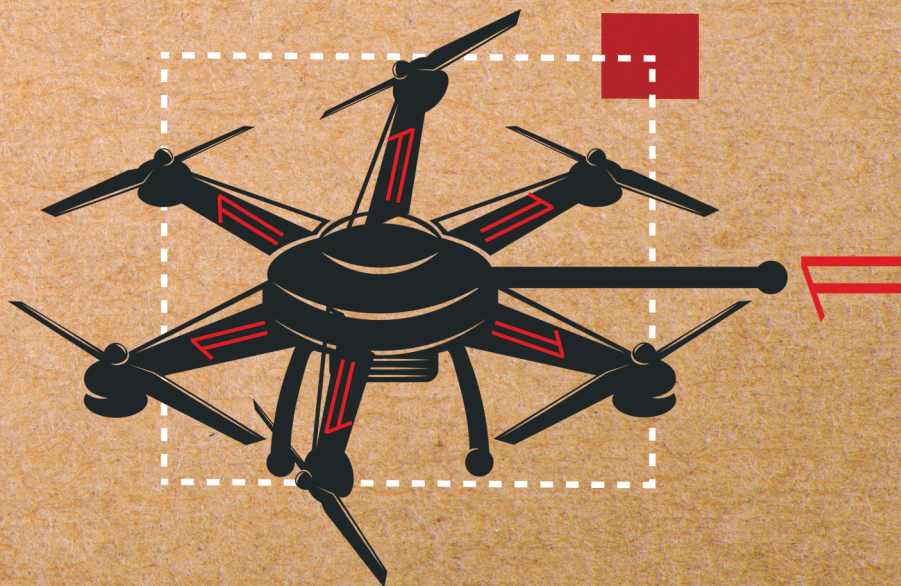
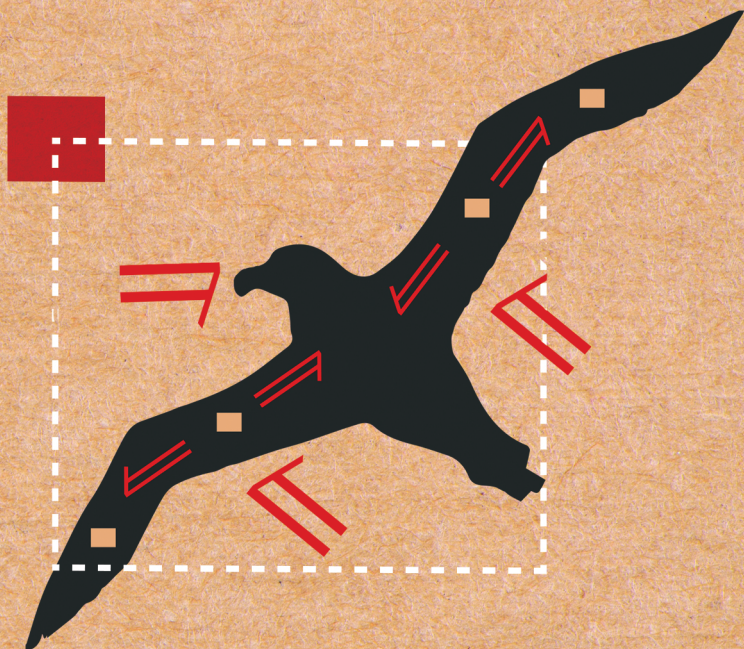


ENERGY-BASED MODELING AND CONTROL OF INTERACTIVE AERIAL ROBOTS: A GEOMETRIC PORT-HAMILTONIAN APPROACH

RAMY RASHAD



**ENERGY-BASED MODELING AND CONTROL
OF INTERACTIVE AERIAL ROBOTS:
A GEOMETRIC PORT-HAMILTONIAN APPROACH**

RAMY RASHAD

PhD dissertation committee:

Chairman and Secretary:

prof.dr. J.N. Kok University of Twente, NL

Promotor:

prof.dr.ir. S. Stramigioli University of Twente, NL

Co-promotor:

dr.ir. F.P. Schuller University of Twente, NL

Members:

prof.dr. A.J. van der Schaft University of Groningen, NL

prof.dr. B. Maschke University of Lyon, FR

prof.dr.ir. B.J. Geurts University of Twente, NL

dr. A. Franchi University of Twente, NL



This research has been funded by the European Research Council via the PortWings project (Grant 787675) and by the cooperation program “INTERREG Deutschland-Nederland” via the SPECTORS project (Grant 143081).



This research has been conducted at the Robotics and Mechatronics group, Faculty of Electrical Engineering, Mathematics and Computer Science, University of Twente.

**UNIVERSITY
OF TWENTE.**

Publisher: University of Twente
P.O. Box 217, 7500 AE, Enschede, The Netherlands

ISBN: 978-90-365-5113-7

DOI: 10.3990/1.9789036551137

Copyright© 2020, by Ramy Rashad, Enschede, The Netherlands.

Printed by ProefschriftMaken in the Netherlands.

Cover design by Yusuf Emad.

**ENERGY-BASED MODELING AND CONTROL
OF INTERACTIVE AERIAL ROBOTS:
A GEOMETRIC PORT-HAMILTONIAN APPROACH**

DISSERTATION

to obtain
the degree of doctor at the University of Twente,
on the authority of the rector magnificus,
prof. dr. ir. A. Veldkamp,
on account of the decision of the Doctorate Board,
to be publicly defended
on Thursday 21 January 2021 at 14:45

by

Ramy Abdelmonem Mohamed Rashad Hashem

born on 10 February 1991
in Sohag, Egypt.

This dissertation has been approved by:

prof.dr.ir. S. Stramigioli, *Promotor*

dr.ir. F.P. Schuller, *Co-promotor*

Copyright© 2020, by Ramy Rashad, Enschede, The Netherlands. All rights reserved. No parts of this thesis may be reproduced, stored in a retrieval system or transmitted in any form or by any means without permission of the author.

ACKNOWLEDGMENTS

فَتَبَسَّ ضَاحِكًا مِّن قَوْلِهَا وَقَالَ رَبِّ أَوْزِعْنِي أَنْ أَشْكُرَ نِعْمَتَكَ الَّتِي أَنْعَمْتَ عَلَيَّ وَعَلَىٰ وَالِدَيَّ وَأَنْ أَعْمَلَ صَالِحًا تَرْضَاهُ وَأَدْخِلْنِي بِرَحْمَتِكَ فِي عِبَادِكَ الصَّالِحِينَ (النمل ١٩)

So he smiled, amused at her speech, and said, "My Lord, enable me to be grateful for Your favor which You have bestowed upon me and upon my parents and to do righteousness of which You approve. And admit me by Your mercy into Your righteous servants." (*The Ants: 19*)

The first people I want to thank are my beloved mother Nahla and father Abdelmonem. No words can express how much they supported me with their care, effort, and prayers to become the person I am today. I am forever grateful to them and hope that they are proud of their son.

Next in line is my wife Yara, the love of my life and mother of my precious jewels, Hla and Malak. This thesis would have never come to the light if it wasn't for her endless support and unconditional love. During the past four years, I was also supported by my sister Mona, brother Ziad, and my wife's family Amira, Gamal, and Mohamed. I want to thank them from all my heart for their constant care and prayers.

I want to also thank my mentor and supervisor Stefano Stramigioli, who I saw in him what it's like to be a dedicated scientist and caring human. His continuous criticism (which on average does not hurt) was the main force for this thesis to reach its final form. I want to thank Stefano for "every" thing he has done and I hope that one day I become an *epsilon* of the scientist he is.

I would like to thank Frederic Schuller who has contributed to this thesis in numerous ways thanks to his invaluable comments and challenging questions. Being a brilliant mathematician and physicist, he made me realize and appreciate the value of mathematics through our many hours of discussion and his unique teaching style.

I would like to thank the other members of my graduation committee: prof. Arjan van der Schaft, prof. Bernhard Maschke, prof. Bernard Geurts, and dr. Antonio Franchi for their time spent reading my thesis and their feedback on it. In addition, I would like to thank Antonio for the pleasurable discussions we had cooperating together and prof. Gijs Krijnen for chairing my defense.

During my Ph.D. thesis, I was very fortunate to be part of not just one great team, but two! I had the pleasure of working with Federico Califano, Alexander Dijkshoorn, Luuk Groot Koerkamp, Riccardo Snee, and Andrea Brugnoli within the Portwings project, as well as Davide Bicego, Santiago Sanchez-Escalonilla, and Ran Jiao within the SPECTORS project. I enjoyed very much all of our fruitful discussions, coffee breaks, online meetings during the lockdowns, and informal chats. Not to mention the memorable trip with Federico, Alexander and Luuk to the Recess College which has been a great opportunity to spend invaluable time together. I would like to specially thank Alexander for his help writing the Samenvatting and to Federico for the countless hours of technical discussions we had together leading to many results presented in this thesis.

I want to thank all twenty-three B.Sc. and M.Sc. students I had the pleasure to supervise and learn from at the University of Twente. I want to express my special gratitude to Asem Khattab, Jelmer Goerres, and Jelle Zult for their outstanding works that contributed significantly to this thesis.

Then, I would like to say a big thank you to all members of RAM for the enjoyable working environment they provided, the wonderful brainstorming days in Zenderen, and the soaking 2019 sailing day in Friesland. Particularly, I would like to say a special thank you to Jolanda for taking care of the whole group, to Gijs Krijnen who I had the pleasure of co-supervising students with, to Marcel Schwartz, Sander Smits, Henny Kuipers, and Gerben Scholten for their friendly support, to Johan Engelen who has been an extremely supportive guide during my first two years teaching me how proper research should be done, and to Momen Abayazid who has been a great friend and brother helping me out on countless occasions since my very first days of foreignness.

Last but not least, I would like to thank Mohamed E. Abdelaziz who was the reason I started my PhD at RAM, and prof. Ayman El-Badawy who taught me the foundations on which this thesis was built.

SUMMARY

This thesis addresses the modeling and control of interactive aerial robots in the port-Hamiltonian paradigm, covering several research problems in both theory and practice. The interactive aerial robots considered in this work are distinguished by the fact that the interaction with the environment is inherent in the modeling, analysis, and control of such dynamical systems. This class of robots includes multi-rotor vehicles interacting physically with the environment and flapping-wing ornithopters.

The first part of the thesis focuses on aspects of the theoretical framework of the port-Hamiltonian systems paradigm. The wide applicability of the paradigm for modeling and controlling multi-domain physical systems, both finite- and infinite-dimensional, is highlighted by an extensive literature review of over 150 research studies conducted in the past twenty years. Using differential geometric tools and Hamiltonian reduction theorems, port-Hamiltonian models of rigid body motion and ideal fluid flow, both compressible and incompressible, are constructed systematically starting from first principles.

The second part of the thesis focuses on the emerging field of aerial physical interaction. An extensive survey of fully-actuated multi-rotor aerial vehicles is presented which highlights a wide range of suitable designs for developing a flying end-effector capable of physical interacting with the environment. Then, it is shown how this physical interaction can be naturally described in the port-Hamiltonian framework via energy-exchange between the aerial robot and the environment. With this description, a motion/impedance control system is derived via the energy-balancing passivity-based control approach. This controller can be interpreted in the control-by-interconnection approach as a virtual physical system interconnected to the aerial robot. This interpretation allows developing an enhanced energy-aware impedance controller utilizing concepts of energy routing and energy tanks. Finally, in a step towards achieving autonomous aerial physical interaction, the thesis addresses the augmentation of the impedance controller with visual-perception of the environment, leading to a general framework for vision-based interaction of aerial robots.

SAMENVATTING

Dit proefschrift behandelt de modellering en besturing van interactieve vliegende robots in het port-Hamiltoniaanse paradigma, en behandelt verschillende onderzoeksproblemen in zowel de theorie als de praktijk. De interactieve vliegende robots die in dit werk aan bod komen, onderscheiden zich door het feit dat de interactie met de omgeving inherent is aan de modellering, analyse en besturing van dergelijke dynamische systemen. Deze klasse van robots omvat voertuigen met meerdere rotors, die fysiek in contact staan met de omgeving, evenals ornithopters, die vliegen door het klappen van vleugels.

Het eerste deel van het proefschrift richt zich op aspecten van het theoretische kader van het port-Hamiltoniaanse systeem paradigma. De brede toepasbaarheid van het paradigma voor het modelleren en regelen van multidomein fysische systemen, zowel eindig als oneindig-dimensionaal, wordt benadrukt door een uitgebreid literatuuroverzicht van meer dan 150 onderzoeken die in de afgelopen twintig jaar zijn uitgevoerd. Met behulp van differentiaalmeetkundige instrumenten en Hamiltoniaanse reductietheorieën worden systematisch port-Hamiltoniaanse modellen van starre lichaamsbewegingen en ideale vloeistofstroming, zowel samendrukbaar als niet-samendrukbaar, geconstrueerd vanaf de basisprincipes.

Het tweede deel van het proefschrift richt zich op het opkomende veld van de fysieke interactie in vlucht. Er wordt een uitgebreid overzicht gepresenteerd van de volledig aangedreven multi-rotor vliegende voertuigen, waarbij een breed scala aan geschikte ontwerpen voor de ontwikkeling van een vliegende eindeffector, die in staat is tot fysieke interactie met de omgeving, wordt belicht. Vervolgens wordt getoond hoe deze fysieke interactie op natuurlijke wijze kan worden beschreven in het port-Hamiltoniaanse kader via energie-uitwisseling tussen de vliegende robot en de omgeving. Met deze beschrijving wordt een bewegings-/impedantie regelsysteem afgeleid via de energie-balancerende, op passiviteit gebaseerde regeltechniek methode. Deze regelaar kan in de regeling-via-interconnectie aanpak worden geïnterpreteerd als een virtueel fysiek systeem dat verbonden is met de vliegende robot. Deze interpretatie maakt het

mogelijk om een verbeterde energiebewuste impedantie regelaar te ontwikkelen die gebruik maakt van concepten van energierouting en energietanks. Ten slotte, in een stap in de richting van het bereiken van autonome fysieke interactie in vlucht, behandelt het proefschrift de uitbreiding van de impedantie regelaar met visuele perceptie van de omgeving, wat leidt tot een algemeen kader voor op visie gebaseerde interactie van vliegende robots.

CONTENTS

1	Introduction	1
1.1	Unmanned Aerial Vehicles: Now and Then	1
1.1.1	UAVs Then	2
1.1.2	UAVs Now	4
1.2	Emerging Fields of Aerial Robotics	6
1.2.1	Aerial Physical Interaction	6
1.2.2	Bio-Inspired Flapping-Flight	8
1.3	Framework for Interactive Aerial Robots	11
1.3.1	Geometric Port-Hamiltonian Framework	12
1.3.2	Port-Hamiltonian View of a Flying End-Effector	13
1.3.3	Port-Hamiltonian View of a Bio-inspired Robotic Bird .	16
1.4	Research Goals of the Thesis	19
1.4.1	SPECTORS Project	20
1.4.2	PortWings Project	20
1.5	Contributions of the Thesis	21
1.6	Outline of the Thesis	25

I	Theoretical Framework	27
----------	------------------------------	-----------

2	Port-Hamiltonian Framework	29
2.1	Foundations of Port-Hamiltonian Systems	30
2.1.1	Finite-dimensional Systems	30
2.1.2	Infinite-dimensional Systems	36
2.2	Relation to Standard Hamiltonian Theory	39
2.2.1	Extending Poisson Structures	40
2.2.2	Difference in Modeling Philosophy	42
2.3	Hamiltonian Reduction	46
2.4	Conclusion	49

3	Twenty Years of Distributed Port-Hamiltonian Systems	51
3.1	Theoretical Framework	52
3.1.1	Stokes-Dirac Structure Formulation	53
3.1.2	Functional Analytic Formulation	54
3.1.3	Jet Bundle Formulation	55
3.1.4	Theoretical Extensions	56
3.2	Modeling of Distributed Parameter Systems	57
3.2.1	Structural Mechanics	57
3.2.2	Electro-Mechanics	58
3.2.3	Fluid Mechanics	59
3.2.4	Magneto-Hydrodynamics	60
3.2.5	Chemical Processes	60
3.3	Analysis and Control of Distributed Parameter Systems	60
3.3.1	Extension of Control by Interconnection	61
3.3.2	Control Design Based on Spatial Discretization	62
3.3.3	Other Control Methods	62
3.3.4	Interpretation as Boundary Control Systems	63
3.4	Discretization of Distributed Parameter Systems	66
3.5	Conclusion	68
4	Port-Hamiltonian Modeling of Rigid Body Motion	71
4.1	Geometric Formulation of Rigid Body Kinematics	72
4.1.1	Coordinate-free Formulation of the Configuration Space	72
4.1.2	Numerical Representation of the Configuration Space	75
4.1.3	Lie-Group Structure of $SO(3)$	79
4.1.4	Lie-Group Structure of $SE(3)$	84
4.2	Port-Hamiltonian Modeling of a Rigid Body	93
4.2.1	Kinetic Co-energy of a Rigid Body	94
4.2.2	Closed Model of Kinetic Energy	95
4.2.3	Port-based Representation	97
4.2.4	Open Model of Kinetic Energy	99
4.2.5	Open Model of Potential Energy	100
4.2.6	Port-Hamiltonian Dynamics of a Rigid Body	101
4.3	Conclusion	106
5	Port-Hamiltonian Modeling of Fluid Flow	107
5.1	Kinematics of Fluid Motion	110
5.1.1	Configuration Space $\mathcal{D}(M)$	110
5.1.2	Lie Group Structure of $\mathcal{D}(M)$	112
5.1.3	Differential Form Representation of Lie algebra	114
5.1.4	Permeable vs. Impermeable Boundaries	116
5.1.5	Dual Space of Lie Algebra	118
5.2	Kinematics of Advected Quantities	119

5.2.1	Mathematical Description	120
5.2.2	Relation Between Fluid Motion and Advected Quantities	124
5.2.3	Right Representation and Semidirect Product Structure	127
5.3	Port-Hamiltonian Modeling of the Kinetic Energy Subsystem	131
5.3.1	Semidirect Product Reduction Theorem	132
5.3.2	Closed Model of Kinetic Energy	133
5.3.3	Port-based Representation	137
5.3.4	Open Model of Kinetic Energy	139
5.3.5	Change of Coordinates to the Velocity Representation	143
5.4	Port-Hamiltonian Modeling of Compressible Flow	150
5.4.1	Isentropic Compressible Flow	152
5.4.2	Adiabatic Compressible Flow	159
5.5	Port-Hamiltonian Modeling of Incompressible Flow	164
5.6	Conclusion	169
II	Aerial Physical Interaction	171
6	Fully-Actuated UAVs	173
6.1	Mechanical Design of Fully-Actuated UAVs	174
6.1.1	Static Control Wrench Analysis	174
6.1.2	Classification of Multi-rotor UAVs	177
6.2	Survey of Fixed-Tilt Concepts	177
6.3	Survey of Variable-Tilt Concepts	185
6.4	Conclusion	189
7	Energy-Balancing Passivity-Based Control of a Flying End-Effector	191
7.1	Survey of Aerial Interaction Control Methods	193
7.1.1	Hybrid Pose/Wrench and Motion Control	193
7.1.2	Impedance and Admittance Control	194
7.1.3	Port-Hamiltonian Control	195
7.2	Port-Hamiltonian Model of a Flying End-Effector	196
7.2.1	Vehicle Description	196
7.2.2	Dynamic Model	197
7.3	Port-Hamiltonian Control System Design	199
7.3.1	Change of Coordinates	200
7.3.2	Control Objective of EB-PBC	201
7.3.3	Energy Shaping Control Procedure	202
7.3.4	Control Law Derivation	204
7.3.5	Closed Loop System Behavior	207
7.4	Experimental Validation	210
7.4.1	Exp.1: Robust Interaction with Rigid Surface	210

7.4.2	Exp.2: Robust Hovering at Maximum Roll	210
7.5	Conclusion	212
8	Energy-Aware Impedance Control of a Flying End-effector	215
8.1	Control-By-Interconnection Interpretation	217
8.1.1	Flying-end Effector	217
8.1.2	Impedance Controller	219
8.1.3	Passivity Analysis of Closed-loop System	223
8.2	Interaction Wrench Regulation	225
8.2.1	Interaction Wrench Observer	226
8.2.2	Stiffness Modulation	227
8.2.3	Variable-Stiffness Spring	228
8.3	Energy-Aware Impedance Controller	229
8.3.1	Idea of Energy Routing	229
8.3.2	Energy Routing using a Dirac Structure	231
8.3.3	Design of the Energy Tank	232
8.3.4	Passivity Analysis of the Closed-loop System	234
8.4	Conclusion	235
9	Vision-Based Impedance Control of an Aerial Robot	237
9.1	Vision Based Interaction Framework	239
9.1.1	Problem Formulation	239
9.1.2	Proposed Method	240
9.1.3	Curve Projection Algorithm	242
9.1.4	Impedance Controller and Control Allocation	244
9.2	Simulation Results	246
9.2.1	Matlab Results	246
9.2.2	Gazebo Results	247
9.3	Preliminary Experimental Results	249
9.4	Discussion	250
9.5	Conclusion	256
III	Discussion and Conclusions	257
10	Conclusions	259
10.1	Research Findings	259
10.2	Future Work	263
10.3	Final Word	265

CHAPTER 1

INTRODUCTION

The focus of this dissertation is on the field of aerial robotics covering research problems from theory to practice. The paradigm that is used in this work to address the modeling and control of aerial robots is the port-Hamiltonian framework. In this first chapter, the problems tackled and the research questions addressed in this dissertation are formulated and clarified. Moreover, the contributions of this work are highlighted with respect to the state of the art. First, the chapter starts by a short introduction to aerial robotics.

1.1 Unmanned Aerial Vehicles: Now and Then

In this section, a quick glimpse of the history of Unmanned Aerial Vehicles (UAVs) is presented to highlight how they evolved. Within the aerospace jargon, aerial robots are usually referred to as UAVs. The definition of a UAV according to the American Institute of Aeronautics and Astronautics [Nonami et al., 2010] is given as “an aircraft which is designed or modified, not to carry a human pilot and is operated through electronic input initiated by the flight controller or by an onboard autonomous flight management control system that does not require flight controller intervention”. Technically, an aerial robot is a more complex system than a UAV due to the extra perceptual and decision-making capabilities of any robot. However, nowadays most UAVs are equipped with some form of robotic technology whether they are autonomous, semi-autonomous, or remotely-piloted. As a result, the two terms, aerial robot and UAV, are interchangeably used by researchers and practitioners of the field.

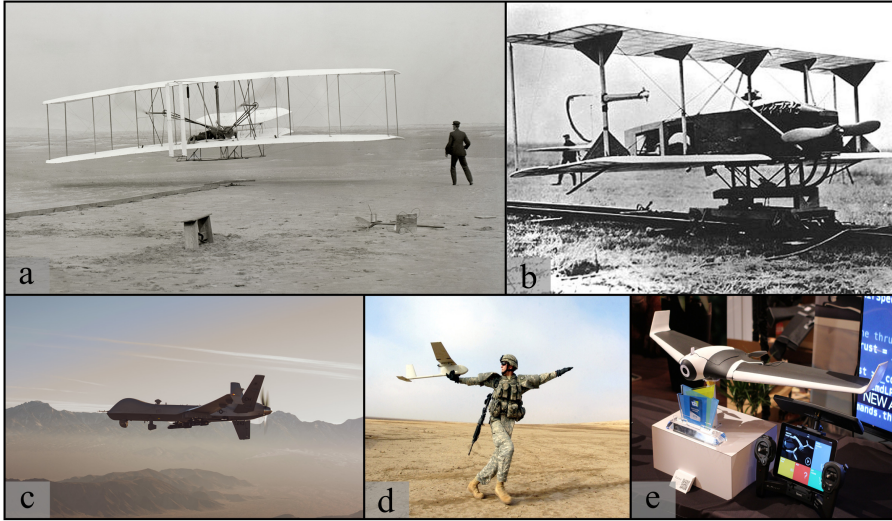


Figure 1.1: Evolution of Fixed Wing UAVs: a. Wright Flyer (Public domain), b. Hewitt-Sperry Automatic Airplane (Public domain), c. MQ-9 Reaper (Credit: U.S. Air Force), d. AeroVironment RQ-11 Raven (Credit: U.S. Army), e. Parrot DISCO drone (CC-BY-2.0).

1.1.1 UAVs Then

What the Wright brothers did on the 17th of December 1903 was a stepping-stone for humanity in its quest to conquer the skies by flying machines of their own creation. A quest that started hundreds of years before with many attempts of human-powered flight mimicking the flapping-behavior of birds. After years full of trial, errors, and crashing bodies, humans converged to the solution of fixed-wing aircrafts for sustained flight and not flapping-wing ones.

Ever since the Wright Flyer (Fig. 1.1.a) flew in 1903, fixed-wing aircrafts have evolved at a tremendous rate motivated, unfortunately, by its hostile capabilities. Only 11 years were enough for powered-aircrafts to become an important branch of the armed forces in World War I. Although, aircrafts were used initially for reconnaissance only, by the end of the war armed air-forces included fighter and bomber aircrafts as well.

The capabilities of aerial vehicles have triggered a massive amount of military funds to be allocated for the development of the technology which in turn accelerated the evolution of fixed-wing aircrafts. Such funds have allowed the increase of the maximum speed of these vehicles from 80 km/h in the beginning of the war in 1914 to 240 km/h at the end of the war in 1918 [Munson, 1969]. It is also remarkable that during this early development stage, the first

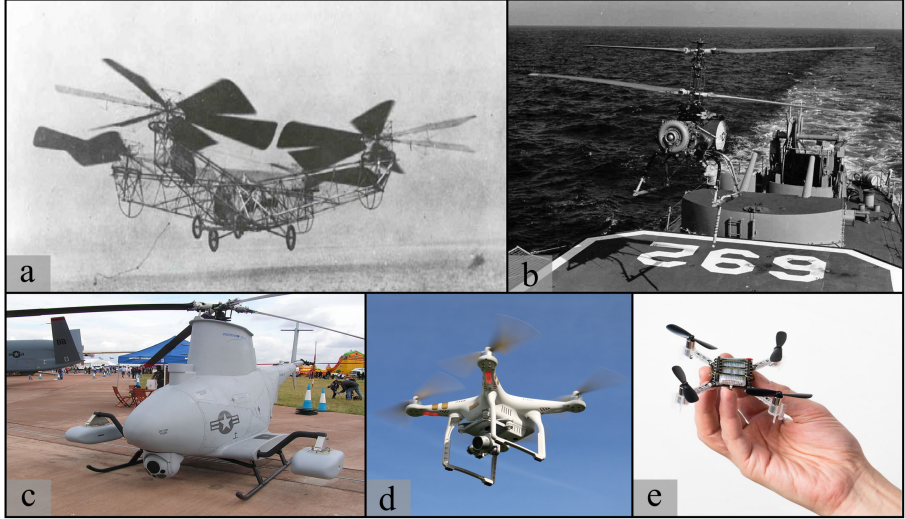


Figure 1.2: Evolution of Rotary Wing UAVs: a. De Bothezat Helicopter (Public domain), b. Gyrodyne QH-50 DASH (Public domain), c. MQ-8 Fire Scout (CC BY-SA 2.5 nl), d. DJI Phantom 3 (Credit: Flickr/Andri Koolme), e. Crazyflie 2.1 (Public domain)

autopilot-controlled UAV (Fig. 1.1.b), designed by P.C. Hewitt and E. Sperry, made its first successful flight on the 12th of September 1917 [Valavanis and Vachtsevanos, 2015].

Most development efforts were concentrated initially on fixed-wing aerial vehicles, which were the most suited for military purposes due to their high endurance and long-range capabilities. However, there were many appealing features in such vehicles such as vertical take-off and landing (VTOL), flying at low altitudes, and hovering. This led to the advent of rotary-wing or multirotor aerial vehicles. The first successful flight of a quad-rotor aircraft took place in the early 1920s by the de Bothezat helicopter (Fig. 1.2.a). Thirty-nine years later, the first unmanned helicopter developed was the QH-50 DASH (Fig. 1.2.b), which demonstrated its first flight in 1959 [Valavanis and Vachtsevanos, 2015].

The military development of fixed-wing and rotary-wing aerial vehicles, both manned and unmanned, continued for decades. Such development yielded a vast variety of designs at many scales. Moreover, the mathematical understanding of the flight dynamics and control of such vehicles evolved greatly in the process.

On the other hand, the development of flapping-wing aerial vehicles (aka

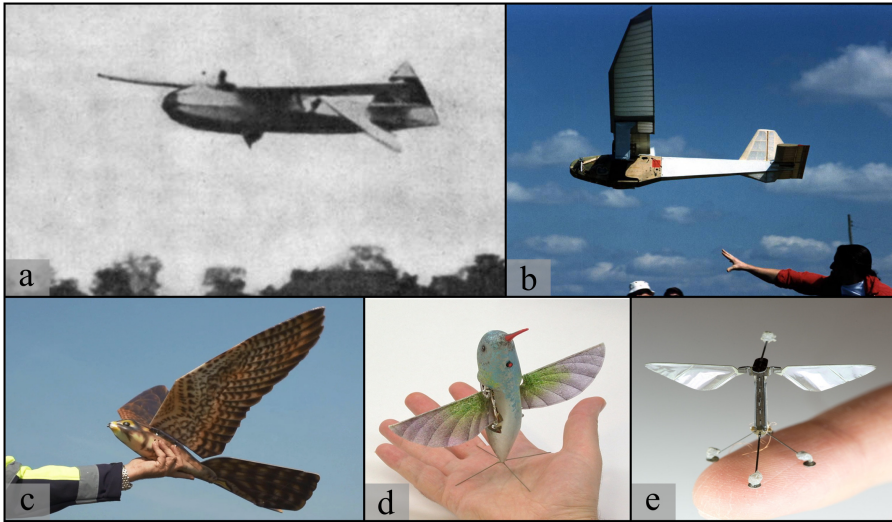


Figure 1.3: Evolution of Flapping Wing UAVs: a. Schmid 1942 Ornithopter (Public domain), b. Mr. Bill’s first launch (Credit: Project Ornithopter), c. Robird (Credit: Clear Flight Solutions), d. AeroVironment Nano Hummingbird (Public domain photo), e. RoboBee (Credit: Wyss Institute at Harvard University)

ornithopters) was overshadowed by the success of fixed-wing and multirotor vehicles. Thus, flapping-wing aerial vehicles were abandoned for many years and considered a futureless technology due to its high complexity [Goodheart, 2011]. However, the old dream of “flying like the birds” motivated a few individual visionaries to unlock the secrets of the flight dynamics of birds and build flapping-wing aerial vehicles, but at a much slower pace compared to fixed-wing and multirotor vehicles. The first human-powered flapping-wing vehicle successfully flew in 1929 as a result of the work of A. Lippish. Seventeen years later, in 1946, the first engine-powered flapping-flight was achieved by A. Schmid (Fig. 1.3.a). Then after another forty-five years, the first successful engine-powered small-scale flapping-wing UAV, known as “Mr. Bill” (Fig. 1.3.b), was designed in September 1991 [Goodheart, 2011].

1.1.2 UAVs Now

Nowadays UAVs have come a very long way in becoming smaller, cheaper, smarter, and closer to people. The advancements in the fields of miniaturized sensors, microprocessors, electric drives, and batteries have allowed the down-scaling of UAVs to a great extent and simultaneously with lower costs. More-

over, the advancement in robotic technologies have allowed the development of advanced UAVs with perception, planning, and decision-making capabilities, that allowed them to accomplish complicated tasks autonomously. The combination of UAVs and robotic technologies gave rise to the field of *aerial robotics*.

The small scale and low cost of current aerial robots have been primary factors that enabled aerial robots to gain unprecedented notability in the civilian market. Historically military applications have been the main driving force for the development of UAV technologies. However, nowadays the market share of civil applications is increasing at a very high pace. According to Finnegan [2019], the commercial unmanned aerial systems (which includes UAVs and their auxiliary equipment) market is expected to increase from \$5 billion in 2019 to \$14.5 billion in 2028. In addition, UAVs are allowing for commercial services and solutions that are estimated to potentially have a market value of over \$127 billion [Mazur and Wiśniewski, 2016]. These market predictions, and others, imply that civilian applications are becoming an equally important driving force, if not more, for the development of UAV technologies.

Multi-rotor aerial robots have gained more popularity in civilian applications as well as academic research compared to fixed-wing ones. This can be contributed to their lower cost, versatility, portability and most importantly its hovering and VTOL capabilities. With the wide variety of sensors that could be mounted onboard, aerial robots enabled many companies to offer cost-effective solutions for various civilian applications such as surveillance, visual inspection, aerial photography, search and rescue, mapping, entertainment, and law enforcement, just to mention a few.

In recent years, there has been also an increasing interest in small-scale flapping-wing UAVs in academic research groups and civilian companies. One factor that helped revive interest in this class of aerial vehicles was their aerodynamic properties at very small scales. The efficient operation of these vehicles at low Reynolds numbers has motivated the development of insect-like micro UAVs such as the RobobBee [Jafferis et al., 2019] as well as hummingbird-like UAVs such as the AeroVironment Nano Hummingbird [Keennon et al., 2012], shown in Fig. 1.3. The natural appearance of bird-like aerial robots, such as the Robird [Folkertsma et al., 2017], has also found a niche market in the civilian sector to be used as a deterrent for real birds at airports, harbors, and waste management facilities. Successful companies that utilized such unique feature of flapping-wing robots include The Drone Bird Company¹ (formerly Clear Flight Solutions) and AERIUM Analytics².

¹<https://www.thedronebird.com>

²<https://www.aeriumanalytics.com>

1.2 Emerging Fields of Aerial Robotics

The field of aerial robotics is an interdisciplinary field that is evolving and progressing at an increasing rate. As a result there exists a wide range of emerging research directions nowadays that could be hardly classified or counted. Out of the tremendous number of different emerging fields of research, the work in this thesis focuses on two fields: aerial physical interaction and bio-inspired flapping-flight. In what follows, a brief introduction to these fields is presented and the challenges in these emerging topics are identified. These challenges serve as the motivation for the research conducted in this thesis.

1.2.1 Aerial Physical Interaction

In recent years there has been an exploding interest in extending the current applications of multirotor UAVs to those that require aerial physical interaction. Most of the currently successful applications of multirotor UAVs, mentioned above, are exploiting UAVs as flying sensors, in the sense that are used to only observe the environment and sense it remotely. However, there have been many research efforts to enable UAVs to physically interact with their environment, and thus acts as flying manipulators instead of flying sensors.

With this new class of aerial robots capable of manipulating and interacting physically with their environment, the potential applications are numerous. The most appealing one is the contact-based inspection and maintenance of hard-to-reach sites e.g. wind turbines, power-lines, or oil/gas pipelines. Other applications include the assembly of structures, the management of construction and demolition wastes, collaborating and assisting humans in domestic and industrial regions, and many more new application that are waiting to be discovered.

The aforementioned potential applications have enticed many research groups and civilian companies to advance the field of aerial physical interaction. Consequently, many synergies have been established worldwide in the past years with the aim of creating flying manipulators. Table 1.1 presents a partial list of such international projects within the European Union alone.

There are two common approaches in the literature for realizing a flying-manipulator. The first approach is to endow a conventional UAV with a robotic manipulator arm as shown in Figs. 1.4.a-c. Although the multi-degrees of freedom of the manipulator allow for high dexterous manipulation, these systems suffer from several drawbacks like inertial coupling, variable center of mass, no exertion of lateral forces, in addition to the limited payload, and force exertion. The second approach for aerial manipulation is the use of fully-actuated UAVs that have non-parallel propellers allowing for controlling all six degrees of freedom of the aerial robot. In this physical interaction paradigm, the UAV itself is considered as a **flying end-effector** which can interact with its environment

Table 1.1: Scientific Research Projects in the European Union with the aim of aerial physical interaction.

	Start Date	End Date	Website
AIROBOTS	Feb 2010	Jan 2013	http://www.airobots.dei.unibo.it
ARCAS	Nov 2011	Nov 2015	http://www.arcas-project.eu
AEROWORKS	Jan 2015	Dec 2017	http://www.aeroworks2020.eu
AEROARMS	Jun 2015	Aug 2019	https://www.aeroarms-project.eu
AEROBI	Dec 2015	Nov 2018	https://www.aerobi.eu
SPECTORS	Dec 2016	Dec 2020	https://www.spectors.eu
HYFLIERS	Jan 2018	Dec 2021	https://www.oulu.fi/hyfliers
AERIAL-CORE	Dec 2019	Nov 2023	https://www.aerial-core.eu

[Ryll et al., 2019]. Although a flying end-effector is mechanically simpler, more robust, and capable of applying lateral forces, it suffers from lower efficiency and thus lower operation time. Examples of some state of the art fully-actuated platforms are shown in Figs. 1.4.d-e. In this thesis, we focus mainly on aerial physical interaction using the flying end-effector approach.

This new field of aerial physical interaction adds a number of challenges in the design, control, and analysis of such aerial robots, compared to the conventional aerial robots and ground-based manipulators. The first challenge is that a flying manipulator does not benefit from ground reaction forces as is the case for ground-based manipulators. As a result, the aerial robot continuously uses its propellers' control thrusts to react the wrench (combined forces and torques) arising during contact with the environment. At the same time, the aerial robot should overcome the gravitational forces to remain airborne.

The second challenge is that a flying manipulator needs information about the interaction wrench. One solution is to equip the aerial robot with a force/torque sensor. Although such solution is very reliable, it only provides measurement of the interaction wrench at a single predefined contact point on the robot. Moreover, the addition of such sensors increases the cost and weight of the robot. A second solution would be to use an observer to estimate the interaction wrench based on a mathematical model of the robot's dynamics. Although such solution does not add to the weight/cost of the robot and can estimate the interaction wrench at any point, the estimated interaction wrench will be corrupted by aerodynamic disturbances and uncertainties in the robot's model.

Another challenge, specific for a flying end-effector, is the number and configuration of the rotors. Unlike the conventional under-actuated multirotor UAVs, a fully-actuated UAV has propellers that are not parallel and not in the same plane. The optimal configuration for the rotors depends on the application through a compromise between efficiency and the generation of lateral forces.



Figure 1.4: State of the art flying-manipulator platforms. a. ARCAS UAV with manipulator [Ruggiero et al., 2018], b. AEROARMS UAV with dual-arm manipulator [Ruggiero et al., 2018], c. DLR Suspended Aerial Manipulator [Bicego, 2019], d. AEROARMS hexarotor robot [Bicego, 2019], e. AEROARMS octarotor robot [Ollero et al., 2018]

The fourth, and most important, challenge is that a successful operation of a flying manipulator requires the stability of the robots not only in free-flight but also in contact with the environment. Once the robot is in contact with the environment, the stability of the overall system depends on the dynamics of the aerial robot's physics, its controller as well as the environment. Since the aerial robot is expected to interact with an unknown environment, the same stability analysis techniques used for conventional aerial robots cannot be used directly for a flying manipulator.

Although there are many research teams and individuals addressing the aforementioned challenges and more, there are many open problems and abundant room for further progress and advancements.

1.2.2 Bio-Inspired Flapping-Flight

The ever-expanding range of potential new applications of aerial robots calls for novel solutions to the existing challenges in the field. Many civilian applications require a power-efficient aerial robot capable of low speed flight with high maneuverability as well as the ability to VTOL and hover. Such aerial robots are required in these applications to fly in urban unstructured environments near humans, maneuver in cluttered restricted locations, and have sufficient flight time to fulfill as many tasks as possible.

Flapping-wing aerial robots possess numerous capabilities that make them viable candidates for many potential new applications. Although the most popular choice of UAV design in currently successful civilian applications is the multirotor UAV, such vehicles have a number of fundamental limitations that could be resolved in flapping-wing UAVs.

First, multirotor UAVs are not safe near humans due to their high-speed rotating propellers. Second, although they are well capable of maneuvering in constrained places, the rigidity of the rotating propellers makes them very sensitive to any contact with the environment. One solution for these two limitations is the usage of protective caging for the whole UAV, as in [Brescianini and D’Andrea, 2018], or for the propellers, as in [Staub et al., 2018]. However, such solution limits greatly the payload of the robot, its maximum allowable interaction wrench, and its flight. Third, due to the usage of multiple rotors, such UAVs consume very high power. Specially, fully-actuated multirotor vehicles consume even more power, compared to conventional underactuated ones, due to their non-parallel rotor configurations.

On the other hand, flapping-wings are usually flexible and low weight which makes them safe to be near humans, robust to contact with the environment, and capable of flying in cluttered spaces. Moreover, flapping-wings allow for both long-range sustained flight and almost vertical take-off and landing, which combines two appealing features of fixed-wing and rotary-wing UAVs. In addition, flapping-flight is more power efficient than using propellers, which implies more flight time for the same battery capacity. Another unique feature of flapping-wing aerial robots is the low aero-acoustic signature of such vehicles. Such property makes them more suitable for operations near humans and in indoor applications. However, the main drawback of realizing such flapping-wing aerial vehicles is the increased complexity of their mechanical design, aerodynamics and flight dynamics.

A rich source of inspiration to address the challenges of realizing flapping-wing UAVs is present in natural flyers such as birds, bats, and insects. These biological creatures showcase effective and optimized solutions to not only flapping-based locomotion, but also to sensing and navigation. Consequently, there is an emerging field of bio-inspired solutions in the robotics community, both aerial and ground robots. Examples of such solutions are bird-inspired perching [Doyle et al., 2011], bat-inspired echolocation [Eliakim et al., 2018], bio-inspired artificial intelligence [Wang et al., 2012], animal-inspired geomagnetic navigation [Liu et al., 2013], and pigeon-like flapping-wing mechanisms [Chang et al., 2020]. In this thesis, we are mainly interested in bio-inspired flapping locomotion, and more specifically **bird-inspired flapping flight**.

The understanding of the aerodynamical, structural, and behavioral patterns of natural birds is essential for the development of robust and high performance flapping-wing aerial robots. However, this is not an easy task! Despite

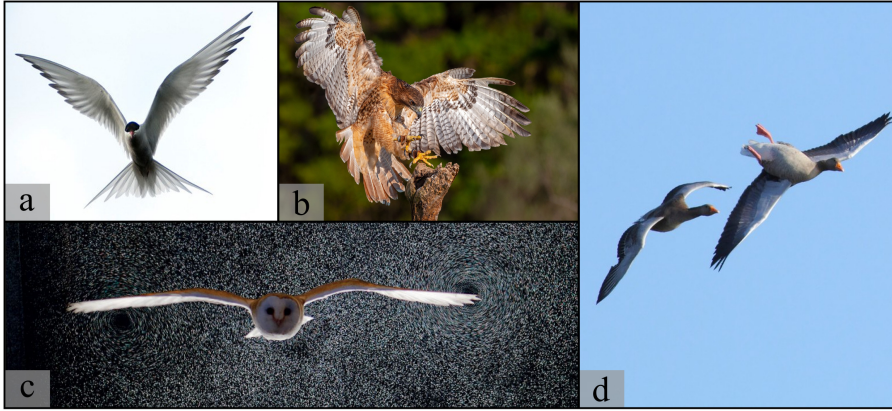


Figure 1.5: Capabilities of Natural Flyers: a. Arctic Tern (Credit: National Park Service/Kent Miller) , b. A falconer's red-tailed hawk landing (CC BY-SA 4.0) , c. Air motions caused by gliding barn owl visualized with bubbles [Usherwood et al., 2020] , d. Whiffling Geese (Credit: Arran Birding)

the many research efforts throughout the past decades, the flight dynamics of natural flyers are still not full understood [Floreano et al., 2009], especially that of bats and birds [Chin and Lentink, 2016].

Natural birds have a number of outstanding features (*cf.* Fig. 1.5) in their locomotion that are challenging to understand [Shyy et al., 2009]. For example (i) they exploit multiple aerodynamic mechanisms for the generation and enhancement of lift and thrust, (ii) they accommodate wind gusts and avoid obstacles via variable kinematic and dynamic patterns using their wings, tail, and body, (iii) they actively change the structural compliance of their wings to achieve wing deformations that improve aerodynamic performance, and (iv) they have distributed actuation and sensing biological units all over their surface that are utilized for flight stability in extreme environment regimes.

Understanding the aforementioned features of natural birds necessitates comprehending their highly unsteady three-dimensional aerodynamics, transition in boundary and shear layers, bilateral fluid-structure interactions, dynamic wing morphologies, and highly nonlinear flight dynamics [Shyy et al., 2009]. After understanding these biological creatures, the following step would be to abstract specific desired features and engineer them into aerial robots, a task that is as complicated as the former. Therefore, in this thesis, the focus is only on decoding and understanding the secrets of bio-inspired flapping flight.

In very recent years there have been a number of scientific projects in the EU

aimed at tackling this field of bio-inspired flapping flight such as GRIFFIN³ and PORTWINGS⁴, which are both European Research Council (ERC) advanced grants taking place from 2018 to 2023. Nevertheless, this interdisciplinary field of understanding flapping-flight and designing flapping-wing aerial robots is extremely fertile with discoveries and scientific achievements, and it will take many more years and research efforts for such field to mature.

1.3 Framework for Interactive Aerial Robots

As mentioned previously, the scope of the work in this thesis focuses on two types of emerging fields in aerial robotics, namely aerial physical interaction and bio-inspired flapping flight. In these two fields, the focus is specifically on two types of aerial robots, a flying end-effector and a bio-inspired robotic bird. While the work in this thesis covers both theoretical and practical aspects of the flying end-effector, the work on the bio-inspired robotic bird is only limited to the theoretical understanding of flapping-flight as a prerequisite for the physical realization of such complicated robot.

Although there are many discrepancies between these two types of aerial robots, viewed as dynamical systems, there exists one substantial common feature that shall be exploited in this thesis. This common feature is that interaction with the environment is fundamental for their purpose and operation. Such aerial robots will be referred to in this work as **interactive aerial robots**.

From a physical point of view, any type of mobile robot interacts with its environment for locomotion, whether it is a ground, underwater, or aerial robot. However, what distinguishes *interactive aerial robots* is that, from a system theoretic point of view, the interaction with the environment is an essential ingredient in the study and control of these robots and is not a “source of disturbances” that need to be rejected by the control system.

As a definition, we say that two systems interact with each other if the behavior of one is influenced by the behavior of the other. For the case of a flying end-effector, its primary purpose is to interact mechanically with the environment, in addition to flying. While in the case of a robotic-bird, its main mechanism for generating upward and forward forces (i.e. lift and thrust) is flapping its wings and changing their morphology. The generated forces are a result of highly coupled fluid-structure interaction between the flexible wings of the bird, as one dynamical system, and the air flow around it, as another separate dynamical system. Therefore, for both aerial robots, it is important to consider and understand the bilateral interaction with environment in the framework used to address these dynamical systems.

³<https://griffin-erc-advanced-grant.eu>

⁴<http://www.portwings.eu>

In what follows we show how the geometric port-Hamiltonian framework is well suited for the modeling, analysis and control of interactive aerial robots. This suitability is the primary motivation for the majority of the work presented in this dissertation. After a brief introduction to the geometric port-Hamiltonian framework and its main features related to this work, we present an overview of how a flying-end effector and a robotic-bird are viewed in this framework.

1.3.1 Geometric Port-Hamiltonian Framework

The geometric port-Hamiltonian framework [Maschke and van der Schaft, 1992] is based on two paradigms as the name suggests: the “port-based” framework and the “Hamiltonian” framework. The port-Hamiltonian framework builds upon the port-based modeling paradigm introduced by H. Paynter in the Bond-Graph formalism [Montbrun-Di Filippo et al., 1991] and describes a complex system as the interconnection of simpler sub-atomic units. Moreover, the port-Hamiltonian framework builds upon the geometric Hamiltonian formalism of mechanics [Marsden and Ratiu, 1999] by explicating the role of the energy of the system and the geometry of the state space in the process of modeling and analyzing a physical system.

At the heart of the port-Hamiltonian framework is the thermodynamical concept of energy, which is a fundamental concept unifying many branches of physics. An interaction between two systems is characterized by the energy exchanged between them in the port-Hamiltonian framework. This interaction takes place through what is called a *power port*. Each power port consists of two dual variables, called an *effort* and *flow*, whose pairing (product) gives the power flowing between the two interacting systems.

The main features of the port-Hamiltonian modeling process of a complex physical system is that (i) it models the overall system as a collection of smaller open subsystems interconnected via power-ports. (ii) The model separates the overall network interconnection structure of the system describing how power flows through it from the constitutive relations of its subsystems. (iii) The model emphasizes and classifies its subsystems based on their energetic behavior into energy-storing, energy-dissipating, energy-suppliers, or energy-routing units.

Another important feature of port-Hamiltonian models is that they are *acausal*, in the sense that each subsystem contains only the constitutive relations describing how its variables evolve dynamically without imposing which is an input and which is an output. This appealing feature makes the port-Hamiltonian framework suitable for *open dynamical systems* that can be interconnected to one another, in contrast to the block diagram approach which lacks compositionality [Duindam et al., 2009].

An important pillar of the geometric port-Hamiltonian framework, that is

highly utilized in this thesis, is differential geometry. Differential geometry is a mathematical formalism that allows describing dynamical systems in a coordinate-free manner. Such intrinsic description allows the separation of the physical characteristics of a dynamical system from details and artifacts available in a specific choice of coordinates. An example of such artifacts in the field of aerial robotics is the gimbal-lock problem of Euler angles and the double-covering problem of quaternions that appear when representing the orientation of rigid bodies [Selig, 2004]. The coordinate-free description of systems in the port-Hamiltonian framework is one of the essential ingredients that allow the framework to incorporate both lumped-parameter (finite-dimensional) and distributed-parameter (infinite-dimensional) systems.

In addition to the systematic procedure for modeling, the port-Hamiltonian framework also allows for a systematic procedure for analyzing and controlling a complex physical system. The system's interconnection structure and its total energy (i.e. Hamiltonian) are utilized for the study of the system properties and the design of controllers [Ortega et al., 2001]. Such systematic procedure allows the analysis and control of both lumped- and distributed-parameter systems using the same fundamental concepts.

One distinguishing feature of the port-Hamiltonian control approach is that the control system can be perceived as another virtual physical system interconnected to the actual system via power ports [Stramigioli, 2001]. The advantages of such physical interpretation of a controller are numerous. First, the interconnection of port-Hamiltonian systems is again a port-Hamiltonian system [Cervera et al., 2007]. Such powerful property allows assessing the properties (e.g. passivity) of the closed loop system by properties of its comprising smaller subsystems. Second, such interpretation may suggest simple and robust solutions for control based on how energy should flow, which led to novel concepts in the literature such as impedance control [Hogan, 1985c,b,a], energy routing and energy tanks [Duindam and Stramigioli, 2004]. Third, the change in behavior introduced by the controller could also be implemented partially by modifying the physical properties of the actual system. If possible, such physical implementation of the controller might reduce the number of sensors and actuators which could lead to more energy-efficient systems, which is a fundamental requirement in the field of aerial robotics.

1.3.2 Port-Hamiltonian View of a Flying End-Effector

In the port-Hamiltonian framework, a flying end effector is modeled as the interconnection of three main subsystems, as shown in Fig. 1.6: the robot's physical system, the controller's virtual system, and the environment. The aerial robot's model has two main multidimensional power ports: a mechanical port representing the energy exchange between the robot and the (unknown) environment which the robot is physically interacting with, and an electrical

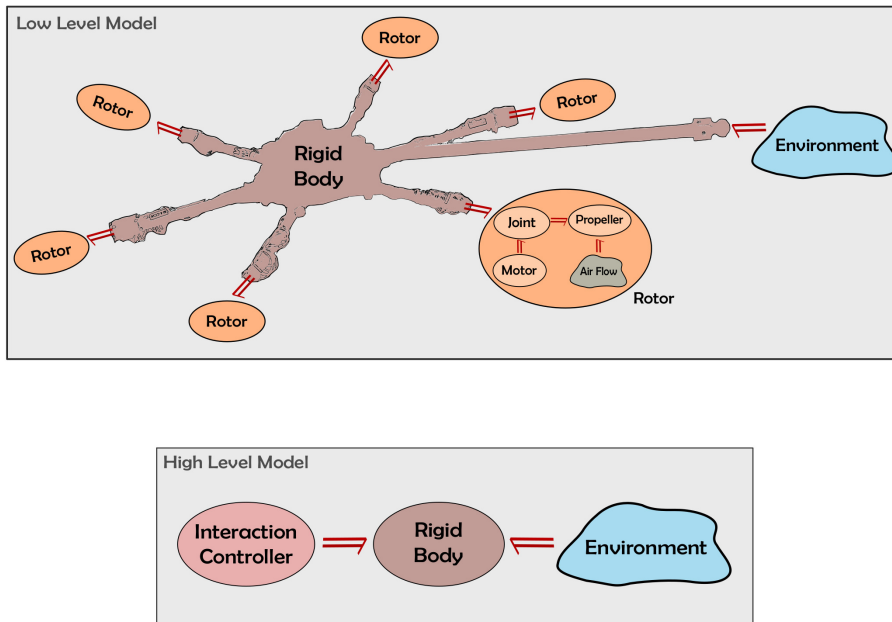


Figure 1.6: Port-Hamiltonian View of a Flying End-Effector as the interconnection of several dynamical systems. Figure shows a fully-actuated hexarotor robot (top), a low level detailed model of the robot (middle), and a high-level model used for control (bottom).

port representing the energy exchange of the control system which is interacting with the electric actuators of the robot to modify its behavior.

As for many other kinds of robots, it is common to treat a flying robot as a multi-body system consisting of a set of bodies linked together via joints that could be either passive or active. For a flying end-effector, the robot's model consists of a single rigid body that is connected to a number of propellers via revolute joints activated by electric motors. The port-Hamiltonian models of the robot's main rigid body and its propellers describe how kinetic and gravitational potential energy evolve. The interaction between each propeller as it rotates and the surrounding air generates the aerodynamic forces that allows the robot to fly. By controlling the electric energy supplied to the electric motors, the aerodynamic forces can be altered such that the robot flies in a desired manner.

For control purposes, it is a common approach to neglect the electric and mechanical dynamics of the UAV's propellers. This is because such dynamics change at a faster time scale compared to the dynamics of the robot's rigid body. Moreover, the interaction between the propellers and the air is usually not modeled and replaced by system identification techniques identifying the relation between a propeller's thrust and rotation speed, or by closed loop speed controllers. Therefore, the high level model shown in Fig. 1.6 is usually sufficient for designing the control system, while the low level model is more realistic and useful for simulation purposes. The aforementioned assumptions are usually valid in the small scale of UAVs considered for academic research and civilian applications.

The control design process of a flying manipulator is fundamentally different than that of a conventional aerial robot used as a flying sensor. For a flying manipulator in general, and a flying end-effector in particular, the port-Hamiltonian framework is a suitable paradigm for the modeling, analysis and control of such systems.

The primary control objective for conventional multirotor UAVs is to achieve stability in free-flight and to reject external disturbances in order to maximize performance. However, for a flying end-effector, in addition to free-flight stability, it should be able to interact with an unknown environment in a stable manner. When the flying end-effector is physically interacting with its environment, the closed loop dynamics of the overall system changes, from a system theoretic perspective. This change in dynamics is unknown in general and could also be discontinuous in a dynamic interaction scenario when contact/non-contact situations occur. Therefore, during contact the environment should be a part of any stability analysis conducted.

In the traditional framework of analyzing the closed-loop dynamical system as an isolated *closed system*, certain assumptions are made to incorporate a model of the environment such as using linear springs and dampers. How-

ever, such unrealistic and simplistic models only guarantee contact stability for very specific and limited types of real environments. On the contrary, the port-Hamiltonian framework models the flying end-effector as an *open system* that can be interconnected to any environment via a power port. By designing controllers that guarantee that the closed loop system fulfills certain requirements as seen from this environment port, the contact stability can be asserted independent of any environment model [Stramigioli, 2015].

Moreover, the traditional framework of modeling a dynamical system using block diagrams, based on unilateral signals, is not suitable for modeling and control of a flying end-effector. In free-flight operation, the output signal of the robot is considered as its pose (i.e. combined position and orientation) which is regulated by a pose controller, whereas in contact operation, the pose of the robot can no longer be controlled as it is constrained by the environment. Moreover, if an additional wrench controller is used to regulate the interaction wrench between the robot and the environment during contact, such wrench can no longer be regulated once the robot loses contact and is in a free-flight situation.

As described in Stramigioli [2001] using the behavioral framework, controlling either the pose or wrench requires perfect knowledge of the environment and when contact occurs or not, which is clearly not possible for practical interactive robots. Instead, the behavior of the controlled robot could be modified independent of the environment. The first one to address this issue in the field of robotics was Neville Hogan in his seminal work [Hogan, 1985c,b,a], which led to the widely used *impedance control* methodology. The port-based framework was an essential ingredient that Hogan used to formalize this control methodology, and in the author's point of view, impedance control can only be understood using the port-based and port-Hamiltonian framework.

Therefore, the aforementioned reasons justify why the port-Hamiltonian framework is the chosen paradigm to model, study, and control a flying end-effector in this thesis.

1.3.3 Port-Hamiltonian View of a Bio-inspired Robotic Bird

In the port-Hamiltonian framework, a flapping bird, viewed as a dynamical system, is abstractly modeled as a number of interconnected subsystems, as shown in Fig. 1.7. First, the main hull of the bird is modeled as a single rigid body interconnected to two wings via joints and power ports. Second, the two wings could be viewed as two flexible bodies with distributed stiffness and mass corresponding to the different components of the biological wing such as bones, muscles, and feathers. Moreover, along the wings are distributed actuators to model mechanisms that birds utilize to actively deform their wings, as well as distributed sensors to model mechanisms that birds for example use

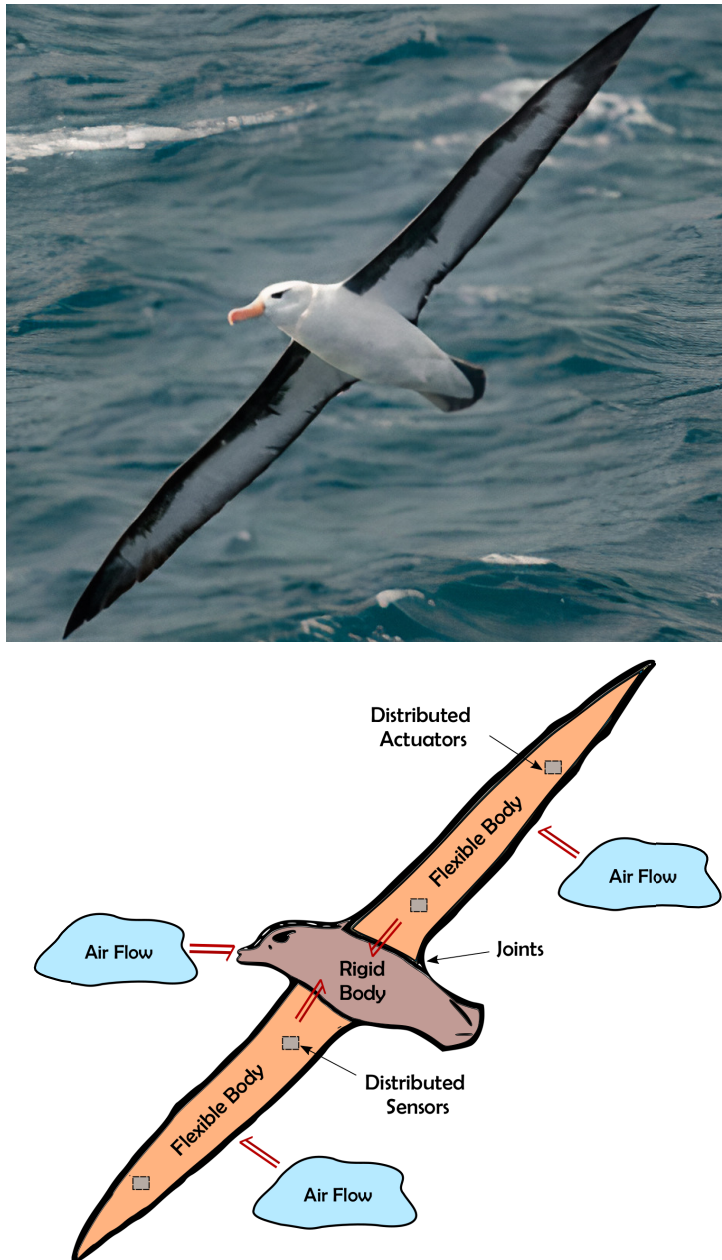


Figure 1.7: Port-Hamiltonian View of a Bio-inspired Robotic Bird viewed as the interconnection of several dynamical systems. Figure shows a flying albatross (top) and a detailed abstract model of a flying bird/robot.

to sense air flow. Third, both the bird's rigid body and flexible wing models are interconnected to another subsystem that represents the dynamics of the air flow. This interconnection and energy exchanged between the different subsystems are characterized by power ports.

In the case of a robotic bird, the overall port-Hamiltonian model would include additional subsystems (not shown in figure) such as the control system interacting, via an electrical port, with the robot's flapping mechanism and distributed actuators engineered to deform the wings or change its stiffness.

The port-Hamiltonian framework has a number of significant features that make it possible to model and decompose bird's flapping flight into the set of smaller subsystems described above. First, the subsystems shown in Fig. 1.7 are a combination of finite- and infinite-dimensional systems. In particular, the rigid body model is a finite-dimensional system represented by ordinary differential equations, whereas the airflow and flexible body models are infinite-dimensional systems represented by partial differential equations. Thanks to its geometric global and unified formulation, the port-Hamiltonian framework can incorporate both finite and infinite dimensional systems. Such capability has been demonstrated for example in modeling robotic manipulators with both rigid and flexible links [Macchelli et al., 2009].

Second, to properly describe in a model the flapping-flight of birds, essential aerodynamic phenomena that need to be considered are viscosity of the airflow and the generation of vortices [Chin and Lentink, 2016]. Consequently, linear or ideal assumptions cannot be made in the mathematical modeling of airflow and the full Navier-Stokes equations have to be used, which makes the airflow model a nonlinear and dissipative dynamical system. Although the traditional Hamiltonian framework, based on Poisson structures, can handle nonlinear infinite-dimensional systems, it is only limited to conservative dynamical systems. On the contrary, the port-Hamiltonian framework overcomes this limitation by exploiting Dirac structures that allow handling complex dissipative systems. Therefore, the Navier-Stokes equations can be described fully in the port-Hamiltonian framework.

Third, to describe a fluid dynamical system or flexible structural system as open systems, that could be interconnected to other systems, the variable (spatial) boundary conditions need to be incorporated. A major limitation of the traditional Hamiltonian treatment of such infinite-dimensional systems is that it handles only boundary conditions that cause zero-power exchange through the boundary [van der Schaft and Maschke, 2002]. Thus, it only allows modeling systems that are isolated and not part of a bigger dynamical system. On the other hand, the port-Hamiltonian framework allows for non-zero power exchange through the boundary and variable boundary conditions, e.g. as demonstrated in the modeling of elastic beam theory in Macchelli et al. [2007a].

Fourth, the port-Hamiltonian framework is capable of incorporating multi-

domain physical systems since it is based on energy-conservation principles. As a result, the same mathematical representations and concepts can be used for the different physical domains available in the model of flapping-flight i.e. structural mechanics and fluid mechanics. In addition, such property is also useful for the modeling of the distributed sensors and actuators that will include the electromagnetic domain as well. Such property has been demonstrated previously in the modeling of complex multi-physical system such as thermo-magento-hydrodynamics [Vu et al., 2016] with coupled fluid mechanical, electromagnetic, and thermodynamic components.

In conclusion, the different properties of the port-Hamiltonian paradigm mentioned above clearly showcase its suitability for the problem at hand and motivates why it is chosen in this thesis to model and study the flapping-flight of birds.

1.4 Research Goals of the Thesis

The primary goal of the research in this thesis is to apply the port-Hamiltonian framework to specific problems related to interactive aerial robotics, namely aerial physical interaction using a flying end-effector and bio-inspired flapping flight using a robotic-bird. The work in this thesis can be divided into theoretical-oriented objectives related to both interactive aerial robots, and more practical-oriented objectives related to aerial physical interaction.

The specific goals of this thesis are formulated in a number of research questions (RQ) as follows:

- **RQ1:** How to systematically construct the port-Hamiltonian models of the different subsystems comprising the models of a flying end-effector and robotic bird?

Such models include rigid-body motion, flexible-body motion, and viscous three-dimensional airflow, as shown in Figs. 1.6 and 1.7. An important aspect is to develop these models in a systematic manner from first principles.

- **RQ2:** How to develop port-Hamiltonian control systems for the flying-end effector model that are stable and robustly performing in both free-flight and in contact-based tasks?

Such control and analysis methods should be able to guarantee the overall system's properties independent of specific models for the environment the robot is expected to interact with.

- **RQ3:** How to design an autonomous control architecture that provides a general flying-manipulator with perceptual and decision-making capa-

bilities utilizing other paradigms outside the scope of the port-Hamiltonian framework?

To enable autonomous accomplishment of aerial physical interaction tasks, a flying manipulator requires additional modules based on “signal -processing” paradigms, such machine learning and computer vision.

The research presented in this thesis has been conducted within two different European projects: SPECTORS and PortWings.

1.4.1 SPECTORS Project

Sensor Products for Enterprises Creating Technological Opportunities in Remote Sensing (SPECTORS) is a four year long innovation program funded by INTERREG V-A Deutschland-Nederland. The project consists of more than 20 Dutch and German small-and-medium sized enterprises. The goal of the project is to exploit the market potential of civil drone technology through sensor innovations for remote sensing, remote monitoring, and big data cloud computing for applications in aerial inspection, precision agriculture, nature conservation and environmental protection.

The main role that the work of this thesis contributes to is the technological development of an aerial robot capable of establishing a robust mechanical surface contact for remote contact-based inspection. All the work in this thesis related to aerial physical interaction has been within the SPECTORS project from end of 2016 to 2020.

1.4.2 PortWings Project

PortWings is a ERC-2018 Advanced grant awarded to S. Stramigioli between 2018 and 2023. The main goal of the project is to understand the secrets of flapping flight of birds using the port-Hamiltonian framework and validate these understandings experimentally by building an advanced bird-inspired aerial robot [Califano et al., 2021].

The project comprises of an interdisciplinary team of six members led by S. Stramigioli tackling different research challenges of the project. For the theoretical challenges, two members of the team work on the system theoretical problems related to the formulation and control of the port-Hamiltonian models. Another member is responsible for the numerical discretization and simulation of such models. For the realization challenges, one team member works on experimental fluid-dynamics validating the constructed port-Hamiltonian models using wind-tunnel and particle image velocimetry facilities. Another member works on the bio-mimetic mechatronic design of the robotic bird, while the last member of the team focuses on the study and fabrication of sensors and actuators needed for the robot.

The main role of the work in this thesis contributes to the theoretical development of the port-Hamiltonian framework by reframing the available methods used in continuum mechanics in the setting of differential geometry and the port-based paradigm. All the work in this thesis related to the port-Hamiltonian theory and infinite-dimensional dynamical systems has been within the PortWings project from end of 2018 to 2020.

1.5 Contributions of the Thesis

According to the primary research goal stated previously, we now highlight in this section the contributions of this thesis. The major contribution of this thesis as a whole is the demonstration of the strengths of the port-Hamiltonian paradigm in addressing complex physical problems such as aerial physical interaction and bio-inspired flapping flight.

The work in this thesis is divided into two distinct parts: Part I deals with aspects of the *Theoretical Framework* of port-Hamiltonian systems covering **RQ1**, related to both aerial physical interaction and flapping flight at an abstract level. Part II focuses only on the topic of *Aerial Physical Interaction* and deals with the control systems design issues of **RQ2** and the autonomy issues of **RQ3**.

In what follows, the specific contributions and publications of this thesis with respect to the three different parts are detailed. For the reader's convenience, Tables 1.2 - 1.3 summarize the main publications that comprise the backbone on which this dissertation is built.

Part I: Theoretical Framework

The first contribution of this thesis in Part I is an extensive survey of over 150 studies related to distributed-parameter port-Hamiltonian systems. This survey highlights the wide applicability of the framework and affirmed its suitability to tackle the complex problem of flapping-flight. The survey has been published in Rashad et al. [2020b].

An outcome of the survey is that there is a short-coming in the literature in understanding the main building block underlying the distributed port-Hamiltonian theory i.e the “Dirac structure”. Using Hamiltonian reduction theory for Lie groups [Marsden and Ratiu, 1999] and the underlying geometry of the state-space, it is shown in this thesis that the Dirac structure underlying the port-Hamiltonian theory can be systematically constructed starting from the Poisson structure used in classical Hamiltonian theory. This exposition led to a systematic procedure for developing port-Hamiltonian models of both finite- and infinite-dimensional mechanical systems whose configuration space is described by Lie groups.

Table 1.2: Summary of publications in Part I.

Part I - Theoretical Framework
1. R. Rashad, , F. Califano, A. van der Schaft & S. Stramigioli. Twenty Years of Distributed Port-Hamiltonian Systems: A Literature Review. <i>IMA Journal of Mathematical Control and Information</i> , 2020.
2. R. Rashad, , F. Califano, F. P. Schuller & S. Stramigioli. Port-Hamiltonian Modeling of Ideal Fluid Flow: Part I. Foundations and Kinetic Energy. <i>Journal of Geometry and Physics</i> , 2021. (<i>Under review</i>)
3. R. Rashad, , F. Califano, F. P. Schuller & S. Stramigioli. Port-Hamiltonian Modeling of Ideal Fluid Flow: Part II. Compressible and Incompressible Flow. <i>Journal of Geometry and Physics</i> , 2021. (<i>Under review</i>)

The second contribution of this thesis is applying the systematic procedure mentioned above to address **RQ1**. As a result, we present a port-Hamiltonian representation of the finite-dimensional model for rigid body motion, and a number of infinite-dimensional models for compressible and incompressible flow. Compared to previous port-Hamiltonian models in the literature for the rigid body [Maschke and van der Schaft, 1997] and a specific case of compressible flow [van der Schaft and Maschke, 2001], the models presented in this thesis have several appealing features. First, these models are derived from first principles by Hamiltonian reduction instead of being postulated or transformed from other representations. Second, the port-Hamiltonian models in this work are more disjoint and teared apart which provides more insight into the underlying structure of these dynamical systems and their comprising units. The work related to the modeling of fluid mechanics is currently under review to be published as a two-parts journal article [Rashad et al., 2021b,c].

Another important contribution of this thesis is the unified formulation of both the rigid body and fluid flow dynamical systems. This global formulation using Lie groups theory has highlighted many similarities between the two different systems. The unified formulation presented in this work is a first step towards a theory coupling the two dynamical systems together which contributes to the important field of fluid-structure interaction.

Part II: Aerial Physical Interaction

The second part of this thesis is more focused on aerial physical interaction using the flying end-effector approach i.e. utilizing a fully-actuated multirotor UAV. The first contribution of the thesis in this part is an extensive survey of multirotor configurations in the literature achieving fully-actuated flight. This literature survey has been published in Rashad et al. [2020c].

Based on the survey conducted, one specific type of fully-actuated UAV has

Table 1.3: Summary of publications in Part II.

Part II: Aerial Physical Interaction	
4.	R. Rashad , J. Goerres, R. G. Aarts, J. B. Engelen, & S. Stramigioli. Fully Actuated Multirotor UAVs: A Literature Review. <i>IEEE Robotics & Automation Magazine</i> , 2020.
5.	R. Rashad , F. Califano, & S. Stramigioli. Port-Hamiltonian passivity-based control on SE (3) of a fully actuated UAV for aerial physical interaction near-hovering. <i>IEEE Robotics and Automation Letters</i> , 4(4), 4378-4385, 2019.
6.	R. Rashad , D. Bicego, J. Zult, S. Sanchez-Escalonilla, R. Jiao, A. Franchi, & S. Stramigioli. Energy-Aware Impedance Control of a Flying End-Effector in the Port-Hamiltonian Framework. <i>IEEE Transactions on Robotics</i> , 2021. (In preparation)
7.	R. Rashad , J. B. Engelen, & S. Stramigioli. Energy tank-based wrench/impedance control of a fully-actuated hexarotor: A geometric port-hamiltonian approach. In <i>Proceedings of the IEEE International Conference on Robotics and Automation (ICRA)</i> , 2019.
8.	B. Sirmacek, R. Rashad , & P. Radl. Autonomous UAV-based 3D-reconstruction of structures for aerial physical interaction. <i>International Archives of the Photogrammetry, Remote Sensing and Spatial Information Sciences</i> , vol. XLII-2/W13, 2019.
9.	R. Rashad , D. Bicego, R. Jiao, S. Sanchez-Escalonilla, & S. Stramigioli. Towards Vision-Based Impedance Control for the Contact Inspection of Unknown Generic Surfaces with a Fully-Actuated Aerial Robot. In <i>Proceedings of the IEEE/RSJ International Conference on Intelligent Robots and Systems (IROS)</i> , October, 2020.

been chosen as the platform to be used within this thesis for aerial physical interaction. The platform selected is a hexarotor with canted propellers, first proposed in Voyles and Jiang [2012], chosen mainly for its simplicity and low mechanical complexity compared to other design concepts. Consequently, an achievement of this thesis is the software and hardware development of a flying end-effector having the configuration of a fully-actuated hexarotor, called “BetaX”. The BetaX aerial robot has been used in all experimental validation work presented in this thesis.

Using the developed aerial robot and the port-Hamiltonian model of a rigid body of **RQ1** as an abstract model for the flying end-effector, the goals of **RQ2** were then addressed. The contribution of this thesis in light of **RQ2** consists of two port-Hamiltonian control systems for aerial physical interaction.

The first controller is based on the energy-balancing passivity-based control (EB-PBC) approach. The developed controller is a reformulation of the geo-

metric impedance controller of [Fasse and Broenink, 1997; Stramigioli, 2001] within the port-Hamiltonian framework. The controller is capable of regulating the pose of the aerial robot as well as enabling it to interact with the environment. Moreover, the contact stability is proven using passivity analysis without an explicit model for the environment, and the robustness of the controller has been verified experimentally. This work has been published as a journal article in Rashad et al. [2019a] as well as presented at the 2019 IEEE/RSJ International Conference on Intelligent Robots and Systems(IROS).

The second controller is based on the control by interconnection approach used to add features to the first controller and enhance its interaction capabilities. The enhanced capabilities include regulating the interaction wrench by variable stiffness control, guaranteed passivity using energy routing with energy tanks, and contact-loss stabilization utilizing energy tanks as energy observers. This work is currently in preparation to be published as a journal article [Rashad et al., 2021a] and a preliminary version of it has been published in Rashad et al. [2019b].

Finally, the goals of **RQ3** were addressed where additional modules were designed that complement the port-Hamiltonian controllers described above in order to accomplish interactive tasks autonomously. The first contribution of this part is an integration of computer-vision techniques with the EB-PBC controller, designed previously, to add perception capabilities to the aerial robot. As a result, the aerial robot could accomplish physical interaction without prior knowledge of the environment’s surface geometry, as demonstrated both in simulation and experiment. This work has been published in Rashad et al. [2020a] and a preliminary version of it has been published in Sirmacek et al. [2019].

The second contribution of this part is an integration of Bayesian-optimization techniques with the EB-PBC controller to improve the performance of the controller over time and have a consistent behavior with different environments. Consequently, aerial physical interaction tasks without prior knowledge of the environment’s mechanical properties have been achieved and validated in simulation. This work has been published in Khattab et al. [2019] and was the winner of the **best paper award** at the 2019 IEEE SSR conference. However, we decided to leave out this work from this thesis since we believe its level of maturity requires substantial effort for improvement which is currently being investigated. Nevertheless, we will highlight on its research findings in the conclusion chapter. Other works that have been co-authored and not reported in this thesis also includes [Jiao et al., 2021; Califano et al., 2021] where the former focuses on the interaction wrench estimation problem and its effect on aerial physical interaction, while the latter addresses how the port-Hamiltonian framework can address the challenges of flapping flight.

Table 1.4: Summary of other contributions not included in the thesis

Other contributions
10. A. Khattab, R. Rashad , J. B. Engelen, & S. Stramigioli. Bayesian-Optimized Impedance Control of an Aerial Robot for Safe Physical Interaction with the Environment. In <i>Proceedings of IEEE International Symposium on Safety, Security, and Rescue Robotics (SSRR)</i> , 2019.
11. R. Jiao, R. Rashad , D. Bicego, W. Chou, & S. Stramigioli. Observer-based Geometric Impedance Control of a Fully-Actuated Hexarotor for Physical Sliding Interaction with Unknown Generic Surfaces. <i>Journal of Intelligent & Robotic Systems</i> , 2021. (<i>Under review</i>)
12. F. Califano, R. Rashad , A. Dijkshoorn, L. Groot Koerkamp, R. Snee, A. Brugnoli, & S. Stramigioli. Decoding and Realising Flapping Flight with Port-Hamiltonian System Theory. <i>Annual Reviews in Control</i> , 2021. (<i>Under review</i>)

1.6 Outline of the Thesis

The remaining chapters of the thesis are organized and structured in three parts that include the two parts discussed in the previous section with an additional part for general discussions. The majority of the chapters are either slightly-adapted or extended versions of the articles listed in Tables 1.2 - 1.3. The extensions added to some chapters include extra background preliminaries, detailed proofs of theorems, and more elaboration on various concepts.

Part I of this thesis consists of Chapters 2-5:

Chapter 2 first introduces the port-Hamiltonian framework and its basic concepts and terminology. Then, the chapter deals with exposing the relation between the traditional Hamiltonian theory and the port-Hamiltonian theory. Using Hamiltonian reduction, it is shown how to systematically derive port-Hamiltonian models for mechanical systems with a configuration space that is a Lie group.

Chapter 3 presents the literature survey of distributed port-Hamiltonian systems [Rashad et al., 2020b], where the surveyed studies are classified into different classes based on their respective research focus.

Chapter 4 deals partially with **RQ1** by the port-Hamiltonian modeling of a rigid body using the method of Chapter 2. The chapter presents a detailed treatment of the geometric formulation of rigid body kinematics and dynamics using the Lie group $SE(3)$. The presented port-Hamiltonian model is one of the basic milestones in modeling flapping-flight of birds and will be used in later chapters for the design of control schemes for aerial physical interaction.

Chapter 5 addresses also **RQ1** by the port-Hamiltonian modeling of fluid flow using an extension of the method presented in Chapter 2. The chapter introduces didactically the geometric formulation of fluid mechanics using exterior calculus instead of the standard vector calculus treatment used commonly in the field. The configuration space of a fluid dynamical system is shown to be the diffeomorphism group $\mathcal{D}(M)$ of the (possibly curved) space on which the fluid flows. The developed port-Hamiltonian model is an important milestone related to modeling flapping-flight of birds via separate interconnected dynamical systems. This chapter is the most mathematically and technically involved part of the dissertation.

Part II consists of Chapters 6-9:

Chapter 6 presents mainly the literature survey of fully-actuated multirotor UAVs [Rashad et al., 2020c]. The survey concepts are classified into fixed- and variable-tilt designs and their corresponding design parameters are identified. Moreover, the chapter presents a review of the optimization criteria used in the literature for choosing these design parameters.

Chapter 7 deals with the port-Hamiltonian control system design of a flying end-effector using the EB-PBC approach within the view of **RQ2**. The port-Hamiltonian rigid body model, developed earlier in Chapter 4, is used as an abstraction of a fully-actuated hexarotor. The chapter presents experimental results that validate the robustness of the controller against uncertainties and input saturation.

Chapter 8 also addresses **RQ2** by an extension of the controller developed in Chapter 7. The chapter utilizes novel concepts exclusive in the port-Hamiltonian framework, such as energy routing using Dirac structures and energy tanks, to enhance conventional impedance control with more enhanced features required for high-performance aerial physical interaction.

Chapter 9 deals with **RQ3** with a shifted focus to the intersection of interaction control and computer-vision techniques. The chapter presents a vision-based impedance control architecture that adds more autonomy to the aerial robot. The proposed architecture is validated in simulation and experiments.

Part III consists of Chapter 10:

Chapter 10 concludes this thesis by summarizing the main contributions of this thesis, reflecting on the limitations of the different presented solutions, and presenting an outlook for the future applications and extensions of the work.

Part I

Theoretical Framework

CHAPTER 2

PORT-HAMILTONIAN FRAMEWORK

This chapter is an introduction to Part I of this thesis dealing with theoretical aspects and foundations of the port-Hamiltonian framework. The purpose of this chapter is twofold. First, to introduce the basic concepts and terminology of the port-Hamiltonian framework used throughout this thesis for both modeling and control. Second, to explicate the relation between the port-Hamiltonian framework relying on Dirac structures and the standard Hamiltonian framework relying on Poisson and symplectic structures.

There are two main messages that are conveyed in this chapter. The first one is that finite-dimensional and infinite-dimensional systems are treated in the geometric port-Hamiltonian framework using the SAME concepts. The second one is that the port-Hamiltonian framework is NOT a “trivial extension” of the standard Hamiltonian framework, but rather a paradigm shift. This is demonstrated by comparing the modeling philosophy and approach of each framework.

The chapter is outlined as follows: Sec. 2.1 introduces the port-Hamiltonian framework for both finite and infinite-dimensional systems, its graphical representation using bond graphs and block diagrams, and the implicit and explicit forms of the dynamical equations. Sec. 2.2 discusses the relationship between the port-Hamiltonian framework and the standard Hamiltonian framework by showing how a Dirac structures extend Poisson structures as well as the difference in their modeling philosophies. Sec. 2.3 provides a brief summary of the central topic of Hamiltonian reduction which will be of utmost significance in later chapters. Finally, we conclude the chapter in Sec. 2.4.

2.1 Foundations of Port-Hamiltonian Systems

The port-Hamiltonian systems paradigm is a framework for the modeling, analysis, design, and control of complex physical dynamical systems. The mentioned complexity arises due to multi-physical domains, inter-domain couplings, nonlinearities, and distributed sensing and actuation. The port-Hamiltonian system theory can handle successfully both lumped-parameter (finite-dimensional) systems [Maschke et al., 1992] and distributed-parameter (infinite-dimensional) systems [van der Schaft and Maschke, 2002].

In what follows, we introduce the basic port-Hamiltonian concepts first for finite-dimensional systems and then we discuss how these concepts are extended for infinite-dimensional systems. For a more extensive introduction to the subject, the reader is referred to [Duindam et al., 2009; van der Schaft and Jeltsema, 2014; van der Schaft, 2020].

2.1.1 Finite-dimensional Systems

A core feature of the port-Hamiltonian framework is the emphasis on power flow between subsystems and the separation of the interconnection structure of the system from its components' constitutive relations. A complex physical system is modeled in the port-Hamiltonian framework as the interconnection of several subsystems or elements, classified based on their relation to energy. Namely, energy storage, energy dissipation¹, energy supply, and energy routing elements.

Power Ports

All subsystems are interconnected by power ports (or bonds), graphically represented by a half-arrow in bond graph notation, as shown in Fig. 2.1. Each port is defined by the pair (e, f) with $f \in \mathcal{F}$ and $e \in \mathcal{E} := \mathcal{F}^*$ referred to as the *flow* and *effort* variables, respectively. The flow and effort variables are usually referred to as *port variables*. In lumped parameter systems, the flow space \mathcal{F} and the effort space \mathcal{E} are both finite-dimensional vector spaces. The duality pairing between a flow f and effort e (i.e. a vector and a covector), denoted by $\langle e | f \rangle_{\mathcal{F}} := e(f)$, represents the power flow through the port (e, f) at a specific instant of time. In the special case where $\mathcal{F} = \mathbb{R}^n$ and $\mathcal{E} \cong \mathbb{R}^n$ are n -dimensional Euclidean spaces, then the duality pairing is given by $\langle e | f \rangle_{\mathcal{F}} = e^{\top} f$.

¹From the first principle of thermodynamics, energy can neither be created nor destroyed, but only transformed from one form to another. In this thesis, dissipation of energy refers to the irreversible transformation of energy to the thermal domain.

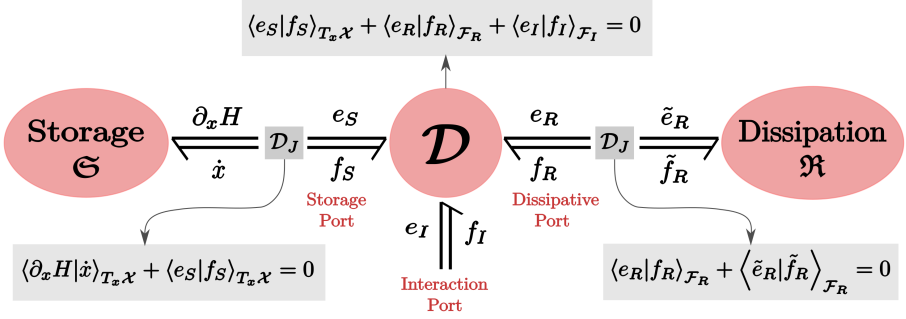


Figure 2.1: Finite-dimensional port-Hamiltonian system consisting of an energy storage subsystem \mathfrak{S} , an energy dissipation subsystem \mathfrak{R} , an external energy supply port (e_I, f_I) , in addition to the Dirac structures \mathcal{D} and \mathcal{D}_J that act as energy routing elements.

Energy Storage

With reference, to Fig. 2.1, the first class of subsystems of a port-Hamiltonian model are the energy storage elements, represented by \mathfrak{S} . Physical examples in the mechanical domain include storage of kinetic and potential energy in inertial and elastic elements, respectively. Other examples in the electromagnetic domain include storage of electric and magnetic energy in capacitive and inductive elements, respectively.

The energy storage subsystem \mathfrak{S} is mathematically defined by the pair (\mathcal{X}, H) where the state space \mathcal{X} is a finite-dimensional manifold and $H : \mathcal{X} \rightarrow \mathbb{R}$ is called the Hamiltonian function denoting the energy stored. The state (or energy variable) of the energy storage system is an element x of the manifold \mathcal{X} . The flow variable of \mathfrak{S} is given by the rate of change of the state variable $\dot{x} \in T_x \mathcal{X}$, while the effort variable is given by the partial derivative of H with respect to the state x , denoted by $\partial_x H(x) := \frac{\partial H}{\partial x}(x) \in T_x^* \mathcal{X}$. The effort variable $\partial_x H(x)$ is usually called the co-energy variable. The rate of change of the energy stored is given by

$$\dot{H} = \langle \partial_x H(x) | \dot{x} \rangle_{T_x \mathcal{X}}, \quad (2.1)$$

where $\langle \cdot | \cdot \rangle_{T_x \mathcal{X}}$ denotes the duality pairing between the effort in $T_x^* \mathcal{X}$ and the flow in $T_x \mathcal{X}$. In the special case where $\mathcal{X} = \mathbb{R}^n$, one has that $T_x \mathcal{X} \cong T_x^* \mathcal{X} \cong \mathbb{R}^n$ and the energy balance (2.1) can be written as

$$\dot{H} = \langle \partial_x H(x) | \dot{x} \rangle_{\mathbb{R}^n} = \partial_x H^\top(x) \dot{x},$$

where $\partial_x H(x)$ is a column vector of partial derivatives of H .

In generalized bond graph terminology, the storage system \mathfrak{S} is graphically represented by a so called \mathbb{C} -element that has its Hamiltonian energy function $H(x)$ written beside it, as illustrated in Fig. 2.2a.

Energy Dissipation

The second class of subsystems of a port-Hamiltonian model corresponds to the internal energy dissipation (or resistive) elements, represented by \mathfrak{R} . Physical examples include mechanical friction, fluid viscosity, and electrical resistance. The effort and flow variables of a resistive system \mathfrak{R} are denoted by $(\tilde{e}_R, \tilde{f}_R) \in \mathcal{F}_R^* \times \mathcal{F}_R$, where \mathcal{F}_R is an m -dimensional vector space. To represent energy dissipation, a resistive system is defined by a static relation between \tilde{e}_R and \tilde{f}_R such that

$$\langle \tilde{e}_R | \tilde{f}_R \rangle_{\mathcal{F}_R} \geq 0. \quad (2.2)$$

This condition implies that energy only goes towards the system \mathfrak{R} which represents the irreversible transfer of energy to the thermal domain.

An important recurrent type of resistive relations is one that could be expressed as an input-output mapping. Such resistive map can be represented in either *impedance* or *admittance* form:

$$\tilde{e}_R = \mathcal{R}(\tilde{f}_R) \quad (\text{impedance}), \quad \tilde{f}_R = \mathcal{R}(\tilde{e}_R) \quad (\text{admittance}).$$

In the special case of a linear static impedance relation for $\mathcal{F}_R = \mathbb{R}^m$ and $\mathcal{F}_R^* \cong \mathbb{R}^m$, the resistive mapping is expressed as $\tilde{e}_R = \tilde{R}\tilde{f}_R$, where $\tilde{R} \in \mathbb{R}^{m \times m}$ is some symmetric positive semi-definite matrix.

In bond graph terminology, the resistive system \mathfrak{R} is graphically represented by an \mathbb{R} -element that has its resistive map (e.g. \tilde{R}) written beside it, as illustrated in Fig. 2.2a.

Energy Supply

The port-Hamiltonian system has an *open* external port $(e_I, f_I) \in \mathcal{F}_I^* \times \mathcal{F}_I =: \mathcal{I}$ called the interaction port, for some finite-dimensional vector space \mathcal{F}_I . This port is a general one used to model the interaction of the port-Hamiltonian system with the rest of its environment. The interaction is characterized by the energy supplied *from the environment to the system*, given by the duality pairing $\langle e_I | f_I \rangle_{\mathcal{F}_I}$.

Energy Routing

The last component of a port-Hamiltonian system is the Dirac structure, denoted by \mathcal{D} as shown in Fig. 2.1. The Dirac structure represents the power-continuous (power-preserving) combination of all energy routing elements linking the various subsystems and their corresponding ports together. The Dirac

structure encodes how the port variables of all its connected ports are related to each other such that the total power associated to the port-variables is zero.

Given a k -th dimensional vector space \mathcal{F} , a Dirac structure is mathematically defined as the k -th dimensional subspace $\mathcal{D} \subset \mathcal{F} \times \mathcal{F}^*$ such that all its elements $(e, f) \in \mathcal{D}$ satisfy

$$\langle e | f \rangle_{\mathcal{F}} = 0. \quad (2.3)$$

For a more general definition of Dirac structures (that is applicable also for infinite-dimensions), see [van der Schaft and Jeltsema, 2014, Pg. 16].

The Dirac structure \mathcal{D} shown in Fig. 2.1 consists of three ports; a storage port $(e_S, f_S) \in T_x^* \mathcal{X} \times T_x \mathcal{X}$, a resistive port $(e_R, f_R) \in \mathcal{F}_R^* \times \mathcal{F}_R$, and an interaction port $(e_I, f_I) \in \mathcal{F}_I^* \times \mathcal{F}_I$. Then, \mathcal{D} is mathematically a subspace of $\mathcal{F}_T \times \mathcal{F}_T^*$, the total port space (or bond space), where $\mathcal{F}_T := T_x \mathcal{X} \times \mathcal{F}_R \times \mathcal{F}_I$. The power balance encoded by the Dirac structure is given by

$$\langle e_S | f_S \rangle_{T_x \mathcal{X}} + \langle e_R | f_R \rangle_{\mathcal{F}_R} + \langle e_I | f_I \rangle_{\mathcal{F}_I} = 0. \quad (2.4)$$

Interconnection

The overall port-Hamiltonian model is then constructed by interconnecting the storage port (e_S, f_S) and the resistive port (e_R, f_R) of the Dirac structure \mathcal{D} with the energy-storage system \mathfrak{S} and the resistive system \mathfrak{R} , respectively. In most cases, we adopt the convention to define the direction of ports to be *entering* each subsystem. Therefore to follow this convention, as shown in Fig. 2.1, the inversion of power-flows is achieved by *junctions* \mathcal{D}_J that implement the equalities

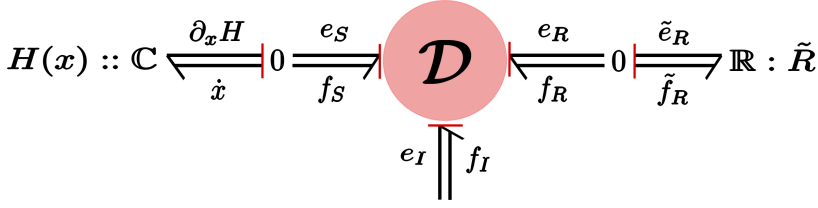
$$\langle \partial_x H(x) | \dot{x} \rangle_{T_x \mathcal{X}} + \langle e_S | f_S \rangle_{T_x \mathcal{X}} = 0, \quad \langle e_R | f_R \rangle_{\mathcal{F}_R} + \langle \tilde{e}_R | \tilde{f}_R \rangle_{\mathcal{F}_R} = 0. \quad (2.5)$$

These junctions are basic examples of a Dirac structure that only serves the purpose of power inversion [Stramigioli, 2001].

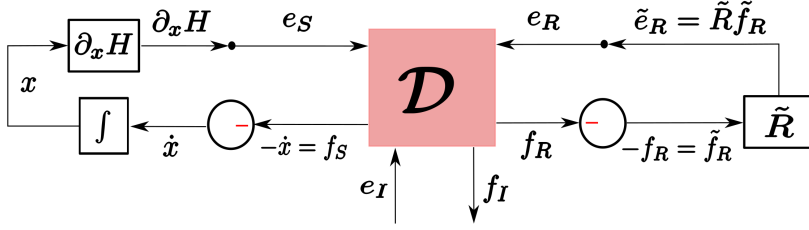
The equalities in (2.5) state that the power flowing *into* each of \mathfrak{S} and \mathfrak{R} is equivalent to the power flowing *out of* the Dirac structure \mathcal{D} . This implies that we cannot simultaneously equate both port-variables of (e_S, f_S) to the port-variables of $(\partial_x H, \dot{x})$, and similarly for the ports connecting \mathfrak{R} and \mathcal{D} . Instead, both ports can have either a *common-flow* and opposite efforts or a *common-effort* and opposite flows. We will follow the common effort convention for interconnecting ports, and thus the constraints implemented by a junction are given by

$$f_S = -\dot{x}, \quad e_S = \partial_x H(x), \quad f_R = -\tilde{f}_R, \quad e_R = \tilde{e}_R. \quad (2.6)$$

In bond graph notation, shown in Fig. 2.2a, the common-effort constraint is implemented by a *zero junction*.



(a) Bond Graph Representation



(b) Block Diagram Representation

Figure 2.2: Example of a basic port-Hamiltonian system with a chosen causality. Namely, an integral (impedance) causality for the \mathbb{C} element, and an impedance causality for both the \mathbb{R} element and the external port.

In conclusion, a coordinate-free description port-Hamiltonian system is completely defined by the tuple $(\mathcal{X}, H, \mathcal{R}, \mathcal{I}, \mathcal{D})$ corresponding to the state manifold, Hamiltonian energy function, the resistive relation, the interaction port space, and the Dirac structure, respectively.

Causality

An extremely important feature of the abstract port-Hamiltonian representation of a physical system presented so far is that no predefined choice of causality is made (i.e. a fixed choice of inputs and outputs). The abstract description of the different storage, resistive, and routing elements above defines relations between their corresponding effort and flow variables (referred to as *constitutive relations*) without a choice of what is input and what is output. The only constraint imposed is that the flow and effort of a port have complementary causality [Stramigioli, 2001, Sec. 3.2]. Therefore, if the flow is an input, the effort is an output (called *impedance causality*), and if the effort is an input, the flow is an output (called *admittance causality*).

This key feature of the port-based paradigm is an important distinction with the standard block-diagram paradigm which describes a particular choice of causality that was made a priori. It is important to realize that often, a real physical system does not have specific imposed causality constraints which are

merely a modeling artifact.

An illustrative example is the direct-current electric motor and direct-current electric generator, where both correspond to the same physical device and only differ in whether electric energy is converted to mechanical energy or vice-versa. Furthermore, if operated as an electric motor, it can have as an input either voltage (effort) or current (flow) and as output either torque (effort) or speed (flow). Therefore, a block-diagram model of the motor, with a predefined choice of input and output, represents 1 out of 4 causality combinations the model could have. On the other hand, only one port-Hamiltonian model that represents all possible causalities of the ports.

In bond graph notation, when the causality information is prescribed, it is graphically represented by a causality stroke on either ends of a port. The location of the stroke identifies the subsystem to which “effort enters as an input”, as shown in Fig. 2.2. Note that in Fig. 2.2, the Dirac structure has its 3 ports in “impedance” causality (effort-in), which is only 1 out of $2^3 = 8$ causality possibilities.

Port-Hamiltonian Dynamics

The Dirac structure plays a central role in defining how the system’s port variables and energy variables evolve, which in turn defines the dynamics of the port-Hamiltonian system. The evolution of the port variables is defined by the constraints imposed by the Dirac structure, such that

$$(f_S(t), f_R(t), f_I(t), e_S(t), e_R(t), e_I(t)) \in \mathcal{D}.$$

Therefore, it follows from the interconnections in (2.6) that the port-Hamiltonian dynamics are implicitly defined by

$$\left(-\dot{x}(t), -\tilde{f}_R(t), f_I(t), \partial_x H(x(t)), \tilde{e}_R, e_I(t)\right) \in \mathcal{D}. \quad (2.7)$$

Consequently, it follows from combining (2.1,2.2,2.4,2.5) that the Hamiltonian energy function $H(x)$ satisfies the energy balance

$$\dot{H} = -\langle \tilde{e}_R | \tilde{f}_R \rangle_{\mathcal{F}_R} + \langle e_I | f_I \rangle_{\mathcal{F}_I} \leq \langle e_I | f_I \rangle_{\mathcal{F}_I}. \quad (2.8)$$

If the Hamiltonian satisfies the extra condition of being positive semi-definite, i.e. $H(x) \geq 0, \forall x \in \mathcal{X}$, then (2.8) implies that the port-Hamiltonian system is passive [van der Schaft, 2000] with respect to interaction port $(e_I, f_I) \in \mathcal{I}$.

In general, the implicit port-Hamiltonian dynamics (2.7) defines algebraic constraints on the state space (energy) variables. Such constrained dynamical systems are represented by a mixed set of differential and algebraic equations (DAEs). A dynamical system described implicitly as presented so far contains only relations between the port and energy variables independent of causality.

Such implicit description is very useful in studying intrinsic system properties in a coordinate-free manner. In addition, it allows arbitrary interconnection to external systems.

On the other hand, for simulation and control purposes, it is usually convenient to use an explicit input-output representation of the dynamics (2.7). One important class of explicit port-Hamiltonian representations that will be used extensively in this thesis is the *input-state-output* port-Hamiltonian system expressed in local coordinates of \mathcal{X} as

$$\begin{aligned}\dot{x} &= (J(x) - R(x))\partial_x H(x) + G(x)u, \\ y &= G^\top(x)\partial_x H(x),\end{aligned}\tag{2.9}$$

where $J(x) = -J^\top(x)$ is the skew-symmetric *structure matrix*, $G(x)$ is the input matrix, and $R(x)$ corresponds to the resistive subsystem. For more details about this form of the port-Hamiltonian dynamics, the reader is referred to [Duindam et al., 2009].

2.1.2 Infinite-dimensional Systems

The port-Hamiltonian framework has been successfully extended in the foundational work of van der Schaft and Maschke [2002] to incorporate distributed parameter (infinite-dimensional) systems using the same generic concepts presented above. Distributed parameter systems are characterized by both time and space as independent parameters on which the port and energy variables are defined. In order to construct coordinate-free port-Hamiltonian models that are globally defined on any choice of spatial domain, differential forms are used to represent port and energy variables of the system.

The spatial manifold, on which physical quantities are defined, is represented mathematically by an n -dimensional manifold M with boundary ∂M . Similar to lumped-parameter systems discussed previously, a distributed port-Hamiltonian model also consists of a number of energy storing, dissipating, supplying, and routing elements interconnected to each other by power ports, as shown in Fig. 2.3

The flow and effort variables of each port are fields of differential forms of complementary orders with respect to the dimension of M . In particular, if a flow variable $f \in \mathcal{F} = \Omega^k(M)$ is a k -differential form on M , then an effort variable $e \in \mathcal{F}^* = \Omega^{n-k}(M)$ is an $n - k$ differential form. Both \mathcal{F} and \mathcal{F}^* are considered as infinite-dimensional vector spaces over the space of real numbers.

The power flowing through the port (e, f) is given by the natural pairing on spaces of differential forms given by

$$\langle e | f \rangle_\Omega := \int_M e \wedge f, \quad e \in \Omega^{n-k}(M), \quad f \in \Omega^k(M)$$

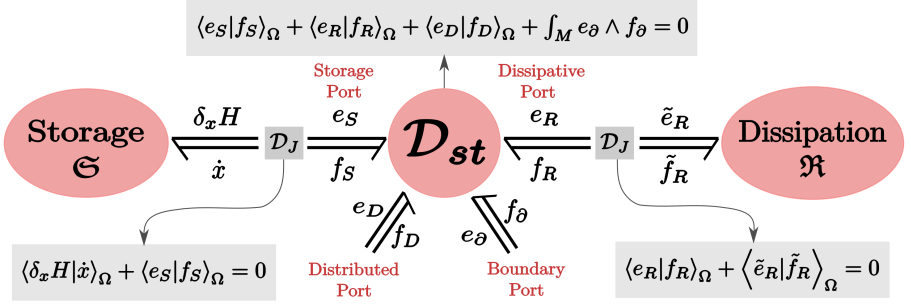


Figure 2.3: Infinite-dimensional port-Hamiltonian system consisting of an energy storage subsystem \mathfrak{S} , an energy dissipation subsystem \mathfrak{R} , and two external energy supply ports (e_D, f_D) and (e_∂, f_∂) . The Stokes Dirac structure \mathcal{D}_{st} and the power inverting junctions \mathcal{D}_J are the energy routing elements.

where \wedge denotes the wedge (or exterior) product.

The energy storage subsystem \mathfrak{S} of a distributed port-Hamiltonian model is also defined by the pair (\mathcal{X}, H) , where now the Hamiltonian energy $H[x]$ is a functional of the state $x \in \mathcal{X}$ given by

$$H[x] := \int_M \mathcal{H}(x), \quad \mathcal{H} : \mathcal{X} \rightarrow \Omega^n(M),$$

with \mathcal{H} called the Hamiltonian energy density that associates to every state x a top-form that may be integrated over the spatial domain M .

In general, the state x consists of a number of differential forms over M corresponding to the different physical energy variables of the system. For simplicity, consider in what follows the state $x \in \mathcal{X} = \Omega^{k_S}(M)$ to correspond to one physical quantity represented by a differential form of order k_S . In that case, the flow variable of \mathfrak{S} is given by $\dot{x} \in T_x \mathcal{X} \cong \Omega^{k_S}(M)$. Whereas, the effort variable is given by the variational derivative of H with respect to the state x , denoted by $\delta_x H(x) := \frac{\delta H}{\delta x}(x) \in T_x^* \mathcal{X} \cong \Omega^{n-k_S}(M)$, and defined as the element of $\Omega^{n-k_S}(M)$ that satisfies for any $x, \delta x \in \mathcal{X}$ and $\epsilon \in \mathbb{R}$

$$\langle \delta_x H(x) | \delta x \rangle_\Omega := \left. \frac{d}{d\epsilon} \right|_{\epsilon=0} H(x + \epsilon \delta x), \quad (2.10)$$

which is assumed to exist for a given $H \in C^\infty(\mathcal{X})$. The rate of change of the energy stored is given by

$$\dot{H} = \langle \delta_x H(x) | \dot{x} \rangle_\Omega = \int_M \delta_x H(x) \wedge \dot{x}. \quad (2.11)$$

The energy dissipation subsystem \mathfrak{R} of a distributed port-Hamiltonian model is very similar to the case of a finite-dimensional system, with the difference

that the effort and flow variables $(\tilde{e}_R, \tilde{f}_R)$ are now differential forms of complementary orders.

On the other hand, energy supply for infinite-dimensional systems is fundamentally different than in finite-dimensions. With reference to Fig. 2.3, there are two ways a distributed port-Hamiltonian system can exchange energy with its surroundings. The first one is through the distributed interaction port

$$(e_D, f_D) \in \Omega^{n-k_D}(M) \times \Omega^{k_D}(M) =: \mathcal{I}_D,$$

while the second one is through the boundary interaction port

$$(e_\partial, f_\partial) \in \Omega^{n-k_\partial-1}(\partial M) \times \Omega^{k_\partial}(\partial M) =: \mathcal{I}_\partial,$$

where $k_D, k_\partial \in \{1, \dots, n\}$ denote the order of the differential forms f_D and f_∂ , respectively. The power flowing through the distributed port, given by $\int_M e_D \wedge f_D$, characterizes energy supply within the spatial domain M , whereas the power flowing through the boundary port, given by $\int_{\partial M} e_\partial \wedge f_\partial$, characterizes energy supply through the boundary ∂M . The boundary port variables correspond to the boundary conditions of the PDEs represented by the port-Hamiltonian model.

The mathematical object used to interconnect the previous components of a distributed port-Hamiltonian system is the infinite-dimensional Dirac structure \mathcal{D}_{st} . The key result used within \mathcal{D}_{st} is Stokes theorem, which allows incorporating the energy flow through the boundary along with other energy flows within the spatial domain. Therefore, the Dirac structure used in distributed port-Hamiltonian systems is usually referred to as a *Stokes-Dirac structure* [van der Schaft and Maschke, 2002]. The power balance encoded by the Stokes-Dirac structure, shown in Fig. 2.3, is given by

$$\langle e_S | f_S \rangle_\Omega + \langle e_R | f_R \rangle_\Omega + \langle e_D | f_D \rangle_\Omega + \int_{\partial M} e_\partial \wedge f_\partial = 0. \quad (2.12)$$

Furthermore, the storage and resistive ports of the Stokes-Dirac structure are connected to \mathfrak{S} and \mathfrak{R} , respectively, via junctions similar to (2.5) and (2.6).

In conclusion, a distributed port-Hamiltonian system is represented abstractly by the tuple $(M, \mathcal{X}, H, \mathcal{R}, \mathcal{I}_D, \mathcal{I}_\partial, \mathcal{D}_{st})$. Similar to (2.7), the implicit port-Hamiltonian dynamics in this case are then given by

$$(-\dot{x}(t), -\tilde{f}_R(t), f_D(t), f_\partial(t), \delta_x H(x(t)), \tilde{e}_R, e_D(t), e_\partial(t)) \in \mathcal{D}_{st}. \quad (2.13)$$

Finally, the Hamiltonian energy functional $H[x]$ satisfies the energy balance

$$\dot{H} \leq \int_M e_D \wedge f_D + \int_{\partial M} e_\partial \wedge f_\partial. \quad (2.14)$$

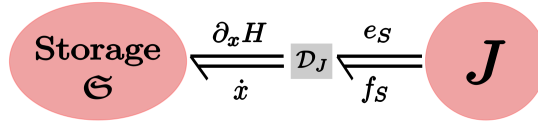


Figure 2.4: A standard Hamiltonian system consisting of an energy storage subsystem \mathfrak{S} and a Poisson structure J . We adopt the convention of defining the power port associated to a Poisson structure to be directing *outwards*. This choice is equivalent to defining the port to be directing inwards into a subsystem defined by $-J$.

2.2 Relation to Standard Hamiltonian Theory

In this section, we address a very important topic which sometimes causes a lot of confusion. Namely, the relation between the standard Hamiltonian framework and the port-Hamiltonian framework.

One of the two pillars of the port-Hamiltonian framework is the standard geometric Hamiltonian theory which has its roots in analytical mechanics. The standard Hamiltonian theory focuses mainly on **conservative closed** systems, which is suitable for analysis purposes, whereas the port-Hamiltonian theory is applicable to **non-conservative open** systems, which is suitable for modular modeling and control. Therefore, the standard Hamiltonian framework addresses the conservative dynamics only of a physical system related to the pair $(\mathfrak{S}, \mathcal{D})$ in finite-dimensions or the pair $(\mathfrak{S}, \mathcal{D}_{st})$ in infinite-dimensions.

For unconstrained physical systems, the Dirac structure is replaced by a Poisson (or a symplectic) structure J , which plays the same structural role in the standard Hamiltonian framework as the Dirac structure in the port-Hamiltonian framework. Thus, compared to the port-Hamiltonian models in Figs. 2.1 and 2.3, a standard Hamiltonian system would be represented graphically as shown in Fig. 2.4.

In what follows, we highlight the differences between the two frameworks by exposing the relation between Poisson and Dirac structures and how the Poisson structure corresponds to the energy-conservation part of the Dirac structure. Furthermore, we discuss a fundamental distinction between the modeling philosophies of the two frameworks, which clarifies how the port-Hamiltonian approach is not a trivial extension of the classical Hamiltonian approach.

First, we start by a brief introduction to the standard Hamiltonian formalism based on Poisson structures presented in local coordinates for simplicity. For a more extensive coordinate-free treatment of the subject, the reader is referred to [Marsden and Ratiu, 1999; Holm et al., 2009].

2.2.1 Extending Poisson Structures

With contrast to the explicit port-Hamiltonian dynamics in (2.9), the standard Hamiltonian formalism based on Poisson structures deals with the “conservative” part of a physical system. A finite-dimensional (generalized) Hamiltonian system is given in local coordinates of the state space manifold \mathcal{X} by

$$\dot{x} = J(x)\partial_x H(x), \quad (2.15)$$

where the map $J(x) : T_x^* \mathcal{X} \rightarrow T_x \mathcal{X}$ is a skew-symmetric matrix.

The structure matrix $J(x)$ can be used to equip the state space manifold \mathcal{X} with a (generalized) Poisson bracket, uniquely determined by $J(x)$ locally in \mathcal{X} , as follows. Consider any smooth function $F \in C^\infty(\mathcal{X})$. Along solutions of the dynamical system (2.15), denoted by the curve $x_t := x(t)$, the rate of change of F is given by

$$\dot{F}(x_t) = \langle \partial_x F(x_t) | \dot{x}_t \rangle_{T_x \mathcal{X}} = \langle \partial_x F(x_t) | J(x_t) \partial_x H(x_t) \rangle_{T_x \mathcal{X}}. \quad (2.16)$$

Therefore, by defining the bilinear map $\{\cdot, \cdot\} : C^\infty(\mathcal{X}) \times C^\infty(\mathcal{X}) \rightarrow C^\infty(\mathcal{X})$ as

$$\{F, K\}(x) := \langle \partial_x F(x) | J(x) \partial_x H(x) \rangle_{T_x \mathcal{X}}, \quad F, K \in C^\infty(\mathcal{X}), \quad (2.17)$$

then one can compactly represent (2.16) as

$$\dot{F}(x(t)) = \{F, H\}(x(t)). \quad (2.18)$$

The map $\{\cdot, \cdot\}$ is known as a *generalized Poisson bracket* and the pair $(\mathcal{X}, \{\cdot, \cdot\})$ is usually called a *Poisson manifold*. Furthermore, the Hamiltonian dynamics (2.15) are fully defined by the pair $(H, \{\cdot, \cdot\})$.

In case $\mathcal{X} = \mathbb{R}^n$ is an n -dimensional Euclidean space, the Poisson bracket (2.17) takes the well-known form

$$\{F, K\}(x) := \partial_x F^\top(x) J(x) \partial_x K(x). \quad (2.19)$$

From the skew symmetry property of $J(x)$, it follows that the generalized Poisson bracket (2.19) is skew-symmetric:

$$\{F, K\} = -\{K, F\},$$

and satisfies for any $\tilde{K} \in C^\infty(\mathcal{X})$ the Leibniz rule:

$$\{F, K \cdot \tilde{K}\} = \{F, K\} \cdot \tilde{K} + K \cdot \{F, \tilde{K}\}.$$

The standard Hamiltonian formalism presented above can be extended to infinite-dimensional systems as well. In that case, the Hamiltonian equations (2.15) take the form

$$\dot{x} = \mathcal{J}(x) \delta_x H(x), \quad (2.20)$$

where \mathcal{X} is now an infinite-dimensional manifold, the state $x \in \mathcal{X}$ consists of differential forms over M , $H[x]$ is a Hamiltonian functional, $\delta_x H$ denotes the variational derivative, and $\mathcal{J}(x) : T_x^* \mathcal{X} \rightarrow T_x \mathcal{X}$ is a skew-symmetric (matrix) operator.

The analog of (2.18) in the infinite-dimensional case is given by

$$\{F, K\}(x) := \langle \delta_x F(x) | \mathcal{J}(x) \delta_x K(x) \rangle_{T_x \mathcal{X}}, \quad F, K \in C^\infty(\mathcal{X}), \quad (2.21)$$

which is also a skew-symmetric bracket satisfying the Leibniz rule as a consequence of the skew-symmetry of the operator $\mathcal{J}(x)$. Similar to (2.18), one can represent the rate of change of any functional $F[x]$ on the state space \mathcal{X} in terms of the Poisson bracket (2.21).

Conservation of the Hamiltonian

An important consequence of the skew-symmetry of the structure maps $J(x)$ and $\mathcal{J}(x)$ is that the Hamiltonian is always a conserved quantity in the formalism above based on Poisson brackets. It follows from the skew-symmetric property of the brackets (2.19), it follows that the rate of change of a Hamiltonian function (or functional) satisfies

$$\dot{H}(x(t)) = \{H, H\}(x(t)) = 0, \quad (2.22)$$

along solutions of the system. Therefore, the generalized Poisson brackets (2.19) and (2.21) represent the *conservative dynamics* of a physical system such that the Hamiltonian H is a conserved quantity. Consequently, the standard Hamiltonian formulation focuses mainly on “closed isolated” physical systems. Such systems have neither internal (free) energy dissipation nor external energy supply.

On the other hand, by comparing the energy balance (2.22) to both (2.8) and (2.14), it can be clearly observed that the Dirac structure, used in the port-Hamiltonian formalism, generalizes the Poisson structure by allowing for **non-zero change** of the energy function H . Therefore, port-Hamiltonian formulation is applicable to physical systems that are “open for interconnection”. In port-Hamiltonian systems, the change of energy happens via the internal dissipation port or the external supply port, which in the case of infinite-dimensional systems could either be within the spatial domain or through the boundary.

In infinite-dimensional standard Hamiltonian systems, the zero energy supply through the boundary has an important implication. In order for the Hamiltonian of the system to be conserved, the boundary conditions of the PDEs represented by (2.20) are restricted to the ones that yield zero energy exchange through the boundary. Whereas the port-Hamiltonian framework allows to model systems with *variable boundary conditions*.

Canonical Poisson Structure

We end the part on Poisson structures by an important special case of the generalized Hamiltonian system (2.15). This special case is when the state space manifold $\mathcal{X} = T^*Q$ is the cotangent bundle of an n -dimensional manifold Q , and the structure matrix is given by the constant matrix

$$J(x) = J_s = \begin{pmatrix} \mathbf{0} & \mathbf{I}_n \\ -\mathbf{I}_n & \mathbf{0} \end{pmatrix},$$

where $\mathbf{I}_n \in \mathbb{R}^{n \times n}$ is the identity matrix. The matrix J_s is known as the *symplectic* structure matrix. If the state is represented by the coordinates $x = (q, p) \in T^*Q$, then the dynamical equations (2.15) can be expressed for a given Hamiltonian $\mathcal{H} : T^*Q \rightarrow \mathbb{R}$ as

$$\begin{pmatrix} \dot{q} \\ \dot{p} \end{pmatrix} = \begin{pmatrix} \partial_p \mathcal{H}(q, p) \\ -\partial_q \mathcal{H}(q, p) \end{pmatrix}, \quad (2.23)$$

which corresponds to the classical Hamilton's equations. A similar construction can be made if Q is an infinite-dimensional manifold, where J_s becomes a constant matrix operator and partial derivatives are replaced by variational ones.

A very important property of the generalized Poisson bracket associated to the symplectic structure matrix J_s is that it is canonically (intrinsically) defined on the cotangent bundle of any manifold, whether it is finite- or infinite-dimensional. We denote this special *canonical Poisson bracket* by $\{\cdot, \cdot\}_c$, and the coordinates (q, p) are usually referred to as the *canonical coordinates*.

2.2.2 Difference in Modeling Philosophy

It is important to realize that the port-Hamiltonian formalism is not a *trivial extension* of the standard Hamiltonian formalism that includes inputs and outputs, which is already present and known in the literature as input-output Hamiltonian systems [Maschke and van der Schaft, 1992]. The two frameworks are in fact fundamentally different in their underlying **modeling philosophy**.

The unique characteristic of the port-Hamiltonian paradigm that separates it from the standard Hamiltonian paradigm is that the overall physical system is modeled as a “network” of energetic units interconnected by ports. This fundamental characteristic is inherited from the classical port-based network approach which is the second pillar underlying the port-Hamiltonian framework. Consequently, the philosophy of the port-Hamiltonian modeling process is based on a *bottom-up* approach, whereas the standard Hamiltonian modeling process relies on a *top-down* approach. We illustrate the two modeling approaches using Fig. 2.5.

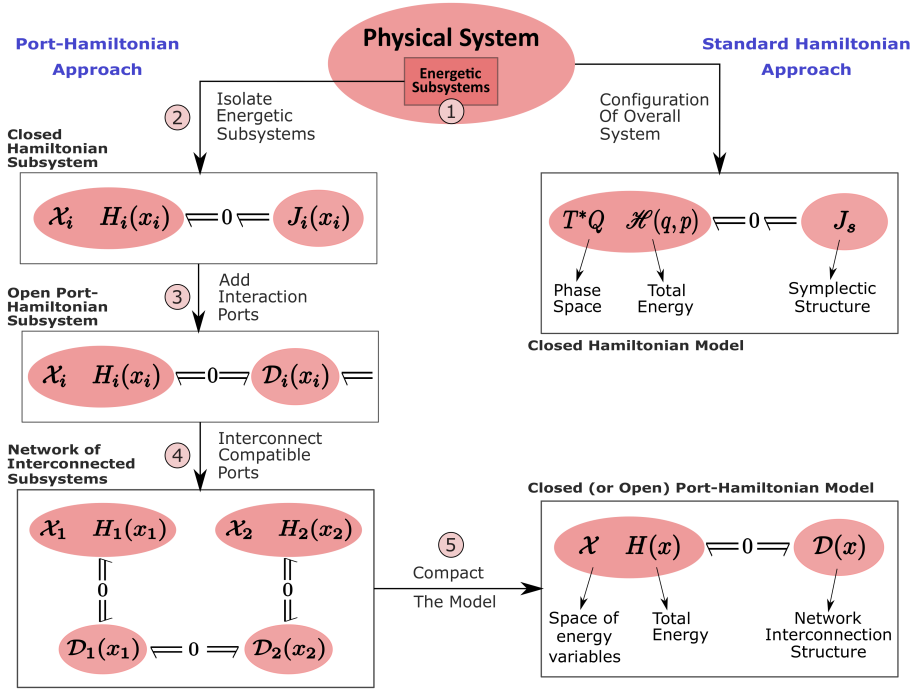


Figure 2.5: Comparison of the bottom-up port-Hamiltonian modeling procedure of a complex physical system compared to the top-down standard Hamiltonian procedure.

Standard Hamiltonian Approach

The standard top-down Hamiltonian approach starts from the concept of a configuration $q \in Q$ representing the degrees of freedom of the overall physical system, as shown in Fig. 2.5. Then, a Lagrangian $\mathcal{L} : TQ \rightarrow \mathbb{R}$, as a function of q and $\dot{q} \in T_q Q$, is defined on the tangent bundle, which is called the velocity phase space. Using the Legendre transformation, the conjugate momentum variable $p := \partial \mathcal{L} / \partial \dot{q} \in T_q^* Q$ can be calculated, and a Hamiltonian $\mathcal{H} : T^*Q \rightarrow \mathbb{R}$ can be constructed on the cotangent bundle T^*Q , referred to as the phase space. The equation of motion governing the dynamical system on the phase space T^*Q are given by the standard Hamiltonian equations (2.23), which are in turn equivalent to the Euler-Lagrange equations on TQ derived from Hamilton's principle of least action. Therefore, as shown in Fig. 2.5, the overall dynamical system is defined by the Hamiltonian \mathcal{H} and the symplectic structure matrix J_s corresponding to the canonical Poisson bracket $\{\cdot, \cdot\}_c$.

Port-Hamiltonian Approach

On the other hand, the bottom-up port-Hamiltonian modeling approach is divided into the following stages, illustrated in Fig. 2.5:

1. **Conceptual tearing:** The starting point for the port-Hamiltonian approach for modeling is a *conceptual tearing* process to the overall physical system, viewing it as a set of interconnected energetic subsystems. The i -th subsystem is characterized by the energy it possess, denoted by $H_i : \mathcal{X}_i \rightarrow \mathbb{R}$. This energy traverses from one subsystem to another through an imaginary boundary dividing both of them. Furthermore, this reasoning can be applied to both lumped-parameter and distributed-parameter systems.
2. **Hamiltonian modeling of isolated energetic subsystems:** After identifying the individual energetic subsystems, one can use the standard Hamiltonian theory at this point to develop a Hamiltonian model for each energetic subsystem *isolated* from the rest of the system. However, the emphasis here is on physical energy variables $x_i \in \mathcal{X}_i$ which do not necessarily correspond to the canonical coordinates of some cotangent bundle. In fact, energy variables that are most physically compelling [Morrison, 1998] or thermodynamically more expressive [Breedveld, 1984] are in general non-canonical. Consequently, the outcome of this stage is a closed Hamiltonian model for each energetic subsystem, defined by the energy function $H_i(x_i)$ and the non-canonical Poisson structure corresponding to $J_i(x_i)$.
3. **Add interaction ports:** The closed Hamiltonian model of each subsystem is now extended to an open port-Hamiltonian model with interaction ports. This corresponds to the port (e_I, f_I) for finite-dimensional systems, and the ports $(e_D, f_D), (e_\partial, f_\partial)$ for infinite-dimensional ones. One then replaces the Poisson structure representing the conservation of H_i by a Dirac structure $\mathcal{D}_i(x_i)$ that allows for non-zero energy exchange via the interaction ports.
4. **Interconnect all energetic subsystems:** The overall physical system is then constructed by interconnecting the different energetic subsystems. This is achieved by specifying the interconnection structure of the open port-Hamiltonian subsystems in the form of constraints on the variables of the interaction ports of each subsystem. For the interconnection to be power consistent, only subsystems with *compatible* interaction ports are interconnected. Additional Dirac structures could be possibly used to resolve incompatibility issues.

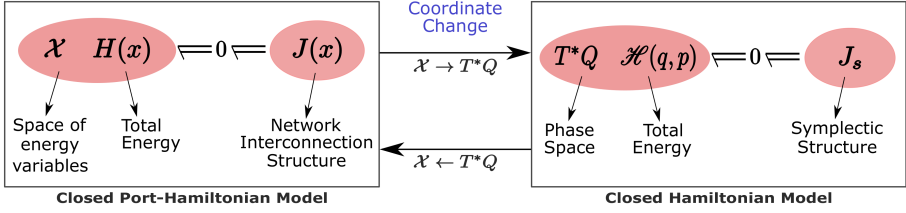


Figure 2.6: Using a coordinate transformation, from the space of energy variables \mathcal{X} to the phase space T^*Q of the overall system, one can link the overall models from the port-Hamiltonian approach to the standard Hamiltonian approach.

5. **Compact the port-Hamiltonian model:** After developing a decomposed model of the physical system in terms of a network of interconnected subsystems, one could (optionally) compact the network into one dynamical system by combining the energy storing elements together and all the Dirac structures into one, denoted by $D(x)$. The compact port-Hamiltonian model would then have a total state space \mathcal{X} and total Hamiltonian $H : \mathcal{X} \rightarrow \mathbb{R}$ given, respectively, by

$$\mathcal{X} := \prod_i \mathcal{X}_i, \quad H(x) := \sum_i H_i(x_i),$$

where $x \in \mathcal{X}$ is the state of the overall system corresponding to the combined energy variables. The compact model could be either a *closed* system, or an *open* one with interaction ports that allows the overall port-Hamiltonian model to be interconnected to its external environment. This concludes the port-Hamiltonian approach modeling procedure.

In case the compact port-Hamiltonian model of the physical system is closed and there are no algebraic constraints on the total state $x \in \mathcal{X}$, one can relate this model to the one derived from the standard Hamiltonian approach, as shown in Fig. 2.6. In such case, the combined Dirac structure $D(x)$ degenerates to a (generalized) Poisson structure represented by $J(x)$. Although the two Hamiltonian functions $H(x)$ and $\mathcal{H}(q, p)$ of the two models correspond to the total energy of the system, the difference lies essentially in the choice of coordinates representing the system. While the standard Hamiltonian approach relies on the canonical coordinates $(q, p) \in T^*Q$ and the canonical Poisson structure J_s , the port-Hamiltonian approach hinges on the (generally) non-canonical energy variables $x \in \mathcal{X}$, and the Poisson structure $J(x)$ which corresponds to the network interconnection structure of the system's energetic components. Using an invertible coordinate transformation from the state space \mathcal{X} to the phase space T^*Q , one can convert from one model to the other.

In conclusion, it is clear from their distinguished strategies in tackling a modeling problem that the port-Hamiltonian framework is fundamentally different from the standard Hamiltonian approach. Unfortunately this unique characteristic of the port-Hamiltonian framework with respect to the classical Hamiltonian framework, known to a broader audience of mathematicians and physicists, is often overseen or underestimated. In the author's opinion, an important reason for this is that this fundamental difference is not well communicated in the port-Hamiltonian literature.

Finally, we conclude by some general remarks.

1. Starting from the port-Hamiltonian approach, one can systematically transform the network and the compact representations of the port-Hamiltonian model to the standard Hamiltonian model. However, starting from the Hamiltonian approach, the opposite transformation is in general not trivial.
2. A significant advantage of the port-Hamiltonian bottom up approach compared to the standard Hamiltonian approach is that, when needed, the overall port-Hamiltonian model can be updated by adding a new subsystem to its open ports without re-deriving the whole dynamical equations.
3. Although the network-based modeling procedure of port-Hamiltonian systems, as described above, is applicable for both lumped-parameter and distributed-parameter systems, it is more popular in the former only. This can be contributed to the fact that the foundational work of distributed port-Hamiltonian theory in [van der Schaft and Maschke, 2002] does not discuss the systematic derivation of the underlying Stokes-Dirac structure and focuses instead on how it generalizes Poisson structures. On the other hand, this approach was clearly highlighted in the foundation work of port-Hamiltonian theory for lumped-parameter systems in the earlier work of Maschke et al. [1992].
4. An immediate benefit in dividing the overall system into isolated energetic subsystems is that one does not have to consider all physical variables of the overall system at once during the Hamiltonian modeling process in stage 2, provided one can separate them. Consequently, this significant step allows one to use the powerful *Hamiltonian reduction theorems*.

2.3 Hamiltonian Reduction

Hamiltonian reduction plays a central role in geometric mechanics and is of great practical significance. It refers to a general process for transforming a

given Hamiltonian system to one of smaller dimension. However, the widely used term reduction is usually misleading since the process does not “actually” reduce the degrees of freedom of the system, but instead allows to exploit the known parts of the system’s dynamics in order to construct solutions in stages [Morrison, 1998]. In this work, Hamiltonian reduction will serve as a tool for systematically deriving the equations of motion of dynamical systems.

Recall that a generalized Hamiltonian system is defined in terms of a Hamiltonian function $H : \mathcal{X} \rightarrow \mathbb{R}$ on a Poisson manifold $(\mathcal{X}, \{\cdot, \cdot\}_{\mathcal{X}})$. The reduction process in its essence is a transformation $\Phi : \mathcal{X} \rightarrow \mathcal{Z}$ applied to the Hamiltonian system. The first part of the reduction, known as kinematic reduction, occurs if one can transform the old Poisson bracket $\{\cdot, \cdot\}_{\mathcal{X}}$ on $C^\infty(\mathcal{X})$ to a new Poisson bracket $\{\cdot, \cdot\}_{\mathcal{Z}}$ on $C^\infty(\mathcal{Z})$ that depends solely on the new coordinates. Similarly, the second part of the reduction, known as dynamic reduction, occurs if the Hamiltonian can be also written in terms of the new coordinates only such that

$$\tilde{H}(z) := H(\Phi(x)) = H(x), \quad \forall x \in \mathcal{X}, z \in \mathcal{Z}.$$

Therefore, the reduction process transforms the Hamiltonian dynamics $(H, \{\cdot, \cdot\}_{\mathcal{X}})$ into $(\tilde{H}, \{\cdot, \cdot\}_{\mathcal{Z}})$.

The transformations that leave the Hamiltonian H invariant are called **symmetries**, which form a group called the **symmetry group** of H , with the group operation being composition of maps. The Hamiltonian reduction theorems formalize the basic idea of the process mentioned above. These general theorems allows one to exploit the symmetries of the Hamiltonian and constants of motion of the system. For an introduction to this sophisticated topic, the reader is referred to [Marsden and Ratiu, 1999; Holm et al., 2009]. In this thesis, we are interested in one specific type of reduction theorems, namely *Lie-Poisson reduction*.

Lie-Poisson Reduction

An important class of dynamical systems are those whose configuration space G has the mathematical structure of a Lie group. This rich class of systems includes dynamics of rigid bodies on the special Euclidean group $SE(3)$ and dynamics of fluid flow on the diffeomorphism group $\mathcal{D}(M)$, which are treated later in Ch.4 and Ch.5, respectively.

Recall that the phase space T^*G of the configuration space G is naturally equipped with a canonical Poisson bracket $\{\cdot, \cdot\}_c$ that defines the Hamiltonian dynamics of the mechanical system for a given Hamiltonian $\mathcal{H} : T^*G \rightarrow \mathbb{R}$. By taking advantage of the Hamiltonian’s symmetries, it is possible to “reduce” the Hamiltonian dynamics of the system from the cotangent bundle T^*G to the dual space \mathfrak{g}^* of either the *left* or *right* Lie algebra \mathfrak{g} corresponding to the Lie group G . The dynamics are reduced to the dual of the left or right Lie algebra

depending on whether \mathcal{H} is *left-invariant* or *right-invariant* with respect to the symmetry transformations, respectively.

Left Lie algebras play an important role in rigid body mechanics while right Lie algebras appear recurrently in general continuum mechanics [Holm et al., 1998; Marsden and Ratiu, 1999]. While the phase space T^*G represents the “material” or “Lagrangian” coordinates of motion of a mechanical system, the dual of the left Lie algebra represents the “body” or “convective” coordinates, and the dual of the right Lie algebra represents the “spatial” or “Eulerian” coordinates of motion.

Remark 2.3.1 (Lie Bracket Sign Convention). Recall that the Lie algebra of G consists of the tangent space $T_e G$ at the identity $e \in G$ equipped with a Lie bracket. One canonical way to construct a Lie bracket for $T_e G$ is by extending the Jacobi-Lie bracket on $\mathfrak{X}_L(G)$, the space of left-invariant vector fields on G . Such Lie bracket is denoted by $[\cdot, \cdot]_L$. Another way is to extend the Jacobi-Lie bracket on $\mathfrak{X}_R(G)$, the space of right-invariant vector fields on G . In this case, the Lie bracket is denoted by $[\cdot, \cdot]_R$.

It can be shown [Marsden and Ratiu, 1999, Pg. 270] that the right and left brackets are related by a minus sign i.e. $[\cdot, \cdot]_R = -[\cdot, \cdot]_L$. Therefore, it is conventional in the literature [Holm et al., 2009, Pg. 316] that the Lie bracket associated to \mathfrak{g} is denoted by $[\cdot, \cdot]_{\mathfrak{g}}$ and chosen to be the one defined by left extension i.e. $[\cdot, \cdot]_{\mathfrak{g}} = [\cdot, \cdot]_L = -[\cdot, \cdot]_R$. Therefore, the left Lie algebra corresponds to the pair $(T_e G, [\cdot, \cdot]_{\mathfrak{g}})$ while the right Lie algebra corresponds to $(T_e G, -[\cdot, \cdot]_{\mathfrak{g}})$.

The Hamiltonian reduction process is achieved using the so called *momentum maps*, which are maps from the phase space T^*G to the dual space \mathfrak{g}^* . The momentum maps are used to derive from the Hamiltonian dynamics on the phase space, defined by $(\mathcal{H}, \{\cdot, \cdot\}_c)$, the **reduced Hamiltonian dynamics**, defined by $(H, \{\cdot, \cdot\}_{\mathfrak{g}^*})$, where

- $H \in C^\infty(\mathfrak{g}^*)$ is the reduced Hamiltonian constructed from the Hamiltonian $\mathcal{H} \in C^\infty(T^*G)$.
- $\{\cdot, \cdot\}_{\mathfrak{g}^*} : C^\infty(\mathfrak{g}^*) \times C^\infty(\mathfrak{g}^*) \rightarrow C^\infty(\mathfrak{g}^*)$ is a reduced Poisson bracket constructed from the canonical Poisson bracket $\{\cdot, \cdot\}_c$.

The reduced Poisson bracket $\{\cdot, \cdot\}_{\mathfrak{g}^*}$ is called the Lie-Poisson bracket and the whole reduction process described above is known as **Lie-Poisson reduction**. For more details, the reader is referred to [Marsden and Ratiu, 1999, Ch.13].

The expressions of the reduced Poisson bracket and the corresponding Hamiltonian dynamical equations depend on whether \mathfrak{g} is a left or right algebra and whether it is finite- or infinite-dimensional.

For the case of a *left finite-dimensional* Lie algebra \mathfrak{g} , the reduced Poisson bracket is defined for any $x \in \mathfrak{g}^*$ and $F, K \in C^\infty(\mathfrak{g}^*)$ by

$$\{F, K\}_{\mathfrak{g}^*}(x) := - \left\langle x \mid [\partial_x F, \partial_x K]_{\mathfrak{g}} \right\rangle_{\mathfrak{g}}, \quad (2.24)$$

where $[\cdot, \cdot]_{\mathfrak{g}} : \mathfrak{g} \times \mathfrak{g} \rightarrow \mathfrak{g}$ denotes the Lie bracket of \mathfrak{g} and $\langle \cdot \mid \cdot \rangle_{\mathfrak{g}} : \mathfrak{g}^* \times \mathfrak{g} \rightarrow \mathbb{R}$ denotes its duality pairing.

Given a Hamiltonian function $H(x)$, the dynamical equations are then expressed by

$$\dot{x} = ad_{\partial_x H}^*(x), \quad (2.25)$$

where for any $\omega \in \mathfrak{g}$, the map $ad_{\omega}^* : \mathfrak{g}^* \rightarrow \mathfrak{g}^*$ is the dual of the adjoint operator $ad_{\omega} : \mathfrak{g} \rightarrow \mathfrak{g}$ defined such that $ad_{\omega}(\cdot) := [\omega, \cdot]_{\mathfrak{g}}$.

For the case of a *right infinite-dimensional* Lie algebra \mathfrak{g} , the reduced Poisson bracket takes the form

$$\{F, K\}_{\mathfrak{g}^*}(x) := \left\langle x \mid [\delta_x F, \delta_x K]_{\mathfrak{g}} \right\rangle_{\mathfrak{g}}, \quad (2.26)$$

where the partial derivatives are replaced by variational derivatives.

Given a Hamiltonian functional $H[x]$, the dynamical equations are now given by

$$\dot{x} = -ad_{\delta_x H}^*(x), \quad (2.27)$$

where in this case, the map ad_{ω}^* is the *formal* dual of the adjoint operator ad_{ω} , i.e. up to a boundary term. As will be discussed in Ch.5, these boundary terms will vanish naturally as a consequence of the skew-symmetry of the structure operator corresponding to the ad_{ω}^* map. The inclusion of these boundary terms will play an important role later in the construction of the Stokes-Dirac structure of the distributed parameter systems considered.

In the less common cases of a *right finite-dimensional* or *left infinite-dimensional* Lie algebra, equations (2.24-2.27) have opposite signs.

Finally, by comparing the form of the Hamiltonian dynamics in (2.25) and (2.27) to the ones in (2.15) and (2.20), one can see that the map given by

$$ad_{(\cdot)}^*(x) : \mathfrak{g} \rightarrow \mathfrak{g}^*,$$

for any $x \in \mathfrak{g}^*$, corresponds (with an additional sign) to the structure matrix $J(x)$ or the structure matrix operator $\mathcal{J}(x)$.

2.4 Conclusion

This chapter has provided the foundations of the port-Hamiltonian paradigm which will be used through the rest of this dissertation for the modeling and

control of interactive aerial robots as motivated in Ch.1. The focus of the chapter was on highlighting two important properties of the port-Hamiltonian paradigm.

The first property is that the port-Hamiltonian framework is capable of handling finite- and infinite-dimensional systems with the same tools and concepts. This is achieved by using appropriate differential geometric tools.

The second property is that the port-Hamiltonian framework extends the standard Hamiltonian framework in a non-trivial way by combining with it the port-based approach for modeling physical systems viewing a complex physical system as the network of energetic subsystems interconnected to each other by power ports in addition to allowing for non-zero change of the system's energy.

These two properties will be demonstrated in subsequent chapters via two case studies to which the port-Hamiltonian theory is applied to. Namely, modeling of rigid body motion and fluid flow on a manifold, treated in Ch.4 and Ch.5, respectively. In these two chapters, we will show how the port-Hamiltonian procedure of Sec. 2.2.2, combined with Hamiltonian reduction theorems and a proper geometric formulation, will lead to a systematic derivation of open port-Hamiltonian models for rigid body motion and fluid flow on a manifold.

CHAPTER 3

TWENTY YEARS OF DISTRIBUTED PORT-HAMILTONIAN SYSTEMS

For the past two decades, the distributed port-Hamiltonian (dpH) systems theory underwent a huge evolution that branched in different directions and is still an active area of research. This chapter reports the results of [Rashad et al., 2020b] which presents a review of the research studies carried out in the past twenty years (approximately) relying on the seminal work of van der Schaft and Maschke [2002].

This chapter highlights the wide applicability of the port-Hamiltonian (pH) framework to complex systems in multi-physical domains. It also highlights one of the key benefits of the pH paradigm which is modeling a wide range of systems in different fields with the same tools and language at all stages, starting from the theoretical modeling to the practical implementation. Moreover, it highlights the main methodologies and techniques developed in the different subfields of pH system theory which helps identifying the existing gaps.

In this work, over a hundred and fifty studies are classified into different classes depending on their respective research focus, as shown in Fig. 3.1. The classes considered include modeling, analysis and control, discretization, theoretical framework, and applications. The first research direction in the literature was in implementing the generic dpH theory for modeling distributed parameter systems in different physical domains. The second direction was the analysis and design of control techniques suitable for pH models by extending the well-established techniques for finite-dimensional pH systems, like energy shaping and damping injection. Another research direction was focused on generating finite dimensional approximations of the dpH models or the

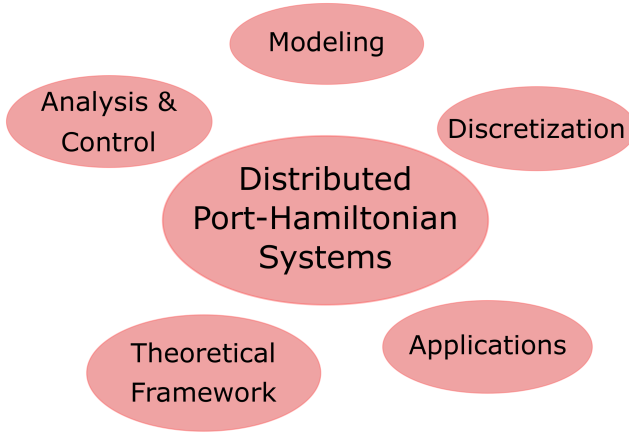


Figure 3.1: The classification of research studies surveyed in this paper.

infinite-dimensional controllers by structure-preserving discretization methods. Furthermore, there has been also a lot of research efforts in different theoretical formulations of pH systems and extensions to the original framework in van der Schaft and Maschke [2002]. Finally, the applications class includes papers that combine other different techniques.

The rest of the chapter is organized as follows: we first start in Sec. 3.1 by a discussion of the class of *theoretical framework* studies in the literature. In Sec. 3.2, we present the *modeling* class which includes the implementation of the framework to a wide range of physical domains. In Sec. 3.3, we present the *analysis and control* class followed by the *discretization* class in Sec. 3.4. Finally, we conclude the chapter and summarize the *applications* class in Sec. 3.5. All the research studies reviewed in this chapter can be accessed through an online bibliographical database¹, classified in their respective groups.

3.1 Theoretical Framework

In this section, we provide an overview of the different formulations of dpH systems introduced in the literature. We recognize and briefly address three main formulations of dpH systems: the *Stokes-Dirac structure approach*, the *functional analytic approach*, and the *jet bundle approach*. Then we present a collection of different results extending these approaches in different directions.

¹<http://dx.doi.org/10.17632/wz6h2xpvg9.1>

3.1.1 Stokes-Dirac Structure Formulation

This formulation of the dpH theory is the one presented in the the foundational work of van der Schaft and Maschke [2002]. In this work, the power-continuous interconnection structure of distributed parameter systems was mathematically modeled by a Stokes-Dirac structure (SDS) denoted by \mathcal{D}_{st} .

For the reader's convenience, we provide a brief summary of the dpH formulation based on a SDS described in Sec. 2.1.2. A non-dissipative distributed port-Hamiltonian system is given by the tuple $(M, \mathcal{X}, H, \mathcal{I}_D, \mathcal{I}_\partial, \mathcal{D}_{st})$, where M is the finite-dimensional manifold representing the spatial domain, with boundary ∂M . The state space \mathcal{X} is composed by a subspace of differential forms over M . The space \mathcal{I}_∂ is a subspace of differential forms over ∂M . Finally $H : \mathcal{X} \rightarrow \mathbb{R}$ is a functional of the state x . The energy storage port of the system is defined by $(\dot{x}, \delta_x H)$, where $\delta_x H$ denotes the variational derivative of the functional H with respect to x . Energy-flow through the boundary into the system is modeled by utilizing Stokes' theorem which defines the boundary port variables $(f_\partial, e_\partial) \in \mathcal{I}_\partial$ used to specify the boundary conditions freely. Distributed port-variables, that allow for energy flow within the spatial domain, can also be included through the interaction port $(f_D, e_D) \in \mathcal{I}_D$.

The implicit pH system dynamics and energy balance are then given by

$$(-\dot{x}, \delta_x H, f_D, e_D, f_\partial, e_\partial) \in \mathcal{D}_{st}, \quad \dot{H} = \int_{\partial M} e_\partial \wedge f_\partial + \int_M e_D \wedge f_D, \quad (3.1)$$

evaluated along solutions $x(t)$ of the system.

After the seminal work of van der Schaft and Maschke [2002] some extensions of dpH formulations were carried out. The work in Macchelli et al. [2004b] was motivated by the need to find a clearer formulation for infinite-dimensional port-Hamiltonian systems, not relying on the definition of the SDS introduced in van der Schaft and Maschke [2002], which was introduced as fundamental building block, but whose generalization for more complex systems was not provided. In particular the definition of a novel class of the SDS was formalized by a proper generalization of constant (i.e. not depending on the state variables) Dirac structures of finite-dimensional pH systems. This has been done by generalizing the matrix operators (representing interconnection, damping and interaction) of finite-dimensional pH systems, to multivariable differential operators suitable for the infinite-dimensional case. The key result is the constructive definition of a SDS starting from a formally skew-adjoint operator acting on vector-valued smooth functions. This represents a further extension with respect to van der Schaft and Maschke [2002] where only scalar-valued smooth functions on the spatial manifold were described as zero differential forms. This generalization is referred to as *multi-variable dpH system* in Macchelli et al. [2004b]. Using Stokes theorem, a linear operator induced on the spatial boundary is formally introduced and depends on the skew-adjoint op-

erator. This operator-based approach has the advantage to describe broader classes of PDEs with respect to the original formulation², e.g. the controversial example of the *heat equation* is described as dpH system in Macchelli et al. [2004b] by introducing a self-adjoint differential operator representing distributed dissipation for the diffusive process.

3.1.2 Functional Analytic Formulation

In what follows, we describe the field that puts together concepts coming from functional analysis and dpH systems. Actually the class of dpH systems that are considered in this framework is very small if compared to the general class presented in van der Schaft and Maschke [2002] and therefore strictly speaking it should not be considered as a separate formulation, but as a subclass. Nevertheless the contributions and the connections with the PDE community have been of such importance and impact, that we consider it valuable to keep this distinction.

The seminal work for this approach is Le Gorrec et al. [2005], which had tremendous impact on the future research and represents one of the most important contributions for dpH systems. The framework introduced in this paper describes the connection between Dirac structures, boundary control systems and skew adjoint-operators using functional analytic tools. This framework would allow to handle rigorously *well-posedness* of the dpH system, in the sense of existence and smoothness of solutions³. In principle this step is necessary to make a control design based on Lyapunov-like arguments, since variations of energy have to be computed *along solutions*, for which these existence and smoothness properties must be known. The price to pay to achieve such a level of mathematical rigour is to diminish dramatically the class of considered systems to linear, one-dimensional spatial domain. The whole approach is based on the definition of the operator \mathcal{J}

$$\mathcal{J}e = \sum_{i=0}^N P(i) \frac{d^i e}{dz^i}(z), \quad z \in [a, b] \quad (3.2)$$

where conditions on matrices $P(i)$ are explicitly assumed in order to make the operator formally skew-adjoint. In this context Dirac structures have been defined on Hilbert spaces and consequently, state variables are not more identified with differential 1-forms as in van der Schaft and Maschke [2002], but with vector-valued L^2 functions. The port variables living on the boundary of

²Nevertheless some systems (e.g. n -dimensional fluid dynamic equation) can not be described by such operator due to their non-constant SDS.

³This is only a rough definition aiming at giving an insight of the problem to the reader. The rigorous definition of well-posedness, often not shared among authors, needs to be carefully addressed in the specific framework that is considered.

the spatial domain (introduced by means of Stokes theorem like in the previous approach) are included in the SDS and parametrized in such a way that the differential operator \mathcal{J} restricted to a proper domain generates a contractive C_0 -semigroup. Consequently a rich description of these systems as boundary control systems was possible, introducing input and output variables as specific linear combinations of state variables restricted on the boundary of the spatial domain. In particular connection to system theoretic properties like *passivity* and more in general *dissipativity* are formalized.

The definition of dpH systems was done by introducing a quadratic energy functional $H(x) = \frac{1}{2}\langle x, \mathcal{L}(z)x \rangle$ with $\mathcal{L}(z)$ a coercive, bounded operator depending in general on the spatial variable z . In this situation the dpH can be abstractly written as

$$\dot{x} = \mathcal{J}\mathcal{L}x, \quad (3.3)$$

with the appropriate boundary conditions. Here the energy function is the norm of a Hilbert space induced by \mathcal{L} itself. The structure of the system led to important results like the possibility of valuating properties which are complex and abstract in principle (e.g. generation of contraction semigroup) by means of simple matrix inequalities and the fact dpH systems of the considered class are dissipative with respect to quadratic supply rates, by considering energy as storage functional. Summarizing, this formulation bridged the more geometric and physical approach started in van der Schaft and Maschke [2002] with a more system and control-theoretic approach.

The contribution after Le Gorrec et al. [2005] grew fast in the relatively small system theoretic community working on the subject. Later in Sec. 3.3, we will briefly go through the main results developed within this formulation in terms of analysis and control.

3.1.3 Jet Bundle Formulation

The SDS formulation of dpH systems in van der Schaft and Maschke [2002] relies on a choice of proper *energy variables* (efforts and flows) such that the Hamiltonian energy density does not depend on their spatial derivatives. However, this choice is not unique at all and in some cases there are convincing arguments that suggest different choices. An important example of this different way of thinking led to a formulation that is based on the jet-bundle structure of the distributed system [Ennsbrunner and Schlacher, 2005; Schöberl and Siuka, 2014]. To give an exhaustive overview of this formulation is out of the scope of this literature review but we briefly highlight the main idea behind this approach, which makes use of differential geometric tools like jet bundles (see e.g. Schlacher [2007] for an introduction to this topic). The main differences between the SDS formulation and the jet-bundle formulation is that in the former differential operators appear in the interconnection map and that

the variational derivative of the Hamiltonian plays a different role. These differences are caused by a different choice of the independent variables for the system, sometimes called *evolutionary variables*, in contrast to the energy variables. This approach bridges theory of dpH systems with classical Hamiltonian field theory developed in physics. A detailed comparison of the two approaches can be found in Schöberl and Siuka [2013] applied on the Mindlin plate as an example. Moreover, the jet-bundle formulation has been extended to second order field theories in Schöberl and Schlacher [2015a,b, 2018].

3.1.4 Theoretical Extensions

There have been many efforts in the past two decades to mathematically explore and extend the fundamental building block in van der Schaft and Maschke [2002] which is the SDS. We briefly list them in this section, for the sake of completeness and in order to provide references for the interested reader.

In Vankerschaver et al. [2010], a method for systematically deriving the SDS for a given system was presented based on symmetry reduction of a canonical Dirac structure on the co-tangent bundle i.e. the unreduced phase space. In Nishida et al. [2008a, 2015], the authors studied an extended SDS with distributed port variables, which makes it a boundary non-integrable structure. Moreover, the authors show that systems with distributed energy flow can be transformed to standard ones, without distributed energy flows. This allows the application of boundary control techniques to the transformed system. The work of Nishida et al. [2008a, 2015] was extended to manifolds with non-trivial topology in Nishida and Maschke [2018].

The pH formulation in van der Schaft and Maschke [2002] was defined on a fixed spatial domain. A relaxation of this assumption for the one-dimensional case was presented in Diagne and Maschke [2013], where the authors studied two systems coupled via a moving boundary interface.

A unified modeling procedure of dpH systems for field equations was presented in Nishida and Yamakita [2005] where a high-order SDS on variational complexes of jet bundles was used. This class of dpH systems is referred to as field port-Lagrangian systems [Nishida and Yamakita, 2005]. It has been shown in Nishida et al. [2006] how field pL systems can be derived systematically from conservation laws with a variational symmetry. Moreover, the authors of Nishida et al. [2006] present a strategy for observing and detecting the breaking of the variational symmetry for field port-Lagrangian systems. The practical significance of such symmetry observer have been discussed in Nishida et al. [2009]. An extension of the work of Nishida et al. [2006] to the case of infinite-dimensional symmetry of bi-Hamiltonian systems can be found in Nishida et al. [2007].

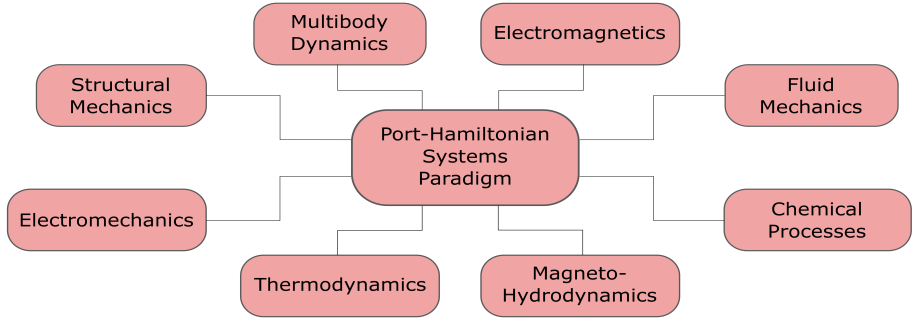


Figure 3.2: The wide variety of physical domains in which the port-Hamiltonian paradigm was applied to in the literature.

3.2 Modeling of Distributed Parameter Systems

There have been many efforts in the pH community for the past two decades to implement the generic dpH framework for modeling distributed-parameter systems in a wide variety of multi-physical domains including mechanical, electrical, magnetic, thermal, and chemical domains, as shown in Fig. 3.2. In this section, we survey the different physical domains of the distributed parameter systems modeled in the pH framework in the literature.

3.2.1 Structural Mechanics

The first class of distributed parameter systems presented is structural mechanical systems with its mechanical energy comprising of kinetic and potential elastic energy. In van der Schaft and Maschke [2002], a model of a vibrating string was presented with the energy variables chosen as the strain and momentum. The underlying SDS of the model was a canonical one with the exterior derivative describing effort-flow relations. In the case of higher-order models like that of the Euler-Bernoulli [Nishida and Yamakita, 2004] or the Timoshenko beam [Macchelli and Melchiorri, 2004], the underlying SDS of the model describes high-order effort-flow differential-relations. The extended structures consist of compositions of the exterior derivative and the Hodge star operator. In Brugnoli et al. [2019a,b] a formulation of the thick plates (using respectively Midlin and Kirchhoff models) that employs tensor variables is given for a coordinate-free pH description. Nonlinear phenomena can be easily incorporated in the framework through the constitutive relations, as in Trivedi et al. [2016], where a nonlinear Euler-Bernoulli beam model was presented including two-dimensional stress-strain relations modeling large deflections of the beam. Another approach for modeling planar beams with large deformations

is the work of Golo et al. [2003], in which screw theory was used. Under the assumption of small deviations around an equilibrium configuration, the longitudinal part of the developed dpH model in Golo et al. [2003] is shown to correspond to the rod equation, while the transversal part corresponds to the Timoshenko beam model. The work of Golo et al. [2003] was extended in Macchelli et al. [2006, 2007a] to describe flexible links with one-dimensional spatial domain deforming in three-dimensional space, where gravity was also included through the use of a distributed port. In Heidari and Zwart [2019] two different port-Hamiltonian models for studying longitudinal vibrations in a nanorod are provided.

In the context of mixed pH systems, i.e. systems merging from the interconnection of finite- and infinite-dimensional pH systems, an inverted pendulum on a cart was modeled in Trivedi et al. [2011], in which the pendulum was described by a flexible beam with a tip mass. Moreover, the work of Macchelli et al. [2007a] was extended to the case of a complete complex multi-body system in Macchelli et al. [2009] with both rigid and flexible links connected through kinematic pairs. An example of such systems is a robot manipulator with flexible links. Along the same line, a simplified model for a rotating flexible spacecraft was presented in Aoues et al. [2017], where the model consists of a center rigid hub, two flexible (Euler-Bernoulli) beams each connected to a tip mass. Finally, in Ramirez et al. [2013], an underactuated simplified model for a flexible nano-gripper for DNA manipulation was presented. The model comprised of a flexible (Timoshenko) beam connected to a network of mass-spring-dampers modeling the DNA bundle, suspension, and actuation mechanisms.

Several pH models of mechanical systems have been also presented using the jet-bundle formalism including the Euler-Bernoulli beam [Schöberl and Schlacher, 2015a], Kirchhoff plate [Schöberl and Schlacher, 2015a, 2018], Timoshenko beam [Schöberl and Siuka, 2014], and Mindlin plate [Schöberl and Siuka, 2013; Schöberl and Schlacher, 2015b].

3.2.2 Electro-Mechanics

The second class of infinite-dimensional systems presented is electro-mechanical systems which consists of two different physical domains interacting with each other in addition to mechanical and electrical ports defined on the boundary of the domain. In Macchelli et al. [2004a], the dynamics of a piezoelectric material, connected to a flexible beam, is modeled with the assumptions of quasi-static electric field, linear behavior and negligible thermal effects. Under the same assumptions, another model of the piezoelectric dynamics has been presented in Schöberl et al. [2008] using jet variables. An extended model for a piezoelectric Timoshenko beam has been studied in Voß and Scherpen [2014] which can represent nonlinear beam deformations as well as dynamic electric fields. The

model studied was used to describe inflatable space structures. Another type of electro-mechanical system that was studied is the Ionic Polymer-Metal Composite [Nishida et al., 2008b, 2011], which is a type of electro-active polymer consisting of a mechanical flexible beam with large deformations in addition to an electric double layer of polymer and metal electrodes. The mechanical and electric parts are coupled through electro-stress diffusion. The presented model incorporated the inherent nonlinearities as well as the multi-spatial-scale structure of the system. A very original example of mixed finite/infinite-dimensional pH description of an electro-mechanical system is present in Falaize and H  lie [2017] where a *Rhodes Piano* is modeled and simulated.

3.2.3 Fluid Mechanics

Fluid-dynamical systems equations are characterized by two conservation laws; the balance of mass and momentum of the fluid. Several models of fluid-dynamical systems have been studied in the literature. The shallow-water equations (*aka* Saint-Venant equations) have been used in Pasumarthy and van der Schaft [2006b]; Hamroun et al. [2006] for the (one-dimensional) modeling of open-channel irrigation systems. An extended model is presented in Hamroun et al. [2007] to include interconnected reaches with slopes and bed frictions. In one of the earliest work on distributed pH systems, the dynamics of an three-dimensional compressible inviscid isentropic fluid was presented in van der Schaft and Maschke [2001]. The same results were also included in the original paper of van der Schaft and Maschke [2002] with the energy variables chosen as the mass density and Eulerian velocity field. The SDS describing the system is nonlinear, however it was also shown that for irrotational flow, the underlying SDS becomes the canonical one. An extended model describing the case of non-isentropic fluids is presented in Polner and van der Vegt [2014] in terms of the vorticity-dilatation variables. Moreover for the spatial one-dimensional case, different pH models of fluid-thermal equations can be found in Lopezlena and Scherpen [2004b], a dpH of Navier Stokes equations for reactive flows can be found in Altmann and Schulze [2017], while jet-bundle formulations of the Kortweg-de Vries and Boussinesq equations can be found in Maschke and van der Schaft [2013].

Some work on fluid-structure interaction has also been conducted in the dpH framework. In Lequeurre and Tucsna  k [2015], the one-dimensional Navier-Stokes equation is coupled with a point mass to describe a simplified model of a gas/piston system. Moreover, in Cardoso-Ribeiro et al. [2017], the shallow water equations in a moving tank are coupled to a flexible beam with piezo-electric actuators. The whole setup is a model for the fuel sloshing in a tank connected to very flexible wings in aeronautical applications.

3.2.4 Magneto-Hydrodynamics

Magneto-hydrodynamical systems are ones in which the fluid's magnetic behavior and electrical conductance is considered. Examples of such systems include electrolytes, liquid metals, and plasmas. Such systems comprise of two physical domains interacting together, i.e. electromagnetism, governed by Maxwell equations, and fluid mechanics, governed by Euler equations of ideal isentropic fluids. The coupling term is a function of the free current density and the magnetic field induction. pH models of the magneto-hydrodynamics equations based on the jet-bundle formalism can be found in Siuka et al. [2010]; Nishida and Sakamoto [2010]. Moreover, if the fluid thermal behavior is taken into consideration, then such models are called thermo-magneto-hydrodynamical systems. Several research studies have been conducted in Vu et al. [2012]; Vu and Lefèvre [2013]; Vu et al. [2016] for pH modeling of plasma in nuclear fusion reactors. The work has also been extended in Vincent et al. [2017] for modeling burning plasma models.

3.2.5 Chemical Processes

The dpH formalism was also applied to the modeling of chemical processes in which heat and mass transport occurs along with chemical reactions. In Eberard and Maschke [2004], the dpH framework was extended to include irreversible thermodynamic processes. Then in Eberard et al. [2005], the diffusion process in a heterogeneous mixture is modeled, with an example of the pressure swing adsorption process.

In Baaij et al. [2009a], the heat and mass transport phenomena with multiscale coupling is modeled. The hydrodynamics of the fluid is not modeled explicitly but is handled by the introduction of a moving reference frame. Several studies have been also devoted for reaction-diffusion systems in which there is coupling between mass transport and chemical reactions. Different pH models can be found in Zhou et al. [2012, 2015, 2017]; Šešljica et al. [2010, 2014b]. A different way to model multi-scale systems stemming from the combination of hyperbolic and diffusive processes is studied in Le Gorrec and Matignon [2013], where fractional integrals and derivatives are used.

3.3 Analysis and Control of Distributed Parameter Systems

In this section, we summarize the main control techniques that have been developed for dpH systems. As a preamble, it is worth mentioning that when dealing with infinite-dimensional systems, some intrinsic difficulties arise in the proofs of stability of equilibria. This is mainly due to the fact that all norms

are not equivalent in infinite-dimensional spaces. Thus in principle, a norm has to be chosen in the specific stability argument [Jacob and Zwart, 2012].

The primary contribution of an infinite-dimensional pH model is not to resolve the aforementioned issues, which are intrinsic in general distributed parameter systems, but rather to provide a physical understanding of the system to be controlled. Normally, the Hamiltonian energy appearing in the system is a good choice for a Lyapunov functional, which can be used for designing the control law in a more intuitive way. The control techniques developed in this context aim at generalizing the procedures of *energy shaping* and *damping injection* established for finite-dimensional pH systems within the *control by interconnection* paradigm, which is discussed next.

3.3.1 Extension of Control by Interconnection

In Macchelli and Melchiorri [2004], the damping injection technique is applied to the dpH Timoshenko model to stabilize the beam both at the distributed and boundary ports. In the same work, control by interconnection to perform energy shaping of the beam is extended to the infinite-dimensional case following the ideas presented in Rodriguez et al. [2001]. This has been done by introducing a finite-dimensional controller and a tip mass on the extremities of the beam and generalizing the concept of Casimir functions for the resulting closed-loop system. In the same spirit as in Macchelli and Melchiorri [2004], the dpH model and damping injection control is performed to the two-dimensional case of the Mildlin plate in Macchelli et al. [2005a].

In Macchelli and Melchiorri [2005], control by interconnection was formalized for a class of mixed pH systems, in the sense of a power conserving interconnection between an infinite-dimensional system, "sandwiched" between two finite-dimensional ones, all of them in pH form. The control by interconnection by means of Casimir generation has been extended to this class of systems, allowing for a structural state feedback law able to shift the equilibrium of the closed-loop system if appropriate conditions on the Casimirs are fulfilled. In Macchelli et al. [2005b], the same idea was applied for closed-loop systems consisting on the interconnection of two systems only, one finite-dimensional and the other distributed. A related work is Pasumarthu and van der Schaft [2005] where only one-dimensional systems are considered. In Pasumarthu and van der Schaft [2007] the problem of characterizing achievable Casimirs is analysed for systems merging from the interconnection of finite-dimensional systems at the boundary of infinite-dimensional ones. Distributed and boundary dissipation are included in the analysis which is substantially limited to one-dimensional spatial domain dpH systems in which the SDS is defined on the space of differential forms. An attempt to tackle the two-dimensional case has been done in Macchelli et al. [2015b] where control by interconnection has been applied on dpH systems with rectangular spatial domains.

3.3.2 Control Design Based on Spatial Discretization

Another control approach is to take advantage of the spatial discretization algorithms for dpH systems and design the regulator on the basis of the finite-dimensional approximation. This has been the strategy in Macchelli and Melchiorri [2009]; Macchelli and Melchiorri [2010]; Macchelli [2011, 2012b] where the Casimirs for the closed-loop system were chosen on the basis of the finite-dimensional closed-loop approximation and where the connection with the corresponding infinite-dimensional Casimirs is studied. In Kotyczka [2014]; Kotyczka and Brandst [2014], the feedforward control problem is studied for spatially discretized dpH systems consisting in hyperbolic systems of two conservation laws. The obtained results rely on the explicit expression of the inverse dynamics, which is available since the discretized system of the considered class possesses a non zero feedthrough term. In Toledo et al. [2019], an observer-based controller is designed on the basis of a spatial discretization of a dpH system in the form (3.4) in such a way that it stabilizes the infinite-dimensional system as well, avoiding spillover effects. In Cardoso-Ribeiro et al. [2019], the nonlinear 2D shallow water equations are discretized and controlled at the boundary. The problem is tackled after a reduction to a one-dimensional system performed by means of symmetry conditions and use of polar coordinates.

3.3.3 Other Control Methods

In Schöberl and Siuka [2011]; Schöberl and Siuka [2013]; Rams and Schöberl [2017]; Malzer et al. [2019], control by interconnection in terms of Casimir generation is analysed in the context of dpH systems described using the jet bundle formulation and not using skew-adjoint operators. In Nishida et al. [2013], optimal control for dpH systems has been used to derive passivity based control laws in a differential geometric setting. A numerical algorithm is then proposed to control a flexible beam with large deformations. In Macchelli [2016a]; Kosaraju et al. [2017], a Brayton-Moser formulation is given for the dpH systems in the form (3.4) and a boundary control algorithms is proposed to shape the mixed-potential function to overcome the dissipation obstacle. In Trenchant et al. [2017b]; Trang Vu et al. [2017], control by structural invariant is extended to shape not only the energy of the closed-loop system, but also its structure. It is shown how a one-dimensional hyperbolic dpH system of two conservation laws can be shaped in a parabolic one. A similar idea was followed in Vu et al. [2017a], where the IDA-PBC synthesis is explicitly addressed for a dpH system with spatial symmetries.

3.3.4 Interpretation as Boundary Control Systems

The following contributions rely on the functional analytic formulation of Le Gorrec et al. [2005]. It is important to realize that the machinery connecting dpH systems and boundary control systems was not yet available at the time at which some of the previously listed control techniques were introduced. As a consequence, in the first works extending control by interconnection to dpH systems, the closed-loop system merging from the designed controller is "solution free" [Macchelli and Melchiorri, 2004], in the sense that existence of trajectories of the closed-loop system was not addressed. This does not take away importance to these works, that in principle can be applied to more general systems than those for which exhaustive functional analysis has been applied on later.

As previously mentioned, the functional-analytic framework is characterized by the following trade-off: the control design gained more rigorously in the sense that existence of solutions for closed-loop the system is addressed explicitly with a dramatic decrease of the class of systems that are considered. In fact, beside some minor variations, the plants on which controllers have been designed are substantially represented by the PDE (3.4). An isolated exception is represented by the work of Kurula and Zwart [2015], where well-posedness of the linear wave equation is studied in an n -dimensional spatial domain. It is important to cite Le Gorrec et al. [2006], where distributed dissipation was added to the framework by means of a symmetric operator.

The work on stabilization of dpH systems by means of finite-dimensional boundary controllers started in Villegas et al. [2005], where *asymptotic* stability results based on static and dynamic feedback of boundary control systems considered in Le Gorrec et al. [2005] were carried out by means of frequency based arguments. It started to be clear that by restricting the class of systems described by the differential operator (3.2) to the case $N = 1$ technical issues necessary for stability were automatically satisfied, leading to the definition of the abstract class of linear dpH systems, on one-dimensional spatial domains, given by

$$\dot{x} = P_1 \frac{\partial}{\partial z} (\mathcal{L}(z)x) + (P_0 - G_0) \mathcal{L}(z)x, \quad (3.4)$$

with P_1 and G_0 being symmetric matrices and P_0 skew-symmetric. Here $z \in [a, b]$ and x lives in the functional space equivalent to $L^2([a, b], \mathbb{R}^n)$ endowed with the inner product that makes its induced norm equal to twice the energy functional. It is clear that the names P_1, P_0 derive from the indices of the truncated series in (3.2) and G_0 is the operator describing distributed dissipation.

In the PhD thesis of Villegas [2007], a great number of results in terms of stability and stabilization have been formalized for systems in form (3.3)-(3.4). Many arguments highlighting the difficulty of extending the functional analytic

approach to higher dimensional spatial domains are present in Villegas [2007]. The key result in Villegas et al. [2009] provided an *exponential* stability argument for boundary control systems in pH form (3.4) by means of adding dissipation on the boundary of the spatial domain. This result has been of great importance since it provided a practical check to evaluate exponential stability and was instrumental for future stabilizability results. In Zwart et al. [2009], results on well-posedness of systems in the form (3.4) are carried out even for the case in which the autonomous system does not generate a contraction semigroup. At this point the richness of the framework was enough to publish the monograph Jacob and Zwart [2012], where the important results for systems (3.4) were collected and developed.

Further important research involving exponential stabilization of boundary control systems in pH form is present in Ramirez et al. [2014], where the methodology developed in Villegas et al. [2009] has been used to study stabilizability of (3.4) by means of finite-dimensional boundary controllers, considered to be finite-dimensional pH systems with non zero feedthrough term. It is worth mentioning that practically every result in stabilizability of systems in form (3.3) or (3.4) make the assumption of a particular input-output parametrization, e.g. impedance passivity [Le Gorrec et al., 2005]. In Macchelli and Califano [2018], the results are extended to any possible parametrization introduced in Le Gorrec et al. [2005] such that the autonomous boundary control systems generates a contraction semigroup and consequently the supply rate can assume any quadratic form of the input-output pair. Here the finite-dimensional controllers are assumed to be general linear-time-invariant systems, and not more in pH form, in order to deal with general supply rates. This result has been instrumental to handle more general systems of coupled PDEs and ODEs and as result *repetitive control systems* [Califano et al., 2017; Macchelli and Califano, 2018] have been cast in this rigorous framework to derive novel stability conditions. In Jacob and Zwart [2018], the operator based analysis to dpH systems is extended to address control theoretic properties like *controllability* and *input-to-state stability*. It is also important to cite the PhD thesis of Augner [2018], where some stability results for the second order case are present.

Several research efforts in the literature focused on interconnecting linear dpH systems with nonlinear controllers, ending up with the difficult task of handling a nonlinear, infinite-dimensional closed-loop systems. This scenario is particularly challenging and only few recent results are present in terms of well-posedness and stabilization. In particular in Ramirez et al. [2017a], a class of nonlinear passive systems stabilizing first asymptotically and then exponentially dpH in form (3.4) is presented. This work has inspired Califano et al. [2018], where stability analysis for nonlinear repetitive control schemes has been performed for a class of systems, subsequently extended in Califano and

Macchelli [2019]. In Augner [2018], a nonlinear semigroup approach is used to prove exponential stability of dpH systems by means of nonlinear dissipative feedback. In Hastir et al. [2019], a different approach is used to study the interconnection of infinite-dimensional linear systems interconnected with a static nonlinearity. The result can be applied in this framework to show well-posedness of a vibrating string in pH form with a nonlinear damper at the boundary.

Many research efforts focused on re-investigating “Casimir generation” for systems in the form (3.4) in order to properly address well-posedness (i.e. existence and smoothness of solutions) for the closed-loop system. In Macchelli [2012a], control by interconnection by means of Casimir generation is revisited in this framework without dissipation (i.e. $G_0 = 0$ in (3.4)) where the closed-loop system merges from the interconnection of the dpH and a finite-dimensional boundary regulator in pH form. Conditions for existence of Casimirs and asymptotic stability conditions are given. In Macchelli [2014, 2013], the class of stabilising controllers has been enlarged by relying on the parametrisation of the system dynamics provided by the image representation of the SDS to overcome the *dissipation obstacle*, i.e. the problem of steering a dynamical system in a state that dissipates energy. In this way the boundary control is not generated implicitly by means of Casimirs of the closed-loop system but directly as feedback control law. The methodology is applied to the whole class of (3.4) in Macchelli et al. [2015a]. In Macchelli [2015], the dissipation obstacle is overcome in a different way: by defining a new passive output and applying control by interconnection to the new input-output pair of the dpH system it was shown how to overcome the dissipation obstacle by means of Casimir generation for the new closed-loop-system. In Le Gorrec et al. [2014], asymptotic stability for (3.4) is proven by means of a boundary finite-dimensional pH controller and Casimir generation for the closed-loop system. The methodology is applied to a nanotweezer DNA-manipulation device. In Macchelli [2016b], the control by interconnection paradigm is augmented with an output feedback control loop providing exponential stability of the closed-loop system of the internally shaped equilibrium.

An important contribution summarizing the ideas about boundary control laws for (3.4) is Macchelli et al. [2017b], where Casimir generation, state feedback control laws able to overcome dissipation obstacle, and asymptotic stabilization with damping injection are extensively addressed. In Ramirez et al. [2017b], a backstepping boundary controller is designed for a simple one-dimensional hyperbolic lossless dpH system, showing that pH structure is able to simplify the control design process for a target system with dissipation. In Macchelli et al. [2017a], the same idea to map system (3.4) into a target one is explored through a proper coordinate transformation preserving the Hamiltonian structure.

Table 3.1: Structure-preserving discretization methods for port-Hamiltonian systems.

Discretization Method	References
Finite Element	Golo et al. [2002]; Talasila et al. [2002]; Golo et al. [2004]; Baaiu et al. [2006]; Bassi et al. [2007]; Baaiu et al. [2009b]; Eberard et al. [2007]; Macchelli et al. [2007b]; Voß and Weiland [2011]; Pasumarthu et al. [2012]; Wu et al. [2015],
Finite Difference	Lopezlena and Scherpen [2004a], Trenchant et al. [2018a], Trenchant et al. [2017a], Trenchant et al. [2018b]
Finite Volume	Kotyczka [2016], Serhani et al. [2018]
Partitioned Finite Element	Cardoso-Ribeiro et al. [2018], Serhani et al. [2019c], Serhani et al. [2019b], Serhani et al. [2019a]
Pseudo-spectral	Harkort and Deutscher [2012], Moulla et al. [2011], Moulla et al. [2012], Vu et al. [2013a], Vu et al. [2017b]
Discrete Exterior Calculus	Kotyczka et al. [2018], Šešlija et al. [2011], Šešlija et al. [2014a], Šešlija et al. [2012]

3.4 Discretization of Distributed Parameter Systems

For numerical simulation and control synthesis, it is necessary to have finite approximations of the infinite-dimensional pH system models or infinite-dimensional controllers discussed earlier. These finite-dimensional approximations should maintain the "openness" property to be able to interconnect it via its ports to other systems. The conventional numerical algorithms emanating from the numerical analysis field fail to preserve the intrinsic pH system structure and properties, such as passivity, symplecticity, and conservation laws [Šešlija et al., 2012].

This has motivated research for the past two decades in developing structure-preserving discretization techniques of dpH systems, summarized in Table 3.1. These methods, similar to traditional ones, are based either on the approximation of equations or the approximation of solutions [Baaiu et al., 2009b]. The first category includes finite-differences methods and finite-volume methods, while the second category includes weighted residual methods and finite-element methods.

One of the earliest works in structure-preserving discretization techniques was the work of Golo et al. [2002, 2003, 2004] where a mixed finite-elements method was presented. The method of Golo et al. [2004] considered the approximation of the differential forms by Whitney forms. The method was used to discretize the telegrapher's equation [Golo et al., 2002], wave equation [Golo et al., 2003], chemical adsorption column [Baaiu et al., 2006], Maxwell's equations [Eberard et al., 2007], and a vibro-acoustic system [Wu et al., 2015].

The work of Golo et al. [2004] was extended to the case of a non-constant SDS in Pasumorthy and van der Schaft [2006a]; Pasumorthy et al. [2012] for the shallow water equations, and extended to irreversible pH systems in Baaiu et al. [2009b]; Voß and Weiland [2011]. Another method that was inspired by Golo et al. [2004] is Bassi et al. [2007] which was formulated for the functional analytic formulation of pH systems discussed in Sec. 3.1.2. The algorithm described in Bassi et al. [2007] was implemented in Macchelli et al. [2007b] for a flexible link.

Structure-preserving discretization methods based on finite differences and finite volumes have also been presented in the literature. In Clemente-Gallardo et al. [2002]; Lopezlena and Scherpen [2004a], a method based on discretizing the spatial domain into a grid of nodes where finite differences are used to approximate the differential form variables of the pH system. A drawback of this method, unlike the method of Golo et al. [2004], is that only uniform grids can be used. This problem was avoided in Trenchant et al. [2017a, 2018b] by using staggered-grids finite differences thus allowing the use of different grids. Rectangular grids have been used in Trenchant et al. [2017a] while cylindrical grids have been used in Trenchant et al. [2018a]. A finite-volume scheme based on the generalized leapfrog method has been introduced for one-dimensional systems in Kotyczka [2016] and extended to two-dimensional systems in Serhani et al. [2018].

A promising and very recent structure-preserving numerical method is the *Partitioned Finite Element Method* (PFEM). It has been introduced in Cardoso-Ribeiro et al. [2018], developed in Serhani et al. [2019c,b,a] and successfully applied for discretization and simulation of thick plate models in the already referred papers Brugnoli et al. [2019a,b]. The method consists in rewriting the system in a weak-form where only some of the equations are integrated by parts. As consequence the SDS and the constitutive equations are discretized separately, preserving the power balance of the open system (including boundary control and observation) at the discrete level.

Another class of discretization methods that has been used in the literature includes pseudo-spectral methods, which can be considered a generalization of mixed finite element methods when low-order polynomials are used for approximation. In Moulla et al. [2011] a method based on polynomial approximation bases, with Lagrange interpolation, is introduced and used to discretize the

Table 3.2: Application research papers combining different aspects of the pH framework. The aspects include Modeling, Discretization, Control, and Experimental Validation.

	Modeling	Discretization	Control	Experiment
Banavar and Dey [2010]	✓		✓	
Hamroun et al. [2010]	✓	✓	✓	✓
Siuka et al. [2011]	✓		✓	
Voß and Weiland [2011]	✓	✓	✓	
Nishida et al. [2012]	✓		✓	✓
Ramirez et al. [2013]	✓		✓	
Vu et al. [2013b]	✓	✓	✓	
Šešljija et al. [2014b]	✓	✓		
Kotyczka and Blancato [2015]	✓	✓	✓	
Trenchant et al. [2015]	✓		✓	
Trivedi et al. [2016]	✓	✓		
Aoues et al. [2017]	✓		✓	✓
Cardoso-Ribeiro et al. [2017]	✓	✓	✓	✓
Brugnoli et al. [2019a,b]	✓	✓		

lossless transmission line [Moulla et al., 2011] and the shallow water equations [Moulla et al., 2012]. The aforementioned method was extended in Vu et al. [2013a, 2017b] using Bessel function bases and applied to a one-dimensional Tokamak model. Another pseudo-spectral method was introduced in Harkort and Deutscher [2012] using a generalized Galerkin projection method for discretizing linear pH systems in the functional analytic approach.

A natural approach to the structure-preserving discretization of pH systems is to mirror the continuous exterior calculus formulation using *discrete exterior calculus*. The framework replaces the smooth structures in exterior calculus by their discrete analogues, e.g. replacing the smooth manifold by a simplicial complex and replacing the differential forms by co-chains. The conventional discrete exterior calculus methods were extended from the Hamiltonian setting to the port-Hamiltonian setting in the work of Šešljija et al. [2011, 2012] in an algebraic topology setting. The main results of Šešljija et al. [2011, 2012] have been made more accessible in Šešljija et al. [2014a] by being rewritten in matrix representations instead of the algebraic topology nomenclature. A closely-related work to the discrete exterior calculus formulation is Kotyczka et al. [2018] which was based on the weak-form of the SDS of the pH system.

3.5 Conclusion

In this survey paper we reviewed the topic of distributed port-Hamiltonian systems that started about 20 years ago. We analyzed and classified over 150

studies that we considered relevant. Our pedagogical classification is based on conceptual approaches and not on chronological order. The aim of this review is to help researchers in consulting and examining relevant references, and also in understanding the conceptual backbone of the topic, together with their variations. This manuscript highlights the fact that the distributed port-Hamiltonian framework provides a deep understanding of the different multiphysical natural phenomena by explicitly separating energetic and interconnection properties of the system.

One of the key benefits of the port-Hamiltonian framework is the unified language and conceptual insight that can be applied for the synthesis of a distributed parameter system; namely the modeling, discretization, analysis, and control, in addition that these powerful techniques are directly usable at the practical level. Table 3.2 lists the research studies that applied the distributed port-Hamiltonian framework through the combination of the aforementioned steps. Taking into consideration also that the pH framework can incorporate both finite and infinite dimensional systems in a similar manner conceptually, we believe this framework to be very fruitful in the near future.

CHAPTER 4

PORT-HAMILTONIAN MODELING OF RIGID BODY MOTION

The study of rigid body modeling is central to the mathematical theories of robotics. The topic of rigid bodies is a recurrent theme for serial and parallel rigid manipulators as well as for ground, underwater, and aerial mobile robots. In this chapter, we consider the problem of modeling rigid body motion in the port-Hamiltonian framework.

The purpose of the port-Hamiltonian modeling of rigid body motion in this chapter is threefold. First, it serves as a case study for the general port-Hamiltonian modeling procedure described in Ch.2. Second, the derived open port-Hamiltonian model will be used for designing control algorithms for aerial physical interaction using a flying-end effector. Third, the model also serves as a building block that could be interconnected to other subsystems to compose more complex port-Hamiltonian models, e.g. fluid-structure interaction.

In this work, we follow the Lie group approach for describing rigid body kinematics. The configuration space of a rigid body is the group of proper isometries of Euclidean spaces, known as the special Euclidean group $SE(3)$. This group is indeed special and significant as evident in this quote by J. M. Selig. [Selig, 2004] “This group is perhaps the most important one for robotics”.

Instead of starting immediately by postulating $SE(3)$ as the configuration space for a rigid body, we take the long route of introducing many concepts first abstractly in a coordinate-free manner, following the approach of [Stramigioli, 2001]. This coordinate-free treatment will clarify many assumptions that are hidden and usually forgotten in coordinate-based representations. This will be achieved by 1) clearly differentiating between the abstract coordinate descrip-

tion of rigid body motion and its coordinate representation using matrices, and 2) highlighting the mathematical nature of the different maps and spaces that arise when describing rigid bodies.

After describing rigid body kinematics geometrically on $SE(3)$, we approach the dynamic modeling problem in the port-Hamiltonian framework. We demonstrate how to apply the procedure described in Ch.2 combined with the Lie-Poisson reduction method for constructing a port-Hamiltonian model for a rigid body. The procedure will cover all stages starting from a conceptual tearing process of rigid body motion into energetic subsystems and ending by an open compact port-Hamiltonian model.

This chapter is organized as follows: In Sec. 4.1, we start by an introduction to the geometric formulation for describing kinematics of rigid body motion, explicating the Lie group structure of $SE(3)$. Then, in Sec. 4.2, we address the port-Hamiltonian modeling procedure of a rigid body starting by modeling its kinetic energy and gravitational potential energy separated from each other, and then combined together. Finally, we conclude this chapter in Sec. 4.3.

4.1 Geometric Formulation of Rigid Body Kinematics

In this section we present the kinematics of a rigid body in a geometric manner using the matrix Lie group approach. As motivated in the introduction of this chapter, we first introduce the abstract concepts related to a rigid body in a coordinate-free manner, followed by its coordinate-based description. The aim of the presented material is to deductively identify how $SE(3)$ is the configuration space of a rigid body.

The interesting feature of $SE(3)$ is that being a manifold as well as a group, it becomes a Lie group. Locally, $SE(3)$ looks like Euclidean space \mathbb{R}^n , but globally it is not isomorphic to \mathbb{R}^n and thus does not have a vector space structure. Therefore, it requires different tools to perform calculus on it. In addition, the rich structure of $SE(3)$ as a matrix Lie group allows us to study rigid body motion using its matrix Lie algebra $\mathfrak{se}(3)$, which will play a central role in the development of a decomposed port-Hamiltonian model.

4.1.1 Coordinate-free Formulation of the Configuration Space

The abstract coordinate-free treatment in what follows is based on the work of Stramigioli [2001] which goes in more depth starting from concepts of projective geometry. This section can be considered a summary of the main points mentioned in Stramigioli [2001], where our starting point will be from the concept

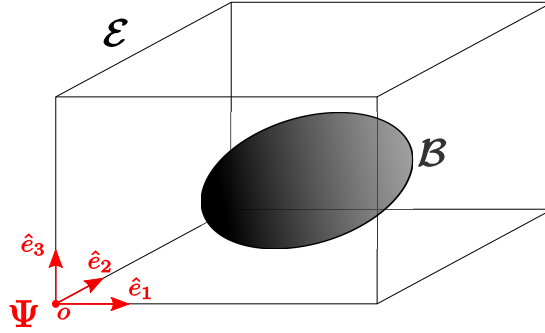


Figure 4.1: An example of a rigid body \mathcal{B} , an Euclidean space \mathcal{E} , and its associated coordinate frame Ψ .

of Euclidean space.

An n -dimensional Euclidean space, denoted by \mathcal{E} , is intuitively an abstraction of the physical space we are living in, and will be the fundamental mathematical structure postulated. Associated to \mathcal{E} is a vector space \mathcal{E}_* equipped with an inner product $\langle\langle, \rangle\rangle : \mathcal{E}_* \times \mathcal{E}_* \rightarrow \mathbb{R}$. Elements of \mathcal{E} are called points and denoted by $p \in \mathcal{E}$, while elements of \mathcal{E}_* are called free vectors, or translation vectors, denoted by $v \in \mathcal{E}_*$. Mathematically, the Euclidean space \mathcal{E} has the structure of oriented metric space that is equipped with 1) a metric $d : \mathcal{E} \times \mathcal{E} \rightarrow \mathbb{R}^+$ defining the distance between any 2 points in \mathcal{E} , 2) an n -form $\Omega : \mathcal{E}_* \times \cdots \times \mathcal{E}_* \rightarrow \mathbb{R}$ specifying the orientation of the space. Intuitively in 2D, Ω allows one to say when a cycle in \mathcal{E} goes around clockwise or counterclockwise, whereas in 3D Ω defines when a figure is left-handed or right-handed.

The abstract space \mathcal{E} is to be distinguished from a specific example of it which is the real n -space \mathbb{R}^n equipped with the standard inner product. Concepts relying on \mathcal{E} are coordinate-free, whereas \mathbb{R}^n allows associating numbers to these concepts. The passage from an n -dimensional Euclidean space \mathcal{E} to the real n -space \mathbb{R}^n is achieved by introducing the concept of a **coordinate frame**.

Definition 4.1.1 (Coordinate Frame). A coordinate frame for the Euclidean space \mathcal{E} is the 4-tuple $\Psi := \{o, \hat{e}_1, \hat{e}_2, \hat{e}_3\}$, with $o \in \mathcal{E}$ and $\hat{e}_1, \hat{e}_2, \hat{e}_3 \in \mathcal{E}_*$ are linearly independent free vectors. We call Ψ a right-handed orthonormal coordinate frame, if the basis $\hat{e}_1, \hat{e}_2, \hat{e}_3$ are orthonormal and $\Omega(\hat{e}_1, \hat{e}_2, \hat{e}_3) = +1$. The point o is called the origin of the frame and is the preferred point in \mathcal{E} representing the zero origin (i.e. identity element) of \mathbb{R}^n .

A fact about Euclidean spaces is that all Euclidean spaces of a given dimension n are isomorphic, i.e. essentially there is only 1 unique Euclidean space of dimension n . Therefore, any information about \mathcal{E} is equivalently available in

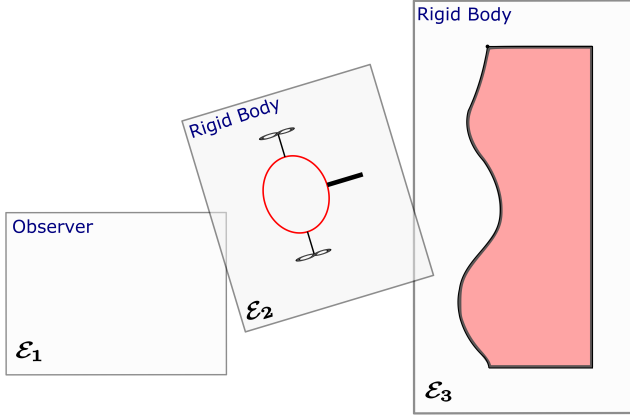


Figure 4.2: Example of a 2D- Euclidean system $S^3(2) = \{\mathcal{E}_1, \mathcal{E}_2, \mathcal{E}_3\}$ consisting of an observer \mathcal{E}_1 and two rigid bodies \mathcal{E}_2 and \mathcal{E}_3 .

studying \mathbb{R}^n using coordinates because \mathcal{E} and \mathbb{R}^n are isomorphic through the use of a coordinate frame Ψ . However, the drawback is that conceptually a coordinate free treatment is more fundamental without a preferred basis and preferred origin. In addition, using coordinates hides the abstract nature of a given mathematical entity and causes conceptual confusion.

Now we introduce the concept of a **rigid body**. A rigid body is mathematically the pair (\mathcal{B}, ρ) where $B \subset \mathcal{E}$ is the matter set which is a compact subset of points of \mathcal{E} where matter is present, and $\rho : \mathcal{B} \rightarrow \mathbb{R}^+$ is the continuous mass density function. The mass density function will be relevant for the dynamics considerations in Sec. 4.2.1. Fig. 4.1 illustrates the different objects introduced so far.

Before defining the configuration of a rigid body we introduce several abstract structures. We start by defining an **Euclidean system**.

Definition 4.1.2 (Euclidean System). An n -dimensional Euclidean system of order m is the set $S^m(n) := \{\mathcal{E}_1, \mathcal{E}_2, \dots, \mathcal{E}_m\}$ of m , n -dimensional oriented Euclidean spaces.

A Euclidean system consists of a collection of rigid bodies and observers. An observer is an example of an Euclidean space with the matter set being the empty set. In practice an observer could correspond to an exteroceptive sensor like a camera or a motion capture system. An example of a two-dimensional Euclidean system (in the plane) is illustrated in Fig. 4.2. The material treated is general and applicable to both 2-dimensional systems (rigid bodies in a plane) and 3-dimensional systems (rigid bodies in a space).

In order to describe the relative pose (position and orientation) of two

Euclidean spaces in an Euclidean system with respect to each other, we need the concept of an **isometry**.

Definition 4.1.3 (Isometry). An isometry is a bijective map $h_i^j : \mathcal{E}_i \rightarrow \mathcal{E}_j$ between the metric spaces (\mathcal{E}_i, d_i) and (\mathcal{E}_j, d_j) such that $d_j(h_i^j(p), h_i^j(q)) = d_i(p, q), \forall p, q \in \mathcal{E}_i$. If $i = j$ we call $h_i := h_i^i$ an auto-isometry of \mathcal{E}_i .

Isometries are the *structure preserving* maps between metric spaces i.e. the maps that preserve the metric associated to each Euclidean space. Examples of isometries include translation, rotation, reflection, and combinations of them. The set of isometries between the n -dimensional Euclidean spaces \mathcal{E}_i and \mathcal{E}_j is denoted by $E_i^j(n)$, while the set of auto-isometries of \mathcal{E}_i is denoted by $E_i(n)$.

As physical rigid body motions include combinations of translations and rotations but no reflections, we should restrict to a subset of $E_i^j(n)$ (and $E_i(n)$) to represent the configuration of a rigid body. We do that by restricting the isometries h_i^j that preserve the orientation Ω_i of the Euclidean space, and thus excluding isometries that include reflection. We refer to the orientation preserving isometries as **positive isometries**. The set of positive isometries from \mathcal{E}_i to \mathcal{E}_j is denoted by $SE_i^j(n)$, while the set of positive auto-isometries of \mathcal{E}_i is denoted by $SE_i(n)$. An element $h_i^j \in SE_i^j(n)$ represents the relative pose of \mathcal{E}_i with respect to \mathcal{E}_j . Whereas an element $h_i \in SE_i(n)$ represents the *configuration of the rigid body* B_i associated to \mathcal{E}_i , and $SE_i(n)$ represents its *configuration space*.

Now the key point that is usually forgotten is that we can identify $SE_i^j(n)$ and $SE_i(n)$ by choosing a specific reference configuration. With reference to Fig. 4.3 (left), we can associate a relative pose $h_i^j \in SE_i^j(n)$ to elements of $SE_i(n)$ and $SE_j(n)$ using a reference relative pose $r_i^j \in SE_i^j(n)$, such that

$$h_i^j = r_i^j \circ h_i = h_j \circ r_i^j. \quad (4.1)$$

Thus, we can use $h_i^j \in SE_i^j(n)$ to represent the configuration of a rigid body B_i in \mathcal{E}_i . Note that $SE_i^j(n)$ represents the space of absolute relative poses between two Euclidean spaces independently of any relative reference pose, thus it is intrinsically defined, whereas the identification of a relative pose by an element of $SE_i(n)$ or $SE_j(n)$ is not intrinsic as it depends on the preferred choice of reference pose r_i^j .

4.1.2 Numerical Representation of the Configuration Space

The material presented so far considers the configuration space of a rigid body and relative poses in an abstract coordinate-free manner. As mentioned earlier, the coordinate representation of the presented concepts in \mathbb{R}^n is achieved by the introduction of a coordinate frame Ψ_k that is associated to each Euclidean space \mathcal{E}_k in an Euclidean system $S^m(n)$.

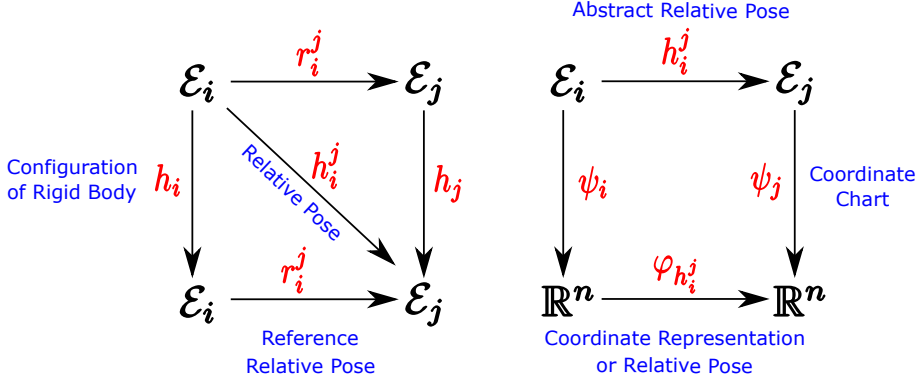


Figure 4.3: Identification of the different isomorphisms related to the configuration of a rigid body. Left diagram shows how to identify $SE_i(n)$ and $SE_j(n)$ with $SE_i^j(n)$, while right diagram shows how to identify $SE_i^j(n)$ with $\text{Iso}(\mathbb{R}^n)$

The coordinate representation of a point $p \in \mathcal{E}$ and a free-vector $\hat{v} \in \mathcal{E}_*$ in Ψ are given respectively by $p = p^i \hat{e}_i$ and $\hat{v} = \hat{v}^i \hat{e}_i$ where the Einstein summation convention has been used. The coordinates $p^i, \hat{v}^i \in \mathbb{R}$ are defined by

$$p^i := \ll (p - o), \hat{e}_i \gg, \quad \hat{v}^i := \ll \hat{v}, \hat{e}_i \gg, \quad i \in \{1, \dots, n\}, \quad (4.2)$$

where \ll, \gg is the inner product associated to \mathcal{E}_* , and $(p - o) \in \mathcal{E}_*$ denotes the vector pointing¹ from the origin o to the point p .

Associated to each frame Ψ_k is an isomorphism $\psi_k : \mathcal{E}_k \rightarrow \mathbb{R}^n$, called the **coordinate chart**, with its component functions given by $\psi_k^i : p \mapsto p^i$ for any $p \in \mathcal{E}_k$. With reference to Fig. 4.3 (right), we can assign an abstract relative pose $h_i^j \in SE_i^j(n)$ to an isomorphism $\phi_{h_i^j} \in \text{Iso}(\mathbb{R}^n)$

$$\phi_{h_i^j} = \psi_j \circ h_i^j \circ \psi_i^{-1}, \quad (4.3)$$

which corresponds to the numerical representation of the relative pose of frame Ψ_i with respect to frame Ψ_j . The link between the coordinate-free formulation and the standard matrix Lie group approach on \mathbb{R}^n is completed by choosing the reference pose $r_i^j \in SE_i^j(n)$ of the Euclidean system in (4.1) such that all coordinate frames coincide, i.e.

$$r_i^j = \psi_j^{-1} \circ \text{id}_{\mathbb{R}^n} \circ \psi_i, \quad (4.4)$$

where $\text{id}_{\mathbb{R}^n}$ denotes the identity map in \mathbb{R}^n . The intuition behind this step is that we identify the identity map as the standard reference(home) configuration. Any subsequent pose of a rigid body (or observer) in a Euclidean

¹which makes sense due to the Euclidean structure via parallel transport.

system is then described by the rigid body transformation that **transforms the reference configuration of the body to its current configuration**.

Now we look in more depth at general isometries ϕ_h of \mathbb{R}^n which preserve the Euclidean distance, and thus represent rigid body transformations (including reflections). It is well known that the action of any isometry $\phi_h : \mathbb{R}^n \rightarrow \mathbb{R}^n$ on a general vector $\mathbf{v} \in \mathbb{R}^n$ can be written as a combination of a rotation and a translation [Selig, 2004]

$$\phi_h(\mathbf{v}) = \mathbf{M}\mathbf{v} + \boldsymbol{\xi}, \quad \mathbf{M} \in O(n), \boldsymbol{\xi} \in \mathbb{R}^n, \quad (4.5)$$

where $\boldsymbol{\xi}$ is a constant translation vector, and \mathbf{M} is an orthogonal matrix belonging to the set of orthogonal transformations of \mathbb{R}^n given by

$$O(n) := \{\mathbf{M} \in \mathbb{R}^{n \times n} | \mathbf{M}\mathbf{M}^\top = \mathbf{I}_n\}. \quad (4.6)$$

Therefore, we can identify any isometry ϕ_h of \mathbb{R}^n by the pair $(\mathbf{M}, \boldsymbol{\xi}) =: \mathbf{h} \in E(n)$. We denote by $E(n)$ the (matrix) Euclidean group that represents rigid body transformations, which is defined as follows.

Definition 4.1.4 (Euclidean group). The Euclidean group is a group $(E(n), \bullet)$, with the set $E(n) := \{\mathbf{h} = (\mathbf{M}, \boldsymbol{\xi}) \in O(n) \times \mathbb{R}^n\}$, the group operation $\bullet : E(n) \times E(n) \rightarrow E(n)$ is defined as $\mathbf{h}_2 \bullet \mathbf{h}_1 = (\mathbf{M}_2\mathbf{M}_1, \mathbf{M}_2\boldsymbol{\xi}_1 + \boldsymbol{\xi}_2)$, for $\mathbf{h}_i = (\mathbf{M}_i, \boldsymbol{\xi}_i), i = \{1, 2\}$, and the inverse operation defined as $\mathbf{h}^{-1} = (\mathbf{M}^{-1}, -\mathbf{M}^{-1}\boldsymbol{\xi})$.

From the previous definition, it can be seen that $E(n)$ is isomorphic to the direct product $O(n) \times \mathbb{R}^n$ as sets but not as groups. Therefore, $E(n)$ is said to be the *semi-direct product* of the groups $O(n)$ and \mathbb{R}^n denoted as

$$E(n) = O(n) \ltimes \mathbb{R}^n, \quad (4.7)$$

where \mathbb{R}^n is considered as a commutative group with the group operation being the addition operator “+”.

An orthogonal matrix $\mathbf{M} \in O(n)$ satisfies $\mathbf{M}\mathbf{M}^\top = \mathbf{I}_n$, which implies that $\det(\mathbf{M}) = \pm 1$. Thus, the set $O(n)$ consists of two disconnected components: the first corresponding to matrices with $\det(\mathbf{M}) = +1$, which correspond to rotations around the origin, and the second are matrices with $\det(\mathbf{M}) = -1$, which correspond to reflection. Therefore, to properly model physical rigid body transformations, excluding reflections, we restrict $O(n)$ to the subgroup defined as

$$SO(n) := \{\mathbf{R} \in O(n) | \det(\mathbf{R}) = +1\},$$

which is known as the **special orthogonal group**, and its elements are called rotation matrices. Consequently, we restrict $E(n)$ to the semidirect product

$$SE(n) := SO(n) \ltimes \mathbb{R}^n \subset E(n),$$

which is known as the **special Euclidean group**, with an element $\mathbf{h} \in SE(n)$ corresponding to the pair $(\mathbf{R}, \boldsymbol{\xi}) \in SO(n) \ltimes \mathbb{R}^n$.

Using concepts from projective geometry [Stramigioli, 2001], there exists a bijective group homomorphism between $SE(3)$ and a subspace of the general linear group $GL(n+1)$ that fortunately allows us to use standard matrix operations to perform rigid body transformations, instead of working with the pair $(\mathbf{R}, \boldsymbol{\xi})$. This group homomorphism is defined by

$$SE(n) \rightarrow HM(n+1) \subset GL(n+1)$$

$$\mathbf{h} = (\mathbf{R}, \boldsymbol{\xi}) \mapsto \begin{pmatrix} \mathbf{R} & \boldsymbol{\xi} \\ \mathbf{0} & 1 \end{pmatrix} =: \mathbf{H}. \quad (4.8)$$

The matrix $\mathbf{H} \in HM(n+1)$ is called the homogeneous representation of $\mathbf{h} \in SE(n)$ and we denote the space of homogeneous matrices by $HM(n+1)$. The *homogeneous* notion is due to the connection with projective transformations [Stramigioli, 2001].

The group and inverse operations of $SE(n)$, given in Def. 4.1.4, are now represented by the matrix multiplication and inverse operations:

$$\mathbf{H}_2 \mathbf{H}_1 = \begin{pmatrix} \mathbf{R}_2 & \boldsymbol{\xi}_2 \\ \mathbf{0} & 1 \end{pmatrix} \begin{pmatrix} \mathbf{R}_1 & \boldsymbol{\xi}_1 \\ \mathbf{0} & 1 \end{pmatrix} = \begin{pmatrix} \mathbf{R}_2 \mathbf{R}_1 & \mathbf{R}_2 \boldsymbol{\xi}_1 + \boldsymbol{\xi}_2 \\ \mathbf{0} & 1 \end{pmatrix}, \quad (4.9)$$

$$\mathbf{H}^{-1} = \begin{pmatrix} \mathbf{R} & \boldsymbol{\xi} \\ \mathbf{0} & 1 \end{pmatrix}^{-1} = \begin{pmatrix} \mathbf{R}^\top & -\mathbf{R}^\top \boldsymbol{\xi} \\ \mathbf{0} & 1 \end{pmatrix}. \quad (4.10)$$

Moreover, the action of $SE(n)$ on \mathbb{R}^n in (4.5) is now identified by the action of $HM(n+1)$ on \mathbb{R}^{n+1} , as follows. First, we assign a vector² $\mathbf{v} \in \mathbb{R}^n$ to a vector $\mathbf{V} \in \mathbb{R}^{n+1}$ defined by $\mathbf{V}^\top := (\mathbf{v}^\top, 1)$. Then, the action of the transformation $\mathbf{H} \in HM(n+1)$ on \mathbf{V} is represented by matrix multiplication such that

$$\mathbf{H} \mathbf{V} = \begin{pmatrix} \mathbf{R} & \boldsymbol{\xi} \\ \mathbf{0} & 1 \end{pmatrix} \begin{pmatrix} \mathbf{v} \\ 1 \end{pmatrix} = \begin{pmatrix} \mathbf{R} \mathbf{v} + \boldsymbol{\xi} \\ 1 \end{pmatrix}, \quad (4.11)$$

which recovers (4.5). The components of $\mathbf{V} \in \mathbb{R}^{n+1}$ are referred to as the homogeneous coordinates of $\mathbf{v} \in \mathbb{R}^n$. More precisely, \mathbf{V} is a representative of the equivalence class that corresponds to \mathbf{v} in the projective space.

In conclusion, we have presented four mathematical objects that correspond to the configuration of a rigid body, summarized in Table 4.1. While the numerical matrices are useful for calculations, the abstract maps are useful for understanding the intrinsic properties of a rigid body (*cf.* [Stramigioli, 2001]), and it is extremely beneficial to distinguish between these different mathematical objects on a conceptual level.

²which corresponds to the coordinate representation of a point in \mathcal{E} .

Abstract Configuration	$h_i \in SE_i(n)$
Abstract Relative Pose	$h_i^j \in SE_i^j(n)$
Rotation Matrix & Translation Vector	$(\mathbf{R}_i^j, \boldsymbol{\xi}_i^j) \in SE(n)$
Homogeneous Matrix	$\mathbf{H}_i^j \in HM(n+1)$

Table 4.1: Different mathematical objects corresponding to the configuration of a rigid body.

Remark 4.1.5. In the remaining of this chapter, we will primarily refer to the configuration space of a rigid body as $SE(n)$, and we will work with homogeneous matrices for calculations. For simplicity of notation, we will abusively refer to the space of homogeneous matrices as $SE(n)$, and thus write $\mathbf{H} \in SE(n)$.

The configuration space $SE(n)$ has been presented so far with the structure of a group that is the semidirect product of two subgroups: $SO(n)$ and \mathbb{R}^n . In fact, $SE(n)$ has both the structure of a smooth manifold and a group. Moreover, with the fact that the group operation (4.9) and the inverse operation (4.10) are smooth maps, $SE(n)$ has consequently the structure of a matrix Lie-group. In addition, $SO(n)$ is a Lie-subgroup of $SE(n)$, with the group operation of matrix multiplication and the inverse operation as the matrix transpose.

In the coming two sections, we discuss the Lie-group structure of $SO(n)$ and how to represent rigid body rotational motion, followed by the Lie-group structure of $SE(n)$ and how to represent general rigid body motion. For convenience of notations, the rest of this chapter will be presented for the three-dimensional case ($n = 3$).

4.1.3 Lie-Group Structure of $SO(3)$

A rigid body rotational motion is represented mathematically by a curve $\gamma_R : t \mapsto \mathbf{R}_t$ on the smooth manifold $SO(3)$, which provides a family of transformation (rotation) matrices \mathbf{R}_t that describe the evolution of the reference configuration to the current configuration, as shown in Fig. 4.4.

As illustrated in Fig. 4.4, the rate of change of the rigid body rotation is represented by the velocity of the curve γ_R at a point \mathbf{R}_t which is an element (vector) of the tangent space to $SO(3)$ at \mathbf{R}_t , denoted by $\dot{\mathbf{R}}_t \in T_{\mathbf{R}_t}SO(3)$. At any point $\mathbf{R} \in SO(3)$ in the manifold, the tangent space $T_{\mathbf{R}}SO(3)$ is defined as

$$T_{\mathbf{R}}SO(3) := \{\dot{\mathbf{R}} \in \mathbb{R}^{3 \times 3} | \dot{\mathbf{R}}\mathbf{R} = -(\dot{\mathbf{R}}\mathbf{R})^\top\}, \quad (4.12)$$

which follows from differentiating the condition $\mathbf{R}\mathbf{R}^\top = \mathbf{I}_3$ in (4.6).

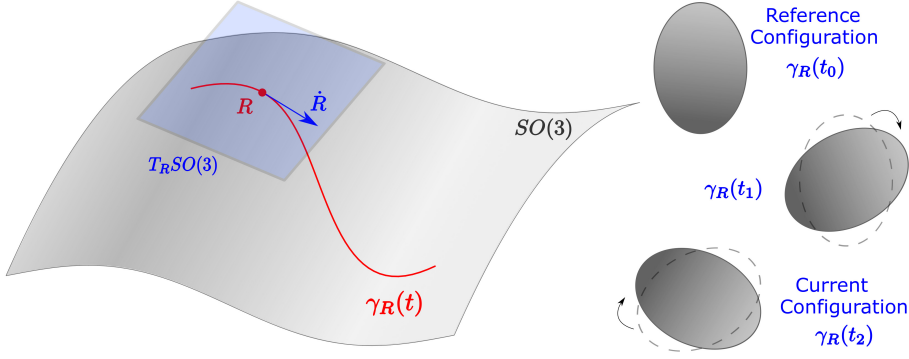


Figure 4.4: Illustration of rigid body rotation as a curve $\gamma_R(t)$ on $SO(3)$ which represents a family of transformation (rotation) matrices on \mathbb{R}^3 .

The tangent space $T_{\mathbf{R}}SO(3)$ at any $\mathbf{R} \in SO(3)$ has the structure of a finite-dimensional vector space, with dimension same as $SO(3)$ i.e. $\dim(T_{\mathbf{R}}SO(3)) = \dim(SO(3)) = 3$. Note that numerically, $\dot{\mathbf{R}}$ is a 3×3 matrix, whereas geometrically it is a vector in the three-dimensional vector space $T_{\mathbf{R}}SO(3)$.

The dual space to $T_{\mathbf{R}}SO(3)$ is called the cotangent space to $SO(3)$ at \mathbf{R} , and is denoted by $T_{\mathbf{R}}^*SO(3)$. The cotangent space consists of all linear maps $\Gamma_{\mathbf{R}} : T_{\mathbf{R}}SO(3) \rightarrow \mathbb{R}$, referred to as covectors (or 1-forms).

A recurrent example of a covector in $T_{\mathbf{R}}^*SO(3)$ is the derivative of any smooth function $F : SO(3) \rightarrow \mathbb{R}$ with respect to $\mathbf{R} \in SO(3)$, given by

$$\frac{dF}{d\mathbf{R}}(\mathbf{R}) \in T_{\mathbf{R}}^*SO(3). \quad (4.13)$$

Furthermore, the rate of change of such smooth function along a curve in $SO(3)$ is expressed by

$$\dot{F}(\mathbf{R}_t) = \left\langle \frac{dF}{d\mathbf{R}}(\mathbf{R}_t) \middle| \dot{\mathbf{R}}_t \right\rangle_{\text{so}}, \quad (4.14)$$

where $\langle \cdot | \cdot \rangle_{\text{so}}$ denotes the duality pairing on the vector space $T_{\mathbf{R}}SO(3)$.

The collection of all tangent spaces at every point $\mathbf{R} \in SO(3)$ comprises the tangent bundle $TSO(3)$. Similarly, the collection of all cotangent spaces at every point $\mathbf{R} \in SO(3)$ comprises the cotangent bundle $T^*SO(3)$. The cotangent bundle is extremely significant in geometric mechanics and plays a fundamental role in Hamiltonian mechanics.

The Lie-algebra $\mathfrak{so}(3)$ of $SO(3)$

By utilizing the Lie-group structure of $SO(3)$, it is possible to describe the rotational motion of a rigid body independent of the current configuration \mathbf{R} .

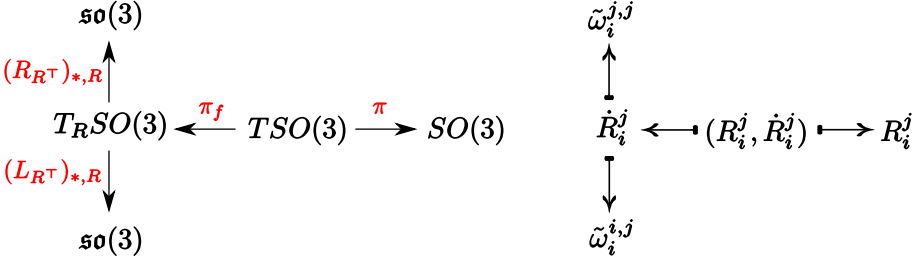


Figure 4.5: Mapping the tangent bundle $TSO(3)$ to the Lie-algebra $\mathfrak{so}(3)$. The maps π and π_f represent the canonical and fiber projections, respectively.

We can map any element $(\mathbf{R}, \dot{\mathbf{R}})$ of the tangent bundle $TSO(3)$ to a unique element of the tangent space $T_I SO(3)$ at the group identity $\mathbf{I} \in SO(3)$, i.e. the matrix Lie-algebra $\mathfrak{so}(3)$. This element corresponds physically to the angular velocity $\tilde{\omega} \in \mathfrak{so}(3)$ of the rigid body which has a geometrical interpretation, unlike $\dot{\mathbf{R}} \in T_{\mathbf{R}} SO(3)$ which depends on the current rotation matrix \mathbf{R} .

The matrix Lie algebra $\mathfrak{so}(3)$ is given by the set of skew-symmetric matrices:

$$\mathfrak{so}(3) = T_I SO(3) = \{\tilde{\omega} \in \mathbb{R}^{3 \times 3} | \tilde{\omega} = -\tilde{\omega}^\top\},$$

which follows from (4.12). It can be shown that the corresponding Lie bracket of $\mathfrak{so}(3)$ is given by the matrix commutator:

$$[\tilde{\omega}_1, \tilde{\omega}_2]_{\mathfrak{so}} = \tilde{\omega}_1 \tilde{\omega}_2 - \tilde{\omega}_2 \tilde{\omega}_1, \quad \tilde{\omega}_1, \tilde{\omega}_2 \in \mathfrak{so}(3). \quad (4.15)$$

The mapping from the tangent bundle to the Lie-algebra can be achieved using the pushforward of two canonical maps on the Lie group $SO(3)$: the right-translation and the left-translation map denoted, respectively, by

$$R_{\mathbf{R}} : SO(3) \rightarrow SO(3), \quad L_{\mathbf{R}} : SO(3) \rightarrow SO(3).$$

Let $\dot{\mathbf{R}}_i^j \in SO(3)$ denote the instantaneous relative rotational motion of a frame Ψ_i with respect to another frame Ψ_j . We can identify $\dot{\mathbf{R}}_i^j$ with two elements of the Lie algebra $\mathfrak{so}(3)$ of the Lie group $SO(3)$, as shown in Fig. 4.5. The first element, denoted by $\tilde{\omega}_i^{j,j} \in \mathfrak{so}(3)$, corresponds to the mapping of $\dot{\mathbf{R}}_i^j$ using the pushforward of the right translation map at $\mathbf{R}_i^j \in SO(3)$

$$(R_{\mathbf{R}_i^j})_{*, \mathbf{R}_i^j} : T_{\mathbf{R}_i^j} SO(3) \rightarrow T_I SO(3).$$

Whereas the second element, denoted by $\tilde{\omega}_i^{i,j} \in \mathfrak{so}(3)$, is achieved by using the pushforward of the left translation map at $\mathbf{R}_i^j \in SO(3)$

$$(L_{\mathbf{R}_i^j})_{*, \mathbf{R}_i^j} : T_{\mathbf{R}_i^j} SO(3) \rightarrow T_I SO(3).$$

The two elements are expressed as

$$\tilde{\omega}_i^{j,j} := (R_{R_j^i})_{*,R_j^i}(\dot{R}_i^j) = \dot{R}_i^j R_j^i \in \mathfrak{so}(3), \quad (4.16)$$

$$\tilde{\omega}_i^{i,j} := (L_{R_j^i})_{*,R_j^i}(\dot{R}_i^j) = R_j^i \dot{R}_i^j \in \mathfrak{so}(3), \quad (4.17)$$

where the pushforward maps are given by matrix multiplication, since $SO(3)$ is a matrix Lie group [Holm et al., 2009, Ch.5].

An element of $\mathfrak{so}(3)$ corresponds to an intrinsic, configuration-independent representation of the rotational motion. Both angular velocities $\tilde{\omega}_i^{j,j}$ and $\tilde{\omega}_i^{i,j}$ describe the rotational motion of Ψ_i with respect to Ψ_j , but $\tilde{\omega}_i^{j,j}$ expresses the motion in Ψ_j , while $\tilde{\omega}_i^{i,j}$ expresses the motion in Ψ_i .

If frame $\Psi_i =: \Psi_B$ is chosen as a frame fixed to a rigid body and frame $\Psi_j =: \Psi_I$ is chosen as an inertial-fixed frame, then the Lie algebra element $\tilde{\omega}_B^{B,I} = \dot{R}_B^I R_I^B$ is usually called the body-angular velocity, whereas $\tilde{\omega}_B^{I,I} = R_I^B \dot{R}_B^I$ is called the spatial (inertial) angular velocity. Note that both elements describe the same (abstract) rotation of the rigid body, but expressed in two different frames.

An important characteristic of $\mathfrak{so}(3)$ is that it can be identified with \mathbb{R}^3 through the isomorphism

$$\begin{aligned} \mathcal{S} : \mathbb{R}^3 &\rightarrow \mathfrak{so}(3) \\ \omega &:= \begin{pmatrix} \omega^1 \\ \omega^2 \\ \omega^3 \end{pmatrix} \mapsto \begin{pmatrix} 0 & -\omega^3 & \omega^2 \\ \omega^3 & 0 & -\omega^1 \\ -\omega^2 & \omega^1 & 0 \end{pmatrix} =: \mathcal{S}(\omega). \end{aligned} \quad (4.18)$$

We will use frequently the notation $\tilde{\omega} := \mathcal{S}(\omega) \in \mathfrak{so}(3)$, where elements of $\mathfrak{so}(3)$ will be always distinguished with a *tilde*. The isomorphism (4.18) is defined such that the following identity holds

$$\tilde{\omega}v = \omega \wedge v, \quad \forall \omega, v \in \mathbb{R}^3, \quad (4.19)$$

with \wedge denoting the vector product on \mathbb{R}^3 .

The dual of the Lie algebra $\mathfrak{so}(3)$

Let $\mathfrak{so}^*(3)$ denote the dual space of the Lie algebra $\mathfrak{so}(3)$ which consists of linear maps $\tilde{\tau}^* : \mathfrak{so}(3) \rightarrow \mathbb{R}$. The duality pairing between a covector $\tilde{\tau}^* \in \mathfrak{so}^*(3)$ and a vector $\tilde{\omega} \in \mathfrak{so}(3)$ is denoted by $\langle \tilde{\tau}^* | \tilde{\omega} \rangle_{\mathfrak{so}} \in \mathbb{R}$.

The dual of the linear map (4.18) provides an isomorphism between the two dual spaces $\mathfrak{so}^*(3)$ and $(\mathbb{R}^3)^* \cong \mathbb{R}^3$ given by

$$\begin{aligned} \mathcal{S}^* : \mathfrak{so}^*(3) &\rightarrow (\mathbb{R}^3)^* \\ \tilde{\tau}^* &\mapsto \mathcal{S}^*(\tilde{\tau}^*) =: \tau^*, \end{aligned} \quad (4.20)$$

defined such that

$$\langle \mathcal{S}^*(\tilde{\tau}^*) | \omega \rangle_{\mathbb{R}^3} = \langle \tilde{\tau}^* | \mathcal{S}(\omega) \rangle_{\mathfrak{so}},$$

or equivalently, using (4.18),

$$\langle \tilde{\tau}^* | \omega \rangle_{\mathbb{R}^3} = \langle \tilde{\tau}^* | \tilde{\omega} \rangle_{\mathfrak{so}}. \quad (4.21)$$

In finite dimensions, we can always identify the dual of a vector space with the *vector space itself* using an inner product. This identification is beneficial for simplifying a lot of notations and calculations e.g. for providing an explicit expression of the duality pairings $\langle \cdot | \cdot \rangle_{\mathfrak{so}}$ and $\langle \cdot | \cdot \rangle_{\mathbb{R}^3}$. However, it is important to conceptually distinguish between a vector space and its dual because they change coordinates differently.

Let $\tilde{\tau} \in \mathfrak{so}(3)$ be the corresponding skew-symmetric matrix that is identified with the linear map $\tilde{\tau}^* \in \mathfrak{so}^*(3)$. Then, one can show [Holm et al., 2009, Pg. 176] that the duality pairing $\langle \cdot | \cdot \rangle_{\mathfrak{so}}$ has the form

$$\langle \tilde{\tau}^* | \tilde{\omega} \rangle_{\mathfrak{so}} = \frac{1}{2} \text{tr}(\tilde{\tau} \tilde{\omega}^\top). \quad (4.22)$$

Furthermore, let $\tau \in \mathbb{R}^3$ be the corresponding (column) vector that is identified with the linear map (row vector) $\tau^* \in (\mathbb{R}^3)^*$. Then, the duality pairing $\langle \cdot | \cdot \rangle_{\mathbb{R}^3}$ has the well-known form

$$\langle \tau^* | \omega \rangle_{\mathbb{R}^3} = \tau^\top \omega. \quad (4.23)$$

In the sequel, we shall usually drop the *asterisk-superscript*(^{*}) from covectors, and use interchangeably the same notation for a covector and its identified vector. Therefore, using (4.23) and (4.22), we can rewrite (4.21) as

$$\langle \tilde{\tau} | \tilde{\omega} \rangle_{\mathfrak{so}} = \frac{1}{2} \text{tr}(\tilde{\tau} \tilde{\omega}^\top) = \tau^\top \omega = \langle \tau | \omega \rangle_{\mathbb{R}^3}, \quad (4.24)$$

where $\tilde{\omega} \in \mathfrak{so}(3)$, $\tilde{\tau} \in \mathfrak{so}^*(3)$, $\omega \in \mathbb{R}^3$, and $\tau \in (\mathbb{R}^3)^*$.

One physical example of a covector $\tau \in (\mathbb{R}^3)^*$ (or $\tilde{\tau} \in \mathfrak{so}^*(3)$) is the torque applied to a rigid body causing it to rotate by the angular velocity $\omega \in \mathbb{R}^3$ (or $\tilde{\omega} \in \mathfrak{so}(3)$). The duality pairing $\langle \tau | \omega \rangle_{\mathbb{R}^3}$ (or $\langle \tilde{\tau} | \tilde{\omega} \rangle_{\mathfrak{so}}$) corresponds then to the mechanical power supplied to the rigid body by the entity that generates the torque. Another physical example of a covector is the angular momentum $P_\omega \in (\mathbb{R}^3)^*$ (or $\tilde{P}_\omega \in \mathfrak{so}^*(3)$) which when paired with the angular velocity corresponds to twice the kinetic energy of the rotating body.

Finally, we conclude this section by showing how covectors in the cotangent space $T_{\mathbf{R}}^*SO(3)$ can be mapped to $\mathfrak{so}^*(3)$. With reference to the commutative diagram in Fig. 4.6, a co-vector $\mathbf{\Gamma}_{\mathbf{R}} \in T_{\mathbf{R}_i}^*SO(3)$ is mapped to $\mathfrak{so}^*(3)$ by using either the pullback of the right translation map at the identity $\mathbf{I} \in SO(3)$,

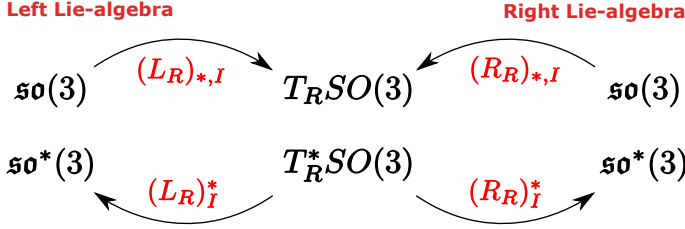


Figure 4.6: Commutative diagram of isomorphisms between the tangent spaces $T_R SO(3)$ and $\mathfrak{so}(3)$ & the cotangent spaces $T_R^* SO(3)$ and $\mathfrak{so}^*(3)$.

denoted by $(R_{R_i^j})_I^*$, or the pullback of the left translation map at the identity $I \in SO(3)$, denoted by $(L_{R_i^j})_I^*$. Therefore, we have that

$$\tilde{\tau}^j := (R_{R_i^j})_I^*(\Gamma_R) \in \mathfrak{so}^*(3), \quad (4.25)$$

$$\tilde{\tau}^i := (L_{R_i^j})_I^*(\Gamma_R) \in \mathfrak{so}^*(3), \quad (4.26)$$

where the pullback maps are defined implicitly by

$$\left\langle (R_{R_i^j})_I^*(\Gamma_R) \middle| \tilde{\omega}_i^{j,j} \right\rangle_{\mathfrak{so}} = \left\langle \Gamma_R \middle| (R_{R_i^j})_{*,I}(\tilde{\omega}_i^{j,j}) \right\rangle_{\mathfrak{so}} \quad (4.27)$$

$$\left\langle (L_{R_i^j})_I^*(\Gamma_R) \middle| \tilde{\omega}_i^{i,j} \right\rangle_{\mathfrak{so}} = \left\langle \Gamma_R \middle| (L_{R_i^j})_{*,I}(\tilde{\omega}_i^{i,j}) \right\rangle_{\mathfrak{so}}. \quad (4.28)$$

In summary, by combining (4.27) and (4.28) with (4.16-4.17) and (4.25-4.26), we have that

$$\langle \tilde{\tau}^j | \tilde{\omega}_i^{j,j} \rangle_{\mathfrak{so}} = \langle \Gamma_R | \dot{R}_i^j \rangle_{\mathfrak{so}} = \langle \tilde{\tau}^i | \tilde{\omega}_i^{i,j} \rangle_{\mathfrak{so}}.$$

4.1.4 Lie-Group Structure of $SE(3)$

Now we present the Lie group structure of $SE(3)$ following the same line of thought of the material presented for rotational motion on $SO(3)$. A general rigid body motion on $SE(3)$ is a combination of rotational and translational motion. The following treatment allows us to describe these two aspects using a single mathematical object, called a *twist*.

A general rigid body motion is represented mathematically by a curve $\gamma_H : t \mapsto \mathbf{H}_t$ on the smooth manifold $SE(3)$, which provides a family of transformation (homogeneous) matrices \mathbf{H}_t that describe the evolution of the reference configuration to the current configuration. The rate of change of the rigid body motion is represented by the velocity of the curve γ_H at a point \mathbf{H}_t which is an element (vector) $\dot{\mathbf{H}}_t \in T_{\mathbf{H}_t} SE(3)$, as illustrated in Fig. 4.7. The

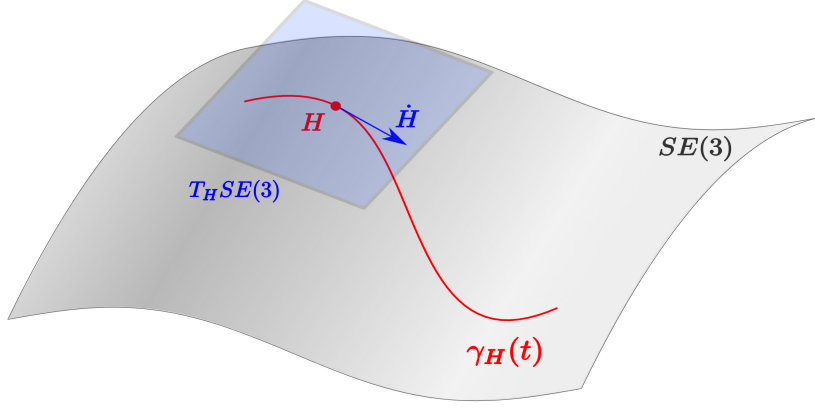


Figure 4.7: Illustration of general rigid body motion as a curve $\gamma_H(t)$ on $SE(3)$ which represents a family of homogeneous transformation matrices on a projective extension of \mathbb{R}^3 .

velocity vector $\dot{\mathbf{H}}_t \in T_{\mathbf{H}_t}SE(3)$ is given in partitioned matrix form by

$$\dot{\mathbf{H}}_t = \begin{pmatrix} \dot{\mathbf{R}}_t & \dot{\boldsymbol{\xi}}_t \\ \mathbf{0} & 0 \end{pmatrix} \in T_{\mathbf{H}_t}SE(3), \quad (4.29)$$

where $\dot{\mathbf{R}}_t \in T_{\mathbf{R}_t}SO(3)$ and $\dot{\boldsymbol{\xi}}_t \in T_{\boldsymbol{\xi}_t}\mathbb{R}^3 \cong \mathbb{R}^3$ are the tangent vectors of the projection curves of γ_H onto the submanifolds $SO(3)$ and \mathbb{R}^3 , respectively. From (4.29) we see that we can identify $\dot{\mathbf{H}}$ by the pair $(\dot{\mathbf{R}}, \dot{\boldsymbol{\xi}})$ and thus we have that as vector spaces

$$T_{\mathbf{H}}SE(3) \cong T_{\mathbf{R}}SO(3) \oplus \mathbb{R}^3.$$

Consequently, we also have that the cotangent space

$$T_{\mathbf{H}}^*SE(3) \cong T_{\mathbf{R}}^*SO(3) \oplus (\mathbb{R}^3)^*.$$

Thus, any covector $\boldsymbol{\Gamma}_H \in T_{\mathbf{H}}^*SE(3)$ can be identified by the pair $(\boldsymbol{\Gamma}_R, \boldsymbol{\Gamma}_F) \in T_{\mathbf{R}}^*SO(3) \times (\mathbb{R}^3)^*$. Moreover, the duality pairing on $T_{\mathbf{H}}SE(3)$ can be expressed as

$$\left\langle \boldsymbol{\Gamma}_H | \dot{\mathbf{H}} \right\rangle_{SE} = \left\langle \boldsymbol{\Gamma}_R | \dot{\mathbf{R}} \right\rangle_{SO} + \left\langle \boldsymbol{\Gamma}_F | \dot{\boldsymbol{\xi}} \right\rangle_{\mathbb{R}^3}. \quad (4.30)$$

Similar to the case of $SO(3)$ in (4.13) and (4.14), one has that the derivative of a general function on $SE(3)$ with respect to $\mathbf{H} \in SE(3)$ is a covector in $T_{\mathbf{H}}^*SE(3)$ and its rate of change can be calculated using (4.30).

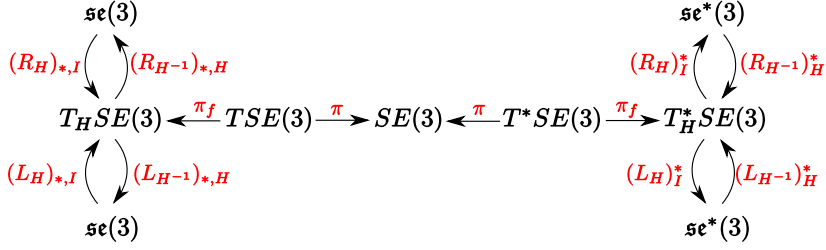


Figure 4.8: Commutative Diagram relating the Lie group $SE(3)$ to the Lie algebra $\mathfrak{se}(3)$ and its dual space $\mathfrak{se}^*(3)$. The maps π and π_f represent the canonical and fiber projections, respectively.

The Lie-algebra $\mathfrak{se}(3)$ of $SE(3)$

The instantaneous relative motion \dot{H}_i^j of a frame Ψ_i with respect to another frame Ψ_j can be identified with two elements of the Lie algebra $\mathfrak{se}(3)$ of the Lie group $SE(3)$, as shown in Fig. 4.8.

The first element, denoted by $\tilde{T}_i^{j,j} \in \mathfrak{se}(3)$, corresponds to the mapping of \dot{H}_i^j using the pushforward the right translation map at $H_i^j \in SE(3)$. Whereas the second element, denoted by $\tilde{T}_i^{i,j} \in \mathfrak{se}(3)$, is calculated by using the pushforward the left translation map at $H_i^j \in SE(3)$. The two elements are expressed using matrix multiplication as

$$\tilde{T}_i^{j,j} := (R_{H_j^i})_{*,H_i^j}(\dot{H}_i^j) = \dot{H}_i^j H_j^i, \quad (4.31)$$

$$\tilde{T}_i^{i,j} := (L_{H_j^i})_{*,H_i^j}(\dot{H}_i^j) = H_j^i \dot{H}_i^j. \quad (4.32)$$

An element of $\mathfrak{se}(3)$ is called a **twist**, which corresponds to a configuration-independent intrinsic representation of the generalized velocity of an Euclidean space. Both twists $\tilde{T}_i^{j,j}$ and $\tilde{T}_i^{i,j}$ describe the general motion (translational and rotational) of Ψ_i with respect to Ψ_j , but $\tilde{T}_i^{j,j}$ expresses the motion in Ψ_j , while $\tilde{T}_i^{i,j}$ expresses the motion in Ψ_i .

Moreover, if $\Psi_i = \Psi_B$ is a body-fixed frame and frame $\Psi_j = \Psi_I$ is an inertial-fixed frame, then the Lie algebra elements

$$\tilde{T}_B^{B,I} = \dot{H}_B^I H_I^B \in \mathfrak{se}(3), \quad \tilde{T}_B^{I,I} = H_I^B \dot{H}_B^I \in \mathfrak{se}(3),$$

are referred to as the **body-twist** and the **spatial-twist**, respectively.

From equations (4.31) and (4.32), it can be deduced that a twist can be represented by a 4×4 square matrix, i.e. $\mathfrak{se}(3) \subset \mathbb{R}^{4 \times 4}$. By expanding equations (4.31-4.32) using the partitioned matrix forms of H_j^i and \dot{H}_i^j in (4.8) and

(4.29) , we can express the twists $\tilde{T}_i^{j,j}$ and $\tilde{T}_i^{i,j}$ as

$$\tilde{T}_i^{j,j} = \begin{pmatrix} \dot{R}_i^j & \dot{\xi}_i^j \\ \mathbf{0} & 0 \end{pmatrix} \begin{pmatrix} R_j^i & \xi_j^i \\ \mathbf{0} & 1 \end{pmatrix} = \begin{pmatrix} \dot{R}_i^j R_j^i & \dot{\xi}_i^j + \dot{R}_i^j \xi_j^i \\ \mathbf{0} & 0 \end{pmatrix}, \quad (4.33)$$

$$\tilde{T}_i^{i,j} = \begin{pmatrix} R_j^i & \xi_j^i \\ \mathbf{0} & 1 \end{pmatrix} \begin{pmatrix} \dot{R}_i^j & \dot{\xi}_i^j \\ \mathbf{0} & 0 \end{pmatrix} = \begin{pmatrix} R_j^i \dot{R}_i^j & R_j^i \dot{\xi}_i^j \\ \mathbf{0} & 0 \end{pmatrix}, \quad (4.34)$$

which can be rewritten for $k = \{i, j\}$ as

$$\tilde{T}_i^{k,j} = \begin{pmatrix} \tilde{\omega}_i^{k,j} & \mathbf{v}_i^{k,j} \\ \mathbf{0} & 0 \end{pmatrix}, \quad (4.35)$$

with $\tilde{\omega}_i^{k,j} \in \mathfrak{so}(3)$, $\mathbf{v}_i^{k,j} \in \mathbb{R}^3$ defined by

$$\tilde{\omega}_i^{j,j} := \dot{R}_i^j R_j^i, \quad \mathbf{v}_i^{j,j} := \dot{\xi}_i^j + \dot{R}_i^j \xi_j^i, \quad (4.36)$$

$$\tilde{\omega}_i^{i,j} := R_j^i \dot{R}_i^j, \quad \mathbf{v}_i^{i,j} := R_j^i \dot{\xi}_i^j. \quad (4.37)$$

Therefore, we can identify any twist $\tilde{T} \in \mathfrak{se}(3)$ by the pair $(\tilde{\omega}, \mathbf{v}) \in \mathfrak{so}(3) \times \mathbb{R}^3$, and thus we have that as vector spaces

$$\mathfrak{se}(3) \cong \mathfrak{so}(3) \oplus \mathbb{R}^3. \quad (4.38)$$

It is important to note that $\mathfrak{se}(3)$ is isomorphic to the direct sum $\mathfrak{so}(3) \oplus \mathbb{R}^3$ only as a vector space. The relation between $\mathfrak{se}(3)$ and $\mathfrak{so}(3) \times \mathbb{R}^3$ as Lie algebras is established from inspecting their Lie brackets. The Lie bracket of $\mathfrak{se}(3)$ is given by the matrix commutator

$$[\tilde{T}_1, \tilde{T}_2]_{\mathfrak{se}} = \tilde{T}_1 \tilde{T}_2 - \tilde{T}_2 \tilde{T}_1, \quad (4.39)$$

which can be expanded using (4.35) as

$$\begin{aligned} [\tilde{T}_1, \tilde{T}_2]_{\mathfrak{se}} &= \begin{pmatrix} \tilde{\omega}_1 \tilde{\omega}_2 - \tilde{\omega}_2 \tilde{\omega}_1 & \tilde{\omega}_1 \mathbf{v}_2 - \tilde{\omega}_2 \mathbf{v}_1 \\ \mathbf{0} & 0 \end{pmatrix} \\ &= \begin{pmatrix} [\tilde{\omega}_1, \tilde{\omega}_2]_{\mathfrak{so}} & \tilde{\omega}_1 \mathbf{v}_2 - \tilde{\omega}_2 \mathbf{v}_1 \\ \mathbf{0} & 0 \end{pmatrix}. \end{aligned} \quad (4.40)$$

Thus, as a Lie algebra, $\mathfrak{se}(3)$ is then equal to the semi-direct product

$$\mathfrak{se}(3) = \mathfrak{so}(3) \ltimes \mathbb{R}^3, \quad (4.41)$$

where $(\mathfrak{so}(3), [\cdot, \cdot]_{\mathfrak{so}})$ is a Lie-subalgebra of $(\mathfrak{se}(3), [\cdot, \cdot]_{\mathfrak{se}})$ and \mathbb{R}^3 is an ideal of $\mathfrak{se}(3)$.

Using the isomorphism (4.18), one can identify the Lie algebra $\mathfrak{se}(3)$ with $\mathbb{R}^3 \oplus \mathbb{R}^3$ and consequently \mathbb{R}^6 . This allows associating to every twist $\tilde{T} \in \mathfrak{se}(3)$

a pair of 3-dimensional vectors $(\boldsymbol{\omega}, \boldsymbol{v}) \in \mathbb{R}^3 \oplus \mathbb{R}^3$, and thus a six-dimensional vector $\boldsymbol{T} \in \mathbb{R}^6$.

For our purposes, the use of the vector representation allows performing different operations involving twists simply by using matrix multiplication. The **vector representation of a twist** is defined as

$$\boldsymbol{T} := \begin{pmatrix} \boldsymbol{\omega} \\ \boldsymbol{v} \end{pmatrix} \in \mathbb{R}^6,$$

which is related to the Lie algebra element in $\mathfrak{se}(3)$ by the vector space isomorphism

$$\begin{aligned} \tilde{\cdot} : \mathbb{R}^6 &\rightarrow \mathfrak{se}(3) \\ \boldsymbol{T} = \begin{pmatrix} \boldsymbol{\omega} \\ \boldsymbol{v} \end{pmatrix} &\mapsto \begin{pmatrix} \tilde{\boldsymbol{\omega}} & \boldsymbol{v} \\ \mathbf{0} & \mathbf{0} \end{pmatrix} = \tilde{\boldsymbol{T}}. \end{aligned} \quad (4.42)$$

With an abuse of notation, we will call both $\tilde{\boldsymbol{T}} \in \mathfrak{se}(3)$ and $\boldsymbol{T} \in \mathbb{R}^6$ a twist, where elements of $\mathfrak{se}(3)$ will always be distinguished with a *tilde*.

Remark 4.1.6 (Screw Representation of Twists). The pair of three-dimensional vectors $(\boldsymbol{\omega}, \boldsymbol{v}) \in \mathbb{R}^3 \oplus \mathbb{R}^3$ have important physical interpretations. On one hand, the two vectors $(\boldsymbol{\omega}, \boldsymbol{v})$ represent the angular and linear velocity components of the twist. On the other hand, these vectors allow associating a screw to the twist $\tilde{\boldsymbol{T}}$.

Screw theory is based on the geometry of lines in \mathbb{R}^3 and is considered an extremely important tool for the study of mechanisms, multi-body dynamics, and computer graphics. Intuitively, a screw is a line in \mathbb{R}^3 with a scalar quantity called the pitch. The vector $\boldsymbol{\omega} \in \mathbb{R}^3$ represents the direction of the line, whereas the vector $\boldsymbol{v} \in \mathbb{R}^3$ corresponds to the moment of the line. The pair of vectors $(\boldsymbol{\omega}, \boldsymbol{v})$ are called the **Plucker coordinates** of the screw corresponding to the infinitesimal rigid body motion.

For a more thorough introduction to screw theory and its relation to the Lie group formulation presented in this sequel, the reader is referred to [Stramigioli, 2001; Selig, 2004].

The dual of the Lie algebra $\mathfrak{se}(3)$

Now we discuss the dual entities to twists which consists of the linear maps $\tilde{\boldsymbol{W}}^* : \mathfrak{se}(3) \rightarrow \mathbb{R}$. The dual space of the Lie algebra $\mathfrak{se}(3)$ is denoted by $\mathfrak{se}^*(3)$, while the duality pairing on $\mathfrak{se}(3)$ is denoted by $\langle \cdot | \cdot \rangle_{\mathfrak{se}}$. We can also identify any linear map $\tilde{\boldsymbol{W}}^* \in \mathfrak{se}^*(3)$ by an element $\tilde{\boldsymbol{W}} \in \mathfrak{se}(3)$. Thus in what follows, we shall drop the asterisk-superscript from covectors.

The dual of the linear map (4.42) provides an isomorphism between $\mathfrak{se}^*(3)$ and $(\mathbb{R}^6)^* \cong \mathbb{R}^6$ given by

$$\begin{aligned}\tilde{\mathcal{S}}^* : \mathfrak{se}^*(3) &\rightarrow (\mathbb{R}^6)^* \\ \tilde{\mathbf{W}} &\mapsto \tilde{\mathcal{S}}^*(\tilde{\mathbf{W}}) =: \mathbf{W},\end{aligned}\tag{4.43}$$

defined implicitly such that

$$\left\langle \tilde{\mathcal{S}}^*(\tilde{\mathbf{W}}) \middle| \mathbf{T} \right\rangle_{\mathbb{R}^6} = \left\langle \tilde{\mathbf{W}} \middle| \tilde{\mathcal{S}}(\mathbf{T}) \right\rangle_{\mathfrak{se}},$$

or equivalently, using (4.42),

$$\langle \mathbf{W} | \mathbf{T} \rangle_{\mathbb{R}^6} = \left\langle \tilde{\mathbf{W}} \middle| \tilde{\mathbf{T}} \right\rangle_{\mathfrak{se}}.$$

To provide an explicit expression of the duality pairing $\langle \cdot | \cdot \rangle_{\mathfrak{se}}$, we utilize the fact that $\mathfrak{se}(3) \cong \mathfrak{so}(3) \oplus \mathbb{R}^3$ which implies that

$$\mathfrak{se}^*(3) \cong \mathfrak{so}^*(3) \oplus (\mathbb{R}^3)^*.\tag{4.44}$$

Therefore, we can identify any $\tilde{\mathbf{W}} \in \mathfrak{se}^*(3)$ by the pair $(\tilde{\boldsymbol{\tau}}, \mathbf{f}) \in \mathfrak{so}^*(3) \oplus (\mathbb{R}^3)^*$. The duality pairing between $\tilde{\mathbf{T}} \in \mathfrak{se}(3)$ and $\tilde{\mathbf{W}} \in \mathfrak{se}^*(3)$ is then expressed by

$$\left\langle \tilde{\mathbf{W}} \middle| \tilde{\mathbf{T}} \right\rangle_{\mathfrak{se}} = \langle \tilde{\boldsymbol{\tau}} | \tilde{\boldsymbol{\omega}} \rangle_{\mathfrak{so}} + \langle \mathbf{f} | \mathbf{v} \rangle_{\mathbb{R}^3} = \langle \boldsymbol{\tau} | \boldsymbol{\omega} \rangle_{\mathbb{R}^3} + \langle \mathbf{f} | \mathbf{v} \rangle_{\mathbb{R}^3} = \boldsymbol{\tau}^\top \boldsymbol{\omega} + \mathbf{f}^\top \mathbf{v},$$

which can be rewritten as

$$\left\langle \tilde{\mathbf{W}} \middle| \tilde{\mathbf{T}} \right\rangle_{\mathfrak{se}} = \mathbf{W}^\top \mathbf{T}, \quad \mathbf{W} = \begin{pmatrix} \boldsymbol{\tau} \\ \mathbf{f} \end{pmatrix} \in \mathbb{R}^6.\tag{4.45}$$

One physical example for a covector $\tilde{\mathbf{W}} \in \mathfrak{se}^*(3)$ corresponds to the **wrench** (i.e. generalized force) that is applied to a rigid body to have a general motion, rotational and translational. Its corresponding component $\tilde{\boldsymbol{\tau}} \in \mathfrak{so}^*(3)$ corresponds to the torque while its other component $\mathbf{f} \in (\mathbb{R}^3)^*$ corresponds to the force. The pairing between $\tilde{\mathbf{W}}$ and $\tilde{\mathbf{T}}$ corresponds to the total power that is supplied to generate the rigid body motion. Another physical example of a covector is the generalized momentum $\tilde{\mathbf{P}}$, which when paired with $\tilde{\mathbf{T}}$ corresponds to twice the total kinetic energy of the body.

Following the same line of thought as we did before for the cotangent spaces of $SO(3)$, we can map a co-vector $\boldsymbol{\Gamma}_H \in T_H^*SE(3)$ to two elements of the dual space $\mathfrak{se}^*(3)$. With reference to the commutative diagram in Fig. 4.8, a co-vector $\boldsymbol{\Gamma}_H \in T_{H_i^j}^*SE(3)$ is mapped to $\mathfrak{se}^*(3)$ by using the pullback at the identity $\mathbf{I} \in SE(3)$ of either the right translation map $(R_{H_i^j})_{\mathbf{I}}^*$ or left

$$\begin{array}{ccc}
T^i \in \mathbb{R}^6 & \xrightarrow{\tilde{S}} & \mathfrak{se}(3) \ni \tilde{T}^i \\
\textcolor{red}{Ad}_{H_i^j} \downarrow & & \downarrow \textcolor{red}{Ad}_{H_i^j} \\
T^j \in \mathbb{R}^6 & \xrightarrow{\tilde{S}} & \mathfrak{se}(3) \ni \tilde{T}^j
\end{array}
\quad
\begin{array}{ccc}
W^i \in (\mathbb{R}^6)^* & \xleftarrow{\tilde{S}^*} & \mathfrak{se}(3) \ni \tilde{W}^i \\
\textcolor{red}{Ad}_{H_i^j}^\top \uparrow & & \uparrow \textcolor{red}{Ad}_{H_i^j}^* \\
W^j \in (\mathbb{R}^6)^* & \xleftarrow{\tilde{S}^*} & \mathfrak{se}(3) \ni \tilde{W}^j
\end{array}$$

Figure 4.9: Matrix representations of the adjoint action of $SE(3)$ on $\mathfrak{se}(3)$ (left) and the coadjoint action of $SE(3)$ on $\mathfrak{se}^*(3)$ (right).

translation map $(L_{H_i^j})_I^*$, such that

$$\tilde{W}^j := (R_{H_i^j})_I^*(\Gamma_H) \in \mathfrak{se}^*(3), \quad (4.46)$$

$$\tilde{W}^i := (L_{H_i^j})_I^*(\Gamma_H) \in \mathfrak{se}^*(3), \quad (4.47)$$

where the pullback maps are defined implicitly by

$$\left\langle (R_{H_i^j})_I^*(\Gamma_H) \middle| \tilde{T}_i^{j,j} \right\rangle_{\mathfrak{se}} = \left\langle \Gamma_H \middle| (R_{H_i^j})_{*,I}(\tilde{T}_i^{j,j}) \right\rangle_{SE} \quad (4.48)$$

$$\left\langle (L_{H_i^j})_I^*(\Gamma_H) \middle| \tilde{T}_i^{i,j} \right\rangle_{\mathfrak{se}} = \left\langle \Gamma_H \middle| (L_{H_i^j})_{*,I}(\tilde{T}_i^{i,j}) \right\rangle_{SE}. \quad (4.49)$$

In summary, by combining (4.48) and (4.49) with (4.31-4.32) and (4.46-4.47), we have that

$$\left\langle \tilde{W}^j \middle| \tilde{T}_i^{j,j} \right\rangle_{\mathfrak{se}} = \left\langle \Gamma_H \middle| \dot{H}_i^j \right\rangle_{SE} = \left\langle \tilde{W}^i \middle| \tilde{T}_i^{i,j} \right\rangle_{\mathfrak{se}}.$$

Adjoint and Coadjoint actions of $SE(3)$

The change of coordinates of twists between any two frames is performed using the adjoint action of $SE(3)$ on $\mathfrak{se}(3)$.

For a given $H \in SE(3)$, the adjoint action Ad_H of the Lie group $SE(3)$ on the vector space $\mathfrak{se}(3)$ is defined as $Ad_H := (R_{H^{-1}} \circ L_H)_{*,I}$. Using (4.31) and (4.32), it follows that Ad_H is given by

$$\begin{aligned}
Ad_H : \mathfrak{se}(3) &\rightarrow \mathfrak{se}(3) \\
\tilde{T} &\mapsto H \tilde{T} H^{-1}.
\end{aligned} \quad (4.50)$$

Therefore, the body representation of a twist $\tilde{T}_B^{B,I}$ and its spatial counterpart $\tilde{T}_B^{I,I}$ are related by

$$\tilde{T}_B^{I,I} = Ad_{H_B^I}(\tilde{T}_B^{B,I}) = H_B^I \tilde{T}_B^{B,I} H_B^B.$$

The change of coordinates of covectors in $\mathfrak{se}^*(3)$ (e.g. wrenches and generalized momenta) can be achieved by the coadjoint action $Ad_H^* : \mathfrak{se}^*(3) \rightarrow \mathfrak{se}^*(3)$. The coadjoint action is the dual of the (4.50) and is defined implicitly by

$$\left\langle Ad_H^*(\tilde{\mathbf{W}}) \middle| \tilde{\mathbf{T}} \right\rangle_{\mathfrak{se}} = \left\langle \tilde{\mathbf{W}} \middle| Ad_H(\tilde{\mathbf{T}}) \right\rangle_{\mathfrak{se}}, \quad \tilde{\mathbf{T}} \in \mathfrak{se}(3), \tilde{\mathbf{W}} \in \mathfrak{se}^*(3). \quad (4.51)$$

It follows from (4.41) and (4.44) that two expressions for the map Ad_H^* can be calculated, one for its $\mathfrak{so}^*(3)$ component and another for its $(\mathbb{R}^3)^*$ component [Holm, 2008, Pg. 145]. Alternatively, one could exploit the vector representations of twists and wrenches to implement the adjoint and coadjoint actions above using matrix multiplication.

With reference to the commutative diagram in Fig. 4.9, the isomorphism (4.42) allows to represent the action of the adjoint map (4.50) by the square matrix $Ad_H : \mathbb{R}^6 \rightarrow \mathbb{R}^6$ defined by

$$Ad_H := \tilde{S}^{-1} \circ Ad_H \circ \tilde{S}. \quad (4.52)$$

Similarly, one can represent the coadjoint action Ad_H^* by the square matrix $Ad_H^\top : (\mathbb{R}^6)^* \rightarrow (\mathbb{R}^6)^*$ defined by

$$Ad_H^\top := \tilde{S}^* \circ Ad_H^* \circ (\tilde{S}^*)^{-1}, \quad (4.53)$$

which is simply the transpose of the one in (4.52).

The exact expressions of these matrices are given by [Stramigioli, 2001, Pg. 24-25]

$$Ad_H := \begin{pmatrix} \mathbf{R} & \mathbf{0} \\ \tilde{\boldsymbol{\xi}} \mathbf{R} & \mathbf{R} \end{pmatrix}, \quad Ad_H^\top := \begin{pmatrix} \mathbf{R}^\top & -\mathbf{R}^\top \tilde{\boldsymbol{\xi}} \\ \mathbf{0} & \mathbf{R}^\top \end{pmatrix}, \quad (4.54)$$

where $(\mathbf{R}, \boldsymbol{\xi}) \in SO(3) \times \mathbb{R}^3$ are the corresponding components for $\mathbf{H} \in SE(3)$.

Therefore, the body representation of the pair $(\mathbf{W}^B, \mathbf{T}_B^{B,I})$ is related to its spatial counterpart $(\mathbf{W}^I, \mathbf{T}_B^{I,I})$ by

$$\mathbf{T}_B^{I,I} = Ad_{H_B^I} \mathbf{T}_B^{B,I}, \quad \mathbf{W}^B = Ad_{H_B^I}^\top \mathbf{W}^I \quad (4.55)$$

Adjoint and Coadjoint actions of $\mathfrak{se}(3)$

The adjoint action of $SE(3)$ on $\mathfrak{se}(3)$ described above induces another adjoint action of $\mathfrak{se}(3)$ on itself. For a given $\tilde{\mathbf{T}} \in \mathfrak{se}(3)$, this induced action³ is denoted by $ad_{\tilde{\mathbf{T}}} : \mathfrak{se}(3) \rightarrow \mathfrak{se}(3)$ and related to (4.50) by

$$ad_{\tilde{\mathbf{T}}} := \left. \frac{d}{dt} \right|_{t=0} Ad_{\gamma_H(t)},$$

³Note that the ad map is usually referred to as the adjoint action of the Lie algebra $\mathfrak{se}(3)$, even though it is not a group action.

where γ_H is the curve with $\tilde{\mathbf{T}} \in \mathfrak{se}(3)$ as its tangent vector at $t = 0$ at $\gamma_H(0) = \mathbf{I}$. The exact expression of the induced adjoint map is given by

$$ad_{\tilde{\mathbf{T}}_1}(\tilde{\mathbf{T}}_2) := [\tilde{\mathbf{T}}_1, \tilde{\mathbf{T}}_2]_{\mathfrak{se}}, \quad \tilde{\mathbf{T}}_1, \tilde{\mathbf{T}}_2 \in \mathfrak{se}(3). \quad (4.56)$$

The coadjoint action $ad_{\tilde{\mathbf{T}}}^* : \mathfrak{se}^*(3) \rightarrow \mathfrak{se}^*(3)$, dual to $ad_{\tilde{\mathbf{T}}}$, will play a central role in the dynamical equations of motion governing rigid body motion, as will be shown later. This dual map is defined implicitly by

$$\left\langle ad_{\tilde{\mathbf{T}}_1}^*(\tilde{\mathbf{W}}) \middle| \tilde{\mathbf{T}}_2 \right\rangle_{\mathfrak{se}} = \left\langle \tilde{\mathbf{W}} \middle| ad_{\tilde{\mathbf{T}}_1}(\tilde{\mathbf{T}}_2) \right\rangle_{\mathfrak{se}}, \quad \tilde{\mathbf{T}}_1, \tilde{\mathbf{T}}_2 \in \mathfrak{se}(3), \tilde{\mathbf{W}} \in \mathfrak{se}^*(3). \quad (4.57)$$

Using the isomorphism (4.42) we can also represent the adjoint action $ad_{\tilde{\mathbf{T}}}$ using the matrix $\mathbf{ad}_{\mathbf{T}} : \mathbb{R}^6 \rightarrow \mathbb{R}^6$ defined by

$$\mathbf{ad}_{\mathbf{T}} := \tilde{\mathcal{S}}^{-1} \circ ad_{\tilde{\mathcal{S}}(\mathbf{T})} \circ \tilde{\mathcal{S}}. \quad (4.58)$$

Consequently, one has the matrix representation of the coadjoint action $ad_{\tilde{\mathbf{T}}}^*$ to be the matrix transpose $\mathbf{ad}_{\mathbf{T}}^\top : (\mathbb{R}^6)^* \rightarrow (\mathbb{R}^6)^*$.

The exact expressions of these matrices are given by [Stramigioli, 2001, Pg. 27]

$$\mathbf{ad}_{\mathbf{T}} = \begin{pmatrix} \tilde{\boldsymbol{\omega}} & \mathbf{0} \\ \tilde{\mathbf{v}} & \tilde{\boldsymbol{\omega}} \end{pmatrix}, \quad \mathbf{ad}_{\mathbf{T}}^\top = \begin{pmatrix} -\tilde{\boldsymbol{\omega}} & -\tilde{\mathbf{v}} \\ \mathbf{0} & -\tilde{\boldsymbol{\omega}} \end{pmatrix}, \quad (4.59)$$

where $\tilde{\boldsymbol{\omega}} = \mathcal{S}(\boldsymbol{\omega})$ and $\tilde{\mathbf{v}} = \mathcal{S}(\mathbf{v})$, while $\boldsymbol{\omega}, \mathbf{v} \in \mathbb{R}^3$ are the components of $\mathbf{T} \in \mathbb{R}^6$.

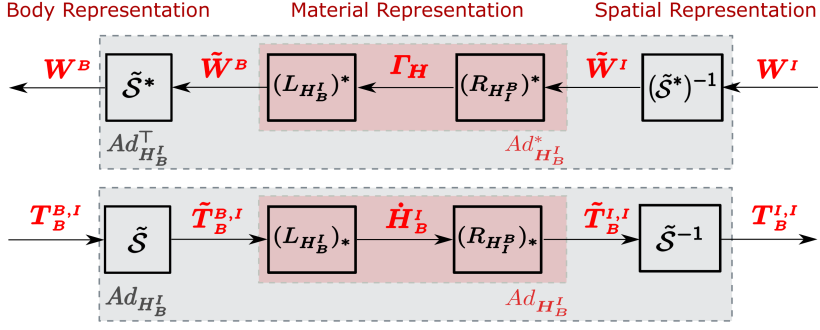
Port-based Interpretation of Duality

Finally, we conclude this section by a summary of the maps presented so far related to the Lie group structure of $SE(3)$, as shown in Fig. 4.10.

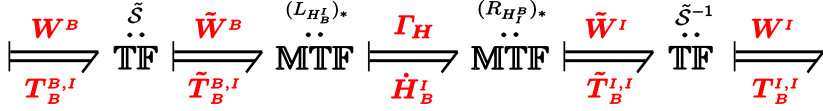
A very important observation that should be noted in Fig. 4.10 is the duality of the different maps and spaces presented. Although the pairs $(\mathbf{T}_H, \dot{\mathbf{H}})$, $(\tilde{\mathbf{W}}, \tilde{\mathbf{T}})$, and (\mathbf{W}, \mathbf{T}) belong to different spaces, their corresponding duality pairings are all equivalent if they are related with the corresponding maps shown in the figure.

From the physical point of view, all the duality pairings represent mechanical power and the variables in the pairs above are all *power-conjugate* variables. While the variables on the left correspond to the *body* representation and the variables on the right correspond to the *spatial* representation of the rigid body motion, the variables in the middle (combined with \mathbf{H}_B^L) represent the *material* representation of the rigid body motion.

In the port-Hamiltonian framework, each pair of the aforementioned ones defines a *power port* and the maps used for changing coordinates are perceived as *power-continuous transformations* from one port to another. The bond graph corresponding to the block diagram in Fig. 4.10a can be seen in Fig. 4.10b.



(a) Block Diagram



(b) Bond Graph

Figure 4.10: Summary of all maps introduced related to the Lie-group structure of $SE(3)$ in block diagram and bond graph representations

4.2 Port-Hamiltonian Modeling of a Rigid Body

In the previous section, we studied how to geometrically describe rigid body motion on its configuration space $SE(3)$. The Lie group structure of $SE(3)$ allowed us to have three representations of the motion: the material representation $(H_B^I, \dot{H}_B^I) \in TSE(3)$, the spatial representation $\tilde{T}_B^{I,I} \in \mathfrak{se}(3)$, and the body representation $\tilde{T}_B^{B,I} \in \mathfrak{se}(3)$.

Now we turn attention to representing the equations of motion governing rigid body dynamics in the port-Hamiltonian framework. As described earlier in Ch.2, the port-Hamiltonian modeling procedure aims for a decomposed model of a rigid body in terms of a network of interconnected energetic subsystems.

The first step in the port-Hamiltonian procedure is to conceptually tear the rigid body, as a dynamical system, into two subsystems; one characterizing kinetic energy and another one characterizing gravitational potential energy. In general, the kinetic energy is a function of the configuration and the generalized velocity, while the potential energy is a function of configuration only. However, when represented in terms of the body twist $\tilde{T}_B^{B,I}$, the kinetic energy can be written in terms of the generalized velocity alone. Consequently, one can model the kinetic energy completely on the Lie algebra $\mathfrak{se}(3)$ independently from the

configuration space $SE(3)$, which represents a symmetry.

In what follows, we will consider the port-Hamiltonian modeling of the kinetic energy subsystem, first as a closed dynamical system and then as an open one. After that we show how the potential energy subsystem is modeled and interconnected to the kinetic energy subsystem. The result will be a port-Hamiltonian dynamical model representing rigid body motion composed of a network of interconnected subsystems.

4.2.1 Kinetic Co-energy of a Rigid Body

Recall from Sec. 4.1.1 that a rigid body is defined as the pair (\mathcal{B}, ρ) , with $\mathcal{B} \subset \mathcal{E} \cong \mathbb{R}^3$ as the matter set and $\rho : \mathcal{B} \rightarrow \mathbb{R}^+$ as the mass density function describing the distribution of matter. Let μ_{vol} denote the standard volume form on \mathbb{R}^3 , $\xi \in \mathcal{B}$ denote a point of the rigid body, Ψ_I denote an inertial-fixed frame, Ψ_B denote a body-fixed coordinate frame, o_B denote the origin of Ψ_B , and $\xi^B \in \mathbb{R}^3$ denote the coordinate representation of the point ξ in the frame Ψ_B . By integrating over all points in \mathcal{B} , considering ξ as the independent variable, we can define the following properties of a rigid body:

1. Mass of the body:

$$m := \int_{\mathcal{B}} \rho(\xi) \mu_{\text{vol}} \in \mathbb{R}^+,$$

2. Center of mass of the body expressed in Ψ_B

$$\xi_{\text{cm}}^B := \frac{1}{m} \int_{\mathcal{B}} \rho(\xi) \xi^B \mu_{\text{vol}} \in \mathbb{R}^3,$$

3. Moment of inertia tensor of the body around o_B expressed in Ψ_B

$$\mathbf{J}^B := \int_{\mathcal{B}} \rho(\xi) (\tilde{\xi}^B)^\top \tilde{\xi}^B \mu_{\text{vol}} \in \mathbb{R}^{3 \times 3},$$

By analogy with the kinetic co-energy of a system of particles, we define the kinetic co-energy of the rigid body E_k^* as

$$E_k^* := \int_{\mathcal{B}} \rho(\xi) (\dot{\xi}^I)^\top \dot{\xi}^I \mu_{\text{vol}} \in \mathbb{R}^+, \quad (4.60)$$

where $\dot{\xi}^I \in \mathbb{R}^3$ denotes the velocity of the point $\xi \in \mathcal{B}$ with respect to the inertial frame Ψ_I and expressed in it.

The kinetic co-energy of a rigid body is given intuitively by the summation of the velocities of its (infinitely many) comprising points. The terminology *co-energy* is used in physical modeling to distinguish between the *energy* E

as a function of the (thermodynamically extensive) state of a dynamic system and the *co-energy* E^* as a function of a port-variable. Since the velocity of a point-mass is a port-variable we refer to E_k^* as the kinetic co-energy. For more discussion on the topic, *cf.* [Duindam et al., 2009, Sec. B.2] and [Breedveld, 1984].

The kinetic co-energy E_k^* given above can be written as a quadratic function in terms of the body twist $\mathbf{T}_B^{B,I} \in \mathbb{R}^6$ as given by the following result.

Proposition 4.2.1. *Let Ψ_I be an inertially-fixed frame and Ψ_B be a body-fixed frame. The total kinetic co-energy of a rigid body (4.60) can be expressed as*

$$E_k^*(\mathbf{T}_B^{B,I}) = \frac{1}{2}(\mathbf{T}_B^{B,I})^\top \mathcal{I}^B \mathbf{T}_B^{B,I}, \quad (4.61)$$

where $\mathcal{I}^B \in \mathbb{R}^{6 \times 6}$ is called the inertia tensor of the body, defined as

$$\mathcal{I}^B := \int_B \rho(\xi) \begin{pmatrix} (\tilde{\xi}^B)^\top \tilde{\xi}^B & \tilde{\xi}^B \\ \tilde{\xi}^B{}^\top & \mathbf{I}_3 \end{pmatrix} \mu_{\text{vol}}. \quad (4.62)$$

Proof. See [Duindam and Stramigioli, 2008, Pg. 38] ■

If the body frame Ψ_B is chosen such that its origin o_B coincides with the center of mass ξ_{cm}^B , and its basis $\{\hat{x}_B, \hat{y}_B, \hat{z}_B\}$ is aligned with principle directions of the inertia ellipsoid of the rigid body [Bullo and Lewis, 2005, Pg. 165], then the inertia tensor has the form of a diagonal matrix given by

$$\mathcal{I}^B = \begin{pmatrix} \mathbf{J}^B & \mathbf{0} \\ \mathbf{0} & m\mathbf{I}_3 \end{pmatrix}, \quad (4.63)$$

where the components of $\mathbf{J}^B = \text{diag}(J_x, J_y, J_z)$ denote the moments of inertia around the \hat{x}_B, \hat{y}_B , and \hat{z}_B axes of Ψ_B , respectively. We will always assume in this work that the body-fixed frame is chosen in such manner, which is always possible for any rigid body of any (fixed) geometry and material.

4.2.2 Closed Model of Kinetic Energy

In this section, the Hamiltonian equations of the kinetic energy subsystem will be derived using Hamiltonian reduction. First, we will derive the Hamiltonian dynamics on $\mathfrak{se}^*(3)$ and then present an equivalent representation on $(\mathbb{R}^6)^*$. For now on, all variables will be expressed in the body-fixed frame Ψ_B and thus all indices will be dropped for simplicity.

The kinetic co-energy introduced previously in (4.61) defines a function $\mathcal{L}_k : \mathfrak{se}(3) \rightarrow \mathbb{R}$ given by

$$\mathcal{L}_k(\tilde{\mathbf{T}}) := \frac{1}{2} \mathbf{T}^\top \mathcal{I} \mathbf{T}, \quad \mathbf{T} = \tilde{\mathcal{S}}^{-1}(\tilde{\mathbf{T}}) \in \mathbb{R}^6, \quad (4.64)$$

where $\mathbf{T} \in \mathbb{R}^6$ denotes the body twist and $\mathcal{I} \in \mathbb{R}^{6 \times 6}$ denotes the inertia tensor of the body given in (4.62).

The function \mathcal{L}_k is in fact a reduced Lagrangian corresponding to the true Lagrangian function $\mathcal{L}_k : TSE(3) \rightarrow \mathbb{R}$ on the tangent bundle defined by

$$\mathcal{L}_k(\mathbf{H}, \dot{\mathbf{H}}) := \mathcal{L}_k((L_{\mathbf{H}^{-1}})_{*, \mathbf{H}}(\dot{\mathbf{H}})), \quad (\mathbf{H}, \dot{\mathbf{H}}) \in TSE(3), \quad (4.65)$$

with the push-forward map is given in (4.32).

Using the Legendre transformation, we can construct the kinetic energy Hamiltonian $\mathcal{H}_k : \mathfrak{se}^*(3) \rightarrow \mathbb{R}$ to be

$$\mathcal{H}_k(\tilde{\mathbf{P}}) := \frac{1}{2} \mathbf{P}^\top \mathcal{I}^{-1} \mathbf{P}, \quad \mathbf{P} = \tilde{\mathcal{S}}^*(\tilde{\mathbf{P}}) \in (\mathbb{R}^6)^*, \quad (4.66)$$

where $\tilde{\mathbf{P}} := \partial \mathcal{L}_k / \partial \tilde{\mathbf{T}} \in \mathfrak{se}^*(3)$ is the conjugate momentum variable with respect to the body twist $\tilde{\mathbf{T}} \in \mathfrak{se}(3)$. Physically, $\tilde{\mathbf{P}} \in \mathfrak{se}^*(3)$ corresponds to the body representation of the **generalized momentum** of the rigid body related to the body-twist by $\mathbf{P} = \mathcal{I}\mathbf{T}$.

The function \mathcal{H}_k is also a reduced Hamiltonian corresponding to the true Hamiltonian $\mathcal{H}_k : T^*SE(3) \rightarrow \mathbb{R}$ on the cotangent bundle defined by

$$\mathcal{H}_k(\mathbf{H}, \mathbf{\Gamma}_H) := \mathcal{H}_k((L_H)_I^*(\mathbf{\Gamma}_H)), \quad (\mathbf{H}, \mathbf{\Gamma}_H) \in T^*SE(3), \quad (4.67)$$

with the pullback map is given in (4.47).

The Lie-Poisson reduction theorem [Marsden and Ratiu, 1999, Ch.13] asserts that the Hamiltonian dynamical equations on $\mathfrak{se}^*(3)$ are then given by

$$\dot{\tilde{\mathbf{P}}} = ad_{\partial_{\tilde{\mathbf{P}}} \mathcal{H}_k}^*(\tilde{\mathbf{P}}), \quad (4.68)$$

where the coadjoint map ad^* is the coadjoint action of $\mathfrak{se}(3)$ introduced earlier in (4.56), and $\partial_{\tilde{\mathbf{P}}} \mathcal{H}_k \in \mathfrak{se}(3)$ denotes the partial derivative of \mathcal{H}_k with respect to $\tilde{\mathbf{P}} \in \mathfrak{se}^*(3)$, which is equivalent to $\partial_{\tilde{\mathbf{P}}} \mathcal{H}_k = \tilde{\mathbf{T}}$.

The Hamiltonian equation (4.68) describes the conservation of kinetic energy which, using (4.56) and (4.57), can be seen from

$$\begin{aligned} \dot{\mathcal{H}}_k &= \left\langle \dot{\tilde{\mathbf{P}}} \left| \partial_{\tilde{\mathbf{P}}} \mathcal{H}_k \right\rangle_{\mathfrak{se}} = \left\langle ad_{\partial_{\tilde{\mathbf{P}}} \mathcal{H}_k}^*(\tilde{\mathbf{P}}) \left| \partial_{\tilde{\mathbf{P}}} \mathcal{H}_k \right\rangle_{\mathfrak{se}} \right. \\ &= \left\langle \tilde{\mathbf{P}} \left| ad_{\partial_{\tilde{\mathbf{P}}} \mathcal{H}_k}(\partial_{\tilde{\mathbf{P}}} \mathcal{H}_k) \right\rangle_{\mathfrak{se}} = \left\langle \tilde{\mathbf{P}} \left| [\partial_{\tilde{\mathbf{P}}} \mathcal{H}_k, \partial_{\tilde{\mathbf{P}}} \mathcal{H}_k]_{\mathfrak{se}} \right\rangle_{\mathfrak{se}} = 0, \end{aligned} \quad (4.69)$$

which follows from the skew-symmetry of the Lie bracket $[\cdot, \cdot]_{\mathfrak{se}}$.

The corresponding Lie-Poisson bracket, denoted by

$$\{\cdot, \cdot\} : C^\infty(\mathfrak{se}^*(3)) \times C^\infty(\mathfrak{se}^*(3)) \rightarrow C^\infty(\mathfrak{se}^*(3)),$$

that is associated to $\mathfrak{se}^*(3)$ and encodes the energy balance (4.69) is given by

$$\{F, G\}(\mathbf{x}) = \langle \mathbf{x} | [\partial_{\mathbf{x}} G, \partial_{\mathbf{x}} F]_{\mathfrak{se}} \rangle_{\mathfrak{se}}, \quad \forall F, G \in C^\infty(\mathfrak{se}^*(3)), \mathbf{x} \in \mathfrak{se}^*(3), \quad (4.70)$$

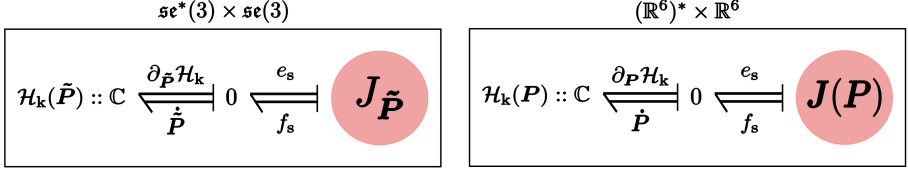


Figure 4.11: Port-based representation of the closed Hamiltonian models (4.68) and (4.71) of the kinetic energy subsystem. The left bond graph represents the dynamical system (4.68), while the right bond graph corresponds to its matrix representation (4.71).

which can be shown to be related to the canonical Poisson bracket on the cotangent bundle $T^*SE(3)$ [Marsden and Ratiu, 1999, Ch.13].

When we use the matrix representation of the coadjoint map ad^* in (4.59) and the corresponding vector representations of elements in $\mathfrak{se}(3)$ and $\mathfrak{se}^*(3)$, the Hamiltonian dynamical equation (4.68) takes the form

$$\dot{P} = ad_{\partial_P \mathcal{H}_k}^\top P, \quad (4.71)$$

where $P \in (\mathbb{R}^6)^*$, $\partial_P \mathcal{H}_k = \mathcal{I}^{-1}P = T \in \mathbb{R}^6$, and the kinetic energy Hamiltonian $\mathcal{H}_k(P) = \mathcal{H}_k(\tilde{P})$ is given by (4.66), where we abusively denote both Hamiltonian functions on $\mathfrak{se}^*(3)$ and $(\mathbb{R}^6)^*$ with \mathcal{H}_k .

4.2.3 Port-based Representation

In the port-based paradigm, the dynamical system described in (4.68) is represented by two elements interconnected using ports, as shown in Fig. 4.11 (left). The first element corresponds to the storage of the kinetic energy (4.66) and the second one corresponds to the interconnection structure encoded in the Lie-Poisson bracket (4.70).

The energy storage element is defined by the state space manifold $\mathfrak{se}^*(3)$ with the kinetic energy Hamiltonian $\mathcal{H}_k : \mathfrak{se}^*(3) \rightarrow \mathbb{R}$. The body momentum $\tilde{P} \in \mathfrak{se}^*(3)$ represents the state variable of the element.

The variables $\dot{\tilde{P}} \in T_{\tilde{P}}\mathfrak{se}^*(3) \cong \mathfrak{se}^*(3)$ and $\partial_{\tilde{P}}\mathcal{H}_k \in T_{\tilde{P}}^*\mathfrak{se}^*(3) \cong \mathfrak{se}(3)$ represent the flow and effort variables of the energy storage element, respectively. The duality pairing of the effort and flow variables correspond to the rate of change of the Hamiltonian $\dot{\mathcal{H}}_k = \left\langle \dot{\tilde{P}} \middle| \partial_{\tilde{P}}\mathcal{H}_k \right\rangle_{\mathfrak{se}}$, which represents the power entering the kinetic energy storage element at a certain instant of time.

The second element corresponds to the Lie-Poisson structure defined by the map $J_{\tilde{P}} : \mathfrak{se}(3) \rightarrow \mathfrak{se}^*(3)$ defined by

$$J_{\tilde{P}}(e_s) := ad_{e_s}^*(\tilde{P}), \quad \tilde{P} \in \mathfrak{se}^*(3), e_s \in \mathfrak{se}(3). \quad (4.72)$$

The effort and flow variables of the Lie-Poisson structure are denoted by $e_s \in \mathfrak{se}(3)$ and $f_s := J_{\tilde{P}}(e_s) \in \mathfrak{se}^*(3)$, respectively.

By connecting the ports (e_s, f_s) and $(\partial_{\tilde{P}}\mathcal{H}_k, \dot{\tilde{P}})$ of the two elements together by the *zero-junction* (or *one-junction*) implementing the constraints

$$f_s = \dot{\tilde{P}}, \quad e_s = \partial_{\tilde{P}}\mathcal{H}_k,$$

one recovers the port-Hamiltonian representation of (4.68) given by

$$\dot{\tilde{P}} = J_{\tilde{P}}(\partial_{\tilde{P}}\mathcal{H}_k). \quad (4.73)$$

Following the same line of thought, the dynamic system (4.73) can also be represented as the interconnection of two elements, as shown in Fig. 4.11 (right). The port-Hamiltonian system corresponding to (4.73) is given by

$$\dot{P} = J(P)\partial_P\mathcal{H}_k, \quad (4.74)$$

where $J(P) = -J^\top(P) \in \mathbb{R}^{6 \times 6}$ is the skew-symmetric matrix

$$J(P) = \begin{pmatrix} \tilde{P}_\omega & \tilde{P}_v \\ \tilde{P}_v & \mathbf{0} \end{pmatrix}, \quad P = \begin{pmatrix} P_\omega \\ P_v \end{pmatrix} \in (\mathbb{R}^6)^*, \quad (4.75)$$

where $\tilde{P}_\omega, \tilde{P}_v$ are the skew-symmetric matrices related to $P_\omega, P_v \in (\mathbb{R}^3)^*$ using (4.20).

The two covectors P_ω, P_v correspond physically to the angular momentum and linear momentum of the rigid body respectively. From the expression of the inertia tensor (4.63), one has that $P_\omega = J\omega$ and $P_v = mv$.

Remark 4.2.2. As a map, $J(P) : \mathbb{R}^6 \rightarrow \mathbb{R}^6$ is related to $J_{\tilde{P}}$ by $J(P) := \tilde{S}^* \circ J_{\tilde{P}} \circ \tilde{S}^{-1}$, with \tilde{S} and \tilde{S}^* given respectively by (4.42) and (4.43). The expression for $J(P)$ in (4.75) can be derived by manipulating the right-hand side of (4.71) using the identity $\tilde{x}y = \tilde{y}^\top x, \forall x, y \in \mathbb{R}^3$.

The skew-symmetry property of $J(P)$ immediately implies the conservation of kinetic energy, that can be seen from

$$\dot{\mathcal{H}}_k = \dot{P}^\top \partial_P \mathcal{H}_k = (\partial_P \mathcal{H}_k)^\top J^\top(P) \partial_P \mathcal{H}_k = 0,$$

which is indeed equivalent to (4.69).

In summary, the closed port-Hamiltonian models (4.73) and (4.74), shown graphically in Fig. 4.11, describe the kinetic energy of a rigid body isolated from the rest of the world such that the kinetic energy Hamiltonian is a conserved quantity.

Next, we show how to allow non-zero exchange by extending the Lie-Poisson structure to a Dirac structure. This non-zero change of the kinetic energy will be due to power supplied to the rigid body as a consequence of an externally applied wrench.

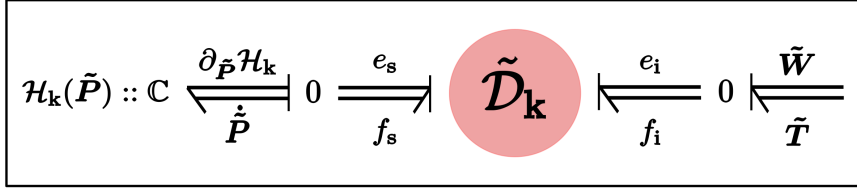
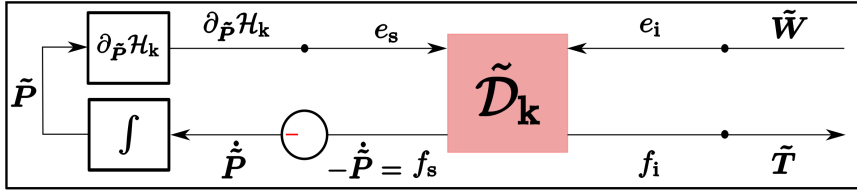
Bond Graph**Block Diagram**

Figure 4.12: Port-based representation of the open port-Hamiltonian model (4.76) of the kinetic energy subsystem.

4.2.4 Open Model of Kinetic Energy

Newton's second law of motion states that the variation of momentum of a rigid body expressed in an inertial frame is equal to the applied wrench on the body. In a body fixed-frame, Newton's law takes the form

$$\dot{\tilde{\mathbf{P}}} = J_{\tilde{\mathbf{P}}}(\partial_{\tilde{\mathbf{P}}} \mathcal{H}_k) + \tilde{\mathbf{W}}, \quad (4.76)$$

where $\tilde{\mathbf{W}} \in \mathfrak{se}^*(3)$ corresponds to the body representation of the wrench externally applied to the rigid body.

Along solutions of the system (4.76), the energy balance (4.69) takes the form:

$$\dot{\mathcal{H}}_k = \left\langle \dot{\tilde{\mathbf{P}}} \middle| \partial_{\tilde{\mathbf{P}}} \mathcal{H}_k \right\rangle_{\mathfrak{se}} = 0 + \left\langle \tilde{\mathbf{W}} \middle| \partial_{\tilde{\mathbf{P}}} \mathcal{H}_k \right\rangle_{\mathfrak{se}} = \left\langle \tilde{\mathbf{W}} \middle| \tilde{\mathbf{T}} \right\rangle_{\mathfrak{se}}, \quad (4.77)$$

where $\left\langle \tilde{\mathbf{W}} \middle| \tilde{\mathbf{T}} \right\rangle_{\mathfrak{se}} \in \mathbb{R}$ corresponds to the power *supplied to* the kinetic energy subsystem *from* the external entity that generates the wrench applied to the rigid body.

From the energy balance (4.77), it can be deduced that the twist $\tilde{\mathbf{T}} \in \mathfrak{se}(3)$ is the power conjugate variable to the external wrench $\tilde{\mathbf{W}} \in \mathfrak{se}^*(3)$. The pair $(\tilde{\mathbf{W}}, \tilde{\mathbf{T}})$ represent the interaction port with which the kinetic energy subsystem can be interconnected to other subsystems, as shown in Fig. 4.12.

The Dirac structure that mediates the kinetic energy stored and the exter-

nally applied power is defined as the subspace

$$\tilde{\mathcal{D}}_k = \left\{ (\mathbf{f}_s, \mathbf{f}_i, \mathbf{e}_s, \mathbf{e}_i) \in \mathcal{F}_k \times \mathcal{E}_k \mid \begin{pmatrix} \mathbf{f}_s \\ \mathbf{f}_i \end{pmatrix} = \begin{pmatrix} -J_{\tilde{\mathbf{P}}} & -1 \\ 1 & 0 \end{pmatrix} \begin{pmatrix} \mathbf{e}_s \\ \mathbf{e}_i \end{pmatrix} \right\}, \quad (4.78)$$

where $\mathcal{F}_k := \mathfrak{se}^*(3) \times \mathfrak{se}(3)$ and $\mathcal{E}_k := \mathcal{F}_k^*$ are the flow and effort spaces on which $\tilde{\mathcal{D}}_k$ is defined. The pair $(\mathbf{e}_s, \mathbf{f}_s)$ is called the storage port of the Dirac structure, whereas $(\mathbf{e}_i, \mathbf{f}_i)$ is called its interaction port, which in the case at hand is simply $(\mathbf{e}_i, \mathbf{f}_i) = (\tilde{\mathbf{W}}, \tilde{\mathbf{T}})$.

The open port-Hamiltonian model for the kinetic energy is now constructed by connecting the storage port of the Dirac structure to the kinetic energy storage element by

$$(\mathbf{e}_s, \mathbf{f}_s) = (\partial_{\tilde{\mathbf{P}}} \mathcal{H}_k, -\dot{\tilde{\mathbf{P}}}).$$

Then, one recovers (4.76) along with the output equation $\tilde{\mathbf{T}} = \partial_{\tilde{\mathbf{P}}} \mathcal{H}_k$. Furthermore, in terms of the matrix representation, the explicit port-Hamiltonian dynamical equations take the form

$$\dot{\tilde{\mathbf{P}}} = \mathbf{J}(\mathbf{P}) \partial_{\mathbf{P}} \mathcal{H}_k + \mathbf{W}, \quad (4.79)$$

$$\mathbf{T} = \partial_{\mathbf{P}} \mathcal{H}_k. \quad (4.80)$$

Similar to the Dirac structure (4.78), one could represent the port-Hamiltonian equations (4.79- 4.80) using another Dirac structure \mathcal{D}_k defined by

$$\mathcal{D}_k = \left\{ (\mathbf{f}_s, \mathbf{f}_i, \mathbf{e}_s, \mathbf{e}_i) \in \mathcal{F}_k \times \mathcal{E}_k \mid \begin{pmatrix} \mathbf{f}_s \\ \mathbf{f}_i \end{pmatrix} = \begin{pmatrix} -\mathbf{J}(\mathbf{P}) & -\mathbf{I}_6 \\ \mathbf{I}_6 & \mathbf{0} \end{pmatrix} \begin{pmatrix} \mathbf{e}_s \\ \mathbf{e}_i \end{pmatrix} \right\}, \quad (4.81)$$

with $\mathbf{I}_6 \in \mathbb{R}^{6 \times 6}$ denoting the identity matrix, and the flow space \mathcal{F}_k is now given by $(\mathbb{R}^6)^* \times \mathbb{R}^6$ and the effort space is accordingly $\mathcal{E}_k := \mathcal{F}_k^*$.

This concludes the construction of the port-Hamiltonian model for the kinetic energy of a rigid body. In the coming sections, we show how the open interaction port $(\tilde{\mathbf{W}}, \tilde{\mathbf{T}})$ (or (\mathbf{W}, \mathbf{T})) will be used to interconnect the kinetic-energy subsystem, presented so far, to another storage subsystem that represents gravitational potential energy.

4.2.5 Open Model of Potential Energy

The storage of the rigid body's gravitational potential energy is represented by a storage subsystem with state manifold $SE(3)$ and its corresponding state variable $\mathbf{H} \in SE(3)$ being the configuration of the body with respect to an inertial frame.

The gravitational potential energy $\mathcal{H}_g : SE(3) \rightarrow \mathbb{R}$ is given by

$$\mathcal{H}_g(\mathbf{H}) = m \boldsymbol{\xi}^\top \mathbf{g}, \quad (4.82)$$

where $\boldsymbol{\xi} \in \mathbb{R}^3$ is the translation component of the configuration and $\mathbf{g} \in \mathbb{R}^3$ is the inverse direction of the gravitational acceleration in the inertial frame. For example, if the inertial frame Ψ_I is chosen such that gravity is aligned with $-\hat{\mathbf{z}}_I$, then $\mathbf{g} = g\hat{\mathbf{z}}_I$, where $g \approx 9.81 \text{ ms}^{-2}$ is the gravitational acceleration constant.

The effort and flow variables of the potential energy storage subsystem are given, respectively, by

$$\partial_{\mathbf{H}}\mathcal{H}_g \in T_{\mathbf{H}}^*SE(3), \quad \dot{\mathbf{H}} \in T_{\mathbf{H}}SE(3).$$

The duality pairing of the effort and flow variables yields the power entering the potential energy subsystem given by

$$\dot{\mathcal{H}}_g = \left\langle \partial_{\mathbf{H}}\mathcal{H}_g \mid \dot{\mathbf{H}} \right\rangle_{\text{SE}},$$

where $\langle \cdot \mid \cdot \rangle_{\text{SE}}$ is the duality pairing associated to the vector space $T_{\mathbf{H}}SE(3)$.

Due to the semi-direct product structure of $SE(3)$, we have from (4.30) that

$$\left\langle \partial_{\mathbf{H}}\mathcal{H}_g \mid \dot{\mathbf{H}} \right\rangle_{\text{SE}} = \left\langle \partial_{\mathbf{R}}\mathcal{H}_g \mid \dot{\mathbf{R}} \right\rangle_{\text{SO}} + \left\langle \partial_{\boldsymbol{\xi}}\mathcal{H}_g \mid \dot{\boldsymbol{\xi}} \right\rangle_{\mathbb{R}^3} = \left\langle \partial_{\boldsymbol{\xi}}\mathcal{H}_g \mid \dot{\boldsymbol{\xi}} \right\rangle_{\mathbb{R}^3} = (m\mathbf{g})^\top \dot{\boldsymbol{\xi}}, \quad (4.83)$$

which follows from the fact that $\partial_{\mathbf{R}}\mathcal{H}_g = \mathbf{0}$ as obvious in (4.82). Therefore, we have that $\partial_{\boldsymbol{\xi}}\mathcal{H}_g = m\mathbf{g} \in (\mathbb{R}^3)^*$.

The conservation of the potential energy $\dot{\mathcal{H}}_g = 0$ simply implies that $\dot{\mathbf{H}} = 0$, since $\partial_{\mathbf{H}}\mathcal{H}_g \neq 0$ as seen from (4.82). Therefore, the trivial equation $\dot{\mathbf{H}} = 0$ corresponds to the Hamiltonian dynamical equations of the potential energy subsystem isolated from the world. However, as an energetic subsystem of the rigid body model, the change in potential energy will be caused by the transformation of kinetic energy, as will be seen next.

4.2.6 Port-Hamiltonian Dynamics of a Rigid Body

So far we have constructed the separated port-Hamiltonian models of the two energetic subsystems comprising a rigid body: one for kinetic energy and one for gravitational potential energy. Now we show how the open interaction port of the kinetic energy subsystem, denoted here by $(\tilde{\mathbf{W}}_g, \tilde{\mathbf{T}})$, will be connected to the gravitational potential energy subsystem such that $\tilde{\mathbf{W}}_g \in \mathfrak{se}^*(3)$ corresponds to the external wrench applied due to gravity.

The first law of thermodynamics states that energy can neither be created, nor destroyed which implies that the change of kinetic energy has to be equivalent to the inverse change of potential energy. Therefore, the power incoming the potential energy subsystem should be equal to the power out-coming the

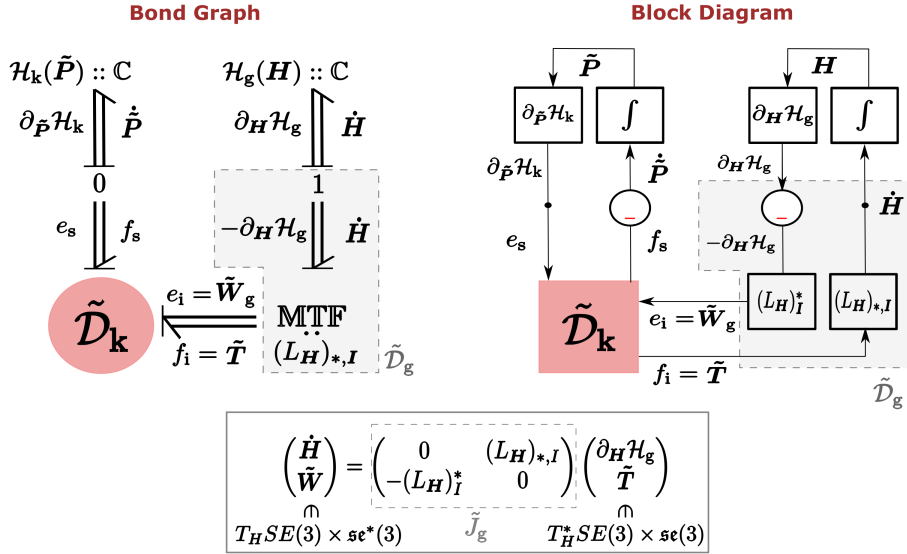


Figure 4.13: Augmenting the kinetic energy subsystem (4.76) with the storage of gravitational potential energy through the interaction port (\tilde{W}_g, \tilde{T}) . The bond graph (left) and block diagram (right) representations are shown.

interaction port of the kinetic energy subsystem i.e.

$$\left\langle \partial_H \mathcal{H}_g | \dot{H} \right\rangle_{SE} = - \left\langle \tilde{W}_g | \tilde{T} \right\rangle_{\mathfrak{se}}. \quad (4.84)$$

To interconnect the external port of the kinetic energy subsystem $(\tilde{W}_g, \tilde{T}) \in \mathfrak{se}^*(3) \times \mathfrak{se}(3)$ with the port of the potential energy subsystem $(\partial_H \mathcal{H}_g, \dot{H}) \in T_H^* SE(3) \times T_H SE(3)$ they should be compatible, which is clearly not the case. However, using the Lie group structure of $SE(3)$, one could then resolve this incompatibility using a power-continuous transformation.

In the bond graph of Fig. 4.13, this transformation is achieved by the modulated transformer element MTF that implements the map

$$\begin{pmatrix} \dot{H} \\ \dot{\tilde{W}}_g \end{pmatrix} = \begin{pmatrix} 0 & (L_H)_{*,I} \\ (L_H)_I^* & 0 \end{pmatrix} \begin{pmatrix} -\partial_H \mathcal{H}_g \\ \tilde{T} \end{pmatrix}, \quad (4.85)$$

where the pushforward map $(L_H)_{*,I} : \mathfrak{se}(3) \rightarrow T_H SE(3)$ and its dual $(L_H)_I^* : T_H^* SE(3) \rightarrow \mathfrak{se}^*(3)$ are given by (4.32) and (4.49), respectively. The minus sign next to $\partial_H \mathcal{H}_g$ in (4.85) is due to the *one-junction* in Fig. 4.13 used to invert the power entering the potential energy subsystem i.e. implementing the equality

$$\left\langle \partial_H \mathcal{H}_g | \dot{H} \right\rangle_{SE} = - \left\langle -\partial_H \mathcal{H}_g | \dot{H} \right\rangle_{SE}.$$

The combination of the one-junction and the MTF represent a power-continuous Dirac structure $\tilde{\mathcal{D}}_g$ given by the relation corresponding to the skew-symmetric map

$$\tilde{J}_g : T_{\mathbf{H}}^*SE(3) \times \mathfrak{se}(3) \rightarrow T_{\mathbf{H}}SE(3) \times \mathfrak{se}^*(3),$$

as illustrated in Fig. 4.13. The Dirac structure $\tilde{\mathcal{D}}_g$ is modulated by the configuration $\mathbf{H} \in SE(3)$ and its power-continuity is a consequence of the skew-symmetry of the map \tilde{J}_g .

Now we show that the previous energy-based construction correctly models a free rigid body moving in a gravitational field. First, we show that the transformations (4.85) model the transfer of kinetic energy to potential energy. Starting from the power supplied to the kinetic energy subsystem $\langle \tilde{\mathbf{W}}_g | \tilde{\mathbf{T}} \rangle_{\mathfrak{se}}$ and using (4.32), (4.49) and (4.85), we have that

$$\begin{aligned} \langle \tilde{\mathbf{W}}_g | \tilde{\mathbf{T}} \rangle_{\mathfrak{se}} &= \langle (L_{\mathbf{H}})_I^* (-\partial_{\mathbf{H}} \mathcal{H}_g) | \tilde{\mathbf{T}} \rangle_{\mathfrak{se}} \\ &= - \langle \partial_{\mathbf{H}} \mathcal{H}_g | (L_{\mathbf{H}})_{*,I}(\tilde{\mathbf{T}}) \rangle_{\text{SE}} = - \langle \partial_{\mathbf{H}} \mathcal{H}_g | \dot{\mathbf{H}} \rangle_{\text{SE}} = -\dot{\mathcal{H}}_g, \end{aligned} \quad (4.86)$$

which satisfies (4.84). Furthermore, by construction, we have that the upper row in (4.85)

$$\dot{\mathbf{H}} = (L_{\mathbf{H}})_{*,I}(\tilde{\mathbf{T}}) = \mathbf{H} \tilde{\mathbf{T}}, \quad (4.87)$$

corresponds to the rigid body kinematics relation in (4.32), while the lower row yields

$$\tilde{\mathbf{W}}_g = (L_{\mathbf{H}})_I^* (-\partial_{\mathbf{H}} \mathcal{H}_g), \quad (4.88)$$

which represents the externally applied wrench due to gravity as shown in the following result.

Proposition 4.2.3. *The wrench due to gravity $\tilde{\mathbf{W}}_g \in \mathfrak{se}^*(3)$ expressed in the body frame given by (4.88) has its corresponding covector $\mathbf{W}_g \in (\mathbb{R}^6)^*$, defined using (4.43), given by*

$$\mathbf{W}_g = \begin{pmatrix} \mathbf{0} \\ -m \mathbf{R}^\top \mathbf{g} \end{pmatrix} \in (\mathbb{R}^6)^*. \quad (4.89)$$

Proof. From (4.45), we have that

$$\langle \tilde{\mathbf{W}}_g | \tilde{\mathbf{T}} \rangle_{\mathfrak{se}} = \langle \tilde{\tau}_g | \tilde{\omega} \rangle_{\mathfrak{so}} + \langle \mathbf{f}_g | \mathbf{v} \rangle_{\mathbb{R}^3},$$

where $(\tilde{\tau}_g, \mathbf{f}_g) \in \mathfrak{so}^*(3) \oplus (\mathbb{R}^3)^*$ are the components of $\tilde{\mathbf{W}}_g \in \mathfrak{se}^*(3)$, and $(\tilde{\omega}, \mathbf{v}) \in \mathfrak{so}(3) \times \mathbb{R}^3$ are the components of $\tilde{\mathbf{T}} \in \mathfrak{se}(3)$. Therefore, using (4.86) and (4.83), we have that

$$\langle \tilde{\mathbf{W}}_g | \tilde{\mathbf{T}} \rangle_{\mathfrak{se}} = \langle \tilde{\tau}_g | \tilde{\omega} \rangle_{\mathfrak{so}} + \langle \mathbf{f}_g | \mathbf{v} \rangle_{\mathbb{R}^3} = - \langle \partial_{\xi} \mathcal{H}_g | \dot{\xi} \rangle_{\mathbb{R}^3} = - \langle m \mathbf{g} | \dot{\xi} \rangle_{\mathbb{R}^3},$$

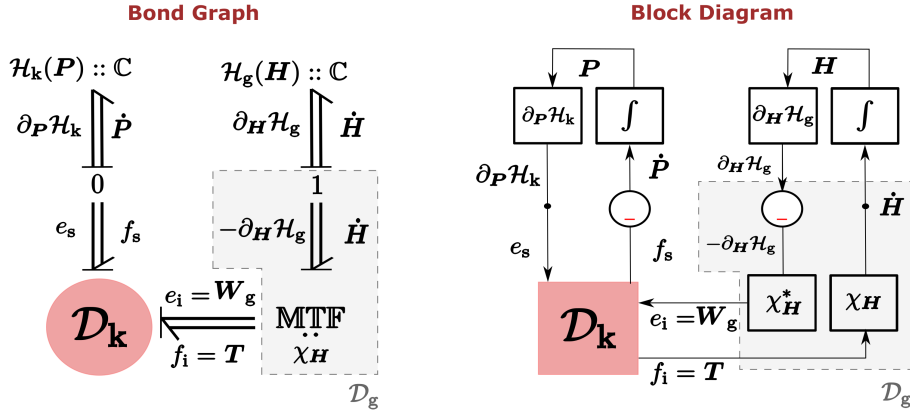


Figure 4.14: Augmenting the kinetic energy subsystem (4.79-4.80) with the storage of gravitational potential energy through the interaction port (W_g, T) . The bond graph (left) and block diagram (right) representations are shown.

which implies that $\tilde{\tau}_g = \mathbf{0}$. Using the relation $\dot{\xi} = Rv$ from (4.37), we have that

$$\langle f_g | v \rangle_{\mathbb{R}^3} = \langle -mg | Rv \rangle_{\mathbb{R}^3} = \langle -mR^\top g | v \rangle_{\mathbb{R}^3},$$

and thus $f_g = -mR^\top g$. ■

In conclusion, the port-Hamiltonian model consisting of the network of interconnected subsystems shown in Fig. 4.13 correctly represents the motion of a free rigid body in a gravitational field. This network consists of the kinetic energy subsystem of Sec. 4.2.4, the potential energy subsystem of Sec. 4.2.5, and the Dirac structure $\tilde{\mathcal{D}}_g$ that mediates the energy flow between them.

The port-Hamiltonian rigid body model can be also constructed using the matrix representation of the kinetic energy subsystem, as shown in Fig. 4.14. In this case, the Dirac structure \mathcal{D}_g that resolves the incompatibility of the ports (W_g, T) and $(\partial_H \mathcal{H}_g, \dot{H})$ is given by the relation corresponding to the skew-symmetric map

$$\begin{pmatrix} \dot{H} \\ W_g \end{pmatrix} = \begin{pmatrix} \mathbf{0} & \chi_H \\ -\chi_H^* & \mathbf{0} \end{pmatrix} \begin{pmatrix} \partial_H \mathcal{H}_g \\ T \end{pmatrix}, \quad (4.90)$$

where the map $\chi_H : \mathbb{R}^6 \rightarrow T_H SE(3)$ and its dual $\chi_H^* : T_H^* SE(3) \rightarrow (\mathbb{R}^6)^*$ are defined by

$$\chi_H := (L_H)_{*,I} \tilde{\mathcal{S}}, \quad \chi_H^* := \tilde{\mathcal{S}}^* \circ (L_H)_I^*. \quad (4.91)$$

We conclude by a compact port-Hamiltonian model that combines the energy storage elements together and combines the Dirac structures together, as

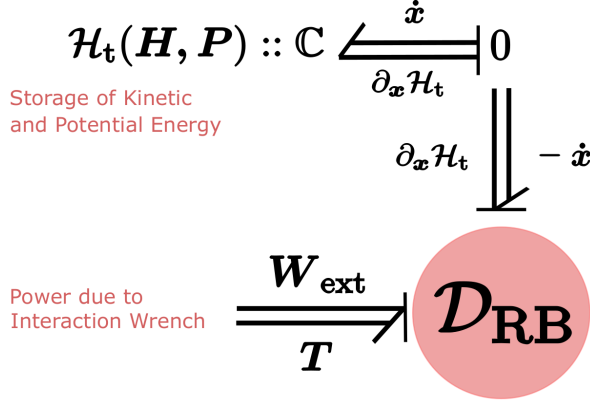


Figure 4.15: Bond graph representation of the compact port-Hamiltonian model (4.95-4.96) for free rigid body motion in a gravitational field.

shown in Fig. 4.15. This open model will include an additional interaction port $(\mathbf{W}_{\text{ext}}, \mathbf{T})$ that represents the power due to external wrenches applied to the rigid body other than gravity. For future reference, we will present this model directly in terms of the matrix representation.

The new storage element has its state variable $\mathbf{x} := (\mathbf{H}, \mathbf{P}) \in SE(3) \times (\mathbb{R}^6)^*$ and its Hamiltonian \mathcal{H}_t given by the sum of kinetic and gravitational potential energy, i.e.

$$\mathcal{H}_t(\mathbf{x}) = \mathcal{H}_t(\mathbf{H}, \mathbf{P}) = \frac{1}{2} \mathbf{P}^\top \mathcal{I}^{-1} \mathbf{P} + m \boldsymbol{\xi}^\top \mathbf{g}. \quad (4.92)$$

The flow and effort variables of the new storage element are given by

$$\dot{\mathbf{x}} = \begin{pmatrix} \dot{\mathbf{H}} \\ \dot{\mathbf{P}} \end{pmatrix} \in T_{\mathbf{H}} SE(3) \times (\mathbb{R}^6)^*, \quad \partial_{\mathbf{x}} \mathcal{H}_t = \begin{pmatrix} \partial_{\mathbf{H}} \mathcal{H}_t \\ \partial_{\mathbf{P}} \mathcal{H}_t \end{pmatrix} \in T_{\mathbf{H}}^* SE(3) \times \mathbb{R}^6.$$

The explicit port-Hamiltonian dynamics of the rigid body moving in a gravitational field is given by

$$\begin{pmatrix} \dot{\mathbf{H}} \\ \dot{\mathbf{P}} \end{pmatrix} = \underbrace{\begin{pmatrix} \mathbf{0} & \chi_{\mathbf{H}} \\ -\chi_{\mathbf{H}}^* & \mathbf{J}(\mathbf{P}) \end{pmatrix}}_{\mathbf{J}_{\text{RB}}(\mathbf{x})} \begin{pmatrix} \partial_{\mathbf{H}} \mathcal{H}_t \\ \partial_{\mathbf{P}} \mathcal{H}_t \end{pmatrix} + \underbrace{\begin{pmatrix} \mathbf{0} \\ \mathbf{I}_6 \end{pmatrix}}_{\mathbf{G}} \mathbf{W}_{\text{ext}} \quad (4.93)$$

$$\mathbf{T} = \underbrace{\begin{pmatrix} \mathbf{0} & \mathbf{I}_6 \end{pmatrix}}_{\mathbf{G}^\top} \begin{pmatrix} \partial_{\mathbf{H}} \mathcal{H}_t \\ \partial_{\mathbf{P}} \mathcal{H}_t \end{pmatrix}, \quad (4.94)$$

or more compactly

$$\dot{\mathbf{x}} = \mathbf{J}_{\text{RB}}(\mathbf{x}) \partial_{\mathbf{x}} \mathcal{H}_t + \mathbf{G} \mathbf{W}_{\text{ext}} \quad (4.95)$$

$$\mathbf{T} = \mathbf{G}^\top \partial_{\mathbf{x}} \mathcal{H}_t. \quad (4.96)$$

Finally, the underlying Dirac structure \mathcal{D}_{RB} of the port-Hamiltonian dynamic model of the rigid body in (4.95,4.96) is given by the relation corresponding to the skew-symmetric map

$$\begin{pmatrix} -\dot{\mathbf{x}} \\ \mathbf{T} \end{pmatrix} = \begin{pmatrix} -\mathbf{J}_{\text{RB}}(\mathbf{x}) & -\mathbf{G} \\ \mathbf{G}^\top & \mathbf{0} \end{pmatrix} \begin{pmatrix} \partial_{\mathbf{x}} \mathcal{H}_t \\ \mathbf{W}_{\text{ext}} \end{pmatrix}. \quad (4.97)$$

4.3 Conclusion

In this chapter, a systematic procedure to model rigid body motion in the port-Hamiltonian framework was presented. The outcome was a decomposed and open port-Hamiltonian model for a rigid body consisting of a network of interconnected energetic elements.

We have shown that central to this network representation of a rigid body is a Dirac structure that mediates the energy flow between the different elements. Furthermore, we have demonstrated that using Lie-Poisson reduction and the proper geometric formulation of the state space, the port-Hamiltonian model of the rigid body can be derived systematically from first principles.

The geometric formulation of the rigid body kinematics on the matrix Lie group $SE(3)$ has allowed a straightforward construction of the port-Hamiltonian model and a unified treatment of the rotational and translational dynamics of the system. While most of the work in this chapter relied on the numerical representation of a rigid body's configuration space, the coordinate-free material presented in the beginning has explicated several assumptions that are usually hidden when using coordinates. This distinction between the coordinate-free and coordinate-based treatments will be essential for extending several concepts to infinite-dimensional mechanical systems, as will be shown in Ch.5.

An important feature of the derived port-Hamiltonian rigid body model is that it is an *open model*. Using the interaction port, the rigid body model can be extended simply by interconnection to compose more complicated mechanical systems or for control design. In Ch.7 and Ch.8, we show how to utilize the derived rigid body model to develop algorithms for motion and interaction control of a flying-end effector.

CHAPTER 5

PORT-HAMILTONIAN MODELING OF FLUID FLOW

Fluid mechanics is one of the most fundamental fields that has stimulated many ideas and concepts that are central to modern mathematical sciences. Throughout history, many research efforts have been conducted analytically, computationally, and experimentally. However, many important achievements in this field were established based on profound analytical studies rather than experiments [Arnold and Khesin, 1998].

Many practitioners and researchers use coordinate-based descriptions for modeling flow in Euclidean space using vector calculus. However, coordinate-free descriptions of mechanical systems in general provide more insights in the fundamental properties of such systems. These coordinate-free descriptions are formulated using tools of differential geometry. The unfamiliar reader is referred to Chorin and Marsden [1993] for an introduction to fluid mechanics using vector calculus, and to Arnold and Khesin [1998] for a geometric treatment of the subject.

In his foundational work [Arnold, 1966], V. Arnold described the motion of inviscid incompressible flow as the geodesic equation of the group of volume-preserving diffeomorphisms. Such description provided significant insights to the nature of the problem. Consequently after three years, D.Ebin and J. Marsden proved the local existence and uniqueness of solutions using techniques based on such geometric formulation [Ebin and Marsden, 1970]. Moreover, the geometric formulation by V. Arnold triggered many developments in studying stability of fluid flows, explicit calculations of Hamiltonian structures for a large number of distributed systems of hydrodynamic origin, and the development of differential geometric tools for dealing with diffeomorphism groups [Khesin

et al., 2020].

Fluid mechanics has been studied in the literature using both the Lagrangian and Hamiltonian formalism. In the classical Hamiltonian theory for fluid dynamical systems, a fundamental difficulty arises in incorporating the spatial boundary conditions of the system, which is also the case for general distributed parameter systems. Previous Hamiltonian formulations of fluid flow in the literature [Marsden and Abraham, 1970; Marsden et al., 1984a,b; Morrison, 1998] tend to focus on conservative systems with no energy-exchange with its surrounding environment. Usually, this is imposed by certain assumptions on the system variables. For example, if the spatial domain is non-compact, it is assumed that the system variables decay at infinity. Whereas if the spatial domain is compact, the boundary is assumed impermeable by imposing that the velocity vector field is tangent to the boundary.

Consequently, the traditional Hamiltonian theory is limited to distributed parameter systems on spatial manifolds without a boundary or ones with zero-energy exchange through the boundary. While this is useful for analyzing a system that is isolated from its surroundings, it is certainly an obstacle for practical applications such as simulation and control. While the traditional Hamiltonian formalism, in its generalized version on Poisson manifolds, focuses on conservative closed systems, the port-Hamiltonian formalism, based on Dirac structures, is applicable to non-conservative open systems capable of energy exchange with its environment.

This chapter describes how fluid dynamical systems are systematically and completely modeled in the port-Hamiltonian framework by a small set of building blocks of open subsystems. Depending on the choice of subsystems one composes in an energetically consistent manner, the geometric description of a number of fluid dynamical systems can be achieved, ranging from incompressible to compressible flows.

This decomposed network-based model of fluid dynamical systems comes at a great technical advantage. Each of the subsystems is described in the structurally simplest possible way, even if other subsystems require a considerably more sophisticated formulation. The composition of such unequal subsystems is mediated by a Dirac structure, which routes the energy flow between all subsystems.

A second tremendous technical simplification is achieved concerning the precise choice of state space underlying each energetic subsystem. For example when treating the kinetic energy of the fluid, no prior assumptions are required on the state space of fluid velocity to handle specific cases, such as impermeable boundaries and incompressibility. Instead, one chooses a state space that treats the general case of a compressible velocity field on any spatial domain (possible curved) that is permeable. Then, a modeling assumption is imposed by composition with a suitable type of subsystem that physically models this

assumption and is simply coupled to the unchanged kinetic-energy system. The equations resulting from this procedure are, in the end, of course the same as those following from the traditional view, but their geometric description is technically simplified and made physically more insightful at the same time.

In addition to the system theoretic advantages of modeling ideal fluid flow in the port-Hamiltonian paradigm, the work we present here serves as a stepping stone for modeling fluid-structure interaction in the quest of understanding the flapping-flight of birds, as motivated in Ch.1.

In this chapter, we start the port-Hamiltonian modeling process of fluid dynamical systems with the construction of the energetic subsystem that stores the kinetic energy of a fluid flowing on a general spatial domain with permeable boundary. The procedure to construct the port-Hamiltonian model we are aiming for relies greatly on understanding the underlying geometric structure of the state space of each energetic subsystem. This geometric formulation, pioneered by Arnold [1966] and Ebin and Marsden [1970], will allow a systematic derivation of the underlying Hamiltonian dynamical equations and Dirac structures, usually postulated a priori in the literature [van der Schaft and Maschke, 2001, 2002; Polner and van der Vegt, 2014; Altmann and Schulze, 2017]. Furthermore, it will allow for the boundary terms, which are always absent in the traditional Hamiltonian picture, to be easily identified and transformed into power ports which can be used for energy exchange through the boundary of the spatial domain.

The geometric description of ideal fluid flow is then used to develop the port-Hamiltonian model of the kinetic energy storage subsystem and the identification of the Dirac structure that routes the energy flowing in and out of the kinetic energy subsystem to a distributed power port (which allows the connection to subsystems that interact with the fluid within the spatial domain) and a boundary power port (which allows the connection to subsystems that allow the exchange of material). Then, we utilize the distributed port of the kinetic energy port-Hamiltonian system for representing a number of fluid-dynamical systems; by adding internal energy we model compressible flow, both adiabatic and isentropic, and by adding constraint forces we model incompressible flow.

This chapter is organized as follows: Sec. 5.1 starts by a general introduction to the coordinate-free formulation of describing kinematics of fluid motion. Then, Sec. 5.2 discusses the kinematics of advected quantities carried along with the fluid, their corresponding governing equations, and the extra mathematical structures they add. Sec. 5.3, will discuss the first three steps of the port-Hamiltonian modeling procedure aiming to construct the open port-Hamiltonian model for the kinetic-energy subsystem with variable boundary conditions and distributed stress forces. Then, we will proceed with the remaining steps of the port-Hamiltonian procedure which will utilize the distributed stress forces added to the port-Hamiltonian model of the kinetic energy to add

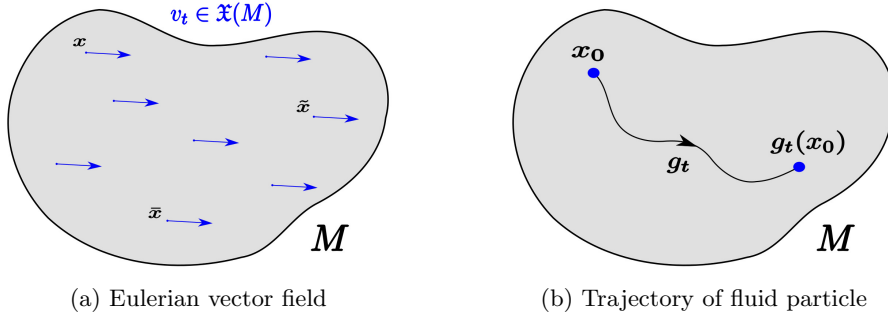


Figure 5.1: The fluid velocity vector fields v_t and its corresponding flow operator g_t .

storage of internal energy for modeling compressible flow in Sec. 5.4, and to add constraint forces to model incompressible flow in Sec. 5.5. Finally, we conclude this chapter in Sec. 5.6.

5.1 Kinematics of Fluid Motion

In this section, the coordinate-free formulation of describing fluid flow using manifolds and differential forms is presented. The goal is to define the configuration and configuration space of a fluid flow.

5.1.1 Configuration Space $\mathcal{D}(M)$

We start by describing the physical space in which the fluid flows. This region is mathematically represented by an n -dimensional compact manifold M , where for non relativistic physically meaningful spaces we are restricted to $n = \{2, 3\}$. We equip the manifold with a Riemannian metric \mathbb{M} and a metric-induced volume form $\mu_{\text{vol}} \in \Omega^n(M)$. The manifold could have a boundary ∂M or could have no boundary ($\partial M = \emptyset$), like for instance our (almost) spherical Earth. As a special case, M could represent a bounded region in Euclidean space ($M \subseteq \mathbb{R}^n$), with the standard Euclidean inner product and volume form.

The mathematical representation of the fluid region as a manifold is a modeling assumption that considers the fluid as a continuum completely filling the whole space. Such assumption ignores the fact that the fluid is made of molecules separated from each other in space. However, for length-scales bigger than the inter-atomic distances, it has proved to be a valid assumption.

As the fluid flows within the domain M , the material particles are transported with the flow. Let $x \in M$ be a point in the spatial domain. With reference to Fig. 5.1a, consider the fluid particle passing through x at time t ,

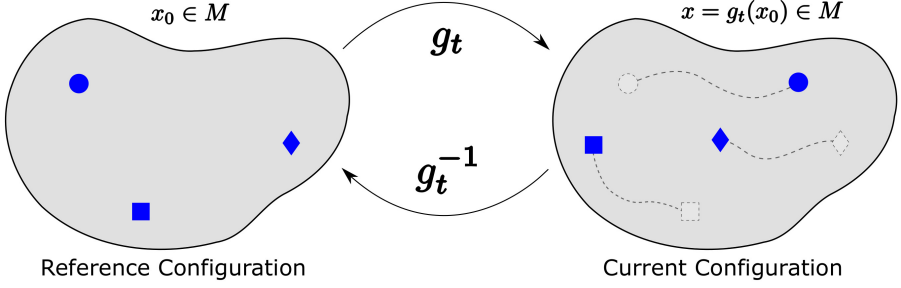


Figure 5.2: Describing the configuration of the fluid using the flow map g_t .

and let $v(t, x)$ denote the velocity of that particle assumed to be smooth in its arguments. For each time t , $v_t := v(t, \cdot) \in \mathfrak{X}(M)$ is a vector field on M i.e., a section of the tangent bundle TM . We denote the set of smooth vector fields on M by $\mathfrak{X}(M)$. Similarly, $v := v(\cdot, \cdot)$ is a time-dependent vector field on M , that can be made into a time-independent vector field on the space-time manifold $\mathbb{R} \times M$. For technical details, the reader is referred to [Abraham et al., 1988, pg. 283-285]. We call v the **Eulerian velocity field** of the fluid.

In the Lagrangian perspective of fluid mechanics, each fluid particle is a physical entity that maintains its identity during the flow. The particle identifier or **label** could be chosen at some specific time as the particle's position in M or as some thermodynamic property of the particle. Labeling all particles at a specific time defines the reference configuration of the fluid, as shown in Fig. 5.2. Without loss of generality, we choose the particle's position $x_0 \in M$ at time $t = 0$ as the Lagrangian label.

The particle at $x_0 \in M$ at time $t = 0$ traverses a well defined trajectory as the fluid flows. The evolution of the fluid particle during a fixed time t is described by the map $g_t : M \rightarrow M$, as shown in Fig. 5.1b. Thus, the particle starting at a point x_0 reaches the point $g_t(x_0) \in M$ after time t . The map $g_t : M \rightarrow M$, referred to as the **flow map**, defines the current configuration of the fluid at time t . Under the assumption that the fluid particles do not overlap, collide, or merge during the flow, the flow map g_t is a bijective map. The forward map $g_t : x_0 \mapsto x$ takes a fluid parcel from its initial position in the reference configuration to its current spatial position in the domain. Whereas, the inverse map $g_t^{-1} : x \mapsto x_0$ assigns the Lagrangian labels to a given spatial point.

The flow map g_t is mathematically the *flow* or *evolution operator* of the time dependent vector field v [Abraham et al., 1988, pg. 285]. The relationship between v and g_t is given by

$$\frac{d}{dt}g_t(x) = v(t, g_t(x)) = v_t(g_t(x)), \quad \forall x \in M. \quad (5.1)$$

By the assumption that v_t is a smooth vector field $\forall t$, we have that g_t is a diffeomorphism on M . Moreover, the map g_t satisfies $\forall x \in M$ (i) $g_0(x) = x$, (ii) $g_t(g_s(x)) = g_{t+s}(x)$. Thus, as a mathematical object, we have that

- i. $g_0 = \text{id}_M$,
- ii. $g_t \circ g_s = g_{t+s}$,
- iii. $g_t^{-1} = g_{-t}$,

where property (iii) is a consequence of the first two.

The set of all diffeomorphisms g_t on M satisfying the aforementioned properties form a group, known as the **diffeomorphism group** $\mathcal{D}(M)$, with the group operation being composition, and the identity element $e := g_0$. This group has a structure modeled on an infinite-dimensional *Frechet* space which makes $\mathcal{D}(M)$ into a Lie group [Marsden and Abraham, 1970]. The Lie group $\mathcal{D}(M)$ serves as the configuration space for the fluid flow.

The term Lie group here is misleading, as for $\mathcal{D}(M)$ right translation is smooth, but group inversion and left translation are only continuous [Holm et al., 1998]. Thus, the usual Lie theorems do not hold for $\mathcal{D}(M)$. However, it shares many important Lie group properties and for the applications considered in this chapter, it is *safe* to consider $\mathcal{D}(M)$ as an infinite dimensional Lie group. Technically $\mathcal{D}(M)$ is a Frechet-Lie group [Modin et al., 2011]. The reader is referred to Ebin and Marsden [1970] for a proper introduction to a functional-analytic treatment of the subject, which is beyond the scope of this thesis.

5.1.2 Lie Group Structure of $\mathcal{D}(M)$

Now we discuss in more details the structure of the configuration space $\mathcal{D}(M)$, which we denote also interchangeably as G for simplicity. A **fluid motion** is represented by the curve $\gamma_g : t \mapsto g_t$ on G which provides a family of diffeomorphisms $g_t : M \rightarrow M$ evolving from the reference configuration to the current configuration in M , as shown in Fig. 5.3. The tangent vector to the curve γ_g is denoted by $\dot{g}_t \in T_{g_t}G$, which also defines a map on M given, for any $x \in M$, by

$$\dot{g}_t(x) = v_t(g_t(x)) \in T_{g_t(x)}M. \quad (5.2)$$

Specifically, for g_0 , we find that

$$\dot{g}_0(x) = v_t(g_0(x)) = v_t(x) \in T_xM, \quad (5.3)$$

which implies that $\dot{g}_0 = v_t$. As a result, the tangent space T_eG at the identity $e \in G$ (the Lie-algebra of G) is equivalent to $\mathfrak{X}(M)$.

The **Lagrangian velocity field** of the fluid is defined as $\dot{g}_t(x_0)$ keeping the particle labels x_0 fixed. By comparing equations (5.2) and (5.3), it can

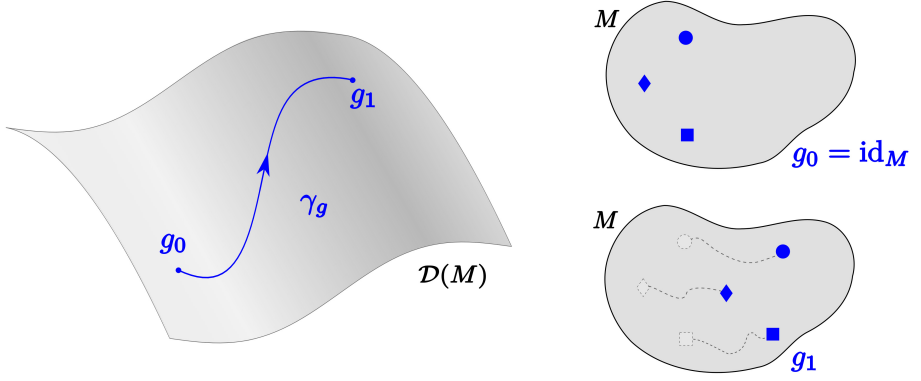


Figure 5.3: Illustration of fluid motion as a curve γ_g on $\mathcal{D}(M)$ which represents a family of diffeomorphisms on M .

be concluded that the Eulerian velocity v_t is a vector field on M , while the Lagrangian velocity \dot{g}_t is not mathematically a vector field, since $\dot{g}_t(x_0) \in T_{g_t(x_0)}M = T_xM$ is not a vector at x_0 .

It follows from (5.2) that at any time t , the Lagrangian velocity field \dot{g}_t is a *right-translation* of the Lie algebra element v_t . Consider the right and left translation maps of G given by $R_\varphi : g \mapsto g \circ \varphi$ and $L_\varphi : g \mapsto \varphi \circ g$, respectively. The corresponding pushforward maps of R_φ and L_φ are expressed as follows: For a point $(g_t, \dot{g}_t) \in TG$ in the tangent bundle of G , let $\gamma_g(t)$ be a curve in G such that $\gamma_g(a) = g_t$ and $\dot{\gamma}_g(a) = \dot{g}_t$. Then, we have that $(R_\varphi)_* : TG \rightarrow TG$ is given at a base point $g_t \in G$ by

$$(R_\varphi)_{*,g_t}(\dot{g}_t) = \left. \frac{d}{dt} \right|_{t=a} (\gamma_g(t) \circ \varphi) = \left. \frac{d}{dt} \right|_{t=a} \gamma_g(t) \circ \varphi = \dot{g}_t \circ \varphi, \quad (5.4)$$

while $(L_\varphi)_* : TG \rightarrow TG$ is similarly given by

$$(L_\varphi)_{*,g_t}(\dot{g}_t) = \left. \frac{d}{dt} \right|_{t=a} (\varphi \circ \gamma_g(t)) = \varphi_* \circ \left. \frac{d}{dt} \right|_{t=a} \gamma_g(t) = \varphi_* \circ \dot{g}_t, \quad (5.5)$$

where φ_* denotes the pushforward map corresponding to φ . For notional convenience, we will write $(R_\varphi)_*(\dot{g}_t) = \dot{g}_t \circ \varphi$ and $(L_\varphi)_*(\dot{g}_t) = \varphi_* \circ \dot{g}_t$, when the base point is clear from the context.

This construction legitimates to consider T_eG the Lie algebra of $\mathcal{D}(M)$. Indeed an element $v \in T_eG$ is related to the tangent vector $\dot{g} \in T_gG$ by right translation such that $v = (R_{g^{-1}})_*\dot{g} = \dot{g} \circ g^{-1}$. Therefore, T_eG is isomorphic as a vector space to $\mathcal{R}(G) \subset \mathfrak{X}(G)$, the space of right invariant vector fields on G , through the isomorphism $v \mapsto X_v$, with $X_v(g) := (R_g)_*(v) \in T_gG$. The Lie

bracket on $T_e G$ is defined by

$$[u, v]_{\mathfrak{X}} := \llbracket X_u, X_v \rrbracket_G(e), \quad \forall u, v \in T_e G, \quad (5.6)$$

where $\llbracket \cdot, \cdot \rrbracket_G$ denotes the Jacobi-Lie Bracket of vector fields on G . Therefore, the vector space $T_e G$ with the Lie bracket $[\cdot, \cdot]_{\mathfrak{X}}$ composes the Lie algebra of $G = \mathcal{D}(M)$ which will be denoted by \mathfrak{g}^v .

A more useful expression for the Lie bracket of \mathfrak{g}^v than the one in (5.6) can be obtained through the adjoint action of the Lie algebra on itself. First, we consider the adjoint action of G on \mathfrak{g}^v . Let $u, v \in \mathfrak{g}^v$ be the tangent vectors at $t = 0$ of the two curves γ, η at $\gamma_0 = \eta_0 = e$, respectively. We use the notation $\gamma_t := \gamma(t) \in G$ and $\eta_t := \eta(t) \in G$ and we denote by $A_\varphi : G \rightarrow G$, with $A_\varphi(g) = L_\varphi \circ R_{\varphi^{-1}}(g)$, the inner automorphism map. The adjoint action $Ad : G \times \mathfrak{g}^v \rightarrow \mathfrak{g}^v$ is defined by [Holm et al., 2009]

$$Ad_\varphi(v) := (A_\varphi)_{*,e}(v) = \left. \frac{d}{dt} \right|_{t=0} A_\varphi(\eta_t) = \left. \frac{d}{dt} \right|_{t=0} \varphi \circ \eta_t \circ \varphi^{-1} = \varphi_* \circ v \circ \varphi^{-1} = \varphi_* v, \quad (5.7)$$

where $Ad_\varphi(v) := Ad(\varphi, v)$. Hence, the adjoint action of G on \mathfrak{g}^v is given by the pushforward operation of vector fields on M . The induced adjoint action of the Lie-algebra \mathfrak{g}^v on itself is defined by

$$ad_u(v) = \left. \frac{d}{dt} \right|_{t=0} Ad_{\gamma_t}(v) = \left. \frac{d}{dt} \right|_{t=0} (\gamma_t)_* v = -\mathcal{L}_u v = -\llbracket u, v \rrbracket_M, \quad (5.8)$$

where $\llbracket \cdot, \cdot \rrbracket_M$ denotes the Jacobi-Lie bracket of vector fields on M , and the last two equalities hold from the definition of the Lie derivative of a vector field. In conclusion, we have that the Lie bracket on \mathfrak{g}^v is given by minus the standard Jacobi-Lie bracket on $\mathfrak{X}(M)$ i.e.

$$[u, v]_{\mathfrak{X}} = ad_u(v) = -\llbracket u, v \rrbracket_M. \quad (5.9)$$

5.1.3 Differential Form Representation of Lie algebra

In this work we rely greatly on representing the Lie algebra \mathfrak{g}^v using the space of differential forms on M . The differential form representation is technically beneficial for a number of reasons. First, the related Grassmannian algebra operators are very efficient in carrying out calculations and proving theorems. Second, well established results like Stokes theorem will be crucial in the development of the Dirac structures of this work. Third, the equations of motion expressed using differential forms are invariant with respect to coordinate changes.

Using the manifold's extra structures provided with it, there are two options for identifying the Lie algebra of vector fields $\mathfrak{g}^v = \mathfrak{X}(M)$ with the space of k -differential forms $\Omega^k(M)$, summarized in Fig. 5.4.

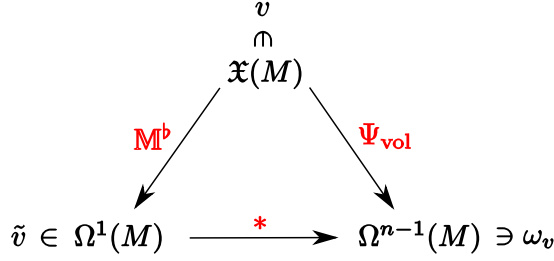


Figure 5.4: Isomorphism between vector fields and corresponding differential forms

The first option is to use the Riemannian metric \mathbb{M} to identify $\mathfrak{X}(M)$ with one-forms $\Omega^1(M)$ via the isomorphism

$$\begin{aligned} \mathbb{M}^\flat : \mathfrak{X}(M) &\rightarrow \Omega^1(M) \\ v &\mapsto \mathbb{M}^\flat(v) := \mathbb{M}(v, \cdot). \end{aligned} \quad (5.10)$$

While the second one is to use the volume form μ_{vol} to identify $\mathfrak{X}(M)$ with $\Omega^{n-1}(M)$ via the isomorphism

$$\begin{aligned} \Psi_{\text{vol}} : \mathfrak{X}(M) &\rightarrow \Omega^{n-1}(M) \\ v &\mapsto \iota_v \mu_{\text{vol}} = \mu_{\text{vol}}(v, -), \end{aligned} \quad (5.11)$$

where $\iota_v : \Omega^n(M) \rightarrow \Omega^{n-1}(M)$ denotes the interior product operator of forms, and the dash indicates all remaining open slots of the volume form μ_{vol} .

For notational convenience we will denote the 1-form and $n-1$ form corresponding to a vector field $v \in \mathfrak{X}(M)$ by $\tilde{v} := \mathbb{M}^\flat(v) \in \Omega^1(M)$ and $\omega_v := \iota_v \mu_{\text{vol}} \in \Omega^{n-1}(M)$, respectively. Moreover, it will be useful later to represent the vector field corresponding to an $n-1$ form $\omega \in \Omega^{n-1}(M)$ by $\hat{\omega} \in \mathfrak{X}(M)$ and similarly the vector field corresponding to a 1-form $\alpha \in \Omega^1(M)$ by $\hat{\alpha} \in \mathfrak{X}(M)$.

Using the Hodge star operator $* : \Omega^k(M) \rightarrow \Omega^{n-k}(M)$, it is possible to map the 1-form representation of $\mathfrak{X}(M)$ to the corresponding $n-1$ -form. In particular, using the general identity

$$\iota_v \alpha = (-1)^{(k+1)(n-k)} * (\tilde{v} \wedge * \alpha), \quad \forall v \in \mathfrak{X}(M), \alpha \in \Omega^k(M), \quad (5.12)$$

and the fact that $\mu_{\text{vol}} = *1$, it holds that

$$\omega_v = \iota_v \mu_{\text{vol}} = \iota_v (*1) = *\tilde{v}, \quad \text{and} \quad \tilde{v} = (-1)^{n-1} * \omega_v. \quad (5.13)$$

Remark 5.1.1. Note that the sign in (5.12) is positive if α is a top form or is of an odd order, which will always be the case where this identity is used in this work.

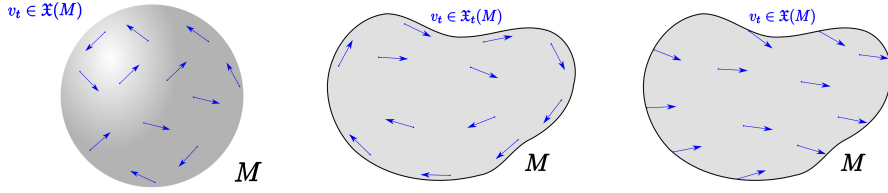


Figure 5.5: Boundary cases for fluid flow on a compact manifold; no boundary (left), impermeable boundary (middle), or permeable boundary (right).

The choice we will make in this work is to represent the Lie algebra of $\mathcal{D}(M)$ using $n - 1$ forms. We denote the differential form representation of the Lie algebra by $\mathfrak{g} = \Omega^{n-1}(M)$ where its corresponding Lie bracket $[\cdot, \cdot]_{\mathfrak{g}}$ is constructed by

$$[\omega_u, \omega_v]_{\mathfrak{g}} := \Psi_{\text{vol}}([\Psi_{\text{vol}}^{-1}(\omega_u), \Psi_{\text{vol}}^{-1}(\omega_v)]_{\mathfrak{X}}), \quad \forall \omega_u, \omega_v \in \mathfrak{g}. \quad (5.14)$$

In other words, the map Ψ_{vol} in (5.11) acts as a Lie-algebra isomorphism between $\mathfrak{g}^{\mathfrak{v}}$ and \mathfrak{g} . The explicit expression of the Lie bracket $[\cdot, \cdot]_{\mathfrak{g}}$ is given by the next result.

Proposition 5.1.2. *The Lie bracket $[\cdot, \cdot]_{\mathfrak{g}} : \mathfrak{g} \times \mathfrak{g} \rightarrow \mathfrak{g}$ defined by (5.14) is given by*

$$[\omega_u, \omega_v]_{\mathfrak{g}} = -\mathcal{L}_u \omega_v + \text{div}(u) \omega_v, \quad (5.15)$$

where $u \in \mathfrak{g}^{\mathfrak{v}}$ is the vector field corresponding to ω_u , and $\text{div}(u) \in C^\infty(M)$ is called the divergence of the vector field $u \in \mathfrak{g}^{\mathfrak{v}}$ and is defined as the function such that $\mathcal{L}_u \mu_{\text{vol}} = \text{div}(u) \mu_{\text{vol}}$.

Proof. By substituting (5.11) and (5.9) in (5.14), one has that

$$\begin{aligned} [\omega_u, \omega_v]_{\mathfrak{g}} &= \Psi_{\text{vol}}([u, v]_{\mathfrak{X}}) = \Psi_{\text{vol}}(-\llbracket u, v \rrbracket_M) = -\iota_{\llbracket u, v \rrbracket_M} \mu_{\text{vol}} \\ &= -\mathcal{L}_u (\iota_v \mu_{\text{vol}}) + \iota_v (\mathcal{L}_u \mu_{\text{vol}}) = -\mathcal{L}_u \omega_v + \iota_v (\text{div}(u) \mu_{\text{vol}}) \\ &= -\mathcal{L}_u \omega_v + \text{div}(u) \iota_v \mu_{\text{vol}} = -\mathcal{L}_u \omega_v + \text{div}(u) \omega_v, \end{aligned}$$

where we used the Lie derivative property

$$\mathcal{L}_u (\iota_v \alpha) = \iota_{\llbracket u, v \rrbracket_M} \alpha + \iota_v (\mathcal{L}_u \alpha), \quad \alpha \in \Omega^k(M). \quad (5.16)$$

■

5.1.4 Permeable vs. Impermeable Boundaries

Before moving on, we turn attention to a fundamental issue that distinguishes between the Hamiltonian and port-Hamiltonian treatments of fluid dynamics with respect to the boundary of the fluid container, as shown in Fig. 5.5.

The construction presented so far in describing the configuration of a fluid flowing using the diffeomorphism group $\mathcal{D}(M)$ rests on the fundamental assumption that the fluid particles always remain within the fluid container. In case M has no boundary, this is obviously always true. However, in case M has a boundary, the Lie algebra of $\mathcal{D}(M)$ is constrained to the subspace $\mathfrak{X}_t(M) \subset \mathfrak{X}(M)$ with $\mathfrak{X}_t(M)$ defined as the subset of vector fields on M that are tangent to ∂M . This extra condition on v is synonymous with the boundary of M being impermeable.

The restriction of \mathfrak{g}^v to vector fields that are tangent to ∂M translates to the condition that its corresponding $n - 1$ form is normal to ∂M , i.e. satisfies $i^*(\omega_v) = 0$, where $i : \partial M \rightarrow M$ is the canonical inclusion map. Differential forms normal to ∂M are said to satisfy the *Dirichlet boundary condition*. Thus, in the case of impermeable boundary, the Lie algebra \mathfrak{g} for impermeable boundaries becomes $\Omega_D^{n-1}(M)$, which denotes the space of normal $n - 1$ forms on M .

The cases for which M has no boundary or ∂M is impermeable correspond to an isolated fluid dynamical system that cannot exchange (mass) flow with its surrounding. Consequently, all results of the traditional Hamiltonian formalism relying on $\mathcal{D}(M)$ and Poisson structures are related to such isolated systems.

In order to treat fluid dynamical systems in the port-Hamiltonian framework, it is necessary to treat the fluid container with a boundary that is permeable by default. This is necessary, for instance, if M is to represent a control volume inside a bigger flow domain. Fortunately, the extension of the known geometric formulation of fluids to permeable boundaries is only obstructed at the group level. At the Lie algebra level, this extension is simply afforded by dropping the previously identified Dirichlet constraint from the vector space $\Omega_D^{n-1}(M)$, which is the algebra for impermeable boundaries, and taking instead all of $\Omega^{n-1}(M)$ as the underlying vector space.

The deceptive simplicity of this step comes with a drastic conceptual shift. The Lie algebra $(\mathfrak{g}, [\cdot, \cdot]_{\mathfrak{g}})$ for permeable boundaries can no longer be the associated Lie algebra of the diffeomorphism group $\mathcal{D}(M)$ or any of its subgroups. The intuition behind it is that the flow map g_t no longer becomes bijective as the fluid particles in the spatial domain M comprising the reference configuration are no longer constrained to remain in M . Therefore, the treatment of permeable boundaries requires nothing more and nothing less than the ability to phrase any question about the fluid in a form that can be treated entirely at Lie algebra level.

The discussion of impermeable and permeable boundaries at this early stage is important, because much of what follows depends on whether one deals with impermeable or permeable boundaries. For instance, the determination of the duals of the vector space underlying the Lie algebra \mathfrak{g} , crucially depends on the nature of ∂M . Another consequence is that boundary terms, which all

vanish for impermeable boundaries, must be carried through in a treatment that aspires to be valid for the three boundary cases.

Indeed, it is precisely the surface terms that make the key difference between the Lie-Poisson structure, underlying the traditional Hamiltonian theory, and the Stokes-Dirac structure, underlying the port-Hamiltonian theory, and will be of extreme importance in this work as it will rigorously reveal the corresponding boundary ports.

5.1.5 Dual Space of Lie Algebra

The dual space \mathfrak{g}^* to the Lie algebra \mathfrak{g} is naturally identified with the space of 1-forms $\Omega^1(M)$ by means of the duality pairing

$$\langle \alpha | \omega \rangle_{\mathfrak{g}} := \int_M \alpha \wedge \omega, \quad \alpha \in \mathfrak{g}^*, \omega \in \mathfrak{g}, \quad (5.17)$$

which is the natural pairing based on integration on M of differential forms of complementary order.

An essential ingredient for deriving the equations of fluid motion in the Hamiltonian formalism is the map $ad_{\omega}^* : \mathfrak{g}^* \rightarrow \mathfrak{g}^*$, which is the formal dual to the adjoint operator of \mathfrak{g} defined by $ad_{\omega}(\cdot) := [\omega, \cdot]_{\mathfrak{g}}$, for a given $\omega \in \mathfrak{g}$. The explicit expression for ad_{ω}^* is given by the following result.

Proposition 5.1.3. *For any $\omega \in \mathfrak{g}$, the dual map ad_{ω}^* of the adjoint operator ad_{ω} of $\mathfrak{g} = \Omega^{n-1}(M)$ is given by*

$$ad_{\omega}^*(\alpha) = \mathcal{L}_{\hat{\omega}}\alpha + \text{div}(\hat{\omega})\alpha, \quad \omega \in \mathfrak{g}, \alpha \in \mathfrak{g}^*. \quad (5.18)$$

For a general manifold M with boundary ∂M , the map ad_{ω}^ in (5.18) satisfies for any $\omega, \beta \in \mathfrak{g}$ and $\alpha \in \mathfrak{g}^*$,*

$$\langle ad_{\omega}^*(\alpha) | \beta \rangle_{\mathfrak{g}} = \langle \alpha | ad_{\omega}(\beta) \rangle_{\mathfrak{g}} + \int_{\partial M} \eta_{ad_{\omega}}(\alpha, \beta)|_{\partial M}, \quad \omega, \beta \in \mathfrak{g}, \alpha \in \mathfrak{g}^*, \quad (5.19)$$

where the $(n-1)$ -form $\eta_{ad_{\omega}}(\alpha, \beta) \in \Omega^{n-1}(M)$ is given by

$$\eta_{ad_{\omega}}(\alpha, \beta) = \iota_{\hat{\omega}}(\alpha \wedge \beta). \quad (5.20)$$

The term $\eta|_{\partial M} \in \Omega^k(\partial M)$ denotes the trace of the form $\eta \in \Omega^k(M)$ which is defined as the pullback of the inclusion map $i : \partial M \rightarrow M$, i.e. $\eta|_{\partial M} := i^\eta$.*

Proof. Consider any $\beta \in \mathfrak{g}$. By using (5.15) we have that

$$\langle \alpha | ad_{\omega}(\beta) \rangle_{\mathfrak{g}} = \int_M \alpha \wedge [\omega, \beta]_{\mathfrak{g}} = \int_M \alpha \wedge \text{div}(\hat{\omega})\beta - \int_M \alpha \wedge \mathcal{L}_{\hat{\omega}}\beta. \quad (5.21)$$

Using the Leibniz rule for the Lie derivative $\mathcal{L}_{\hat{\omega}}(\alpha \wedge \beta) = \mathcal{L}_{\hat{\omega}}\alpha \wedge \beta + \alpha \wedge \mathcal{L}_{\hat{\omega}}\beta$ and Cartan's magic formula $\mathcal{L}_{\hat{\omega}} = d\iota_{\hat{\omega}} + \iota_{\hat{\omega}}d$ the second integrand in (5.21) becomes

$$-\alpha \wedge \mathcal{L}_{\hat{\omega}}\beta = \mathcal{L}_{\hat{\omega}}(\alpha \wedge \beta) - d\iota_{\hat{\omega}}(\alpha \wedge \beta). \quad (5.22)$$

Substituting (5.22) in (5.21), using the definition of divergence and Stokes theorem we have that

$$\begin{aligned} \langle \alpha | ad_{\omega}(\beta) \rangle_{\mathfrak{g}} &= \langle \text{div}(\hat{\omega})\alpha + \mathcal{L}_{\hat{\omega}}\alpha | \beta \rangle_{\mathfrak{g}} - \int_{\partial M} i^*(\iota_{\hat{\omega}}(\alpha \wedge \beta)) \\ &= \langle ad_{\omega}^*(\alpha) | \beta \rangle_{\mathfrak{g}} - \int_{\partial M} (\iota_{\hat{\omega}}(\alpha \wedge \beta))|_{\partial M}. \end{aligned}$$

■

Remark 5.1.4. Interestingly (but not surprisingly), this condition on representatives of the Lie algebra in case of impermeable boundary, is exactly the one that nullifies the boundary term in (5.19), which is easily verified because the pullback in the trace distributes over the wedge. This consideration sheds light on the fact that in classical Hamiltonian theory the state space is constrained such that no energy exchange can happen on the boundary of the spatial manifold, and the surface term in the duality pairing (5.19) is consequently neglected.

As will be shown in what follows, the surface terms are the key difference between the Lie-Poisson structure, underlying the traditional Hamiltonian theory, and the Stokes-Dirac structure, underlying the port-Hamiltonian theory, and will be of extreme importance in this work. Our methodology does not rely on constraining the state space of the fluid, but to consider duality pairings like (5.19) in their full generality, which will reveal rigorously boundary ports that can be used for modeling or control purposes.

5.2 Kinematics of Advected Quantities

In ideal continuum flow, the material parcels of the fluid are carried by the flow. These parcels are transported (advected) by the ideal flow along with extensive thermodynamic properties such as the parcels' mass and heat. The properties transported by the flow are referred to as **advected quantities**.

The presence of advected quantities adds more structure to the spaces underlying the motion of fluids \mathfrak{g} and \mathfrak{g}^* . Understanding this additional structure is crucial for the development of the decomposed model of fluid dynamics we aim for in this work as well as the derivation of the Stokes-Dirac structure underlying the kinetic energy subsystem.

Next, we describe mathematically advected quantities and their governing evolution equations. Then, we introduce the interconnection maps that will allow relating the spaces of fluid motion and the spaces of advected quantities to each other. Finally, we discuss the added *semi-direct algebra* structure that the presence of these advected quantities introduces into the geometric picture.

5.2.1 Mathematical Description

An advected quantity a_t is represented mathematically, in general, as a time-dependent tensor field. We denote the vector space of advected quantities by $V^* \subset \mathcal{T}(M)$ which is usually a subspace of the space of tensor fields $\mathcal{T}(M)$ on M . Specific examples include scalar fields (e.g. buoyancy, entropy), vector fields (e.g. magnetic field), 2-forms (e.g. vorticity), and top forms (e.g. mass form). Another example of advected quantities also includes the Lagrangian labels x_0 , interpreted as passive scalars. All advected quantities that will be considered later in this chapter will be represented by differential forms.

Let $a(t, x) \in V^*$ denote a time-dependent advected quantity of the fluid, expressed in terms of the spatial coordinates x of the manifold M . Thus, $a(t, x) = a_t(x)$ is an Eulerian representation of the advected quantity. The corresponding Lagrangian representation of the same advected quantity is denoted by $\tilde{a}(t, x_0) = \tilde{a}_t(x_0)$ which is a function of the Lagrangian labels x_0 which are kept fixed. Due to the choice of the Lagrangian labels x_0 to be the particle's position at $t = 0$, the Eulerian and Lagrangian forms of the advected quantity coincide in the reference configuration i.e.

$$a_0(x) = \tilde{a}_0(x_0) \in V^*. \quad (5.23)$$

The relation between the tensor field a_t at $t > 0$ and its initial value a_0 is given the pullback of the flow map $g_t \in G$,

$$a_0(x_0) = (g_t^* a_t)(x_0), \quad (5.24)$$

and similarly, since g_t is a diffeomorphism,

$$a_t(x) = ((g_t^{-1})^* a_0)(x). \quad (5.25)$$

Therefore, we have that $a_0 = g_t^* a_t$ or $a_t = (g_t^{-1})^* a_0$. An important observation is that the Eulerian advected quantity a_t is completely determined by the flow map g_t and its initial value a_0 .

In the Lagrangian view, the condition for a time-dependent advected quantity $\tilde{a}(t, x_0)$ to be advected with the flow is given by $\frac{d}{dt} \tilde{a}(t, x_0) = 0$. Conversely, in the Eulerian view, the tensor field a_t is advected with the flow if $\forall t$

$$\left(\frac{\partial}{\partial t} + \mathcal{L}_v \right) a_t = 0, \quad (5.26)$$

which is an immediate consequence of the Lie derivative formula for time-dependent tensor fields [Abraham et al., 1988, Pg. 372],

$$\frac{d}{dt}(g_t^* a_t) = g_t^* \left(\frac{\partial}{\partial t} a_t + \mathcal{L}_v a_t \right). \quad (5.27)$$

An advected quantity is also referred to as being invariant under the flow, frozen into the fluid, or Lie dragged with the flow.

Next we consider several examples of advected quantities.

Conservation of Mass

The prototypical case of an advected quantity that occurs in all continuum flows is the mass top-form given by $\mu_t := \rho_t \mu_{\text{vol}} \in \Omega^n(M)$, where $\rho_t \in C^\infty(M)$ denotes the mass density function. We have that $\mu_t \in V^* = \Omega^n(M)$.

The mass conservation condition can be written in terms of the mass form as $g_t^* \mu_t = \mu_0$, or equivalently

$$\frac{\partial}{\partial t} \mu_t + \mathcal{L}_v \mu_t = 0, \quad (5.28)$$

where \mathcal{L}_v denotes the Lie derivative operator along vector field v . Equation (5.28) is referred to as the mass continuity equation.

To express the mass continuity in terms of the density function ρ_t , we substitute $\mu_t = \rho_t \mu_{\text{vol}}$ in (5.28)

$$\frac{\partial}{\partial t}(\rho_t \mu_{\text{vol}}) + \mathcal{L}_v(\rho_t \mu_{\text{vol}}) = \frac{\partial}{\partial t}(\rho_t) \mu_{\text{vol}} + \mathcal{L}_v(\rho_t) \mu_{\text{vol}} + \rho_t \mathcal{L}_v(\mu_{\text{vol}}), \quad (5.29)$$

$$= \left(\frac{\partial}{\partial t}(\rho_t) + \mathcal{L}_v(\rho_t) + \rho_t \operatorname{div}(v) \right) \mu_{\text{vol}} = 0, \quad (5.30)$$

which follows from the Leibniz rule of the Lie derivative and the definition of $\operatorname{div}(v) \in C^\infty(M)$. Therefore, the mass continuity equation in terms of the density function $\rho_t \in C^\infty(M)$ is expressed as

$$\frac{\partial}{\partial t} \rho_t + \mathcal{L}_v \rho_t + \rho_t \operatorname{div}(v) = 0. \quad (5.31)$$

By comparing the mass continuity equation in its two forms (5.28) and (5.31), it is observed that in general, the mass form μ_t is an advected quantity while the mass density function ρ_t is not. This observation is the main reason why μ_t will be chosen as a state variable later for representing the fluid's kinetic energy E_{kin} , which depends on the density and velocity of the flow.

Conservation of Entropy

Another quantity of interest that is associated with fluid flow is the specific entropy function $s_t \in C^\infty(M)$. The entropy in general is not an advected quantity. However, in the case of *adiabatic compressible flow*, s_t is advected with the flow. Thus, it satisfies $g_t^* s_t = s_0$, or equivalently

$$\frac{\partial}{\partial t} s_t + \mathcal{L}_v s_t = 0. \quad (5.32)$$

A consequence of the entropy conservation (5.32), is that if the entropy is homogeneous in space initially (i.e. $s_0(x_0) = s_0$ is constant) then it remains constant for all time (i.e. $s_t(x) = s_0, \forall t > 0, x \in M$). In such case, the compressible flow is called isentropic.

In compressible flow, the total energy of the fluid consists of kinetic energy E_{kin} and internal energy E_{int} . In adiabatic compressible flow, the internal energy of the fluid depends on the entropy function s_t and the density function ρ_t . Whereas, in isentropic compressible flow, E_{int} depends only on the density function ρ_t .

Conservation of Volume

In the physical world, it is observed from experiments that the compressibility of a fluid could be neglected when the speed of a body within the fluid is much lower than the speed of sound. In this case, the flow is approximated to be incompressible which is characterized mathematically by the conservation of the volume form $g_t^* \mu_{\text{vol}} = \mu_{\text{vol}}$.

Let the top-form given by $g_t^* \mu_{\text{vol}}$ have a density $J(g_t) \in C^\infty(M)$ defined such that $g_t^* \mu_{\text{vol}} = J(g_t) \mu_{\text{vol}}$. In the case of Euclidean space ($M \subseteq \mathbb{R}^n$) with the standard volume form, the function $J(g_t)$ corresponds to the determinant of the Jacobian matrix associated with the diffeomorphism g_t . The incompressibility condition implies that $J(g_t) = 1$ for all times and at all points $x \in M$.

By the Lie derivative rule, we have that

$$\frac{d}{dt}(g_t^* \mu_{\text{vol}}) = g_t^*(\mathcal{L}_v \mu_{\text{vol}}). \quad (5.33)$$

Thus, an equivalent condition for incompressible flow is $\mathcal{L}_v \mu_{\text{vol}} = 0$. Therefore, in incompressible flow the time-independent volume form is also an advected quantity, or more correctly it is frozen in the fluid.

Using properties of the Lie derivative, one also has that

$$\mathcal{L}_v \mu_{\text{vol}} = \text{div}(v) \mu_{\text{vol}} = 0 \implies \text{div}(v) = 0, \quad (5.34)$$

as well as

$$\mathcal{L}_v \mu_{\text{vol}} = d\iota_v \mu_{\text{vol}} = d\omega_v = 0. \quad (5.35)$$

Flow Type	Advected Quantities	Total Energy
Compressible Adiabatic	μ_t, s_t	$E_{\text{kin}}(\rho_t, v_t) + E_{\text{int}}(\rho_t, s_t)$
Compressible Isentropic	$\mu_t, s_t = s_0$	$E_{\text{kin}}(\rho_t, v_t) + E_{\text{int}}(\rho_t)$
Incompressible Inhomogeneous	$\mu_t, \rho_t, \mu_{\text{vol}}$	$E_{\text{kin}}(\rho_t, v_t)$
Incompressible Homogeneous	$\mu_t = \mu_0, \rho_t = \rho_0, \mu_{\text{vol}}$	$E_{\text{kin}}(v_t)$

Table 5.1: Flow types and corresponding advected quantities

Therefore, the following are all equivalent conditions for incompressible flow:

- i) $J(g_t) = 1$, ii) $\mathcal{L}_v \mu_{\text{vol}} = 0$, iii) $\text{div}(v) = 0$, iv) $d\omega_v = 0$.

In the case of incompressible flow, the aforementioned conditions restricts the configuration space of the fluid flow to a subgroup of $\mathcal{D}(M)$ defined by

$$\mathcal{D}_{\text{vol}}(M) := \{g \in \mathcal{D}(M) | J(g) = 1\}, \quad (5.36)$$

This subgroup is known in the literature as the volume-preserving diffeomorphism group, which was shown in Ebin and Marsden [1970] to be a Lie-subgroup of $\mathcal{D}(M)$. The corresponding Lie sub-algebra is given by the divergence-free vector fields $\mathfrak{X}_{\text{vol}}(M)$ defined as

$$\mathfrak{X}_{\text{vol}}(M) := \{v \in \mathfrak{X}(M) | \text{div}(v) = 0\}. \quad (5.37)$$

Condition (iv) also implies that the differential form representation of the Lie algebra $\mathfrak{X}_{\text{vol}}(M)$ corresponds to the closed $n - 1$ forms.

As a consequence of the incompressibility condition $\text{div}(v) = 0$, the mass continuity equation (5.31) becomes

$$\frac{\partial}{\partial t} \rho_t + \mathcal{L}_v \rho_t = 0, \quad (5.38)$$

which implies that ρ_t is also advected with the flow if it is incompressible. Therefore, if the mass density is homogeneous in space initially, then it remains constant for all time (i.e. $\rho_t(x) = \rho_0, \forall t > 0, x \in M$), and consequently μ_t remains constant as well. In such case, the incompressible flow is called homogeneous, while the former case with time-varying density is called inhomogeneous flow. In homogeneous incompressible flow, the kinetic energy E_{kin} becomes a function of the fluid's velocity only.

A summary of the previously discussed fluid types and advected quantities is shown in Table 5.1.

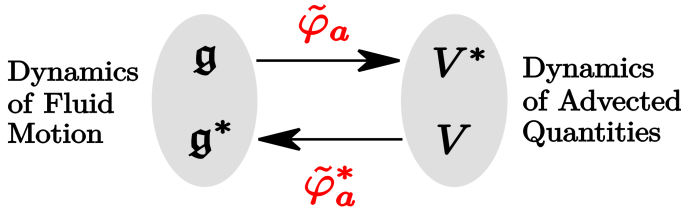


Figure 5.6: Interconnection maps relating the space of fluid motion to the space of advected quantities.

5.2.2 Relation Between Fluid Motion and Advected Quantities

In order to build a decomposed model of fluid flow, it is important to describe the dynamics of advected quantities separately from the dynamics of fluid motion. With reference to Fig. 5.6, the dynamics of the fluid motion are defined on the space $(\mathfrak{g} \times \mathfrak{g}^*)$, whereas the dynamics of advected quantities are defined on $(V^* \times V)$. The dual space of $V^* = \Omega^k(M)$ is $V = \Omega^{n-k}(M)$ with respect to the duality pairing $\langle \cdot | \cdot \rangle_{V^*} : V \times V^* \rightarrow \mathbb{R}$ given by the integral of the wedge product, i.e.

$$\langle \bar{a} | a \rangle_{V^*} := \int_M \bar{a} \wedge a, \quad a \in V^*, \bar{a} \in V. \quad (5.39)$$

As discussed in Sec. 5.2.1, the evolution of an advected quantity depends on the fluid motion described by $\omega \in \mathfrak{g}$. On the other hand, the advected quantity carried by the flow influences the flow motion in a power-consistent manner through the *bidirectional exchange* of kinetic energy of the fluid and the additional energy characterized by the advected quantity (e.g. potential or magnetic energy).

The effect of the fluid motion ($\omega \in \mathfrak{g}$) on the advected quantity $a \in V^*$ is encoded in the primary map $\tilde{\varphi}_a : \mathfrak{g} \rightarrow V^*$, which is defined by

$$\begin{aligned} \tilde{\varphi}_a : \mathfrak{g} &\rightarrow V^* \\ \omega &\mapsto \tilde{\varphi}_a(\omega) := \mathcal{L}_\omega a. \end{aligned} \quad (5.40)$$

In terms of this primary map, the governing equation of an advected quantity (5.26) is rewritten as $\dot{a}_t = -\tilde{\varphi}_a(\omega)$, with $\omega = \Psi_{\text{vol}}(v)$.

The reverse effect, which the advected quantities has on the fluid motion, is characterized by the (formal) dual map of $\tilde{\varphi}_a$ given by

$$\begin{aligned} \tilde{\varphi}_a^* : V &\rightarrow \mathfrak{g}^* \\ \bar{a} &\mapsto \tilde{\varphi}_a^*(\bar{a}). \end{aligned} \quad (5.41)$$

We refer to the two maps $\tilde{\varphi}_a, \tilde{\varphi}_a^*$ as the **interconnection maps** (cf. Fig. 5.6) as they will serve the fundamental role of interconnecting the space of advected quantities with the space of fluid motion in the port-Hamiltonian model, as will be shown later in this chapter.

The explicit expression for $\tilde{\varphi}_a^*$ is given by the following result which depends on a specific choice of V^* . For our purpose, we only consider the cases of top-forms and smooth functions relevant to the advected quantities of mass form ($V^* = \Omega^n(M) \ni \mu$) and entropy ($V^* = \Omega^0(M) \ni s$).

Proposition 5.2.1. *For a given $a \in V^*$, consider the map $\tilde{\varphi}_a$ defined by (5.40) and consider its dual map $\tilde{\varphi}_a^*: V \rightarrow \mathfrak{g}^*$. For a general manifold M with boundary ∂M , the dual map $\tilde{\varphi}_a^*$ satisfies for any $\omega \in \mathfrak{g}$*

$$\langle \tilde{\varphi}_a^*(\bar{a}) | \omega \rangle_{\mathfrak{g}} = \langle \bar{a} | \tilde{\varphi}_a(\omega) \rangle_{V^*} + \int_{\partial M} \eta_{\tilde{\varphi}_a}(\omega, \bar{a})|_{\partial M}, \quad (5.42)$$

where $\eta_{\tilde{\varphi}_a}(\omega, \bar{a}) \in \Omega^{n-1}(M)$ is the corresponding $n-1$ form representing the surface term.

i) In case $V = \Omega^0(M)$ and $V^* = \Omega^n(M)$,

$$\tilde{\varphi}_a^*(\bar{a}) = -(*a) d\bar{a}, \quad \eta_{\tilde{\varphi}_a}(\omega, \bar{a}) = -(*a) \omega \wedge \bar{a},$$

ii) In case $V = \Omega^n(M)$ and $V^* = \Omega^0(M)$,

$$\tilde{\varphi}_a^*(\bar{a}) = (*\bar{a}) da, \quad \eta_{\tilde{\varphi}_a}(\omega, \bar{a}) = 0,$$

where $*$ denotes the Hodge star operator and d denotes the exterior derivative operator.

Proof. i) Let $\bar{a} \in V = \Omega^0(M)$ and $a \in V^* = \Omega^n(M)$, where a can be written as $a = (*a) \mu_{\text{vol}}$. Let $\omega \in \mathfrak{g}$ and let $\hat{\omega} \in \mathfrak{X}(M)$ be its corresponding vector field.

Using the fact that $\bar{a} \in C^\infty(M)$ and the Leibniz rule for the exterior derivative, we can write

$$\begin{aligned} \langle \bar{a} | \tilde{\varphi}_a(\omega) \rangle_{V^*} &= \int_M \bar{a} \wedge \mathcal{L}_{\hat{\omega}} a = \int_M \bar{a} \wedge d\iota_{\hat{\omega}} a = \int_M \bar{a} \wedge d((*a) \iota_{\hat{\omega}} \mu_{\text{vol}}), \\ &= \int_M \bar{a} \wedge d(*a \omega) = \int_M d(\bar{a} \wedge (*a \omega)) - d\bar{a} \wedge (*a) \omega, \\ &= \int_{\partial M} (*a) \omega \wedge \bar{a} - \int_M (*a) d\bar{a} \wedge \omega, \\ &= \int_{\partial M} -\eta_{\tilde{\varphi}_a}(\omega, \bar{a}) + \langle -(*a) d\bar{a} | \omega \rangle_{\mathfrak{g}}, \end{aligned}$$

which concludes the proof of (i).

Advection Quantity (a)	Advection Space (V^*)	$\tilde{\varphi}_a(\omega)$	$\tilde{\varphi}_a^*(\bar{a})$	$\eta_{\tilde{\varphi}_a}(a, \bar{a})$
Mass form (μ)	$\Omega^n(M)$	$\mathcal{L}_{\hat{\omega}}\mu$	$-(\mu)\mathrm{d}\bar{\mu}$	$-(\mu)\omega \wedge \bar{\mu}$
Entropy (s)	$\Omega^0(M)$	$\mathcal{L}_{\hat{\omega}}s$	$(s)\mathrm{d}s$	0

Table 5.2: Summary of interconnection maps for the advected quantities: mass form $\mu \in \Omega^n(M)$ and entropy function $s \in \Omega^0(M)$. Their associated dual elements are denoted by $\bar{\mu} \in \Omega^0(M)$ and $\bar{s} \in \Omega^n(M)$, respectively.

- ii) Let $\bar{b} \in V = \Omega^n(M)$ and $b \in V^* = \Omega^0(M)$, where \bar{b} can be written as $\bar{b} = (*\bar{b})\mu_{\text{vol}}$.

Using the definition of $\tilde{\varphi}_b(\omega)$ and the fact that $b \in C^\infty(M)$, we write

$$\langle \bar{b} | \tilde{\varphi}_b(\omega) \rangle_{V^*} = \int_M \bar{b} \wedge \mathcal{L}_{\hat{\omega}}b = \int_M \bar{b} \wedge \iota_{\hat{\omega}}\mathrm{d}b = \int_M \iota_{\hat{\omega}}\mathrm{d}b \wedge \bar{b}.$$

Using the Leibniz rule for the interior product it holds $\iota_{\hat{\omega}}(\mathrm{d}b \wedge \bar{b}) = \iota_{\hat{\omega}}(\mathrm{d}b) \wedge \bar{b} - \mathrm{d}b \wedge \iota_{\hat{\omega}}(\bar{b}) = 0$, since, as an $n+1$ form, $\mathrm{d}b \wedge \bar{b} = 0$. It follows

$$\begin{aligned} \int_M \iota_{\hat{\omega}}\mathrm{d}b \wedge \bar{b} &= \int_M \mathrm{d}b \wedge \iota_{\hat{\omega}}\bar{b} = \int_M \mathrm{d}b \wedge (*\bar{b})\iota_{\hat{\omega}}\mu_{\text{vol}} \\ &= \int_M (*\bar{b})\mathrm{d}b \wedge \omega = \langle \tilde{\varphi}_b^*(\bar{b}) | \omega \rangle_{\mathfrak{g}} \end{aligned}$$

Moreover, from (5.42) we have that $\eta_{\tilde{\varphi}_b}(\omega, \bar{b}) = 0$. ■

For the reader's convenience, a summary of the interconnection maps is provided in Table 5.2. Finally, we conclude this section by the following remark.

Remark 5.2.2. It is important to distinguish in (5.40) that the map $\tilde{\varphi}_a$ is modulated by the state $a \in V^*$, while the image of ω under $\tilde{\varphi}_a$ belongs to the tangent space at $a \in V^*$, i.e.

$$\tilde{\varphi}_a(\omega) = -\dot{a} \in T_a V^* \cong V^*.$$

Moreover, the range of the map $\tilde{\varphi}_a^*$ is the cotangent space at $a \in V^*$, i.e. $T_a^* V^* \cong V$. These three spaces correspond to variables of different physical nature. In the port-Hamiltonian formalism, presented later, this physical difference is highlighted by referring to the state $a \in V^*$ as the energy variable, to its rate of change $\dot{a} \in V^*$ as the flow variable, and to an element of V as the co-energy variable.

5.2.3 Right Representation and Semidirect Product Structure

The presence of advected quantities adds more structure to the Lie algebra structure of \mathfrak{g} that will be central for deriving the Hamiltonian dynamics in the coming section.

On the group level (valid only for impermeable or no boundary), the pullback operation of a flow map $g_t \in \mathcal{D}(M)$ on an advected quantity $a_t \in V^*$ defines a right linear action (i.e. representation) of the group $\mathcal{D}(M)$ on the vector space V^* , which induces another representation on its dual space V , given also by the pullback operation [Holm et al., 2009]. Thus, both V and V^* are representation spaces of $\mathcal{D}(M)$.

On the algebra level, the representation of $\mathcal{D}(M)$ on V and V^* induces two other representations of \mathfrak{g} on V and V^* that are both related to the Lie derivative operator [Holm et al., 2009]. This representation will allow constructing the semi-direct product algebra $\mathfrak{s} = \mathfrak{g} \ltimes V$, where its dual will be the state space on which the Hamiltonian dynamical equations will be represented.

In what follows next, we present the semi-direct product structure of \mathfrak{s} , but first provide the technical details of the representations of both $\mathcal{D}(M)$ and \mathfrak{g} on V and V^* . Readers who are familiar with the action of Lie groups on vector spaces, can freely skip the next technical subsection and continue directly to the discussion on the semi-direct product structure.

Right Representations of G and \mathfrak{g} on V and V^*

The action of the Lie group G on the vector space V is defined by

$$\begin{aligned} \Phi : G \times V &\rightarrow V \\ (g, \bar{a}) &\mapsto g^*(\bar{a}). \end{aligned} \quad (5.43)$$

Thus, $\Phi_g : \bar{a} \mapsto g^*(\bar{a})$ is a linear isomorphism on V for every $g \in G$. The action (5.43) is a **right action** because we have $\forall \bar{a} \in V, \forall g_1, g_2 \in G$

- i) $\Phi_e(\bar{a}) = e^*(\bar{a}) = \bar{a}$,
- ii) $\Phi_{g_1 \circ g_2}(\bar{a}) = (g_1 \circ g_2)^*(\bar{a}) = g_2^*(g_1^*\bar{a}) = \Phi_{g_2} \circ \Phi_{g_1}(\bar{a})$.

Let the duality pairing $\langle \cdot | \cdot \rangle_V : V^* \times V \rightarrow \mathbb{R}$ to be given by

$$\langle a | \bar{a} \rangle_V := \int_M a \wedge \bar{a}, \quad a \in V^*, \bar{a} \in V. \quad (5.44)$$

The induced right action of G on V^* is equal to the inverse of the dual map

of Φ_g . The dual isomorphism Φ_g^* is defined such that for any $\bar{a} \in V$ and $a \in V^*$

$$\langle \Phi_g^*(a) | \bar{a} \rangle_V = \langle a | \Phi_g(\bar{a}) \rangle_V = \int_M a \wedge g^* \bar{a} \quad (5.45)$$

$$= \int_M g^*((g^{-1})^* a \wedge \bar{a}) = \int_M (g^{-1})^* a \wedge \bar{a} = \langle (g^{-1})^* a | \bar{a} \rangle_V, \quad (5.46)$$

thus, $\Phi_g^*(a) = (g^{-1})^*(a)$. Now we define the induced action of G on V^* by

$$\begin{aligned} \tilde{\Phi} : G \times V^* &\rightarrow V^* \\ (g, a) &\mapsto \tilde{\Phi}(g, a) := \Phi_{g^{-1}}^*(a). \end{aligned} \quad (5.47)$$

Therefore, we have that $\tilde{\Phi}_g := \tilde{\Phi}(g, \cdot)$ is given by

$$\tilde{\Phi}_g(a) = \Phi_{g^{-1}}^*(a) = g^* a. \quad (5.48)$$

In conclusion, the representation of G on both V and V^* is given by the pullback operation.

The induced actions of the Lie algebra $\mathfrak{g}^v = \mathfrak{X}(M)$ on V and on V^* , are given respectively by the maps $\phi : \mathfrak{g}^v \times V \rightarrow V$ and $\tilde{\phi} : \mathfrak{g}^v \times V^* \rightarrow V^*$, defined such that

$$\phi_v(\bar{a}) := \phi(v, \bar{a}) := \left. \frac{d}{dt} \right|_{t=0} \Phi_{g(t)}(\bar{a}), \quad \tilde{\phi}_v(a) := \tilde{\phi}(v, a) := \left. \frac{d}{dt} \right|_{t=0} \tilde{\Phi}_{g(t)}(a),$$

where $g(t) \in G$ is the curve with $g(0) = e$ and $\dot{g}(0) = v$.

Therefore, for the representations (5.43) and (5.48), we have that

$$\phi_v(\bar{a}) = \left. \frac{d}{dt} \right|_{t=0} g^*(t)(\bar{a}) = \mathcal{L}_v \bar{a}, \quad \tilde{\phi}_v(a) = \left. \frac{d}{dt} \right|_{t=0} g^*(t)(a) = \mathcal{L}_v a,$$

which follows from the definition of the Lie-derivative.

Using the isomorphism Ψ_{vol} in (5.11), it is possible to construct an action of the differential form representation of the Lie algebra \mathfrak{g} on V and V^* as follows. For a given $\omega \in \mathfrak{g}$, we define the maps

$$\begin{aligned} \varphi_\omega : V &\rightarrow V & \tilde{\varphi}_\omega : V^* &\rightarrow V^* \\ \bar{a} &\mapsto \varphi_\omega(\bar{a}) := \phi(\hat{\omega}, \bar{a}), & a &\mapsto \tilde{\varphi}_\omega(a) := \tilde{\phi}(\hat{\omega}, a), \end{aligned} \quad (5.49)$$

where $\hat{\omega} = \Psi_{\text{vol}}^{-1}(\omega)$. Thus, we explicitly have that $\varphi_\omega(\bar{a}) = \mathcal{L}_{\hat{\omega}} \bar{a}$ and $\tilde{\varphi}_\omega(a) = \mathcal{L}_{\hat{\omega}} a$.

Finally, a summary of the aforementioned maps is presented in Table 5.3.

	G	\mathfrak{g}^v	\mathfrak{g}
V	$\Phi_g = g^*$	$\phi_v = \frac{d}{dt} _{t=0} \Phi_{g(t)} = \mathcal{L}_v$	$\varphi_\omega = \phi(\Psi_{\text{vol}}^{-1}(\omega), \cdot) = \mathcal{L}_{\hat{\omega}}$
V^*	$\tilde{\Phi}_g = \Phi_{g^{-1}}^* = g^*$	$\tilde{\phi}_v = \frac{d}{dt} _{t=0} \tilde{\Phi}_{g(t)} = \mathcal{L}_v$	$\tilde{\varphi}_\omega = \tilde{\phi}(\Psi_{\text{vol}}^{-1}(\omega), \cdot) = \mathcal{L}_{\hat{\omega}}$

Table 5.3: Summary of notations for Actions on V and V^*

Semidirect Product Structure

Given the group $\mathcal{D}(M)$, vector space $V = \Omega^k(M)$, and the right representation given by the pullback operation, we define the semi-direct product Lie group S as the group with underlying manifold $\mathcal{D}(M) \times V$ and group operation $\bullet : S \times S \rightarrow S$ defined by

$$(g_1, \bar{a}_1) \bullet (g_2, \bar{a}_2) = (g_1 \circ g_2, g_2^*(\bar{a}_1) + \bar{a}_2). \quad (5.50)$$

Usually S is denoted by $\mathcal{D}(M) \ltimes V$. The Lie algebra of S is then given by the semi-direct product algebra $\mathfrak{s} = \mathfrak{g} \ltimes V$, with its corresponding bracket $[\cdot, \cdot]_{\mathfrak{s}} : \mathfrak{s} \times \mathfrak{s} \rightarrow \mathfrak{s}$, is defined using the Lie bracket on \mathfrak{g} in (5.15) and the induced action of \mathfrak{g} on V as

$$[(\omega_1, \bar{a}_1), (\omega_2, \bar{a}_2)]_{\mathfrak{s}} := ([\omega_1, \omega_2]_{\mathfrak{g}}, \mathcal{L}_{\hat{\omega}_2} \bar{a}_1 - \mathcal{L}_{\hat{\omega}_1} \bar{a}_2). \quad (5.51)$$

The dual space $\mathfrak{s}^* = \mathfrak{g}^* \times V^*$ to the Lie algebra \mathfrak{s} will serve as the Poisson manifold on which the dynamical equations of motion will be formulated later. The duality pairing between an element $(\alpha, a) \in \mathfrak{s}^*$ and an element $(\omega, \bar{a}) \in \mathfrak{s}$ is given by

$$\langle (\alpha, a) | (\omega, \bar{a}) \rangle_{\mathfrak{s}} := \langle \alpha | \omega \rangle_{\mathfrak{g}} + \langle a | \bar{a} \rangle_V = \int_M \alpha \wedge \omega + a \wedge \bar{a}. \quad (5.52)$$

As usual we define the adjoint operator $\mathbf{ad}_{(\omega, \bar{a})} : \mathfrak{s} \rightarrow \mathfrak{s}$ for a given $(\omega, \bar{a}) \in \mathfrak{s}$ by $\mathbf{ad}_{(\omega, \bar{a})} := [(\omega, \bar{a}), \cdot]_{\mathfrak{s}}$. Note that the *bold* notation for $\mathbf{ad}_{(\omega, \bar{a})}$ is to distinguish it from the ad_{ω} operator of the Lie algebra \mathfrak{g} . Then the dual map $\mathbf{ad}_{(\omega, \bar{a})}^* : \mathfrak{s}^* \rightarrow \mathfrak{s}^*$ is given by the following result, which is an extension of Prop. 5.1.3 for the case of the semi-direct product \mathfrak{s} .

Theorem 5.2.3. *For a given $(\omega, \bar{a}) \in \mathfrak{s}$, the formal dual $\mathbf{ad}_{(\omega, \bar{a})}^*$ of the adjoint operator $\mathbf{ad}_{(\omega, \bar{a})}$ and (5.51) is given explicitly by*

$$\mathbf{ad}_{(\omega, \bar{a})}^*(\alpha, a) = (ad_{\omega}^*(\alpha) + \bar{a} \diamond a, \mathcal{L}_{\hat{\omega}} a), \quad (\alpha, a) \in \mathfrak{s}^*, \quad (5.53)$$

where $ad_{\omega}^* : \mathfrak{g}^* \rightarrow \mathfrak{g}^*$ is given by Prop. 5.1.3, and the diamond map $\diamond : V \times V^* \rightarrow \mathfrak{g}^*$ is given by

$$\bar{a} \diamond a := (-1)^{c+1} \tilde{\varphi}_a^*(a), \quad \bar{a} \in V = \Omega^k(M), a \in V^* = \Omega^{n-k}(M),$$

where $c = k(n - k) \in \mathbb{R}$.

For a general n -dimensional manifold M with boundary ∂M , the map $\mathbf{ad}_{(\omega_1, \bar{a}_1)}^*$ satisfies the following equality for any $(\omega_1, \bar{a}_1), (\omega_2, \bar{a}_2) \in \mathfrak{s}$ and $(\alpha, a) \in \mathfrak{s}^*$

$$\begin{aligned} \left\langle \mathbf{ad}_{(\omega_1, \bar{a}_1)}^*(\alpha, a) \middle| (\omega_2, \bar{a}_2) \right\rangle_{\mathfrak{s}} &= \left\langle (\alpha, a) \middle| \mathbf{ad}_{(\omega_1, \bar{a}_1)}(\omega_2, \bar{a}_2) \right\rangle_{\mathfrak{s}} \\ &\quad + \int_{\partial M} \eta_{\mathbf{ad}_{(\omega_1, \bar{a}_1)}}(\alpha, a, \omega_2, \bar{a}_2)|_{\partial M}, \end{aligned} \quad (5.54)$$

where the surface term $\eta_{\mathbf{ad}_{(\omega_1, \bar{a}_1)}}(\alpha, a, \omega_2, \bar{a}_2) \in \Omega^{n-1}(M)$ is expressed as

$$\begin{aligned} \eta_{\mathbf{ad}_{(\omega_1, \bar{a}_1)}}(\alpha, a, \omega_2, \bar{a}_2) &= \eta_{ad_{\omega_1}}(\alpha, \omega_2) + (-1)^{c+1} \eta_{\tilde{\varphi}_a}(\omega_2, \bar{a}_1) \\ &\quad - \iota_{\omega_2}(a \wedge \bar{a}_1) + \iota_{\omega_1}(a \wedge \bar{a}_2), \end{aligned} \quad (5.55)$$

where the expressions of the surface terms are given in (5.20) and in Prop. 5.2.1.

Proof. Consider $(\omega_1, \bar{a}_1), (\omega_2, \bar{a}_2) \in \mathfrak{s}$. Using the definition of the bracket in (5.51), the duality pairing in (5.52), and the identity

$$\int_M a \wedge \mathcal{L}_{\hat{\omega}} \bar{a} + \mathcal{L}_{\hat{\omega}} a \wedge \bar{a} = \int_{\partial M} \iota_{\hat{\omega}}(a \wedge \bar{a}),$$

we have that

$$\begin{aligned} \left\langle (\alpha, a) \middle| \mathbf{ad}_{(\omega_1, \bar{a}_1)}(\omega_2, \bar{a}_2) \right\rangle_{\mathfrak{s}} &= \left\langle (\alpha, a) \middle| ([\omega_1, \omega_2]_{\mathfrak{g}}, \mathcal{L}_{\hat{\omega}_2} \bar{a}_1 - \mathcal{L}_{\hat{\omega}_1} \bar{a}_2) \right\rangle_{\mathfrak{s}} \\ &= \langle \alpha | ad_{\omega_1}(\omega_2) \rangle_{\mathfrak{g}} + \langle a | \mathcal{L}_{\hat{\omega}_2} \bar{a}_1 \rangle_V - \langle a | \mathcal{L}_{\hat{\omega}_1} \bar{a}_2 \rangle_V \\ &= \langle \alpha | ad_{\omega_1}(\omega_2) \rangle_{\mathfrak{g}} - \langle \mathcal{L}_{\hat{\omega}_2} a | \bar{a}_1 \rangle_V + \langle \mathcal{L}_{\hat{\omega}_1} a | \bar{a}_2 \rangle_V \\ &\quad + \int_{\partial M} \iota_{\hat{\omega}_2}(a \wedge \bar{a}_1)|_{\partial M} - \int_{\partial M} \iota_{\hat{\omega}_1}(a \wedge \bar{a}_2)|_{\partial M}. \end{aligned}$$

Let $c := k(n - k) \in \mathbb{R}$. Using the wedge product properties and (5.42), the term $-\langle \mathcal{L}_{\hat{\omega}_2} a | \bar{a}_1 \rangle_V$ can be expressed as

$$\begin{aligned} - \int_M \mathcal{L}_{\hat{\omega}_2} a \wedge \bar{a}_1 &= \int_M (-1)^{c+1} \bar{a}_1 \wedge \mathcal{L}_{\hat{\omega}_2} a = (-1)^{c+1} \langle \bar{a}_1 | \tilde{\varphi}_a(\omega_2) \rangle_{V^*} \\ &= (-1)^{c+1} \left(\langle \tilde{\varphi}_a^*(\bar{a}_1) | \omega_2 \rangle_{\mathfrak{g}} - \int_{\partial M} \eta_{\tilde{\varphi}_a}(\omega_2, \bar{a}_1)|_{\partial M} \right) \\ &= \langle \bar{a}_1 \diamond a | \omega_2 \rangle_{\mathfrak{g}} - \int_{\partial M} (-1)^{c+1} \eta_{\tilde{\varphi}_a}(\omega_2, \bar{a}_1)|_{\partial M}. \end{aligned} \quad (5.56)$$

Using the pairing equalities (5.19) and (5.56), we have that

$$\begin{aligned}
& \langle (\alpha, a) | \mathbf{ad}_{(\omega_1, \bar{a}_1)}(\omega_2, \bar{a}_2) \rangle_{\mathfrak{s}} \\
&= \langle \mathbf{ad}_{\omega_1}^*(\alpha) | \omega_2 \rangle_{\mathfrak{g}} - \int_{\partial M} \eta_{ad_{\omega_1}}(\alpha, \omega_2)|_{\partial M} + \langle \bar{a}_1 \diamond a | \omega_2 \rangle_{\mathfrak{g}} \\
&- \int_{\partial M} (-1)^{c+1} \eta_{\bar{\varphi}_a}(\omega_2, \bar{a}_1)|_{\partial M} + \langle \mathcal{L}_{\hat{\omega}_1} a | \bar{a}_2 \rangle_V \\
&+ \int_{\partial M} \iota_{\hat{\omega}_2}(a \wedge \bar{a}_1)|_{\partial M} - \int_{\partial M} \iota_{\hat{\omega}_1}(a \wedge \bar{a}_2)|_{\partial M} \\
&= \langle \mathbf{ad}_{\omega_1}^*(\alpha) + \bar{a}_1 \diamond a | \omega_2 \rangle_{\mathfrak{g}} + \langle \mathcal{L}_{\hat{\omega}_1} a | \bar{a}_2 \rangle_V - \int_{\partial M} [\eta_{ad_{\omega_1}}(\alpha, \omega_2) \\
&+ (-1)^{c+1} \eta_{\bar{\varphi}_a}(\omega_2, \bar{a}_1) - \iota_{\hat{\omega}_2}(a \wedge \bar{a}_1) + \iota_{\hat{\omega}_1}(a \wedge \bar{a}_2)]|_{\partial M}, \\
&= \langle \mathbf{ad}_{(\omega_1, \bar{a}_1)}^*(\alpha, a) | (\omega_2, \bar{a}_2) \rangle_{\mathfrak{s}} - \int_{\partial M} \eta_{ad_{(\omega_1, \bar{a}_1)}}(\alpha, a, \omega_2, \bar{a}_2)|_{\partial M},
\end{aligned}$$

which concludes the proof. ■

Remark 5.2.4. The diamond operator $\diamond : V \times V^* \rightarrow \mathfrak{g}^*$ in (5.53) is usually introduced in the Hamiltonian mechanics literature, e.g. [Marsden et al., 1984a; Holm et al., 1998; Modin et al., 2011], as a short-hand notation for the dual map (5.41) and it describes the effect that the advected quantities impose on the motion of the fluid.

5.3 Port-Hamiltonian Modeling of the Kinetic Energy Subsystem

Now we start the port-Hamiltonian modeling procedure of a fluid dynamical system flowing on an arbitrary spatial manifold. Unlike the standard *top-down* approach in classical Hamiltonian theory for modeling a fluid system starting from the configuration space $\mathcal{D}(M)$, the philosophy of the port-Hamiltonian modeling process is based on a *bottom-up* approach, as discussed in Ch.2.

For the fluid dynamical system at hand, the first step of the port-Hamiltonian modeling procedure, i.e. the conceptual tearing process, yields two energetic subsystems; One for storage of kinetic energy and another for storage of internal energy (for the general case of compressible flow). In this section, we will only focus on the application of the second and third steps for modeling the kinetic energy subsystem. Indeed, we will derive it as a closed Hamiltonian model and then extend it to an open port-Hamiltonian model.

The non-canonical coordinates we choose to develop the Hamiltonian model belong to the dual space $\mathfrak{s}^* = \mathfrak{g}^* \times V^*$ of the semi-direct Lie-algebra $\mathfrak{s} = \mathfrak{g} \ltimes V$.

In the classical fluid dynamics literature, these coordinates are referred to as the Eulerian representation of the fluid motion, in contrast to the Lagrangian representation corresponding to the canonical coordinates on the cotangent bundle of $\mathcal{D}(M)$.

Using the *semi-direct product reduction theorem* [Marsden et al., 1984a,b], we will show in the coming section that the Hamiltonian dynamical equations in terms of the Eulerian variables is derivable from the canonical symplectic Hamiltonian dynamics in terms of the Lagrangian variables. This procedure will yield the Hamiltonian dynamics on the dual space $\mathfrak{s}^* = \mathfrak{g}^* \times V^*$ of the semi-direct Lie-algebra $\mathfrak{s} = \mathfrak{g} \ltimes V$. It is important to note that this is the only stage where the diffeomorphism group is used, which is possible since we will deal with an isolated closed dynamical system. Moreover, the material presented in this work will be a mere reproduction of the results of [Marsden et al., 1984a,b] with a slight difference that the algebra considered here is $n - 1$ differential forms.

Afterwards, we will show the derived Hamiltonian model and its corresponding Lie-Poisson structure are extended to an open port-Hamiltonian model based on a Stokes-Dirac structure. In this open model, the group structure will be no longer valid, but all the constructions on the algebra will be extended directly to incorporate the permeable boundaries.

5.3.1 Semidirect Product Reduction Theorem

In order to derive the Hamiltonian dynamics of the kinetic energy subsystem in terms of the Eulerian variables we will use the *semi-direct product reduction theorem* [Marsden et al., 1984a,b], which requires an extension of the configuration space to incorporate also advected quantities. This procedure will yield the Hamiltonian dynamics on the dual space $\mathfrak{s}^* = \mathfrak{g}^* \times V^*$ of the semi-direct Lie-algebra $\mathfrak{s} = \mathfrak{g} \ltimes V$.

The main reason why one needs the semi-direct product reduction theorem is that the kinetic energy Hamiltonian on the phase space, i.e. the cotangent bundle $T^*\mathcal{D}(M)$, depends parametrically on a variable corresponding to the static reference value of the mass form, which becomes dynamic when reduction is performed.

For the reader's convenience, we provide a very brief overview of the procedure, without technical details.

- Let $\mathbf{H}_{a_0} : T^*G \rightarrow \mathbb{R}$ be a Hamiltonian function on the phase space T^*G that depends parametrically on a variable $a_0 \in V^*$.
- Let $\mathbf{H} : T^*G \times V^* \rightarrow \mathbb{R}$, defined for $(g, \pi) \in T^*G$ by $\mathbf{H}(g, \pi, a_0) := \mathbf{H}_{a_0}(g, \pi)$, be invariant on T^*G under the action of G on $T^*G \times V^*$.

- Consequently we have on the semi-direct product group S that the function \mathbf{H} is invariant on $T^*S = T^*(G \times V) \cong T^*G \times V \times V^*$ which is extended to be constant in V under the action of the semi-direct product.
- The semi-direct product reduction theorem ensures that the dynamics of \mathbf{H}_{a_0} reduced by the symmetry group G_{a_0} (i.e. the stabilizer group of a_0) is symplectically equivalent to the Lie-Poisson dynamics on the dual space $\mathfrak{s}^* = \mathfrak{g}^* \times V^*$ of the semi-direct product Lie algebra $\mathfrak{s} = \mathfrak{g} \times V$ in terms of an induced Hamiltonian $H : \mathfrak{s}^* \rightarrow \mathbb{R}$.

Although the semidirect product reduction theorem has been shown in the literature to be applicable to a wide range of finite-dimensional systems (e.g., heavy-top) and infinite-dimensional systems (e.g. compressible flow and magneto-hydrodynamics), the theorem is usually applied backwards. The reason is that starting from the cotangent bundle T^*G , it is not obvious a priori what the representation space V and its corresponding action (similar to (5.43)) should be [Marsden et al., 1984a]. Next, we illustrate how the theorem is applied for the kinetic energy Hamiltonian defined on \mathfrak{s}^* .

5.3.2 Closed Model of Kinetic Energy

The *kinetic co-energy*¹ of the fluid flow can be used to construct a (reduced) Hamiltonian functional on $\mathfrak{s}^* = \mathfrak{g}^* \times V^*$. By analogy with the kinetic co-energy of a system of particles, we define the co-energy of the fluid flowing on a manifold M to be

$$E_k^*(v, \rho) := \int_M \frac{1}{2} \rho \mathbb{M}(v, v) \mu_{\text{vol}}, \quad (5.57)$$

where \mathbb{M} is the Riemannian metric on M .

Now we wish to represent the kinetic co-energy of the fluid in terms of the Lie algebra \mathfrak{g} and the space of advected quantities V^* , which is expressed as

$$L_k(\omega_v, \mu) = \int_M \frac{1}{2} (*\mu) \omega_v \wedge *\omega_v, \quad (5.58)$$

which follows from $\rho = *\mu$ and the equalities

$$\mathbb{M}(v, v) \mu_{\text{vol}} = \iota_v \tilde{v} \mu_{\text{vol}} = \tilde{v} \wedge *\tilde{v} = (-1)^{n-1} * \omega_v \wedge \omega_v = \omega_v \wedge *\omega_v, \quad (5.59)$$

where the second equality follows from identity (5.12). Thus, $L_k : \mathfrak{g} \times V^* \rightarrow \mathbb{R}$ is a (reduced Lagrangian) functional on the Lie algebra of $\mathcal{D}(M)$ that depends parametrically on $\mu \in V^*$. Using a partial Legendre transformation, we can thus of course represent the *kinetic energy* as a functional on $\mathfrak{g}^* \times V^*$ as follows.

¹For the motivation behind using the co-energy and energy terminologies, see [Duindam et al., 2009, Sec. B.2].

Theorem 5.3.1. *The Legendre transformation of $L_k : \mathfrak{g} \times V^* \rightarrow \mathbb{R}$, as given by (5.58), is the functional $H_k : \mathfrak{g}^* \times V^* \rightarrow \mathbb{R}$ given by*

$$H_k(\alpha, \mu) = \int_M \frac{1}{2(*\mu)} \alpha \wedge *\alpha, \quad (5.60)$$

where $\alpha := (-1)^{n-1}(*\mu) * \omega_v \in \mathfrak{g}^*$ denotes the momentum of the fluid.

The variational derivatives $\delta_\alpha H_k \in T_\alpha^* \mathfrak{g}^* \cong \mathfrak{g} = \Omega^{n-1}(M)$ and $\delta_\mu H_k \in T_\mu^* V^* \cong V = \Omega^0(M)$ with respect to the states $\alpha \in \mathfrak{g}^*$ and $\mu \in V^*$, respectively, are given by

$$\delta_\alpha H_k = \frac{*\alpha}{*\mu}, \quad \delta_\mu H_k = -\frac{1}{2(*\mu)^2} \iota_{\hat{\alpha}} \alpha, \quad (5.61)$$

where $\hat{\alpha} \in \mathfrak{X}(M)$ denotes the vector field corresponding to the 1-form α .

Proof. First we start by the variational derivatives of (5.58) with respect to its variables. The variational derivative $\delta_\mu L_k := \frac{\delta L_k}{\delta \mu}$ of L_k with respect to $\mu \in V^*$ is the element of V that satisfies for any $\delta \mu \in V^*$,

$$\langle \delta_\mu L_k | \delta \mu \rangle_{V^*} = \langle \delta \mu | \delta_\mu L_k \rangle_V = \left. \frac{d}{d\epsilon} \right|_{\epsilon=0} L_k(\omega_v, \mu + \epsilon \delta \mu).$$

By rewriting (5.58) as

$$L_k(\omega_v, \mu) = \int_M \frac{1}{2}(*\mu) \wedge \omega_v \wedge *\omega_v = \int_M \frac{1}{2} * (\omega_v \wedge *\omega_v) \wedge \mu,$$

then one has that

$$\delta_\mu L_k = \frac{1}{2} * (\omega_v \wedge *\omega_v),$$

by definition of the variational derivative.

The variational derivative $\delta_{\omega_v} L_k := \frac{\delta L_k}{\delta \omega_v}$ of L_k with respect to $\omega_v \in \mathfrak{g}$ is the element of \mathfrak{g}^* that satisfies for any $\delta \omega \in \mathfrak{g}$

$$\langle \delta_{\omega_v} L_k | \delta \omega \rangle_{\mathfrak{g}} = \left. \frac{d}{d\epsilon} \right|_{\epsilon=0} L_k(\omega_v + \epsilon \delta \omega, \mu).$$

By rewriting (5.58) as

$$L_k(\omega_v, \mu) = \int_M \frac{1}{2}(*\mu) \omega_v \wedge *\omega_v = \int_M \frac{1}{2}(-1)^{n-1}(*\mu) * \omega_v \wedge \omega_v,$$

and the observation that L_k is quadratic in ω_v , it follows, again simply by definition of the variational derivative, that

$$\delta_{\omega_v} L_k = (-1)^{n-1}(*\mu) * \omega_v.$$

Now define the conjugate momentum variable $\alpha \in \mathfrak{g}^*$ by $\alpha := \delta_{\omega_v} L_k = (-1)^{n-1}(*\mu) * \omega_v$. The partial Legendre transform of L_k is by definition the change of variables, and its corresponding inverse,

$$(\omega_v, \mu) \mapsto (\alpha, \mu) = ((-1)^{n-1}(*\mu) * \omega_v, \mu), \quad (\alpha, \mu) \mapsto (\omega_v, \mu) = \left(\frac{* \alpha}{* \mu}, \mu\right).$$

Using (5.13), we have that physically $\alpha = (*\mu)\tilde{v} = \rho\tilde{v}$ is the 1-form corresponding to the momentum of the fluid.

Since the Legendre transformation is a diffeomorphism, then L_k is hyperregular, and one can define the Hamiltonian $H_k : \mathfrak{g}^* \times V^* \rightarrow \mathbb{R}$

$$H_k(\alpha, \mu) := \langle \alpha | \omega_v \rangle_{\mathfrak{g}} - L_k(\omega_v, \mu), \quad (5.62)$$

which could be expressed as

$$\begin{aligned} H_k(\alpha, \mu) &= \int_M \alpha \wedge \omega_v - \frac{1}{2}(-1)^{n-1}(*\mu) * \omega_v \wedge \omega_v, \\ &= \int_M \left(\alpha - \frac{1}{2}(-1)^{n-1}(*\mu) * \omega_v\right) \wedge \omega_v, \\ &= \int_M \left(\alpha - \frac{1}{2}\alpha\right) \wedge \frac{* \alpha}{* \mu}, \\ &= \int_M \frac{1}{2(*\mu)} \alpha \wedge * \alpha. \end{aligned}$$

The variational derivative of H with respect to α follows immediately by applying the chain rule to the construction in (5.62)

$$\frac{\delta H_k}{\delta \alpha} = \omega_v + \left\langle \alpha \left| \frac{\delta \omega_v}{\delta \alpha} \right. \right\rangle_{\mathfrak{g}} - \left\langle \frac{\delta L_k}{\delta \omega_v} \left| \frac{\delta \omega_v}{\delta \alpha} \right. \right\rangle_{\mathfrak{g}} = \omega_v = \frac{* \alpha}{* \mu}. \quad (5.63)$$

Similarly, the variational derivative of H with respect to μ is given by

$$\frac{\delta H_k}{\delta \mu} = -\frac{\delta L_k}{\delta \mu} = -\frac{1}{2} * (\omega_v \wedge * \omega_v) = -\frac{1}{2(*\mu)^2} * (\alpha \wedge * \alpha) = -\frac{1}{2(*\mu)^2} \iota_{\hat{\alpha}} \alpha,$$

where identity (5.12) was used. This concludes the proof. \blacksquare

One of the benefits of the previous systematic construction of the (reduced) Hamiltonian H_k is that the correct *conjugate momentum* variable with respect to $\omega_v \in \mathfrak{g}$ is chosen, and all variational derivatives are correctly derived.

As for the governing equations of motion, the semi-direct product reduction theorem asserts that the Hamiltonian dynamics on $\mathfrak{s}^* = \mathfrak{g}^* \times V^*$ is given as follows.

Theorem 5.3.2. *The Hamiltonian dynamical equations of fluid flow in terms of Eulerian variables on the dual space $\mathfrak{s}^* = \mathfrak{g}^* \times V^*$ are given by*

$$\begin{pmatrix} \dot{\alpha} \\ \dot{\mu} \end{pmatrix} = -\mathbf{ad}_{(\delta_\alpha H_k, \delta_\mu H_k)}^*(\alpha, \mu) = \begin{pmatrix} -\mathbf{ad}_{\delta_\alpha H_k}^*(\alpha) - \delta_\mu H_k \diamond \mu \\ -\mathcal{L}_{(\delta_\alpha H_k)^\wedge}(\mu) \end{pmatrix}, \quad (5.64)$$

where the Hamiltonian $H_k(\alpha, \mu)$ and its corresponding variational derivatives are given by Theorem 5.3.1.

The corresponding Lie-Poisson bracket underlying these dynamical equations is given by

$$\{F, G\}(\alpha, \mu) = \left\langle \alpha \mid [\delta_\alpha F, \delta_\alpha G]_{\mathfrak{g}} \right\rangle_{\mathfrak{g}} + \left\langle \mu \mid \mathcal{L}_{(\delta_\alpha G)^\wedge} \delta_\mu F - \mathcal{L}_{(\delta_\alpha F)^\wedge} \delta_\mu G \right\rangle_V, \quad (5.65)$$

where $F, G \in C^\infty(\mathfrak{s}^*)$ are smooth functions on \mathfrak{s}^* .

Proof. To derive the Hamiltonian dynamics using the semidirect product reduction theorem, we need the Hamiltonian \mathbf{H}_{a_0} described on the phase space $T^*\mathcal{D}(M)$. The goal is to extend the Hamiltonian functional $H_k : \mathfrak{g}^* \times V^* \rightarrow \mathbb{R}$ in (5.60) to one on $T^*\mathcal{D}(M)$. Consider the isomorphism $\Gamma : T^*\mathcal{D}(M) \times V^* \rightarrow \mathfrak{g}^* \times V^*$ defined by

$$\Gamma(g, \pi, \mu_0) = ((R_g)^*(\pi), (g^{-1})^*\mu_0), \quad (5.66)$$

which physically represents the map from the space $(T^*\mathcal{D}(M) \times V^*)$ of Lagrangian coordinates to the space $(\mathfrak{g}^* \times V^*)$ of Eulerian coordinates. The action of Γ on $(g, \pi) \in T^*\mathcal{D}(M)$ is given by the pullback of the right translation map $R_g : \mathcal{D}(M) \rightarrow \mathcal{D}(M)$, whereas the action of Γ on $\mu_0 \in V^*$ is given by the pullback operator. Then, by construction, the functional

$$\mathbf{H}(g, \pi, \mu_0) := H_k \circ \Gamma(g, \pi, \mu_0) = H_k(\alpha, \mu)$$

is a Hamiltonian on $T^*\mathcal{D}(M) \times V^*$. Moreover, define the Hamiltonian $\mathbf{H}_{a_0} : T^*\mathcal{D}(M) \rightarrow \mathbb{R}$ by $\mathbf{H}_{\mu_0}(g, \pi) = \mathbf{H}(g, \pi, \mu_0)$. By construction, \mathbf{H}_{a_0} is right-invariant under the action of the stabilizer group G_{μ_0} of $\mu_0 \in V^*$ given by

$$G_{\mu_0} := \{g \in \mathcal{D}(M) \mid (g^{-1})^*\mu_0 = \mu_0\}.$$

As a consequence of the previous construction, the semi-direct product reduction theorem asserts that, for a given Hamiltonian functional $H : \mathfrak{s}^* \rightarrow \mathbb{R}$, the Hamiltonian dynamics on $\mathfrak{s}^* = \mathfrak{g}^* \times V^*$ are given by

$$\dot{x} = -\mathbf{ad}_{\delta_x H}^*(x),$$

where $\delta_x H \in \mathfrak{s}$ is the variational derivative of H with respect to x , and $\mathbf{ad}_{\delta_x H}^*$ is the dual of the adjoint operator $\mathbf{ad}_{\delta_x H}$ of \mathfrak{s} given in (5.53).

The corresponding Lie-Poisson bracket associated to \mathfrak{s}^* is defined by

$$\{F, G\}(x) := \left\langle x \left| \left[\frac{\delta F}{\delta x}, \frac{\delta G}{\delta x} \right]_{\mathfrak{s}} \right. \right\rangle_{\mathfrak{s}}, \quad (5.67)$$

for any $F, G \in C^\infty(\mathfrak{s}^*)$ and $x \in \mathfrak{s}^*$. ■

A key advantage of the equations of motion in the Hamiltonian form (5.64) is that the structure of the equations clearly separates the kinetic energy functional $H_k(\alpha, \mu)$ from the underlying interconnection structure governing the evolution of the energy variables (α, μ) . Note that the second equation in (5.64) represents the advection law for the conservation of mass, whereas the term with the diamond operator in the first equation corresponds to the effect of advection on the momentum balance. Next, we present the port-based interpretation of the Hamiltonian system (5.64).

5.3.3 Port-based Representation

In what follows, Bond graphs will be exploited to graphically represent the different models and constructions performed. For readers unfamiliar with bond graphs, we also accompany most of the bond graphs by their corresponding block diagrams.

In the port-based paradigm, the system described by the equations (5.64) is represented by two subsystems that are connected together using ports. The first subsystem corresponds to the storage property of the system's energy (5.60), while the second subsystem corresponds to the interconnection structure encoded in the Lie-Poisson bracket (5.65).

In general, an energy-storage system (or element) in the port-Hamiltonian framework is defined by the smooth state space manifold \mathcal{X} with a Hamiltonian functional $H : \mathcal{X} \rightarrow \mathbb{R}$ representing the stored energy, and $x \in \mathcal{X}$ is called the energy variable. The rate of change of the energy is given by $\dot{H} = \langle \delta_x H | \dot{x} \rangle_{\mathcal{X}}$, where $(\delta_x H, \dot{x}) \in T_x^* \mathcal{X} \times T_x \mathcal{X}$ are referred to as the effort and flow variables of the energy storage element, respectively. The duality pairing between an effort in $T_x^* \mathcal{X}$ and a flow in $T_x \mathcal{X}$ corresponds to the power entering the energy-storage element at a certain instant of time.

For the case of the kinetic energy Hamiltonian H_k in (5.60), the state space manifold is given by $\mathcal{X} = \mathfrak{s}^*$, the energy variables are given by $x = (\alpha, \mu)$, while the effort variable $\delta_x H_k$ and flow variable \dot{x} are given by

$$\delta_x H_k = (\delta_\alpha H_k, \delta_\mu H_k) \in T_{(\alpha, \mu)}^* \mathfrak{s}^* \cong \mathfrak{g} \times V, \quad (5.68)$$

$$\dot{x} = (\dot{\alpha}, \dot{\mu}) \in T_{(\alpha, \mu)} \mathfrak{s}^* \cong \mathfrak{g}^* \times V^*. \quad (5.69)$$

The energy balance is expressed by

$$\begin{aligned}\dot{H}_k &= \langle \dot{x} | \delta_x H_k \rangle_{\mathfrak{s}} = \langle (\dot{\alpha}, \dot{\mu}) | (\delta_{\alpha} H_k, \delta_{\mu} H_k) \rangle_{\mathfrak{s}} \\ &= \langle \dot{\alpha} | \delta_{\alpha} H_k \rangle_{\mathfrak{g}} + \langle \dot{\mu} | \delta_{\mu} H_k \rangle_V = \int_M \dot{\alpha} \wedge \delta_{\alpha} H_k + \dot{\mu} \wedge \delta_{\mu} H_k.\end{aligned}\quad (5.70)$$

Thus, this represents the first subsystem corresponding to the storage of the kinetic energy H_k in (5.60).

The second subsystem corresponds to the Lie-Poisson structure defined by the map

$$\begin{aligned}J_x : T_x^* \mathfrak{s}^* &\cong \mathfrak{s} \rightarrow T_x \mathfrak{s}^* \cong \mathfrak{s}^* \\ e_{sk} &\mapsto J_x(e_{sk}) =: f_{sk}.\end{aligned}\quad (5.71)$$

For the energy variables, $x = (\alpha, \mu) \in \mathfrak{g}^* \times V^*$, we have that $e_{sk} = (e_{\alpha}, e_{\mu})$ and $f_{sk} = (f_{\alpha}, f_{\mu})$. Then we can express the Lie-Poisson structure as

$$J_x(e_{\alpha}, e_{\mu}) = \begin{pmatrix} -ad_{e_{\alpha}}^*(\alpha) - e_{\mu} \diamond \mu \\ -\mathcal{L}_{\hat{e}_{\alpha}}(\mu) \end{pmatrix}, \quad (e_{\alpha}, e_{\mu}) \in \mathfrak{s} = \mathfrak{g} \times V. \quad (5.72)$$

By substituting the expressions of ad^* in Prop. 5.1.3 and the diamond operator in Prop. 5.2.1 (case 1), we can rewrite the Lie-Poisson structure (5.72) as

$$J_x(e_{\alpha}, e_{\mu}) = \begin{pmatrix} -\mathcal{L}_{\hat{e}_{\alpha}}(\alpha) - \operatorname{div}(\hat{e}_{\alpha})\alpha - (*\mu)\operatorname{de}_{\mu} \\ -\operatorname{d}((*\mu)e_{\alpha}) \end{pmatrix}, \quad (5.73)$$

where the second row in (5.73) follows from $\mathcal{L}_{\hat{e}_{\alpha}}(\mu) = \operatorname{d}\iota_{\hat{e}_{\alpha}}(\mu) = \operatorname{d}((*\mu)\iota_{\hat{e}_{\alpha}}\mu_{\operatorname{vol}}) = \operatorname{d}((*\mu)e_{\alpha})$, using identity $\iota_{\hat{\omega}}\mu_{\operatorname{vol}} = \omega$ for any $\omega \in \mathfrak{g}$, and the fact that μ is a top form. Thus, this represents the second subsystem corresponding the interconnection structure of the system. Since the Lie-Poisson structure (5.73) is defined in terms of the momentum variable α , we refer to it as the **momentum representation** of the Lie-Poisson structure.

The port-Hamiltonian representation of the system (5.64) is now given by

$$\dot{x} = J_x(\delta_x H_k), \quad (5.74)$$

which is constructed by connecting the two ports (e_{sk}, f_{sk}) and $(\delta_x H_k, \dot{x})$ together:

$$f_{sk} = \dot{x} = (\dot{\alpha}, \dot{\mu}), \quad e_{sk} = \delta_x H_k = (\delta_{\alpha} H_k, \delta_{\mu} H_k).$$

Graphically, the port-based representation of the Hamiltonian dynamics (5.64) is shown in Fig. 5.7, where the left figure is represented using bond graphs and the right figure is represented using block diagrams, explicating causality. The kinetic energy storage subsystem is denoted in generalized bond graphs [Breedveld, 1984] by a C-element with its energy functional H_k . The

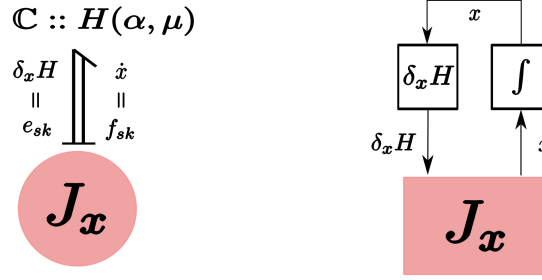


Figure 5.7: Port-based representation of the Hamiltonian dynamics (5.64) corresponding to the system's kinetic energy.

storage subsystem is connected to the Lie-Poisson structure J_x through a port denoted by a double half-arrow. The flow and effort variables are indicated on the right and left of the port, respectively.

At any instant of time, the duality pairing between the flow \dot{x} and the effort $\delta_x H$ equals the power (rate of change of kinetic energy). The conservation of energy can be seen from

$$\begin{aligned}\dot{H}_k &= \langle \dot{x} | \delta_x H_k \rangle_{\mathfrak{s}} = \langle J_x(\delta_x H_k) | \delta_x H_k \rangle_{\mathfrak{s}} = \langle -\mathbf{ad}_{\delta_x H_k}^*(x) | \delta_x H_k \rangle_{\mathfrak{s}} \\ &= -\langle x | \mathbf{ad}_{\delta_x H_k} \delta_x H_k \rangle_{\mathfrak{s}} = -\langle x | [\delta_x H_k, \delta_x H_k]_{\mathfrak{s}} \rangle_{\mathfrak{s}} = 0,\end{aligned}\quad (5.75)$$

which follows from the skew-symmetry of the Lie bracket of \mathfrak{s} . Consequently, the Lie-Poisson structure J_x is a skew-symmetric operator, which corresponds to it being a power-continuous element in port-based terminology. It is extremely important to note that in the energy balance (5.75), the surface terms (5.54) that should appear in the fourth equality naturally disappear for the closed system (5.64).

In summary, the closed port-Hamiltonian system shown in Fig. 5.7 describes the conservation of kinetic energy H_k and the corresponding evolution of the energy variables (α, μ) . The conservation of energy follows from the skew-symmetry of the Lie-Poisson structure. The aforementioned port-Hamiltonian system is still equivalent to the *standard* Hamiltonian one that describes a conservative system that is isolated from any energy-exchange with the external world. Next, we discuss how to allow non-zero energy exchange by replacing the underlying Lie-Poisson structure with a *Stokes-Dirac structure*.

5.3.4 Open Model of Kinetic Energy

There are two ways in which the port-Hamiltonian system (5.74) can interact and exchange energy with the world; either through the boundary ∂M of the spatial manifold M or within the domain itself through a distributed port that

allows energy exchange at every point in M . The former allows exchange of kinetic energy by mass inflow or outflow, while the latter allows transformation of kinetic energy to another form in a reversible (or irreversible) way.

To add a distributed port based on Newton's second law, a *distributed force* field $\mathbf{f}_s \in \mathfrak{g}^* = \Omega^1(M)$ is added to the momentum balance equation such that the port-Hamiltonian system (5.64) is rewritten, using (5.73) as

$$\begin{pmatrix} \dot{\alpha} \\ \dot{\mu} \end{pmatrix} = \begin{pmatrix} -\mathcal{L}_{(\delta_\alpha H_k)^\wedge}(\alpha) - \operatorname{div}((\delta_\alpha H_k)^\wedge)\alpha - (*\mu)d\delta_\mu H_k + \mathbf{f}_s \\ -d((*\mu)\delta_\alpha H_k) \end{pmatrix}, \quad (5.76)$$

$$H_k(\alpha, \mu) = \int_M \frac{1}{2(*\mu)} \alpha \wedge *\alpha. \quad (5.77)$$

It is worth noticing how our previous choice of the Lie algebra \mathfrak{g} as $\Omega^{n-1}(M)$ effects the external force field \mathbf{f}_s on the dual algebra \mathfrak{g}^* to be a co-vector field, which is the correct geometrical representation of a force field. We can write (5.76) more compactly as

$$\dot{x} = J_x(\delta_x H_k) + G\mathbf{f}_s, \quad (5.78)$$

with J_x given by (5.73) and $G : \mathfrak{g}^* \rightarrow \mathfrak{g}^* \times V^*$, $G = \begin{pmatrix} 1 & 0 \end{pmatrix}^\top$ representing the input map. The force one-form (co-vector field) \mathbf{f}_s will be used later in Part II to model stress forces due to pressure. In general, the distributed force can be used for modeling other stress forces due to viscosity, as well as any body (external) forces on the continuum (e.g. due to magnetic fields or gravity and electrostatic accelerations).

The Hamiltonian energy (5.77), as a functional $H_k : \mathfrak{s}^* \rightarrow \mathbb{R}$, admits its rate of change such that along trajectories $x(t)$, parameterized by time $t \in \mathbb{R}$, it holds that

$$\dot{H}_k = \langle \dot{x} | \delta_x H_k \rangle_{\mathfrak{s}} = \int_M \dot{x} \wedge \delta_x H_k. \quad (5.79)$$

As shown in (5.75), for an isolated fluid system on a closed manifold (corresponding to $G = 0$, and either $\partial M = \emptyset$ or ∂M is impermeable) the kinetic energy is always conserved. However, for a general open fluid system, the expression for the kinetic energy balance (5.79) is given by the following result.

Theorem 5.3.3. *The rate of change of the Hamiltonian (5.77) along trajectories of the port-Hamiltonian system (5.78) is given by*

$$\dot{H}_k = \int_{\partial M} e_{\partial k} \wedge f_{\partial k} + \int_M e_d \wedge f_d, \quad (5.80)$$

where the boundary port variables $e_{\partial k}, f_{\partial k} \in \Omega^0(\partial M) \times \Omega^{n-1}(\partial M)$ and dis-

tributed port variables $e_d, f_d \in \Omega^1(M) \times \Omega^{n-1}(M)$ are defined by

$$\begin{aligned} e_{\partial k} &:= \left(\frac{\iota_{(\delta_\alpha H_k)^\wedge}(\alpha)}{* \mu} + \delta_\mu H_k \right) |_{\partial M}, & e_d &:= f_s, \\ f_{\partial k} &:= -(*\mu) \delta_\alpha H_k |_{\partial M}, & f_d &:= \delta_\alpha H_k, \end{aligned}$$

where $\eta|_{\partial M} \in \Omega^k(\partial M)$ denotes the trace of the form $\eta \in \Omega^k(M)$.

Proof. For notational simplicity, we denote $(e_\alpha, e_\mu) = (\delta_\alpha H_k, \delta_\mu H_k)$. By substituting (5.78) in (5.79), we have that

$$\begin{aligned} \dot{H}_k &= \langle J_x(e_\alpha, e_\mu) | (e_\alpha, e_\mu) \rangle_s + \langle G f_s | (e_\alpha, e_\mu) \rangle_s \\ &= - \left\langle \mathbf{ad}_{(e_\alpha, e_\mu)}^*(\alpha, \mu) \middle| (e_\alpha, e_\mu) \right\rangle_s + \langle f_s | G^\top(e_\alpha, e_\mu) \rangle_s \\ &= - \underbrace{\langle (\alpha, \mu) | \mathbf{ad}_{(e_\alpha, e_\mu)}(e_\alpha, e_\mu) \rangle_s}_{=0} - \int_{\partial M} \eta_{\mathbf{ad}_{(e_\alpha, e_\mu)}}(\alpha, \mu, e_\alpha, e_\mu) |_{\partial M} + \langle f_s | e_\alpha \rangle_g, \end{aligned}$$

where (5.54) was used, and the first term in the last equality vanishes due to the skew-symmetry property of the Lie bracket $\mathbf{ad} = [\cdot, \cdot]_s$. Using (5.55), (5.20), and Prop. 5.2.1 (case i), we can express the surface term as

$$\begin{aligned} \eta_{\mathbf{ad}_{(e_\alpha, e_\mu)}}(\alpha, \mu, e_\alpha, e_\mu) &= \eta_{ad_{e_\alpha}}(\alpha, e_\alpha) - \eta_{\tilde{\varphi}_\mu}(e_\alpha, e_\mu) - \iota_{\hat{e}_\alpha}(\mu \wedge e_\mu) + \iota_{\hat{e}_\alpha}(\mu \wedge e_\mu), \\ &= \iota_{\hat{e}_\alpha}(\alpha \wedge e_\alpha) - (-(*\mu)e_\alpha \wedge e_\mu) + 0. \end{aligned}$$

Using the interior product properties, we have that

$$\begin{aligned} \iota_{\hat{e}_\alpha}(\alpha \wedge e_\alpha) &= \iota_{\hat{e}_\alpha}(\alpha) \wedge e_\alpha - \alpha \wedge \iota_{\hat{e}_\alpha}(e_\alpha) \\ &= \iota_{\hat{e}_\alpha}(\alpha) \wedge e_\alpha - \alpha \wedge \iota_{\hat{e}_\alpha} \circ \iota_{\hat{e}_\alpha}(\mu \text{vol}) = \iota_{\hat{e}_\alpha}(\alpha) \wedge e_\alpha, \end{aligned}$$

where the nil-potency property of the interior product was used in the last equality. Therefore, finally we have that

$$\dot{H}_k = \int_{\partial M} \left(\frac{\iota_{\hat{e}_\alpha}(\alpha)}{* \mu} + e_\mu \right) |_{\partial M} \wedge -(*\mu)e_\alpha |_{\partial M} + \int_M f_s \wedge e_\alpha, \quad (5.81)$$

which concludes the proof. ■

It is interesting to note the physical interpretation of the boundary flow variable $f_{\partial k}$. Using (5.61) we have that

$$f_{\partial k} = -(*\mu) \delta_\alpha H_k |_{\partial M} = -*\alpha |_{\partial M} = -(*\mu)\omega_v |_{\partial M} = -\iota_v \mu |_{\partial M},$$

which represents the incoming mass flow through the boundary. As discussed before in Sec. 5.1.4, the condition $\omega_v|_{\partial M} = 0$ corresponds to an impermeable

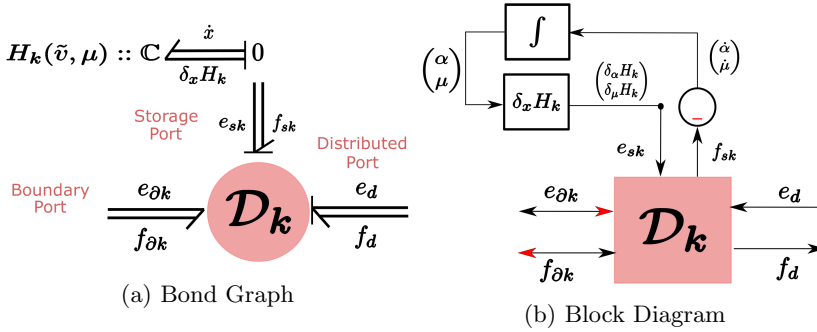


Figure 5.8: Graphical Representation of the Kinetic Energy Subsystem (5.76) in terms of the state variables: momentum one-form α and the mass top-form μ .

boundary ∂M which implies that $f_{\partial k} = 0$ and thus results in no exchange of power through the boundary, as seen in (5.80). The physical interpretation of the boundary effort variable $e_{\partial k}$ will be discussed later.

With reference to Fig. 5.8, the port-Hamiltonian system now has 3 ports; an energy storage port (e_{sk}, f_{sk}) , a boundary port $(e_{\partial k}, f_{\partial k})$, and a distributed port (e_d, f_d) . The port $(e_{\partial k}, f_{\partial k})$ represents the power incoming to the system through the boundary, while the port (e_d, f_d) represents the power flow from an external distributed source in the spatial domain. The 3 ports are connected together through a power-conserving structure \mathcal{D}_k that encodes the power balance equation (5.80). Such mathematical structure is called a **Stokes-Dirac structure** defined as

$$\begin{aligned}
 \mathcal{D}_k &= \{(f_{sk}, f_{\partial k}, f_d, e_{sk}, e_{\partial k}, e_d) \in \mathcal{B}_k \mid \\
 &\quad \begin{pmatrix} f_\alpha \\ f_\mu \end{pmatrix} = \begin{pmatrix} \mathcal{L}_{\hat{e}_\alpha}(\alpha) + \text{div}(\hat{e}_\alpha)\alpha + (*\mu)\text{d}e_\mu \\ \text{d}((*\mu)e_\alpha) \end{pmatrix} - \begin{pmatrix} 1 \\ 0 \end{pmatrix} e_d, \\
 &\quad f_d = \begin{pmatrix} 1 & 0 \end{pmatrix} \begin{pmatrix} e_\alpha \\ e_\mu \end{pmatrix}, \\
 &\quad \begin{pmatrix} e_{\partial k} \\ f_{\partial k} \end{pmatrix} = \begin{pmatrix} \left(\frac{\iota_{\hat{e}_\alpha}(\alpha)}{*\mu} + e_\mu \right) |_{\partial M} \\ -(*\mu)e_\alpha |_{\partial M} \end{pmatrix} \},
 \end{aligned} \tag{5.82}$$

where the storage port variables are given by $f_{sk} = (f_\alpha, f_\mu) \in \mathfrak{s}^* = \Omega^1(M) \times \Omega^n(M)$ and $e_{sk} = (e_\alpha, e_\mu) \in \mathfrak{s} = \Omega^{n-1}(M) \times \Omega^0(M)$. The bond-space $\mathcal{B}_k = \mathcal{F}_k \times \mathcal{E}_k$ is the product space of the flow space $\mathcal{F}_k = \Omega^1(M) \times \Omega^n(M) \times \Omega^{n-1}(\partial M) \times \Omega^{n-1}(M)$ and the effort space $\mathcal{E}_k = \Omega^{n-1}(M) \times \Omega^0(M) \times \Omega^0(\partial M) \times \Omega^1(M)$, represented by smooth differential forms of the appropriate degree.

The Dirac structure (5.82) is a modulated one, in the sense that it depends

on the state variables $x = (\alpha, \mu)$. In the absence of the distributed force ($e_d = 0$) and in case of an impermeable (or no) boundary ($f_{\partial k} = 0$), the Stokes-Dirac structure degenerates to the Lie-Poisson structure (5.73) which encodes the conservation of kinetic energy ($\dot{H}_k = 0$). The sign difference between the Lie-Poisson structure in (5.73) and its counterpart in (5.82) is due to the choice of having all power ports entering the Dirac structure. This can be clearly seen in the graphical representation of the port-Hamiltonian system in Fig. 5.8 in terms of bond graph and block diagram notation.

It is interesting to note that the three power ports shown in Fig. 5.8 are of different natures and result from different duality pairings. The power in the storage port is expressed by the pairing $\langle e_{sk} | f_{sk} \rangle_s$, the power in the distributed port is expressed by the pairing $\langle e_d | f_d \rangle_g$, while the power in the distributed port is expressed by $\int_{\partial M} e_{\partial k} \wedge f_{\partial k}$.

The port-Hamiltonian system (5.76) can be recovered from the Stokes-Dirac structure (5.82) by imposing

$$\begin{aligned} e_{sk} &= \begin{pmatrix} e_\alpha \\ e_\mu \end{pmatrix} = \begin{pmatrix} \delta_\alpha H_k \\ \delta_\mu H_k \end{pmatrix}, & f_{sk} &= \begin{pmatrix} f_\alpha \\ f_\mu \end{pmatrix} = \begin{pmatrix} -\dot{\alpha} \\ -\dot{\mu} \end{pmatrix}, \\ e_d &= f_s, & f_d &= \delta_\alpha H_k, \end{aligned}$$

where the minus sign is due to the choice of having the storage port entering the Dirac structure, as shown in Fig. 5.8. Therefore the implicit port-Hamiltonian dynamics are governed by

$$((-\dot{\alpha}, -\dot{\mu}), f_{\partial k}, \delta_\alpha H_k, (\delta_\alpha H_k, \delta_\mu H_k), e_{\partial k}, f_s) \in \mathcal{D}_k. \quad (5.83)$$

5.3.5 Change of Coordinates to the Velocity Representation

In the work of van der Schaft and Maschke [2002], the port-Hamiltonian model for compressible isentropic flow was given in terms of the velocity 1-form $\tilde{v} \in \Omega^1(M)$ and the mass top-form $\mu \in \Omega^n(M)$ as the underlying energy variables. The arguments behind this choice of coordinates were not connected to the geometric structure underlying the state space, as we presented so far in this work. Instead, in [van der Schaft and Maschke, 2002] the authors defined a canonical version of a Stokes Dirac structure based on exterior derivatives, that is representative of a number of physical systems based on conservation laws of different nature. Then, the authors modified this canonical Dirac structure to represent the fluid dynamical system with the velocity and mass forms as energy variables.

One of the contributions of this article is to present a rigorous derivation of the Stokes Dirac structure presented in [van der Schaft and Maschke, 2002], starting from (5.82) based on semi-direct product theory. We will represent

the port-Hamiltonian system in (5.76) in terms of the same energy variables in [van der Schaft and Maschke, 2002] by means of a change of coordinates, recovering the Dirac structure which was introduced there without a formal derivation.

The following change of coordinates procedure was introduced by Vankerschaver et al. [2010] for the Lie-Poisson structure only. In this work we extend the coordinate change for the full Stokes-Dirac structure and emphasize its port-based interpretation. It will turn out that in terms of the new variables, the expression of the Dirac structure will be simpler than the momentum representation in (5.73). In addition, this description yields further advantages such as a trivial derivation of the vorticity equation.

Consider the (nonlinear) diffeomorphism

$$\Phi : (\alpha, \mu) \mapsto (\tilde{v}, \tilde{\mu}) := \left(\frac{\alpha}{*\mu}, \mu \right). \quad (5.84)$$

We denote the new state variables $(\tilde{v}, \tilde{\mu})$ by $\tilde{x} \in \mathfrak{s}^*$, i.e. $\Phi : x \mapsto \tilde{x}$. Consider the pushforward map $(\Phi_*)_x$ and pullback map $(\Phi^*)_x$ of Φ at a point $x \in \mathfrak{s}^*$

$$\begin{aligned} (\Phi_*)_x : T_x \mathfrak{s}^* &\rightarrow T_{\tilde{x}} \mathfrak{s}^* & (\Phi^*)_x : T_{\tilde{x}}^* \mathfrak{s}^* &\rightarrow T_x^* \mathfrak{s}^* \\ (\dot{\alpha}, \dot{\mu}) &\mapsto (\dot{\tilde{v}}, \dot{\tilde{\mu}}), & (e_{\tilde{v}}, e_{\tilde{\mu}}) &\mapsto (e_{\alpha}, e_{\mu}), \end{aligned} \quad (5.85)$$

Now we consider the coordinate change for the Lie-Poisson part (5.73) of the Stokes-Dirac structure. The **velocity representation** of the Lie-Poisson structure is the map $\tilde{J}_{\tilde{x}} : T_{\tilde{x}}^* \mathfrak{s}^* \rightarrow T_{\tilde{x}} \mathfrak{s}^*$, defined by

$$\tilde{J}_{\tilde{x}} := (\Phi_*)_x \circ J_x \circ (\Phi^*)_x. \quad (5.86)$$

The change of coordinates described above can be represented graphically in an elegant way in the port-based framework as shown in the Fig. 5.9.

The exact expressions for the maps $(\Phi_*)_x$, $(\Phi^*)_x$, and $\tilde{J}_{\tilde{x}}$ are given by the following theorem [Vankerschaver et al., 2010].

Proposition 5.3.4. *The pushforward $(\Phi_*)_x$ and pullback map $(\Phi^*)_x$ of the diffeomorphism (5.84) at a point $x = (\alpha, \mu) \in \mathfrak{s}^*$ are given respectively by*

$$(\Phi_*)_x(\dot{\alpha}, \dot{\mu}) = \left(\frac{\dot{\alpha} - (*\dot{\mu})\tilde{v}}{*\tilde{\mu}}, \dot{\mu} \right) =: (\dot{\tilde{v}}, \dot{\tilde{\mu}}), \quad (5.87)$$

$$(\Phi^*)_x(e_{\tilde{v}}, e_{\tilde{\mu}}) = \left(\frac{e_{\tilde{v}}}{*\tilde{\mu}}, e_{\tilde{\mu}} - \frac{*(\tilde{v} \wedge e_{\tilde{v}})}{*\tilde{\mu}} \right) =: (e_{\alpha}, e_{\mu}), \quad (5.88)$$

where $(\tilde{v}, \tilde{\mu}) = \Phi(\alpha, \mu)$. The velocity representation of the Lie-Poisson structure defined by (5.86) is expressed as

$$\tilde{J}_{\tilde{x}}(e_{\tilde{v}}, e_{\tilde{\mu}}) = \begin{pmatrix} -de_{\tilde{\mu}} - \frac{1}{*\tilde{\mu}} \iota_{\tilde{e}_{\tilde{v}}} d\tilde{v} \\ -de_{\tilde{v}} \end{pmatrix}. \quad (5.89)$$

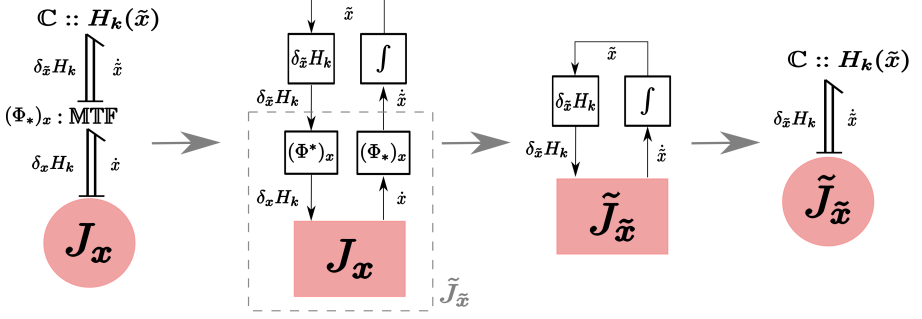


Figure 5.9: Graphical representation of change of coordinates from the momentum-representation J_x to the velocity representation $\tilde{J}_{\tilde{x}}$ of the Lie-Poisson structure.

Proof. For notational simplicity in this proof we denote $*\mu = *\tilde{\mu}$ by ρ when needed. The derivation of the pushforward map $(\Phi_*)_x$ follows from the rate of change of $\alpha = \rho\tilde{v}$

$$\dot{\alpha} = \dot{\rho}\tilde{v} + \rho\dot{\tilde{v}} \implies \dot{\tilde{v}} = \frac{\dot{\alpha} - \dot{\rho}\tilde{v}}{\rho} = \frac{\dot{\alpha} - (*\dot{\mu})\tilde{v}}{*\tilde{\mu}}, \quad (5.90)$$

where $\dot{\rho}$ is the density of the top-form $\dot{\mu} = \dot{\tilde{\mu}}$. This concludes the proof of (5.87).

The pullback map $(\Phi^*)_x$ is defined implicitly by

$$\langle (\dot{\alpha}, \dot{\mu}) | (\Phi^*)_x(e_{\tilde{v}}, e_{\tilde{\mu}}) \rangle_s = \langle (\Phi^*)_x(\dot{\alpha}, \dot{\mu}) | (e_{\tilde{v}}, e_{\tilde{\mu}}) \rangle_s = \langle (\dot{\tilde{v}}, \dot{\tilde{\mu}}) | (e_{\tilde{v}}, e_{\tilde{\mu}}) \rangle_s.$$

Using the duality pairing definition (5.52), we have that

$$\begin{aligned} \langle (\dot{\alpha}, \dot{\mu}) | (e_{\alpha}, e_{\mu}) \rangle_s &= \int_M \dot{\tilde{v}} \wedge e_{\tilde{v}} + \dot{\tilde{\mu}} \wedge e_{\tilde{\mu}} = \int_M \left(\frac{\dot{\alpha} - (*\dot{\mu})\tilde{v}}{\rho} \right) \wedge e_{\tilde{v}} + \dot{\mu} \wedge e_{\tilde{\mu}} \\ &= \int_M \frac{\dot{\alpha}}{\rho} \wedge e_{\tilde{v}} - *\dot{\mu} \frac{\tilde{v}}{\rho} \wedge e_{\tilde{v}} + \dot{\mu} \wedge e_{\tilde{\mu}} \\ &= \int_M \dot{\alpha} \wedge \frac{e_{\tilde{v}}}{\rho} - *\dot{\mu} \wedge \frac{\tilde{v} \wedge e_{\tilde{v}}}{\rho} + \dot{\mu} \wedge e_{\tilde{\mu}} \\ &= \int_M \dot{\alpha} \wedge \frac{e_{\tilde{v}}}{\rho} - \dot{\mu} \wedge \frac{*(\tilde{v} \wedge e_{\tilde{v}})}{\rho} + \dot{\mu} \wedge e_{\tilde{\mu}} \\ &= \left\langle (\dot{\alpha}, \dot{\mu}) \left| \left(\frac{e_{\tilde{v}}}{\rho}, e_{\tilde{\mu}} - \frac{*(\tilde{v} \wedge e_{\tilde{v}})}{\rho} \right) \right|_s \right\rangle, \end{aligned}$$

which concludes the proof of (5.88).

Finally the proof of the Lie-Poisson structure (5.86) is as follows. Let (e_α, e_μ) be given by (5.88). Then using (5.73) one has that

$$\begin{pmatrix} \dot{\alpha} \\ \dot{\mu} \end{pmatrix} = J_x(e_\alpha, e_\mu) = \begin{pmatrix} -\mathcal{L}_{X_{\tilde{v}}}(\alpha) - \operatorname{div}(X_{\tilde{v}})\alpha - \rho d(e_{\tilde{\mu}} - \frac{*(\tilde{v} \wedge e_{\tilde{v}})}{\rho}) \\ -d(\rho \frac{e_{\tilde{v}}}{\rho}) \end{pmatrix}, \quad (5.91)$$

where $X_{\tilde{v}} := (\frac{e_{\tilde{v}}}{\rho})^\wedge$ is the vector field corresponding to the $n-1$ form $\frac{e_{\tilde{v}}}{\rho} = e_\alpha$ which is defined such that $\iota_{X_{\tilde{v}}} \mu_{\text{vol}} = \frac{e_{\tilde{v}}}{\rho} = *\tilde{X}_{\tilde{v}}$.

The first row in (5.91) could be massaged as follows

$$\begin{aligned} \dot{\alpha} &= -\mathcal{L}_{X_{\tilde{v}}}(\rho \tilde{v}) - \operatorname{div}(X_{\tilde{v}})\rho \tilde{v} - \rho d e_{\tilde{\mu}} + \rho d * (\tilde{v} \wedge \frac{e_{\tilde{v}}}{\rho}) \\ &= -\rho \mathcal{L}_{X_{\tilde{v}}} \tilde{v} - \mathcal{L}_{X_{\tilde{v}}}(\rho) \tilde{v} - \operatorname{div}(X_{\tilde{v}})\rho \tilde{v} - \rho d e_{\tilde{\mu}} + \rho d * (\tilde{v} \wedge *\tilde{X}_{\tilde{v}}) \\ &= -\rho d \iota_{X_{\tilde{v}}} \tilde{v} - \rho \iota_{X_{\tilde{v}}} d \tilde{v} - (\mathcal{L}_{X_{\tilde{v}}} \rho + \operatorname{div}(X_{\tilde{v}})\rho) \tilde{v} - \rho d e_{\tilde{\mu}} + \rho d * (\tilde{X}_{\tilde{v}} \wedge *\tilde{v}) \\ &= -\rho \iota_{X_{\tilde{v}}} d \tilde{v} - (\mathcal{L}_{X_{\tilde{v}}} \rho + \operatorname{div}(X_{\tilde{v}})\rho) \tilde{v} - \rho d e_{\tilde{\mu}}, \end{aligned} \quad (5.92)$$

where the Leibniz rule for the Lie derivative and Cartan's homotopy formula were used, and the last equality follows from $-\iota_{X_{\tilde{v}}} \tilde{v} + *(\tilde{X}_{\tilde{v}} \wedge *\tilde{v}) = -\iota_{X_{\tilde{v}}} \tilde{v} + \iota_{X_{\tilde{v}}} \tilde{v} = 0$, using identity (5.12). The second row in (5.91), and consequently the second row in (5.89), can be written simply as

$$\dot{\mu} = -d e_{\tilde{v}} = \dot{\tilde{\mu}}. \quad (5.93)$$

By substituting the expressions (5.92) in the expression of $\dot{\tilde{v}}$ in (5.87), we have that

$$\dot{\tilde{v}} = \frac{1}{\rho}(\dot{\alpha} - \rho \tilde{v}) = -\iota_{X_{\tilde{v}}} d \tilde{v} - \underbrace{\frac{1}{\rho}(\dot{\rho} + \mathcal{L}_{X_{\tilde{v}}} \rho + \operatorname{div}(X_{\tilde{v}})\rho)}_{=0} \tilde{v} - d e_{\tilde{\mu}} = -\iota_{X_{\tilde{v}}} d \tilde{v} - d e_{\tilde{\mu}},$$

where the term in the parenthesis vanishes as a consequence of the mass continuity equation (5.31). Thus, finally using $\iota_{X_{\tilde{v}}} d \tilde{v} = \iota_{(\frac{e_{\tilde{v}}}{\rho})^\wedge} d \tilde{v} = \frac{1}{\rho} \iota_{\tilde{e}_{\tilde{v}}} d \tilde{v}$, the proof of (5.89) is concluded. \blacksquare

In terms of the new energy variables, the kinetic energy Hamiltonian functional and its variational derivatives are given by the following result.

Proposition 5.3.5. *The kinetic energy Hamiltonian given by (5.60) in terms of the velocity 1-form \tilde{v} and the mass top-form μ is given by*

$$H_k(\tilde{v}, \mu) = \int_M \frac{1}{2} (*\mu) \tilde{v} \wedge *\tilde{v}. \quad (5.94)$$

The variational derivatives $\delta_{\tilde{v}} H_k \in T_{\tilde{v}}^* \mathfrak{g}^* \cong \mathfrak{g} = \Omega^{n-1}(M)$ and $\delta_\mu H_k \in T_\mu^* V^* \cong V = \Omega^0(M)$ with respect to the states $\tilde{v} \in \mathfrak{g}^*$ and $\mu \in V^*$, respectively, are given by

$$\delta_{\tilde{v}} H_k = (*\mu) * \tilde{v} = \iota_v \mu, \quad \delta_\mu H_k = \frac{1}{2} \iota_v \tilde{v}, \quad (5.95)$$

Proof. The new functional $\tilde{H}_k(\tilde{v}, \mu)$ is defined by $\tilde{H}_k = H_k \circ \Phi^{-1}$. By substituting $\Phi^{-1}(\tilde{v}, \mu) = ((*\tilde{\mu})\tilde{v}, \mu)$ in (5.60) as

$$\tilde{H}_k(\tilde{v}, \mu) = H_k(\Phi^{-1}(\tilde{v}, \mu)) = \int_M \frac{1}{2(*\mu)} (*\mu)\tilde{v} \wedge (*\mu)\tilde{v} = \int_M \frac{1}{2}(*\mu)\tilde{v} \wedge *\tilde{v}.$$

For notational simplicity, we drop the *tilde* from the mass form $\mu = \tilde{\mu} \in V^*$ as well as the tilde over the new energy functional and denote it by $H_k(\tilde{v}, \mu)$.

The variational derivative of H_k with respect to $\tilde{v} \in \mathfrak{g}^*$ can be found out by rewriting (5.94) as

$$H_k(\tilde{v}, \mu) = \int_M \frac{1}{2}\tilde{v} \wedge ((*\mu) * \tilde{v}),$$

where we have that $\delta_{\tilde{v}}H_k = (*\mu) * \tilde{v}$ from the fact that H_k is quadratic in \tilde{v} . Furthermore, we can express $\delta_{\tilde{v}}H_k$ as

$$\delta_{\tilde{v}}H_k = (*\mu) * \tilde{v} = (*\mu)\iota_v\mu_{\text{vol}} = \iota_v(*\mu\mu_{\text{vol}}) = \iota_v\mu.$$

Similarly, the variational derivative of H_k with respect to $\mu \in V^*$ can be found out by rewriting (5.94) as

$$H_k(\tilde{v}, \mu) = \int_M \frac{1}{2}(*\mu) \wedge (\tilde{v} \wedge *\tilde{v}) = \int_M \mu \wedge \frac{1}{2} * (\tilde{v} \wedge *\tilde{v}),$$

where an immediate consequence of the definition of the variational derivative is that

$$\delta_{\mu}H_k = \frac{1}{2} * (\tilde{v} \wedge *\tilde{v}).$$

Using identity (5.12) allows one to write $\delta_{\mu}H_k$ as in (5.95), which concludes the proof. \blacksquare

The new energy balance for the kinetic energy Hamiltonian (5.94) instead of (5.80) can be now calculated using the pullback map $(\Phi^*)_x$ in (5.88) as follows.

Theorem 5.3.6. *The rate of change of the kinetic energy Hamiltonian (5.94) in terms of the new state variables (\tilde{v}, μ) is given by*

$$\dot{H}_k = \int_{\partial M} e_{\partial k} \wedge f_{\partial k} + \int_M e_d \wedge f_d, \quad (5.96)$$

where the boundary port variables $e_{\partial k}, f_{\partial k} \in \Omega^0(\partial M) \times \Omega^{n-1}(\partial M)$ and the distributed port variables $(e_d, f_d) \in \Omega^1(M) \times \Omega^{n-1}(M)$ are expressed using the new coordinates (\tilde{v}, μ) by

$$\begin{aligned} e_{\partial k} &= \delta_{\mu}H_k|_{\partial M} = \frac{1}{2}\iota_v\tilde{v}|_{\partial M}, & e_d &= \mathbf{f}_s, \\ f_{\partial k} &= -\delta_{\tilde{v}}H_k|_{\partial M} = -\iota_v\mu|_{\partial M}, & f_d &= \frac{\delta_{\tilde{v}}H_k}{*\mu} = \omega_v, \end{aligned}$$

where the variational derivatives of H_k in (5.94) are given by (5.95), and $\omega_v = \iota_v \mu_{\text{vol}} \in \Omega^{n-1}(M)$.

Proof. In this proof we denote by $(e_\alpha, e_\mu) = (\delta_\alpha H_k, \delta_\mu H_k)$ and by $(e_{\tilde{v}}, e_{\tilde{\mu}}) = (\delta_{\tilde{v}} H_k, \delta_{\tilde{\mu}} H_k)$. By substituting (e_α, e_μ) defined by (5.88) and $(\alpha, \mu) = (*\mu\tilde{v}, \mu)$ in the energy balance expression in terms of (α, μ) given by (5.81)

$$\begin{aligned} \dot{H}_k &= \int_{\partial M} \left(\frac{\iota_{X_\alpha}(\alpha)}{* \mu} + e_\mu \right) |_{\partial M} \wedge -(*\mu)e_\alpha|_{\partial M} + \int_M \mathbf{f}_s \wedge e_\alpha, \\ &= \int_{\partial M} \left(\iota_{X_\alpha}(\tilde{v}) + e_{\tilde{\mu}} - \frac{*(\tilde{v} \wedge e_{\tilde{v}})}{* \mu} \right) |_{\partial M} \wedge -e_{\tilde{v}}|_{\partial M} + \int_M \mathbf{f}_s \wedge \frac{e_{\tilde{v}}}{* \mu}, \end{aligned}$$

where X_α is defined such that $\iota_{X_\alpha} \mu_{\text{vol}} = e_\alpha = \frac{e_{\tilde{v}}}{* \mu}$. Consequently, we have that $\frac{e_{\tilde{v}}}{* \mu} = *\tilde{X}_\alpha$. The term $\frac{*(\tilde{v} \wedge e_{\tilde{v}})}{* \mu}$ can be rewritten using identity (5.12) as

$$\frac{*(\tilde{v} \wedge e_{\tilde{v}})}{* \mu} = *(\tilde{v} \wedge \frac{e_{\tilde{v}}}{* \mu}) = *(\tilde{v} \wedge *\tilde{X}_\alpha) = *(\tilde{X}_\alpha \wedge *\tilde{v}) = \iota_{X_\alpha} \tilde{v}.$$

Therefore, we have that

$$\begin{aligned} \dot{H}_k &= \int_{\partial M} \left(\iota_{X_\alpha}(\tilde{v}) + e_{\tilde{\mu}} - \frac{*(\tilde{v} \wedge e_{\tilde{v}})}{* \mu} \right) |_{\partial M} \wedge -e_{\tilde{v}}|_{\partial M} + \int_M \mathbf{f}_s \wedge \frac{e_{\tilde{v}}}{* \mu}, \\ &= \int_{\partial M} e_{\tilde{\mu}} |_{\partial M} \wedge -e_{\tilde{v}}|_{\partial M} + \int_M \mathbf{f}_s \wedge \frac{e_{\tilde{v}}}{* \mu}. \end{aligned}$$

Therefore, $e_{\tilde{v}} = \delta_{\tilde{v}} H_k$ and $e_{\tilde{\mu}} = \delta_{\tilde{\mu}} H_k$ are given in (5.95) (where $\tilde{\mu} = \mu$ is used). Moreover, the term $\frac{e_{\tilde{v}}}{* \mu}$ could be rewritten using (5.95) as

$$\frac{e_{\tilde{v}}}{* \mu} = \frac{\delta_{\tilde{v}} H_k}{* \mu} = \frac{1}{* \mu} \iota_v \mu = \iota_v \left(\frac{\mu}{* \mu} \right) = \iota_v \mu_{\text{vol}},$$

which concludes the proof. ■

As mentioned before, the boundary flow variable $f_{\partial k}$ is physically the incoming mass flow through the boundary. On the other hand, the boundary effort variable $e_{\partial k}$ is physically the dynamic pressure (modulo the density) which is the only pressure that exists related to the kinetic energy of the fluid since we have not modeled yet any thermodynamic potential.

The new Stokes-Dirac structure $\tilde{\mathcal{D}}_k$ in terms of the state variables (\tilde{v}, μ) can now be constructed using the velocity representation of the Lie-Poisson structure (5.89) and the definitions of the boundary and distributed port variables

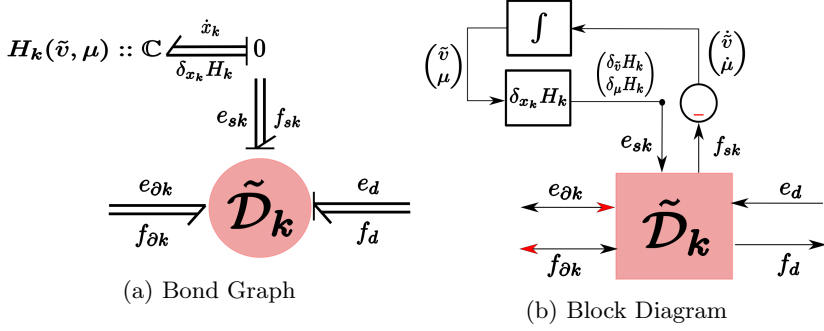


Figure 5.10: Graphical Representation of the Kinetic Energy Subsystem (5.98) in terms of the state variables: velocity one-form \tilde{v} and the mass top-form μ .

in Theorem 5.3.6. The expression for $\tilde{\mathcal{D}}_k$ is given by

$$\begin{aligned}
 \tilde{\mathcal{D}}_k &= \{(f_{sk}, f_{\partial k}, f_d, e_{sk}, e_{\partial k}, e_d) \in \mathcal{B}_k | \\
 &\quad \begin{pmatrix} f_{\tilde{v}} \\ f_{\mu} \end{pmatrix} = \begin{pmatrix} de_{\mu} + \frac{1}{*\mu} \iota_{\tilde{e}_{\tilde{v}}} d\tilde{v} \\ de_{\tilde{v}} \end{pmatrix} - \begin{pmatrix} \frac{1}{*\mu} \\ 0 \end{pmatrix} e_d, \\
 &\quad f_d = \begin{pmatrix} \frac{1}{*\mu} & 0 \end{pmatrix} \begin{pmatrix} e_{\tilde{v}} \\ e_{\mu} \end{pmatrix}, \\
 &\quad \begin{pmatrix} e_{\partial k} \\ f_{\partial k} \end{pmatrix} = \begin{pmatrix} 0 & 1 \\ -1 & 0 \end{pmatrix} \begin{pmatrix} e_{\tilde{v}}|_{\partial M} \\ e_{\mu}|_{\partial M} \end{pmatrix} \},
 \end{aligned} \tag{5.97}$$

where the storage port variables are now given by $f_{sk} = (f_{\tilde{v}}, f_{\mu}) \in \mathfrak{s}^* = \Omega^1(M) \times \Omega^n(M)$ and $e_{sk} = (e_{\tilde{v}}, e_{\mu}) \in \mathfrak{s} = \Omega^{n-1}(M) \times \Omega^0(M)$. The bond-space \mathcal{B}_k is the same as the one defined before for \mathcal{D}_k in (5.82).

By excluding the distributed port (e_d, f_d) , the Stokes-Dirac structure (5.97) coincides with the one postulated in [van der Schaft and Maschke, 2002] for an ideal fluid and considered as an extended version of with respect to the one containing only exterior derivative operators.

To summarize, the explicit port-Hamiltonian dynamical model in terms of the kinetic energy state variable $x_k := \tilde{x} = (\tilde{v}, \mu) \in \mathcal{X} = \mathfrak{s}^*$ is given by

$$\begin{pmatrix} \dot{\tilde{v}} \\ \dot{\mu} \end{pmatrix} = \begin{pmatrix} -d(\delta_{\mu} H_k) - \iota_{\tilde{v}} d\tilde{v} \\ -d(\delta_{\tilde{v}} H_k) \end{pmatrix} + \begin{pmatrix} \frac{1}{*\mu} \\ 0 \end{pmatrix} \mathfrak{f}_s, \tag{5.98}$$

$$\omega_v = \begin{pmatrix} \frac{1}{*\mu} & 0 \end{pmatrix} \begin{pmatrix} \delta_{\tilde{v}} H_k \\ \delta_{\mu} H_k \end{pmatrix}, \tag{5.99}$$

$$H_k(x_k) = H_k(\tilde{v}, \mu) = \int_M \frac{1}{2} (*\mu) \tilde{v} \wedge *\tilde{v}, \tag{5.100}$$

where the variational derivatives are given by Prop. 5.3.5. The term $\iota_v d\tilde{v}$ is equivalent to $\frac{1}{*\mu} \iota_{\hat{e}_{\tilde{v}}} d\tilde{v} = \iota_{(\hat{e}_{\tilde{v}}/*\mu)} d\tilde{v}$ in (5.89), which follows from

$$\frac{\hat{e}_{\tilde{v}}}{*\mu} = \frac{(\delta_{\tilde{v}} H_k)^\wedge}{*\mu} = \frac{(*\mu * \tilde{v})^\wedge}{*\mu} = (*\tilde{v})^\wedge = v.$$

Moreover, the port-Hamiltonian dynamics (5.98-5.100) are recovered from the Dirac structure $\tilde{\mathcal{D}}_k$ in (5.97) by

$$((-\dot{\tilde{v}}, -\dot{\mu}), f_{\partial k}, \omega_v, (\delta_{\tilde{v}} H_k, \delta_\mu H_k), e_{\partial k}, f_s) \in \tilde{\mathcal{D}}_k. \quad (5.101)$$

The graphical representation of the kinetic energy port-Hamiltonian system (5.98-5.100) is shown in Fig. 5.10.

This concludes the port-Hamiltonian modeling procedure of the kinetic energy subsystem. In the coming sections, we show how to utilize the distributed stress forces for modeling internal energy to represent compressible flow, and modeling constraint forces to represent incompressible flow.

5.4 Port-Hamiltonian Modeling of Compressible Flow

The distributed force f_s present in the model (5.98) originates physically from the random motion and collisions of the molecules that comprise the fluid. The force f_s is defined through averaging the momentum transfer of a large group of molecules over a short time scale, compared to the macroscopic motion of the fluid encoded by the vector field v . Thus, the transfer of momentum on the microscopic scale is equivalent to the continuous force f_s acting at each point in the spatial domain M at the macroscopic scale.

There are two types of basic forces due to the microscopic motion of the fluid; pressure forces and viscous friction forces. Both pressure and viscous forces are *forces of stress*. In this work, we will consider ideal flow, and thus model pressure forces only, while modeling the viscous forces is an issue of future work.

The molecular kinetic and vibration energy is encoded, at the macroscopic scale, as a continuous function $\tilde{U} := \rho U \in C^\infty(M)$, called the internal energy density, where ρ is the mass density function, and U is the specific internal energy (i.e. per unit mass). The first law of thermodynamics states that the internal energy \tilde{U} is conserved only if the system is isolated, i.e. does not interact with its surrounding. The internal energy of a system changes if there is transfer of mass and heat to or from the system, and by work done on or by the system.

The specific internal energy $U(\nu, s)$ depends on the fluid's specific volume $\nu = 1/\rho \in C^\infty(M)$ and the fluid's specific entropy $s \in C^\infty(M)$. The differential

of the internal energy $dU \in \Omega^1(M)$ is given by the famous Gibbs equation

$$dU(\nu, s) = -p d\nu + T ds, \quad (5.102)$$

where $T ds$ corresponds to the heat exchanged per unit mass, and $p d\nu$ corresponds to the mechanical work done by the fluid system due to pressure forces. Note that from (5.102) we have that

$$\frac{\partial U}{\partial \nu} = -p, \quad \frac{\partial U}{\partial s} = T, \quad (5.103)$$

are the components of the one-form dU .

A more convenient form of Gibbs equation is given by

$$dU(\rho, s) = \frac{p}{\rho^2} d\rho + T ds, \quad (5.104)$$

which follows from the chain rule $\frac{\partial U}{\partial \rho} = \frac{\partial U}{\partial \nu} \frac{\partial \nu}{\partial \rho} = p/\rho^2$. The relation between the pressure p , specific internal energy U and the mass density, given by

$$p = \rho^2 \frac{\partial U}{\partial \rho}, \quad (5.105)$$

is known as the *equation of state* of the fluid, which should be specified for a choice of fluid.

Another useful thermodynamic variable is the specific enthalpy $h \in C^\infty(M)$, related to the internal energy by the Legendre transformation. The enthalpy can be expressed as

$$h = U + \frac{p}{\rho} = U + \rho \frac{\partial U}{\partial \rho} = \frac{\partial}{\partial \rho}(\rho U), \quad (5.106)$$

where the second equality follows from (5.105), while the last equality follows from the chain rule. In terms of the enthalpy, the Gibbs equation becomes

$$dh = dU + d\left(\frac{p}{\rho}\right) = dU + d(p\nu) = -p d\nu + T ds + dp\nu + p d\nu = dp\nu + T ds,$$

thus we have that

$$dh(\rho, s) = \frac{dp}{\rho} + T ds. \quad (5.107)$$

In the case of isentropic flow, one has that the entropy s is constant in space throughout the fluid for all time, and thus $ds = 0$. In this case, the specific internal energy $U(\rho)$ depends on the density ρ only, and thus the two forms of Gibbs equations (5.102) and (5.107) become

$$dU(\rho) = \frac{p}{\rho^2} d\rho, \quad dh(\rho) = \frac{dp}{\rho}. \quad (5.108)$$

Next, we show how to systematically represent the pressure forces using the distributed force f_s in (5.98) acting on an infinitesimal fluid element at a point in M . For ease of presentation, we first consider the case of isentropic flow, followed by the slightly more general case of adiabatic flow, describing a fluid with no irreversible thermodynamic phenomena, but in which the advected entropy function s_t , might not be constant in space.

5.4.1 Isentropic Compressible Flow

In the port-Hamiltonian system (5.98) in which only kinetic energy is present, the distributed port (e_d, f_d) could be used to add storage of internal energy of the fluid. The storage of the fluid's total internal energy $H_i(\mu)$ is represented by a storage element with state manifold $\mathcal{X}_i = V^* = \Omega^n(M)$ and its corresponding state variable $x_i = \mu$ being the mass form. The internal energy Hamiltonian $H_i : \mathcal{X}_i \rightarrow \mathbb{R}$ is given by

$$H_i(\mu) = \int_M U(*\mu)\mu, \quad (5.109)$$

where $U(*\mu) = U(\rho)$ is the specific internal energy introduced earlier.

The effort and flow variables of the internal energy storage element are given by

$$\delta_\mu H_i \in T_{x_i}^* \mathcal{X}_i \cong V = \Omega^0(M), \quad \dot{\mu} \in T_{x_i} \mathcal{X}_i \cong V^* = \Omega^n(M), \quad (5.110)$$

where $\delta_\mu H_i$ is given by the following result.

Proposition 5.4.1. *The variational derivative of the Hamiltonian functional $H_i : V^* \rightarrow \mathbb{R}$ in (5.109) with respect to $\mu \in V^* = \Omega^n(M)$, denoted by $\delta_\mu H_i \in V = \Omega^0(M)$, is equal to the enthalpy function (5.106):*

$$\delta_\mu H_i = h \in C^\infty(M). \quad (5.111)$$

Proof. The variational derivative $\delta_\mu H_i \in C^\infty(M)$ is defined implicitly as the function satisfying

$$\langle \delta_\mu H_i | \delta\mu \rangle_{V^*} = \left. \frac{d}{d\epsilon} \right|_{\epsilon=0} H_i(\mu + \epsilon\delta\mu), \quad (5.112)$$

for any $\epsilon \in \mathbb{R}$ and $\delta\mu \in \Omega^n(M)$. For notational simplicity, we introduce $\mu_\epsilon := \mu + \epsilon\delta\mu \in \Omega^n(M)$, $\rho := *\mu \in C^\infty(M)$, and $\delta\rho := *\delta\mu \in C^\infty(M)$. Consequently, we have that $\rho_\epsilon := \rho + \epsilon\delta\rho = *\mu_\epsilon$, as well as

$$\left. \frac{d}{d\epsilon} \right|_{\epsilon=0} \mu_\epsilon = \delta\mu. \quad (5.113)$$

Using (5.109), (5.113), and the Leibniz rule, we can rewrite (5.112) as

$$\begin{aligned}
 \int_M \delta_\mu H_i \wedge \delta\mu &= \int_M \frac{d}{d\epsilon} \Big|_{\epsilon=0} (U(*\mu_\epsilon) \wedge \mu_\epsilon), \\
 &= \int_M \frac{d}{d\epsilon} \Big|_{\epsilon=0} U(*\mu_\epsilon) \wedge \mu_\epsilon + U(*\mu_\epsilon) \wedge \frac{d}{d\epsilon} \Big|_{\epsilon=0} \mu_\epsilon, \\
 &= \int_M \frac{d}{d\epsilon} \Big|_{\epsilon=0} U(*\mu_\epsilon) \wedge \mu_\epsilon + U(*\mu) \wedge \delta\mu. \tag{5.114}
 \end{aligned}$$

Since $U : C^\infty(M) \rightarrow C^\infty(M)$ is a function on $C^\infty(M)$, its derivative $\frac{dU}{d\rho}(\rho) \in C^\infty(M)$ is defined implicitly as the function satisfying

$$\frac{dU}{d\rho}(\rho) \cdot \delta\rho = \frac{d}{d\epsilon} \Big|_{\epsilon=0} U(\rho_\epsilon). \tag{5.115}$$

By substituting (5.115) into (5.114), we get

$$\int_M \delta_\mu H_i \wedge \delta\mu = \int_M \frac{dU}{d\rho}(\rho) \cdot \delta\rho \wedge \mu + U(\rho) \wedge \delta\mu. \tag{5.116}$$

Using the equality $\delta\rho \wedge \mu = \delta\rho \cdot \rho \wedge \mu_{\text{vol}} = \rho \cdot \delta\rho \wedge \mu_{\text{vol}} = \rho \cdot \wedge \delta\mu$, we can rewrite (5.116) as

$$\int_M \delta_\mu H_i \wedge \delta\mu = \int_M \left(\frac{dU}{d\rho}(\rho) \cdot \rho + U(\rho) \right) \wedge \delta\mu. \tag{5.117}$$

Therefore, using the chain rule, we have that

$$\delta_\mu H_i = \frac{dU}{d\rho}(\rho) \cdot \rho + U(\rho) = \frac{d}{d\rho}(\rho \cdot U(\rho)), \tag{5.118}$$

which is equal to the enthalpy as defined by (5.106). Note that in case U is a multi-variable function of ρ , the derivative $\frac{dU}{d\rho}$ in this proof is replaced by a partial derivative. ■

The Hamiltonian H_i satisfies the power balance

$$\dot{H}_i = \langle \delta_\mu H_i | \dot{\mu} \rangle_{V^*}. \tag{5.119}$$

Since the flow does not exchange heat with its surrounding, any change in the internal energy of the system is caused by the transformation of kinetic energy (if we assume there is no mass-flow through the boundary). The power incoming the internal energy storage element $\langle \delta_\mu H_i | \dot{\mu} \rangle_{V^*}$ is then equal to the power outcoming the distributed port of the kinetic energy subsystem, i.e.

$$\langle \delta_\mu H_i | \dot{\mu} \rangle_{V^*} = - \langle e_d | f_d \rangle_{\mathfrak{g}} = \langle f_s | -\omega_v \rangle_{\mathfrak{g}}, \tag{5.120}$$

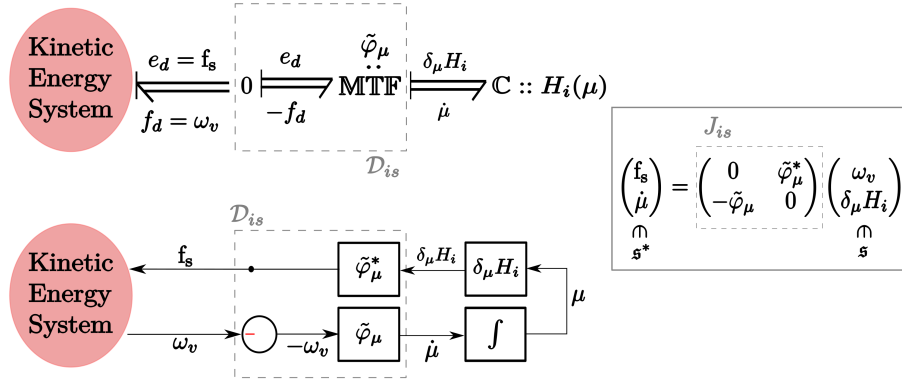


Figure 5.11: Augmenting the kinetic energy system (5.98) with the storage of internal energy through the distributed port (e_d, f_d) . The model corresponds to isentropic compressible flow on a manifold without boundary. The Bond graph (top) and block diagram (bottom) representations are shown.

as shown in Fig. 5.11.

However, to interconnect the internal energy storage port to the kinetic energy distributed port they should be compatible. Their incompatibility lies in the fact that $(\delta_\mu H_i, \dot{\mu}) \in V \times V^*$ while $(e_d, f_d) \in \mathfrak{g} \times \mathfrak{g}^*$ by their definitions. The key to connecting these two ports is related to the semi-direct product structure of \mathfrak{g} and V , and more precisely the interconnection maps introduced earlier in Sec. 5.2.2. For simplicity, we first introduce the idea of interconnecting the two ports assuming M has no boundary, then we consider the general case with the boundary port variables.

The two ports are made compatible by the use of a power-conserving transformation that relates the efforts of the two ports to each other, and relates the flows of the two ports to each other. In the bond graph in Fig. 5.11, the modulated transformer element MTF implements the map

$$\begin{pmatrix} e_d \\ \dot{\mu} \end{pmatrix} = \begin{pmatrix} 0 & \tilde{\varphi}_\mu^* \\ \tilde{\varphi}_\mu & 0 \end{pmatrix} \begin{pmatrix} -f_d \\ \delta_\mu H_i \end{pmatrix}, \quad (5.121)$$

where the map $\tilde{\varphi}_\mu : \mathfrak{g} \rightarrow V^*$ and its dual $\tilde{\varphi}_\mu^* : V \rightarrow \mathfrak{g}^*$ are given in Table 1 for μ as the advected parameter (i.e, $a = \mu \in V^*$). The minus sign next to f_d in (5.121) is due to the zero junction in Fig. 5.11, used to represent the power inversion (from inflow to outflow) given by

$$\langle e_d | f_d \rangle_{\mathfrak{g}} = -\langle e_d | -f_d \rangle_{\mathfrak{g}}. \quad (5.122)$$

Both the zero-junction and the MTF combined represent a power-conserving Dirac structure \mathcal{D}_{is} , given by the relation corresponding to the map $J_{is} : \mathfrak{s} \rightarrow$

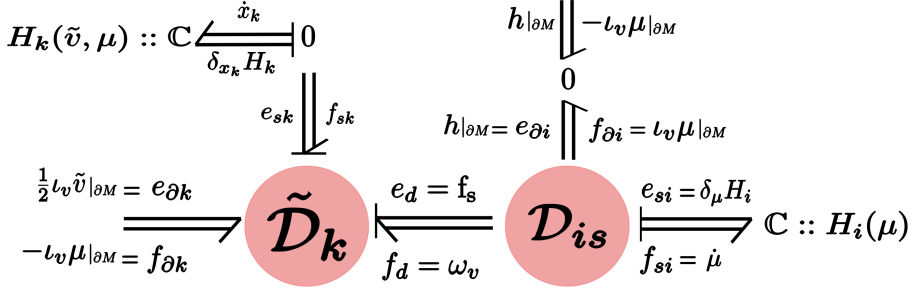


Figure 5.12: Augmenting the kinetic energy system (5.98) with the storage of internal energy through the distributed port (e_d, f_d) . The model corresponds to compressible isentropic flow on a general manifold with permeable boundary.

\mathfrak{s}^* , as illustrated in Fig. 5.11. The Dirac structure \mathcal{D}_{is} is modulated by the mass form μ (as a state of advected quantity), and its power-preserving property is clearly visible by the skew-symmetry of the map J_{is} .

Now we show that the previous energy-based construction correctly models compressible isentropic flow. Consider the following equalities

$$\langle f_s | -\omega_v \rangle_{\mathfrak{g}} = \langle \tilde{\varphi}_\mu^*(\delta_\mu H_i) | -\omega_v \rangle_{\mathfrak{g}} = \langle \delta_\mu H_i | \tilde{\varphi}_\mu(-\omega_v) \rangle_{V^*} = \langle \delta_\mu H_i | \dot{\mu} \rangle_{V^*} = \dot{H}_i, \quad (5.123)$$

which follows using (5.121) and the port variables definitions. Therefore, using the expressions of $\tilde{\varphi}_\mu$ and $\tilde{\varphi}_\mu^*$ in Table 5.2, we have that

$$\dot{\mu} = \tilde{\varphi}_\mu(-\omega_v) = -\tilde{\varphi}_\mu(\omega_v) = -\mathcal{L}_{\tilde{\omega}_v} \mu = -\mathcal{L}_v \mu, \quad (5.124)$$

$$f_s = \tilde{\varphi}_\mu^*(\delta_\mu H_i) = -(*\mu)d(\delta_\mu H_i) = -(*\mu)dh = -dp. \quad (5.125)$$

Therefore, (5.124) correctly represents the evolution of μ as being advected with the flow, while (5.125) correctly represents the stress forces due to pressure applied within M [Abraham et al., 1988, pg. 588].

Now in case M has a permeable boundary, the pairing equality (5.123) is no longer valid and should be augmented with a surface term $\eta_{\tilde{\varphi}_\mu}$ from (5.42). In this case, using the expression of $\eta_{\tilde{\varphi}_\mu}$ in Table 5.2, (5.123) is rewritten as

$$\begin{aligned} \langle f_s | -\omega_v \rangle_{\mathfrak{g}} &= \langle \tilde{\varphi}_\mu^*(\delta_\mu H_i) | -\omega_v \rangle_{\mathfrak{g}} \\ &= \langle \delta_\mu H_i | \tilde{\varphi}_\mu(-\omega_v) \rangle_{V^*} + \int_{\partial M} -(*\mu)(-\omega_v)|_{\partial M} \wedge \delta_\mu H_i|_{\partial M} \\ &= \langle \delta_\mu H_i | \dot{\mu} \rangle_{V^*} + \int_{\partial M} h|_{\partial M} \wedge (*\mu)\omega_v|_{\partial M} \\ &= \dot{H}_i + \int_{\partial M} h|_{\partial M} \wedge \iota_v \mu|_{\partial M}. \end{aligned} \quad (5.126)$$

By defining the boundary port variables $e_{\partial i} := h|_{\partial M} = \delta_\mu H_i|_{\partial M}$ and $f_{\partial i} := \iota_v \mu|_{\partial M}$, the pairing equality (5.126) becomes

$$\langle f_s | \omega_v \rangle_{\mathfrak{g}} + \dot{H}_i + \int_{\partial M} e_{\partial i} \wedge f_{\partial i} = 0. \quad (5.127)$$

Therefore, as shown in Fig. 5.12, the interconnection to model isentropic flow is achieved by the Dirac structure \mathcal{D}_{is} given by

$$\begin{aligned} \mathcal{D}_{is} = \{ & (f_{si}, f_{\partial i}, f_d, e_{si}, e_{\partial i}, e_d) \in \mathcal{B}_{is} | \\ & \begin{pmatrix} e_d \\ f_{si} \end{pmatrix} = \begin{pmatrix} 0 & \tilde{\varphi}_\mu^* \\ -\tilde{\varphi}_\mu & 0 \end{pmatrix} \begin{pmatrix} f_d \\ e_{si} \end{pmatrix}, \\ & \begin{pmatrix} e_{\partial i} \\ f_{\partial i} \end{pmatrix} = \begin{pmatrix} 1 & 0 \\ 0 & *\mu|_{\partial M} \end{pmatrix} \begin{pmatrix} e_{si}|_{\partial M} \\ f_d|_{\partial M} \end{pmatrix} \}, \end{aligned} \quad (5.128)$$

where the bond-space $\mathcal{B}_{is} = \mathcal{F}_{is} \times \mathcal{E}_{is}$ is the product space of the flow space $\mathcal{F}_{is} = \Omega^n(M) \times \Omega^{n-1}(\partial M) \times \Omega^{n-1}(M)$ and the effort space $\mathcal{E}_{is} = \Omega^0(M) \times \Omega^0(\partial M) \times \Omega^1(M)$. The Dirac structure (5.128) is modulated by the mass form $\mu \in V^*$, and encodes the power balance

$$\langle e_d | f_d \rangle_{\mathfrak{g}} + \langle e_{si} | f_{si} \rangle_{V^*} + \int_{\partial M} e_{\partial i} \wedge f_{\partial i} = 0,$$

which is equivalent to (5.127) by setting the ports of \mathcal{D}_{is} by

$$(\dot{\mu}, \iota_v \mu|_{\partial M}, \omega_v, \delta_\mu H_i, h|_{\partial M}, f_s) \in \mathcal{D}_{is},$$

as illustrated in Fig. 5.12, and thus restoring (5.124) and (5.125).

In conclusion, the port-Hamiltonian model for compressible isentropic flow consists of two storage elements for kinetic and internal energy, two boundary ports $(e_{\partial k}, f_{\partial k})$ and $(e_{\partial i}, f_{\partial i})$ representing power through the boundary of M due to mass inflow, and all the remaining power conserving elements that allow the interconnection of the aforementioned ports, shown in Fig. 5.12.

It is interesting to combine all the energy storage elements into one as well as combine all the power conserving elements to a new Stokes Dirac structure $\mathcal{D}_{c,i}$, as shown in Fig. 5.13. The new storage element has its state variables $x_t = (\tilde{v}, \mu)$ and its Hamiltonian H_t given by the total energy of the system (the sum of kinetic and internal), i.e.,

$$H_t(\tilde{v}, \mu) = H_k(\tilde{v}, \mu) + H_i(\mu) = \int_M \frac{1}{2}(*\mu)\tilde{v} \wedge *\tilde{v} + U(*\mu)\mu, \quad (5.129)$$

with flow and effort variables

$$\dot{x}_t = \begin{pmatrix} \dot{\tilde{v}} \\ \dot{\mu} \end{pmatrix}, \quad \delta_{x_t} H_t = \begin{pmatrix} \delta_{\tilde{v}} H_t \\ \delta_\mu H_t \end{pmatrix} = \begin{pmatrix} \iota_v \mu \\ \frac{1}{2} \iota_v \tilde{v} + h \end{pmatrix}. \quad (5.130)$$

The new energy balance for H_t is given by the following result.

Proposition 5.4.2. *The rate of change of the total Hamiltonian H_t , given by (5.129), along trajectories of its state variables $x_t = (\tilde{v}, \mu)$ is expressed as*

$$\dot{H}_t = \int_{\partial M} e_{\partial} \wedge f_{\partial}, \quad (5.131)$$

where the new boundary port variables $(e_{\partial}, f_{\partial}) \in \Omega^0(\partial M) \times \Omega^{n-1}(\partial M)$ are defined by

$$e_{\partial} := \delta_{\mu} H_t|_{\partial M} = \left(\frac{1}{2} \iota_v \tilde{v} + h\right)|_{\partial M}, \quad f_{\partial} := -\delta_{\tilde{v}} H_t|_{\partial M} = -(\iota_v \mu)|_{\partial M}. \quad (5.132)$$

Proof. By starting from the energy balance for \dot{H}_k in (5.96) and using the equality (5.127), we have that

$$\begin{aligned} \dot{H}_k &= \int_{\partial M} e_{\partial k} \wedge f_{\partial k} + \int_M e_d \wedge f_d \\ &= \int_{\partial M} \frac{1}{2} \iota_v \tilde{v}|_{\partial M} \wedge -\iota_v \mu|_{\partial M} + \langle f_s | \omega_v \rangle_{\mathfrak{g}} \\ &= \int_{\partial M} \frac{1}{2} \iota_v \tilde{v}|_{\partial M} \wedge -\iota_v \mu|_{\partial M} - \langle \delta_{\mu} H_i | \dot{\mu} \rangle_{V^*} - \int_{\partial M} e_{\partial i} \wedge f_{\partial i} \\ &= \int_{\partial M} \frac{1}{2} \iota_v \tilde{v}|_{\partial M} \wedge -\iota_v \mu|_{\partial M} - \dot{H}_i - \int_{\partial M} h|_{\partial M} \wedge \iota_v \mu|_{\partial M} \\ &= \int_{\partial M} \left(\frac{1}{2} \iota_v \tilde{v} + h\right)|_{\partial M} \wedge -\iota_v \mu|_{\partial M} - \dot{H}_i. \end{aligned}$$

Thus, we have that

$$\dot{H}_t = \dot{H}_k + \dot{H}_i = \int_{\partial M} \left(\frac{1}{2} \iota_v \tilde{v} + h\right)|_{\partial M} \wedge -\iota_v \mu|_{\partial M},$$

which concludes the proof using (5.132). ■

Physically the boundary effort variable e_{∂} is known as the stagnation or total enthalpy at the boundary, while the boundary flow variable f_{∂} represents the mass inflow through the boundary. The power in the port $(e_{\partial}, f_{\partial})$ represent the energy change due to the exchange of mass flow between the isentropic compressible flow system and its surroundings.

The overall Stokes-Dirac structure $\mathcal{D}_{c,i}$ for isentropic compressible flow that implements the power balance in (5.131) is given by

$$\begin{aligned} \mathcal{D}_{c,i} &= \{(f_s, f_{\partial}, e_s, e_{\partial}) \in \mathcal{B}_{c,i} | \\ &\quad \begin{pmatrix} f_{\tilde{v}} \\ f_{\mu} \end{pmatrix} = \begin{pmatrix} de_{\mu} + \frac{1}{*\mu} \iota_{\hat{e}_{\tilde{v}}} d\tilde{v} \\ de_{\tilde{v}} \end{pmatrix}, \\ &\quad \begin{pmatrix} e_{\partial} \\ f_{\partial} \end{pmatrix} = \begin{pmatrix} 0 & 1 \\ -1 & 0 \end{pmatrix} \begin{pmatrix} e_{\tilde{v}}|_{\partial M} \\ e_{\mu}|_{\partial M} \end{pmatrix}\}, \end{aligned} \quad (5.133)$$

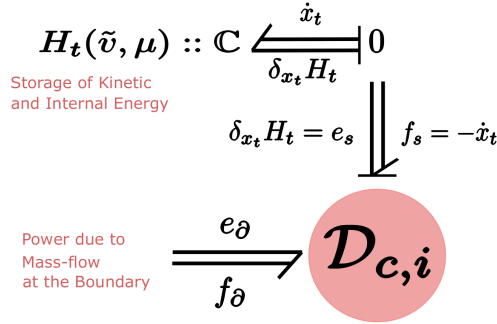


Figure 5.13: Port-based representation of Euler Equation (5.134) of compressible isentropic flow.

where the total storage port variables are given by $f_s = (f_{\tilde{v}}, f_\mu) \in \mathfrak{s}^*$ and $e_s = (e_{\tilde{v}}, e_\mu) \in \mathfrak{s}$. The bond-space is now given by $\mathcal{B}_{c,i} = \mathcal{F}_{c,i} \times \mathcal{E}_{c,i}$, with the flow space $\mathcal{F}_{c,i} = \Omega^1(M) \times \Omega^n(M) \times \Omega^0(\partial M)$ and the effort space $\mathcal{E}_{c,i} = \Omega^{n-1}(M) \times \Omega^0(M) \times \Omega^{n-1}(\partial M)$.

The port-Hamiltonian dynamics for compressible isentropic flow is then recovered by setting $((-\dot{\tilde{v}}, -\dot{\mu}), f_\partial, (\delta_{\tilde{v}} H_t, \delta_\mu H_t), e_\partial) \in \mathcal{D}_{c,i}$, which yields

$$\begin{pmatrix} \dot{\tilde{v}} \\ \dot{\mu} \end{pmatrix} = \begin{pmatrix} -d(\delta_\mu H_t) - \iota_v d\tilde{v} \\ -d(\delta_{\tilde{v}} H_t) \end{pmatrix}, \quad (5.134)$$

$$H_t(x_t) = H_t(\tilde{v}, \mu) = \int_M \frac{1}{2} (*\mu) \tilde{v} \wedge *\tilde{v} + U(*\mu)\mu. \quad (5.135)$$

where the variational derivatives of H_t are given by (5.130), and the boundary conditions are specified by the boundary port-variables (e_∂, f_∂) given by (5.132).

Finally we conclude by some remarks about the Dirac structure (5.133) derived in this section. First, this is exactly the Dirac structure which was just defined as a fundamental object in [van der Schaft and Maschke, 2002]. Here the geometrical structure that underpins this object has been rigorously explicated.

Second, the Dirac structure $\mathcal{D}_{c,i}$ given by (5.133) is modulated by the state variables (\tilde{v}, μ) . An interesting case occurs when the 2-form $d\tilde{v} =: \omega \in \Omega^2(M)$ is zero $\forall t$. In such case, the term $\iota_v d\tilde{v}$ in (5.133) vanishes and the Dirac structure becomes a constant one in the bond space $\mathcal{B}_{c,i}$. The 2-form ω is known as the *vorticity form* which is also advected with the flow in ideal fluid flow [Abraham et al., 1988, Pg. 596]. Therefore, if the vorticity form is zero at $t = 0$, it remains zero for all $t > 0$. Such type of fluid flow is called *irrotational flow*².

²In van der Schaft and Maschke [2002] it is erroneously remarked that the term $\iota_v d\tilde{v}$ also

Third, compared to the Dirac structure of the kinetic subsystem in (5.97), the overall Dirac structure (5.133) is exactly the same (if we exclude the distributed port). This equivalence is due to the fact that both systems have the same state variables (\tilde{v}, μ) , but only differ in the Hamiltonian function which is independent from the underlying structure of the system. This underlying structure composed of the external boundary port variables combined with the Lie-Poisson structure which governs the evolution equations of (\tilde{v}, μ) independent of the Hamiltonian energy function.

5.4.2 Adiabatic Compressible Flow

Following the same line of thought as for the isentropic case, we can also extend the kinetic energy port-Hamiltonian system using the distributed port (e_d, f_d) to model adiabatic flow. The exact same procedure is applied for the internal energy storage element but for the extended state variable $x_i = (\mu, s) \in \mathcal{X}_i = V^*$. Both the energy variables (μ, s) are advected quantities of the fluid. Thus the space of advected quantities in this case is $\bar{V}^* = \Omega^n(M) \times \Omega^0(M)$.

The internal energy Hamiltonian $H_i : \mathcal{X}_i \rightarrow \mathbb{R}$ is now given by

$$H_i(\mu, s) = \int_M U(*\mu, s)\mu, \quad (5.136)$$

where the specific internal energy $U(*\mu, s) = U(\rho, s)$ depends now on entropy as well.

The effort and flow variables of the internal energy storage element are given by

$$\begin{aligned} \delta_{x_i} H_i &= \begin{pmatrix} \delta_\mu H_i \\ \delta_s H_i \end{pmatrix} \in T_{x_i}^* \mathcal{X}_i \cong \bar{V} = \Omega^0(M) \times \Omega^n(M), \\ \dot{x}_i &= \begin{pmatrix} \dot{\mu} \\ \dot{s} \end{pmatrix} \in T_{x_i} \mathcal{X}_i \cong \bar{V}^* = \Omega^n(M) \times \Omega^0(M). \end{aligned} \quad (5.137)$$

The variational derivative of H_i with respect to μ is given by Prop. 5.4.1 while the variational derivative of H_i with respect to s is given by

$$\delta_s H_i = \frac{\partial U}{\partial s} \mu = T\mu, \quad (5.138)$$

using (5.103). The internal energy H_i satisfies now the power balance

$$\dot{H}_i = \langle \delta_{x_i} H_i | \dot{x}_i \rangle_{V^*} = \langle \delta_\mu H_i | \dot{\mu} \rangle_{V^*} + \langle \delta_s H_i | \dot{s} \rangle_{V^*}. \quad (5.139)$$

With reference to Fig. 5.14, the Dirac structure \mathcal{D}_{ad} used for connecting the internal energy port $(\delta_{x_i} H_i, \dot{x}_i)$ to the distributed port (e_d, f_d) is given by

vanishes in two-dimensional flow, which is not the case.

$$\begin{aligned}
\mathcal{D}_{ad} = \{ & (f_{si}, f_{\partial i}, f_d, e_{si}, e_{\partial i}, e_d) \in \mathcal{B}_{ad} | \\
& \begin{pmatrix} e_d \\ f_{si} \end{pmatrix} = \begin{pmatrix} 0 & \tilde{\varphi}_{(\mu,s)}^* \\ -\tilde{\varphi}_{(\mu,s)} & 0 \end{pmatrix} \begin{pmatrix} f_d \\ e_{si} \end{pmatrix}, \\
& \begin{pmatrix} e_{\partial i} \\ f_{\partial i} \end{pmatrix} = \begin{pmatrix} 1 & 0 & 0 \\ 0 & 0 & *\mu|_{\partial M} \end{pmatrix} \begin{pmatrix} e_\mu|_{\partial M} \\ e_s|_{\partial M} \\ f_d|_{\partial M} \end{pmatrix} \},
\end{aligned} \tag{5.140}$$

where $f_{si} := (f_\mu, f_s) \in \bar{V}^* = \Omega^n(M) \times \Omega^0(M)$ and $e_{si} := (e_\mu, e_s) \in \bar{V} = \Omega^0(M) \times \Omega^n(M)$, $(f_{\partial i}, e_{\partial i}) \in \Omega^0(\partial M) \times \Omega^{n-1}(\partial M)$, and $(e_d, f_d) \in \Omega^1(M) \times \Omega^{n-1}(M)$. The bond-space \mathcal{B}_{ad} is then given by the product of the aforementioned spaces of forms.

The map $\tilde{\varphi}_{(\mu,s)} : \mathfrak{g} \rightarrow \bar{V}^*$ and its dual $\tilde{\varphi}_{(\mu,s)}^* : \bar{V} \rightarrow \mathfrak{g}^*$ are defined, respectively, for any $\omega \in \mathfrak{g}$ and $(e_\mu, e_s) \in \bar{V}$ as

$$\tilde{\varphi}_{(\mu,s)}(\omega) := \begin{pmatrix} \tilde{\varphi}_\mu(\omega) \\ \tilde{\varphi}_s(\omega) \end{pmatrix}, \quad \tilde{\varphi}_{(\mu,s)}^*(e_\mu, e_s) = \tilde{\varphi}_\mu^*(e_\mu) + \tilde{\varphi}_s^*(e_s), \tag{5.141}$$

which allows one to rewrite the first equation in (5.140) as

$$\begin{pmatrix} e_d \\ f_\mu \\ f_s \end{pmatrix} = \begin{pmatrix} 0 & \tilde{\varphi}_\mu^* & \tilde{\varphi}_s^* \\ -\tilde{\varphi}_\mu & 0 & 0 \\ -\tilde{\varphi}_s & 0 & 0 \end{pmatrix} \begin{pmatrix} f_d \\ e_\mu \\ e_s \end{pmatrix}. \tag{5.142}$$

For the choice of μ and s as the advected parameters, the maps $\tilde{\varphi}_\mu, \tilde{\varphi}_s$ and $\tilde{\varphi}_\mu^*, \tilde{\varphi}_s^*$ are given in Table 5.2.

The power balance that the Dirac structure \mathcal{D}_{ad} encodes is given by the following result.

Proposition 5.4.3. *The Dirac structure \mathcal{D}_{ad} given by (5.140) is a power continuous structure, such that*

$$\langle e_d | f_d \rangle_{\mathfrak{g}} + \langle e_{si} | f_{si} \rangle_{\bar{V}^*} + \int_{\partial M} e_{\partial i} \wedge f_{\partial i} = 0. \tag{5.143}$$

Proof. Using (5.140 - 5.142), we have that

$$\begin{aligned}
\langle e_d | f_d \rangle_{\mathfrak{g}} &= \langle \tilde{\varphi}_\mu^*(e_\mu) | f_d \rangle_{\mathfrak{g}} + \langle \tilde{\varphi}_s^*(e_s) | f_d \rangle_{\mathfrak{g}} \\
&= \langle e_\mu | \tilde{\varphi}_\mu(f_d) \rangle_{V^*} + \int_{\partial M} \eta_{\tilde{\varphi}_{f_d}}(\mu, e_\mu) \\
&\quad + \langle e_s | \tilde{\varphi}_s(f_d) \rangle_{V^*} + \int_{\partial M} \eta_{\tilde{\varphi}_{f_d}}(s, e_s) \\
&= \langle e_\mu | -f_\mu \rangle_{V^*} - \int_{\partial M} (*\mu f_d)|_{\partial M} \wedge e_\mu|_{\partial M} + \langle e_s | -f_s \rangle_{V^*} + 0, \\
&= -\langle e_{si} | f_{si} \rangle_{\bar{V}^*} - \int_{\partial M} e_{\partial i} \wedge f_{\partial i},
\end{aligned}$$

which follows from (5.42) and the interconnection map expressions (and their corresponding surface terms) in Table 5.2. \blacksquare

With reference to Fig. 5.14, the Dirac structure \mathcal{D}_{ad} is used to model adiabatic compressible flow by setting its ports to

$$(\langle \dot{\mu}, \dot{s} \rangle, \iota_v \mu|_{\partial M}, \omega_v, (\delta_\mu H_i, \delta_s H_i), h|_{\partial M}, f_s) \in \mathcal{D}_{ad}.$$

Therefore, following exactly the steps shown in (5.124), the evolution of s is given by

$$\dot{s} = -\tilde{\varphi}_s(\omega_v) = -\mathcal{L}_v s, \quad (5.144)$$

and the evolution of μ is the same as the isentropic case in (5.124). Moreover, using (5.125) and the definition of $\tilde{\varphi}_s^*$ we have that

$$\begin{aligned}
f_s &= \tilde{\varphi}_\mu^*(\delta_\mu H_i) + \tilde{\varphi}_s^*(\delta_s H_i) = -(*\mu)dh + *(\delta_s H_i)ds \\
&= -(*\mu)dh + *(T\mu)ds = -(*\mu)dh + T(*\mu)ds = -dp,
\end{aligned} \quad (5.145)$$

where the fourth equality follows from the commutativity of the Hodge star with functions, and the final results follows from Gibbs equation (5.107). Therefore, both (5.144) and (5.124) correctly represent the evolution of the entropy s and the mass form μ as being advected with the flow, while (5.145) correctly represents the stress forces due to pressure consistent with the thermodynamics of the system.

Finally we conclude by a more compact port-Hamiltonian model for adiabatic compressible flow, as shown in Fig. 5.14. The new storage element has its state variables $\bar{x}_t := (\tilde{v}, \mu, s)$ and the total Hamiltonian \bar{H}_t given by

$$\bar{H}_t(\tilde{v}, \mu, s) = \int_M \frac{1}{2}(*\mu)\tilde{v} \wedge *\tilde{v} + U(*\mu, s)\mu, \quad (5.146)$$

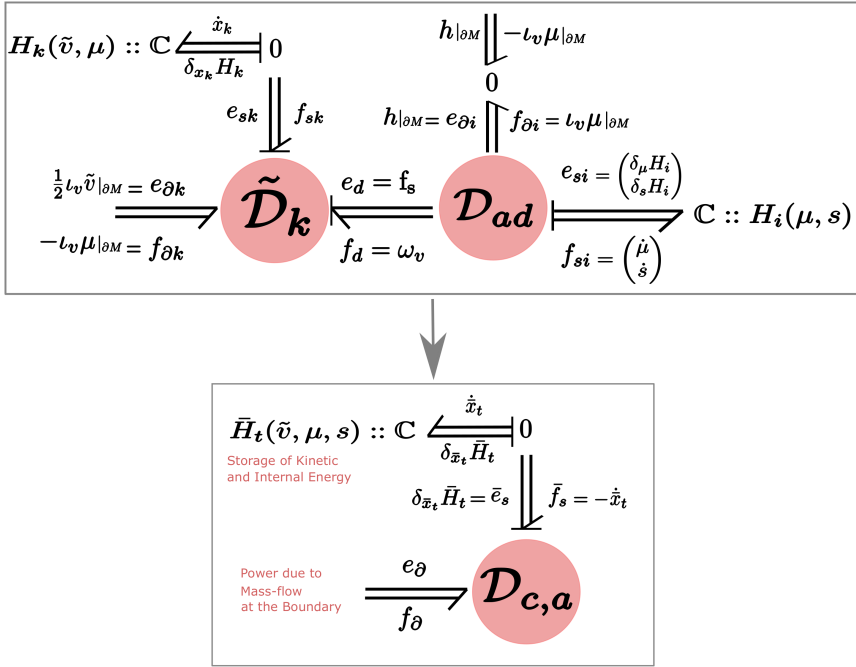


Figure 5.14: Compressible adiabatic flow on a general manifold with permeable boundary. Top figure shows how to augment the kinetic energy system (5.98) with the storage of internal energy, while the bottom figure shows a compact model with a combined storage element, Dirac structure, and boundary port.

with flow and effort variables

$$\dot{\bar{x}}_t = \begin{pmatrix} \dot{\bar{v}} \\ \dot{\mu} \\ \dot{s} \end{pmatrix}, \quad \delta_{\bar{x}_t} \bar{H}_t = \begin{pmatrix} \delta_{\bar{v}} \bar{H}_t \\ \delta_{\mu} \bar{H}_t \\ \delta_s \bar{H}_t \end{pmatrix} = \begin{pmatrix} \iota_v \mu \\ \frac{1}{2} \iota_v \bar{v} + h \\ T \mu \end{pmatrix}. \quad (5.147)$$

Interestingly, the new energy balance for \bar{H}_t is given by the same power balance as for the isentropic case as will be proven in the following.

Proposition 5.4.4. *The rate of change of the total Hamiltonian \bar{H}_t , given by (5.146), along trajectories of its state variables $\bar{x}_t = (\bar{v}, \mu, s)$ is expressed as*

$$\dot{\bar{H}}_t = \int_{\partial M} e_{\partial} \wedge f_{\partial}, \quad (5.148)$$

where the same boundary port variables defined before in (5.132).

Proof. The proof follows exactly the one of Prop. 5.4.2, where the pairing $\langle e_d | f_d \rangle_{\mathfrak{g}} = \langle f_s | \omega_v \rangle_{\mathfrak{g}}$ is substituted by the power balance given by Prop. 5.4.3. ■

Remark 5.4.5. The reason why the energy balance (5.148) for adiabatic flow is equivalent to the one for isentropic flow in (5.131) is mainly due to the vanishing of the surface term $\eta_{\tilde{\varphi}_{f_d}}(s, e_s)$ in the proof of Prop. 5.4.3, which follows from Table 5.2. The physical intuition behind this observation is the fact that adiabatic flow corresponds to conservation of entropy due to no exchange of heat with the surroundings. Thus, it is natural that no increase of internal energy occurs due to heat exchange through the boundary, and the only way for internal energy to increase is due to mass flow through the boundary.

The overall Stokes-Dirac structure $\mathcal{D}_{c,a}$ for adiabatic compressible flow that implements the power balance in (5.148) is given by

$$\begin{aligned} \mathcal{D}_{c,a} = \{(\bar{e}_s, \bar{f}_s, e_{\partial}, f_{\partial}) \in \mathcal{B}_{c,a} \mid \\ \begin{pmatrix} f_{\bar{v}} \\ f_{\mu} \\ f_s \end{pmatrix} &= \begin{pmatrix} de_{\mu} + \frac{1}{*\mu} \iota_{\hat{e}_{\bar{v}}} d\bar{v} - \frac{**e_s}{*\mu} ds \\ de_{\bar{v}} \\ \frac{1}{*\mu} \iota_{\hat{e}_{\bar{v}}} ds \end{pmatrix}, \\ \begin{pmatrix} e_{\partial} \\ f_{\partial} \end{pmatrix} &= \begin{pmatrix} 0 & 1 & 0 \\ -1 & 0 & 0 \end{pmatrix} \begin{pmatrix} e_{\bar{v}}|_{\partial M} \\ e_{\mu}|_{\partial M} \\ e_s|_{\partial M} \end{pmatrix} \}, \end{aligned} \quad (5.149)$$

where the total storage port variables are given by $\bar{f}_s = (f_{\bar{v}}, f_{\mu}, f_s) \in \Omega^1(M) \times \Omega^n(M) \times \Omega^0(M)$ and $\bar{e}_s = (e_{\bar{v}}, e_{\mu}, e_s) \in \Omega^{n-1}(M) \times \Omega^0(M) \times \Omega^n(M)$. The bond-space is given by $\mathcal{B}_{c,a} = \mathcal{F}_{c,a} \times \mathcal{E}_{c,a}$, with the flow space $\mathcal{F}_{c,a} = \Omega^1(M) \times$

$\Omega^n(M) \times \Omega^0(M) \times \Omega^0(\partial M)$ and the effort space $\mathcal{E}_{c,a} = \Omega^{n-1}(M) \times \Omega^0(M) \times \Omega^n(M) \times \Omega^{n-1}(\partial M)$.

Finally, the port-Hamiltonian dynamics for compressible adiabatic flow is then recovered by setting $((-\dot{\tilde{v}}, -\dot{\mu}, -\dot{s}), f_\partial, (\delta_{\tilde{v}}\bar{H}_t, \delta_\mu\bar{H}_t, \delta_s\bar{H}_t), e_\partial) \in \mathcal{D}_{c,a}$, which yields

$$\begin{pmatrix} \dot{\tilde{v}} \\ \dot{\mu} \\ \dot{s} \end{pmatrix} = \begin{pmatrix} -d(\delta_\mu\bar{H}_t) - \iota_v d\tilde{v} + (*\delta_s\bar{H}_t / *\mu)ds \\ -d(\delta_{\tilde{v}}\bar{H}_t) \\ -\iota_v ds \end{pmatrix}, \quad (5.150)$$

$$\bar{H}_t(\bar{x}_t) = \bar{H}_t(\tilde{v}, \mu, s) = \int_M \frac{1}{2}(*\mu)\tilde{v} \wedge *\tilde{v} + U(*\mu, s)\mu, \quad (5.151)$$

where the following equality was used

$$-\dot{s} = \mathcal{L}_v s = d\iota_v s + \iota_v ds = \iota_v ds = \frac{1}{*\mu} \iota_{\hat{e}_{\tilde{v}}} ds. \quad (5.152)$$

The variational derivatives of \bar{H}_t are given by (5.147), and the boundary conditions are specified by the boundary port-variables (e_∂, f_∂) given by (5.132).

5.5 Port-Hamiltonian Modeling of Incompressible Flow

As discussed before in Sec. 5.2, for low speed flows it is possible to neglect the compressibility of the fluid and assume incompressible flow. Such flow is known as incompressible subsonic flow and usually identified when the ratio of the flow speed compared to the speed of sound (the Mach number) is approximately less than 0.3.

In incompressible flow, the fluid is characterized only by kinetic energy and no internal energy is present. The pressure function in incompressible flow no longer has its thermodynamic nature as in compressible flow, but rather acts as a Lagrange multiplier that enforces the incompressibility of the flow. Therefore, an incompressible flow system is classified as a constrained mechanical system, not a thermodynamic system.

To represent incompressible flow in the port-Hamiltonian framework, the kinetic energy subsystem (5.98-5.100) already contains all the energy stored, its energy variables, and its corresponding interconnection structure. The difference now is that the system (5.98) no longer has the state space $\mathcal{X} = \mathfrak{s}^* = \mathfrak{g}^* \times V^* = \Omega^1(M) \times \Omega^n(M)$, but instead the constrained state space \mathcal{X}_c defined by

$$\mathcal{X}_c := \mathfrak{g}_c^* \times V^* = \tilde{C}^1(M) \times \Omega^n(M), \quad (5.153)$$

where $\mathbf{g}_c^* := \tilde{C}^1(M) \subset \Omega^1(M)$ denotes the space of co-closed 1-forms defined by

$$\tilde{C}^1(M) := \{\tilde{v} \in \Omega^1(M) \mid d * \tilde{v} = 0\}.$$

The incompressibility constraint $d * \tilde{v} = d\omega_v = 0$ is equivalent to the conservation of the volume form, as discussed in Sec. 5.2.

For the port-Hamiltonian system (5.98) to correctly represent incompressible flow, the distributed port $(e_d, f_d) = (f_s, \omega_v)$ needs to be adapted to model stress forces that impose the incompressibility constraint. Following the exact same manner as in the previous section, the key point that allows building the port-based model of incompressible flow is that the volume form μ_{vol} is frozen in the fluid (i.e. an advected quantity).

With reference to Fig. 5.15, the interconnection to model incompressible flow is achieved by the Dirac structure \mathcal{D}_{inc} given by

$$\begin{aligned} \mathcal{D}_{inc} = \{ & (f_{\partial i}, f_{di}, e_{\partial i}, e_{di}) \in \mathcal{B}_{inc} \mid \\ & \begin{pmatrix} e_{di} \\ 0 \end{pmatrix} = \begin{pmatrix} 0 & \tilde{\varphi}_{\mu_{\text{vol}}}^* \\ -\tilde{\varphi}_{\mu_{\text{vol}}} & 0 \end{pmatrix} \begin{pmatrix} f_d \\ p \end{pmatrix}, \\ & \begin{pmatrix} e_{\partial i} \\ f_{\partial i} \end{pmatrix} = \begin{pmatrix} 1 & 0 \\ 0 & 1 \end{pmatrix} \begin{pmatrix} p|_{\partial M} \\ f_d|_{\partial M} \end{pmatrix} \}, \end{aligned} \quad (5.154)$$

where the bond-space $\mathcal{B}_{inc} = \mathcal{F}_{inc} \times \mathcal{E}_{inc}$ is the product space of the flow space $\mathcal{F}_{inc} = \Omega^{n-1}(\partial M) \times \Omega^{n-1}(M)$ and the effort space $\mathcal{E}_{inc} = \Omega^0(\partial M) \times \Omega^1(M)$.

The power continuity of \mathcal{D}_{inc} is given by the following result.

Proposition 5.5.1. *The Dirac structure \mathcal{D}_{inc} given by (5.154) is a power continuous structure, such that*

$$\langle e_{di} | f_{di} \rangle_{\mathbf{g}} + \int_{\partial M} e_{\partial i} \wedge f_{\partial i} = 0. \quad (5.155)$$

Proof. Using (5.42) and (5.154), we have that

$$\begin{aligned} \langle e_{di} | f_{di} \rangle_{\mathbf{g}} &= \langle \tilde{\varphi}_{\mu_{\text{vol}}}^*(p) | f_d \rangle_{\mathbf{g}} = \langle p | \tilde{\varphi}_{\mu_{\text{vol}}}(f_d) \rangle_{V^*} + \int_{\partial M} \eta_{\tilde{\varphi}_{f_d}}(\mu_{\text{vol}}, p) \\ &= \langle p | 0 \rangle_{V^*} - \int_{\partial M} f_d|_{\partial M} \wedge p|_{\partial M} = - \int_{\partial M} e_{\partial i} \wedge f_{\partial i}, \end{aligned}$$

which follows from the definition of $\tilde{\varphi}_{\mu_{\text{vol}}}^*$ and $\eta_{\tilde{\varphi}_{f_d}}$ given in Table 5.2 with μ_{vol} instead of μ as the advected quantity. \blacksquare

Remark 5.5.2. A special feature of the Dirac structure \mathcal{D}_{inc} is that it has three ports, one of which, namely $(p, 0)$, does not affect the power balance (5.155). The power flowing through the port $(p, 0)$ is always zero such that the

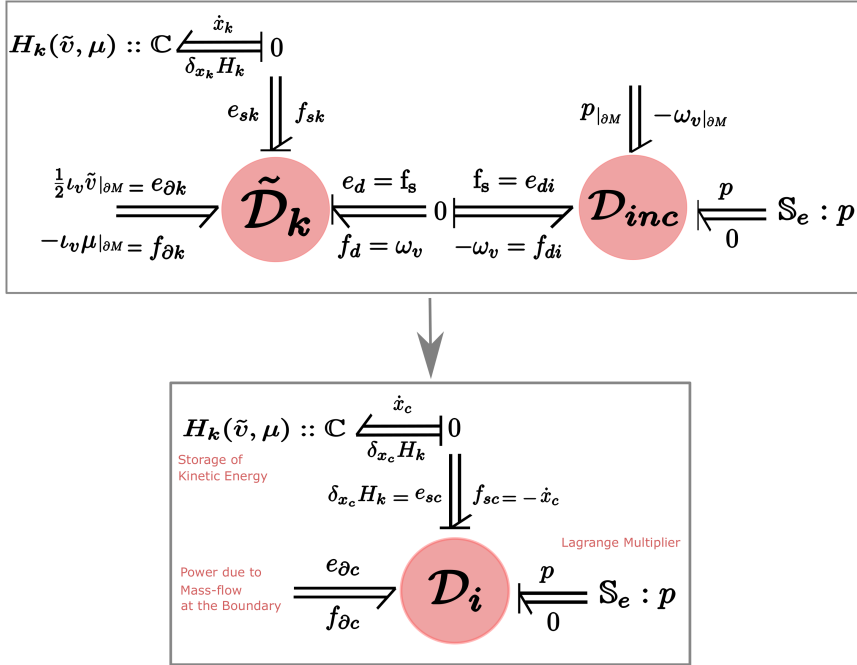


Figure 5.15: Incompressible inhomogeneous flow on a general manifold with permeable boundary. Top figure shows how to augment the kinetic energy system (5.98) with the pressure as a Lagrange multiplier, while the bottom figure shows a compact model with a combined storage element, Dirac structure, boundary port, and constraint distributed port.

pressure function acts as a Lagrange multiplier enforcing the incompressibility constraint. A direct consequence is that the Dirac structure \mathcal{D}_{inc} is defined as a subspace on the two ports $(e_{\partial i}, f_{\partial i})$ and (e_{di}, f_{di}) only, as shown in (5.154).

The Dirac structure (5.154) is then used to model incompressible flow by setting its ports to $(\iota_v \mu|_{\partial M}, -\omega_v, p|_{\partial M}, f_s) \in \mathcal{D}_{inc}$. Therefore from (5.154) it follows that

$$0 = -\tilde{\varphi}_{\mu_{vol}}(-\omega_v) = \mathcal{L}_v \mu_{vol} = d\iota_v \mu_{vol} = d * \tilde{v}, \quad (5.156)$$

and similarly

$$f_s = \tilde{\varphi}_{\mu_{vol}}^*(p) = -dp. \quad (5.157)$$

Thus, both the incompressibility constraint and the forces due to pressure are properly modeled in (5.156) and (5.157), respectively.

Remark 5.5.3. From the power balance (5.155) it is worth noticing that if we neglect the surface term, the power flow through distributed port $(e_d, f_d) = (f_s, \omega_v)$ is equal to zero, which is a consequence that the work done due to the pressure $\langle p|0 \rangle_{V^*}$ is equal to zero. The pressure p acts as a Lagrange multiplier that only enforces the incompressibility constraint, and no longer has its thermodynamic nature in incompressible flow, which is considered a limit case of the general compressible flow.

To summarize, the explicit port-Hamiltonian dynamical model of (inhomogeneous) incompressible flow in terms of the constrained state variable $x_c := (\tilde{v}, \mu) \in \mathcal{X}_c = \mathfrak{g}_c^* \times V^*$ is given by

$$\begin{pmatrix} \dot{\tilde{v}} \\ \dot{\mu} \end{pmatrix} = \begin{pmatrix} -d(\delta_\mu H_k) - \iota_v d\tilde{v} \\ -d(\delta_{\tilde{v}} H_k) \end{pmatrix} - \begin{pmatrix} \frac{1}{*\mu} \circ d \\ 0 \end{pmatrix} p, \quad (5.158)$$

$$0 = (d \circ \frac{1}{*\mu} \quad 0) \begin{pmatrix} \delta_{\tilde{v}} H_k \\ \delta_\mu H_k \end{pmatrix}, \quad (5.159)$$

$$H_k(x_c) = H_k(\tilde{v}, \mu) = \int_M \frac{1}{2} (*\mu) \tilde{v} \wedge *\tilde{v}. \quad (5.160)$$

where the variational derivatives are given by (5.95), and the pressure function $p \in C^\infty(M)$ is a distributed Lagrange multiplier. The energy balance for H_k is given by the following result.

Proposition 5.5.4. *The rate of change of the total Hamiltonian H_k , given by (5.160), along trajectories of (5.158) is expressed as*

$$\dot{H}_k = \int_{\partial M} e_{\partial c} \wedge f_{\partial c}, \quad (5.161)$$

where the boundary port variables $e_{\partial c}, f_{\partial c} \in \Omega^0(\partial M) \times \Omega^{n-1}(\partial M)$ are defined by

$$\begin{aligned} e_{\partial c} &:= \delta_\mu H_k|_{\partial M} + \left(\frac{p}{*\mu} \right)|_{\partial M} = \left(\frac{1}{2} \iota_v \tilde{v} + \frac{p}{*\mu} \right)|_{\partial M}, \\ f_{\partial c} &:= -\delta_{\tilde{v}} H_k|_{\partial M} = -(\iota_v \mu)|_{\partial M}. \end{aligned} \quad (5.162)$$

Proof. By starting from the energy balance for \dot{H}_k in (5.96) and using the equality (5.155) with $\langle e_{di}|f_{di} \rangle_{\mathfrak{g}} = \langle f_s|-\omega_v \rangle_{\mathfrak{g}}$, we have that

$$\begin{aligned} \dot{H}_k &= \int_{\partial M} e_{\partial k} \wedge f_{\partial k} + \int_M e_d \wedge f_d \\ &= \int_{\partial M} \frac{1}{2} \iota_v \tilde{v}|_{\partial M} \wedge -\iota_v \mu|_{\partial M} - \langle f_s|-\omega_v \rangle_{\mathfrak{g}} \\ &= \int_{\partial M} \frac{1}{2} \iota_v \tilde{v}|_{\partial M} \wedge -\iota_v \mu|_{\partial M} + \int_{\partial M} e_{\partial i} \wedge f_{\partial i} \\ &= \int_{\partial M} \frac{1}{2} \iota_v \tilde{v}|_{\partial M} \wedge -\iota_v \mu|_{\partial M} + \int_{\partial M} p|_{\partial M} \wedge -\omega_v|_{\partial M} \\ &= \int_{\partial M} \frac{1}{2} \iota_v \tilde{v}|_{\partial M} \wedge -\iota_v \mu|_{\partial M} + \int_{\partial M} \left(\frac{p}{*\mu} \right)|_{\partial M} \wedge -\iota_v \mu|_{\partial M} \\ &= \int_{\partial M} \left(\frac{1}{2} \iota_v \tilde{v} + \frac{p}{*\mu} \right)|_{\partial M} \wedge -\iota_v \mu|_{\partial M}. \end{aligned}$$

■

Finally, the Stokes-Dirac structure \mathcal{D}_i that encodes the power balance (5.161) is given by

$$\begin{aligned} \mathcal{D}_i &= \{(f_{sc}, f_{\partial c}, e_{sc}, e_{\partial c}) \in \mathcal{B}_i| \\ &\quad \begin{pmatrix} f_{\tilde{v}} \\ f_\mu \end{pmatrix} = \begin{pmatrix} de_\mu + \frac{1}{*\mu} \iota_{\tilde{e}_{\tilde{v}}} d\tilde{v} \\ de_{\tilde{v}} \end{pmatrix} + \begin{pmatrix} \frac{1}{*\mu} \circ d \\ 0 \end{pmatrix} p, \\ &\quad 0 = (d \circ \frac{1}{*\mu} \quad 0) \begin{pmatrix} e_{\tilde{v}} \\ e_\mu \end{pmatrix}, \\ &\quad \begin{pmatrix} e_{\partial c} \\ f_{\partial c} \end{pmatrix} = \begin{pmatrix} 0 & 1 \\ -1 & 0 \end{pmatrix} \begin{pmatrix} e_{\tilde{v}}|_{\partial M} \\ e_\mu|_{\partial M} \end{pmatrix} + \begin{pmatrix} \frac{1}{*\mu} \\ 0 \end{pmatrix} p|_{\partial M}\}, \end{aligned} \quad (5.163)$$

where the boundary port variables $e_{\partial c}, f_{\partial c} \in \Omega^0(\partial M) \times \Omega^{n-1}(\partial M)$ and total storage port variables are given by $f_{sc} = (f_{\tilde{v}}, f_\mu) \in \tilde{C}^1(M) \times \Omega^n(M)$ and $e_{sc} = (e_{\tilde{v}}, e_\mu) \in C^{n-1}(M) \times \Omega^0(M)$, where $C^{n-1}(M) \subset \Omega^{n-1}(M)$ is the space of closed $n-1$ forms. The bond-space \mathcal{B}_i is given accordingly by the product of the aforementioned spaces, as usual.

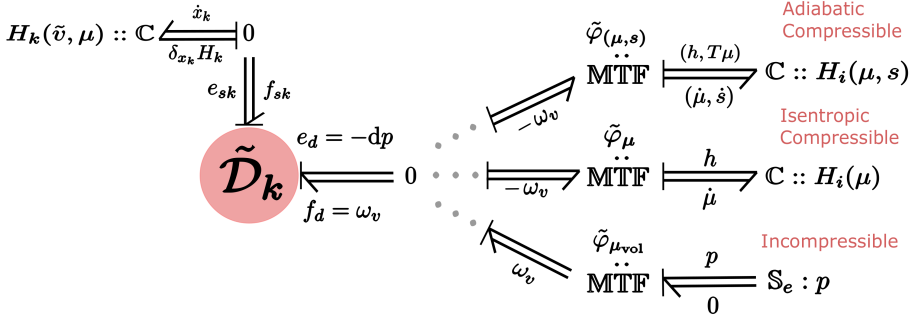


Figure 5.16: Graphical representation of compressible and incompressible Euler Equations on a closed manifold ($\partial M = \emptyset$) showing modularity of the port-Hamiltonian framework. For a general permeable manifold, the interconnection is achieved using Dirac structures.

Remark 5.5.5. For inhomogeneous incompressible flow, one can derive the Lie-Poisson part of the Dirac structure (5.163) by semi-direct product reduction (*cf.* [Marsden, 1976]) starting from the configuration space $\mathcal{D}_{\text{vol}}(M) \ltimes V$, where $\mathcal{D}_{\text{vol}}(M)$ represents the volume preserving diffeomorphisms on M . However, in the modular approach we presented, a re-derivation of the underlying structure is unnecessary as the open ports of the system (5.100) were used to constraint the state space to the dual of the Lie algebra of $\mathcal{D}_{\text{vol}}(M) \ltimes V$.

For the case of homogeneous incompressible flow, one no longer has the semi-direct product structure as the mass form becomes constant in space and is no longer advected. In this case, the standard Hamiltonian reduction theorems can be used to derive the Lie-Poisson structure as in [Ebin and Marsden, 1970; Arnold and Khesin, 1998; Modin et al., 2011].

5.6 Conclusion

In this chapter, a systematic procedure to model a variety of fluid dynamical systems on general Riemannian manifolds was presented. The procedure was demonstrated for developing decomposed and open port-Hamiltonian models for (ideal) compressible and incompressible flow with variable boundary conditions. The models presented are all geometric and thus are globally defined independently of a choice of coordinates on the spatial manifold M , thanks to the formulation of the equations using exterior calculus.

Using the geometric nature and the semi-direct product algebra structure of the state space underlying the energy variables of the kinetic energy subsystem, we showed that its Stokes-Dirac structure could be systematically constructed

in two steps. First one uses Poisson reduction [Marsden et al., 1984a,b] to construct the underlying Lie-Poisson structure and its corresponding bracket. The second step then extends the Lie-Poisson structure to a Stokes-Dirac structure that allows non-zero exchange of kinetic energy within the spatial domain and through its boundary. All the surface terms were easily identified thanks to the duality pairings of the different maps constructed on the algebra \mathfrak{s} .

This systematic two-step procedure coincide with the Stokes-Dirac structure of compressible isentropic flow heuristically obtained in [van der Schaft and Maschke, 2001, 2002] based on the velocity of the flow as the energy variable. We also presented an alternative Stokes-Dirac structure based on the momentum of the flow, and showed how to relate both representations.

We have highlighted in this chapter that the philosophy of port-Hamiltonian modeling is different from the classic approach of deriving Hamiltonian equations using variational principles [Arnold and Khesin, 1998; Marsden et al., 1972, 1984a]. The philosophy of the latter approach is a top-down procedure starting from the *total* energy (Hamiltonian) defined on the cotangent bundle of the system's configuration space and then deriving the *total* equations of motion governing the system. Whereas, the philosophy of the port-Hamiltonian framework is a bottom-up procedure starting from subsystems that are interconnected together to form the complex total system. The straightforward advantage compared to the variational approach, is that simply the model is updated by adding a new subsystem without re-deriving the whole dynamical equations. This has been demonstrated by extending the subsystem corresponding to kinetic energy storage to three models, shown in Fig. 5.16.

One advantage of our presented decomposed models is that they are *open models*. Using the *open boundary port* or an extra distributed port, the derived models can be extended to more complicated fluid systems with (potentially) other physical domains, like e.g. structural mechanics or electromagnetism. The only constraint when coupling subsystems of different nature is that one finds the physical reason for why they can be coupled in the first place. If systems of different complexity are to be coupled (such as a fluid and a structure) a physical condition must be present that effects the suitable complexity reduction of the ports of the more complex system (such as the no-slip condition for coupling fluids and structures) so that they can be coupled.

Another advantage of our work is that our framework allows to decompose a fluid domain into several imaginary subdomains whose equally imaginary boundaries of course do not prevent the flow between these subdomains. But since the thus constituted subsystems must now be connected through a Dirac structure that routes the energy, between adjoining domains, we obtain control over precisely this energy flow. This promises an avenue to ensure compatibility of our energy-aware decomposition with correspondingly designed structure-preserving numerical schemes, e.g. [Šešljija et al., 2011, 2012].

Part II

Aerial Physical Interaction

CHAPTER 6

FULLY-ACTUATED UAVS

This chapter reports the results of [Rashad et al., 2020c] which is an extensive literature survey of UAVs capable of full-actuation. These fully-actuated vehicles are suitable candidates to be used as a flying-end effector for the purpose of aerial physical interaction.

Conventional multirotor UAV designs, like the quadrotor or hexarotor, are optimized for maximum flight time. As a result, all rotors of such UAVs have parallel directions to collectively counteract gravity. Consequently, conventional multirotor UAVs have underactuated dynamics due to the coupling between horizontal translational dynamics and rotational dynamics.

For many applications, the underactuation property of conventional designs has been alleviated by the use of gimbals to mount sensors onboard. However, the applicability of multirotor UAVs can be extended if full actuation of these UAVs could be achieved. One example of such applications is the field of aerial physical interaction addressed in this thesis.

Several fully-actuated multirotor platforms have been introduced in the past decade to overcome the underactuation property of conventional multirotors. Full-actuation has been mainly realized by two techniques; either by having fixed propellers with dissimilar orientations, which we refer to as *fixed-tilt concepts*, or by actively tilting propellers using extra actuators, which we refer to as *variable-tilt concepts*.

The problem with fully-actuated UAV concepts is that the optimal rotor configuration is application-dependent, contrary to underactuated concepts which usually have the orientation of their rotors to be vertical in an in-plane symmetric configuration. To achieve full-actuation, the orientation and loca-

tion of the rotors needs to be altered, which results in a wide range of possible rotor configurations. Depending on the requirements of the application, this results in a vast variety of different possible concepts.

In this chapter we present a review of the available concepts in the aerial robotics literature suggested for achieving fully-actuated flight. The focus is mainly on fully-actuated multi-rotor UAVs using propellers only for propulsion since they are more popular in the aerial robotics literature. The surveyed concepts are divided into fixed-tilt multirotors and variable-tilt multirotors. This work also includes a review of the optimization criteria used in the literature for optimizing the design parameters of fixed-tilt multirotor UAVs. Moreover, a static wrench analysis has been utilized to systematically derive the control allocation matrix in a unified frame of reference for all the surveyed concepts.

The rest of the chapter is organized as follows: in Sec. 6.1, we present some background preliminaries of the fully-actuated wrench generation of multirotors. We present the surveyed concepts in Sec. 6.2 and Sec. 6.3, which include the fixed-tilt and variable-tilt designs, respectively. Finally, we conclude in Sec. 6.4 with some remarks on the optimization criteria and control-system architecture used in the literature.

6.1 Mechanical Design of Fully-Actuated UAVs

6.1.1 Static Control Wrench Analysis

In this section, we show how to derive the control allocation matrix, which maps the control inputs of the UAV, i.e. the propellers' thrusts, to the total aerodynamic wrench applied to the UAV's body. This is done first by defining the reference frames used, followed by a static wrench analysis and the classification of multirotor UAVs based on the mapping matrix. For a more comprehensive introduction to the topic, the reader is referred to textbooks like Austin [2011]; Valavanis and Vachtsevanos [2015].

Coordinate Frames

First we introduce the notion of a coordinate frame which is represented by the quadruple $\{\Psi_i : o_i, \hat{\mathbf{x}}_i, \hat{\mathbf{y}}_i, \hat{\mathbf{z}}_i\}$, where o_i represents the origin of the frame and $(\hat{\mathbf{x}}_i, \hat{\mathbf{y}}_i, \hat{\mathbf{z}}_i)$ is a triad of (right) mutually orthonormal basis vectors. Let $\{\Psi_B : o_B, \hat{\mathbf{x}}_B, \hat{\mathbf{y}}_B, \hat{\mathbf{z}}_B\}$ denote a body-fixed frame with o_B attached to the center-of-mass (CoM), $\hat{\mathbf{z}}_B$ is chosen such that gravity acts oppositely when the UAV is rested on a flat ground, and $\hat{\mathbf{x}}_B$ represents the UAV's forward direction such that when aligned to point North, $\hat{\mathbf{y}}_B$ would point West, as shown in Fig.6.1.

Associated to the i -th propeller is the frame $\{\Psi_{p_i} : o_{p_i}, \hat{\mathbf{x}}_{p_i}, \hat{\mathbf{y}}_{p_i}, \hat{\mathbf{z}}_{p_i}\}$ with

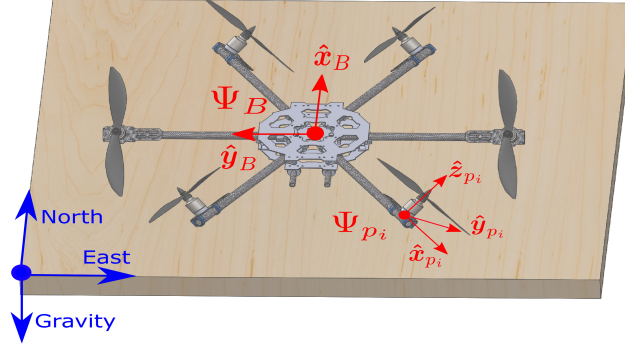


Figure 6.1: Schematic view of the reference frames used, illustrated on a fully-actuated hexarotor.

the origin o_{p_i} coinciding with the CoM of the i -th rotor, and \hat{z}_{p_i} is oriented with the direction of generated thrust (i.e. normal to the spinning disk area). As for the axis \hat{x}_{p_i} , it is chosen such that it is collinear to the line connecting o_B to o_{p_i} , while \hat{y}_{p_i} completes the right-oriented triad as shown in Fig.6.1. The propeller frame Ψ_{p_i} does not rotate with the propeller's spinning i.e. it is also a body-fixed frame for the case of fixed-tilt concepts. However, for variable tilt-concepts \hat{z}_{p_i} is always aligned with the variable thrust generation direction.

With the aforementioned definitions of the coordinate frames used, the configuration of each rotor/propeller now can be determined by the displacement vector $\xi_i \in \mathbb{R}^3$ and the orientation vector $u_i \in \mathbb{S}^2$ given by

$$\xi_i := \xi_{p_i}^B, \quad u_i(t) := R_{p_i}^B(t)\hat{z}, \quad (6.1)$$

where $\xi_{p_i}^B \in \mathbb{R}^3$, $R_{p_i}^B \in SO(3)$ denote the position and orientation of Ψ_{p_i} with respect to Ψ_B , respectively, and $\hat{z} = (0, 0, 1)^\top$. The explicit time-dependence in (6.1) is for the case of variable-tilt UAVs, whereas for fixed-tilt UAVs both ξ_i and u_i are constants.

In the case of a planar multirotor, i.e. a design with coplanar rotor positions, it is possible to parametrize the orientation matrix $R_{p_i}^B$ by three angles such that

$$R_{p_i}^B = R_z(\psi_i)R_y(\beta_i)R_x(\alpha_i), \quad (6.2)$$

where $R_k(\cdot)$ is the standard rotation matrix around the k -th axis, while the angles α_i and β_i uniquely define the direction of the thrust generation axis \hat{z}_{p_i} in Ψ_B . The angle ψ_i denotes the heading, while α_i, β_i will be referred to, respectively, as the cant and dihedral angles.

Static Analysis

The aerodynamic wrench produced by the rotors can be derived based on a static wrench analysis. A wrench represents the generalized force acting on a rigid body, consisting of a linear force component $\mathbf{f} \in \mathbb{R}^3$ and a rotational torque component $\boldsymbol{\tau} \in \mathbb{R}^3$. A wrench applied to the origin of Ψ_i with its components specified in Ψ_i is denoted by $\mathbf{W}^i = (\boldsymbol{\tau}^{i\top}, \mathbf{f}^{i\top})^\top$. The change of coordinates of a wrench between any two frames Ψ_i and Ψ_k can be performed by

$$\mathbf{W}^k = \mathbf{Ad}_{\mathbf{H}_k^i}^\top \mathbf{W}^i, \quad \mathbf{Ad}_{\mathbf{H}_k^i}^\top = \begin{pmatrix} \mathbf{R}_i^k & \tilde{\boldsymbol{\xi}}_i^k \mathbf{R}_i^k \\ \mathbf{0} & \mathbf{R}_i^k \end{pmatrix}, \quad (6.3)$$

where $\boldsymbol{\xi}_i^k, \mathbf{R}_i^k$ denote the position and orientation of Ψ_i with respect to Ψ_k , respectively. The skew-symmetric matrix $\tilde{\boldsymbol{\xi}}$ in (6.3) is defined such that $\tilde{\boldsymbol{\xi}}\mathbf{x} = \boldsymbol{\xi} \wedge \mathbf{x}, \forall \mathbf{x} \in \mathbb{R}^3$, where \wedge denotes the cross product on \mathbb{R}^3 . In differential geometric terms as discussed in Ch.4, the matrix $\mathbf{Ad}_{\mathbf{H}_k^i}^\top$ corresponds to the coadjoint operator of $SE(3)$, while the components of \mathbf{W}^i correspond to the Plucker coordinates of the wrench screw.

It is well known from the aerial robotics literature that, in quasi-static flights, the aerodynamic thrust and drag torque of a propeller are both approximately proportional to the square of the propeller's spinning velocity Mahony et al. [2012]. This simple aerodynamic wrench model neglects many high-order effects such as blade-flapping and induced drag, which induce forces in the $\hat{\mathbf{x}}_{p_i}$ - $\hat{\mathbf{y}}_{p_i}$ plane. However, for the scale of multi-rotor UAVs used in robotics, these effects cause minor perturbations and are usually neglected in the control design process Mahony et al. [2012]. Thus, the aerodynamic wrench generation direction is only along $\hat{\mathbf{z}}_{p_i}$.

The thrust magnitude generated by the i -th propeller in Ψ_{p_i} will be denoted by λ_i , while the drag torque will be expressed as $\tau_{d,i} = \gamma \sigma_i \lambda_i$, where γ is the propeller's drag-to-thrust ratio, and $\sigma_i \in \{-1, 1\}$ specifies the propeller's rotation direction (with $\sigma_i = 1$ for clockwise rotation). The individual aerodynamic wrench generated from the i -th propeller, applied to the UAV's body at the origin of Ψ_{p_i} , is expressed in Ψ_{p_i} as

$$\mathbf{W}_c^{p_i} = \lambda_i(0, 0, \gamma \sigma_i, 0, 0, 1)^\top. \quad (6.4)$$

By summing over i , the cumulative aerodynamic control wrench \mathbf{W}_c^B from the total number of rotors N_p , expressed in Ψ_B , can be written as

$$\mathbf{W}_c^B = \sum_i^{N_p} \mathbf{Ad}_{\mathbf{H}_B^{p_i}}^\top \mathbf{W}_c^{p_i}, \quad (6.5)$$

which can be expanded as

$$\begin{pmatrix} \tau_c^B \\ f_c^B \end{pmatrix} = \sum_i^{N_p} \lambda_i \begin{pmatrix} \mathbf{R}_{p_i}^B & \tilde{\xi}_i \mathbf{R}_{p_i}^B \\ \mathbf{0} & \mathbf{R}_{p_i}^B \end{pmatrix} \begin{pmatrix} \gamma \sigma_i \hat{\mathbf{z}} \\ \hat{\mathbf{z}} \end{pmatrix} = \sum_i^{N_p} \lambda_i \begin{pmatrix} \gamma \sigma_i \mathbf{u}_i + \xi_i \wedge \mathbf{u}_i \\ \mathbf{u}_i \end{pmatrix}, \quad (6.6)$$

where the definitions in (6.1) have been used. We can rewrite (6.6) in a compact form as

$$\mathbf{W}_c^B = \mathbf{M} \boldsymbol{\lambda}, \quad (6.7)$$

where $\boldsymbol{\lambda} = (\lambda_1, \dots, \lambda_{N_p})^\top \in \Lambda$ is the rotors thrust vector, and $\mathbf{M} \in \mathbb{R}^{6 \times N_p}$ is the control allocation/distribution matrix.

6.1.2 Classification of Multi-rotor UAVs

As shown in (6.7), the UAV's rotors configuration defines the mapping matrix \mathbf{M} which maps the allowable propellers' thrust space Λ to the allowable aerodynamic control wrench space \mathbb{W} . For fixed-tilt UAV designs, \mathbf{M} is a constant matrix, while for variable-tilt designs, it is a function of N_a angles representing the number of additional actuators used to actively-tilt the propellers.

For the case of a fixed-tilt design concept, the UAV can be classified as follows: if $\text{rank}(\mathbf{M}) < 6$, then the UAV is said to be *underactuated*, if $\text{rank}(\mathbf{M}) = 6$ and $N_p = 6$, then the UAV is *fully-actuated*, and if $\text{rank}(\mathbf{M}) = 6$ and $N_p > 6$, then the UAV is *over-actuated*, i.e fully-actuated with redundancy. The variable-tilt concepts have the advantage of converting from one class to another as the rotors are actively-tilted and consequently $\text{rank}(\mathbf{M})$ changes.

The structure of the allowable thrust space Λ depends on the type of propellers used in the UAV's design; whether the propeller has unidirectional or bidirectional thrust generation capability. In general, Λ can be expressed as

$$\Lambda = \{\boldsymbol{\lambda} \in \mathbb{R}^{N_p} \mid 0 \leq \lambda_i \leq \lambda_{\max} \text{ or } |\lambda_i| \leq \lambda_{\max}\}, \quad (6.8)$$

depending on whether the i -th propeller is unidirectional or bidirectional, for $1 \leq i \leq N_p$, with the assumption that all propellers have the same thrust generation capabilities and that bidirectional rotors are symmetric in their maximum thrust produced, which is common in practice. The allowable aerodynamic wrench space \mathbb{W} is simply the image of Λ under the map \mathbf{M} . In the case that \mathbb{W} is large enough such that the UAV is able to produce an aerodynamic wrench that fully counteracts gravity in any direction in Ψ_B , the UAV is classified as an *omnidirectional* vehicle.

6.2 Survey of Fixed-Tilt Concepts

In this section, we present the survey of fixed-tilt multirotor UAV designs which have been classified into *nine* different concepts, listed in Table 6.1.

Table 6.1: The abbreviations of the fixed-tilt UAV concepts described in Sec. 6.2.

Concept	Abbreviation
Quadrotor with four horizontal rotors	Quad4Hor
Hexarotor with canted rotors	HexC
Hexarotor with canted and dihedral rotors	HexCD
Coaxial Hexagon with 12 canted rotors	CoHexC
Double tetrahedron hexarotor	HexDTet
Heptarotor with minimized frame	HeptF
Heptarotor with maximized wrench	HeptW
Octarotor cube	OctCu
Octarotor beam	OctB

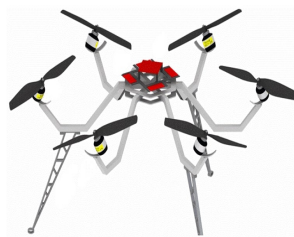
Each fixed-tilt concept is also displayed in Fig. 6.2, along with an illustrative plot of its rotor configurations. Moreover, in Table 6.2, the mapping matrix variables of the concepts are presented, which include the rotor displacements ξ_i , orientations \mathbf{u}_i , rotation direction σ_i , as well as the design parameters selected differently in different versions of the concept.

Quadrotor with four horizontal rotors

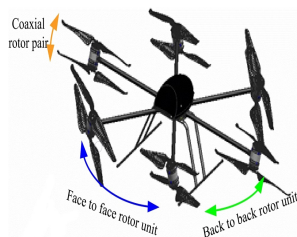
The first concept is an extension of the conventional quadrotor which achieves full-actuation by adding four (unidirectional) horizontal rotors (indexed 5-8). There have been two different implementations of this concept in the literature. In the work of von Frankenberg and Nokleby [2017], the additional rotors are positioned between the quadrotor rotor arms, as shown in Fig. 6.2a. As a result, these added rotors do not create a moment around the CoM and the airflow interference between the rotors is minimized. The other implementation is by Salazar et al. [2009] with the horizontal rotors are located under the vertical rotors. However, the interference of airflow in the design of [Salazar et al., 2009] has negative effects on the controllability of the UAV. It is also worth mentioning that the work [Salazar et al., 2009] was one of the earliest attempts to obtain horizontal actuation with a multirotor UAV.

Hexarotor with Canted Rotors

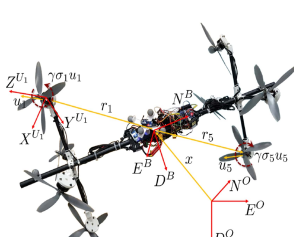
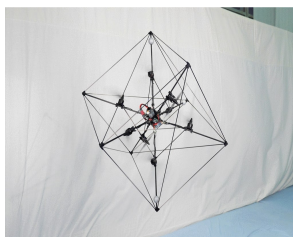
The HexC concept (Fig. 6.2b) can be considered the simplest modification to conventional multirotors in order to achieve fully actuated flight. The rotor positioning is the same as the conventional hexarotor, with all six rotors placed on the vertices of a planar hexagon. Full actuation is achieved by tilting the



(a) Quad4Hor [von Frankenberg and Nokleby, 2017] (b) HexC [Jiang and Voyles, 2013] (c) HexCD [Rajappa et al., 2015]



(d) CoHexC [Lei et al., 2017] (e) HexDTet [Toratani, 2012] (f) HeptF [Nikou et al., 2015]



(g) HeptW [Tognon and Franchi, 2018] (h) OctCu [Brescianini and D'Andrea, 2016] (i) OctB [Park et al., 2018]

Figure 6.2: The Fixed-Tilt Concepts surveyed in this thesis.

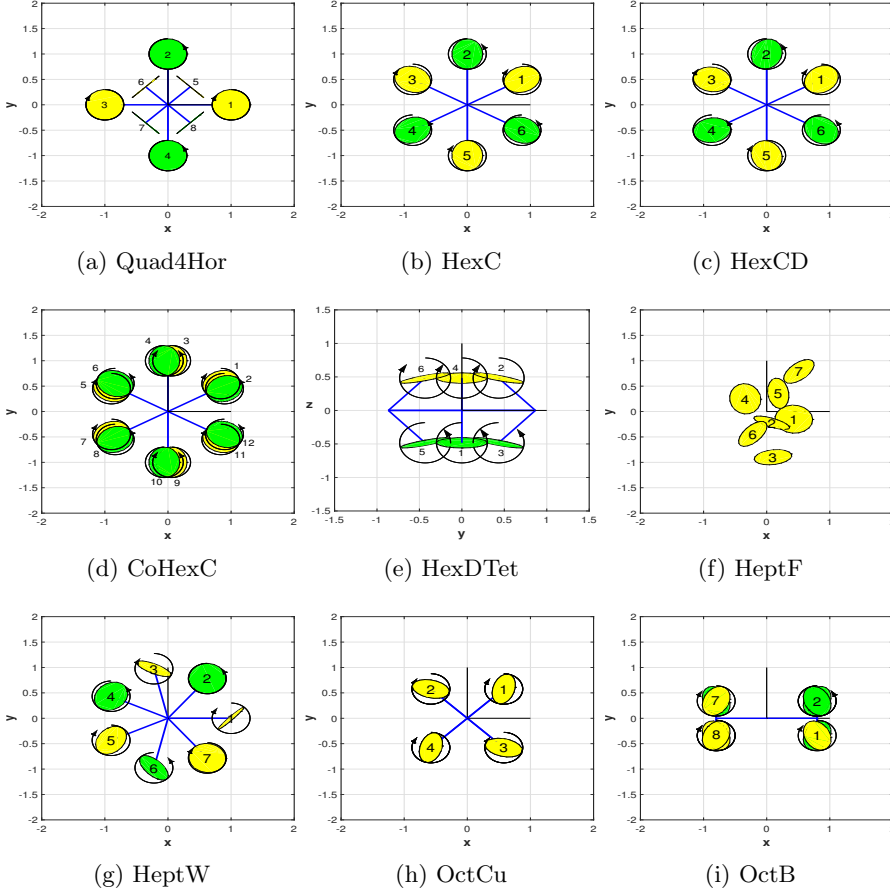


Figure 6.3: Illustration of the top/side view of the rotor configuration for each fixed-tilt concept. Clockwise rotating rotors are colored yellow, while the counter-clockwise ones are displayed in green.

Concept	Index (i)	Rotation Direction (σ_i)	Orientation (u_i)	Displacement (ξ_i)	Fixed Parameters
Quad4Hor	1 - 4	$\sigma_1 = \sigma_3 = 1,$ $\sigma_2 = \sigma_4 = -1$	$u_i = (0, 0, 1)$	$\xi_i = (Lc_{\psi_i}, Ls_{\psi_i}, 0)$	$\psi_i = (i - 1)\frac{\pi}{2}$
	5 - 8	$\sigma_5 = \sigma_6 = 1,$ $\sigma_7 = \sigma_8 = -1$	$u_i = (c_{\psi_i}, s_{\psi_i}, 0)$	$\xi_i = (\bar{L}c_{\psi_i}, \bar{L}s_{\psi_i}, 0)$	$\psi_i = (i - 1)\frac{\pi}{2} + \tilde{\psi}$
HexC	1 - 6	$\sigma_i = (-1)^{i+1}$	$u_i = (s_{\psi_i}s_{\alpha_i}, -c_{\psi_i}s_{\alpha_i}, c_{\alpha_i})$	$\xi_i = (Lc_{\psi_i}, Ls_{\psi_i}, 0)$	$\psi_i = (i - 1)\frac{\pi}{3} + \frac{\pi}{6},$ $\alpha_i = \hat{\alpha}(-1)^{i+1}$
HexCD	1 - 6	$\sigma_i = (-1)^{i+1}$	$u_i = (c_{\psi_i}s_{\beta_i} + s_{\psi_i}s_{\alpha_i}c_{\beta_i},$ $s_{\psi_i}s_{\beta_i} - c_{\psi_i}s_{\alpha_i}c_{\beta_i},$ $c_{\alpha_i}c_{\beta_i})$	$\xi_i = (Lc_{\psi_i}, Ls_{\psi_i}, 0)$	$\psi_i = (i - 1)\frac{\pi}{3} + \frac{\pi}{6},$ $\alpha_i = \hat{\alpha}(-1)^{i+1}$ $\beta_i = \tilde{\beta}$
CoHexC	1 - 12	$\sigma_i = (-1)^{i+1}$	$u_i = (s_{\psi_i}s_{\alpha_i}, -c_{\psi_i}s_{\alpha_i}, c_{\alpha_i})$	$\xi_i = (Lc_{\psi_i}, Ls_{\psi_i}, 0)$	$\psi_i = (i - 1)\frac{\pi}{3} + \frac{\pi}{6},$ $\alpha_i = \hat{\alpha}(-1)^{i+1}$
HexDTet	1 - 6	$\sigma_i = (-1)^i$	$u_i = (c_{\psi_i}c_{\eta}, s_{\psi_i}c_{\eta}, s_{\eta})$	$\xi_i = (Lc_{\psi_i}, Ls_{\psi_i}, (-1)^{i+1}Ls_{\eta})$	$\psi_i = (i - 1)\frac{\pi}{3}$
HeptF	1 - 7	$\sigma_i = 1$	$u_1 = (0.08, 0.39, 0.92)$ $u_2 = (-0.33, -0.90, 0.29)$ $u_3 = (0.13, -0.87, -0.48)$ $u_4 = (0.56, 0.08, 0.82)$ $u_5 = (0.83, 0.11, -0.55)$ $u_6 = (-0.66, 0.57, -0.49)$ $u_7 = (-0.59, 0.62, -0.51)$	$\xi_1 = (0.43, -0.15, -0.44)$ $\xi_2 = (0.08, -0.22, -0.14)$ $\xi_3 = (0.1, -0.9, -0.2)$ $\xi_4 = (-0.34, 0.25, 0.006)$ $\xi_5 = (0.184, 0.359, -0.254)$ $\xi_6 = (-0.22, -0.44, -0.04)$ $\xi_7 = (0.51, 0.79, -0.06)$	
HeptW	1 - 7	$\sigma_i = (-1)^{i+1}$	$u_1 = (-0.71, 0.67, 0.11)$ $u_2 = (0.11, 0.04, -0.98)$ $u_3 = (0.41, 0.85, 0.31)$ $u_4 = (0.44, -0.35, 0.81)$ $u_5 = (0.57, -0.38, -0.72)$ $u_6 = (-0.64, -0.58, -0.48)$ $u_7 = (-0.17, -0.26, 0.94)$	$\xi_i = (Lc_{\psi_i}, Ls_{\psi_i}, 0)$	$\psi_i = (i - 1)\frac{2\pi}{7}$
OctCu	1 - 8	$\sigma_i = 1$	$u_1 = u_8 = (-a, b, c)$ $u_2 = u_7 = (b, a, -c)$ $u_3 = u_6 = (-b, -a, c)$ $u_4 = u_5 = (a, -b, c)$	$\xi_1 = -\xi_8 = (d, d, d)$ $\xi_2 = -\xi_7 = (-d, d, d)$ $\xi_3 = -\xi_6 = (d, -d, d)$ $\xi_4 = -\xi_5 = (-d, -d, d)$	$a = 1/2 + 1/\sqrt{12}$ $b = 1/2 - 1/\sqrt{12}$ $c = 1/\sqrt{3}$ $d = 0.577\text{m}$
OctB	1 - 8	$\sigma_1 = \sigma_6 = 1$ $\sigma_7 = \sigma_8 = 1$ $\sigma_2 = \sigma_3 = -1$ $\sigma_4 = \sigma_5 = -1$	$u_1 = u_5 = (a, b, a)$ $u_2 = u_6 = (a, b, -a)$ $u_3 = u_7 = (a, -b, a)$ $u_4 = u_8 = (a, -b, -a)$	$\xi_1 = -\xi_5 = (L_1, -L_2, L_2)$ $\xi_2 = -\xi_6 = (L_1, L_2, L_2)$ $\xi_3 = -\xi_7 = (L_1, -L_2, -L_2)$ $\xi_4 = -\xi_8 = (L_1, L_2, -L_2)$	$a = 0.68$ $b = 0.28$ $L_1 = 0.4\text{m}$ $L_2 = 0.17\text{m}$

Table 6.2: Variables of the Mapping Matrix for Fixed-Tilt Concepts

rotors around the axis collinear with the rotor arm. This tilting, denoted by α , is referred to as canting as discussed in Sec. 6.1.1. By canting the rotors, they will not only produce thrust vertically, but also horizontally. The canting angle of all rotors are equal and the canting direction and rotation direction of the rotors is alternating (*cf.* Table 6.2), resulting in three symmetric rotor pairs with opposite rotation direction. Due to the design's symmetry, the drag torque of the rotors is counteracted. The amount of canting depends on the application: a large cant angle leads to high horizontal forces, while a small cant angle leads to higher flying efficiency. The angle is limited by the minimum required upward thrust for overcoming gravity.

This concept has been first proposed by Voyles and Jiang [2012] and successfully demonstrating experiments of fully-actuated flight with a cant angle $\alpha = 20^\circ$. The same authors have shown in [Jiang and Voyles, 2013, 2014] that the HexC concept has better disturbance rejection capabilities to lateral wind gusts compared to the conventional hexarotor. A higher cant angle of 47° has been used by Rashad et al. [2019b] in order to maximize the horizontal force applied in a contact-based scenario. An experimental demonstration of a 2kg HexC platform was able to apply 1kg of force to a vertical surface without pitching. Omnidirectional versions of the HexC concept have been proposed in [Roque and Ventura, 2016; Kaufman et al., 2014]. In [Roque and Ventura, 2016] a version, with a cant angle optimized for maximum wrench, has been proposed as a cobot for space applications. Due to the absence of gravity in the intended application, the optimal cant angle is higher: 55° instead of 47° of [Rashad et al., 2019b]. Finally, another omnidirectional version was proposed in [Kaufman et al., 2014], which utilized variable-pitch propellers in order to generate bidirectional thrust, unlike all previously presented designs which use fixed-pitch unidirectional propellers.

Hexarotor with canted and dihedral rotors

The HexCD concept, shown in Fig. 6.2c, is considered an extension of the HexC concept. In its design, the rotors of the hexarotor are not only canted but also tilted along the axis perpendicular to the rotor's arm, which called a dihedral angle (β), as discussed in Sec. 6.1.1. This concept is the most studied/used design in the literature so far with different angles optimized for different criteria. The concept was originally proposed by Rajappa et al. [2015] who chose α and β in order to minimize the required total thrust for full-pose UAV controllability for a given trajectory. The optimal angles are shown to depend heavily on the trajectory, for instance for an in-hover pitching maneuver, the optimal dihedral angle was shown to be nonzero. Moreover, it was shown in [Rajappa et al., 2015] that the direction of the dihedral angle (positive or negative) does not influence the performance of the UAV. However, the maximum dihedral angle is more limited by the UAV's frame when the rotor

is tilted inward ($\beta < 0$), thus all rotors are tilted outward ($\beta > 0$).

The HexCD concept was also used for physical interaction in [Staub et al., 2018; Ryll et al., 2017] with angles $\alpha = 30^\circ$ and $\beta = 10^\circ$. Another study in [Mehmood et al., 2016] analyzed how different angles change the maximum achievable lateral-accelerations as well as the dynamic maneuverability of the UAV. Moreover, in [Jiang et al., 2017, 2018], a multi-objective optimization was performed for determining the cant and dihedral angles for a physical interaction application. The objective function was chosen as a weighted sum of three criteria; the maximum lateral forces, the flying efficiency, and the dihedral effect. The interesting result in [Jiang et al., 2017, 2018] is that the optimal set of angles can be chosen in most cases such that $\beta = 0$. A similar result was shown in [Tadokoro et al., 2017] by using the dynamic maneuverability as the optimization criteria. In such a case, the HexCD concept becomes equivalent to the HexC discussed previously.

The reason for favoring $\beta = 0$ is related to the fact that a non-zero dihedral angle causes part of the generated thrust to be transformed into internal stresses in the $\hat{\mathbf{x}}_{p_i}$ axis. Consequently, this reduces the torque contribution of the rotor (mainly around the $\hat{\mathbf{z}}_B$ axis) and thus the UAV's maneuverability. This implies that the HexC concept has higher maneuverability compared to the HexCD concept. However, a recent study in [Michieletto et al., 2018] has proved that a non-zero β provides the HexCD concept with robustness against rotor failure, a feature which a HexC UAV does not have.

Coaxial Hexagon with Twelve Canted Rotors

This concept (Fig. 6.2d), by Lei et al. [2017], consists of twelve rotors that are positioned in pairs of two in a hexagonal configuration. These pairs are called coaxial rotor pairs, because the rotors rotate around the same axis. Both rotors rotate at the same speed but in opposite directions, such that the drag torque from one rotor is counteracted by the other. The advantage of coaxial rotor pairs is that the amount of thrust that can be produced increases compared to a single rotor. As for the interference of airflow between the top and bottom rotor, the drawbacks are less severe in this design (and for coaxial rotors in general) compared to the Quad4Hor design of [Salazar et al., 2009] as both rotors have the same speed. Finally, some preliminary experiments on a test-rig have been carried out in [Lei et al., 2017], but unfortunately the cant angle by which the rotors were tilted was not provided by the authors.

Double Tetrahedron Hexarotor

This concept, proposed by Toratani [2012], can be considered the first attempt to produce a hexarotor with non-coplanar rotors. The design consists of six rotors restricted to the shape of two opposite tetrahedrons as shown in Fig.

6.2e. Both tetrahedrons have a common base, which lies in the $\hat{\mathbf{x}}_B\text{-}\hat{\mathbf{y}}_B$ plane. Each one of the six rotors is attached on an edge of the two tetrahedrons and the design parameter of this concept is the elevation angle η , which is the angle between the common base and the edge containing a rotor. All rotors have the same elevation angle as seen in the rotor configuration in Fig. 6.2e. As mentioned in Table 6.2, the elevation angle η was chosen in [Toratani, 2012] as 75° . This choice of angle was based on an optimization process, however the authors in [Toratani, 2012] didn't provide any details on the optimization criteria. The work of designing non-coplanar hexarotors was also studied in [Kiso et al., 2015], in which the dynamic maneuverability and maximum lateral-translations measures were used to compute the optimal configurations of the three rotor-pairs.

Heptarotor with Minimized Frame

The UAV concept, proposed by Nikou et al. [2015] and shown in Fig. 6.2f, was one of the first attempts in the literature to create an omnidirectional UAV with unidirectional rotors only. It was shown mathematically that a minimum of seven rotors is required to achieve this. The rotor configurations have been optimized to minimize the volume of the frame. The airflow interference between rotors has been taken into account in the optimization by imposing a minimum distance between the rotors such that airflow interference is avoided. The aforementioned distance was determined empirically based on CFD-analysis (computational fluid dynamics). Since no symmetry requirements were imposed on the UAV, all rotors were designed to rotate clockwise.

Heptarotor with Maximized Wrench

The concept (Fig. 6.2g), proposed by Tognon and Franchi [2018], is another omnidirectional UAV with seven unidirectional rotors, similar to the HeptF concept presented in the previous section. The rotors are placed on the vertices of a heptagon in the horizontal plane and rotate in alternating direction. The orientation of the rotors is optimized for maximum omnidirectional wrench generation. The UAV concept was only introduced in [Tognon and Franchi, 2018] and an operational prototype has been presented in [Hamandi et al., 2020].

Octarotor Cube

The concept (Fig. 6.2h), designed by Brescianini and D'Andrea [2016], is considered the first multirotor UAV to successfully perform omnidirectional flight. The rotor positions are fixed to the vertices of a cube, while the orientation of the rotors are optimized for maximizing the vehicle's agility which is measured

by the maximum attainable omnidirectional wrench. All rotors are designed to rotate in the same direction and symmetric propellers have been used to provide bidirectional thrust. The UAV is surrounded by a cage-like frame to allow human-robot interaction without risk of injury from collision with the propellers. A detailed analysis of the proposed UAV concept and prototype can be found in [Brescianini and D’Andrea, 2018].

Octarotor Beam

The concept by Park et al. [2018], shown in Fig. 6.2i, is an omnidirectional octarotor UAV, with a beam-like shape. The UAV was designed for aerial physical-interaction tasks that require full wrench generation. This concept is considered a second-generation version of the authors’ previously designed beam-like hexarotor in [Park et al., 2016]. Each side of the beam contains four rotors placed on the vertices of a square with rotors 1 and 6-8 rotating clockwise and rotors 2-5 rotating counterclockwise. The rotor configurations are optimized for omnidirectional wrench generation, while imposing the minimum rotor distance such that airflow interference is avoided. The UAV achieves omnidirectional flight by the use of bi-directional rotors. The bidirectional thrust generation is achieved by stacking two unidirectional propellers in the opposite direction. Thus, the OctB design proposed contains 16 propellers. Contrary to the preliminary work in [Park et al., 2016], the authors presented a technique in [Park et al., 2018] to shape the wrench generation by weighing the different wrench generation directions. Finally, the OctB concept has been utilized to create a serial-chain of multiple fully-actuated UAVs connected by spherical joints in [Yang et al., 2018]. The highly-complex system was shown to perform several experimental dexterous manipulation tasks.

6.3 Survey of Variable-Tilt Concepts

In the same style of the previous section, here we present the survey of *six* variable-tilt multirotor concepts. The figures of the concepts can be found in Fig. 6.4, while the mapping matrix variables can be found in Table 6.4.

Quadrotor with Variable Cant Rotors

The concept, shown in Fig. 6.4a, was introduced by Ryll et al. [2012]. The full-actuation is achieved by adding four tilting actuators to the rotors of a conventional quadrotor. These actuators actively cant each rotor individually around the $\hat{\mathbf{x}}_{p_i}$ axis. Since the rotors used were unidirectional and the tilting actuators had maximum limits, the maximum UAV’s achievable pitch/roll angle during hovering was limited to approximately 30 degrees.

Table 6.3: The abbreviations of the variable-tilt UAV concepts described in Sec. 6.3.

Concept	Abbreviation
Quadrotor with variable cant rotors	QuadvC
Quadrotor with variable dihedral rotors	QuadvD
Quadrotor with variable cant and dihedral rotors	QuadvCD
Quadrotor with coupled variable cant and dihedral rotors	QuadvCDc
Hexarotor with variable cant rotors	HexvC
Hexarotor with coupled variable cant rotors	HexvCc

Table 6.4: Variables of the Mapping Matrix for Variable-Tilt Concepts

Concept	Index (i)	Rotation Direction (σ_i)	Orientation (u_i)	Displacement (ξ_i)	Fixed Parameters	Active Tilt
QuadvC	1 - 4	$\sigma_i = (-1)^{i+1}$	$u_i = (s_{\psi_i} s_{\alpha_i}, -c_{\psi_i} s_{\alpha_i}, c_{\alpha_i})$	$\xi_i = (Lc_{\psi_i}, Ls_{\psi_i}, 0)$	$\psi_i = (i-1)\frac{\pi}{2}$	α_i
QuadvD	1 - 4	$\sigma_1 = \sigma_2 = 1$ $\sigma_3 = \sigma_4 = -1$	$u_i = (c_{\psi_i} s_{\beta_i}, s_{\psi_i} s_{\beta_i}, c_{\beta_i})$		$\psi_i = (i-1)\frac{\pi}{2}$	β_i
QuadvCD	1 - 4	$\sigma_i = (-1)^{i+1}$	$u_i = (c_{\psi_i} s_{\beta_i} + s_{\psi_i} s_{\alpha_i} c_{\beta_i},$ $s_{\psi_i} s_{\beta_i} - c_{\psi_i} s_{\alpha_i} c_{\beta_i},$ $c_{\alpha_i} c_{\beta_i})$		$\psi_i = (i-1)\frac{\pi}{2}$	α_i β_i
QuadvCDc	1 - 4				$\psi_i = (i-1)\frac{\pi}{2}$ $\alpha_1 = -\alpha_3 = \alpha_m$ $\alpha_2 = -\alpha_4 = \beta_m$ $\beta_1 = -\beta_3 = \beta_m$ $\beta_2 = -\beta_4 = -\alpha_m$	α_m β_m
HexvC	1 - 6	$\sigma_i = (-1)^{i+1}$	$u_i = (s_{\psi_i} s_{\alpha_i}, -c_{\psi_i} s_{\alpha_i}, c_{\alpha_i})$	$\xi_i = (Lc_{\psi_i}, Ls_{\psi_i}, 0)$	$\psi_i = (i-1)\frac{\pi}{3}$	α_i
HexvCc	1 - 6				$\psi_i = (i-1)\frac{\pi}{3}$ $\alpha_i = \alpha_m(-1)^{i+1}$	α_m

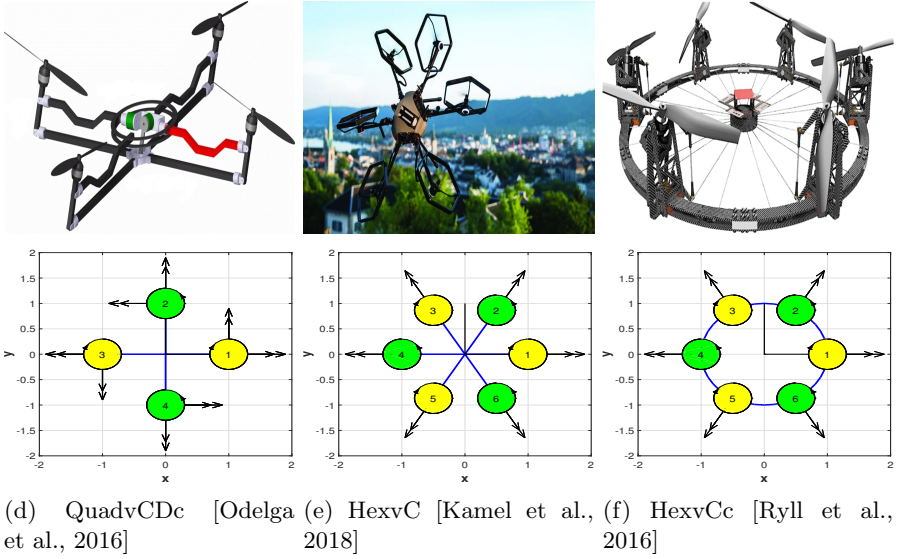
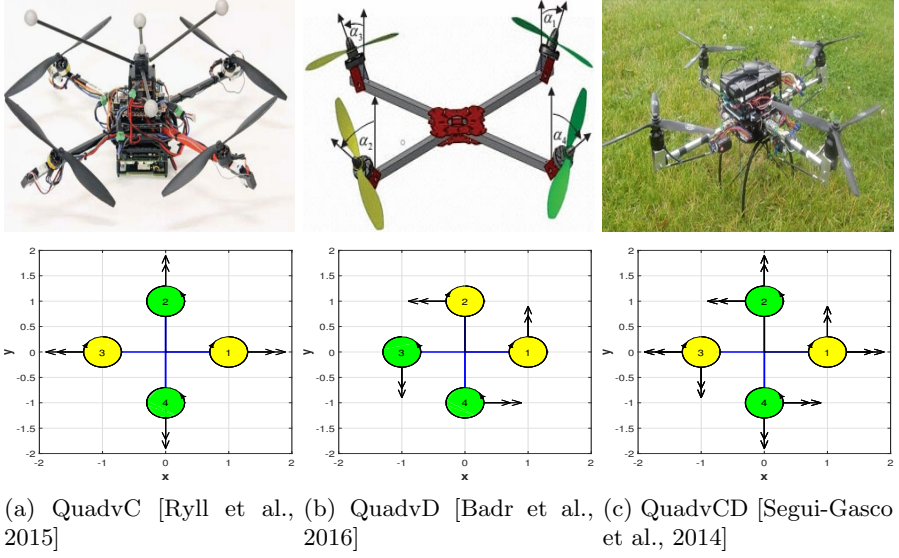


Figure 6.4: Figures of Variable-Tilt Concepts. Each concept is complemented with an illustration of the top view of the rotor configuration. Clockwise rotating rotors are colored yellow, while the counter-clockwise ones are displayed in green, and that double arrows indicate the active tilt-axis.

Quadrotor with Variable Dihedral Rotors

This concept (Fig. 6.4b), by Badr et al. [2016], resembles the QuadvC concept presented in the previous section. Instead of the cant angle, the dihedral angle is actively tilted by an extra actuator. Contrary to the cant angle, the inward dihedral angle is limited by the frame, which interferes with the rotor blades at large dihedral angles. Another difference with variable cant rotors is that dihedral angle does not contribute to the yaw torque, effectively reducing the total torque.

Quadrotor with Variable Cant and Dihedral Rotors

This concept (Fig. 6.4c), by Segui-Gasco et al. [2014], is a combination of the last two concepts. The UAV has two actuators added to each rotor of a conventional quadrotor to actively tilt the rotors around that cant and dihedral angle. Thus, the UAV has 8 actuators for the thrust vectoring. For the dihedral tilt actuation, a push pull mechanism was used, which limits the maximum achievable dihedral angle. However, an alternative actuation method for the cant and dihedral tilting was proposed by Ryll et al. [2015] that can be used to extend the range of achievable cant and dihedral angles.

Quadrotor with Coupled Variable Cant and Dihedral Rotors

This concept (Fig. 6.4d) is by Odelga et al. [2016], who proposed to actuate the angle of all quadrotor propellers with a single actuator using parallelogram linkage mechanism, instead of actuating each rotor separately. This linkage mechanism tilts all rotors in the same direction. For a second rotation direction another similar linkage is used. In this way all rotors always have the same orientation and cannot be orientated individually contrary to the QuadvCD concept. A drawback of such coupling feature is that the maximum tilting angle of all rotors in all directions is now limited by the maximum inward dihedral angle. The main advantage however is that this actuation method reduces the amount of actuators required for cant and dihedral actuation from eight to two. In [Odelga et al., 2016] only a conceptual proposition of the design has been provided and a working prototype has not yet been reported.

Hexarotor with Variable Cant Rotors

The concept shown in Fig. 6.4e and presented in [Kamel et al., 2018] is the first variable-tilt concept to achieve successful omnidirectional flight. The concept contains a canting actuator added to each rotor of a conventional hexarotor to achieve omnidirectional flight with unidirectional thrust generation. The UAV was developed by a group of students from Swiss Federal Institute of Technology (ETH Zurich) and Zurich University of the Arts. A modified version of

Table 6.5: Table of optimization criteria for designing fixed-tilt concepts

Optimization Criteria	References
Max. allowed wrench	[Rashad et al., 2017], [Roque and Ventura, 2016], [Jiang et al., 2017],[Jiang et al., 2018], [Tognon and Franchi, 2018],[Brescianini and D’Andrea, 2018],[Park et al., 2018]
Max. allowed accelerations	[Mehmood et al., 2016],[Kiso et al., 2015]
Min. control effort	[Rajappa et al., 2015]
Max. flying efficiency	[Jiang et al., 2017],[Jiang et al., 2018]
Min. dihedral effect	[Jiang et al., 2018]
Max. dynamic maneuverability	[Tadokoro et al., 2017], [Kiso et al., 2015]
Min. volume of vehicle	[Nikou et al., 2015]

this concept has been proposed in [Bodie et al., 2018] for contact-based aerial inspection applications. The UAV design used in [Bodie et al., 2018] had coaxial rotors in order to increase the thrust generation capabilities of the UAV, with all other design aspects kept the same.

Hexarotor with Coupled Variable Cant Rotors

Finally, the concept (Fig. 6.4f), by Ryll et al. [2016], uses a single actuator to cant all rotors of a hexarotor. This coupled rotor tilting is achieved using a wire mechanism. The cant angle is alternating, similar to the HexC concept, while the maximum achievable cant angle is limited by the frame. The advantage of a single actuator instead of six actuators to cant the rotors is that the energy consumption and total mass of the system is greatly reduced compared to the parallel mechanism of the QuadvCDc concept. However, the maneuverability of the UAV is reduced by the lower bandwidth of the tilting mechanism using wires.

6.4 Conclusion

In this chapter we presented a review of multirotor UAV concepts that have been proposed in the literature for the past decade. The concepts were classified into fixed-tilt and variable tilt UAVs in which the mapping matrix is structurally different. Moreover, all design variables for reconstructing the mapping matrix of all the concepts were provided as well. We conclude with some remarks on different issues related to the work.

First, the HexC and HexCD concepts are the most widely used ones in

the literature, which is a consequence of their mechanical simplicity and the ease of transforming the (already existing) conventional hexarotor into a fully-actuated vehicle. Moreover, the mechanical simplicity of these concepts is also translated into reduced effort for optimizing the design for a given application due to the low number of design parameters.

Second, different fixed-tilt designs were optimized based on a variety of criteria summarized in Table 6.5. The most used measure is maximizing the generated control wrench (6.7), either in specific directions or in all directions (for omnidirectional UAVs). However, it is important to know that equation (6.7) is based on a static analysis and does not take the UAV's inertia parameters into account like the dynamic maneuverability measure or the generated control accelerations measure. As an example of the false intuition this criteria can provide, the maximum wrench of the CoHexC concept would be twice that of the HexC design (assuming identical propellers and cant angle). However, taking into account that the CoHexC has (roughly) double the inertia parameters as the HexC, the maximum accelerations is (roughly) the same.

Finally, we close with a remark about the control-system architecture of the presented UAVs. In most of the works surveyed in this paper, a two stage control-architecture is used where first the control wrench (6.7) is considered as a virtual input to the rigid body model of the UAV. Then the mapping matrix is used to compute the desired propeller thrusts. For fixed-tilt concepts, this involves computing the inverse/pseudo-inverse of the \mathbf{M} matrix, which is guaranteed to exist as shown in Sec. 6.1.2. However, for variable-tilt designs, the control allocation problem is more involved as the rank of the \mathbf{M} matrix might change during operation and the UAV might operate in an underactuated configuration. This calls for nonlinear control allocation techniques in addition to control algorithms that can handle the different UAV operating conditions, like e.g. [Franchi et al., 2018].

CHAPTER 7

ENERGY-BALANCING PASSIVITY-BASED CONTROL OF A FLYING END-EFFECTOR

There is an increasing interest in the aerial robotics community to transition the use of unmanned aerial vehicles (UAVs) from passive tasks, like visual inspection and remote sensing, to active interaction tasks, like contact-based inspection and manipulation. Compared to ground-based manipulators, control of physical interaction using UAVs is more challenging as the controller is required to constantly overcome gravity, stabilize the UAV's inherently unstable dynamics, comply with the environment's constraints, and exert the required forces and torques on the environment.

This chapter reports the results of [Rashad et al., 2019a] which addresses the interaction control problem of a fully-actuated UAV in the port-Hamiltonian framework. Compared to other approaches for aerial interaction, like endowing conventional UAVs with a robotic manipulator arm (*cf.* Ch.1), a fully-actuated UAV has the ability to exert lateral forces and is mechanically simpler as it does not suffer from inertial coupling and variations in its center of mass. Therefore, a fully-actuated UAV is controlled simply as a *flying end-effector*.

There are several methods that have been applied in the robotics literature for the interaction control problem of both ground and aerial manipulators. One method is to use pure motion-controllers, which in general are not suited for interaction as they are designed for minimizing tracking errors and rejecting disturbances. Another method is to use hybrid pose/wrench controllers, which control the interaction wrench in certain directions and control the pose in other “orthogonal” directions. From a practical point of view, such control approach requires an accurate model of the aerial robot and the contact properties of



Figure 7.1: The fully-actuated UAV used for experimental validation of the proposed controller. The photo shows the UAV hovering at a non-zero pitch and roll angle in free-flight.

the environment, which usually limits its applications. From a mathematical point of view, hybrid pose/wrench control techniques suffers from a geometric inconsistency problem related to the orthogonality of wrenches and twists Duffy [1990].

The interaction behavior of an aerial robot can be modeled effectively and elegantly by power ports in port-Hamiltonian systems theory. In this paradigm the interaction is perceived as an exchange of energy between the aerial robot and the environment, instead of an independent control of pose or wrench. Thus, the control system of a robot is no longer perceived as a signal processor, but as a virtual physical system that is connected to the aerial robot via power ports. This is the underlying basic idea of the widely used impedance control technique introduced in Hogan [1985c].

The concepts considered in this work are presented in a geometrically consistent manner by modeling the flying-end effector as a floating rigid body with the special Euclidean group $SE(3)$ as its configuration manifold. Therefore, the designed motion and interaction controllers will be invariant to changes of the inertial coordinate frame, as we do not treat the rotational dynamics and the translational dynamics of the UAV separately [Bullo and Murray, 1999].

Our work is inspired by Fasse and Broenink [1997]; Fasse [1997]; Stramigioli [2001] in which the geometric impedance control problem of ground manipulators is studied. In Fasse and Broenink [1997], a geometric impedance controller was designed in the Lagrangian framework for a rigid manipulator, which only allowed diagonal stiffness and damping parameters. The work of Fasse and Broenink [1997]; Fasse [1997] was generalized in Stramigioli [2001]

in the port-Hamiltonian framework as an interconnection of mechanical structures, for robot grasping. The impedance controller of Stramigioli [2001] enabled achieving arbitrary stiffness control and was invariant to changes of the inertial coordinate frame.

The main contribution of this chapter is the reformulation of the geometric impedance controller of Stramigioli [2001] as an energy-balancing passivity-based control (EB-PBC) problem for a fully-actuated UAV modeled geometrically on $SE(3)$. We extend the work of Stramigioli [2001] by applying it for both the motion and interaction control of a UAV, in addition to a rigorous mathematical derivation and analysis of the closed loop system in free-flight and during contact. Moreover, we validate the presented controller experimentally on a fully-actuated hexarotor to show that its passivity-based nature allows full exploitation of the UAV's capabilities. This is demonstrated by controlling the UAV near its control input limits without losing stability.

This chapter is outlined as follows: Sec. 7.1 presents a literature survey of the different interaction control methods implemented for flying manipulators. Sec. 7.2 discusses the port-Hamiltonian dynamic model of the UAV that will be used for the control system design. In Sec. 7.3, we present the derivation of the controller using the EB-PBC method along with the stability analysis of the closed-loop system. Then, in Sec. 7.4 we present the experimental validation results of the derived controller on a physical aerial robot, and we conclude this chapter in Sec. 7.5.

7.1 Survey of Aerial Interaction Control Methods

In this section, a literature review of the different control approaches used for physical interaction in the context of aerial robotics will be presented. For an introduction to the subject, the reader is referred to [Villani and De Schutter, 2016] for the topic of interaction using ground-based manipulators, to [Ollero and Merino, 2004] for a review of control and perception techniques of aerial robots, and to [Ruggiero et al., 2018] for a review of interaction using aerial manipulators.

7.1.1 Hybrid Pose/Wrench and Motion Control

In the context of hybrid pose/wrench control of UAVs, Bellens et al. [2012] applied this approach to control a quadrotor UAV. The pose controller consisted of a standard cascaded PID, while another PI algorithm was adopted for the interaction wrench regulation. The interaction wrench was estimated based on an offline mapping to the quadrotor's control inputs, which is only valid when the UAV is in contact. In [Darivianakis et al., 2014; Alexis et al.,

2016], a controller based on hybrid model predictive control was proposed. The approach was validated experimentally through an aerial writing application using an underactuated quadrotor. In [Nguyen and Lee, 2013; Nguyen et al., 2015], the authors proposed a hybrid interaction control algorithm and studied the internal dynamics of the interactive quadrotor due to its underactuation. The authors in Papachristos et al. [2014] utilized a hybrid approach where switching between the motion control mode and wrench control mode was achieved through a finite state machine. The switching between modes is conducted based on contact feedback from tactile switches in the end effector. Furthermore, in [Nava et al., 2019], a hybrid force-motion control system was designed by formulating the controller design as a quadratic programming problem that is solved online.

Other works in the literature which used motion-controllers for interaction include [Suseong Kim et al., 2013; Korpela et al., 2014b; Orsag et al., 2014, 2017]. In [Suseong Kim et al., 2013], an adaptive sliding mode controller was implemented on a quadrotor with a 2 DOF manipulator. The external interaction wrench was considered a disturbance to be rejected by the robust controller. In [Korpela et al., 2014b; Orsag et al., 2014], the yaw motion controller of a quadrotor with a 2 DOF arm was used to address the problem of valve turning.

7.1.2 Impedance and Admittance Control

In the context of indirect force control of UAVs, Lippiello and Ruggiero [2012a,b] presented a Cartesian impedance controller for the dynamic model of a quadrotor equipped with a 3-DOF manipulator in the Euler-Lagrange framework. The followed approach was not geometric and this complicates the tuning of the impedance parameters and the generalization of the results. Forte et al. [2012] applied an impedance controller for a ducted-fan UAV. Separate control laws for the manipulator, vertical, and lateral dynamics were designed and validated in simulation. Similarly, in [Fumagalli et al., 2012; Fumagalli and Carloni, 2013; Fumagalli et al., 2014], an impedance controller for a quadrotor was implemented and validated experimentally for contact-based inspection applications using a compliant delta manipulator. Mersha et al. [2014] presented a variable impedance controller for aerial interaction of a quadrotor. A force regulator is implemented as an outer loop of the variable impedance controller. The external force is estimated by the position information and stiffness of the environment, which is assumed to be a linear spring. In [Suarez et al., 2018], a physical-virtual impedance controller was implemented by incorporating a compliant robotic arm with a multi-rotor platform. In [Korpela et al., 2014a] a stiffness control algorithm was used for interaction based on a linear motion controller. The stiffness mapping between the position error and interaction force was chosen as a linear map, which is not geometrically consistent. Cataldi

et al. [2016] followed a multi-layer control admittance control approach for a quadrotor/manipulator system. In addition to representing orientation in local coordinates, the approach depends on an inverse kinematics algorithm that uses null space projectors to resolve redundancy, which yields a non-passive controller.

In [Tomic and Haddadin, 2014; Tomić et al., 2017], the authors presented a unified passivity-based framework for impedance and admittance control. The desired interactive behavior is imposed by cancellation of the nonlinear dynamics of the system and a feedback of the external wrench through an estimation algorithm, while the UAV's rotation was represented using quaternions. The passivity proof of the closed loop system and modifications for underactuated vehicles were presented. In [Ryll et al., 2017, 2019], an admittance controller with an external wrench observer was implemented on a fully-actuated hexarotor platform. The approach relied on the geometric trajectory tracking controller introduced by Lee et al. [2010], in which the controllers for the rotational and translational dynamics are designed separately.

In contrast to our proposed framework, the approaches followed in [Tomic and Haddadin, 2014; Tomić et al., 2017; Ryll et al., 2019] lack consistency in respecting the geometric structure of the configuration space $SE(3)$. Controllers designed in this manner has been shown to suffer from not being invariant to coordinate changes [Bullo and Murray, 1999]. Such geometric inconsistency could lead to many practical problems particularly for interactive robots, *cf.* e.g. [Villani and De Schutter, 2016].

7.1.3 Port-Hamiltonian Control

In recent years there has been an increasing interest in port-Hamiltonian control approaches. The first use of port-based modeling and control concepts in the aerial robotics literature was in Mersha et al. [2011], where stabilization and tracking controllers were derived for generic underactuated vehicles and simulated for a ducted-fan UAV. Although the controllers were designed by standard passivity-based techniques, the presented approach included compensation of the UAV dynamics, non-passive projection, and added robustness by using integral action, which destroyed the passivity of the motion controller. In [Yuksel et al., 2014b,a], the authors used the interconnection and damping assignment PBC (IDA-PBC) approach to change the interactive behavior of a quadrotor. The presented controller, combined with an external wrench observer, was derived in Euler angles and tested in simulations with a passive environment. In [Acosta et al., 2014, 2016], Acosta et al. utilized the IDA-PBC approach for the decentralized control of a quadrotor/manipulator system. The approach was validated through some free-flight simulations.

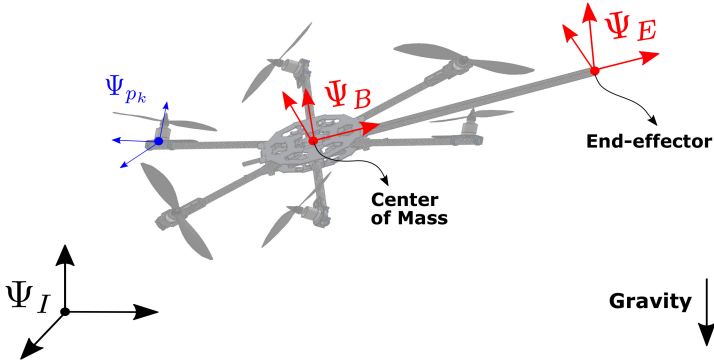


Figure 7.2: Schematic view of the reference frames used to model the UAV.

7.2 Port-Hamiltonian Model of a Flying End-Effector

7.2.1 Vehicle Description

The flying-end effector used in this work is a fully-actuated hexarotor with canted rotors, similar to the work of Ryll et al. [2017]; Jiang et al. [2018]. This specific platform was chosen due to its mechanical simplicity compared to other designs, as surveyed in Ch.6. A conventional hexarotor consists of six parallel propellers placed at the vertices of a planar hexagon, thus it can only generate thrust normal to the rotating plane of the propellers. To modify a traditional hexarotor in order to be fully-actuated, the six rotors should point in different directions. Each rotor's orientation is fixed and parameterized by a cant angle.

The reference frames used to describe the configuration of the UAV are depicted in Fig. 7.2. Let $\{\Psi_I : o_I, \hat{x}_I, \hat{y}_I, \hat{z}_I\}$ denote an orthonormal inertial frame and $\{\Psi_B : o_B, \hat{x}_B, \hat{y}_B, \hat{z}_B\}$ denote a body-fixed frame attached to the vehicle's center of mass and aligned with its principal axes of inertia. We denote the frame associated with the k -th rotor by $\{\Psi_{p_k} : o_{p_k}, \hat{x}_{p_k}, \hat{y}_{p_k}, \hat{z}_{p_k}\}$, with \hat{z}_{p_k} chosen as the direction of the generated thrust, and its origin o_{p_k} coinciding with the center of mass of the rotor. We denote the displacement vector of the k -th rotor in the body-frame Ψ_B by

$$\xi_k := \mathbf{R}_z(\psi_k)[L, 0, 0]^\top \in \mathbb{R}^3,$$

where $\mathbf{R}_z(\cdot) \in SO(3)$ is the standard rotation matrix about the z -axis, $L \in \mathbb{R}^+$ is the distance from the hexarotor's central axis \hat{z}_B to each rotor, and $\psi_k := (k-1)\frac{\pi}{3}$ denotes the heading angle. Moreover, we denote the thrust generation direction of the k -th rotor by $\mathbf{u}_k := \mathbf{R}_{p_k}^B \hat{e}_3 \in \mathbb{S}^2$, where \hat{e}_j is a vector of zeros

with one at the j -th element, and $\mathbf{R}_{p_k}^B \in SO(3)$ denotes the orientation of Ψ_{p_k} with respect to Ψ_B given by

$$\mathbf{R}_{p_k}^B = \mathbf{R}_z(\psi_k) \mathbf{R}_x(\alpha_k),$$

where α_k denotes the cant angle of the k -th rotor and $\mathbf{R}_x(\cdot) \in SO(3)$ is the standard rotation matrix about the x -axis.

The cant angles of the rotors are chosen to maximize the aerodynamic wrench that can be generated laterally by the propellers on the body of the UAV. This in turn will maximize the agility of the UAV, the maximum angle the UAV can hover at, and the interaction wrench that the UAV can apply to the environment in physical contact. However, the hovering efficiency of the UAV deteriorates as a consequence. In case of particular requirements on the aforementioned properties of the UAV, the cant angles can be computed from an optimization process as described in Ch.6. However, the main focus of this work is the design of interaction controllers and thus the cant angles are chosen based on the work of [Jiang et al., 2017] as $\alpha_k = (-1)^{k+1} \alpha^*$, where $\alpha^* = 47^\circ$, while the rotation directions of the rotors are given by $\sigma_k = (-1)^k$.

7.2.2 Dynamic Model

From a dynamical point-of-view, the fully-actuated hexarotor is considered as a rigid body connected to six propellers via revolute joints that are activated by electric motors. The interaction between the rotating propellers and the air generates the aerodynamic forces that are controlled to move the UAV in space as desired. Due to the low speed nature of multirotor UAVs in general and flying manipulators in particular, it is a conventional assumption to neglect the electric and mechanical dynamics of an UAV's propellers. Therefore, for control purposes, we treat the fully-actuated aerial robot as a controlled rigid body floating in a gravitational field.

The port-Hamiltonian dynamical model of a floating rigid body has been studied in details in Ch.4. The state of the dynamical system comprised of the UAV's pose $\mathbf{H}_B^I \in SE(3)$ and its generalized momentum¹ given by $\mathbf{P}^B := \mathcal{I} \mathbf{T}_B^{B,I} \in (\mathbb{R}^6)^*$, where $\mathcal{I} \in \mathbb{R}^{6 \times 6}$ denotes the generalized inertia tensor expressed in Ψ_B . We will denote in what follows the state of the rigid body by

$$\bar{\mathbf{x}} := (\mathbf{H}_B^I, \mathbf{P}^B) \in SE(3) \times (\mathbb{R}^6)^*. \quad (7.1)$$

The Hamiltonian of the system is given by the sum of the UAV's kinetic and potential energies:

$$\mathcal{H}(\bar{\mathbf{x}}) = \mathcal{H}_k(\mathbf{P}^B) + \mathcal{H}_g(\mathbf{H}_B^I) = \frac{1}{2} (\mathbf{P}^B)^\top \mathcal{I}^{-1} \mathbf{P}^B + m(\boldsymbol{\xi}_B^I)^\top \mathbf{g}, \quad (7.2)$$

¹Although we have that $(\mathbb{R}^6)^* \cong \mathbb{R}^6$, we denote the space of generalized momenta and wrenches by $(\mathbb{R}^6)^*$ to stress their covector nature.

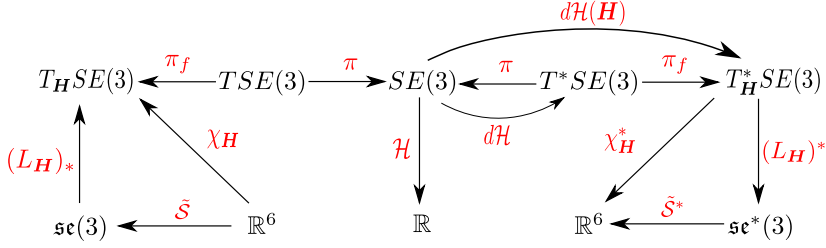


Figure 7.3: Commutative Diagram relating the Lie group $SE(3)$ to the Lie algebra $\mathfrak{se}(3)$ and its dual space $\mathfrak{se}^*(3)$. The maps π and π_f represent the canonical and fiber projections, respectively.

where m is the UAV's mass, $\mathbf{g} := g\hat{\mathbf{z}}_I \in \mathbb{R}^3$ is the inverse of gravity vector, and $g \approx 9.81 \text{ m s}^{-2}$ is the gravitational acceleration constant.

The explicit port-Hamiltonian model of a floating rigid body, repeated here for convenience, is given by

$$\begin{aligned} \frac{d}{dt} \begin{pmatrix} \mathbf{H}_B^I \\ \mathbf{P}^B \end{pmatrix} &= \begin{pmatrix} \mathbf{0} & \chi_{\mathbf{H}_B^I} \\ -\chi_{\mathbf{H}_B^I}^* & \mathbf{J}_k(\mathbf{P}^B) \end{pmatrix} \begin{pmatrix} \partial\mathcal{H}/\partial\mathbf{H}_B^I \\ \partial\mathcal{H}/\partial\mathbf{P}^B \end{pmatrix} + \begin{pmatrix} \mathbf{0} \\ \mathbf{I}_6 \end{pmatrix} \mathbf{W}^B, \\ \mathbf{T}_B^{B,I} &= \begin{pmatrix} \mathbf{0} & \mathbf{I}_6 \end{pmatrix} \begin{pmatrix} \partial\mathcal{H}/\partial\mathbf{H}_B^I \\ \partial\mathcal{H}/\partial\mathbf{P}^B \end{pmatrix}, \end{aligned} \quad (7.3)$$

where the skew-symmetric matrix $\mathbf{J}_k(\mathbf{P}^B)$ is given by

$$\mathbf{J}_k(\mathbf{P}) := \begin{pmatrix} \tilde{\mathbf{P}}_\omega & \tilde{\mathbf{P}}_v \\ \tilde{\mathbf{P}}_v & \mathbf{0} \end{pmatrix}, \quad \mathbf{P} = \begin{pmatrix} \mathbf{P}_\omega \\ \mathbf{P}_v \end{pmatrix} \in (\mathbb{R}^6)^*.$$

The map $\chi_{\mathbf{H}_B^I} : \mathbb{R}^6 \rightarrow T_H SE(3)$ its dual $\chi_{\mathbf{H}_B^I}^* : T_H^* SE(3) \rightarrow (\mathbb{R}^6)^*$ are given by the compositions in (4.91) and illustrated in the commutative diagram of Fig 7.3. Furthermore, $\mathbf{W}^B \in (\mathbb{R}^6)^*$ denotes the total wrench applied to the UAV's rigid body, given by the sum

$$\mathbf{W}^B = \mathbf{W}_c^B + \mathbf{W}_{\text{int}}^B, \quad (7.4)$$

with $\mathbf{W}_c^B \in (\mathbb{R}^6)^*$ denoting the aerodynamic control wrench and $\mathbf{W}_{\text{int}}^B \in (\mathbb{R}^6)^*$ denoting the physical interaction wrench *applied to* the UAV by the environment.

The control wrench produced by the rotors can be derived based on a static wrench analysis, as described in Ch.6. The wrench generated from each propeller on the UAV's body is expressed in Ψ_B as

$$\mathbf{W}_{p_k}^B = \lambda_k \mathbf{A} d_{\mathbf{H}_B^{p_k}}^\top (0, 0, \gamma \sigma_k, 0, 0, 1)^\top,$$

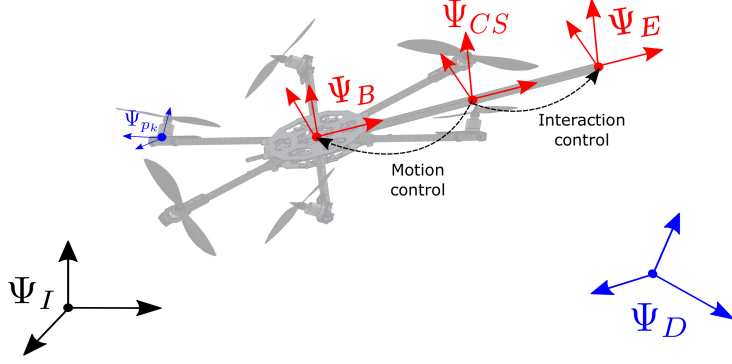


Figure 7.4: Illustration of the center-of-stiffness frame Ψ_{CS} and the desired frame Ψ_D . The relative pose between these two frames \mathbf{H}_{CS}^D corresponds to the new state of the system.

where $\lambda_k \in \mathbb{R}^+$ denotes the unidirectional thrust force generated by the k -th propeller in Ψ_{p_k} , γ is the propeller's drag-to-thrust ratio, and $\sigma_k \in \{-1, 1\}$ specifies the propeller's rotation direction (with $\sigma_k = 1$ for clockwise rotation). By summing over k , the cumulative aerodynamic control wrench \mathbf{W}_c^B expressed in Ψ_B can be written as

$$\mathbf{W}_c^B = \begin{pmatrix} \tau_c^B \\ \mathbf{f}_c^B \end{pmatrix} = \sum_k \lambda_k \begin{pmatrix} \tilde{\xi}_k \mathbf{u}_k + \gamma \sigma_k \mathbf{u}_k \\ \mathbf{u}_k \end{pmatrix}, \quad (7.5)$$

which can be rewritten as

$$\mathbf{W}_c^B = \mathbf{M} \boldsymbol{\lambda}, \quad (7.6)$$

where $\boldsymbol{\lambda} = [\lambda_1, \dots, \lambda_6]^\top$ corresponds to the combined rotor thrusts, and $\mathbf{M} \in \mathbb{R}^{6 \times 6}$ is referred to as the control allocation matrix.

7.3 Port-Hamiltonian Control System Design

Using the port-Hamiltonian rigid body model (7.3), we will design a stabilization control that will be used for two purposes: motion and interaction control. The control approach used is the Energy-Balancing Passivity-Based Control (EB-PBC) approach [Ortega et al., 2001]. The formulation of the UAV geometric control design as an EB-PBC problem is one of the contributions of this work.

7.3.1 Change of Coordinates

We first start by a useful change of coordinates for the dynamical system (7.3). With reference to Fig. 7.4, let Ψ_D be the (virtual) desired frame of the UAV, and let Ψ_{CS} be another body-fixed frame, called the *center of stiffness* frame, which has the same orientation as Ψ_B but a different location, i.e.

$$\mathbf{H}_{CS}^B = \begin{pmatrix} \mathbf{I}_3 & \boldsymbol{\xi}_{CS}^B \\ \mathbf{0} & 1 \end{pmatrix} \in SE(3). \quad (7.7)$$

The location of Ψ_{CS} will vary according to the control task². For motion control Ψ_{CS} coincides with Ψ_B (i.e. $\boldsymbol{\xi}_{CS}^B = 0$), while for interaction control Ψ_{CS} coincides with the end-effector frame Ψ_E .

The new state of the system

$$\mathbf{x} := (\mathbf{H}_{CS}^D, \mathbf{P}^B) \in SE(3) \times (\mathbb{R}^6)^*,$$

is related to the old state $\bar{\mathbf{x}}$ by

$$(\mathbf{H}_{CS}^D, \mathbf{P}^B) = (\mathbf{H}_I^D \mathbf{H}_B^I \mathbf{H}_{CS}^B, \mathbf{P}^B), \quad (7.8)$$

where $\mathbf{H}_{CS}^B \in SE(3)$ is given by (7.7) and $\mathbf{H}_I^D \in SE(3)$ denotes the relative configuration of the desired frame Ψ_D with respect to the inertial frame. In this work, we consider only stabilization (set-point) control, i.e. $\dot{\mathbf{H}}_I^D = 0$ for all time. Therefore, we have that the aforementioned change of coordinates is time-invariant. However, in practice the virtual set-point is changed in a piece-wise manner to achieve the desired behavior of the UAV.

In terms of the rotation and translation components of the homogeneous matrices, it is straightforward to check that the change of coordinates in (7.8) can be expressed

$$\mathbf{R}_{CS}^D = \mathbf{R}_I^D \mathbf{R}_B^I, \quad \boldsymbol{\xi}_{CS}^D = \boldsymbol{\xi}_I^D + \mathbf{R}_I^D \boldsymbol{\xi}_B^I + \mathbf{R}_I^D \mathbf{R}_B^I \boldsymbol{\xi}_{CS}^B, \quad (7.9)$$

whereas its inverse can be expressed as

$$\mathbf{R}_B^I = \mathbf{R}_D^I \mathbf{R}_{CS}^D, \quad \boldsymbol{\xi}_B^I = \boldsymbol{\xi}_D^I + \mathbf{R}_D^I \boldsymbol{\xi}_{CS}^D + \mathbf{R}_D^I \mathbf{R}_{CS}^D \boldsymbol{\xi}_B^{CS}. \quad (7.10)$$

The port-Hamiltonian system (7.3) can be written in terms of the new coordinates as follows. First, we have that the twist of Ψ_{CS} with respect to Ψ_D is equivalent to the twist of Ψ_B with respect Ψ_I :

$$\mathbf{T}_{CS}^{*,D} = \mathbf{T}_{CS}^{*,I} - \underbrace{\mathbf{T}_D^{*,I}}_{=0} = \underbrace{\mathbf{T}_{CS}^{*,B}}_{=0} - \mathbf{T}_I^{*,B} = \mathbf{T}_B^{*,I}, \quad (7.11)$$

²In general, the Ψ_{CS} frame can also be made variable, see e.g. [Stramigioli, 2001].

where $\mathbf{T}_D^{*,I} = 0$ follows from the stabilization control assumption and $\mathbf{T}_{CS}^{*,B} = 0$ follows from the fact that both Ψ_B and Ψ_{CS} are fixed to the same body.

Using (7.11), the kinematics relation $\dot{\mathbf{H}}_{CS}^D = \chi_{\mathbf{H}_{CS}^D}(\mathbf{T}_{CS}^{CS,D})$ can be rewritten as

$$\begin{aligned}\dot{\mathbf{H}}_{CS}^D &= \chi_{\mathbf{H}_{CS}^D}(\mathbf{T}_{CS}^{CS,D}) = \chi_{\mathbf{H}_{CS}^D}(\mathbf{Ad}_{\mathbf{H}_{CS}^D} \mathbf{T}_{CS}^{B,D}) \\ &= \chi_{\mathbf{H}_{CS}^D}(\mathbf{Ad}_{\mathbf{H}_B^{CS}} \mathbf{T}_B^{B,I}) = \chi_{\mathbf{H}_{CS}^D} \circ \mathbf{Ad}_{\mathbf{H}_B^{CS}}(\partial\mathcal{H}/\partial\mathbf{P}^B),\end{aligned}\quad (7.12)$$

with \circ denoting the composition of maps.

By rewriting the time derivative of \mathbf{P}^B in the new coordinates using the dual of the last map in (7.12), the open-loop port-Hamiltonian system (7.3) can be rewritten now as

$$\begin{aligned}\dot{\mathbf{x}} &= \mathbf{J}(\mathbf{x}) \frac{\partial\mathcal{H}(\mathbf{x})}{\partial\mathbf{x}} + \mathbf{G}\mathbf{W}^B, \\ \mathbf{T}_B^{B,I} &= \mathbf{G}^\top \frac{\partial\mathcal{H}(\mathbf{x})}{\partial\mathbf{x}},\end{aligned}\quad (7.13)$$

where \mathbf{W}^B is given by (7.4), while the skew-symmetric structure matrix operator $\mathbf{J}(\mathbf{x})$ and the input matrix \mathbf{G} are given by

$$\mathbf{J}(\mathbf{x}) = \begin{pmatrix} \mathbf{0} & \chi_{\mathbf{H}_{CS}^D} \circ \mathbf{Ad}_{\mathbf{H}_B^{CS}} \\ -\mathbf{Ad}_{\mathbf{H}_B^{CS}}^\top \circ \chi_{\mathbf{H}_{CS}^D}^* & \mathbf{J}_k(\mathbf{P}^B) \end{pmatrix}, \quad \mathbf{G} = \begin{pmatrix} \mathbf{0} \\ \mathbf{I}_6 \end{pmatrix}. \quad (7.14)$$

The Hamiltonian total energy of the system (7.2) is given in terms of the new coordinates $\mathbf{x} = (\mathbf{H}_{CS}^D, \mathbf{P}^B)$ by

$$\begin{aligned}\mathcal{H}(\mathbf{x}) &= \mathcal{H}_k(\mathbf{P}^B) + \mathcal{H}_g(\mathbf{H}_{CS}^D) \\ &= \frac{1}{2}(\mathbf{P}^B)^\top \mathcal{I}^{-1} \mathbf{P}^B + m(\boldsymbol{\xi}_D^I + \mathbf{R}_D^I \boldsymbol{\xi}_{CS}^D + \mathbf{R}_D^I \mathbf{R}_{CS}^D \boldsymbol{\xi}_B^{CS})^\top \mathbf{g},\end{aligned}\quad (7.15)$$

which follows from substituting (7.10) in (7.2).

7.3.2 Control Objective of EB-PBC

Considering the port Hamiltonian system (7.13) without the interaction wrench $\mathbf{W}_{\text{int}}^B$, the control objective of the EB-PBC approach is to find a control law that consists of the sum of an energy shaping term \mathbf{W}_{es}^B and a damping injection term \mathbf{W}_{di}^B i.e.

$$\mathbf{W}_c^B = \mathbf{W}_{\text{es}}^B(\mathbf{x}) + \mathbf{W}_{\text{di}}^B, \quad (7.16)$$

such that the closed loop system will retain the port-Hamiltonian structure:

$$\begin{aligned}\dot{\mathbf{x}} &= \mathbf{J}(\mathbf{x}) \frac{\partial\mathcal{H}_{\text{cl}}(\mathbf{x})}{\partial\mathbf{x}} + \mathbf{G}\mathbf{W}_{\text{di}}^B, \\ \mathbf{T}_B^{B,I} &= \mathbf{G}^\top \frac{\partial\mathcal{H}_{\text{cl}}(\mathbf{x})}{\partial\mathbf{x}}.\end{aligned}\quad (7.17)$$

The closed loop system is chosen such that it has the same interconnection structure (defined by $\mathbf{J}(\mathbf{x})$ and \mathbf{G}) but with a different energy function $\mathcal{H}_{\text{cl}}(\mathbf{x})$ that has a desired strict minimum at $\mathbf{x}^* = (\mathbf{I}_4, \mathbf{0})$, which corresponds to the stabilization of Ψ_{CS} to coincide with Ψ_D .

The first wrench \mathbf{W}_{es}^B of the control law (7.16) is the state feedback component responsible for the energy shaping, while the wrench \mathbf{W}_{di}^B is the output feedback component responsible for injecting damping such that asymptotic stabilization is achieved in free-flight. This can be achieved by choosing the damping injection control law as

$$\mathbf{W}_{\text{di}}^B = -\mathbf{K}_d \mathbf{T}_B^{B,I}, \quad (7.18)$$

where $\mathbf{K}_d \in \mathbb{R}^{6 \times 6}$ is a symmetric positive definite matrix.

7.3.3 Energy Shaping Control Procedure

Now we present the procedure by which the energy shaping control wrench \mathbf{W}_{es}^B is calculated. For system's that do not have internal dissipation, such as the UAV's model (7.13), the closed loop energy $\mathcal{H}_{\text{cl}}(\mathbf{x})$ can be chosen as

$$\mathcal{H}_{\text{cl}}(\mathbf{x}) = \mathcal{H}(\mathbf{x}) + \mathcal{H}_a(\mathbf{x}), \quad (7.19)$$

where $\mathcal{H}(\mathbf{x})$ is the original total energy of the system, whereas $\mathcal{H}_a(\mathbf{x})$ is the energy added by the controller to the system. By substituting (7.16) in (7.13) and (7.19) in (7.17), then comparing both systems together, we get the partial differential equation

$$\mathbf{J}(\mathbf{x}) \frac{\partial \mathcal{H}_a(\mathbf{x})}{\partial \mathbf{x}} = \mathbf{G} \mathbf{W}_{\text{es}}^B(\mathbf{x}), \quad (7.20)$$

which should be solved to find the energy shaping control term \mathbf{W}_{es}^B , given a desired energy function $\mathcal{H}_a(\mathbf{x})$. Equation (7.20) is usually referred to as the *matching equation*.

Using the expressions for $\mathbf{J}(\mathbf{x})$ and \mathbf{G} in (7.14), it can be shown that the matching equation (7.20) takes the form

$$\partial \mathcal{H}_a / \partial \mathbf{P}^B = 0, \quad (7.21)$$

$$-\mathbf{A} d_{\mathbf{H}_B^{CS}}^\top \circ \chi_{\mathbf{H}_{CS}^D}^* (\partial \mathcal{H}_a / \partial \mathbf{H}_{CS}^D) = \mathbf{W}_{\text{es}}^B. \quad (7.22)$$

The solution of (7.21) implies that the added energy function should be independent of \mathbf{P}^B , i.e. $\mathcal{H}_a(\mathbf{x}) = \mathcal{H}_a(\mathbf{H}_{CS}^D)$. Therefore, the control problem has been reduced to solving (7.22), which will be discussed next.

From the definition of $\chi_{\mathbf{H}_{CS}^D}^*$, we can refactor (7.22) as

$$\mathbf{W}_{\text{es}}^B = \mathbf{A} d_{\mathbf{H}_B^{CS}}^\top \mathbf{W}_{\text{es}}^{CS}, \quad (7.23)$$

$$\tilde{\mathbf{W}}_{\text{es}}^{CS} = -(\mathbf{L}_{\mathbf{H}_{CS}^D})^* (d\mathcal{H}_a(\mathbf{H}_{CS}^D)), \quad (7.24)$$

where $\partial\mathcal{H}_a/\partial\mathbf{H}_{CS}^D \in T_{\mathbf{H}_{CS}^D}^*SE(3)$ will be denoted in what follows as $d\mathcal{H}_a(\mathbf{H}_{CS}^D)$, highlighting that it is the differential of the smooth function $\mathcal{H}_a : SE(3) \rightarrow \mathbb{R}$ at \mathbf{H}_{CS}^D , as illustrated in Fig. 7.3.

The action of the pullback in (7.24) is defined as

$$\left\langle (L_{\mathbf{H}_{CS}^D}^D)^*(d\mathcal{H}_a(\mathbf{H}_{CS}^D)) \middle| \delta\tilde{\mathbf{T}}_{CS}^{CS,D} \right\rangle_{\mathfrak{se}} = \left\langle d\mathcal{H}_a(\mathbf{H}_{CS}^D) \middle| (L_{\mathbf{H}_{CS}^D}^D)_*(\delta\tilde{\mathbf{T}}_{CS}^{CS,D}) \right\rangle_{SE}, \quad (7.25)$$

where $\delta\tilde{\mathbf{T}}_{CS}^{CS,D} \in \mathfrak{se}(3)$ is an infinitesimal twist displacement, $\langle \cdot | \cdot \rangle_{\mathfrak{se}}$ denotes the duality pairing on $\mathfrak{se}(3)$, and $\langle \cdot | \cdot \rangle_{SE}$ denotes the duality pairing on $T_{\mathbf{H}_{CS}^D}SE(3)$.

By defining $d\mathbf{H}_{CS}^D \in T_{\mathbf{H}_{CS}^D}SE(3)$ as

$$d\mathbf{H}_{CS}^D = (L_{\mathbf{H}_{CS}^D}^D)_*(\delta\tilde{\mathbf{T}}_{CS}^{CS,D}) = \mathbf{H}_{CS}^D \delta\tilde{\mathbf{T}}_{CS}^{CS,D} = -\mathbf{H}_{CS}^D \delta\tilde{\mathbf{T}}_D^{CS,CS}, \quad (7.26)$$

and using (7.24), we can rewrite (7.25) as

$$\left\langle \tilde{\mathbf{W}}_{es}^{CS} \middle| \delta\tilde{\mathbf{T}}_D^{CS} \right\rangle_{\mathfrak{se}} = \left\langle d\mathcal{H}_a(\mathbf{H}_{CS}^D) \middle| d\mathbf{H}_{CS}^D \right\rangle_{SE}, \quad (7.27)$$

where $\delta\tilde{\mathbf{T}}_D^{CS} \in \mathfrak{se}(3)$ is introduced as a shorthand notation for $\delta\tilde{\mathbf{T}}_D^{CS,CS} \in \mathfrak{se}(3)$.

Remark 7.3.1. Note that the pairing in (7.27) represents infinitesimal virtual work, in contrast to the pairing in (4.49) which represents mechanical power, which is the first-order time-derivative of the energy. Similar to Fasse [1997], we choose to follow the variational approach which will simplify the controller derivation.

The right-hand side of (7.27) can be calculated by

$$\left\langle d\mathcal{H}_a(\mathbf{H}_{CS}^D) \middle| d\mathbf{H}_{CS}^D \right\rangle_{SE} = \mathcal{H}_a(\mathbf{H}_{CS}^D + d\mathbf{H}_{CS}^D) - \mathcal{H}_a(\mathbf{H}_{CS}^D). \quad (7.28)$$

As a consequence of the product structure of $\mathfrak{se}(3)$, we can express the left-hand side of (7.27) as

$$\left\langle \tilde{\mathbf{W}}_{es}^{CS} \middle| \delta\tilde{\mathbf{T}}_D^{CS} \right\rangle_{\mathfrak{se}} = \left\langle \tilde{\boldsymbol{\tau}}_{es}^{CS} \middle| \delta\tilde{\boldsymbol{\theta}}_D^{CS} \right\rangle_{\mathfrak{so}} + \left\langle \mathbf{f}_{es}^{CS} \middle| \delta\boldsymbol{\xi}_D^{CS} \right\rangle_{\mathbb{R}^3} \quad (7.29)$$

where $\delta\tilde{\boldsymbol{\theta}}_D^{CS} \in \mathfrak{so}(3)$ and $\delta\boldsymbol{\xi}_D^{CS} \in \mathbb{R}^3$ are the components of the infinitesimal twist displacement $\delta\tilde{\mathbf{T}}_D^{CS} \in \mathfrak{se}(3)$, while $\tilde{\boldsymbol{\tau}}_{es}^{CS} \in \mathfrak{so}^*(3)$ and $\mathbf{f}_{es}^{CS} \in (\mathbb{R}^3)^*$ are the components of the wrench $\tilde{\mathbf{W}}_{es}^{CS} \in \mathfrak{se}^*(3)$.

The components of $\delta\tilde{\mathbf{T}}_D^{CS} \in \mathfrak{se}(3)$ are related to the components of $d\mathbf{H}_{CS}^D \in T_{\mathbf{H}_{CS}^D}SE(3)$ by

$$d\mathbf{R}_{CS}^D = -\mathbf{R}_{CS}^D \delta\tilde{\boldsymbol{\theta}}_D^{CS}, \quad d\boldsymbol{\xi}_{CS}^D = -\mathbf{R}_{CS}^D \delta\boldsymbol{\xi}_D^{CS}. \quad (7.30)$$

Therefore, using the expressions for the duality pairings $\langle \cdot | \cdot \rangle_{\mathfrak{so}}$ and $\langle \cdot | \cdot \rangle_{\mathbb{R}^3}$ in Ch.4, we can rewrite (7.29) either in the form

$$\left\langle \tilde{\mathbf{W}}_{\text{es}}^{CS} \middle| \delta \tilde{\mathbf{T}}_D^{CS} \right\rangle_{\mathfrak{se}} = (\boldsymbol{\tau}_{\text{es}}^{CS})^\top \delta \boldsymbol{\theta}_D^{CS} + (\mathbf{f}_{\text{es}}^{CS})^\top \delta \boldsymbol{\xi}_D^{CS}, \quad (7.31)$$

or in the form

$$\left\langle \tilde{\mathbf{W}}_{\text{es}}^{CS} \middle| \delta \tilde{\mathbf{T}}_D^{CS} \right\rangle_{\mathfrak{se}} = -\frac{1}{2} \text{tr}(\tilde{\boldsymbol{\tau}}_{\text{es}}^{CS} \delta \tilde{\boldsymbol{\theta}}_D^{CS}) - \frac{1}{2} \text{tr}(\tilde{\mathbf{f}}_{\text{es}}^{CS} \delta \tilde{\boldsymbol{\xi}}_D^{CS}). \quad (7.32)$$

In summary, the expression for the energy shaping control wrench (7.24) will be derived by comparing the expressions in the right-hand side of the pairing equality (7.27), given by (7.28), to its left-hand side, given by (7.31) or (7.32).

7.3.4 Control Law Derivation

In this work, the controller's added energy \mathcal{H}_a is chosen to comprise of an elastic potential energy \mathcal{H}_p and to compensate for the gravitational potential energy \mathcal{H}_g of the system. Thus, we have that

$$\mathcal{H}_a(\mathbf{H}_{CS}^D) = \mathcal{H}_p(\mathbf{H}_{CS}^D) - \mathcal{H}_g(\mathbf{H}_{CS}^D), \quad (7.33)$$

with \mathcal{H}_g is given by (7.15) and \mathcal{H}_p chosen based on the work of Stramigioli [2001] to be

$$\begin{aligned} \mathcal{H}_p(\mathbf{R}, \boldsymbol{\xi}) &= \mathcal{H}_{t,1}(\boldsymbol{\xi}) + \mathcal{H}_{t,2}(\mathbf{R}, \boldsymbol{\xi}) + \mathcal{H}_o(\mathbf{R}) \\ &= \frac{1}{4} \boldsymbol{\xi}^\top \mathbf{K}_t \boldsymbol{\xi} + \frac{1}{4} \boldsymbol{\xi}^\top \mathbf{R} \mathbf{K}_t \mathbf{R}^\top \boldsymbol{\xi} - \text{tr}(\mathbf{G}_o(\mathbf{R} - \mathbf{I}_3)). \end{aligned} \quad (7.34)$$

The potential energy function (7.34) is parameterized by the translational stiffness matrix $\mathbf{K}_t \in \mathbb{R}^{3 \times 3}$ and the orientational co-stiffness matrix $\mathbf{G}_o \in \mathbb{R}^{3 \times 3}$. Stiffness and co-stiffness matrices are related to each other by

$$\mathbf{K}_x = \text{tr}(\mathbf{G}_x) \mathbf{I}_3 - \mathbf{G}_x, \quad \mathbf{G}_x = \frac{1}{2} \text{tr}(\mathbf{K}_x) \mathbf{I}_3 - \mathbf{K}_x, \quad (7.35)$$

for $x \in \{t, o\}$. Both $\mathbf{K}_x, \mathbf{G}_x$ are symmetric and their eigenvectors coincide with one another i.e.

$$\mathbf{K}_x = \mathbf{R}_x \boldsymbol{\Lambda}_x \mathbf{R}_x^\top, \quad \mathbf{G}_x = \mathbf{R}_x \boldsymbol{\Gamma}_x \mathbf{R}_x^\top, \quad (7.36)$$

where $\mathbf{R}_x = (\mathbf{e}_{x_1}, \mathbf{e}_{x_2}, \mathbf{e}_{x_3}) \in SO(3)$ represents the principal axes of stiffness, while $\boldsymbol{\Gamma}_x = \text{diag}(\gamma_{x_1}, \gamma_{x_2}, \gamma_{x_3})$ and $\boldsymbol{\Lambda}_x = \text{diag}(\lambda_{x_1}, \lambda_{x_2}, \lambda_{x_3})$ represent the principal stiffness and co-stiffness values along the axes, respectively. We assume that the principal stiffness gains γ_{x_i} , for $i = \{1, 2, 3\}$, are strictly positive and chosen such that the principal costiffness gains λ_{x_i} are distinct.

Remark 7.3.2. Note that in (7.34), the first term is the usual potential energy considered for a translational spring, while the third term represents a misalignment of \mathbf{R} from the identity [Bullo and Murray, 1999]. The second term in (7.34) is the term that allows for arbitrary non-diagonal stiffness \mathbf{K}_t such that the controller maintains invariance to changes of the inertial coordinate frame Ψ_I [Stramigioli, 2001; Bullo and Murray, 1999]. This term can be only included by considering the dynamics fully on $SE(3)$ without splitting the rotational and translational dynamics.

The exact expression for the energy shaping control law is given by the following result.

Theorem 7.3.3. *For the choice of the added energy (7.33), the energy shaping control law defined by (7.22) can be expressed as*

$$\mathbf{W}_{\text{es}}^B = \text{Ad}_{\mathbf{H}_B^{CS}}^\top (\mathbf{W}_{\text{p}}^{CS} - \mathbf{W}_{\text{g}}^{CS}), \quad (7.37)$$

where $\mathbf{W}_{\text{p}}^{CS}, \mathbf{W}_{\text{g}}^{CS} \in (\mathbb{R}^6)^*$ are the control wrenches defined by

$$\mathbf{W}_{\text{p}}^{CS} = -\chi_{\mathbf{H}_{CS}^D}^* (d\mathcal{H}_{\text{p}}(\mathbf{H}_{CS}^D)), \quad \mathbf{W}_{\text{g}}^{CS} = -\chi_{\mathbf{H}_{CS}^D}^* (d\mathcal{H}_{\text{g}}(\mathbf{H}_{CS}^D)), \quad (7.38)$$

with \mathcal{H}_{p} given by (7.34) and \mathcal{H}_{g} given by (7.15). Furthermore, let

$$\mathbf{W}_{\text{p}}^{CS} = \begin{pmatrix} \boldsymbol{\tau}_{\text{p}}^{CS} \\ \mathbf{f}_{\text{p}}^{CS} \end{pmatrix}, \quad \mathbf{W}_{\text{g}}^{CS} = \begin{pmatrix} \boldsymbol{\tau}_{\text{g}}^{CS} \\ \mathbf{f}_{\text{g}}^{CS} \end{pmatrix}, \quad (7.39)$$

then we have that

$$\tilde{\boldsymbol{\tau}}_{\text{p}}^{CS} = -2\text{sk}(\mathbf{G}_o \mathbf{R}_{CS}^D) - \text{sk}(\mathbf{G}_t \mathbf{R}_D^{CS} \tilde{\boldsymbol{\xi}}_{CS}^D \tilde{\boldsymbol{\xi}}_{CS}^D \mathbf{R}_{CS}^D), \quad (7.40)$$

$$\tilde{\mathbf{f}}_{\text{p}}^{CS} = -\mathbf{R}_D^{CS} \text{sk}(\mathbf{G}_t \tilde{\boldsymbol{\xi}}_{CS}^D) \mathbf{R}_{CS}^D - \text{sk}(\mathbf{G}_t \mathbf{R}_D^{CS} \tilde{\boldsymbol{\xi}}_{CS}^D \mathbf{R}_{CS}^D), \quad (7.41)$$

$$\boldsymbol{\tau}_{\text{g}}^{CS} = -m \tilde{\boldsymbol{\xi}}_B^{CS} \mathbf{R}_D^{CS} \mathbf{R}_I^D \mathbf{g}, \quad (7.42)$$

$$\mathbf{f}_{\text{g}}^{CS} = -m \mathbf{R}_D^{CS} \mathbf{R}_I^D \mathbf{g}, \quad (7.43)$$

where $\tilde{\boldsymbol{\tau}}_{\text{p}}^{CS}, \tilde{\mathbf{f}}_{\text{p}}^{CS} \in \mathfrak{so}^*(3)$ are the skew-symmetric matrices related to the covectors $\boldsymbol{\tau}_{\text{p}}^{CS}, \mathbf{f}_{\text{p}}^{CS} \in (\mathbb{R}^3)^*$ by (4.20).

Proof. We present the derivation of the energy-shaping control law for each separate energy term in (7.33).

For the orientational energy $\mathcal{H}_o(\mathbf{R}_{CS}^D)$, from the definition of \mathcal{H}_o and (7.28), we get

$$\begin{aligned} \langle d\mathcal{H}_o(\mathbf{R}_{CS}^D) | d\mathbf{R}_{CS}^D \rangle &= -\text{tr}(\mathbf{G}_o(\mathbf{R}_{CS}^D + d\mathbf{R}_{CS}^D - \mathbf{I}_3)) + \text{tr}(\mathbf{G}_o(\mathbf{R}_{CS}^D - \mathbf{I}_3)), \\ &= -\text{tr}(\mathbf{G}_o d\mathbf{R}_{CS}^D) = \text{tr}(\mathbf{G}_o \mathbf{R}_{CS}^D \delta \tilde{\boldsymbol{\theta}}_B^{CS}), \\ &= \text{tr}(\text{sk}(\mathbf{G}_o \mathbf{R}_{CS}^D) \delta \tilde{\boldsymbol{\theta}}_B^{CS}), \end{aligned} \quad (7.44)$$

where the second equality results from the linearity of the *trace* map, the third equality results from (7.30), and the last equality results from identity

$$\text{tr}(\mathbf{AB}) = \text{tr}(\text{sym}(\mathbf{A})\text{sym}(\mathbf{B})) + \text{tr}(\text{sk}(\mathbf{A})\text{sk}(\mathbf{B})). \quad (7.45)$$

By comparing equations (7.44) and (7.32), we conclude that the corresponding control wrench for $\mathcal{H}_o(\mathbf{R}_{CS}^D)$ is given by

$$\tilde{\boldsymbol{\tau}}_o^{cs} = -2\text{sk}(\mathbf{G}_o\mathbf{R}_{CS}^D), \quad \tilde{\mathbf{f}}_o^{cs} = \mathbf{0}. \quad (7.46)$$

By following the same steps for the first term of the translational energy $\mathcal{H}_{t,1}(\boldsymbol{\xi})$, we get

$$\begin{aligned} \langle d\mathcal{H}_{t,1}(\boldsymbol{\xi}_{CS}^D) | d\boldsymbol{\xi}_{CS}^D \rangle &= \frac{1}{4}(\mathbf{R}_{CS}^D \delta \boldsymbol{\xi}_B^{cs})^\top \mathbf{K}_t(\mathbf{R}_{CS}^D \delta \boldsymbol{\xi}_B^{cs}) \\ &\quad - \frac{1}{4}(\mathbf{R}_{CS}^D \delta \boldsymbol{\xi}_B^{cs})^\top \mathbf{K}_t \boldsymbol{\xi}_{CS}^D - \frac{1}{4}(\boldsymbol{\xi}_{CS}^D)^\top \mathbf{K}_t \mathbf{R}_{CS}^D \delta \boldsymbol{\xi}_B^{cs}, \end{aligned}$$

where the first can be neglected since it is a second order term [Fasse, 1997], thus we get

$$\langle d\mathcal{H}_{t,1}(\boldsymbol{\xi}_{CS}^D) | d\boldsymbol{\xi}_{CS}^D \rangle = -\frac{1}{2}(\delta \boldsymbol{\xi}_B^{cs})^\top (\mathbf{R}_{CS}^D)^\top \mathbf{K}_t \boldsymbol{\xi}_{CS}^D.$$

By comparison to (7.31), we conclude that

$$\mathbf{f}_{t,1}^{cs} = -\frac{1}{2}\mathbf{R}_D^{CS} \mathbf{K}_t \boldsymbol{\xi}_{CS}^D, \quad \boldsymbol{\tau}_{t,1}^{cs} = \mathbf{0}. \quad (7.47)$$

By using (7.35) and the identities

$$\mathbf{v} = (\text{tr}(\mathbf{A})\mathbf{I}_3 - \mathbf{A}^\top)\mathbf{w} \Leftrightarrow \tilde{\mathbf{v}} = 2\text{sk}(\mathbf{A}\tilde{\mathbf{w}}), \quad (7.48)$$

$$(\mathbf{R}\mathbf{v})^\sim = \mathbf{R}\tilde{\mathbf{v}}\mathbf{R}^\top, \quad (7.49)$$

we can show that $(\mathbf{K}_t \boldsymbol{\xi}_{CS}^D)^\sim = 2\text{sk}(\mathbf{G}_t \tilde{\boldsymbol{\xi}}_{CS}^D)$, which allows us to rewrite (7.47) as

$$\tilde{\mathbf{f}}_{t,1}^{cs} = -\mathbf{R}_D^{CS} \text{sk}(\mathbf{G}_t \tilde{\boldsymbol{\xi}}_{CS}^D) \mathbf{R}_{CS}^D, \quad \tilde{\boldsymbol{\tau}}_{t,1}^{cs} = \mathbf{0}. \quad (7.50)$$

To simplify the control derivation for the second term of the translational energy $\mathcal{H}_{t,2}(\boldsymbol{\xi})$, it is useful to rewrite it as [Stramigioli, 2001]

$$\mathcal{H}_{t,2}(\mathbf{H}_{CS}^D) = \mathcal{H}_{t,2}(\mathbf{R}_{CS}^D, \boldsymbol{\xi}_{CS}^D) = -\frac{1}{4}\text{tr}(\tilde{\boldsymbol{\xi}}_{CS}^D \mathbf{R}_{CS}^D \mathbf{G}_t \mathbf{R}_D^{CS} \tilde{\boldsymbol{\xi}}_{CS}^D).$$

By following the same line of thought and some lengthy calculations [Stramigioli, 2001], we can express the infinitesimal work as

$$\begin{aligned} \langle d\mathcal{H}_{t,2}(\mathbf{H}_{CS}^D) | d\mathbf{H}_{CS}^D \rangle &= \frac{1}{2}\text{tr}(\text{sk}(\mathbf{G}_t \mathbf{R}_D^{CS} \tilde{\boldsymbol{\xi}}_{CS}^D \tilde{\boldsymbol{\xi}}_{CS}^D \mathbf{R}_{CS}^D) \delta \tilde{\boldsymbol{\theta}}_B^{cs}) \\ &\quad + \frac{1}{2}\text{tr}(\text{sk}(\mathbf{G}_t \mathbf{R}_D^{CS} \tilde{\boldsymbol{\xi}}_{CS}^D \mathbf{R}_{CS}^D) \delta \tilde{\boldsymbol{\xi}}_B^{cs}). \end{aligned}$$

By comparison to (7.32), we conclude that

$$\tilde{\mathbf{f}}_{t,2}^{CS} = -\text{sk}(\mathbf{G}_t \mathbf{R}_D^{CS} \tilde{\boldsymbol{\xi}}_{CS}^D \mathbf{R}_{CS}^D), \quad \tilde{\boldsymbol{\tau}}_{t,2}^{CS} = -\text{sk}(\mathbf{G}_t \mathbf{R}_D^{CS} \tilde{\boldsymbol{\xi}}_{CS}^D \tilde{\boldsymbol{\xi}}_{CS}^D \mathbf{R}_{CS}^D). \quad (7.51)$$

By using the identity

$$\tilde{\mathbf{v}} \mathbf{w} = -\tilde{\mathbf{w}} \mathbf{v} = \tilde{\mathbf{w}}^\top \mathbf{v}, \quad (7.52)$$

in addition to (7.48) and (7.35), we can rewrite the force component as

$$\mathbf{f}_{t,2}^{CS} = -\frac{1}{2} \mathbf{K}_t \mathbf{R}_D^{CS} \boldsymbol{\xi}_{CS}^D. \quad (7.53)$$

Therefore, using the fact that

$$\boldsymbol{\tau}_p^{CS} = \boldsymbol{\tau}_o^{CS} + \boldsymbol{\tau}_{t,1}^{CS} + \boldsymbol{\tau}_{t,2}^{CS}, \quad \mathbf{f}_p^{CS} = \mathbf{f}_o^{CS} + \mathbf{f}_{t,1}^{CS} + \mathbf{f}_{t,2}^{CS},$$

the derivation of the control wrench \mathbf{W}_p^{CS} is complete.

Finally, by evaluating the infinitesimal work (7.28) for the gravitational energy $\mathcal{H}_g(\mathbf{H}_{CS}^D)$ and using identity (7.52), one has that

$$\begin{aligned} \langle d\mathcal{H}_g(\boldsymbol{\xi}_{CS}^D) | d\boldsymbol{\xi}_{CS}^D \rangle &= -m[(\mathbf{R}_D^I \mathbf{R}_{CS}^D \delta \boldsymbol{\xi}_D^{CS})^\top + (\mathbf{R}_D^I \mathbf{R}_{CS}^D \delta \tilde{\boldsymbol{\theta}}_D^{CS} \boldsymbol{\xi}_{CS}^B)^\top] \mathbf{g} \\ &= -m(\delta \boldsymbol{\xi}_D^{CS})^\top \mathbf{R}_D^{CS} \mathbf{R}_I^D \mathbf{g} - m(\delta \tilde{\boldsymbol{\theta}}_D^{CS})^\top \tilde{\boldsymbol{\xi}}_B^{CS} \mathbf{R}_D^{CS} \mathbf{R}_I^D \mathbf{g}. \end{aligned}$$

By comparison to (7.31), we get

$$\mathbf{f}_g^{CS} = -m \mathbf{R}_D^{CS} \mathbf{R}_I^D \mathbf{g}, \quad \boldsymbol{\tau}_g^{CS} = \tilde{\boldsymbol{\xi}}_B^{CS} \mathbf{f}_g^{CS}. \quad (7.54)$$

This concludes the derivation of the energy shaping control law (7.37). \blacksquare

To summarize, the total EB-PBC control law is given by

$$\mathbf{W}_c^B = \mathbf{A} d_{\mathbf{H}_B^{CS}}^\top (\mathbf{W}_p^{CS} - \mathbf{W}_g^{CS}) + \mathbf{W}_{di}^B, \quad (7.55)$$

combined with (7.18) and (7.39-7.43).

7.3.5 Closed Loop System Behavior

In this section, we examine the closed loop system's behavior. Using the control law (7.55) we can write the closed loop system as

$$\dot{\mathbf{x}} = (\mathbf{J}(\mathbf{x}) - \mathbf{R}) \frac{\partial \mathcal{H}_{cl}(\mathbf{x})}{\partial \mathbf{x}} + \mathbf{G} \mathbf{W}_{int}^B, \quad (7.56)$$

with the damping matrix \mathbf{R} given by

$$\mathbf{R} = \begin{pmatrix} \mathbf{0} & \mathbf{0} \\ \mathbf{0} & \mathbf{K}_d \end{pmatrix}, \quad (7.57)$$

and the closed loop Hamiltonian given by $\mathcal{H}_{\text{cl}} = \mathcal{H}_{\text{kin}} + \mathcal{H}_{\text{t},1} + \mathcal{H}_{\text{t},2} + \mathcal{H}_{\text{o}}$. In what follows, we present the *almost*³ global asymptotic stability of the system in free flight ($\mathbf{W}_{\text{int}}^B = \mathbf{0}, \mathbf{H}_{CS}^B = \mathbf{I}_4$), followed by the contact stability and impedance behavior of the system in contact ($\mathbf{W}_{\text{int}}^B \neq \mathbf{0}, \mathbf{H}_{CS}^B = \mathbf{H}_E^B$).

Free-flight Stability

The boundedness of \mathcal{H}_{cl} can be proven by the fact that its first three terms are quadratic in $\mathbf{P}^B, \boldsymbol{\xi}_{CS}^D$, and $(\mathbf{R}_D^{CS} \boldsymbol{\xi}_{CS}^D)$ respectively, thus are bounded from below. As for \mathcal{H}_{o} , due to its smoothness and the compactness of $SO(3)$ as a topological space, \mathcal{H}_{o} is also bounded from below [Bullo and Lewis, 2005].

As a consequence of the stiffness and co-stiffness matrices as in (7.35), the closed loop system has *four* isolated equilibrium points $\mathbf{x}_i^* = (\mathbf{H}_i^*, \mathbf{P}_i^*)$, where for all four points $\boldsymbol{\xi}_i^* = \mathbf{0}$ and $\mathbf{P}_i^* = \mathbf{0}$. The equilibrium orientations are given by [Bullo and Lewis, 2005]

$$\mathbf{R}_i^* = \exp(\pi \tilde{\mathbf{e}}_{o_i}), \quad i = \{1, 2, 3\}, \quad \mathbf{R}_4^* = \mathbf{I}_3, \quad (7.58)$$

where \mathbf{e}_{o_i} are the principal axes of \mathbf{K}_o , as shown in (7.36).

The time derivative of \mathcal{H}_{cl} is given by

$$\dot{\mathcal{H}}_{\text{cl}} = \frac{\partial \mathcal{H}_{\text{cl}}}{\partial \mathbf{x}}^\top (\mathbf{J}(\mathbf{x}) - \mathbf{R}) \frac{\partial \mathcal{H}_{\text{cl}}}{\partial \mathbf{x}} = -(\mathbf{P}^B)^\top \boldsymbol{\mathcal{I}}^{-\top} \mathbf{K}_d \boldsymbol{\mathcal{I}}^{-1} \mathbf{P}^B \leq 0, \quad (7.59)$$

which follows from the skew-symmetry of $\mathbf{J}(\mathbf{x})$, and the positive definiteness of \mathbf{K}_d and $\boldsymbol{\mathcal{I}}$. Thus, we conclude the system's passivity using \mathcal{H}_{cl} as a storage function.

By applying LaSalle's invariance principle, it can be shown that the largest invariance set consists of the union of all equilibrium points \mathbf{x}_i^* , which results from

$$\dot{\mathcal{H}}_{\text{cl}} = 0 \quad \Rightarrow \quad \mathbf{P}^B = \mathbf{0} \quad \Rightarrow \quad \dot{\mathbf{P}}^B = \mathbf{0} \quad \Rightarrow \quad \mathbf{W}_p^{CS}(\mathbf{H}_{CS}^D) = 0.$$

Thus, all solutions of the system (7.56), converge to one of the four equilibrium points. However, it will turn out that only the equilibrium $\mathbf{x}_4^* = (\mathbf{I}_4, \mathbf{0})$ is asymptotically stable, while the rest are unstable. This can be shown by examining the local linearized behavior of the control term $\mathbf{W}_p^{CS}(\mathbf{H}_{CS}^D)$ around the equilibrium points. By substituting

$$\mathbf{R}_{CS}^D = \mathbf{R}_i^* - \mathbf{R}_i^* \delta \tilde{\boldsymbol{\theta}}_D^{CS}, \quad \boldsymbol{\xi}_{CS}^D = \mathbf{0} - \mathbf{R}_i^* \delta \boldsymbol{\xi}_D^{CS},$$

in equations (7.46, 7.47, 7.51, 7.53), and discarding high order terms, we get

$$\begin{aligned} \tilde{\boldsymbol{\tau}}_o^{CS} &= 2\text{sk}(\mathbf{G}_o \mathbf{R}_i^* \delta \tilde{\boldsymbol{\theta}}_D^{CS}), & \tilde{\boldsymbol{\tau}}_{\text{t},2}^{CS} &= \mathbf{0}, \\ \mathbf{f}_{\text{t},1}^{CS} &= \frac{1}{2}(\mathbf{R}_i^*)^\top \mathbf{K}_t \mathbf{R}_i^* \delta \boldsymbol{\xi}_D^{CS}, & \mathbf{f}_{\text{t},2}^{CS} &= \frac{1}{2} \mathbf{K}_t \delta \boldsymbol{\xi}_D^{CS}, \end{aligned}$$

³As is it impossible topologically to achieve global asymptotic stability on $SO(3)$ and consequently $SE(3)$.

which allows rewriting the equivalent wrench in (7.40,7.41) as

$$\mathbf{W}_p^{CS} = \mathbf{W}_p^B = -\mathbf{K}_i^* \delta \mathbf{T}_B^{B,I} = \mathbf{K}_i^* \delta \mathbf{T}_D^{CS}, \quad (7.60)$$

with $\mathbf{K}_i^* \in \mathbb{R}^{6 \times 6}$ given by

$$\mathbf{K}_i^* = \begin{pmatrix} \text{tr}(\mathbf{G}_o \mathbf{R}_i^*) \mathbf{I}_3 - (\mathbf{G}_o \mathbf{R}_i^*)^\top & \mathbf{0} \\ \mathbf{0} & \frac{1}{2}[(\mathbf{R}_i^*)^\top \mathbf{K}_t \mathbf{R}_i^* + \mathbf{K}_t] \end{pmatrix}.$$

By evaluating the stiffness matrix \mathbf{K}_i^* at $\mathbf{R}_4^* = \mathbf{I}_3$, we get the positive definite matrix

$$\mathbf{K}_s := \mathbf{K}_4^* = \begin{pmatrix} \mathbf{K}_o & \mathbf{0} \\ \mathbf{0} & \mathbf{K}_t \end{pmatrix}, \quad (7.61)$$

which shows that the potential control term (7.60) resembles a linear elastic wrench near the equilibrium \mathbf{R}_4^* . Similar to the analysis in Fasse and Broenink [1997], it can be shown that the stiffness matrix evaluated at the remaining equilibrium points is not positive definite. Finally, this concludes the *almost global* asymptotic stability of the equilibrium point $\mathbf{x}_4^* = (\mathbf{I}_4, \mathbf{0})$ with respect to the closed loop system (7.56).

Interaction behavior

In the interaction control mode, the passivity of the system with respect to the interaction power port $(\mathbf{T}_B^{B,I}, \mathbf{W}_{\text{int}}^B)$ can be analyzed by rewriting (7.59) as

$$\dot{\mathcal{H}}_{\text{cl}} = -(\mathbf{P}^B)^\top \mathcal{I}^{-\top} \mathbf{K}_d \mathcal{I}^{-1} \mathbf{P}^B + (\mathcal{I}^{-1} \mathbf{P}^B)^\top \mathbf{W}_{\text{int}}^B \leq (\mathbf{W}_{\text{int}}^B)^\top \mathbf{T}_B^{B,I}. \quad (7.62)$$

This guarantees the contact stability of the UAV with any passive arbitrary environment.

The impedance behavior of the UAV's end effector with respect to the environment can be calculated by representing all terms of the momentum dynamics in (7.56) in frame Ψ_E . The linearized impedance behavior in terms of an infinitesimal twist displacement $\delta \mathbf{T}_E^{E,D}$ can be shown to be

$$\mathcal{I}^E \delta \ddot{\mathbf{T}}_E^{E,D} + \mathbf{K}_d^E \delta \dot{\mathbf{T}}_E^{E,D} + \mathbf{K}_s \delta \mathbf{T}_E^{E,D} = \mathbf{W}_{\text{int}}^E, \quad (7.63)$$

where the apparent inertia \mathcal{I}^E and damping \mathbf{K}_d^E matrices are given, respectively, by

$$\mathcal{I}^E = \mathbf{A} d_{\mathbf{H}_E^B}^\top \mathcal{I} \mathbf{A} d_{\mathbf{H}_E^B}, \quad \mathbf{K}_d^E = \mathbf{A} d_{\mathbf{H}_E^B}^\top \mathbf{K}_d \mathbf{A} d_{\mathbf{H}_E^B},$$

while the stiffness matrix \mathbf{K}_s is given by (7.61).

To conclude, during contact with the environment, the EB-PBC control law (7.55) acts as an impedance controller with the impedance behavior (7.63).

Remark 7.3.4. Note that the passivity result in (7.62) actually holds for any external power port to the system. Consider the *actual* control wrench in (7.4) which is equal to the *desired* control wrench in (7.55) only if ($\Delta \mathbf{W}_c = \mathbf{0}$) which represents the wrench due to modeling uncertainties like unmodeled dynamics or input constraints. In case $\Delta \mathbf{W}_c \neq \mathbf{0}$, the closed loop system (7.56) would have an additional term ($\mathbf{G}\Delta \mathbf{W}_c$), and the system's passivity can be easily shown as in (7.62).

7.4 Experimental Validation

The experimental setup used to validate the proposed control approach consists of a fully-actuated hexarotor UAV with unidirectional rotors. Details of the hardware and software architecture used to implement the control law (7.55) can be found in [Rashad et al., 2019b]. The experiments are conducted in an indoor lab with a motion-capture system. The experiments consist of two scenarios, one for interaction control and the other for motion control. The controller gains in both experiments are chosen as $\mathbf{K}_t = \text{diag}(12, 12, 12)$, $\mathbf{K}_o = \text{diag}(0.8, 0.8, 0.5)$, and $\mathbf{K}_d = \text{diag}(3.6, 3.5, 2.1, 7, 7, 7)$. The results are presented next, while recordings of the experiments can be found in the supplementary video.

7.4.1 Exp.1: Robust Interaction with Rigid Surface

The first experiment comprises of the UAV applying a normal force to a vertical surface rigidly connected to an ATI mini40 force/torque sensor (ATI Industrial Automation), as shown in Fig 7.5. The measured normal force and commanded rotor PWM signals are displayed in Figs. 7.6 and 7.7, respectively. The applied force is increased by slowly increasing ξ_E^D , until its maximum allowed normal force is achieved, as shown by the force measurement in Fig. 7.6. In Fig. 7.7, it can be seen that this maximum force is achieved with λ_2 at its lower limit. Therefore, there are instants in which the hexarotor interacts while hovering with its second motor turned off, as shown in the snapshot in Fig. 7.5.

7.4.2 Exp.2: Robust Hovering at Maximum Roll

The second experiment consists of the UAV hovering at different roll angles. In Fig. 7.8, snapshots of the UAV hovering at an angle of 0, 15, and 25 deg are shown. The UAV is commanded to hover at the roll angle $\phi_B = 25$ deg for $t \geq 130$ s, as shown in Fig. 7.9. In order for the UAV to hover at this maximum angle, λ_4 is commanded to be zero for an interval about 40 seconds, as shown in Fig. 7.10. Thus, the UAV hovers at this maximum angle with *five* rotors only. However, due to the inability of the UAV to maintain its desired position



Figure 7.5: Experiment 1: Snapshot ($t = 215\text{s}$) showing the UAV hovering with one rotor off and applying an $\approx 10\text{ N}$ force to a vertical surface rigidly connected to a force/torque sensor.

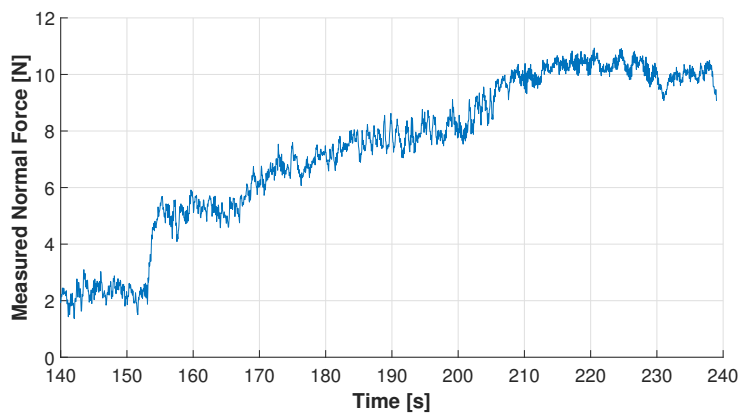


Figure 7.6: Experiment 1: Measured normal force applied by the UAV to the vertical surface. The applied force is gradually increased until it reaches its maximum allowed value due to the actuator limits.

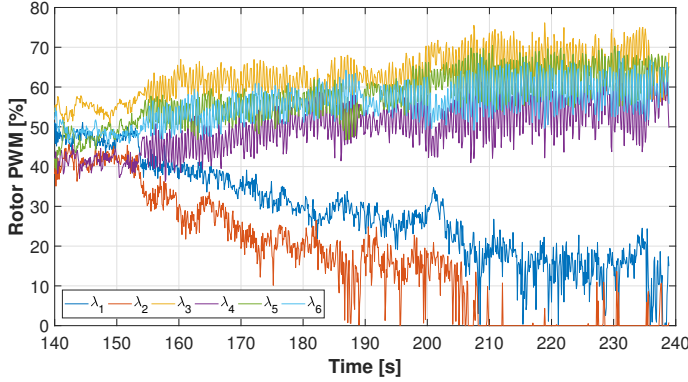


Figure 7.7: Experiment 1: The commanded rotor PWM signals during the interaction where the second rotor hits its lower limit.

against wind disturbances, the UAV drifts which then requires a non-zero λ_4 to be able to reduce the position error.

The main feature of the controller that the two aforementioned experiments demonstrate is its robustness to the actuator limits and in general any uncertainties in the model. This is implied mathematically from the system's passivity in (7.62) against any disturbances to the UAV's model and not only the interaction wrench, as discussed in Remark 7.3.4. Therefore, near the UAV's maximum physical capabilities, the nonlinear saturation of the motor inputs did not destabilize the system.

7.5 Conclusion

In this work, we presented a geometric port-Hamiltonian controller for a fully-actuated UAV suitable for both motion and interaction control. The controller was designed using the EB-PBC approach and was shown to provide almost global asymptotic stability (in the absence of uncertainties) in free-flight as well as guaranteed contact stability with any passive environment.

The main feature of the presented controller is that it is formulated respecting the geometric structure of the underlying state space. Furthermore, the geometric formulation allowed for a compact derivation and rigorous mathematical analysis of the control system. Although the port-Hamiltonian control of fully-actuated mechanical systems is a well studied topic, the problem considered in this work was not trivial, due to the non-symplectic structure of the dynamic model. The experiments showed the validity and robustness of the control approach especially to unmodeled uncertainties such as input saturation, aerodynamic disturbances, and communication delays.

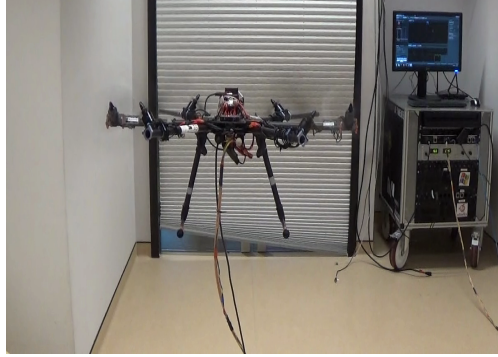
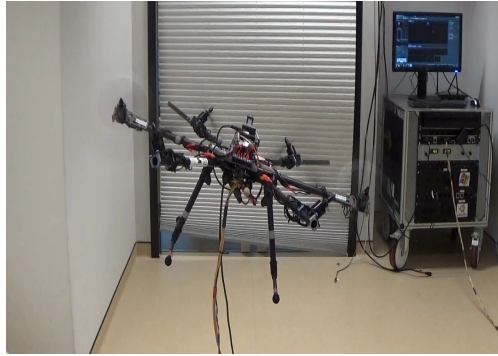
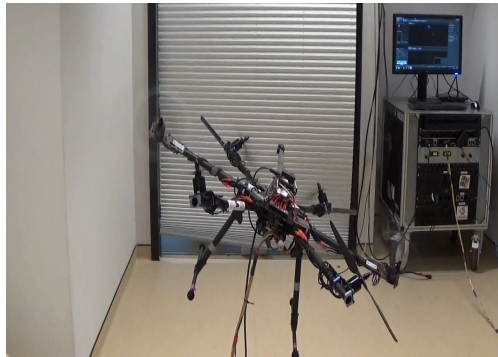
(a) $\phi_B = 0^\circ$, $t = 20$ s(b) $\phi_B = 15^\circ$, $t = 68$ s(c) $\phi_B = 25^\circ$, $t = 141$ s

Figure 7.8: Experiment 2: Snapshots of the UAV hovering at different roll angles ϕ_B . Snapshot (c) shows the UAV hovering at its maximum allowed angle with one of its rotors off.

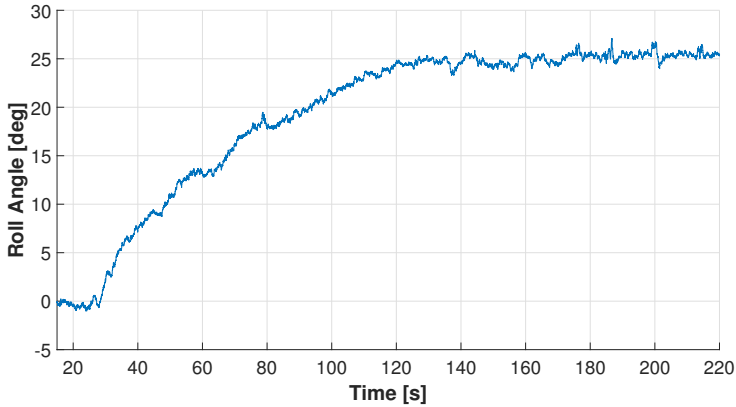


Figure 7.9: Experiment 2: The UAV's roll angle increasing gradually while hovering in free-flight until it reaches its maximum allowed value due to the actuator limits.

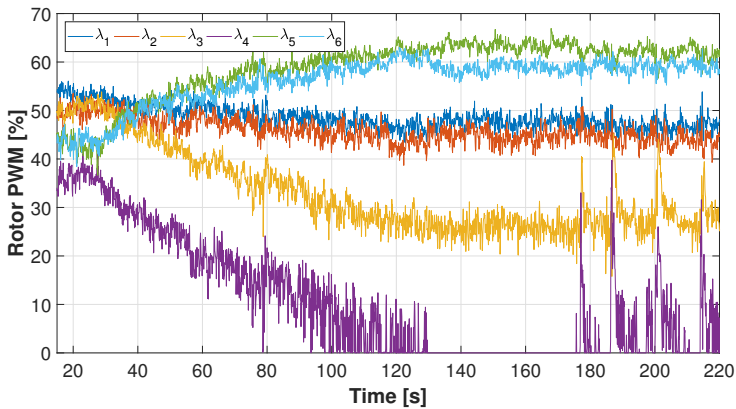


Figure 7.10: Experiment 2: The commanded rotor PWM signals during hovering at a non-zero roll angle where the fourth rotor hits its lower limit.

CHAPTER 8

ENERGY-AWARE IMPEDANCE CONTROL OF A FLYING END-EFFECTOR

We have shown in Ch.7 that the impedance control problem of a flying end-effector can be formulated in the port-Hamiltonian framework as an energy-balancing passivity-based control (EB-PBC) problem. Compared to signal-based techniques, such as hybrid pose/wrench control, our proposed energy-based controller is more suited for physical interaction with uncertain environments. By using the passivity property of the closed loop system as the criterion for stability, the contact stability of the aerial robot interacting with any conceivable passive environment was shown to be guaranteed.

Generally in impedance control, the interaction wrench applied by the aerial robot to the environment depends on the values chosen for the controller's gains and the relative configuration between the virtual desired frame and the end-effector frame. For the application of a specific desired interaction wrench, a priori knowledge of the contact target's geometrical and mechanical properties is required. However, such knowledge is difficult to acquire in practice and in fact this contradicts the key advantage of impedance control to work in uncertain environments.

A solution for the aforementioned drawback is to utilize information about the interaction wrench, either using force/torque measurements or model-based estimation, for modulating the stiffness of the impedance controller in order to regulate the interaction wrench to a desired value. However, the interaction wrench regulation comes at the cost of violating the passivity of the closed-loop system and as a consequence, the contact stability is no longer guaranteed.

The work of this chapter focuses on enhancing the basic geometric impedance

control approach with wrench regulation capabilities while maintaining passivity using the concept of an energy-tank. The concept of energy tanks has been often used in various sub-domains of robotics, e.g. bilateral tele-manipulation [Franken et al., 2011; Secchi et al., 2012] and impedance control of ground-based manipulators [Schindlbeck and Haddadin, 2015; Ferraguti et al., 2013, 2015; Kronander and Billard, 2016; Dietrich et al., 2017; Raiola et al., 2018; Shahriari et al., 2018]. Control by energy tanks and energy-routing, first proposed in Duindam and Stramigioli [2004], is an example of the wider concept of energy-aware robotics [Stramigioli, 2015].

The intuitive idea of an energy-tank is that it stores the “free energy dissipated” by the control system and uses it to implement control actions that could violate the passivity of the closed-loop system, for instance the regulation of the interaction wrench in our case. With this simple idea, energy is routed from one subsystem to another within the controller and the total energy of the closed loop system does not increase. Hence, passivity is guaranteed. On top of that, energy tanks allow the energy flow within the system to be observed and possibly used for high-level purposes, thus the controller becomes more *energy-aware* [Stramigioli, 2015].

In this chapter, we present an *energy-aware impedance control* approach for aerial physical interaction in the port-Hamiltonian framework. A unique feature of the presented controller is that it relies on the *control-by-interconnection* principle in which the control system is treated as a virtual physical system connected to the actual physical robot via power-ports. Furthermore, the controller itself will be constructed as a network of energetic subsystems interconnected to each other in a power-preserving manner.

The first advantage of this control-by-interconnection approach is that the designer can physically interpret the control system which in turn greatly simplifies the tuning process of its design parameters. Second, using the intuitive fact that two passive systems connected by a power-preserving interconnection is again a passive system, the stability analysis of the overall closed loop system can be divided into simpler passivity checks of each energetic subsystem. In addition, these checks do not have to be repeated if extra modules are added. Third, by exploiting bond graphs for graphically representing the different dynamical systems, the passivity analysis becomes an even easier task that can be performed by inspection. Thus, eliminating the need for lengthy calculations encountered in analytical analysis of passivity.

The work in this chapter is based on the work of Zult [2020] which is also used in preparation of a journal paper to be submitted soon. A preliminary version of it has already been published in Rashad et al. [2019b]. The work presented here reformulates many of the concepts in [Zult, 2020; Rashad et al., 2019b] in the port-Hamiltonian framework utilizing Dirac structures which highlights the energy-based nature of the proposed concepts to a big extent.

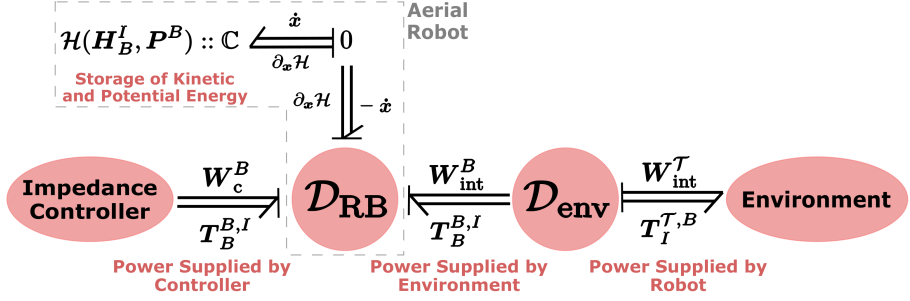


Figure 8.1: Port-based representation of the aerial robot's port-Hamiltonian model connected to its controller and the environment via power ports characterizing the energy exchange between them.

The rest of this chapter is outlined as follows: Sec. 8.1 addresses the control-by-interconnection interpretation of the impedance controller derived in Ch.7. In this point of view, the controller is represented by a number of energetic subsystems that are interconnected to each other via power ports. In Sec. 8.2, we present how the impedance controller can be augmented with wrench regulation capabilities by varying the stiffness of the controller and show how this comes at the cost of losing the passivity of the closed-loop system. Sec. 8.3 presents the details of the energy-aware impedance controller that will utilize energy routing and an energy tank to allow the implementation of the wrench regulation without violating the passivity of the system. Finally, we conclude with some remarks in Sec. 8.4.

8.1 Control-By-Interconnection Interpretation

In this section, we will present the control-by-interconnection representation of the impedance controller designed in Ch.7 by interpreting the controller as a network of energetic subsystems interconnected via power ports. First, we start by the port-based representation of the aerial robot interacting physically with its environment, acting as a flying-end effector.

8.1.1 Flying-end Effector

In the port-Hamiltonian framework, the aerial robot is modeled dynamically as a rigid body interacting with its controller and the environment via power ports, as shown in Fig. 8.1. The aerial robot's port-Hamiltonian model consists of i) an energy storage C-element that characterizes the kinetic energy and gravitational potential energy of the robot, and ii) a Dirac structure \mathcal{D}_{RB} that

characterizes the exchange of energy between the robot and the external world including the impedance controller and the environment.

Recall from Sec. 4.2.6, that the energy storage element has its state variable $\mathbf{x} := (\mathbf{H}_B^I, \mathbf{P}^B) \in SE(3) \times (\mathbb{R}^6)^*$ and its Hamiltonian $\mathcal{H}(\mathbf{x})$ given by the sum of kinetic and gravitational potential energy, i.e.

$$\mathcal{H}(\mathbf{x}) = \mathcal{H}_k(\mathbf{P}^B) + \mathcal{H}_g(\mathbf{H}_B^I) = \frac{1}{2}(\mathbf{P}^B)^\top \mathcal{I}^{-1} \mathbf{P}^B + m(\boldsymbol{\xi}_B^I)^\top \mathbf{g}. \quad (8.1)$$

Furthermore, the flow and effort variables of the energy storage element are given, respectively, by

$$\dot{\mathbf{x}} = \begin{pmatrix} \dot{\mathbf{H}}_B^I \\ \dot{\mathbf{P}}^B \end{pmatrix} \in T_{\mathbf{H}_B^I} SE(3) \times (\mathbb{R}^6)^*, \quad \partial_{\mathbf{x}} \mathcal{H} = \begin{pmatrix} \partial_{\mathbf{H}_B^I} \mathcal{H} \\ \partial_{\mathbf{P}^B} \mathcal{H} \end{pmatrix} \in T_{\mathbf{H}_B^I}^* SE(3) \times \mathbb{R}^6.$$

The Dirac structure \mathcal{D}_{RB} is defined as the relation corresponding to the skew-symmetric map

$$\begin{pmatrix} -\dot{\mathbf{H}}_B^I \\ -\dot{\mathbf{P}}^B \\ \mathbf{T}_B^{B,I} \\ \mathbf{T}_B^{B,I} \end{pmatrix} = \begin{pmatrix} \mathbf{0} & -\chi_{\mathbf{H}_B^I} & \mathbf{0} & \mathbf{0} \\ \chi_{\mathbf{H}_B^I}^* & -\mathbf{J}_k(\mathbf{P}^B) & -\mathbf{I}_6 & -\mathbf{I}_6 \\ \mathbf{0} & \mathbf{I}_6 & \mathbf{0} & \mathbf{0} \\ \mathbf{0} & \mathbf{I}_6 & \mathbf{0} & \mathbf{0} \end{pmatrix} \begin{pmatrix} \partial_{\mathbf{H}_B^I} \mathcal{H} \\ \partial_{\mathbf{P}^B} \mathcal{H} \\ \mathbf{W}_c^B \\ \mathbf{W}_{\text{int}}^B \end{pmatrix}, \quad (8.2)$$

which is a reformulation of the UAV's port-Hamiltonian dynamic model presented in (7.3-7.4). The Dirac structure \mathcal{D}_{RB} encodes the energy balance given by

$$\left\langle \partial_{\mathbf{H}_B^I} \mathcal{H} \middle| \dot{\mathbf{H}}_B^I \right\rangle_{SE} + \left\langle \partial_{\mathbf{P}^B} \mathcal{H} \middle| \dot{\mathbf{P}}^B \right\rangle_{\mathbb{R}^6} = \langle \mathbf{W}_c^B | \mathbf{T}_B^{B,I} \rangle_{\mathbb{R}^6} + \langle \mathbf{W}_{\text{int}}^B | \mathbf{T}_B^{B,I} \rangle_{\mathbb{R}^6},$$

or equivalently

$$\dot{\mathcal{H}}_g + \dot{\mathcal{H}}_k = (\mathbf{W}_c^B)^\top \mathbf{T}_B^{B,I} + (\mathbf{W}_{\text{int}}^B)^\top \mathbf{T}_B^{B,I}, \quad (8.3)$$

which simply states that the rate of change in the total energy $\mathcal{H} = \mathcal{H}_g + \mathcal{H}_k$ stored by the UAV along solutions of the dynamical system represented in (8.2) is equal to the power supplied by the controller and the environment, as illustrated in the bond graph of Fig. 8.1.

It is useful to describe the interaction between the robot and the environment in a frame $\Psi_{\mathcal{T}}$ fixed to the target to be physically contacted by the aerial robot. The robot's body twist $\mathbf{T}_B^{B,I}$ and the interaction wrench applied to the robot $\mathbf{W}_{\text{int}}^B$ are related to their counterparts in the target frame $\Psi_{\mathcal{T}}$ by the skew-symmetric map

$$\begin{pmatrix} \mathbf{W}_{\text{int}}^B \\ \mathbf{T}_I^{\mathcal{T},B} \end{pmatrix} = \begin{pmatrix} \mathbf{0} & \mathbf{Ad}_{\mathbf{H}_B^{\mathcal{T}}}^\top \\ -\mathbf{Ad}_{\mathbf{H}_B^{\mathcal{T}}} & \mathbf{0} \end{pmatrix} \begin{pmatrix} \mathbf{T}_B^{B,I} \\ \mathbf{W}_{\text{int}}^B \end{pmatrix}. \quad (8.4)$$

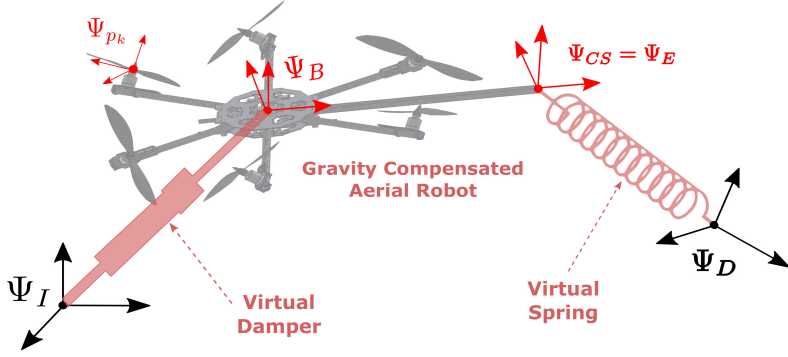


Figure 8.2: Control-by-interconnection interpretation of the impedance controller as a virtual spring and a virtual damper attached to the aerial robot with gravity-compensated.

The Dirac structure \mathcal{D}_{env} , given by the relation corresponding to the map (8.4), states that the power supplied by the environment to the aerial robot is equivalent to *minus* the power supplied by the robot to the environment, i.e.

$$(\mathbf{W}_{\text{int}}^B)^\top \mathbf{T}_{B,I}^{B,I} = -(\mathbf{W}_{\text{int}}^T)^\top \mathbf{T}_I^{T,B}. \quad (8.5)$$

8.1.2 Impedance Controller

Now we turn attention to the control-by-interconnection interpretation of the impedance controller. Recall that the impedance control law \mathbf{W}_c^B given in (7.55) comprised of an energy shaping term \mathbf{W}_{es}^B and a damping injection term \mathbf{W}_{di}^B . The energy shaping wrench corresponded to the added energy by the controller which was chosen as the sum of an elastic potential energy \mathcal{H}_p and minus the gravitational potential energy \mathcal{H}_g to compensate for the aerial robot's gravity.

With reference to Fig. 8.2, the impedance controller derived in Ch.7 emulates a virtual spring and a virtual damper attached to the aerial robot with the gravity being compensated by the controller. The virtual spring is connected between the center of stiffness frame Ψ_{CS} (placed at the robot's end effector frame Ψ_E) and the desired frame Ψ_D . Whereas, the virtual damper is connected between the robot's body frame Ψ_B and the inertial frame Ψ_I .

Virtual spring

A virtual spring with constant stiffness is represented in the port-Hamiltonian framework by the combination of an energy storage element and a transformation, as shown in Fig. 8.3. The energy storage element, denoted by \mathbb{C} ,

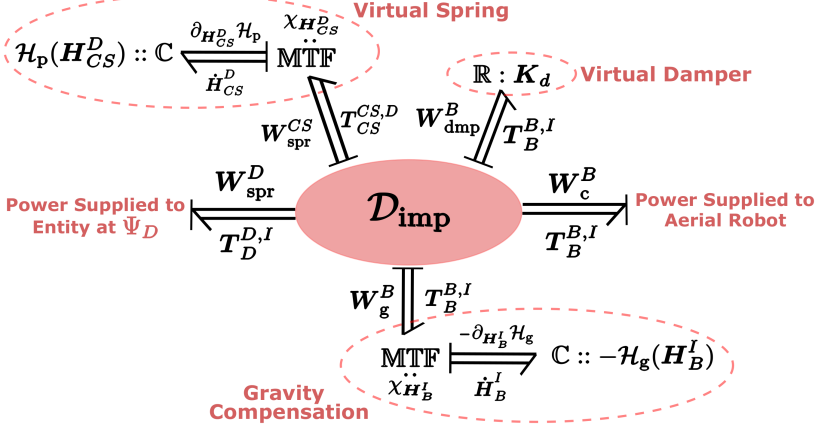


Figure 8.3: Port-based representation of the impedance controller as a number of energetic subsystems.

is characterized by the state variable $\mathbf{H}_{CS}^D \in SE(3)$ and the elastic potential energy Hamiltonian $\mathcal{H}_p : SE(3) \rightarrow \mathbb{R}$ given by

$$\mathcal{H}_p(\mathbf{H}_{CS}^D) = \frac{1}{4}(\xi_{CS}^D)^\top \mathbf{K}_t \xi_{CS}^D + \frac{1}{4}(\xi_{CS}^D)^\top \mathbf{R}_{CS}^D \mathbf{K}_t (\mathbf{R}_{CS}^D)^\top \xi_{CS}^D - \text{tr}(\mathbf{G}_o(\mathbf{R}_{CS}^D - \mathbf{I}_3)), \quad (8.6)$$

where $\mathbf{K}_t \in \mathbb{R}^{3 \times 3}$ is the constant translation stiffness matrix, $\mathbf{G}_o \in \mathbb{R}^{3 \times 3}$ is the constant orientation co-stiffness matrix, and $\mathbf{R}_{CS}^D \in SO(3)$ and $\xi_{CS}^D \in \mathbb{R}^3$ are the rotation and translation components of $\mathbf{H}_{CS}^D \in SE(3)$. The flow and effort variables of the storage element are given respectively by $\dot{\mathbf{H}}_{CS}^D \in T_{\mathbf{H}_{CS}^D} SE(3)$ and $\partial_{\mathbf{H}_{CS}^D} \mathcal{H}_p \in T_{\mathbf{H}_{CS}^D}^* SE(3)$, with their dual product corresponding to the rate of change of energy stored, i.e.

$$\dot{\mathcal{H}}_p = \left\langle \partial_{\mathbf{H}_{CS}^D} \mathcal{H}_p \middle| \dot{\mathbf{H}}_{CS}^D \right\rangle_{SE}. \quad (8.7)$$

The modulated transformer MTF implements the map

$$\begin{pmatrix} \dot{\mathbf{H}}_{CS}^D \\ \mathbf{W}_{spr}^{CS} \end{pmatrix} = \begin{pmatrix} \mathbf{0} & \chi_{\mathbf{H}_{CS}^D} \\ \chi_{\mathbf{H}_{CS}^D}^* & \mathbf{0} \end{pmatrix} \begin{pmatrix} \partial_{\mathbf{H}_{CS}^D} \mathcal{H}_p \\ \mathbf{T}_{CS}^{CS,D} \end{pmatrix}, \quad (8.8)$$

where the first equation corresponds to the kinematics relation between $\dot{\mathbf{H}}_{CS}^D$ and $\mathbf{T}_{CS}^{CS,D} \in \mathbb{R}^6$ which is the relative twist between the two ends of the spring (i.e. Ψ_{CS} and Ψ_D). The second equation in (8.8) relates the differential of the potential function (8.6) to $\mathbf{W}_{spr}^{CS} \in (\mathbb{R}^6)^*$ which corresponds to the wrench applied to the spring by the body it is attached to at Ψ_{CS} (i.e. the aerial

robot). The exact expression of the wrench is given by Theorem 7.3.3 (with a sign difference) as

$$\mathbf{W}_{\text{spr}}^{CS} = \begin{pmatrix} \boldsymbol{\tau}_{\text{spr}}^{CS} \\ \mathbf{f}_{\text{spr}}^{CS} \end{pmatrix}, \quad (8.9)$$

$$\tilde{\boldsymbol{\tau}}_{\text{spr}}^{CS} = 2\text{sk}(\mathbf{G}_o \mathbf{R}_{CS}^D) + \text{sk}(\mathbf{G}_t \mathbf{R}_D^{CS} \tilde{\boldsymbol{\xi}}_{CS}^D \tilde{\boldsymbol{\xi}}_{CS}^D \mathbf{R}_{CS}^D), \quad (8.10)$$

$$\tilde{\mathbf{f}}_{\text{spr}}^{CS} = \mathbf{R}_D^{CS} \text{sk}(\mathbf{G}_t \tilde{\boldsymbol{\xi}}_{CS}^D) \mathbf{R}_{CS}^D + \text{sk}(\mathbf{G}_t \mathbf{R}_D^{CS} \tilde{\boldsymbol{\xi}}_{CS}^D \mathbf{R}_{CS}^D). \quad (8.11)$$

where $\mathbf{G}_t \in \mathbb{R}^{3 \times 3}$ is the translation co-stiffness matrix corresponding to \mathbf{K}_t , and $\tilde{\boldsymbol{\tau}}_{\text{spr}}^{CS}, \tilde{\mathbf{f}}_{\text{spr}}^{CS} \in \mathfrak{so}^*(3)$ are the skew-symmetric matrices related to the covectors $\boldsymbol{\tau}_{\text{spr}}^{CS}, \mathbf{f}_{\text{spr}}^{CS} \in (\mathbb{R}^3)^*$ by (4.20).

Using (8.8), one can rewrite the energy balance (8.7) as

$$\begin{aligned} \dot{\mathcal{H}}_p &= \left\langle \partial_{\mathbf{H}_{CS}^D} \mathcal{H}_p \middle| \chi_{\mathbf{H}_{CS}^D}(\mathbf{T}_{CS}^{CS,D}) \right\rangle_{\text{SE}} \\ &= \left\langle \chi_{\mathbf{H}_{CS}^D}^* (\partial_{\mathbf{H}_{CS}^D} \mathcal{H}_p) \middle| \mathbf{T}_{CS}^{CS,D} \right\rangle_{\mathbb{R}^6} = (\mathbf{W}_{\text{spr}}^{CS})^\top \mathbf{T}_{CS}^{CS,D}. \end{aligned} \quad (8.12)$$

Remark 8.1.1. Note that the sign difference between $\mathbf{W}_{\text{spr}}^{CS}$ in (8.9) and \mathbf{W}_p^{CS} in (7.38) is simply because the latter is the spring wrench applied to the body and the former is its reaction.

Gravity compensation

Similar to the virtual spring, the gravity compensation is also represented by a combination of an energy storage element and a transformation, as shown in Fig. 8.3. The storage element is characterized by the state $\mathbf{H}_B^I \in SE(3)$ and minus the gravitational potential energy Hamiltonian $-\mathcal{H}_g : SE(3) \rightarrow \mathbb{R}$ given by

$$-\mathcal{H}_g(\mathbf{H}_B^I) = -m(\boldsymbol{\xi}_B^I)^\top \mathbf{g}. \quad (8.13)$$

The rate of change of the stored energy is given by

$$-\dot{\mathcal{H}}_g = \left\langle -\partial_{\mathbf{H}_B^I} \mathcal{H}_g \middle| \dot{\mathbf{H}}_B^I \right\rangle_{\text{SE}}, \quad (8.14)$$

where $\dot{\mathbf{H}}_B^I \in T_{\mathbf{H}_B^I} SE(3)$ and $-\partial_{\mathbf{H}_B^I} \mathcal{H}_g \in T_{\mathbf{H}_B^I}^* SE(3)$ are the flow and effort variables of the energy storage element, respectively.

The modulated transformer associated to the storage element implements the map

$$\begin{pmatrix} \dot{\mathbf{H}}_B^I \\ \mathbf{W}_g^B \end{pmatrix} = \begin{pmatrix} \mathbf{0} & \chi_{\mathbf{H}_B^I} \\ \chi_{\mathbf{H}_B^I}^* & \mathbf{0} \end{pmatrix} \begin{pmatrix} -\partial_{\mathbf{H}_B^I} \mathcal{H}_g \\ \mathbf{T}_B^{B,I} \end{pmatrix}, \quad (8.15)$$

where the first equation is a kinematics relation and the second corresponds to the wrench $\mathbf{W}_g^B \in (\mathbb{R}^6)^*$ applied to the aerial robot due to gravity, and $\mathbf{T}_B^{B,I} \in \mathbb{R}^6$ is the robot's body twist.

Similar to (8.12), one can rewrite the energy balance (8.14) as

$$-\dot{\mathcal{H}}_g = (\mathbf{W}_g^B)^\top \mathbf{T}_B^{B,I}. \quad (8.16)$$

Virtual damper

The virtual damper is represented in the bond graph of Fig. 8.3 by an energy dissipation element, denoted by \mathbb{R} , which is characterized by the static relation between its flow $\mathbf{T}_B^{B,I} \in \mathbb{R}^6$ and effort $\mathbf{W}_{\text{dmp}}^B \in (\mathbb{R}^6)^*$ defined as

$$\mathbf{W}_{\text{dmp}}^B = \mathbf{K}_d \mathbf{T}_B^{B,I}, \quad (8.17)$$

where $\mathbf{K}_d \in \mathbb{R}^{6 \times 6}$ is a symmetric positive semi-definite matrix. This static relation implies that power always flows towards the dissipation element, i.e.

$$\langle \mathbf{W}_{\text{dmp}}^B | \mathbf{T}_B^{B,I} \rangle_{\mathbb{R}^6} = (\mathbf{T}_B^{B,I})^\top \mathbf{K}_d \mathbf{T}_B^{B,I} \geq 0, \quad (8.18)$$

which represents the “free energy” dissipated by the controller emulating a virtual damper.

External power ports

The impedance controller depicted in Fig. 8.3 has two power ports that are open for interconnection to external systems. The first port $(\mathbf{W}_c^B, \mathbf{T}_B^{B,I})$ characterizes the power supplied to the aerial robot for control. The causality of this port is such that the body twist $\mathbf{T}_B^{B,I}$ is directed from the aerial robot to the impedance controller, whereas the control wrench \mathbf{W}_c^B is directed from the impedance controller to the aerial robot.

The second port $(\mathbf{W}_{\text{spr}}^D, \mathbf{T}_D^{D,I})$ characterizes the power flowing between the impedance controller and the entity connected to the virtual desired frame Ψ_D . This entity should provide the twist of Ψ_D with respect to Ψ_I as an input to the impedance controller, which in our case is a trajectory or set-point generation algorithm. However, it is important to note that changing the desired virtual set-point affects the energy stored of the controller as a dynamical system. This can be clearly seen in Fig. 8.2 since Ψ_D corresponds to one end of the virtual spring. Thus, changing the virtual set-point will affect the passivity of the closed-loop system, as will be discussed later.

Dirac structure

Central to the control-by-interconnection interpretation of the impedance controller in Fig. 8.3 is the Dirac structure \mathcal{D}_{imp} given by the relation correspond-

ing to the skew-symmetric map

$$\begin{pmatrix} \mathbf{T}_{CS}^{CS,D} \\ \mathbf{T}_B^{B,I} \\ \mathbf{T}_B^{B,I} \\ \mathbf{W}_{\text{spr}}^D \\ \mathbf{W}_c^B \end{pmatrix} = \begin{pmatrix} 0 & 0 & 0 & -\mathbf{Ad}_{\mathbf{H}_D^{CS}} & \mathbf{Ad}_{\mathbf{H}_B^{CS}} \\ 0 & 0 & 0 & 0 & \mathbf{I}_6 \\ 0 & 0 & 0 & 0 & \mathbf{I}_6 \\ \mathbf{Ad}_{\mathbf{H}_D^{CS}}^\top & 0 & 0 & 0 & 0 \\ -\mathbf{Ad}_{\mathbf{H}_B^{CS}}^\top & -\mathbf{I}_6 & -\mathbf{I}_6 & 0 & 0 \end{pmatrix} \begin{pmatrix} \mathbf{W}_{\text{spr}}^{CS} \\ \mathbf{W}_g^B \\ \mathbf{W}_{\text{dmp}}^B \\ \mathbf{T}_D^{D,I} \\ \mathbf{T}_B^{B,I} \end{pmatrix}. \quad (8.19)$$

The first equation in (8.19) corresponds to the twist relation

$$\mathbf{T}_{CS}^{CS,D} = \mathbf{Ad}_{\mathbf{H}_B^{CS}} \mathbf{T}_B^{B,I} - \mathbf{Ad}_{\mathbf{H}_D^{CS}} \mathbf{T}_D^{D,I} = \mathbf{T}_B^{CS,I} - \mathbf{T}_D^{CS,I} = \mathbf{T}_B^{CS,D},$$

which is true since Ψ_B and Ψ_{CS} are both attached to the same body. The fourth equation corresponds to the change of coordinates of the spring wrench from Ψ_{CS} to Ψ_D . Finally, the last equation corresponds to the impedance control law

$$\mathbf{W}_c^B = -\mathbf{Ad}_{\mathbf{H}_B^{CS}}^\top \mathbf{W}_{\text{spr}}^{CS} - \mathbf{W}_g^B - \mathbf{W}_{\text{dmp}}^B, \quad (8.20)$$

which is equivalent to the EB-PBC law in (7.55) using the fact that $\mathbf{W}_{\text{spr}}^{CS} = -\mathbf{W}_p^{CS}$ and $\mathbf{W}_{\text{dmp}}^B = -\mathbf{W}_d^B$ as per the sign difference in their definitions.

It is straightforward to check that the Dirac structure \mathcal{D}_{imp} corresponding to (8.19) encodes the power balance given by

$$(\mathbf{W}_{\text{spr}}^{CS})^\top \mathbf{T}_{CS}^{CS,D} + (\mathbf{W}_g^B)^\top \mathbf{T}_B^{B,I} + (\mathbf{W}_{\text{dmp}}^B)^\top \mathbf{T}_B^{B,I} + (\mathbf{W}_{\text{spr}}^D)^\top \mathbf{T}_D^{D,I} + (\mathbf{W}_c^B)^\top \mathbf{T}_B^{B,I} = 0. \quad (8.21)$$

Therefore, the power supplied by the controller $(\mathbf{W}_c^B)^\top \mathbf{T}_B^{B,I}$ can be expressed, using (8.12, 8.16, 8.18), as

$$(\mathbf{W}_c^B)^\top \mathbf{T}_B^{B,I} = -\dot{\mathcal{H}}_p + \dot{\mathcal{H}}_g - (\mathbf{T}_B^{B,I})^\top \mathbf{K}_d \mathbf{T}_B^{B,I} - (\mathbf{W}_{\text{spr}}^D)^\top \mathbf{T}_D^{D,I}. \quad (8.22)$$

In conclusion, the network of interconnected elements depicted in Fig. 8.3 is the control by interconnection interpretation of the impedance controller derived by EB-PBC in Ch.7. This controller emulates a virtual spring and virtual damper attached to the gravity-compensated aerial robot.

8.1.3 Passivity Analysis of Closed-loop System

Now we turn attention to analyzing the passivity of the closed-loop system, that includes the aerial robot and the impedance controller, with respect to the interaction port $(\mathbf{W}_{\text{int}}^B, \mathbf{T}_B^{B,I})$ characterizing the power supplied by the environment, as shown in Fig. 8.4. Intuitively speaking, a passive system is a system that can only dissipate or store energy, thus its total stored power is always non-increasing.

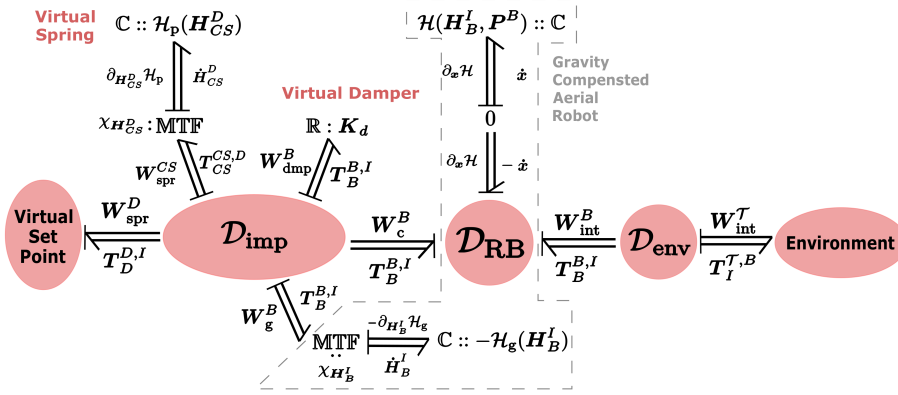


Figure 8.4: Port-based representation of the closed-loop system consisting of the impedance controller, the aerial robot, and the environment.

In the context of physical interaction, guaranteeing passivity of the closed-loop system is an effective way to ensure stable physical contact with an unknown passive environment without assuming a specific structure or model for it. In fact, it has been shown in Stramigioli [2015] that for any non-passive closed-loop system, one can always construct a passive environment that results in unstable behavior during interaction.

Thanks to the port-Hamiltonian formulation of the overall system presented above, the passivity analysis is easily performed by combining the energy balances of the Dirac structures shown in Fig. 8.4. By substituting the energy supplied by the controller (8.22) in the aerial robot's energy balance (8.3), one has that

$$\dot{\mathcal{H}}_g + \dot{\mathcal{H}}_k = -\dot{\mathcal{H}}_p + \dot{\mathcal{H}}_g - (\mathbf{T}_B^{B,I})^\top \mathbf{K}_d \mathbf{T}_B^{B,I} - (\mathbf{W}_{\text{spr}}^D)^\top \mathbf{T}_D^{D,I} + (\mathbf{W}_{\text{int}}^B)^\top \mathbf{T}_B^{B,I},$$

which can be rewritten as

$$\dot{\mathcal{H}}_k + \dot{\mathcal{H}}_p = -(\mathbf{T}_B^{B,I})^\top \mathbf{K}_d \mathbf{T}_B^{B,I} - (\mathbf{W}_{\text{spr}}^D)^\top \mathbf{T}_D^{D,I} + (\mathbf{W}_{\text{int}}^B)^\top \mathbf{T}_B^{B,I}, \quad (8.23)$$

under the assumption that the gravitational energy of the aerial robot has been perfectly compensated by the controller.

Now we take a closer look at the energy balance (8.23) to assess passivity. The left-hand-side of (8.23) corresponds to the rate of change of the total energy stored by the closed-loop system. Whereas the right-hand-side consists of the sum of the power dissipated by the virtual damper, the power due to changing the virtual spring's end connected to Ψ_D , and the power exchanged with the environment during interaction.

First, the power dissipated by the virtual damper $(\mathbf{T}_B^{B,I})^\top \mathbf{K}_d \mathbf{T}_B^{B,I}$ is always non-negative and thus contributes positively to the passivity of the system. As

for the power due to changing Ψ_D , by the subsystem named *virtual set-point* in Fig. 8.4, its power is indefinite. Thus, it is a non-passive action that could inject energy into the virtual spring. However, under the assumption that Ψ_D changes during interaction in a piece-wise constant or quasi-static manner such that

$$(\mathbf{W}_{\text{spr}}^D)^\top \mathbf{T}_D^{D,I} < (\mathbf{T}_B^{B,I})^\top \mathbf{K}_d \mathbf{T}_B^{B,I}, \quad (8.24)$$

then changing the virtual set-point does not violate the passivity.

Another factor that could potentially violate the passivity of the closed-loop system is imperfect gravity compensation. In that case, the right-hand side of (8.23) would have an extra sign-indefinite term given by $(\delta \mathbf{W}_g^B)^\top \mathbf{T}_B^{B,I}$ where $\delta \mathbf{W}_g^B \in (\mathbb{R}^6)^*$ corresponds to the error in estimating the gravitational wrench applied on the aerial robot. However, from (8.13) it can be seen that this error depends on the parametric uncertainty of the robot's mass and gravitational acceleration which in practice could be easily identified empirically. Therefore, the power injected due to imperfect gravity compensation could be assumed to be negligible compared to the power dissipated by the virtual damper. In fact, this should also be assumed for other uncertainties such as modeling errors and communication delays.

To summarize, under the aforementioned assumptions, we can express the energy balance (8.23) as

$$\dot{\mathcal{H}}_k + \dot{\mathcal{H}}_p \leq (\mathbf{W}_{\text{int}}^B)^\top \mathbf{T}_B^{B,I}, \quad (8.25)$$

which ensures the closed-loop system's passivity with respect to the interaction port $(\mathbf{W}_{\text{int}}^B, \mathbf{T}_B^{B,I})$. Thus, contact stability of the impedance-controlled aerial robot interacting with any conceivable passive environment is guaranteed.

8.2 Interaction Wrench Regulation

The basic impedance controller presented above does not allow regulating the interaction wrench with the environment to a desired value. In practice, such missing feature is certainly a prerequisite for high-precision interaction tasks.

In this section, we show how the interaction wrench can be regulated by modulating the stiffness of an additional virtual spring. Thus, the proposed impedance controller will comprise of two virtual springs, one with constant stiffness and another with variable stiffness, as shown in Fig. 8.5.

The choice of adding a new virtual spring with modulated stiffness has the advantage of *separation of concerns*. On one hand, the constant stiffness spring can be tuned for optimized motion control as well as shaping the general impedance behavior of the robot, for instance when establishing initial contact. On the other hand, the variable stiffness can be designed focusing on the goal of wrench regulation which will be shown to be a passivity-violating action.

(8.27) which yields

$$\dot{\hat{\mathbf{W}}}_{\text{int}}^B + \mathbf{K}_o \hat{\mathbf{W}}_{\text{int}}^B = \mathbf{K}_o \mathbf{W}_{\text{int}}^B, \quad (8.29)$$

which represents six first-order filters for each component of the interaction wrench, since \mathbf{K}_o is a diagonal matrix by construction.

In practice, the actual momentum dynamics (8.26) includes other external wrenches e.g. aerodynamic disturbances, unmodeled dynamics, and parametric uncertainties. The wrench computed from the observer (8.27,8.28) will actually be an estimate of all the external disturbances of the system and not just the interaction wrench.

8.2.2 Stiffness Modulation

Using the estimate of the interaction wrench applied to the aerial robot $\hat{\mathbf{W}}_{\text{int}}^B$, we will modulate the stiffness of the virtual spring in order to regulate the interaction wrench to a desired value $\mathbf{W}_{\text{des}}^T$, which is assumed, without loss of generality, to be specified in the task frame $\Psi_{\mathcal{T}}$. In this way, the desired interaction wrench can be defined independent from the orientation of the end-effector's (body-fixed) frame which is subject to aerodynamic disturbances.

Let $\bar{\mathbf{K}}^T \in \mathbb{R}^{6 \times 6}$ denote the time-varying diagonal stiffness matrix of the variable spring expressed in $\Psi_{\mathcal{T}}$. In order to achieve regulation of the interaction wrench, the six components of $\bar{\mathbf{K}}^T$ are calculated such that the wrench regulation error is steered to zero. For this purpose, we employ the simple proportional controller

$$\dot{\bar{\mathbf{K}}}^T = \mathbf{K}_{p,w} (\mathbf{W}_{\text{des}}^T - \mathbf{Ad}_{\mathbf{H}_{\mathcal{T}}^B}^\top \hat{\mathbf{W}}_{\text{int}}^B), \quad (8.30)$$

where $\mathbf{K}_{p,w} \in \mathbb{R}^{6 \times 6}$ is a diagonal matrix of positive proportional gains and the term $\mathbf{Ad}_{\mathbf{H}_{\mathcal{T}}^B}^\top \hat{\mathbf{W}}_{\text{int}}^B$ corresponds to the estimated interaction wrench applied to the aerial robot expressed in the task frame $\Psi_{\mathcal{T}}$.

In order to use the stiffness matrix $\bar{\mathbf{K}}^T$ for calculating the corresponding spring wrench, we should represent it in the center-of-stiffness frame Ψ_{CS} . We denote this representation of the stiffness matrix by $\bar{\mathbf{K}}^{CS} \in \mathbb{R}^{6 \times 6}$ and it is calculated by the following coordinate transformation

$$\bar{\mathbf{K}}^{CS} = \mathbf{Ad}_{\mathbf{H}_{CS}^T}^\top \bar{\mathbf{K}}^T \mathbf{Ad}_{\mathbf{H}_{CS}^T}. \quad (8.31)$$

While $\bar{\mathbf{K}}^T$ was designed to be a diagonal stiffness matrix, its counterpart $\bar{\mathbf{K}}^{CS}$ will not be diagonal in general. Instead, the stiffness matrix $\bar{\mathbf{K}}^{CS}$ will be a symmetric matrix of the form

$$\bar{\mathbf{K}}^{CS} = \begin{pmatrix} \bar{\mathbf{K}}_o & \bar{\mathbf{K}}_c \\ \bar{\mathbf{K}}_c^\top & \bar{\mathbf{K}}_t \end{pmatrix}, \quad (8.32)$$

with $\bar{\mathbf{K}}_o, \bar{\mathbf{K}}_c, \bar{\mathbf{K}}_t \in \mathbb{R}^{3 \times 3}$ denoting the orientation, coupling, and translation parts of the time-varying stiffness matrix $\bar{\mathbf{K}}^{CS}$, respectively.

8.2.3 Variable-Stiffness Spring

With reference to Fig. 8.5, the wrench component $\mathbf{W}_{\text{spr}}^{CS}$ of the impedance controller originates from two springs; one with constant stiffness and another with variable stiffness. The total wrench due to both springs is given by

$$\begin{aligned} \mathbf{W}_{\text{spr}}^{CS} &= \chi_{\mathbf{H}_{CS}^D}^* (\partial_{\mathbf{H}_{CS}^D} \mathcal{H}_p) \\ &= \chi_{\mathbf{H}_{CS}^D}^* (\partial_{\mathbf{H}_{CS}^D} \mathcal{H}_{p,c}) + \chi_{\mathbf{H}_{CS}^D}^* (\partial_{\mathbf{H}_{CS}^D} \mathcal{H}_{p,v}) =: \mathbf{W}_{\text{spr},c}^{CS} + \mathbf{W}_{\text{spr},v}^{CS}, \end{aligned} \quad (8.33)$$

where $\mathcal{H}_{p,c}, \mathcal{H}_{p,v}$ denote the potential energy functions of the constant and variable springs, respectively, and $\mathbf{W}_{\text{spr},c}^{CS}, \mathbf{W}_{\text{spr},v}^{CS} \in (\mathbb{R}^6)^*$ denotes their corresponding wrenches.

The potential function $\mathcal{H}_{p,c}$ of the constant spring has \mathbf{H}_{CS}^D as its state variable and is identical to (8.6). Thus, similar to (8.12), it satisfies the energy balance

$$\dot{\mathcal{H}}_{p,c} = \langle \mathbf{W}_{\text{spr},c}^{CS} | \mathbf{T}_{CS,D}^{CS,D} \rangle_{\mathbb{R}^6}. \quad (8.34)$$

On the other hand, the potential function $\mathcal{H}_{p,v}$ has two differences compared to (8.6). First, it depends on the pair $(\mathbf{H}_{CS}^D, \bar{\mathbf{K}}^{CS})$ as state variables. Second, its expression includes an additional term that models the effect of the coupling part of the stiffness matrix (8.32) such that it is expressed by [Stramigioli, 2001, Pg. 168]

$$\begin{aligned} \mathcal{H}_{p,v}(\mathbf{H}_{CS}^D, \bar{\mathbf{K}}^{CS}) &= \frac{1}{4}(\boldsymbol{\xi}_{CS}^D)^\top \bar{\mathbf{K}}_t \boldsymbol{\xi}_{CS}^D + \frac{1}{4}(\boldsymbol{\xi}_{CS}^D)^\top \mathbf{R}_{CS}^D \bar{\mathbf{K}}_t (\mathbf{R}_{CS}^D)^\top \boldsymbol{\xi}_{CS}^D \\ &\quad - \text{tr}(\bar{\mathbf{G}}_o(\mathbf{R}_{CS}^D - \mathbf{I}_3)) + \text{tr}(\bar{\mathbf{G}}_c(\mathbf{R}_{CS}^D)^\top \boldsymbol{\xi}_{CS}^D), \end{aligned} \quad (8.35)$$

where $\bar{\mathbf{G}}_o, \bar{\mathbf{G}}_c \in \mathbb{R}^{3 \times 3}$ are the co-stiffness matrices corresponding to the stiffness matrices $\bar{\mathbf{K}}_o$ and $\bar{\mathbf{K}}_c$, respectively.

The spring wrench corresponding to (8.35) will consequently contain extra terms compared to (8.9) which can be shown to be equal to [Stramigioli, 2001]

$$\mathbf{W}_{\text{spr},v}^{CS} = \begin{pmatrix} \boldsymbol{\tau}_{\text{spr},v}^{CS} \\ \mathbf{f}_{\text{spr},v}^{CS} \end{pmatrix}, \quad (8.36)$$

$$\tilde{\boldsymbol{\tau}}_{\text{spr},v}^{CS} = 2\text{sk}(\bar{\mathbf{G}}_o \mathbf{R}_{CS}^D) + \text{sk}(\bar{\mathbf{G}}_t \mathbf{R}_{CS}^D \tilde{\boldsymbol{\xi}}_{CS}^D \tilde{\boldsymbol{\xi}}_{CS}^D \mathbf{R}_{CS}^D) + 2\text{sk}(\bar{\mathbf{G}}_c \tilde{\boldsymbol{\xi}}_{CS}^D \mathbf{R}_{CS}^D), \quad (8.37)$$

$$\tilde{\mathbf{f}}_{\text{spr},v}^{CS} = \mathbf{R}_D^{CS} \text{sk}(\bar{\mathbf{G}}_t \tilde{\boldsymbol{\xi}}_{CS}^D) \mathbf{R}_{CS}^D + \text{sk}(\bar{\mathbf{G}}_t \mathbf{R}_D^{CS} \tilde{\boldsymbol{\xi}}_{CS}^D \mathbf{R}_{CS}^D) + 2\text{sk}(\bar{\mathbf{G}}_c \mathbf{R}_{CS}^D), \quad (8.38)$$

where $\bar{\mathbf{G}}_t \in \mathbb{R}^{3 \times 3}$ is the translation co-stiffness matrix corresponding to $\bar{\mathbf{K}}_t$.

The potential function of the variable-stiffness spring $\mathcal{H}_{p,v}$ satisfies the energy balance

$$\dot{\mathcal{H}}_{p,v} = \langle \mathbf{W}_{\text{spr},v}^{CS} | \mathbf{T}_{CS,D}^{CS,D} \rangle_{\mathbb{R}^6} + \left\langle \partial_{\bar{\mathbf{K}}^{CS}} \mathcal{H}_{p,v} | \dot{\bar{\mathbf{K}}}^{CS} \right\rangle_{\mathbb{R}^{6 \times 6}}, \quad (8.39)$$

where the second term corresponds to the change in energy due to varying the stiffness of the spring by the proportional law (8.30-8.31). In bond graph notation, the storage of the potential energy $\mathcal{H}_{p,v}$ is represented by a 2-port \mathbb{C} -element, as shown in Fig. 8.5.

By repeating the passivity analysis in Sec. 8.1.3 for the new impedance controller with stiffness modulation, one can easily show that the second term in (8.39) violates the passivity of the closed-loop system since it is a sign indefinite term. This can also be concluded easily by graphically inspecting the bond graph in Fig. 8.5 since the direction of the power supplied by the “stiffness modulation” module via the port $(\partial_{\dot{\mathbf{K}}^{CS}} \mathcal{H}_{p,v}, \dot{\mathbf{K}}^{CS})$ is indefinite.

In conclusion, although the variable-stiffness impedance controller has the ability to regulate the interaction wrench, the contact stability is no longer guaranteed. In the next section, we present an alternative implementation of the variable-stiffness impedance controller utilizing energy tanks and energy routing without compromising the passivity of the closed-loop system.

8.3 Energy-Aware Impedance Controller

A way to restore the passivity, violated because of regulating the interaction wrench, is by using energy routing and energy tanks [Duijndam and Stramigioli, 2004; Stramigioli, 2015]. The basic idea behind energy routing is that energy within the controller is directed from certain parts and stored in a virtual tank. This stored energy can then be used to implement the non-passive control action of wrench regulation. In this way, the total energy content of the closed-loop system remains unaffected. Thus, the contact stability of the aerial robot interacting with a passive environment is guaranteed again.

In what follows, we present the details of augmenting the impedance control with energy tanks and the effect it has on the overall closed-loop system’s passivity.

8.3.1 Idea of Energy Routing

In the modified controller augmented with an energy tank, the total spring wrench $\mathbf{W}_{\text{spr}}^{CS}$ of the impedance control law (8.20) will not be designed as in (8.33). Instead, the inclusion of the variable spring wrench $\mathbf{W}_{\text{spr},v}^{CS}$ will depend on whether there is enough energy in the virtual tank to implement this non-passive control action or not. Therefore, instead of (8.33), the total spring wrench $\mathbf{W}_{\text{spr}}^{CS}$ is calculated by

$$\mathbf{W}_{\text{spr}}^{CS} = \mathbf{W}_{\text{spr},c}^{CS} + \mathbf{W}_{\text{reg}}^{CS}, \quad (8.40)$$

where $\mathbf{W}_{\text{reg}}^{CS} \in (\mathbb{R}^6)^*$ denotes the control wrench for regulating the interaction wrench, which is chosen as

$$\mathbf{W}_{\text{reg}}^{CS} = \alpha \mathbf{W}_{\text{spr,v}}^{CS}, \quad (8.41)$$

where $0 \leq \alpha \leq 1$ is referred to as the *valve gain* which is regulated by the energy tank.

In normal operation when there is sufficient energy in the virtual tank available for wrench regulation, we have that $\alpha = 1$. Consequently, $\mathbf{W}_{\text{reg}}^{CS}$ is then equal to $\mathbf{W}_{\text{spr,v}}^{CS}$ in (8.36) and the controller emulates the virtual spring with variable-stiffness. The power \mathcal{P}_{reg} that is required for regulating the interaction wrench is given by

$$\mathcal{P}_{\text{reg}} = (\mathbf{W}_{\text{reg}}^{CS})^\top \mathbf{T}_{CS,D}^{CS,D} = \alpha (\mathbf{W}_{\text{spr,v}}^{CS})^\top \mathbf{T}_{CS,D}^{CS,D}. \quad (8.42)$$

This power is drawn from the energy tank, which is initialized by the control designer with a certain *energy budget* that is known a priori to be sufficient for achieving the desired interaction task. Once the energy tank depletes, it sets the valve gain α to zero and hence it follows that $\mathbf{W}_{\text{reg}}^{CS} = 0$. In this situation, the wrench regulation stops and the variable-stiffness spring is de-attached from the aerial robot.

If the depletion of the energy tank occurs before the interaction goal has been completely fulfilled, there could be two possibilities. One one hand, there could exist some sort of uncertainty during the interaction with the unknown environment that caused the depletion. In this case, the valve-based energy tank prevents the instabilities that could potentially occur due to continuation of the wrench regulation. On the other hand, it could be that the allocated energy budget was insufficient for the interaction task. In this case, a high-level strategy can be designed to analyze whether it is safe or not to allocate more energy in the tank to allow further regulation of the interaction wrench.

An important source of internal power that could be used to increase the energy stored in the virtual tank is the power dissipated by the virtual damper given by

$$\mathcal{P}_{\text{dmp}} = (\mathbf{W}_{\text{dmp}}^B)^\top \mathbf{T}_B^{B,I}, \quad (8.43)$$

which is always positive by construction. Instead of “throwing away” all of this power, only a certain portion of it \mathcal{P}_{dis} can be dissipated, which is given by

$$\mathcal{P}_{\text{dis}} = (1 - \eta) \mathcal{P}_{\text{dmp}}, \quad 0 < \eta \leq 1, \quad (8.44)$$

while the remainder, given by $\eta \mathcal{P}_{\text{dmp}}$ can be routed to the virtual tank to be stored. In this way, the energy dissipated by the virtual damper is exploited for implementing the wrench regulation.

Note that it is not advantageous to route all of the damper’s energy to the virtual tank (i.e. choose $\eta = 1$) since this will result in a lossless closed-loop

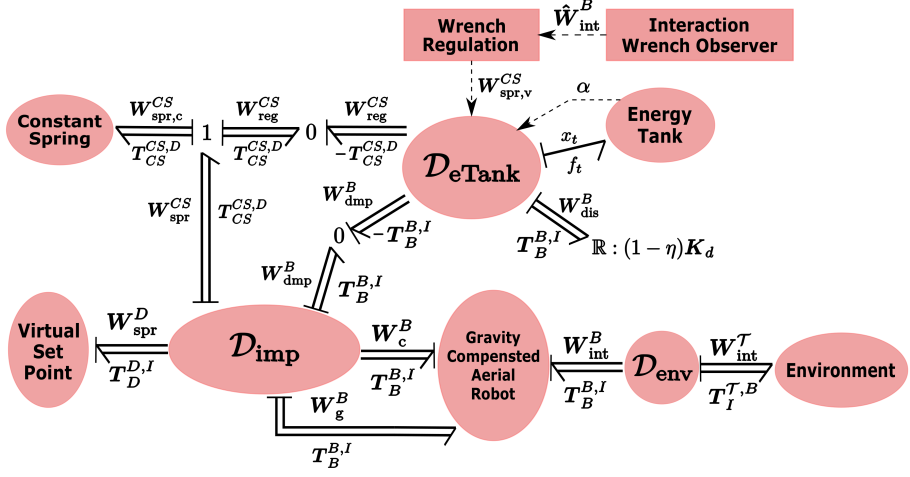


Figure 8.6: Port-based representation of the closed-loop system showing the energy-aware impedance controller which supplies the power needed for wrench regulation using an energy tank and the Dirac structure $\mathcal{D}_{\text{eTank}}$ for energy routing.

system. Since a lossless system is on the border of passivity, choosing $\eta < 1$ allows for some passivity margin which could be beneficial in the presence of other passivity violation sources, such as modeling uncertainties and changing the virtual set-point during interaction.

8.3.2 Energy Routing using a Dirac Structure

The energy routing concept described above is implemented mathematically by the Dirac structure $\mathcal{D}_{\text{eTank}}$ which mediates energy between four power ports, as shown in Fig. 8.6. The first port is $(\mathbf{W}_{\text{dmp}}^B, -\mathbf{T}_B^{B,I})$ which corresponds to $-\mathcal{P}_{\text{dmp}}$, while the second port is $(\mathbf{W}_{\text{dis}}^B, \mathbf{T}_B^{B,I})$ which corresponds to the dissipated power \mathcal{P}_{dis} , with its effort and flow variables related by the static relation

$$\mathbf{W}_{\text{dis}}^B = (1 - \eta)K_d \mathbf{T}_B^{B,I}. \quad (8.45)$$

The third port is $(\mathbf{W}_{\text{reg}}^{CS}, -\mathbf{T}_{CS}^{CS,D})$ which corresponds to $-\mathcal{P}_{\text{reg}}$, while the fourth port is (x_t, f_t) with $x_t, f_t \in \mathbb{R}$ denoting the effort and flow variables of the energy tank and their product

$$\mathcal{P}_t := x_t f_t, \quad (8.46)$$

denoting the power entering the energy tank subsystem.

The Dirac structure $\mathcal{D}_{\text{eTank}}$ connecting the aforementioned ports is defined as the relation corresponding to the skew-symmetric map given by

$$\begin{pmatrix} \mathbf{W}_{\text{reg}}^{CS} \\ \mathbf{W}_{\text{dmp}}^B \\ \mathbf{T}_B^{B,I} \\ f_t \end{pmatrix} = \begin{pmatrix} \mathbf{0} & \mathbf{0} & \mathbf{0} & \frac{\alpha}{x_t} \mathbf{W}_{\text{spr,v}}^{CS} \\ \mathbf{0} & \mathbf{0} & \mathbf{I}_6 & \frac{\eta}{x_t} \mathbf{K}_d \mathbf{T}_B^{B,I} \\ \mathbf{0} & -\mathbf{I}_6 & \mathbf{0} & \mathbf{0} \\ -\frac{\alpha}{x_t} (\mathbf{W}_{\text{spr,v}}^{CS})^\top & -\frac{\eta}{x_t} (\mathbf{K}_d \mathbf{T}_B^{B,I})^\top & \mathbf{0} & \mathbf{0} \end{pmatrix} \begin{pmatrix} -\mathbf{T}_{CS}^{CS,D} \\ -\mathbf{T}_B^{B,I} \\ \mathbf{W}_{\text{dis}}^B \\ x_t \end{pmatrix}. \quad (8.47)$$

The first equation in (8.47) implements the wrench regulation control law (8.41). The second equation can be expressed using (8.45) as

$$\mathbf{W}_{\text{dmp}}^B = \mathbf{W}_{\text{dis}}^B + \eta \mathbf{K}_d \mathbf{T}_B^{B,I} = (1 - \eta) \mathbf{K}_d \mathbf{T}_B^{B,I} + \eta \mathbf{K}_d \mathbf{T}_B^{B,I} = \mathbf{K}_d \mathbf{T}_B^{B,I}, \quad (8.48)$$

which recovers the virtual damper's wrench (8.17). The last equation in (8.47) corresponds to the flow entering the energy tank system, which can be expressed as

$$f_t = \frac{\alpha}{x_t} (\mathbf{W}_{\text{spr,v}}^{CS})^\top \mathbf{T}_{CS}^{CS,D} + \frac{\eta}{x_t} (\mathbf{K}_d \mathbf{T}_B^{B,I})^\top \mathbf{T}_B^{B,I}. \quad (8.49)$$

The energy balance encoded in the Dirac structure corresponding to (8.47) is given by

$$x_t f_t + (\mathbf{W}_{\text{dis}}^B)^\top \mathbf{T}_B^{B,I} = (\mathbf{W}_{\text{reg}}^{CS})^\top \mathbf{T}_{CS}^{CS,D} + (\mathbf{W}_{\text{dmp}}^B)^\top \mathbf{T}_B^{B,I}, \quad (8.50)$$

which can be rewritten using (8.42-8.46) as

$$\begin{aligned} \mathcal{P}_t &= \mathcal{P}_{\text{reg}} + \mathcal{P}_{\text{dmp}} - \mathcal{P}_{\text{dis}} \\ &= \mathcal{P}_{\text{reg}} + \mathcal{P}_{\text{dmp}} - (1 - \eta) \mathcal{P}_{\text{dmp}} \\ &= \mathcal{P}_{\text{reg}} + \eta \mathcal{P}_{\text{dmp}}. \end{aligned} \quad (8.51)$$

The expression (8.51) states that the power flowing into the energy tank is the sum of the power needed for regulating the interaction wrench and a portion of the virtual damper's energy. While the direction of \mathcal{P}_{dmp} is always flowing from the damper to the tank, the flow of \mathcal{P}_{reg} can be in both directions.

In conclusion, the power-preserving Dirac structure corresponding to (8.47) implements the desired energy routing concept which directs the power required to implement the wrench regulation control action from the energy tank, while exploiting a portion of the virtual damper's energy to fill the energy tank and dissipate the remainder. As long as the energy tank includes sufficient energy, the wrench regulation is equivalent to the action of a variable-stiffness virtual spring.

8.3.3 Design of the Energy Tank

With reference to Fig. 8.7, the energy tank is represented by a storage element \mathbb{C} with its state $x_t \in \mathbb{R}$ and energy function E_t given by

$$E_t(x_t) = \frac{1}{2} x_t^2. \quad (8.52)$$

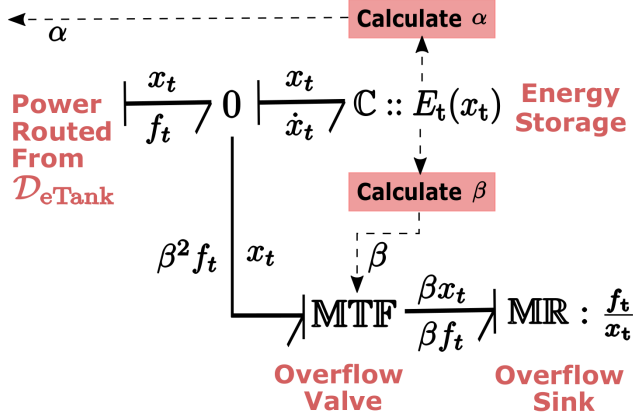


Figure 8.7: Port-based representation of the energy tank.

By construction, one has that the effort and flow variables of the storage element are given by $(x_t, \dot{x}_t) \in \mathbb{R} \times \mathbb{R}$.

The energy tank is designed such that, in addition to energy storage, it adheres to two important behaviors. First, the level of energy in the tank should never reach zero as this implies that $x_t = 0$ which would create a singularity in (8.49) and (8.41). Therefore, the tank energy should never drop below a pre-specified lower limit E_t^- . This can be enforced by setting the valve gain $\alpha = 0$ when $E_t \leq E_t^-$ and $\alpha = 1$ otherwise. To avoid discontinuities in (8.49) and (8.41) and the consequent chattering in the robot's control signals, the transition between 0 and 1 can be made smooth, as suggested by [Shahriari et al., 2018]:

$$\alpha = \begin{cases} 0 & \text{if } E_t \leq E_t^- \\ \frac{1}{2} \left[1 - \cos \left(\frac{E_t - E_t^-}{\delta E} \pi \right) \right] & \text{if } E_t^- < E_t < (E_t^- + \delta E) \\ 1 & \text{otherwise,} \end{cases} \quad (8.53)$$

for some $\delta E > 0$.

Second, the maximum level of energy in the tank should be limited to avoid a steady increase of E_t . In this way, the energy budget allocated to perform the wrench regulation can be kept under control. This maximum energy level allowed in the tank E_t^+ can be enforced by the use of an overflow valve and sink implemented using a modulated transformer and modulated resistive element, as shown in Fig. 8.7.

The flow variables of the three ports connected by the zero-junction in Fig. 8.7 satisfy the condition

$$\dot{x}_t = f_t - \beta^2 f_t = (1 - \beta^2) f_t. \quad (8.54)$$

By multiplying both sides of (8.54) we have that the power stored in the tank (i.e. $\dot{E}_t = x_t \dot{x}_t$) and the power directed from $\mathcal{D}_{\text{eTank}}$ (i.e. $\mathcal{P}_t = x_t f_t$) are related by

$$\dot{E}_t = (1 - \beta^2) \mathcal{P}_t, \quad (8.55)$$

where $\beta \in \{0, 1\}$ is a scalar that represents the state of the overflow valve calculated by

$$\beta = \begin{cases} 1 & \text{if } E_t \geq E_t^+ \text{ \& } \mathcal{P}_t > 0, \\ 0 & \text{otherwise.} \end{cases} \quad (8.56)$$

In this way, all the power that is routed from $\mathcal{D}_{\text{eTank}}$ is stored in the energy tank when $\beta = 0$. Whereas, when $\beta = 1$, all the power routed is dissipated by the modulated resistor and the maximum of E_t is ensured to be E_t^+ . Thus, the MTF emulates a virtual overflow valve.

Remark 8.3.1. Note that the discontinuity of β in (8.56) will only affect the power stored in the \mathbb{C} -element and will cause no chattering to the control signals of the robot.

8.3.4 Passivity Analysis of the Closed-loop System

Finally, we conclude this section with an analysis of the passivity of the closed loop system shown in Fig. 8.6. Recall that the passivity of the closed loop system is assessed by ensuring that the total energy stored in the system is non-increasing. Such assessment is straightforward by graphical inspection of the bond graph in Fig. 8.6, which eliminates the need of an analytic proof of passivity.

The closed-loop system (excluding the environment) consists of five dynamical systems that are interconnected together: 1) the gravity compensated aerial robot, 2) the constant virtual spring, 3) the resistive element, 4) the virtual set-point generator, and 5) the energy tank. Other modules in the system consists of the power ports, junctions, Dirac structures, and the *signal processing* parts of the controller that include the interaction wrench regulation and observer algorithms.

All the power ports, junctions, and Dirac structures are power-preserving by construction. In other words, they only route the power flowing through them without increasing or decreasing the total power. As for the signal-processing modules, they are connected such that they do not inject energy into system but instead modulate the Dirac structure $\mathcal{D}_{\text{eTank}}$. Therefore, the overall system's passivity is guaranteed if each of the individual dynamical subsystems is passive.

By construction, we have that the constant spring, the resistive element, and the energy tank are all passive dynamical systems, whereas the environment is passive by assumption. As for the gravity compensated aerial robot, it is

passive under the assumption of perfect gravity compensation. As for the virtual set-point generator, similar to Sec. 8.1.3, under the assumption that the virtual set-point Ψ_D changes during physical interaction in a piece-wise constant or quasi-static manner such that the power injected is less than that dissipated i.e.

$$(\mathbf{W}_{\text{spr}}^D)^\top \mathbf{T}_D^{D,I} < (1 - \eta)(\mathbf{T}_B^{B,I})^\top \mathbf{K}_d \mathbf{T}_B^{B,I}, \quad (8.57)$$

then the it does not violate the passivity.

In conclusion, with the above graphical inspection of Fig. 8.6, the contact stability between any passive environment and the aerial robot controlled by the proposed energy-aware impedance controller is guaranteed.

8.4 Conclusion

This chapter presented an enhanced impedance control system capable of regulating the interaction wrench of a flying end-effector while ensuring stable physical interaction with the environment.

Although the passivity of the control system was a major goal in the design process, the proposed controller relies more on the concept of “energy-awareness” rather than passivity [Stramigioli, 2015]. The addition of an energy tank did not allow the interaction wrench to be regulated passively in *any circumstance*. Instead, it allowed for means to be aware of the energy used to regulate the interaction wrench by exploiting the dissipated free energy in the controller and the estimated energy budget allowed for accomplishing the task. Therefore, the energy tank acts in fact as a safety mechanism that prevents injecting an uncontrolled amount of energy into the system that could lead to instability.

Furthermore, the advantages of the energy aware control approach presented goes beyond standard passivity-based control techniques in ensuring both *stable and safe* physical interaction. From a system-theoretic point of view, a passive system only stores or dissipates energy which implies stability. From a practical point of view, if the stored energy is huge, it could possibly be transformed into high kinetic energy of the robot leading subsequently to high-impact collisions. However, by utilizing the awareness of the energy flow within the controller, high-level algorithms could be designed to ensure additional safety requirements. Examples of these extensions can be found in [Schindlbeck and Haddadin, 2015; Raiola et al., 2018; Zult, 2020].

Finally, the simulation and experimental results validating the controller presented in this chapter can be found in [Zult, 2020] and [Rashad et al., 2021a], respectively.

CHAPTER 9

VISION-BASED IMPEDANCE CONTROL OF AN AERIAL ROBOT

In impedance control, the contact force between the UAV's end-effector and the environment is directly related to the controller's stiffness and damping parameters, as discussed in Ch.7. However, achieving a consistent performance of the UAV during interaction tasks requires a-priori knowledge of the environment's geometry and contact properties. This contradicts the main advantage of impedance control to effectively work with unmodeled environments, as well as hinders autonomous operation in unstructured environments.

In this chapter, the results of [Rashad et al., 2020a] are reported, where we present a solution combining computer-vision with impedance control such that the aerial robot is able to perceive the environment it will interact with.

The topic of vision-based interaction control is already known in the literature of industrial ground manipulators and its study has led to the accomplishment of a wide spectrum of interesting tasks. In the view of automatizing labor-intensive works, the authors in Zhou et al. [2019] proposed a combination of vision-based and impedance control to perform polishing of flat surfaces like, e.g., walls. A similar approach has been fostered also in Bonilla et al. [2010], where the authors achieved the tracking of a desired force on a non-planar surface of unknown geometry. Following the same line of thoughts, a semi-autonomous robotic pen-drawing system has been presented in Song et al. [2018].

On the other hand, despite the compelling breakthroughs recently delivered by the research related to computer vision and state estimation (*cf.* Cadena et al. [2016] for a broad overview) considerable effort has still to be made to

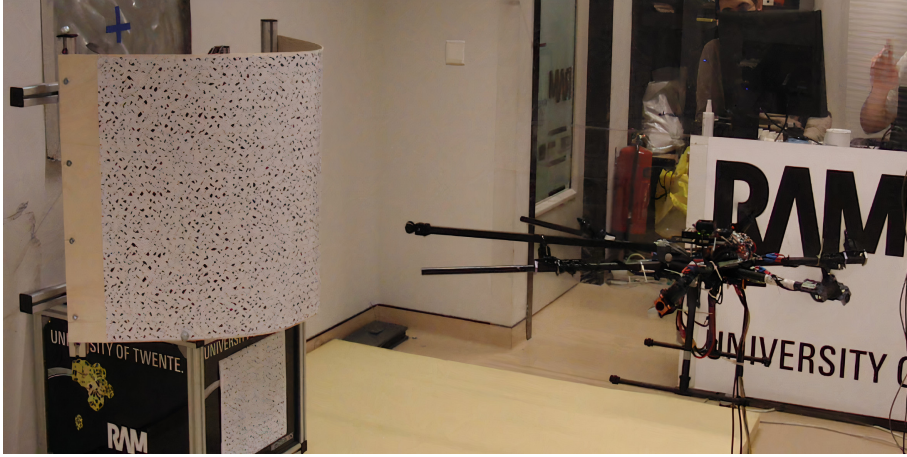


Figure 9.1: Photo of our fully-actuated aerial robot scanning an unknown curved surface prior to interaction.

integrate these techniques with interaction control in the field of aerial robotics. As a matter of fact, impressive experimental results of aerial robots interacting with the environment have been demonstrated in Alexis et al. [2016]; Staub et al. [2018]; Tognon et al. [2019]; Ryll et al. [2019], which however rely on partial a priori knowledge of the interaction target. Towards the direction of vision-aided interaction, the authors in Bodie et al. [2019] exploit depth servoing to locally reconstruct the normal directions of a ceiling vault and use an impedance-controlled omni-directional UAV to perform punctual interaction tasks.

Driven by the aim to exploit vision algorithms in more global way with respect to the object and to extend the nice results presented in Bodie et al. [2019], the work in this chapter consists of a novel **vision-based interaction framework** which allows to design a complete desired trajectory for the robot end-effector on the surface of unknown objects endowed, naturally or artificially, with features.

In this chapter, we consider the challenging task of inspecting by contact the surface of an unknown physical object by means of a flying end-effector endowed with a simple rigid tool. The accomplishment of this operation represents a proof of concept towards the tackling of a wide set of meaningful use-case applications like, e.g., the remote detection of cracks on a gas pipeline or on the blade of a wind-mill, referring to an industrial scenario, or the autonomous cleaning/painting of tall buildings, in a civil context. Differently from other approaches in the field of aerial interaction, we do not require any a priori model of the object, apart from an initial guess of its position and bounding

dimensions. More specifically, the contributions presented in this work are the following:

- the integration of a computer graphics algorithm for the projection of any 2D desired path specified by the user onto an unknown generic interaction surface without the need to analytically reconstruct it, and of an energy-based impedance controller for exerting a force;
- realistic numerical simulations in ROS/Gazebo, showing the effectiveness of our approach in different scenarios;
- preliminary experimental validation tests with a fully-actuated aerial robot interacting with planar and curved surfaces.

The chapter outline is structured as follows: In Sec. 9.1 we provide the details of the vision based interaction methodology. To validate our approach, we present the results of both numerical simulations and real experiments in Sec. 9.2 and in Sec. 9.3, respectively. In Sec. 9.4, the limitations of our proposed system are discussed, and finally we conclude this chapter in Sec. 9.5.

9.1 Vision Based Interaction Framework

9.1.1 Problem Formulation

In this work, we consider the problem of an aerial robot physically interacting with a single target of unknown pose and geometry, as shown in Figs. 9.1–9.2. The interaction task of the aerial robot consists in sliding over the target’s surface. The task is defined in terms of a desired curve and wrench profile to be tracked by the UAV along the target surface. With reference to Fig. 9.2, this desired path is a parameterized curve γ_d defined in the end-effector’s frame. The goal is then to project this desired curve in a desired normal direction \hat{n} onto the target’s surface, as shown in Fig. 9.2. The interaction planner then commands the UAV’s end-effector to the projected curve γ_p on the surface and aligns the end-effector axis with the surface normal along the curve.

With the assumption that the target surface is endowed with enough visual features, we use images from an on-board camera to perceive the object, instead of relying on an a priori computer-aided design (CAD) model. To recover information about the 3D structure of the target, one could use simultaneous localization and mapping (SLAM)-algorithms to approximately gain a spatial representation of the target as well as an estimate of the UAV’s pose relative to it. For this purpose, we employ the ORB-SLAM2 algorithm [Mur-Artal and Tardós, 2017] due to its robust properties identified in the comparative study [Gaspar et al., 2017], and its support for stereo and RGB-D cameras. The ORB-SLAM2 algorithm extracts visual features (referred to as ORBs)

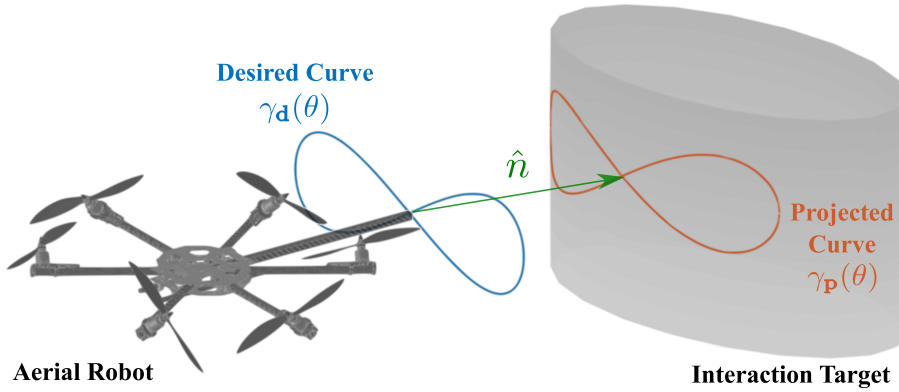


Figure 9.2: An Illustration of the curve projection idea, showing the desired curve $\gamma_d(\theta)$ in blue and the projected curve $\gamma_p(\theta)$ in orange, where θ is the curve parameter.

from the camera images and locates their relative position with respect to the estimated camera pose. The output of ORB-SLAM2 is an estimated pose of the camera and a point-cloud, where each point corresponds to the ORB features identified on the surface of the target object.

The key problem now is projecting the desired curve γ_d onto the ORB-SLAM2 point-cloud representing the point-sampled surface of the target object. In addition, we also need to estimate the normal directions to the surface.

9.1.2 Proposed Method

The problem of projecting a point/curve onto a parametric or implicit surface is a well studied problem in the computer-graphics community. Using the point-cloud generated by ORB-SLAM2, one possible solution is to reconstruct the surface from the sampled points and then use one of the traditional techniques to project the desired curve onto the reconstructed surface and estimate its normals. However, there are several practical limitations for the implementation of the aforementioned solution on point clouds generated visually on an aerial robot. First, the errors introduced due to the surface reconstruction methods of the noisy point cloud will affect the projected curve and consequently, the precision of the interaction task. Second, traditional surface reconstruction methods often fail for large and complex point clouds. Moreover, it requires high computational power and memory space which are usually scarce in small-scale UAVs.

An alternative solution is to project the curve directly to the point cloud without reconstructing the surface. In fact, point-projection algorithms onto

point clouds are used as a lower-level modules in some surface reconstruction algorithms [Liu et al., 2006]. We opt for this curve-projection method in our architecture and use for that purpose the directed projection (DP) algorithm proposed by Azariadis and Sapidis [2005] with a slight modification for increasing computational efficiency for the considered interaction application, cf. Sec. 9.2.1.

The overall interaction planning architecture is depicted in Fig. 9.3. The desired curve $\gamma_{\mathbf{d}}(\theta) \in \mathbb{R}^2$ and desired normal force profile $f_{\mathbf{d}}(\theta) \in \mathbb{R}$ are specified by the user, where $\theta \in [a, b]$ is the curve parameter for some $a, b \in \mathbb{R}$. The user also is required to specify the desired normal direction $\hat{n} \in S^2$ for which the curve is to be projected, as shown in Fig. 9.2. Let $\mathbb{C}_N = \{\xi_i \in \mathbb{R}^3 | i \in \{1, \dots, N\}\}$ denote the set of unorganized data points representing the sampling of the target object's surface generated through ORB-SLAM2. We suppose the point cloud \mathbb{C}_N to have a non-uniform distribution with possibly noise.

The curve $\gamma_{\mathbf{d}}$ is projected by discretizing it to a sequence of points N_c where we denote the k -th point by $\xi_{des,k}$ for $k \in \{1, \dots, N_c\}$. The set of points corresponding to the discretized curve is given by

$$\{\xi_{des,1}, \dots, \xi_{des,N_c}\} = \{\gamma_{\mathbf{d}}(a), \dots, \gamma_{\mathbf{d}}(b)\}. \quad (9.1)$$

For each point $\xi_{des,k}$ in (9.1), the corresponding projection point along the desired projection direction \hat{n} onto the point-cloud \mathbb{C}_N is computed by the DP algorithm. This projected point is referred to as the *foot-point* of $\xi_{des,k}$ and the set of all foot-points comprise the projected curve $\gamma_{\mathbf{p}}$.

9.1.3 Curve Projection Algorithm

In what follows, we present a summary of the DP algorithm [Azariadis and Sapidis, 2005] used for finding the foot-point of each point in (9.1) corresponding to the desired curve $\gamma_{\mathbf{d}}$.

Consider the test point $\xi_{\text{test}} := \xi_{des,k}$ that we wish to project along the direction \hat{n} onto the point-cloud \mathbb{C}_N . Each point $\xi_i \in \mathbb{C}_N$ in the point-cloud is associated with a positive weight α_i that takes into account both its distance from the test point ξ_{test} as well as its deviation from the projection direction \hat{n} . The corresponding footpoint ξ_{proj} of ξ_{test} is expressed as

$$\xi_{\text{proj}}(\tilde{t}) = \xi_{\text{test}} + \tilde{t}\hat{n}, \quad (9.2)$$

where the parameter $\tilde{t} \in \mathbb{R}$ is chosen to minimize the weighted sum

$$E(\tilde{t}) = \sum_{i=1}^N \alpha_i \|\xi_{\text{proj}}(\tilde{t}) - \xi_i\|^2. \quad (9.3)$$

The optimal parameter \tilde{t}^* is given by [Azariadis and Sapidis, 2005]

$$\tilde{t}^* = \frac{\beta - \xi_{\text{test}}^\top \hat{n}}{\|\hat{n}\|^2}, \quad \beta = \frac{c^\top \hat{n}}{c_0}, \quad (9.4)$$

where

$$c_0 = \sum_{i=1}^N \alpha_i \in \mathbb{R}^+, \quad c = \sum_{i=1}^N \alpha_i \xi_i \in \mathbb{R}^3. \quad (9.5)$$

The choice of the weights α_i affects significantly the performance of the projection algorithm. We used the same weight function suggested by Azariadis and Sapidis [2005], i.e.

$$\alpha_i = \frac{1}{1 + \|e_i\|^2 \|e_i \wedge \hat{n}\|^2}, \quad e_i := \xi_i - \xi_{\text{test}} \in \mathbb{R}^3, \quad (9.6)$$

with \wedge denoting the vector product in \mathbb{R}^3 . Intuitively, the weight function (9.6) is maximum (i.e. $\alpha_i = 1$) if ξ_{test} is on the point cloud (i.e. $e_i = 0$) or when ξ_i lies onto the projection axis \hat{n} (i.e. $e_i \wedge \hat{n} = 0$).

Due to the noise inherent in the point cloud \mathbb{C}_N , calculating the footnote corresponding to ξ_{test} by (9.2) might be erroneous. Therefore, the projection process is achieved through an iterative procedure described next and summarized in Algorithm 1.

In each iteration, a working point cloud \mathbb{C}_k is constructed (which is initially equal to \mathbb{C}_N in [Azariadis and Sapidis, 2005]), and gradually reduced by removing from it points that have low weights. After the weight α_i is calculated for each point in \mathbb{C}_k , the mean (α_{mean}) and maximum (α_{max}) weight of the point cloud \mathbb{C}_k is computed. The points that are removed in the j -th iteration are the ones with corresponding weights less than α_{lim} which is calculated as [Azariadis and Sapidis, 2005]

$$\alpha_{\text{lim}} = \begin{cases} \alpha_{\text{mean}} + \frac{\alpha_{\text{max}} - \alpha_{\text{mean}}}{10 - j} & j < 9, \\ \alpha_{\text{mean}} + \frac{\alpha_{\text{max}} - \alpha_{\text{mean}}}{2} & \text{otherwise.} \end{cases} \quad (9.7)$$

The algorithm iterates until the distance between the current projection estimation ξ_{proj} and the current test point ξ_{test} is less than a threshold ϵ or $\alpha_{\text{max}} = 1$. In the opposite case, the test point is moved to the current estimation ξ_{proj} and the new iteration starts with the smaller working point cloud that includes points with weights smaller than α_{lim} . When the algorithm terminates, it returns the foot-point ξ_{proj} of the desired point $\xi_{\text{des},k}$ we started with. The process is then repeated for each point of the desired curve to be projected.

In our work, we introduce a slight modification of the algorithm presented above in terms of the initialization of the working point \mathbb{C}_k . In the original DP algorithm in Azariadis and Sapidis [2005], the working point cloud is initially equal to \mathbb{C}_N . However, in our case we initialize \mathbb{C}_k in a different way that utilizes knowledge of the desired projection direction \hat{n} . The details of this initialization will be presented in Sec. 9.2.1.

Finally, after the projected curve $\gamma_{\mathbf{p}}$ is identified, the surface normals $\hat{n}_{\mathbf{p}}$ along the curve are estimated using the work of Rusu [2009] by estimating the normal of the tangent plane on the surface. The plane is constructed by least-square fitting of a specified number of cloud points near each point of $\gamma_{\mathbf{p}}$. Note that for our purpose of physical interaction, only the normals along $\gamma_{\mathbf{p}}$ are needed which eliminates the need to compute the normals of the whole point cloud, and consequently saves a considerable amount of computational power.

Algorithm 1: Point Projection Algorithm onto Point Cloud

```

1 Get point cloud  $\mathbb{C}_N$ , projection direction  $\hat{n}$ , selection cylinder radius
    $\rho_{cyl}$ , and desired curve point  $\xi_{des,k}$ 
2 for  $i = 1, \dots, N$  do
3   | Select  $\xi_i$  that lies within the selection cylinder
4   | Build working point cloud  $\mathbb{C}_k$  with  $N_k$  points
5  $\xi_{test} = \xi_{des,k}$ 
6 for  $j = 1, \dots, j_{max}$  do
7   | for  $i = 1, \dots, N_k$  do
8   |   | Calculate  $\alpha_i$  by (9.6)
9   |   | Calculate  $\xi_{proj}$  by (9.2,9.4,9.5)
10  |   | Calculate  $\alpha_{max}$ ,  $\alpha_{mean}$ , and  $\alpha_{lim}$  (9.7)
11  |   | if  $\|\xi_{test} - \xi_{proj}\| \leq \epsilon$  or  $\alpha_{max} = 1$  then
12  |   |   | return
13  |   | for  $i = 1, \dots, N_k$  do
14  |   |   | if  $\alpha_i < \alpha_{lim}$  then
15  |   |   |   | remove  $\xi_i$  from  $\mathbb{C}_k$ 
16  |   |  $\xi_{test} = \xi_{proj}$ 

```

9.1.4 Impedance Controller and Control Allocation

The methodology used in this work for the UAV to interact with the environment is the geometric impedance controller of Ch.7. For the reader's convenience, we provide a summary of the controller in what follows.

The impedance control law \mathbf{W}_c^B consists of the sum of an energy shaping

wrench \mathbf{W}_{es}^B and a damping injection wrench \mathbf{W}_{di}^B . The control wrench component \mathbf{W}_{di}^B is added to implement a virtual linear damper connected between the UAV's frame Ψ_B and the inertial frame Ψ_I such that energy of the closed-loop system is damped in free-flight. The role of \mathbf{W}_{es}^B is to add energy to the UAV to compensate the gravitational potential energy and to implement a virtual spatial nonlinear spring connected between the end-effector frame Ψ_E and the virtual desired frame Ψ_D . For small deviations between Ψ_E and Ψ_D , the spring control law behaves as a linear spring, decoupled in its axes.

The control for the robot is derived such that it outputs the desired control wrench \mathbf{W}_c^B on the vehicle's body. Then, in a model-based manner, the desired propellers' thrust λ are computed by the inverse of the mapping \mathbf{M} (i.e. $\lambda = \mathbf{M}^{-1}\mathbf{W}_c^B$), where the platform specific map \mathbf{M} , known as *allocation map* (cf. Ch.7), is invertible in our case thanks to the full-actuation of the robot.

Using the projected curve $\gamma_{\mathbf{p}}(\theta) \in \mathbb{R}^3$ and the surface normal directions along the curve $\hat{n}_{\mathbf{p}}(\theta) \in S^2$ calculated as discussed above, the desired (virtual) pose Ψ_D is computed as follows. First, the user specifies a function $\theta(t)$ that is used to convert the projected curve $\gamma_{\mathbf{p}}(\theta)$ and surface normals $\hat{n}_{\mathbf{p}}(\theta)$ to the time-trajectories $\gamma_{\mathbf{p}}(t)$ and $\hat{n}_{\mathbf{p}}(t)$, respectively.

Then, the end-effector's desired (virtual) orientation is denoted by $\mathbf{R}_D^I(t) \in SO(3)$. By choosing the \hat{x}_D axis of \mathbf{R}_D^I to be aligned with the surface normal, a degree of freedom is remaining to be specified by the user in choosing a desired roll angle ϕ_{des} . Then we can compute $\mathbf{R}_D^I(t)$ by

$$\begin{aligned}\mathbf{R}_D^I &= (\hat{x}_D, \hat{z}_D \wedge \hat{x}_D, \hat{z}_D), \\ \hat{x}_D(t) &= -\hat{n}_{\mathbf{p}}(t), \\ \hat{z}_D(t) &= \frac{\hat{x}_D(t) \wedge \hat{y}_D(t)}{\|\hat{x}_D(t) \wedge \hat{y}_D(t)\|}, \\ \hat{y}_D(t) &= (0, \cos(\phi_{des}(t)), \sin(\phi_{des}(t)))^\top.\end{aligned}$$

The end-effector's desired (virtual) position $\xi_D^I(t) \in \mathbb{R}^3$ is calculated by

$$\xi_D^I(t) = \gamma_{\mathbf{p}}(t) - \delta_{off}(t)\hat{n}_{\mathbf{p}}(t), \quad (9.8)$$

where $\delta_{off} \in \mathbb{R}^+$ is a positive offset specified into the target object which causes a force to be exerted by the aerial robot to the target object. Let $K_{t,x}$ denotes the translational stiffness gain along the \hat{x}_D axis, choosing the offset $\delta_{off}(t)$ by

$$\delta_{off}(t) = \frac{f_{\mathbf{d}}(t)}{K_{t,x}}, \quad (9.9)$$

could (ideally) change the force exerted by the UAV on the environment. Furthermore, if a regulation of the desired force $f_{\mathbf{d}}(t)$ is necessary for the interaction task, then the energy-aware impedance controller of Ch.8 can be used.

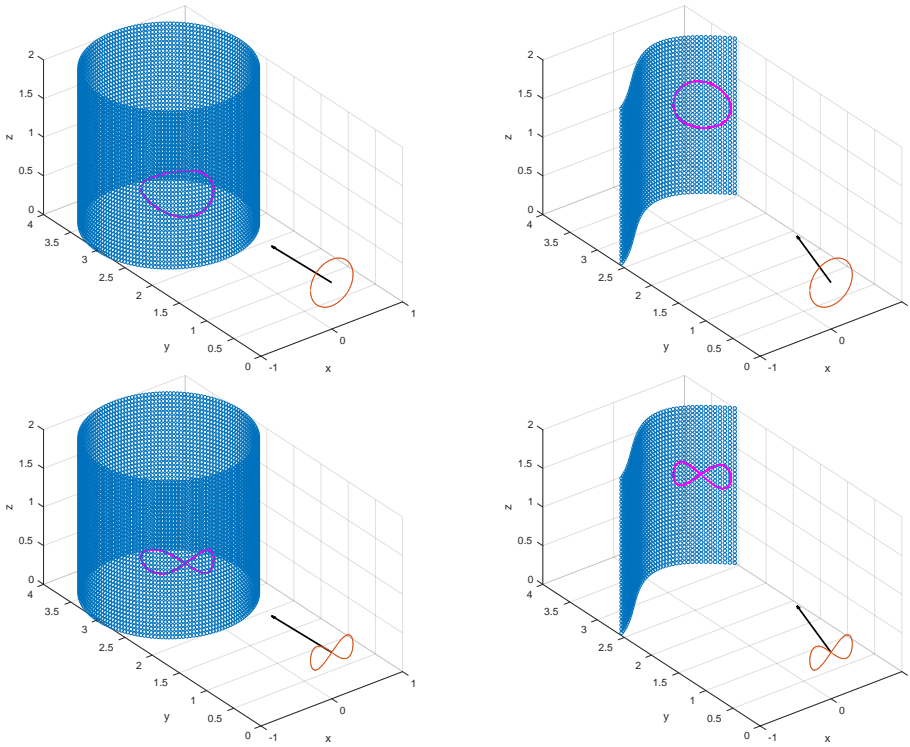


Figure 9.4: Projection algorithm tested with different trajectories and heterogeneous surfaces.

9.2 Simulation Results

9.2.1 Matlab Results

In order to improve the performance and the robustness of the original DP algorithm presented in Sec. 9.1.3 before integrating it in our vision-based interaction framework, we performed preliminary tests in a Matlab environment. In order to decrease the computational load of the algorithm when dealing with big point clouds, we observed that to project a sampled point $\xi_{\text{des},k}$ of $\gamma_{\mathbf{d}}$, it is not needed to take into account the entire point cloud \mathbb{C}_N but it is possible to consider just a subset \mathbb{C}_k of it, which should intuitively depend on $\xi_{\text{des},k}$ and on the direction \hat{n} . Our choice has been to define \mathbb{C}_k as the set of points obtained intersecting \mathbb{C}_N with a virtual cylinder centered on $\xi_{\text{des},k}$ and aligned with \hat{n} . The radius ρ_{cyl} of the cylinder is a function of the point cloud, i.e., it should guarantee that \mathbb{C}_k is not empty. If this happens, \mathbb{C}_k can be re-initialized with

\mathbb{C}_N . Fig. 9.5 depicts the execution of the modified projection algorithm.

It is worth to remark that this shrewdness does not only decrease the computational time of the algorithm, but also improves its robustness. As a matter of fact, by limiting the query set in this way, only the point closed to the “true” projection are considered, thus guaranteeing a better outlier rejection and, as a consequence, a more precise projection. However, when dealing with a pre-scanned 3D object, it could still happen that some points on the backside surface are considered, as shown in Fig. 9.5 (*cf.* the red points). To deal with this side effect, we further modify the algorithm in order to discard the furthest points based on an adaptive threshold. The resulting algorithm was extensively tested in different scenarios providing good results, as shown in Fig. 9.4.

9.2.2 Gazebo Results

In order to assess the validity our approach upon unknown surfaces in a more realistic scenario, the overall vision-based interaction framework was implemented and extensively tested in a simulation environment based on Gazebo [Koenig and Howard, 2004], the RotorS plugin [Furrer et al., 2016], and a software-in-the-loop (SITL) version of the PX4 software [Meier et al., 2015]. The SITL receives the same commands through through ROS, as the real experimental setup. This significantly reduces the time required to validate the theory with

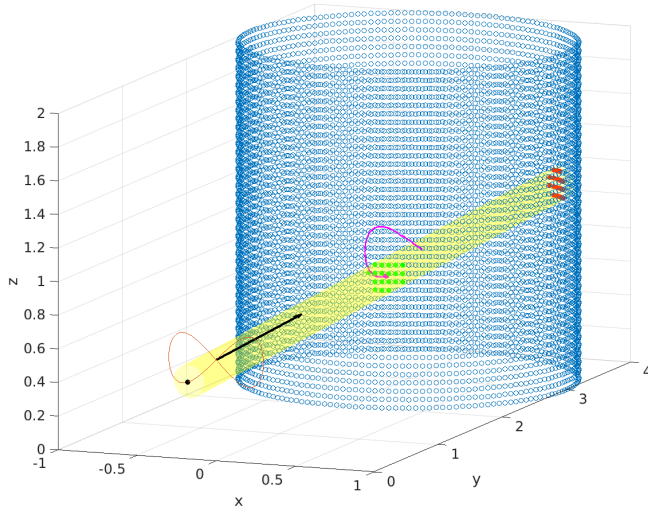
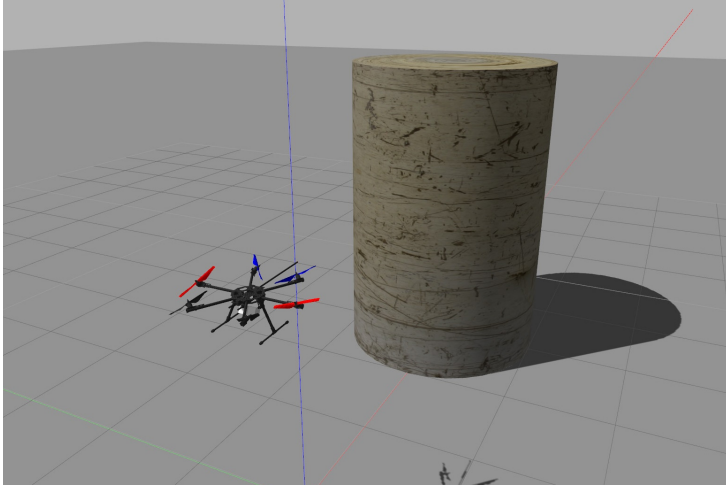
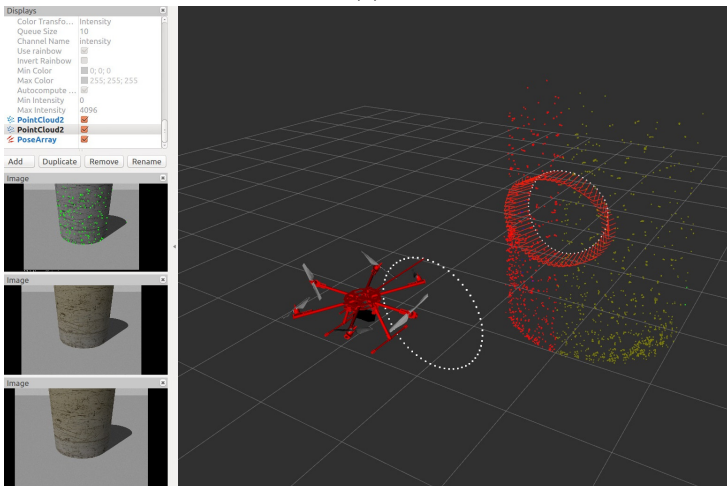


Figure 9.5: Our modified version of the projection algorithm during execution. For each of the point to be projected, only a subset of entire point cloud is used (*cf.* the green points).



(a)



(b)

Figure 9.6: The aerial robot and the target object in the simulated environment in Gazebo (a) and a snapshot of the successful execution of the vision-based interaction planner obtained using RVIZ (b).

real experiments and helps with tuning the different gains present in the control system. The simulated robot is a fully-actuated hexarotor, cf. Rashad et al. [2019b], also employed in the experimental validation. In the aforementioned scenario, we modeled the interaction target as a cylindric solid object whose surface is endowed with multiple features, cf. Fig. 9.6a.

At the beginning of the presented simulation, the aerial robot starts from a stationary initial configuration and is manually moved around the object of interest, whose position and bounding-box are supposed to be known, in order to scan the target object (phase 1). The implicit surface reconstruction is achieved from a stereo camera attached to the hexarotor's frame by extracting a dense point cloud of the environment using ORB-SLAM2 [Mur-Artal and Tardós, 2017]. To obtain the point cloud of projected curve and the estimated normal directions on the interaction surface, the interaction planning algorithm module is activated and the desired path for the robot end-effector, defined by the user in its frame, is projected on the extracted point cloud along the specified direction (phase 2). As the path is parameterized in time, the resulting trajectory is autonomously tracked by the robot under the energy-based impedance controller. The correct execution of the projection algorithm can be appreciated from the snapshot of Fig. 9.6b, which depicts the scene in the ROS 3D visualization tool RVIZ, showing the aerial robot's frame, the desired trajectory and its projection on the surface, and the associated normal vectors necessary to define the robot orientation during the interaction.

9.3 Preliminary Experimental Results

In this section, we experimentally validate the proposed vision-based interaction framework using the BetaX aerial robot. The results of two different validation tests are presented and discussed. The interested reader can find the footage of such experiments in the supplementary video.

The validation scenario for our vision-based framework is an interaction experiment with a textured surface, as shown in Fig. 9.7 and in Fig. 9.8. In particular, as inspection targets we used both a planar-tilted board and a curved-panel with cylindrical shape.

The experimental setup used differs from the simulation for what concerns the sensor source used by ORB-SLAM2 for the point cloud extraction. Instead of a stereo camera, it uses an Intel RealSense D435 RGB-D camera. Apart from this hardware detail, the rest of the architecture remain unchanged.

Although ORB-SLAM2 provides an estimate of the camera pose (which can be related to the UAV pose), we do not use this information for the UAV control. As a matter of fact, we use the Optitrack motion capture system both in the state estimation and as a ground-truth for our vision-based framework at this preliminary stage, focusing only on indoor scenarios. We accomplish

that by comparing the estimated camera pose and the measured camera pose (by Optitrack). Consequently, an error in the camera pose will also affect the estimation of the target surface.

The interaction planner executes two phases; the first is scanning the unknown target to get a dense point cloud. A series of snapshots showing the robot scanning the target surfaces and the generated point cloud can be seen in Figs. 9.7 and 9.8. The assumption of high density features is needed for a correct operation of ORB-SLAM2, but might be alleviated by choosing another SLAM algorithm. The scanning phase is done by manual operation of the UAV, while extending it to autonomous scanning is a topic of future work.

The second phase is projecting the desired curve, namely the (sampled) circle shown in Fig. 9.6b, using the aforementioned DP algorithm. After that, the normal directions along the curve are calculated. The results of the curve projection in Fig. 9.9 shows the robustness of our framework to the incompleteness and noise of the sampled surface. In addition, a significant feature of our approach is that it eliminates the need to explicitly reconstruct the target's surface, which is a challenging task to perform relying only on-board computational capabilities.

In order to indirectly validate the accuracy of the constructed point cloud, we compare the 3D position of the camera estimated by ORB-SLAM2 with the one measured by the motion capture system, as shown in Fig. 9.10 Initially the estimation error was zero, as ORB-SLAM2 was initialized with the actual camera pose. The UAV takes off at about $t = 20$ s in case of the planar surface (*cf.* Fig. 9.10a) and $t = 30$ s in case of the curved surface (*cf.* Fig. 9.10b). Then, the UAV is manually controlled to scan the surface until a sufficiently representative point cloud is generated signaled by a convergence of the estimation error of the camera's position. As shown in Fig. 9.11, the norm of the estimation error decreases with time to an average norm of 10 cm after some loop closure is detected by ORB-SLAM2.

9.4 Discussion

This section describes some of the limitations present in our vision-based interaction framework and lists some possible adverse scenarios that might cause loss in the performance.

Following the block diagram in Fig. 9.3, the three main building modules of the framework can be observed: the vision-based perception module (left), the interaction planner (middle) and the geometric impedance controller (right). Each of these blocks influence the final result of the presented approach and, therefore, its own limitations are inherited in the overall solution. The perception module chosen for our experiments consists of an Intel RealSense D435 RGB-D camera feeding Orbslam 2, the go-to algorithm for localization and

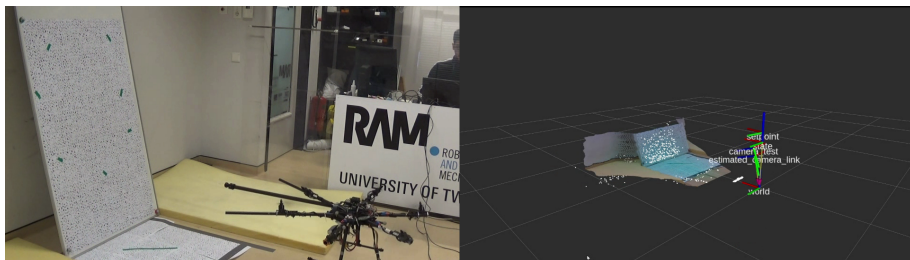
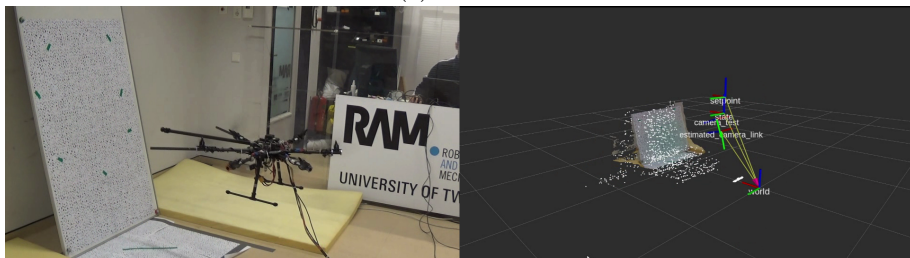
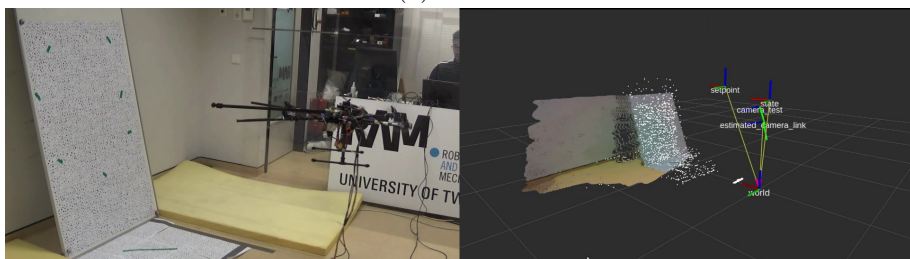
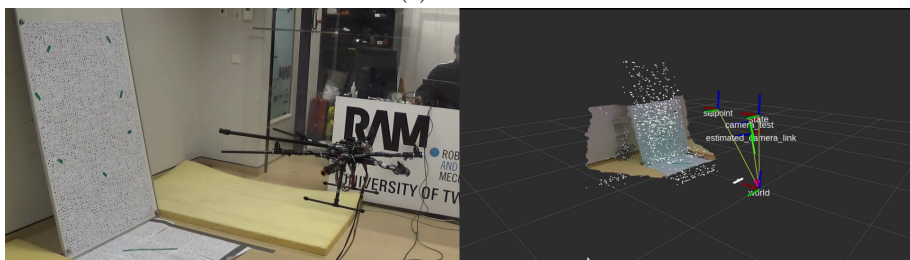
(a) $t = 24$ s(b) $t = 35$ s(c) $t = 96$ s(d) $t = 146$ s

Figure 9.7: Experiment 1: Snapshots of the UAV scanning a planar-tilted surface (left) in addition to the generated point cloud and the RGB-D camera view visualized in RVIZ (right)

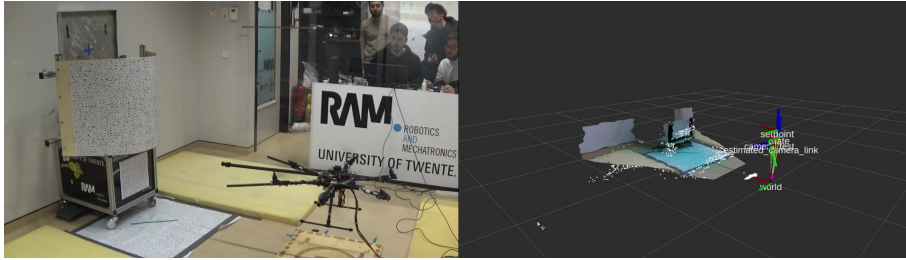
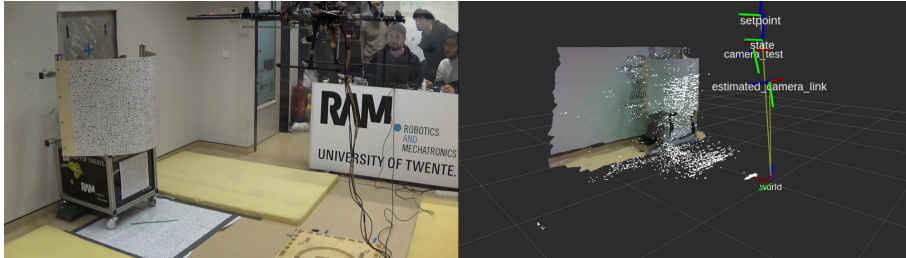
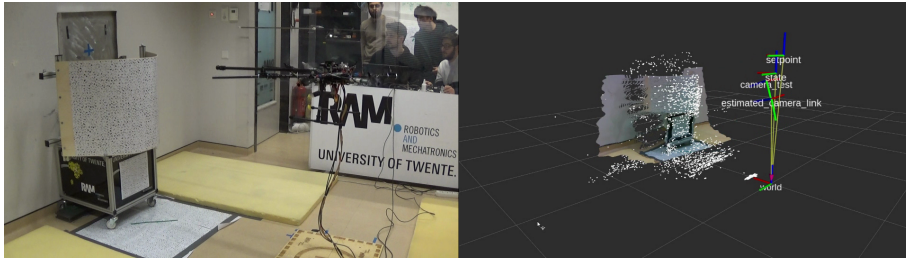
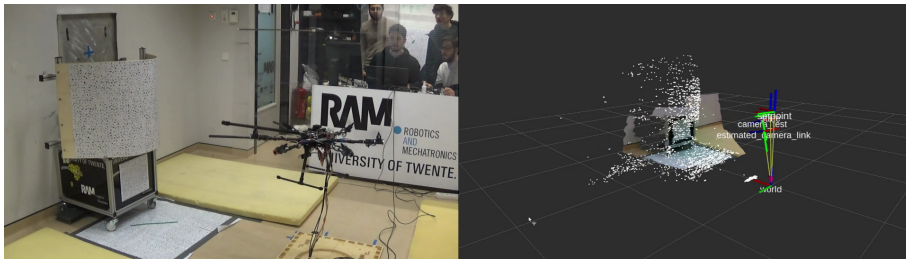
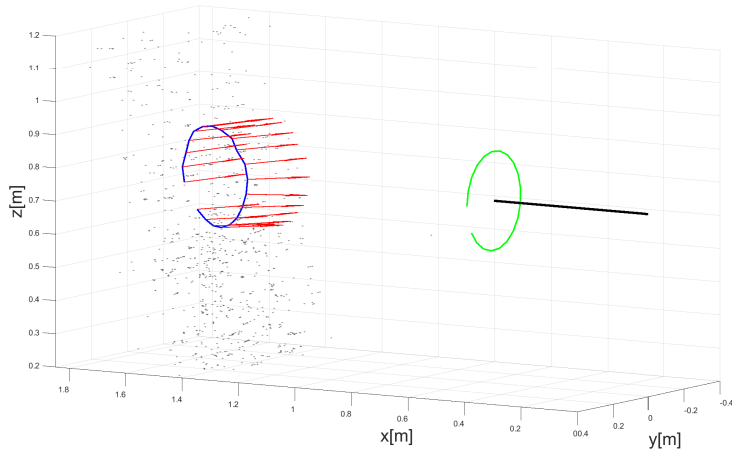
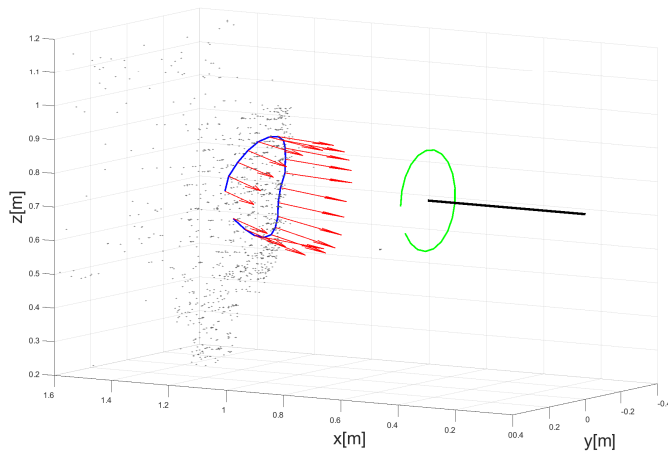
(a) $t = 27$ s(b) $t = 51$ s(c) $t = 113$ s(d) $t = 156$ s

Figure 9.8: Experiment 2: Snapshots of the UAV scanning a curved surface (left) in addition to the generated point cloud and the RGB-D camera view visualized in RVIZ (right)

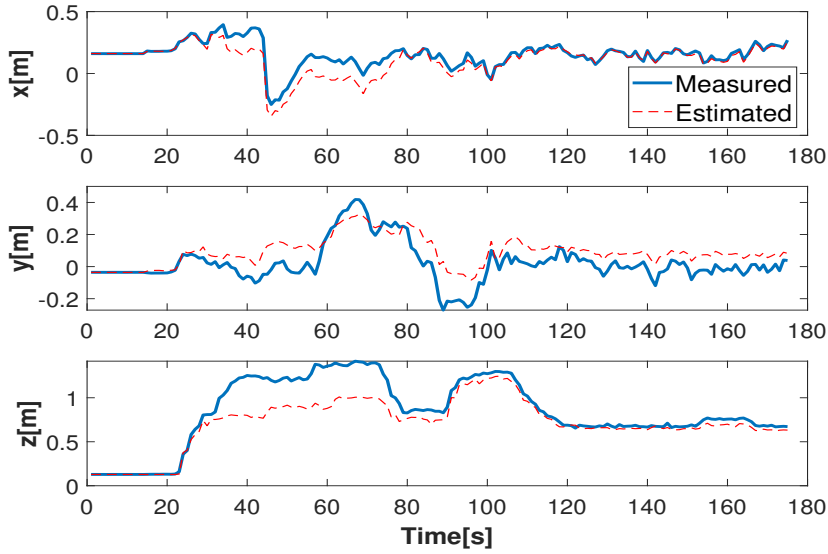


(a) Planar tilted surface

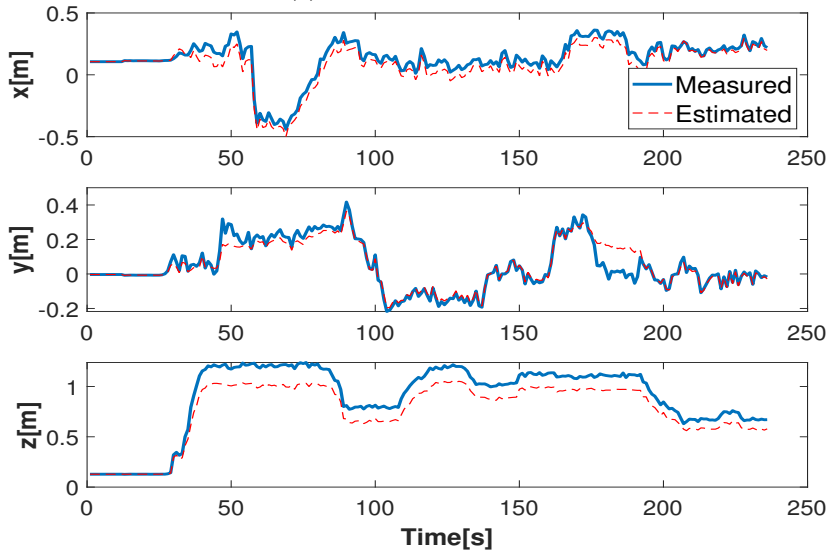


(b) Curved half-cylinder surface

Figure 9.9: Exp. Result: Validation of the Interaction Planner for two target surfaces, showing the desired curve (green) in a plane fixed to the UAV's end-effector (black line). The projected curve (blue) onto the point cloud and the surface normals (red) are also shown.



(a) Planar tilted surface



(b) Curved half-cylinder surface

Figure 9.10: Exp. Results: The Cartesian components of the estimated camera position (dashed red) by ORB-SLAM2 and the ground truth position (solid blue) captured by OptiTrack.

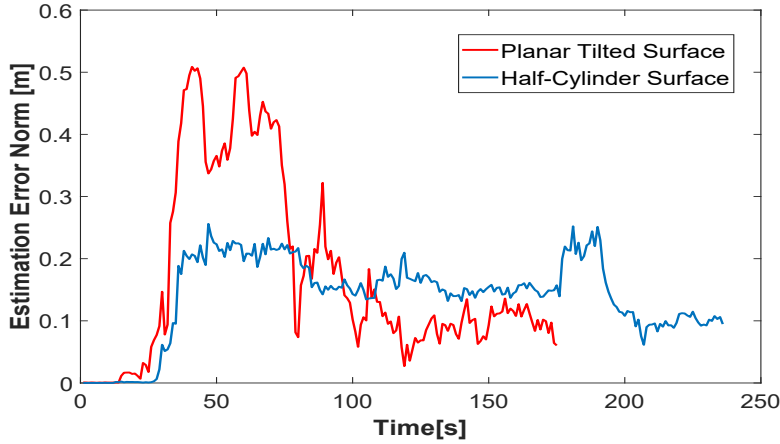


Figure 9.11: Exp. Results: Norm of estimation error of the camera position during the scanning phase for two target surfaces

point-cloud building. This type of system uses the visible features present in the environment for mapping and localization purposes. As a consequence, environments that are poor in features would not suffice our intention. This limitation can be circumvented by adding permanent or temporal artificial features to the surface of interest (*cf.* Fig. 9.1). An additional pitfall of RGB-D cameras are surfaces that are highly or poorly reflective, which can cause false readings in the depth sensor.

The proposed interaction planner algorithm presented in Sec. 9.1 assumes the viability of the curve projection on the surface and a perfect disturbance rejection to satisfy both pose and force profiles. Some situations in which this algorithm might fail are, e.g., projection on surfaces which cannot contain the target curve or with projection vector parallel to the surface of concern, and scenarios with strong external disturbances jeopardizing the interaction.

Lastly, the employed geometric impedance controller (Sec. 9.1.4) could in principle be used to interact with any surface geometry as long as it satisfies the maximum roll and pitch angles of the UAV. Moreover, the controller adopts the assumption of interaction with a passive environment. A violation of this assumption will not guarantee the contact-stability peculiar to this kind of controller.

All in all, the main contribution of this work should be considered the interaction planner module in addition to the vision-based interaction control framework as a whole, whereas some modules can be replaced by alternatives, e.g. different SLAM or interaction control algorithms.

9.5 Conclusion

In this paper, we have presented a vision-based impedance control framework for the accomplishment of aerial interaction tasks which involve the physical contact with unknown textured surfaces. Thanks to our approach, an user-defined trajectory for the robot end-effector can be projected on an arbitrarily-shaped target surface, which can subsequently be inspected by the exertion of a contact force using impedance control. The presented results obtained in preliminary experimental validations with a fully-actuated hexarotor validate our approach and open the way to new research questions, which call for solutions to more advanced problems towards autonomous aerial physical interaction.

Part III

Discussion and Conclusions

CHAPTER 10

CONCLUSIONS

10.1 Research Findings

The primary goal of this thesis was to apply the port-Hamiltonian framework for the modeling and control of a class of aerial robots that inherently interact physically with their environment. In this section, we reflect on the main findings of this thesis in light of the research questions formulated in Sec. 1.4.

The Port-Hamiltonian and Hamiltonian paradigms

Chapter 2 highlighted two fundamental differences between the port-Hamiltonian paradigm and the classic Hamiltonian paradigm. The first one was that the port-Hamiltonian framework is more suited for open dynamical systems that are essential for control. The second one was that even for a closed dynamical system, a port-Hamiltonian network-based model explicates the structure of the system more than a Hamiltonian model. This “object-oriented” property of the port-Hamiltonian paradigm is conceptually beneficial, for the modular modeling of dynamical systems, as well as practically beneficial, for the development of software tools that utilize this inherent composability. While commercial tools already exist for modeling lumped-parameter systems, e.g. 20-sim¹, so far there are no similar tools for simulating distributed-parameter systems.

Another point that was highlighted in Chapter 2 is that the well-established Hamiltonian theory can be used *within* the port-Hamiltonian modeling procedure for deriving the equations of motion of the individual subsystems com-

¹<https://www.20sim.com/>

prising the complex physical system isolated from one another. With this procedure, in light of **RQ1**, a port-Hamiltonian model of a system can be systematically derived and not constructed in an ad-hoc manner by manipulating equations.

Chapter 3 highlighted the wide applicability of the port-Hamiltonian framework to multi-physical infinite-dimensional dynamical systems by surveying over 150 research studies. The first outcome of this survey is that the majority of the research studies utilize the fact that, unlike Hamiltonian theory, the port-Hamiltonian theory allows for modeling systems with energy flow through the boundary or within the spatial domain. However, only a few number of studies apply the port-based network modeling approach when constructing port-Hamiltonian models. This is partly attributed to the presentation of the foundational work of van der Schaft and Maschke [2002] that did not highlight this network approach in infinite-dimensional systems compared to their presentation for finite-dimensional systems [Maschke et al., 1992].

The second outcome of the survey is that the Stokes-Dirac structure underlying the port-Hamiltonian models of infinite-dimensional systems is usually not derived from first principles but rather constructed by manipulating partial-differential equations. However, by understanding the relation between Dirac structures and Poisson structures, as highlighted in Chapter 2, one can use Hamiltonian-reduction techniques to systemically construct the Stokes-Dirac structure.

Rigid body motion and ideal fluid flow

Chapter 4 and 5 presented two case studies that demonstrate the systematic port-Hamiltonian modeling approach addressing **RQ1**. At first sight, a rigid body floating in a gravitational field seem to have very little in common with the flow of liquid or air on a (possible curved) surface. However, from a geometric and energetic point of view, the two systems have a lot of similarities which are usually hidden in coordinate representations using Euler angles or quaternions, in the case of rigid body motion, or using vector calculus, in the case of fluid dynamics.

The treatment presented in Chapters 4 and 5 emphasizes the fundamental fact that both a rigid body and a fluid flowing have infinitely many mass particles that move in space. For a rigid body all the particles are constrained to remain within the same distance from each other at all times, and thus this reduces the degrees of freedom to only six. On the other hand, the particles in fluid dynamics do not have this constraint and thus have infinite degrees of freedom. Consequently, the configuration space of rigid body motion was six-dimensional, while the configuration space of ideal fluid flow was infinite-dimensional.

The key common feature of rigid body motion and fluid flow that was ex-

ploited for deriving the equations of motion, is that they both have a state space that is a Lie algebra. Therefore, the port-Hamiltonian model of the kinetic energy-subsystem of both systems was derived using Lie-Poisson reduction. Furthermore, the addition of gravitational potential energy, for rigid body motion, and internal energy, for fluid flow, was easily achieved by understanding the underlying geometric structure of the state space. This understanding is of uttermost importance for the port-Hamiltonian modeling of general infinite-dimensional systems since it allows a straightforward identification of the boundary ports.

Interaction control of aerial robots

Chapter 6 surveyed a wide range of fully-actuated UAV designs that serve as candidates for developing aerial robots capable of physical interaction with the environment. Compared to other aerial manipulation solutions, such as equipping an underactuated UAV with a robotic arm, fully-actuated UAVs are mechanically simpler, which is the main motive for the popularity of multi-rotor UAVs in general.

Chapters 7 and 8 addressed **RQ2** and highlighted that physical interaction can be understood and described naturally in the port-Hamiltonian framework via energy-exchange and not by unilateral signal flow of position or force. We have shown in Chapter 7 that the motion control and impedance control problems can be formulated in terms of the effect on the system's energy caused by the controller. In this point of view, the control system is treated as a virtual dynamical system rather than a signal processor. Using passivity as the criterion for stability, the proposed control system was shown to be robust in free-flight and during interaction even when the actuators are saturated.

Chapter 8 advanced the aforementioned controller one step further by interpreting it as an interconnection of virtual physical systems. Unlike the treatment in Chapter 7 which had a more system-theoretic flavor, the work in Chapter 8 utilized deeply the port-based and energy-based paradigm. This interpretation of the impedance controller has permitted the enhancement of its capabilities using energy routing and energy tank concepts that are exclusively understood in the port-Hamiltonian paradigm. The graphical representation of the control system and the aerial robot in bond graphs allowed the visualization of the interconnection structure leading consequently to a straightforward intuition of energy tanks and energy routing.

The passivity analysis of the proposed control systems was shown to be very compact and easy. This is accredited to the port-Hamiltonian formulation which resulted in all power flow due to the interconnection structure of the system to vanish from the analysis, no matter how complex the network is. This result is a powerful well known theorem in network theory known as Tellegen's theorem. Furthermore, the passivity analysis becomes an even easier process

that can be accomplished by graphical inspection of bond graphs representing the port-Hamiltonian model.

Perception and machine-learning for aerial robots

In this thesis, **RQ3** addressed the augmentation of an impedance controlled aerial robot with signal-processing modules that are complementary to the port-Hamiltonian control system. The complement is in the sense that these modules are driven by performance optimization, whereas the goal of the port-Hamiltonian controller is to achieve stable and safe control. The work in Chapter 9 focused on the design of a module for visually perceiving the environment, whereas the work in [Khattab et al., 2019], which was not reported in this thesis, focused on enhancing the interaction performance over-time using machine learning.

Chapter 9 highlighted a general framework for vision-based aerial interaction that includes a visual-perception module and an interaction planner augmented to the impedance controller. During the integration of this framework, it was observed that visual perception solutions for mobile robots in general have evolved tremendously. This has lead to many light-weight, power-efficient, and modular solutions that can be easily integrated to aerial robots.

On the other hand, this was not the case for integrating machine learning algorithms with aerial robots due to several challenges. First, aerial robots are inherently unstable systems. Therefore, for safe operation and legislation issues, it is a necessity that a control system has 100% guaranteed stability, from a system-theoretic point of view. Consequently, end-to-end machine learning algorithms are ill-suited for the control of aerial robots, even with very high success rates. Second, due to their origin in data science, machine learning algorithms are mainly oriented to find correlations in sensory data and thus do not exploit the physical nature of robots that obey certain physical laws and causality constraints. Third, training algorithms experimentally is an extremely expensive process for aerial robots because of their high energy consumption² and intolerance for crashes that cost a lot of maintenance time.

The work in [Khattab et al., 2019] addressed the first and second challenges by employing machine learning as a high-level module that selects the design parameters of the impedance controller. In this way, the stability of the controlled aerial robot is guaranteed, the theoretical limits of the control gains are considered, and the knowledge of the physical system is exploited. As for the third challenge, the proposed learning module relied on Bayesian-optimization which has demonstrated sample-efficient behavior.

²The electrical power required for hovering the 2 kg fully-actuated hexarotor used in this thesis was ≈ 410 W.

10.2 Future Work

It is the nature of any scientific endeavor to not only answer specific research questions, but to also formulate new questions that are quite often more interesting than the original ones. In this section, some of these questions are discussed and indicated.

Modeling of flapping-wings

One of the main motivations for the study of rigid body motion and fluid flow in this thesis was to apply this knowledge in understanding the aerodynamic mechanisms used by flapping-wing creatures for flying. Such understanding would then be used to abstract specific design principles that are used to engineer flapping-wing aerial robots within the ongoing Portwings project.

The next steps to be founded on the work of Chapters 4 and 5 are the following:

- i) **Adding viscous effects:** The treatment in Chapter 5 considered only ideal fluid flow that contains stress forces due to pressure but not viscosity, which is known from experiments to be a crucial component for thrust generation in birds. For the addition of viscous effects, an important question arises: how to incorporate the Cauchy stress tensor, which is a symmetric 2-rank tensor, into the covariant formulation presented using differential forms?

Through ongoing investigations to this question, it was discovered that vector-valued forms are needed to geometrically describe viscous effects which, through a power-preserving interconnection, can be added to the ideal flow port-Hamiltonian model which was formulated in Chapter 5 using scalar-valued forms.

- ii) **Coupling fluid flow with rigid bodies:** Another interesting prerequisite for modeling flapping wings is to know how to couple the rigid body model of Chapter 4 to the fluid flow model of Chapter 5 through their open power ports. The new questions then are: how should the fluid's model be modified to allow for a time-varying spatial domain? What is the power-preserving interconnection needed to relate the boundary port variables of the fluid model to those of the rigid body model? Does the combined fluid-body model coincide with ones in the literature derived by traditional Hamiltonian theory?
- iii) **Modeling flexibility:** The next milestone is modeling flexibility effects which are naturally present in an actual bird's wing. One interesting question that arises is that whether an infinite-dimensional elastic model

is needed to capture the dynamics of a bird's wing or is it possible to do so by a network with a finite number of rigid bodies and spatial springs?

Structure-preserving simulation tool

In order to understand the behavior of the fluid-structure models mentioned above, it is necessary to have finite-approximations of the infinite-dimensional port-Hamiltonian models for simulation purposes. A drawback of conventional simulation tools, focusing only on numerical aspects, is that they fail in preserving the intrinsic properties of the models, such as passivity and conserved quantities. This created a need for structure-preserving discretization methods which is an active research direction in the port-Hamiltonian community.

A natural way of discretizing the distributed port-Hamiltonian models presented in Chapter 5 is to use discrete exterior calculus [Hirani, 2003]. By mirroring many concepts of the continuous exterior calculus formulation using chains and co-chains, such discretization methods allows a natural transfer of knowledge between analytical and computational results. Important questions that arise include: how do such structure preserving algorithms compare to the well-established conventional methods in terms of accuracy and performance and what are their limitations?

Energy-aware interaction framework

As a continuation of the energy-aware interaction framework proposed in Chapter 8, an important question that has not been tackled is: how should the energy budget allocated to the virtual tank be determined? This design parameter of the energy-aware controller has a significant effect on its behavior. If a low energy budget is allocated, then the interaction task can not be fulfilled, whereas a high energy budget could potentially lead to an unsafe interaction.

One potential solution is to rely on simulation-based approximations of the environment to estimate the required budget for normal operation. In general, this topic requires further investigation.

Autonomous outdoor aerial interaction

All of the aerial physical interaction experiments in this thesis were conducted by manual operation of the aerial robot in an indoor environment relying on high-accuracy exteroceptive sensors. Repeating the same experiments autonomously in an outdoor scenario adds tremendous challenges and opens the door for many questions.

Luckily enough, there are many research efforts in the robotics community at large that aim for the development of generic solutions for autonomous outdoor navigation and operation. However, further investigation is needed to

evaluate the applicability of these generic solutions to aerial physical interaction scenarios. One instance of such scenarios is the contact-based inspection of wind turbine blades. In this situation, navigation solutions relying on visual-perception are expected to fail due to the absence of visual-features in the environment. Thus, research into more specialized navigation solutions might be needed.

10.3 Final Word

In the end, the work in this thesis has clearly demonstrated the strengths of the geometric port-Hamiltonian paradigm, however “there ain’t no such thing as a free lunch”³. The learning process involves a considerable amount of time and effort that should be invested in understanding many known concepts in a different, but equivalent, way based on energy. It is only through this paradigm shift process that one can utilize the full capabilities of the port-Hamiltonian framework. The real compensation for the time and effort spent occurs when one crosses the borders of physical domains and dimensionality using a few abstract energetic concepts. From this point onward, one realizes that...

Energy is a powerful ally, even though we
don’t know what it really is.

Ramy Rashad.

³Robert Heinlein (1966), “The Moon is a Harsh Mistress”

BIBLIOGRAPHY

- Abraham, R., Marsden, J. E., and Ratiu, T. (1988). *Manifolds, Tensor Analysis, and Applications*, volume 75 of *Applied Mathematical Sciences*. Springer New York.
- Acosta, J., de Cos, C., and Ollero, A. (2016). A robust decentralised strategy for multi-task control of unmanned aerial systems. application on underactuated aerial manipulator. In *International Conference on Unmanned Aircraft Systems (ICUAS)*, pages 1075–1084. IEEE.
- Acosta, J., Sanchez, M., and Ollero, A. (2014). Robust control of underactuated Aerial Manipulators via IDA-PBC. In *IEEE Conference on Decision and Control (CDC)*, pages 673–678. IEEE.
- Alexis, K., Darivianakis, G., Burri, M., and Siegwart, R. (2016). Aerial robotic contact-based inspection: planning and control. *Autonomous Robots*, 40(4):631–655.
- Altmann, R. and Schulze, P. (2017). A port-Hamiltonian formulation of the Navier Stokes equations for reactive flows. *Systems and Control Letters*, 100:51–55.
- Aoues, S., Cardoso-Ribeiro, F. L., Matignon, D., and Alazard, D. (2017). Modeling and control of a rotating flexible spacecraft: a port-Hamiltonian approach. *IEEE Transactions on Control Systems Technology*, 27(1):355–362.
- Arnold, V. (1966). Sur la géométrie différentielle des groupes de lie de dimension infinie et ses applications à l’hydrodynamique des fluides parfaits. In *Annales de l’institut Fourier*, volume 16, pages 319–361.
- Arnold, V. I. and Khesin, B. A. (1998). *Topological Methods In Hydrodynamics*, volume 24. Springer-Verlag New York.

- Augner, B. (2018). *Stabilisation of infinite-dimensional port-Hamiltonian systems via dissipative boundary feedback*. PhD thesis, Universität Wuppertal, Fakultät für Mathematik und Naturwissenschaften.
- Austin, R. (2011). *Unmanned aircraft systems: UAVS design, development and deployment*, volume 54. John Wiley & Sons.
- Azariadis, P. N. and Sapidis, N. S. (2005). Drawing curves onto a cloud of points for point-based modelling. *Computer-Aided Design*, 37(1):109–122.
- Baaiu, A., Couenne, F., Eberard, D., Jallut, C., Lefevre, L., Le Gorrec, Y., and Maschke, B. (2009a). Port-based modelling of mass transport phenomena. *Mathematical and Computer Modelling of Dynamical Systems*, 15(3):233–254.
- Baaiu, A., Couenne, F., Lefevre, L., Le Gorrec, Y., and Tayakout, M. (2006). Energy based discretization of an adsorption column. *IFAC Proceedings Volumes*, 39(2):753–758.
- Baaiu, A., Couenne, F., Lefevre, L., Le Gorrec, Y., and Tayakout, M. (2009b). Structure-preserving infinite dimensional model reduction: Application to adsorption processes. *Journal of Process Control*, 19(3):394–404.
- Badr, S., Mehrez, O., and Kabeel, A. E. (2016). A novel modification for a quadrotor design. In *International Conference on Unmanned Aircraft Systems (ICUAS)*, pages 702–710. IEEE.
- Banavar, R. and Dey, B. (2010). Stabilizing a flexible beam on a cart: A distributed approach Port-Hamiltonian approach. *Journal of Nonlinear Science and Applications*, 20(2):131–151.
- Bassi, L., Macchelli, A., and Melchiorri, C. (2007). An Algorithm to Discretize One-Dimensional Distributed Port Hamiltonian Systems. In *Lagrangian and Hamiltonian Methods for Nonlinear Control 2006*, pages 61–73. Springer.
- Bellens, S., De Schutter, J., and Bruyninckx, H. (2012). A hybrid pose / wrench control framework for quadrotor helicopters. In *IEEE International Conference on Robotics and Automation (ICRA)*, pages 2269–2274. IEEE.
- Bicego, D. (2019). *Design and Control of Multi-Directional Thrust Multi-Rotor Aerial Vehicles with applications to Aerial Physical Interaction Tasks*. PhD thesis, Institut national des sciences appliquées de Toulouse.
- Bodie, K., Brunner, M., Pantic, M., Walser, S., Pfändler, P., Angst, U., Siegart, R., and Nieto, J. (2019). An omnidirectional aerial manipulation platform for contact-based inspection. *arXiv preprint arXiv:1905.03502*.

- Bodie, K., Taylor, Z., Kamel, M., and Siegwart, R. (2018). Towards efficient full pose omnidirectionality with overactuated mavs. In *International Symposium on Experimental Robotics*, pages 85–95. Springer.
- Bonilla, I., Gonzalez-Galvan, E. J., Chavez-Olivares, C., Mendoza, M., Loredon-Flores, A., Reyes, F., and Zhang, B. (2010). A vision-based, impedance control strategy for industrial robot manipulators. In *2010 IEEE International Conference on Automation Science and Engineering*, pages 216–221. IEEE.
- Breedveld, P. C. (1984). *Physical systems theory in terms of bond graphs*. PhD thesis, Technische Hogeschool Twente.
- Brescianini, D. and D’Andrea, R. (2016). Design, modeling and control of an omni-directional aerial vehicle. In *IEEE International Conference on Robotics and Automation (ICRA)*, pages 3261–3266. IEEE.
- Brescianini, D. and D’Andrea, R. (2018). An omni-directional multirotor vehicle. *Mechatronics*, 55:76–93.
- Brugnoli, A., Alazard, D., Pommier-Budinger, V., and Matignon, D. (2019a). Port-Hamiltonian formulation and symplectic discretization of plate models Part I: Mindlin model for thick plates. *Applied Mathematical Modelling*, 75:940–960.
- Brugnoli, A., Alazard, D., Pommier-budinger, V., and Matignon, D. (2019b). Port-Hamiltonian formulation and symplectic discretization of plate models Part II : Kirchhoff model for thin plates. *Applied Mathematical Modelling*, 75:961–981.
- Bullo, F. and Lewis, A. D. (2005). *Geometric Control of Mechanical Systems*. Springer New York.
- Bullo, F. and Murray, R. M. (1999). Tracking for fully actuated mechanical systems: a geometric framework. *Automatica*, 35(1):17–34.
- Cadena, C., Carlone, L., Carrillo, H., Latif, Y., Scaramuzza, D., Neira, J., Reid, I., and Leonard, J. J. (2016). Past, present, and future of simultaneous localization and mapping: Toward the robust-perception age. *IEEE Transactions on robotics*, 32(6):1309–1332.
- Califano, F., Bin, M., Macchelli, A., and Melchiorri, C. (2018). Stability Analysis of Nonlinear Repetitive Control Schemes. *IEEE Control Systems Letters*, 2(4):773–778.

- Califano, F. and Macchelli, A. (2019). A Stability Analysis Based on Dissipativity of Linear and Nonlinear Repetitive Control. *IFAC-PapersOnLine*, 52(2):40–45.
- Califano, F., Macchelli, A., and Melchiorri, C. (2017). Stability analysis of repetitive control: The port-Hamiltonian approach. In *IEEE Conference on Decision and Control (CDC)*, volume 2018, pages 1894–1899. IEEE.
- Califano, F., Rashad, R., Dijkshoorn, A., Groot Koerkamp, L., Sneep, R., Brugnoli, A., and Stramigioli, S. (2021). Decoding and realising flapping flight with port-hamiltonian system theory. *Annual Reviews in Control (to be published)*.
- Cardoso-Ribeiro, F. L., Brugnoli, A., Matignon, D., and Lefèvre, L. (2019). Port-Hamiltonian modeling, discretization and feedback control of a circular water tank. In *IEEE Conference on Decision and Control (CDC)*, pages 6881–6886.
- Cardoso-Ribeiro, F. L., Matignon, D., and Lefèvre, L. (2018). A structure-preserving partitioned finite element method for the 2d wave equation. *IFAC-PapersOnLine*, 51(3):119–124.
- Cardoso-Ribeiro, F. L., Matignon, D., and Pommier-Budinger, V. (2017). A port-Hamiltonian model of liquid sloshing in moving containers and application to a fluid-structure system. *Journal of Fluids and Structures*, 69:402–427.
- Cataldi, E., Muscio, G., Trujillo, M. A., Rodriguez, Y., Pierri, F., Antonelli, G., Caccavale, F., Viguria, A., Chiaverini, S., and Ollero, A. (2016). Impedance Control of an aerial-manipulator : Preliminary results. In *IEEE/RSJ International Conference on Intelligent Robots and Systems (IROS)*, pages 3848–3853. IEEE.
- Cervera, J., van der Schaft, A. J., and Baños, A. (2007). Interconnection of port-hamiltonian systems and composition of Dirac structures. *Automatica*, 43(2):212–225.
- Chang, E., Matloff, L. Y., Stowers, A. K., and Lentink, D. (2020). Soft biohybrid morphing wings with feathers underactuated by wrist and finger motion. *Science Robotics*, 5(38).
- Chin, D. D. and Lentink, D. (2016). Flapping wing aerodynamics: from insects to vertebrates. *Journal of Experimental Biology*, 219(7):920–932.
- Chorin, A. J. and Marsden, J. E. (1993). *A Mathematical Introduction to Fluid Mechanics*, volume 4 of *Texts in Applied Mathematics*. Springer-Verlag New York, New York, NY.

- Clemente-Gallardo, J., Lopezlena, R., and Scherpen, J. (2002). Geometric discretization of fluid dynamics. In *IEEE Conference on Decision and Control (CDC)*, volume 4, pages 4185–4190. IEEE.
- Darivianakis, G., Alexis, K., Burri, M., and Siegwart, R. (2014). Hybrid predictive control for aerial robotic physical interaction towards inspection operations. In *IEEE International Conference on Robotics and Automation (ICRA)*, pages 53–58.
- De Luca, A., Albu-Schaffer, A., Haddadin, S., and Hirzinger, G. (2006). Collision detection and safe reaction with the dlr-iii lightweight manipulator arm. In *IEEE/RSJ International Conference on Intelligent Robots and Systems (IROS)*, pages 1623–1630. IEEE.
- De Luca, A. and Mattone, R. (2005). Sensorless robot collision detection and hybrid force/motion control. In *IEEE International Conference on Robotics and Automation (ICRA)*, pages 999–1004. IEEE.
- Diagne, M. and Maschke, B. (2013). Port Hamiltonian formulation of a system of two conservation laws with a moving interface. *European Journal of Control*, 19(6):495–504.
- Dietrich, A., Wu, X., Bussmann, K., Ott, C., Albu-Schaffer, A., and Stramigioli, S. (2017). Passive Hierarchical Impedance Control Via Energy Tanks. *IEEE Robotics and Automation Letters*, 2(2):522–529.
- Doyle, C. E., Bird, J. J., Isom, T. A., Johnson, C. J., Kallman, J. C., Simpson, J. A., King, R. J., Abbott, J. J., and Minor, M. A. (2011). Avian-inspired passive perching mechanism for robotic rotorcraft. In *IEEE/RSJ International Conference on Intelligent Robots and Systems*, pages 4975–4980. IEEE.
- Duffy, J. (1990). The fallacy of modern hybrid control theory that is based on orthogonal complements of twist and wrench spaces. *Journal of Robotic Systems*, 7(2):139–144.
- Duindam, V., Macchelli, A., Stramigioli, S., and Bruyninckx, H. (2009). *Modeling and control of complex physical systems: the port-Hamiltonian approach*. Springer Science & Business Media.
- Duindam, V. and Stramigioli, S. (2004). Port-based asymptotic curve tracking for mechanical systems. *European Journal of Control*, 10(5):411–420.
- Duindam, V. and Stramigioli, S. (2008). *Modeling and control for efficient bipedal walking robots: A port-based approach*, volume 53. Springer.

- Eberard, D., Lefevre, L., and Maschke, B. (2005). Multiscale coupling in heterogeneous diffusion processes : a port-based approach. In *Proceedings of 2005 International Conference Physics and Control.*, pages 543–547. IEEE.
- Eberard, D. and Maschke, B. (2004). Port Hamiltonian systems extended to irreversible systems : The example of the heat conduction. *IFAC Proceedings Volumes*, 37(13):243–248.
- Eberard, D., Maschke, B., and van der Schaft, A. (2007). On the interconnection structures of discretized port-Hamiltonian systems. In *PAMM: Proceedings in Applied Mathematics and Mechanics*, volume 7, pages 3030005–3030006. Wiley Online Library.
- Ebin, D. G. and Marsden, J. (1970). Groups of diffeomorphisms and the motion of an incompressible fluid. *Annals of Mathematics*, pages 102–163.
- Eliakim, I., Cohen, Z., Kosa, G., and Yovel, Y. (2018). A fully autonomous terrestrial bat-like acoustic robot. *PLOS Computational Biology*, 14(9):1–13.
- Ennsbrunner, H. and Schlacher, K. (2005). On the geometrical representation and interconnection of infinite dimensional port controlled Hamiltonian systems. In *IEEE Conference on Decision and Control (CDC)*, pages 5263–5268. IEEE.
- Falaize, A. and Hélie, T. (2017). Passive simulation of the nonlinear port-Hamiltonian modeling of a Rhodes Piano. *Journal of Sound and Vibration*, 390:289–309.
- Fasse, E. D. (1997). On the Spatial Compliance of Robotic Manipulators. *Journal of Dynamic Systems, Measurement and Control*, 119(4):839–844.
- Fasse, E. D. and Broenink, J. F. (1997). A spatial impedance controller for robotic manipulation. *IEEE Transactions on Robotics and Automation*, 13(4):546–556.
- Ferraguti, F., Preda, N., Manurung, A., Bonfe, M., Lambercy, O., Gassert, R., Muradore, R., Fiorini, P., and Secchi, C. (2015). An energy tank-based interactive control architecture for autonomous and teleoperated robotic surgery. *IEEE Transactions on Robotics*, 31(5):1073–1088.
- Ferraguti, F., Secchi, C., and Fantuzzi, C. (2013). A tank-based approach to impedance control with variable stiffness. In *IEEE International Conference on Robotics and Automation (ICRA)*, pages 4948–4953. IEEE.
- Finnegan, P. (2019). World civil unmanned aerial systems market profile & forecast 2019. Technical report, Teal Group Corporation, Fairfax, VA, USA.

- Floreano, D., Zufferey, J.-C., Srinivasan, M. V., and Ellington, C. (2009). *Flying insects and robots*. Springer.
- Folkertsma, G. A., Straatman, W., Nijenhuis, N., Venner, C. H., and Stramigioli, S. (2017). Robird: a robotic bird of prey. *IEEE Robotics and Automation Magazine*, 24(3):22–29.
- Forte, F., Naldi, R., Macchelli, A., and Marconi, L. (2012). Impedance control of an aerial manipulator. In *American Control Conference (ACC)*, pages 3839–3844. IEEE.
- Franchi, A., Carli, R., Bicego, D., and Ryll, M. (2018). Full-pose tracking control for aerial robotic systems with laterally bounded input force. *IEEE Transactions on Robotics*, 34(2):534–541.
- Franken, M., Stramigioli, S., Misra, S., Secchi, C., and Macchelli, A. (2011). Bilateral telemanipulation with time delays: A two-layer approach combining passivity and transparency. *IEEE transactions on robotics*, 27(4):741–756.
- Fumagalli, M. and Carloni, R. (2013). A modified impedance control for physical interaction of UAVs. In *IEEE/RSJ International Conference on Intelligent Robots and Systems (IROS)*, pages 1979–1984. IEEE.
- Fumagalli, M., Naldi, R., Macchelli, A., Carloni, R., Stramigioli, S., and Marconi, L. (2012). Modeling and control of a flying robot for contact inspection. In *IEEE/RSJ International Conference on Intelligent Robots and Systems (IROS)*, pages 3532–3537. IEEE.
- Fumagalli, M., Naldi, R., Macchelli, A., Forte, F., Keemink, A. Q., Stramigioli, S., Carloni, R., and Marconi, L. (2014). Developing an Aerial Manipulator Prototype: Physical Interaction with the Environment. *IEEE Robotics and Automation Magazine*, 21(3):41–50.
- Furrer, F., Burri, M., Achtelik, M., and Siegwart, R. (2016). Rotors—a modular gazebo mav simulator framework. In *Robot Operating System (ROS)*, pages 595–625. Springer.
- Gaspar, A. R., Nunes, A., Pinto, A., and Matos, A. (2017). Comparative study of visual odometry and slam techniques. In *Iberian Robotics conference*, pages 463–474. Springer.
- Golo, G., Talasila, V., and van der Schaft, A. (2002). Approximation of the Telegrapher’s equations. In *IEEE Conference on Decision and Control (CDC)*, volume 4, pages 4587–4592. IEEE.
- Golo, G., Talasila, V., van der Schaft, A., and Maschke, B. (2004). Hamiltonian discretization of boundary control systems. *Automatica*, 40(5):757–771.

- Golo, G., van der Schaft, A., and Stramigioli, S. (2003). Hamiltonian Formulation of Planar Beams. *IFAC Proceedings Volumes*, 36(2):147–152.
- Goodheart, B. J. (2011). Tracing the history of the ornithopter: Past, present, and future. *Journal of Aviation/Aerospace Education & Research*, 21(1):31–44.
- Hamandi, M., Sawant, K., Tognon, M., and Franchi, A. (2020). Omni-plus-seven (o7+): An omnidirectional aerial prototype with a minimal number of unidirectional thrusters. In *International Conference on Unmanned Aircraft Systems (ICUAS)*, pages 754–761. IEEE.
- Hamroun, B., Dimofte, A., Lefèvre, L., and Mendes, E. (2010). Control by Interconnection and Energy-Shaping Methods of Port Hamiltonian Models. Application to the Shallow Water Equations. *European Journal of Control*, 16(5):545–563.
- Hamroun, B., Lefèvre, L., and Mendes, E. (2006). Port-based modelling for open channel irrigation systems. *Transactions on Fluid Mechanics*, 1(12):995–1009.
- Hamroun, B., Lefèvre, L., and Mendes, E. (2007). Port-based modelling and geometric reduction for open channel irrigation systems. In *Proceedings of the IEEE Conference on Decision and Control*, pages 1578–1583.
- Harkort, C. and Deutscher, J. (2012). Stability and passivity preserving Petrov-Galerkin approximation of linear infinite-dimensional systems. *Automatica*, 48(7):1347–1352.
- Hastir, A., Califano, F., and Zwart, H. (2019). Well-posedness of infinite-dimensional linear systems with nonlinear feedback. *Systems and Control Letters*, 128:19–25.
- Heidari, H. and Zwart, H. (2019). Port-Hamiltonian modelling of nonlocal longitudinal vibrations in a viscoelastic nanorod. *Mathematical and Computer Modelling of Dynamical Systems*, 25(5):447–462.
- Hirani, A. N. (2003). *Discrete exterior calculus*. PhD thesis, California Institute of Technology.
- Hogan, N. (1985a). Impedance control: An approach to manipulation: Part III—Applications. *Journal of Dynamic Systems, Measurement and Control*, 107(1):17–24.
- Hogan, N. (1985b). Impedance control: An approach to manipulation: Part II—Implementation. *Journal of Dynamic Systems, Measurement and Control*, 107(1):8–16.

- Hogan, N. (1985c). Impedance control: An approach to manipulation: Part I—Theory. *Journal of Dynamic Systems, Measurement and Control*, 107(1):1–7.
- Holm, D. D. (2008). *Geometric Mechanics: Part II: Rotating, Translating and Rolling*. World Scientific Publishing Company.
- Holm, D. D., Marsden, J. E., and Ratiu, T. S. (1998). The Euler–Poincaré equations and semidirect products with applications to continuum theories. *Advances in Mathematics*, 137(1):1–81.
- Holm, D. D., Schmah, T., and Stoica, C. (2009). *Geometric mechanics and symmetry: from finite to infinite dimensions*, volume 12. Oxford University Press.
- Jacob, B. and Zwart, H. (2012). *Linear Port-Hamiltonian Systems on Infinite-dimensional Spaces*, volume 223 of *Operator Theory: Advances and Applications*. Birkhäuser, Basel.
- Jacob, B. and Zwart, H. (2018). An operator theoretic approach to infinite-dimensional control systems. *GAMM Mitteilungen*, 41(4):1–14.
- Jafferis, N. T., Helbling, E. F., Karpelson, M., and Wood, R. J. (2019). Untethered flight of an insect-sized flapping-wing microscale aerial vehicle. *Nature*, 570(7762):491–495.
- Jiang, G. and Voyles, R. (2013). Hexrotor uav platform enabling dextrous interaction with structures-flight test. In *IEEE International Symposium on Safety, Security and Rescue Robotics (SSRR)*, pages 1–6. IEEE.
- Jiang, G. and Voyles, R. (2014). A nonparallel hexrotor uav with faster response to disturbances for precision position keeping. In *IEEE International Symposium on Safety, Security and Rescue Robotics (SSRR)*, pages 1–5. IEEE.
- Jiang, G., Voyles, R., Sebesta, K., and Greiner, H. (2017). Estimation and optimization of fully-actuated multirotor platform with nonparallel actuation mechanism. In *IEEE/RSJ International Conference on Intelligent Robots and Systems (IROS)*, pages 6843–6848. IEEE.
- Jiang, G., Voyles, R. M., and Choi, J. J. (2018). Precision fully-actuated uav for visual and physical inspection of structures for nuclear decommissioning and search and rescue. In *IEEE International Symposium on Safety, Security and Rescue Robotics (SSRR)*, pages 1–7. IEEE.
- Jiao, R., Rashad, R., Bicego, D., Chou, W., and Stramigioli, S. (2021). Observer-based geometric impedance control of a fully-actuated hexarotor for physical sliding interaction with unknown generic surfaces. *Journal of Intelligent & Robotic Systems(to be published)*.

- Kamel, M., Verling, S., Elkhatib, O., Sprecher, C., Wulkop, P., Taylor, Z., Siegwart, R., and Gilitschenski, I. (2018). The voliro omniorientational hexacopter: An agile and maneuverable tilttable-rotor aerial vehicle. *IEEE Robotics and Automation Magazine*, 25(4):34–44.
- Kaufman, E., Caldwell, K., Lee, D., and Lee, T. (2014). Design and development of a free-floating hexrotor uav for 6-dof maneuvers. In *IEEE Aerospace Conference*, pages 1–10. IEEE.
- Keennon, M., Klingebiel, K., and Won, H. (2012). Development of the nano hummingbird: A tailless flapping wing micro air vehicle. In *50th AIAA aerospace sciences meeting including the new horizons forum and aerospace exposition*, page 588.
- Khattab, A., Rashad, R., Engelen, J. B., and Stramigioli, S. (2019). Bayesian-optimized impedance control of an aerial robot for safe physical interaction with the environment. In *2019 IEEE International Symposium on Safety, Security, and Rescue Robotics (SSRR)*, pages 172–179. IEEE.
- Khesin, B., Misiolek, G., and Modin, K. (2020). Geometric hydrodynamics of compressible fluids. *arXiv preprint arXiv:2001.01143*.
- Kim, K.-S., Rew, K.-H., and Kim, S. (2010). Disturbance observer for estimating higher order disturbances in time series expansion. *IEEE Transactions on automatic control*, 55(8):1905–1911.
- Kiso, K., Ibuki, T., Yasuda, M., and Sampei, M. (2015). Structural optimization of hexrotors based on dynamic manipulability and the maximum translational acceleration. In *IEEE Conference on Control Applications (CCA)*, pages 774–779.
- Koenig, N. and Howard, A. (2004). Design and use paradigms for gazebo, an open-source multi-robot simulator. In *IEEE/RSJ International Conference on Intelligent Robots and Systems (IROS)*, volume 3, pages 2149–2154. IEEE.
- Korpela, C., Orsag, M., Danko, T., and Oh, P. (2014a). Insertion tasks using an aerial manipulator. In *IEEE International Conference on Technologies for Practical Robot Applications*, pages 1–6. IEEE.
- Korpela, C., Orsag, M., and Oh, P. (2014b). Towards valve turning using a dual-arm aerial manipulator. In *IEEE/RSJ International Conference on Intelligent Robots and Systems (IROS)*, number Iros, pages 3411–3416. IEEE.
- Kosaraju, K. C., Pasumarth, R., Singh, N. M., and Fradkov, A. L. (2017). Control using new passivity property with differentiation at both ports. In *Proceedings of the 2017 Indian Control Conference*, pages 7–11. IEEE.

- Kotyczka, P. (2014). On the feedforward control problem for discretized port-Hamiltonian systems. *IFAC Proceedings Volumes*, 47(3):652–658.
- Kotyczka, P. (2016). Finite Volume Structure-Preserving Discretization of 1D Distributed-Parameter Port-Hamiltonian Systems. *IFAC-PapersOnLine*, 49(8):298–303.
- Kotyczka, P. and Blancato, A. (2015). Feedforward control of a channel flow based on a discretized port-Hamiltonian model. *IFAC-PapersOnLine*, 28(13):194–199.
- Kotyczka, P. and Brandst, S. (2014). Inversion-based feedforward control for discretized port-Hamiltonian systems. In *Proceedings of the 21st International Symposium on Mathematical Theory of Networks and Systems*, pages 729–735.
- Kotyczka, P., Maschke, B., and Lefèvre, L. (2018). Weak form of Stokes-Dirac structures and geometric discretization of port-Hamiltonian systems. *Journal of Computational Physics*, 361:442–476.
- Kronander, K. and Billard, A. (2016). Passive interaction control with dynamical systems. *IEEE Robotics and Automation Letters*, 1(1):106–113.
- Kurula, M. and Zwart, H. (2015). Linear wave systems on n -D spatial domains. *International Journal of Control*, 88(5):1063–1077.
- Le Gorrec, Y., Macchelli, A., Ramirez, H., and Zwart, H. (2014). Energy shaping of boundary controlled linear port-Hamiltonian systems. *IFAC Proceedings Volumes*, 19(3):1580–1585.
- Le Gorrec, Y., Maschke, B., Villegas, J. A., and Zwart, H. (2006). Dissipative boundary control systems with application to distributed parameters reactors. In *Proceedings of the IEEE International Conference on Control Applications*, number 3, pages 668–673. IEEE.
- Le Gorrec, Y. and Matignon, D. (2013). Coupling between hyperbolic and diffusive systems: A port-Hamiltonian formulation. *European Journal of Control*, 19(6):505–512.
- Le Gorrec, Y., Zwart, H., and Maschke, B. (2005). Dirac structures and Boundary Control Systems associated with Skew-Symmetric Differential Operators. *SIAM Journal on Control and Optimization*, 44(5):1864–1892.
- Lee, T., Leoky, M., and McClamroch, N. H. (2010). Geometric tracking control of a quadrotor UAV on SE(3). In *IEEE Conference on Decision and Control (CDC)*, pages 5420–5425. IEEE.

- Lei, Y., Ji, Y., Wang, C., Bai, Y., and Xu, Z. (2017). Aerodynamic design on the non-planar rotor system of a multi-rotor flying robot. In *IEEE 3rd International Symposium in Robotics and Manufacturing Automation*, pages 1–5.
- Lequeurre, J. and Tucsna, M. (2015). The piston problem in a port-Hamiltonian formalism. *IFAC-PapersOnLine*, 28(13):212–216.
- Lippiello, V. and Ruggiero, F. (2012a). Cartesian Impedance Control of a UAV with a Robotic Arm. *IFAC Proc. Vol.*, 45(22):704–709.
- Lippiello, V. and Ruggiero, F. (2012b). Exploiting redundancy in Cartesian impedance control of UAVs equipped with a robotic arm. In *IEEE/RSJ International Conference on Intelligent Robots and Systems (IROS)*, pages 3768–3773. IEEE.
- Liu, M., Liu, K., Yang, P., Lei, X., and Li, H. (2013). Bio-inspired navigation based on geomagnetic. In *2013 IEEE International Conference on Robotics and Biomimetics (ROBIO)*, pages 2339–2344. IEEE.
- Liu, Y.-S., Paul, J.-C., Yong, J.-H., Yu, P.-Q., Zhang, H., Sun, J.-G., and Ramani, K. (2006). Automatic least-squares projection of points onto point clouds with applications in reverse engineering. *Computer-Aided Design*, 38(12):1251–1263.
- Lopezlena, R. and Scherpen, J. M. (2004a). Lumped Approximation of Transmission Line with an Alternative Geometric Discretization. *IFAC Proceedings Volumes*, 37(21):381–386.
- Lopezlena, R. and Scherpen, J. M. (2004b). On distributed port-Hamiltonian process systems. *IFAC Proceedings Volumes*, 37(13):973–978.
- Macchelli, A. (2011). Energy shaping of distributed parameter port-Hamiltonian systems based on finite element approximation. *Systems and Control Letters*, 60(8):579–589.
- Macchelli, A. (2012a). Asymptotic stability of forced equilibria for distributed port-Hamiltonian systems. In *IEEE Conference on Decision and Control (CDC)*, pages 2934–2939. IEEE.
- Macchelli, A. (2012b). Energy-Based Control of Spatially-Discretized Distributed Port-Hamiltonian Systems. *IFAC Proceedings Volumes*, 45(2):786–791.
- Macchelli, A. (2013). On the use of Dirac structures on Hilbert spaces in the synthesis of boundary control laws for port-Hamiltonian systems. In *IEEE Conference on Decision and Control (CDC)*, pages 3267–3272. IEEE.

- Macchelli, A. (2014). Dirac structures on Hilbert spaces and boundary control of distributed port-Hamiltonian systems. *Systems and Control Letters*, 68:43 – 50.
- Macchelli, A. (2015). Control by interconnection beyond the dissipation obstacle of finite and infinite dimensional port-Hamiltonian systems. In *IEEE Conference on Decision and Control (CDC)*, pages 2489–2494. IEEE.
- Macchelli, A. (2016a). Brayton-Moser formulation of infinite dimensional port-Hamiltonian systems with application to boundary control. In *IEEE Conference on Decision and Control (CDC)*, pages 543–548. IEEE.
- Macchelli, A. (2016b). On the control by interconnection and exponential stabilisation of infinite dimensional port-Hamiltonian systems. In *IEEE Conference on Decision and Control (CDC)*, pages 3137–3142. IEEE.
- Macchelli, A. and Califano, F. (2018). Dissipativity-based boundary control of linear distributed port-Hamiltonian systems. *Automatica*, 95:54–62.
- Macchelli, A., Le Gorrec, Y., and Ramírez, H. (2015a). Asymptotic stabilisation of distributed port-Hamiltonian systems by boundary energy-shaping control. *IFAC-PapersOnLine*, 28(1):488–493.
- Macchelli, A., Le Gorrec, Y., and Ramirez, H. (2015b). Boundary L2-gain stabilisation of a distributed Port-Hamiltonian system with rectangular domain. In *IEEE Conference on Decision and Control (CDC)*, pages 1236–1241. IEEE.
- Macchelli, A., Le Gorrec, Y., and Ramirez, H. (2017a). Boundary control of distributed port-Hamiltonian systems via generalised canonical transformations. In *IEEE Conference on Decision and Control (CDC)*, pages 70–75.
- Macchelli, A., Le Gorrec, Y., Ramirez, H., and Zwart, H. (2017b). On the synthesis of boundary control laws for distributed port-Hamiltonian systems. *IEEE Transactions on Automatic Control*, 62(4):1700–1713.
- Macchelli, A. and Melchiorri, C. (2004). Modeling and Control of the Timoshenko Beam. The Distributed Port Hamiltonian Approach. *SIAM Journal on Control and Optimization*, 43(2):743–767.
- Macchelli, A. and Melchiorri, C. (2005). Control by interconnection of mixed port-Hamiltonian systems. *IEEE Transactions on Automatic Control*, 50(11):1839–1844.
- Macchelli, A. and Melchiorri, C. (2009). Control by interconnection of distributed port-Hamiltonian systems based on finite elements approximation. In *Proceedings of the 48th IEEE Conference on Decision and Control (CDC), and the 2009 28th Chinese Control Conference*, pages 5133–5138.

- Macchelli, A. and Melchiorri, C. (2010). Passivity-based control of spatially discretized port-Hamiltonian system. *IFAC Proceedings Volumes*, 43(14):849–854.
- Macchelli, A., Melchiorri, C., and Bassi, L. (2005a). Port-based modelling and control of the Mindlin plate. In *Proceedings of the 44th IEEE Conference on Decision and Control, and the European Control Conference, CDC-ECC '05*, volume 2005, pages 5989–5994. IEEE.
- Macchelli, A., Melchiorri, C., and Stramigioli, S. (2007a). Port-based modeling of a flexible link. *IEEE Transactions on Robotics*, 23(4):650–660.
- Macchelli, A., Melchiorri, C., and Stramigioli, S. (2009). Port-based modeling and simulation of mechanical systems with rigid and flexible links. *IEEE Transactions on Robotics*, 25(5):1016–1029.
- Macchelli, A., Stramigioli, S., and Melchiorri, C. (2006). Port-based modelling of manipulators with flexible links. In *IEEE International Conference on Robotics and Automation (ICRA)*, volume 2006, pages 1886–1891. IEEE.
- Macchelli, A., Stramigioli, S., and Melchiorri, C. (2007b). Port-based finite element model of a flexible link. *IFAC Proceedings Volumes*, 40(12):158–163.
- Macchelli, A., van der Schaft, A., and Melchiorri, C. (2004a). Multi-variable port-Hamiltonian model of piezoelectric material. In *IEEE/RSJ International Conference on Intelligent Robots and Systems (IROS)*, volume 1, pages 897–902. IEEE.
- Macchelli, A., van der Schaft, A., and Melchiorri, C. (2004b). Port Hamiltonian formulation of infinite dimensional systems I. Modeling. In *IEEE Conference on Decision and Control (CDC)*, volume 4, pages 3762–3767 Vol.4. IEEE.
- Macchelli, A., van der Schaft, A., and Melchiorri, C. (2005b). Control By Interconnection for Distributed Port Hamiltonian Systems. *IFAC Proceedings Volumes*, 38(1):489–494.
- Mahony, R., Kumar, V., and Corke, P. (2012). Multirotor aerial vehicles. *IEEE Robotics and Automation Magazine*, 20(32):20–32.
- Malzer, T., Rams, H., and Schöberl, M. (2019). Energy-based in-domain control of a piezo-actuated Euler-Bernoulli beam. *IFAC-PapersOnLine*, 52(2):144–149.
- Marsden, J. and Abraham, R. (1970). Hamiltonian mechanics on lie groups and hydrodynamics. In *Proceedings of Symposia in Pure Mathematics*, volume 16, pages 237–244.

- Marsden, J. E. (1976). Well-posedness of the equations of a non-homogeneous perfect fluid. *Communications in Partial Differential Equations*, 1(3):215–230.
- Marsden, J. E., Ebin, D. G., and Fischer, A. E. (1972). Diffeomorphism groups, hydrodynamics, and relativity. *Proceedings of the 13th Biennial Seminar of the Canadian Mathematical Congress*, pages 135–279.
- Marsden, J. E., Ratiu, T., and Weinstein, A. (1984a). Semidirect products and reduction in mechanics. *Transactions of the American Mathematical Society*, 281(1):147–177.
- Marsden, J. E. and Ratiu, T. S. (1999). *Introduction to Mechanics and Symmetry*, volume 17 of *Texts in Applied Mathematics*. Springer-Verlag New York.
- Marsden, J. E., Ratiu, T. S., and Weinstein, A. (1984b). Reduction and hamiltonian structures on duals of semidirect product lie algebras. *Contemporary Mathematics AMS*, 28:55–100.
- Maschke, B. and van der Schaft, A. (1997). Interconnected mechanical systems, part ii: the dynamics of spatial mechanical networks. In *Modelling and control of mechanical systems*, pages 17–30. World Scientific.
- Maschke, B. and van der Schaft, A. J. (2013). On alternative Poisson brackets for fluid dynamical systems and their extension to Stokes-Dirac structures. *IFAC Proceedings Volumes*, 46(26):109–114.
- Maschke, B. M. and van der Schaft, A. J. (1992). Port-controlled hamiltonian systems: modelling origins and systemtheoretic properties. *IFAC Proceedings Volumes*, 25(13):359–365.
- Maschke, B. M., van der Schaft, A. J., and Breedveld, P. C. (1992). An intrinsic hamiltonian formulation of network dynamics: Non-standard poisson structures and gyrators. *Journal of the Franklin institute*, 329(5):923–966.
- Mazur, M. and Wiśniewski, A. (2016). Clarity from above-pwc global report on the commercial applications of drone technology. Technical report, PwC Polska, Warszawa, Poland.
- Mehmood, H., Nakamura, T., and Johnson, E. N. (2016). A maneuverability analysis of a novel hexarotor UAV concept. In *International Conference on Unmanned Aircraft Systems (ICUAS)*, pages 437–446. IEEE.
- Meier, L., Honegger, D., and Pollefeys, M. (2015). Px4: A node-based multi-threaded open source robotics framework for deeply embedded platforms. In *IEEE International Conference on Robotics and Automation (ICRA)*, pages 6235–6240. IEEE.

- Mersha, A. Y., Carloni, R., and Stramigioli, S. (2011). Port-based modeling and control of underactuated aerial vehicles. In *IEEE International Conference on Robotics and Automation (ICRA)*, pages 14–19. IEEE.
- Mersha, A. Y., Stramigioli, S., and Carloni, R. (2014). Variable impedance control for aerial interaction. *IEEE/RSJ International Conference on Intelligent Robots and Systems (IROS)*, pages 3435–3440.
- Michieletto, G., Ryll, M., and Franchi, A. (2018). Fundamental actuation properties of multirotors: Force–moment decoupling and fail–safe robustness. *IEEE Transactions on Robotics*, 34(3):702–715.
- Modin, K., Perlmutter, M., Marsland, S., and McLachlan, R. (2011). On Euler–Arnold equations and totally geodesic subgroups. *Journal of Geometry and Physics*, 61(8):1446–1461.
- Montbrun-Di Filippo, J., Delgado, M., Brie, C., and Paynter, H. M. (1991). A survey of bond graphs: Theory, applications and programs. *Journal of the Franklin Institute*, 328(5-6):565–606.
- Morrison, P. J. (1998). Hamiltonian description of the ideal fluid. *Reviews of modern physics*, 70(2):467.
- Moulla, R., Lefèvre, L., and Maschke, B. (2011). Geometric pseudospectral method for spatial integration of dynamical systems. *Mathematical and Computer Modelling of Dynamical Systems*, 17(1):85–104.
- Moulla, R., Lefèvre, L., and Maschke, B. (2012). Pseudo-spectral methods for the spatial symplectic reduction of open systems of conservation laws. *Journal of Computational Physics*, 231(4):1272–1292.
- Munson, K. G. (1969). *Aircraft of World War I*. Ian Allan Ltd.
- Mur-Artal, R. and Tardós, J. D. (2017). Orb-slam2: An open-source slam system for monocular, stereo, and rgb-d cameras. *IEEE Transactions on Robotics*, 33(5):1255–1262.
- Nava, G., Sablé, Q., Tognon, M., Pucci, D., and Franchi, A. (2019). Direct force feedback control and online multi-task optimization for aerial manipulators. *IEEE Robotics and Automation Letters*, 5(2):331–338.
- Nguyen, H.-N., Ha, C., and Lee, D. (2015). Mechanics, control and internal dynamics of quadrotor tool operation. *Automatica*, 61:289–301.
- Nguyen, H.-N. and Lee, D. (2013). Hybrid force/motion control and internal dynamics of quadrotors for tool operation. In *IEEE/RSJ International Conference on Intelligent Robots and Systems (IROS)*, pages 3458–3464. IEEE.

- Nikou, A., Gavridis, G. C., and Kyriakopoulos, K. J. (2015). Mechanical Design, Modelling and Control of a Novel Aerial Manipulator. In *IEEE International Conference on Robotics and Automation (ICRA)*, pages 4698–4703.
- Nishida, G. and Maschke, B. (2018). Topological geometric extension of Stokes-Dirac structures for global energy flows. In *2019 18th European Control Conference (ECC)*, pages 1878–1883. EUCA.
- Nishida, G., Maschke, B., and Ikeura, R. (2015). Boundary Integrability of Multiple Stokes-Dirac Structures. *SIAM Journal on Control and Optimization*, 53(2):800–815.
- Nishida, G., Maschke, B., and Yamakita, M. (2008a). Topological geometry and control for distributed port-Hamiltonian systems with non-integrable structures. In *IEEE Conference on Decision and Control (CDC)*, pages 1291–1297.
- Nishida, G. and Sakamoto, N. (2010). Port-based modeling of magnetohydrodynamics equations for tokamaks. In *IEEE International Conference on Control Applications*, pages 842–847. IEEE.
- Nishida, G., Sugiura, M., Yamakita, M., Maschke, B., and Ikeura, R. (2009). Boundary detection of variational symmetry breaking using port-representation of conservation laws. In *IEEE Conference on Decision and Control (CDC)*, pages 2861–2868. IEEE.
- Nishida, G., Sugiura, M., Yamakita, M., Maschke, B., and Ikeura, R. (2012). Multi-input multi-output integrated ionic polymer-metal composite for energy controls. *Micromachines*, 3(1):126–136.
- Nishida, G., Takagi, K., Maschke, B., and Luo, Z. (2008b). Multi-scale distributed port-Hamiltonian representation of ionic polymer-metal composite. *IFAC Proceedings Volumes*, 17(1):2300–2305.
- Nishida, G., Takagi, K., Maschke, B., and Osada, T. (2011). Multi-scale distributed parameter modeling of ionic polymer-metal composite soft actuator. *Control Engineering Practice*, 19(4):321–334.
- Nishida, G., Yamaguchi, K., and Sakamoto, N. (2013). Optimality of passivity-based controls for distributed port-Hamiltonian systems. *IFAC Proceedings Volumes*, 46(23):146–151.
- Nishida, G. and Yamakita, M. (2004). A higher order Stokes-Dirac structure for distributed-parameter port-Hamiltonian systems. In *American Control Conference (ACC)*, pages 5004–5009 vol.6. IEEE.

- Nishida, G. and Yamakita, M. (2005). Formal distributed port-Hamiltonian representation of field equations. In *Proceedings of the 44th IEEE Conference on Decision and Control, and the European Control Conference*, volume 2005, pages 6009–6015. IEEE.
- Nishida, G., Yamakita, M., and Luo, Z. (2006). Field Port-Lagrangian Representation of Conservation Laws for Variational Symmetries. In *IEEE Conference on Decision and Control (CDC)*, pages 5875–5881. IEEE.
- Nishida, G., Yamakita, M., and Luo, Z. W. (2007). Port-representation of bi-Hamiltonian structure for infinite-dimensional symmetry. In *IEEE Conference on Decision and Control (CDC)*, pages 5588–5593.
- Nonami, K., Kendoul, F., Suzuki, S., Wang, W., and Nakazawa, D. (2010). *Autonomous flying robots: unmanned aerial vehicles and micro aerial vehicles*. Springer Science & Business Media.
- Odelga, M., Stegagno, P., and Bulthoff, H. H. (2016). A fully actuated quadrotor UAV with a propeller tilting mechanism: Modeling and control. In *IEEE/ASME International Conference on Advanced Intelligent Mechatronics*, volume 2016-Septe, pages 306–311. IEEE.
- Ollero, A., Heredia, G., Franchi, A., Antonelli, G., Kondak, K., Sanfeliu, A., Viguria, A., Martinez-de Dios, J. R., Pierri, F., Cortés, J., et al. (2018). The AEROARMS project: Aerial robots with advanced manipulation capabilities for inspection and maintenance. *IEEE Robotics & Automation Magazine*, 25(4):12–23.
- Ollero, A. and Merino, L. (2004). Control and perception techniques for aerial robotics. *Annual reviews in Control*, 28(2):167–178.
- Orsag, M., Korpela, C., Bogdan, S., and Oh, P. (2014). Valve turning using a dual-arm aerial manipulator. In *International Conference on Unmanned Aircraft Systems (ICUAS)*, pages 836–841. IEEE.
- Orsag, M., Korpela, C., Bogdan, S., and Oh, P. (2017). Dexterous Aerial Robots—Mobile Manipulation Using Unmanned Aerial Systems. *IEEE Transactions on Robotics*, 33(6):1453–1466.
- Ortega, R., van der Schaft, A. J., Mareels, I., and Maschke, B. (2001). Putting energy back in control. *IEEE Control Systems Magazine*, 21(2):18–33.
- Papachristos, C., Alexis, K., and Tzes, A. (2014). Efficient force exertion for aerial robotic manipulation: Exploiting the thrust-vectoring authority of a tri-tiltrotor UAV. In *IEEE International Conference on Robotics and Automation (ICRA)*, pages 4500–4505. IEEE.

- Park, S., Her, J., Kim, J., and Lee, D. (2016). Design, modeling and control of omni-directional aerial robot. In *IEEE/RSJ International Conference on Intelligent Robots and Systems (IROS)*, pages 1570–1575. IEEE.
- Park, S., Lee, J., Ahn, J., Kim, M., Her, J., Yang, G.-H., and Lee, D. (2018). Odar: Aerial manipulation platform enabling omnidirectional wrench generation. *IEEE/ASME Transactions on Mechatronics*, 23(4):1907–1918.
- Pasumathly, R., Ambati, V. R., and van der Schaft, A. J. (2012). Port-Hamiltonian discretization for open channel flows. *Systems and Control Letters*, 61(9):950–958.
- Pasumathly, R. and van der Schaft, A. (2005). Stability and stabilization of mixed lumped and distributed parameter systems. In *International Symposium on Nonlinear Theory and its Applications*.
- Pasumathly, R. and van der Schaft, A. (2006a). A finite dimensional approximation of the shallow water equations: The port-Hamiltonian approach. In *IEEE Conference on Decision and Control (CDC)*, pages 3984–3989. IEEE.
- Pasumathly, R. and van der Schaft, A. J. (2006b). A port-Hamiltonian approach to modeling and interconnections of canal systems. In *16th International Symposium on Mathematical Theory of Networks and Systems*, number 2, pages 1436–1443.
- Pasumathly, R. and van der Schaft, A. J. (2007). Achievable Casimirs and its implications on control of port-Hamiltonian systems. *International Journal of Control*, 80(9):1421–1438.
- Polner, M. and van der Vegt, J. J. (2014). A Hamiltonian vorticity-dilatation formulation of the compressible Euler equations. *Nonlinear analysis: theory, methods & applications*, 109:113–135.
- Raiola, G., Cardenas, C. A., Tadele, T. S., de Vries, T., and Stramigioli, S. (2018). Development of a safety-and energy-aware impedance controller for collaborative robots. *IEEE Robotics and Automation Letters*, 3(2):1237–1244.
- Rajappa, S., Ryll, M., Bulthoff, H. H., and Franchi, A. (2015). Modeling, control and design optimization for a fully-actuated hexarotor aerial vehicle with tilted propellers. In *IEEE International Conference on Robotics and Automation (ICRA)*, volume 2015-June, pages 4006–4013.
- Ramirez, H., Le Gorrec, Y., Macchelli, A., and Zwart, H. (2014). Exponential stabilization of boundary controlled port-Hamiltonian systems with dynamic feedback. *IEEE Transactions on Automatic Control*, 59(10):2849–2855.

- Ramirez, H., Le Gorrec, Y., and Zwart, H. (2013). Exponential stabilization of a class of flexible microgrippers using dynamic boundary port-Hamiltonian control. In *IEEE Conference on Decision and Control (CDC)*, pages 460–465. IEEE.
- Ramirez, H., Zwart, H., and Le Gorrec, Y. (2017a). Stabilization of infinite dimensional port-Hamiltonian systems by nonlinear dynamic boundary control. *Automatica*, 85:61–69.
- Ramirez, H., Zwart, H., Le Gorrec, Y., and Macchelli, A. (2017b). On backstepping boundary control for a class of linear port-Hamiltonian systems. In *IEEE Conference on Decision and Control (CDC)*, pages 658–663.
- Rams, H. and Schöberl, M. (2017). On structural invariants in the energy based control of port-Hamiltonian systems with second-order Hamiltonian. In *American Control Conference (ACC)*, pages 1139–1144.
- Rashad, R., Bicego, D., Jiao, R., Sanchez-Escalonilla, S., and Stramigioli, S. (2020a). Towards vision-based impedance control for the contact inspection of unknown generic surfaces with a fully-actuated aerial robot. In *IEEE/RSJ International Conference on Intelligent Robots and Systems (IROS)*, pages 1605–1612. IEEE.
- Rashad, R., Bicego, D., Zult, J., Sanchez-Escalonilla, S., Jiao, R., Franchi, A., and Stramigioli, S. (2021a). Energy-Aware Impedance Control of a Flying End-Effector in the Port-Hamiltonian Framework. *IEEE Transactions on Robotics (to be published)*.
- Rashad, R., Califano, F., Schuller, F. P., and Stramigioli, S. (2021b). Port-Hamiltonian Modeling of Ideal Fluid Flow: Part I. Foundations and Kinetic Energy. *Journal of Geometry and Physics(to be published)*.
- Rashad, R., Califano, F., Schuller, F. P., and Stramigioli, S. (2021c). Port-Hamiltonian Modeling of Ideal Fluid Flow: Part II. Compressible and Incompressible Flow. *Journal of Geometry and Physics(to be published)*.
- Rashad, R., Califano, F., and Stramigioli, S. (2019a). Port-Hamiltonian passivity-based control on $SE(3)$ of a fully actuated UAV for aerial physical interaction near-hovering. *IEEE Robotics and Automation Letters*, 4(4):4378–4385.
- Rashad, R., Califano, F., van der Schaft, A., and Stramigioli, S. (2020b). Twenty Years of Distributed Port-Hamiltonian Systems: A Literature Review. *IMA Journal of Mathematical Control and Information*, 37(4):1400–1422.

- Rashad, R., Engelen, J. B., and Stramigioli, S. (2019b). Energy tank-based wrench/impedance control of a fully-actuated hexarotor: A geometric port-Hamiltonian approach. In *IEEE International Conference on Robotics and Automation (ICRA)*, pages 6418–6424. IEEE.
- Rashad, R., Goerres, J., Aarts, R. G., Engelen, J. B., and Stramigioli, S. (2020c). Fully Actuated Multirotor UAVs: A Literature Review. *IEEE Robotics and Automation Magazine*, 27(3):97 – 107.
- Rashad, R., Kuipers, P., Engelen, J., and Stramigioli, S. (2017). Design, modeling, and geometric control on se (3) of a fully-actuated hexarotor for aerial interaction. *arXiv preprint arXiv:1709.05398*.
- Rodriguez, H., van der Schaft, A. J., and Ortega, R. (2001). On stabilization of nonlinear distributed parameter port-controlled Hamiltonian systems via energy shaping. In *IEEE Conference on Decision and Control (CDC)*, volume 1, pages 131–136 vol.1.
- Roque, P. and Ventura, R. (2016). Space cobot: Modular design of an holo-nomic aerial robot for indoor microgravity environments. In *IEEE/RSJ International Conference on Intelligent Robots and Systems (IROS)*, pages 4383–4390. IEEE.
- Ruggiero, F., Lippiello, V., and Ollero, A. (2018). Aerial manipulation: A literature review. *IEEE Robotics and Automation Letters*, 3(3):1957–1964.
- Rusu, R. B. (2009). *Semantic 3D Object Maps for Everyday Manipulation in Human Living Environments*. PhD thesis, Computer Science department, Technische Universitaet Muenchen, Germany.
- Ryll, M., Bicego, D., and Franchi, A. (2016). Modeling and control of FAST-Hex: A fully-actuated by synchronized-tilting hexarotor. In *IEEE/RSJ International Conference on Intelligent Robots and Systems (IROS)*, pages 1689–1694. IEEE.
- Ryll, M., Bühlhoff, H. H., and Giordano, P. R. (2012). Modeling and control of a quadrotor uav with tilting propellers. In *IEEE International Conference on Robotics and Automation (ICRA)*, pages 4606–4613.
- Ryll, M., Bühlhoff, H. H., and Giordano, P. R. (2015). A novel overactuated quadrotor unmanned aerial vehicle: Modeling, control, and experimental validation. *IEEE Transactions on Control Systems Technology*, 23(2):540–556.
- Ryll, M., Muscio, G., Pierri, F., Cataldi, E., Antonelli, G., Caccavale, F., Bicego, D., and Franchi, A. (2019). 6D interaction control with aerial robots:

- The flying end-effector paradigm. *The International Journal of Robotics Research*, 38(9):1045–1062.
- Ryll, M., Muscio, G., Pierri, F., Cataldi, E., Antonelli, G., Caccavale, F., and Franchi, A. (2017). 6D physical interaction with a fully actuated aerial robot. In *IEEE International Conference on Robotics and Automation (ICRA)*, pages 5190–5195. IEEE.
- Salazar, S., Romero, H., Lozano, R., and Castillo, P. (2009). Modeling and real-time stabilization of an aircraft having eight rotors. *Journal of Intelligent and Robotic Systems*, 54(1):455–470.
- Schindlbeck, C. and Haddadin, S. (2015). Unified passivity-based cartesian force/impedance control for rigid and flexible joint robots via task-energy tanks. In *IEEE International Conference on Robotics and Automation (ICRA)*, pages 440–447. IEEE.
- Schlacher, K. (2007). Distributed PCHD-systems, from the lumped to the distributed parameter case. In *Advances in Control Theory and Applications*, pages 239–255. Springer.
- Schöberl, M., Ennsbrunner, H., and Schlacher, K. (2008). Modelling of piezoelectric structures - A Hamiltonian approach. *Mathematical and Computer Modelling of Dynamical Systems*, 14(3):179–193.
- Schöberl, M. and Schlacher, K. (2015a). Lagrangian and Port-Hamiltonian formulation for distributed-parameter systems. *IFAC-PapersOnLine*, 28(1):610–615.
- Schöberl, M. and Schlacher, K. (2015b). Port-Hamiltonian formulation for Higher-order PDEs. *IFAC-PapersOnLine*, 28(13):244–249.
- Schöberl, M. and Schlacher, K. (2018). On the extraction of the boundary conditions and the boundary ports in second-order field theories. *Journal of Mathematical Physics*, 59(10).
- Schöberl, M. and Siuka, A. (2011). On Casimir functionals for field theories in Port-Hamiltonian description for control purposes. In *IEEE Conference on Decision and Control (CDC)*, pages 7759–7764.
- Schöberl, M. and Siuka, A. (2013). Analysis and comparison of port-Hamiltonian formulations for field theories - demonstrated by means of the Mindlin plate. In *2013 European Control Conference (ECC)*, volume 1, pages 548–553. IEEE.

- Schöberl, M. and Siuka, A. (2013). On Casimir functionals for infinite-dimensional port-Hamiltonian control systems. *IEEE Transactions on Automatic Control*, 58(7):1823–1828.
- Schöberl, M. and Siuka, A. (2014). Jet bundle formulation of infinite-dimensional port-Hamiltonian systems using differential operators. *Automatica*, 50(2):607–613.
- Secchi, C., Franchi, A., Bühlhoff, H. H., and Giordano, P. R. (2012). Bilateral teleoperation of a group of uavs with communication delays and switching topology. In *IEEE International Conference on Robotics and Automation (ICRA)*, pages 4307–4314. IEEE.
- Segui-Gasco, P., Al-Rihani, Y., Shin, H.-S., and Savvaris, A. (2014). A Novel Actuation Concept for a Multi Rotor UAV. *Journal of Intelligent and Robotic Systems*, 74(1-2):173–191.
- Selig, J. M. (2004). *Geometric fundamentals of robotics*. Springer Science & Business Media.
- Serhani, A., Haine, G., and Matignon, D. (2019a). Anisotropic heterogeneous nd heat equation with boundary control and observation: Ii. structure-preserving discretization. *IFAC-PapersOnLine*, 52(7):57–62.
- Serhani, A., Matignon, D., and Haine, G. (2018). Structure-Preserving Finite Volume Method for 2D Linear and Non-Linear Port-Hamiltonian Systems . *IFAC-PapersOnLine*, 51(3):131–136.
- Serhani, A., Matignon, D., and Haine, G. (2019b). Partitioned finite element method for port-Hamiltonian systems with boundary damping: Anisotropic heterogeneous 2d wave equations. *IFAC-PapersOnLine*, 52(2):96–101.
- Serhani, A., Matignon, D., and Haine, G. (2019c). A partitioned finite element method for the structure-preserving discretization of damped infinite-dimensional port-Hamiltonian systems with boundary control. In *International Conference on Geometric Science of Information*, pages 549–558. Springer.
- Šešlija, M., Scherpen, J. M., and van der Schaft, A. (2011). A discrete exterior approach to structure-preserving discretization of distributed-parameter port-Hamiltonian systems. In *IEEE Conference on Decision and Control (CDC)*, pages 7003–7008. IEEE.
- Šešlija, M., Scherpen, J. M., and van der Schaft, A. (2014a). Explicit simplicial discretization of distributed-parameter port-Hamiltonian systems. *Automatica*, 50(2):369–377.

- Šešlija, M., van der Schaft, A., and Scherpen, J. M. (2010). Reaction-diffusion systems in the port-Hamiltonian framework. *IFAC Proceedings Volumes*, 43(14):837–842.
- Šešlija, M., van der Schaft, A., and Scherpen, J. M. (2012). Discrete exterior geometry approach to structure-preserving discretization of distributed-parameter port-Hamiltonian systems. *Journal of Geometry and Physics*, 62(6):1509–1531.
- Šešlija, M., van der Schaft, A., and Scherpen, J. M. A. (2014b). Hamiltonian perspective on compartmental reaction-diffusion networks. *Automatica*, 50(3):737–746.
- Shahriari, E., Johansmeier, L., and Haddadin, S. (2018). Valve-based virtual energy tanks: A framework to simultaneously passify controls and embed control objectives. In *American Control Conference (ACC)*, pages 3634–3641. IEEE.
- Shyy, W., Lian, Y., Chimakurthi, S., Tang, J., Cesnik, C., Stanford, B., and Ifju, P. G. (2009). Flexible wings and fluid-structure interactions for micro-air vehicles. In *Flying Insects and Robots*, pages 143–157. Springer.
- Sirmacek, B., Rashad, R., and Radl, P. (2019). Autonomous uav-based 3d-reconstruction of structures for aerial physical interaction. *International Archives of the Photogrammetry, Remote Sensing and Spatial Information Sciences*, pages 601–605.
- Siuka, A., Schöberl, M., and Schlacher, K. (2010). Hamiltonian evolution equations of inductionless magnetohydrodynamics. In *Proceedings of the 19th International Symposium on Mathematical Theory of Networks and Systems—MTNS*, volume 5.
- Siuka, A., Schöberl, M., and Schlacher, K. (2011). Port-Hamiltonian modelling and energy-based control of the Timoshenko beam. *Acta Mechanica*, 222(1-2):69–89.
- Song, D., Lee, T., and Kim, Y. J. (2018). Artistic pen drawing on an arbitrary surface using an impedance-controlled robot. In *IEEE International Conference on Robotics and Automation (ICRA)*, pages 4085–4090. IEEE.
- Staub, N., Bicego, D., Sablé, Q., Arellano, V., Mishra, S., and Franchi, A. (2018). Towards a flying assistant paradigm: The othex. In *2018 IEEE International Conference on Robotics and Automation (ICRA)*, pages 6997–7002. IEEE.
- Stramigioli, S. (2001). *Modeling and IPC Control of Interactive Mechanical Systems - A Coordinate-Free Approach*. Springer-Verlag London.

- Stramigioli, S. (2015). Energy-aware robotics. In *Mathematical Control Theory I*, pages 37–50. Springer.
- Suarez, A., Heredia, G., and Ollero, A. (2018). Physical-Virtual Impedance Control in Ultralightweight and Compliant Dual-Arm Aerial Manipulators. *IEEE Robotics and Automation Letters*, 3(3):2553–2560.
- Suseong Kim, Seungwon Choi, and Kim, H. J. (2013). Aerial manipulation using a quadrotor with a two DOF robotic arm. In *IEEE/RSJ International Conference on Intelligent Robots and Systems (IROS)*, pages 4990–4995. IEEE.
- Tadokoro, Y., Ibuki, T., and Sampei, M. (2017). Maneuverability analysis of a fully-actuated hexrotor uav considering tilt angles and arrangement of rotors. *IFAC-PapersOnLine*, 50(1):8981 – 8986. 20th IFAC World Congress.
- Talasila, V., Golo, G., and van der Schaft, A. J. (2002). The wave equation as a port-Hamiltonian system and a finite-dimensional approximation. In *Proceedings of the 15th International Symposium on Mathematical Theory of Networks and Systems*, pages 1–15.
- Tognon, M., Chávez, H. A. T., Gasparin, E., Sablé, Q., Bicego, D., Mallet, A., Lany, M., Santi, G., Revaz, B., Cortés, J., et al. (2019). A truly-redundant aerial manipulator system with application to push-and-slide inspection in industrial plants. *IEEE Robotics and Automation Letters*, 4(2):1846–1851.
- Tognon, M. and Franchi, A. (2018). Omnidirectional aerial vehicles with unidirectional thrusters: Theory, optimal design, and control. *IEEE Robotics and Automation Letters*, 3(3):2277–2282.
- Toledo, J., Wu, Y., Ramirez, H., and Le Gorrec, Y. (2019). Observer-based state feedback controller for a class of distributed parameter systems. *IFAC-PapersOnLine*, 52(2):114 – 119.
- Tomic, T. and Haddadin, S. (2014). A unified framework for external wrench estimation, interaction control and collision reflexes for flying robots. In *IEEE/RSJ International Conference on Intelligent Robots and Systems (IROS)*, pages 4197–4204. IEEE.
- Tomić, T., Ott, C., and Haddadin, S. (2017). External wrench estimation, collision detection, and reflex reaction for flying robots. *IEEE Transactions on Robotics*, 33(6):1467–1482.
- Toratani, D. (2012). Research and development of double tetrahedron hexarotorcraft (dot-hr). In *28th Congress of the International Council of the Aeronautical Sciences*, pages 1–8.

- Trang Vu, N. M., Trenchant, V., Ramirez, H., Lefèvre, L., and Le Gorrec, Y. (2017). Parabolic matching of hyperbolic system using Control by Interconnection. *IFAC-PapersOnLine*, 50(1):5574–5579.
- Trenchant, V., Fares, Y., Ramirez, H., Le Gorrec, Y., and Ouisse, M. (2015). A port-Hamiltonian formulation of a 2d boundary controlled acoustic system. *IFAC-PapersOnLine*, 28(13):235–240.
- Trenchant, V., Hu, W., Ramirez, H., and Le Gorrec, Y. (2018a). Structure Preserving Finite Differences in Polar Coordinates for Heat and Wave Equations. *IFAC-PapersOnLine*, 51(2):571–576.
- Trenchant, V., Ramirez, H., Le Gorrec, Y., and Kotyczka, P. (2017a). Structure preserving spatial discretization of 2D hyperbolic systems using staggered grids finite difference. In *American Control Conference (ACC)*, volume 5, pages 2491–2496. AACC.
- Trenchant, V., Ramirez, H., Le Gorrec, Y., and Kotyczka, P. (2018b). Finite differences on staggered grids preserving the port-Hamiltonian structure with application to an acoustic duct. *Journal of Computational Physics*, 373:673–697.
- Trenchant, V., Vu, T., Ramirez, H., Lefevre, L., and Le Gorrec, Y. (2017b). On the use of structural invariants for the distributed control of infinite dimensional port-Hamiltonian systems. In *IEEE Conference on Decision and Control (CDC)*, pages 47–52.
- Trivedi, M. V., Banavar, R. N., and Kotyczka, P. (2016). Hamiltonian modelling and buckling analysis of a nonlinear flexible beam with actuation at the bottom. *Mathematical and Computer Modelling of Dynamical Systems*, 22(5):475–492.
- Trivedi, M. V., Banavar, R. N., and Maschke, B. (2011). Modeling of hybrid lumped-distributed parameter mechanical systems with multiple equilibria. *IFAC Proceedings Volumes*, 44(1):7696–7701.
- Usherwood, J. R., Cheney, J. A., Song, J., Windsor, S. P., Stevenson, J. P., Dierksheide, U., Nila, A., and Bomphrey, R. J. (2020). High aerodynamic lift from the tail reduces drag in gliding raptors. *Journal of Experimental Biology*, 223(3).
- Valavanis, K. P. and Vachtsevanos, G. J. (2015). *Handbook of unmanned aerial vehicles*, volume 1. Springer.
- van der Schaft, A. (2020). Port-Hamiltonian modeling for control. *Annual Review of Control, Robotics, and Autonomous Systems*, 3:393–416.

- van der Schaft, A. and Jeltsema, D. (2014). Port-Hamiltonian systems theory: An introductory overview. *Foundations and Trends in Systems and Control*, 1(2-3):173–378.
- van der Schaft, A. and Maschke, B. (2001). Fluid dynamical systems as Hamiltonian boundary control systems. In *IEEE Conference on Decision and Control (CDC)*, volume 5, pages 4497–4502. IEEE.
- van der Schaft, A. and Maschke, B. M. (2002). Hamiltonian formulation of distributed-parameter systems with boundary energy flow. *Journal of Geometry and physics*, 42(1-2):166–194.
- van der Schaft, A. J. (2000). *L2-gain and passivity techniques in nonlinear control*, volume 2. Springer.
- Vankerschaver, J., Yoshimura, H., Leok, M., and Marsden, J. E. (2010). Stokes-Dirac structures through reduction of infinite-dimensional Dirac structures. In *IEEE Conference on Decision and Control (CDC)*, pages 6265–6270. IEEE.
- Villani, L. and De Schutter, J. (2016). Force control. In *Springer handbook of robotics*, pages 195–220. Springer.
- Villegas, J. A. (2007). *A Port-Hamiltonian Approach to Distributed Parameter Systems*. PhD thesis, University of Twente.
- Villegas, J. A., Zwart, H., Le Gorrec, Y., and Maschke, B. (2009). Exponential Stability of a Class of Boundary Control Systems. *IEEE Transactions on Automatic Control*, 54(1):142–147.
- Villegas, J. A., Zwart, H., Le Gorrec, Y., Maschke, B., and van der Schaft, A. J. (2005). Stability and stabilization of a class of boundary control systems. In *Proceedings of the 44th IEEE Conference on Decision and Control, and the European Control Conference*, number 10, pages 3850–3855. IEEE.
- Vincent, B., Hudon, N., Lefèvre, L., and Dochain, D. (2017). Burning magneto-hydrodynamics plasmas model: A port-based modelling approach. *IFAC-PapersOnLine*, 50(1):13038–13043.
- von Frankenberg, F. and Nogleby, S. (2017). Disturbance rejection in multi-rotor unmanned aerial vehicles using a novel rotor geometry. In *4th International Conference of Control, Dynamic Systems*, pages 1–10.
- Voß, T. and Scherpen, J. M. A. (2014). Port-Hamiltonian Modeling of a Non-linear Timoshenko Beam with Piezo Actuation. *SIAM Journal on Control and Optimization*, 52(1):493–519.

- Voß, T. and Weiland, S. (2011). Structure preserving spatial discretization of 1D convection-diffusion port-Hamiltonian systems. In *Proceedings of the IEEE Conference on Decision and Control*, pages 6979–6984. IEEE.
- Voyles, R. and Jiang, G. (2012). Hexrotor uav platform enabling dextrous interaction with structures—preliminary work. In *IEEE International Symposium on Safety, Security, and Rescue Robotics (SSRR)*, pages 1–7. IEEE.
- Vu, N. M. T. and Lefèvre, L. (2013). Material balance and closure equations for plasmas in Tokamaks. *IFAC Proceedings Volumes*, 1:60–65.
- Vu, N. M. T., Lefevre, L., and Maschke, B. (2012). Port-hamiltonian formulation for systems of conservation laws: application to plasma dynamics in tokamak reactors. *IFAC Proceedings Volumes*, 45(19):108–113.
- Vu, N. M. T., Lefèvre, L., and Maschke, B. (2016). A structured control model for the thermo-magneto-hydrodynamics of plasmas in tokamaks. *Mathematical and Computer Modelling of Dynamical Systems*, 22(3):181–206.
- Vu, N. M. T., Lefèvre, L., and Nouailletas, R. (2017a). Distributed and backstepping boundary controls for port-Hamiltonian systems with symmetries. *Mathematical and Computer Modelling of Dynamical Systems*, 23(1):55–76.
- Vu, N. M. T., Lefevre, L., Nouailletas, R., and Bremond, S. (2013a). Geometric discretization for a plasma control model. *IFAC Proceedings Volumes*, 46(2):755–760.
- Vu, N. M. T., Lefèvre, L., Nouailletas, R., and Brémond, S. (2017b). Symplectic spatial integration schemes for systems of balance equations. *Journal of Process Control*, 51:1–17.
- Vu, N. M. T., Nouailletas, R., Lefevre, L., and Bremond, S. (2013b). An IDA -PBC approach for the control of ID plasma profile in tokamaks. In *Proceedings of the IEEE Conference on Decision and Control*, pages 4176–4181. IEEE.
- Wang, L., Yang, S. X., and Biglarbegian, M. (2012). Bio-inspired navigation of mobile robots. In *International Conference on Autonomous and Intelligent Systems*, pages 59–68. Springer.
- Wu, Y., Hamroun, B., Le Gorrec, Y., and Maschke, B. (2015). Power preserving model reduction of 2D vibro-acoustic system: A port-Hamiltonian approach. *IFAC-PapersOnLine*, 28(13):206–211.
- Yang, H., Park, S., Lee, J., Ahn, J., Son, D., and Lee, D. (2018). Lasdra: Large-size aerial skeleton system with distributed rotor actuation. In *IEEE International Conference on Robotics and Automation (ICRA)*, pages 7017–7023. IEEE.

- Yuksel, B., Secchi, C., Bulthoff, H. H., and Franchi, A. (2014a). A nonlinear force observer for quadrotors and application to physical interactive tasks. In *IEEE/ASME International Conference on Advanced Intelligent Mechatronics*, pages 433–440. IEEE.
- Yuksel, B., Secchi, C., Bulthoff, H. H., and Franchi, A. (2014b). Reshaping the physical properties of a quadrotor through IDA-PBC and its application to aerial physical interaction. In *IEEE International Conference on Robotics and Automation (ICRA)*, pages 6258–6265. IEEE.
- Zhou, W., Hamroun, B., Couenne, F., and Le Gorrec, Y. (2017). Distributed port-Hamiltonian modelling for irreversible processes. *Mathematical and Computer Modelling of Dynamical Systems*, 23(1):3–22.
- Zhou, W., Hamroun, B., Le Gorrec, Y., and Couenne, F. (2012). Infinite dimensional port-Hamiltonian representation of chemical reactors. *IFAC Proceedings Volumes*, 45(19):248–253.
- Zhou, W., Hamroun, B., Le Gorrec, Y., and Couenne, F. (2015). Infinite dimensional port-Hamiltonian representation of reaction diffusion processes. *IFAC-PapersOnLine*, 28(1):476–481.
- Zhou, Y., Li, X., Yue, L., Gui, L., Sun, G., Jiang, X., and Liu, Y.-H. (2019). Global vision-based impedance control for robotic wall polishing. In *IEEE/RSJ International Conference on Intelligent Robots and Systems (IROS)*, pages 6022–6027. IEEE.
- Zult, J. (2020). Achieving stable and safe physical interaction for a fully actuated aerial robot using energy tank-based interaction control. Master’s thesis, University of Twente.
- Zwart, H., Le Gorrec, Y., Maschke, B., and Villegas, J. (2009). Well-posedness and regularity of hyperbolic boundary control systems on a one-dimensional spatial domain. *ESAIM: Control, Optimisation and Calculus of Variations*, 16(4):1077–1093.

ABOUT THE AUTHOR

Ramy Rashad, or more precisely Ramy Abdelmonem Mohamed Rashad Hashem, was born in Sohag, Egypt, in the winter of 1991. After completing the International General Certificate of Secondary Education program in 2008, he started his BSc studies in Mechatronics engineering at the German University in Cairo (GUC) in Egypt, which he completed in 2013 with highest honors ranking among the top 5 of his class. During the summer of 2012, he spent three months at the Julius Maximilians University Weurzburg in Germany, where he worked on his BSc thesis under the supervision of prof. Klaus Schilling.



In 2013, he started his MSc studies in the field of aerial robotics at the GUC. Simultaneously, he started working as a teaching assistant in the Mechatronics engineering department at the GUC, teaching a wide range of courses for three consecutive years. During the winter of 2014, he was assigned to the GUC-branch in Berlin, Germany for four months.

After receiving his MSc degree in 2015 with highest honors under the supervision of prof. Ayman El-Badawy, he started sending out numerous applications for pursuing a PhD degree. After more than 16 unsuccessful attempts, he started his PhD research in 2016 at the Robotics and Mechatronics group at the University of Twente, which has led to the creation of this dissertation. Currently, he is living in Enschede with his wife and their two precious jewels.

Supervised by
Stefano Stramigioli
Frederic P. Schuller

Defended on
21 Jan. 2021